Studies of a dipolar quantum gas: Towards Er-K mixture



Jiri Kucera

Balliol College
University of Oxford

This thesis is submitted for the degree of
Doctor of Philosophy

Trinity 2024

Abstract

In this work we present an overview of the current state of the Oxford erbium-potassium experiment and the scientific discoveries that have been made with it.

Namely, we describe the experimental procedure and techniques that lead to a production of a large ($> 200 \times 10^3$) Bose-Einstein condensates of ^{166}Er in a crossed-beam optical dipole trap with atomic transport capabilities using focus-tunable lenses.

We then discuss our measurement of the three-body loss in ^{166}Er between 0-4 G. Our findings reveal new features that display strong temperature dependence, hinting at their higher partial wave character due to the anisotropic dipole-dipole interactions (DDIs) between erbium atoms. We also present a refined model of the three-body loss process which accounts for secondary collisions and excess heating.

The richness of physical phenomena brought about by the long-range DDI is furthermore demonstrated by considering its contribution to the shift in the critical temperature of a dipolar condensate and its depletion as compared to the purely contact interaction case. We present the first experimental measurement of this effect together with an outline of the theoretical model that accounts for our observations.

Lastly, we report on the construction of a 2D+ magneto-optical trap (MOT) for potassium. We describe the technical details of our optical setup and vacuum assembly as well as present initial measurements of the 2D MOTs performance as a steady source of cold atoms. Successful implementation of this stage marks a major step towards the realization of the first ultracold Er-K mixture.

We conclude by discussing the future of our experiment – both the short term goals which include construction of a dual species 3D MOT and inter-species Feshbach resonance measurements, as well as the long term goals which revolve around utilizing a novel, quasi-2D potential for studying impurity physics in homogeneous degenerate dipolar gases.

Acknowledgements



This thesis is the result of me spending the last four years in an underground lab learning how to do 'cool science stuff with lasers'. However, it is also a direct consequence of more than twenty years of education, upbringing and tremendous amount of support that I have had the privilege of receiving. A long list of people contributed to where I am now, each in their own way, and I will never be able to express my gratitude to every individual. What I can try and do instead is a technique I learnt throughout the course of my DPhil – minimise the damage and hope you can make it up to people with a nice piece of baking.

First and foremost, my biggest thanks goes to my family. To my parents, Ivana and Jáchym, whose unconditional love and support of everything I do or ever wanted to do (yes, even when I decided to build a steam engine out of syringes, a glass flask and a candle) made me never doubt myself and whose gentle, thoughtful and fun upbringing made me into the person I am today. To my grandparents, Maria, Marie and František, who constantly fueled my young intrigue with stories and adventures around the world. And to my brother, aunt and cousins, Josef, Renata, Ondřej and Matyáš, for bringing out the playful side of me whenever I started to feel like a boring adult.

Turning from personal to academic matters, my gratitude then goes to all my colleagues. Fortunately, within our research group, 'personal' and 'academic' aren't mutually exclusive. Firstly, I need to thank my supervisor, Professor Robert Smith, for his continued support throughout my studies and for his invaluable (and often brilliantly intuitive) insight into the world of experimental quantum physics. Under Rob's guidance, there always seemed to be a way forward. If a fraction of his wisdom rubbed off on me, I would consider my DPhil a success. Second thanks goes to Dr. Milan Krstajić. If Rob was the Father of the experiment, Milan would certainly be the Mother. His knowledge of the machine and physics in general is only second to his kindness and determination. Consequently, not only am I grateful for having been able to constantly rely on his help and advice but also, and more importantly, for being able to call him my friend. The same applies to Gavin Lamb, whose endless enthusiasm and fascination with just about anything in combination with his charming Scottish accent made even the most difficult days in the lab joyful. Being able to bond over common struggles and bounce my ideas (sometimes completely wrong) off him while listening to his has been invaluable. Although

our times in Oxford only partially overlapped, Dr. Lucas Hofer was one of the first people to adopt me into the Er-K family and make me feel at home. His combination of humour and great working ethic have been an inspiration for me, especially when it comes to programming and career ambitions. Dr. Péter Juhász, similarly to Lucas, belonged to an earlier generation of DPhil students in our lab. From Péter, I learnt that in science presentation is as important as the contents and that the phrase 'charming physicist' is not an oxymoron. Lastly, although our time together was short, I would like to thank Dr. Anna Marchant for making me feel like an invaluable part of the team despite my clear lack of experience.

My physics journey has been influenced by several mentor figures whose teaching fueled my curiosity and whose encouragement gave me the confidence to try and tackle such an arcane subject head-on. In addition to Rob, I have to thank Professor Zoran Hadzibabic, Professor Malte Grosche and my alma mater, Trinity College, Cambridge. Zoran single-handedly ignited my passion for quantum physics and showed me that the gap between students and academics isn't as wide as it seems whilst Malte's career advice and genuine interest in my progress made a huge impact on my decision to start a DPhil. I also have to thank the Johannes Kepler Grammar School for creating an environment in which learning and discussion are encouraged and in which studying abroad is thought of as a thrilling possibility rather than a ridiculous idea. Specifically, I want to thank Martin Kapoun, Petr Višňovský, Helena Kommová and Mirka Lahodová for going above and beyond and showing me the beauty of physics and mathematics outside of the standard curriculum.

I wouldn't have been able to undertake my undergraduate studies without the financial support from the Bakala Foudation and the Krsek Foundation. I am extremely grateful for their trust and for their continued investment in the education of Czech students. I also thank all the donors of the Oxford Physics Endowment for Graduates which made my DPhil and, in return, this thesis possible. To give for the sake of science and not want anything in return is admirable and humbling.

I will conclude this section with a not-so-specific yet very important group of people - my friends. It is a great privilege and joy of one's life to be able to share it with others. In friends we find inspiration, reassurance and everyday fun - all of which were essential for getting me through challenging times. Rather than naming individuals (maybe except for one), I would like to thank all my fellow volleyball team mates (I haven't forgotten about you, Beachie boys), runners, rowers and Trinity scientists for being a second family to me throughout the years. Special thanks also goes to you, 'Koumáci'. I have always felt a bit sad for leaving behind a lot of great friendships when I moved to the UK but whenever we meet up back home or online for a gaming session, it almost feels like I never left in the first place. Finally, I am very grateful to the 21 Walton Well Road squad. It's funny to think that we all semi-randomly ended up together because of the Covid-19 pandemic. Not only have you kept me sane during my first year and the lockdown but you have (almost) all became great friends. In fact, there is one that became a bit more than that. Amelia, thank you for your TLC (I bet you wish you hadn't taught me that), for always being there and for reminding me about the important things in life.

Contents

1 Introduction **8**

1.1 The Oxford Er-K experiment . . . 14

1.2 Thesis structure . . . 15

I Erbium **18**

2 Erbium–the dipolar star of the show **19**

2.1 The element . . . 19

2.2 The atom . . . 21

2.2.1 Electronic structure . . . 21

2.2.2 Magnetic properties . . . 25

2.3 Interactions . . . 28

2.3.1 Contact interaction . . . 28

2.3.2 Dipole-dipole interaction . . . 30

2.3.3 Ultracold scattering . . . 34

2.3.4 Feshbach resonances . . . 42

2.4 Dipolar Bose-Einstein condensates . . . 45

2.4.1 Thermodynamics of non-interacting BECs . . . 46

2.4.2 Physics of weakly interacting, dipolar condensates . . . 49

2.4.3 Excitations . . . 52

3 Experimental setup–reaching the Doppler limit **58**

3.1 Experimental overview . . . 58

3.1.1 Vacuum . . . 61

3.1.2 Magnetic fields . . . 66

3.1.3 Imaging . . . 71

3.1.4 Computer control and data acquisition . . . 74

3.2 Laser cooling . . . 75

3.2.1 Light-scattering force . . . 75

3.2.2 The Blue–401 nm . . . 76

3.2.3 The Yellow–532 nm . . . 83

4 Production of large ^{166}Er BECs **90**

4.1 Optical dipole trapping . . . 90

4.1.1 Polarizability . . . 91

4.1.2 Trapping potential . . . 94

4.1.3 Characterizing the trap . . . 98

4.1.4 Optical system . . . 102

4.2 Loading . . . 105
4.3 Evaporative cooling . . . 107
4.3.1 Evaporation procedure . . . 110
4.4 Degenerate dipolar gas . . . 112
4.4.1 Characterizing erbium BECs . . . 113
4.4.2 Quantum droplets and supersolidity . . . 116
4.5 Tunable lenses . . . 117
4.5.1 Stabilization . . . 119
4.5.2 Transport . . . 124

5 Three-body loss in ^{166}Er 130
5.1 Measuring three-body loss . . . 132
5.1.1 The experiment . . . 132
5.1.2 Fitting procedure . . . 133
5.2 Results . . . 136
5.2.1 The loss spectrum . . . 136
5.2.2 Temperature dependence and light shift . . . 137
5.2.3 Comparison with theory . . . 139
5.2.4 Conclusion . . . 141
5.3 Extended loss model . . . 142
5.3.1 General m-body loss . . . 142
5.3.2 One-body loss . . . 145
5.3.3 Three-body loss . . . 145
5.3.4 Secondary collisions . . . 146
5.3.5 Experimental comparison . . . 157

6 Dipolar T_c shift 159
6.1 Theory . . . 160
6.1.1 Finite size correction . . . 161
6.1.2 Trap geometry . . . 162
6.1.3 Contact interactions . . . 163
6.1.4 Dipole-dipole interactions . . . 166
6.2 Non-saturation . . . 167
6.2.1 Dipolar non-saturation . . . 171
6.3 Experimental design . . . 174
6.3.1 The Sequence . . . 175
6.3.2 Image fitting procedure . . . 175
6.3.3 Temperature corrections . . . 178
6.4 Results . . . 184
6.4.1 Dipolar T_c shift and non-saturation . . . 185
6.4.2 Dependence on contact interactions . . . 186
6.4.3 Conclusion . . . 187

II Potassium **188**

7 Potassium–an impurity **189**
7.1 Why potassium? Everyone likes vanilla . . . 190
7.2 The atom . . . 190
7.2.1 Electronic structure . . . 191
7.3 Cooling of potassium . . . 192
7.3.1 2D+ MOT . . . 194
7.3.2 3D MOT . . . 194
7.3.3 Grey molasses . . . 196
7.3.4 Evaporation . . . 198
7.4 Light preparation . . . 198
7.4.1 Table optics . . . 199
7.4.2 Locking . . . 201
7.4.3 Spliceless arrays . . . 202

8 Building a source of cold K **204**
8.1 Design . . . 204
8.1.1 Vacuum . . . 204
8.1.2 Oven . . . 208
8.1.3 Coils . . . 210
8.1.4 Optics . . . 210
8.2 Construction . . . 213
8.2.1 Gluing and drilling . . . 213
8.2.2 Assembly and the glass cell . . . 215
8.2.3 Bake-out . . . 216
8.2.4 The full setup . . . 219
8.3 2D+ MOT . . . 219
8.3.1 Optimal parameters . . . 220
8.3.2 Searching procedure–who you gonna call? . . . 222

III The Mixture **225**

9 Conclusion and Outlook **226**
9.1 The future of our experiment . . . 227
9.1.1 Box potential . . . 227
9.1.2 Mixture physics . . . 230

IV Appendix **233**

A Electronic circuits **234**
A.1 Magnetometer . . . 234
A.2 Tunable lens driver . . . 234

A.3 Bake-out temperature and pressure logging 236

B Tunable lens stabilization **237**
B.1 Error signal sensitivity 237
B.2 Vibration compensation 240

C Simulating atomic transport and evaporation **243**
C.1 Transport ramps 243
C.2 DSMC 245
C.3 Evaporation theory 247
C.4 Simulating evaporation 251
C.4.1 Full treatment 252
C.4.2 Harmonic approximation 253
C.4.3 Method comparison 254

D Temperature corrections after ToF expansion **257**

E Lab BINGO **259**

1. Introduction



The formulation and subsequent development of quantum mechanics in the first half of the 20$^{\text{th}}$ century marked an important shift in our understanding of the microscopic world. It successfully explained the internal structure of atoms and described the fundamental forces that facilitate their mutual interactions. It also postulated the existence of spin– an intrinsic property of particles that ascribes to them a specific angular momentum and the statistics they obey. However, despite its indisputable achievements and elegant mathematical formulation, quantum mechanics and the associated phenomena stand in stark contrast with our everyday experience. The physics of small and few is seemingly irreconcilable with the physics of large and many.

At this point, statistics comes to the rescue, replacing definite coherent quantum states capable of entanglement and teleportation [1] with their statistical ensembles. At high enough temperatures or, equivalently, energy scales, any single-state quantum character is lost in the incoherent mixture of many states, leaving behind the classical counterpart of the quantum system. As the system gets colder, the collective quantum properties emerge from the thermal noise. The exact temperature at which this onset of the so called *quantum degeneracy* happens depends on the the underlying particle statistics and the available phase space [2]. In 1925, Albert Einstein predicted [3] that for a collection of bosons cooled to a sufficiently low temperature, a macroscopic occupation of the ground state would form–the Bose-Einstein condensate. The condensate sparked the intrigue of theorists and experimentalists alike because it presented a gateway to studying many-body quantum effects on a macroscopic scale. However, the temperatures required to observe this new state of matter remained unattainable for decades.

Fortunately, the second half of the 20th century brought major advances in the field of atomic physics. The generation of coherent, single frequency light in the form of a laser allowed for an unprecedented level of control and manipulation through addressing the internal quantum states of atoms. Subsequent developments in laser cooling and trapping techniques [4]–[6] led to the first experimental realisations of degenerate bosonic gases in 1995 using Rubidium (Rb) [7] and Sodium (Na) [8]. The first fermionic species followed shortly thereafter [9] and the repertoire of 'coolable' atoms has been growing ever since. Cold atom physicists currently have a plethora of standard techniques at their disposal and the related technology is improving at a fast pace [10]–[12]. Light-modulating devices are regularly employed to provide more flexible ways of shaping the trapping potentials

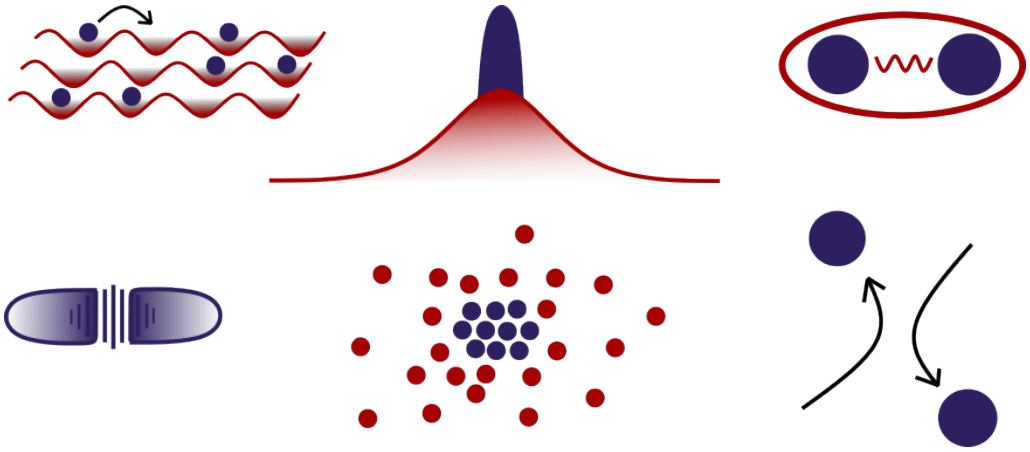


Figure 1.1: The versatility of cold atoms as quantum simulators. Through interaction tuning and trapping in arbitrary potentials, cold atom platforms can simulate a wide range of physical systems ranging from crystalline lattices to black hole event horizons.

[13]–[16]. Narrow line and high power lasers, on the other hand, give access to more efficient cooling schemes that push the Doppler limit by orders of magnitude or entirely bypass it [17]–[21]. Over the last ten years, a considerable effort has also been put into the cooling of molecules [22]–[24].

The early achievements of cold atom physics paved the way for a wider range of experiments in which ultra-cold atoms are prepared in a desired state by being subject to a carefully chosen set of external electromagnetic fields. Under such artificial conditions, the Hamiltonian of the system can formally reproduce that of an entirely different physical system and as such showcase the same properties and phenomena. These *quantum simulators*–as coined by Richard Feynman [25] and depicted in figure 1.1–can be used to study many-body physics of hypothetical or experimentally inaccessible systems with the added benefit of a complete control over some physical parameters such as the interaction strength or dimensionality [26].

In this way, cold atom experiments have been used to investigate the physics of superfluidity [27], [28] and the Josephson effect [29]–[32] as well as their link to superconductivity via probing the BEC-BCS crossover regime [33]–[35]. Through careful manipulation and excitation of degenerate gases, experimentalists were able to observe the dynamics of quantum phase transitions [36]–[38] and the formation of solitons [39], [40] and superfluid vortices [41]–[43] which are relevant in other branches of physics [44]. The advances in trapping techniques, on the other hand, led to experimental realisations of homogeneous gases [45] suitable for the research of turbulence, energy transfer and weak collapse in systems with translational symmetry [46]–[48]. Furthermore, periodic trapping in the form of optical lattices bridged the gap between ultracold gases and solid state physics [49], allowing for the study of the Mott insulator to superfluid transition [50] and quantum magnetism [51]; observation of exotic states such as Anderson localization [52] or Bose glasses [53]; and shedding more light into topological phases of matter [54], [55]. Last but not least, recent theoretical propositions demonstrated a link between ultracold quantum

physics and the physics of large-scale astronomical objects such as black holes and galaxies, suggesting possible avenues for studying such phenomena in room-sized labs [56], [57].

Even though fundamental research remains a strong driving force behind the field, low energies, long lifetimes and high sensitivity to external perturbations have also made cold atom experiments suitable for more applied purposes. For example, cold atomic clocks are widely used as a standard of timekeeping [58] and the recent miniaturization efforts have brought them even closer to everyday use [59]. By measuring the coherent change of the atomic wavefunction in response to an external field, devices based on cold atoms have been utilized for high resolution sensing [60]. Researchers are now able to deploy portable gravimetric devices for measuring, for instance, the density fluctuations of the Earth's crust or for locating underground anomalies such as caves or oil deposits [61]–[63]. Other cases have seen cold atoms used for measuring magnetic fields [64], finding application in engineering and particularly in medicine [65], where the resolution can allow for detecting signals from individual nerve cells. Furthermore, recent collaborations and works have embraced cold atoms as potential candidates for dark matter and gravitational wave detection [66], [67].

The list of possible applications of cold atoms wouldn't be complete without mentioning another field of great interest–quantum computing. The main appeal of cold atoms as opposed to other platforms such as trapped ions [68] or superconductors [69] lies in their simultaneous scalability and relatively long coherence times [70]. The latter is a direct consequence of the low energies involved and the diluteness of the gases. The former is a result of the versatility of the trapping techniques in combination with large atom numbers on one hand and the single atom addressability on the other [71]. A neutral atom qubit can be realised by encoding the quantum information in the internal states of the atom. Inter-qubit coupling can then be facilitated by direct interaction between the atoms [72], [73] or through particle exchange [74]. One of the most promising candidates are optical tweezer arrays loaded with dipolar molecules or Rydberg atoms [75], [76]. The main challenge lies in creating a reproducible high-fidelity state that allows for the implementation of a universal set of quantum gates.

The ability to arbitrarily shape and dynamically change the trapping potential is, in itself, a strong selling point of ultracold atom systems. However, perhaps even more important and appealing is the possibility of tuning the particle interaction strength–a feat not so easily achievable in other fields of physics. The interaction strength is deeply linked to the properties of a quantum gas such as its shape, energy, stability and excitation spectrum [77] but also, more intuitively, to the particle scattering rates responsible for thermalization and, in some cases, losses [78]. At low energies and densities, interaction strength can be described by a single parameter–the s-wave scattering length–independent of the energy of the colliding atoms [79]. The exact value of this parameter is a result of an intricate interplay between the input scattering states and the potential output states. Consequently, it also depends on the energy of these states. By applying an external magnetic field, it is possible to shift the energy levels relative to each other via the Zeeman effect [79], [80]. When the energy difference approaches zero, the s-wave

scattering length and hence the interaction strength is greatly enhanced to a point of divergence while its sign changes. The existence of this so called *Feshbach resonance* [81], [82] can therefore be used to tune the interparticle interactions with a single set of coils and provides an easy way of accessing a multitude of regimes. For example, at a resonance the scattering length is much larger than the average particle spacing and the gas undergoes a transition into the unitary regime [83], [84], displaying universal behaviour irrespective of the species. The interaction can also be made attractive, inducing instability in a gas of bosons and potentially leading to a violent collapse in the form of a Bosenova [85] or facilitating particle pairing in a gas of fermions, probing the BEC-BCS crossover [86], [87]. It is also possible to completely turn off the interaction, posing interesting questions about the dynamics of quantum phase transitions [88], [89].

The interactions described by the s-wave scattering length are short range and therefore local in nature. This somewhat limits the richness of the resulting physics. In order to go beyond the landscape of contact interactions, one either needs to facilitate the exchange of (quasi)particles between the atoms over large distances [90] or to introduce a new type of interaction. The latter can be achieved, for example, by using species with a permanent dipole moment, displaying long-range, anisotropic dipole-dipole interactions (DDI) on top of the short range contact ones. Such species have been one of the focal points of cold atom research for the past two decades. This is in part due to the geometry-dependent, exotic quantum properties displayed by dipolar gases [91] and in part because of the relevance of the DDI in other physical phenomena such as magnetism [92] and quantum chemistry [93].

When it comes to the choice of a suitable dipolar species, there are two main options– electric or magnetic dipoles. Electric dipoles interact more strongly but come with their own set of challenges. They are harder to prepare due to the absence of linear stark shift in hydrogen-like atoms in their ground state. This means that one has to use either polar molecules or highly excited atomic states. The former are difficult to cool and so one usually resorts to cooling the constituent atomic species separately and then inducing molecule formation via a Feshbach resonance [94]. Such molecules are short lived and decay via mutual collisions [95], limiting the time available for experiments unless loaded into a trap with constrained dimensionality [96]. That being said, there exist more involved schemes to suppress losses [97] and the recent advancements in molecule cooling led to the first production of a ground state molecular BEC [98]. The other electric dipole species, known as Rydberg atoms, require a more involved preparation procedure and their lifetime is, in general, limited by spontaneous emissions [99], [100]. The shortcomings of both species can be partially mitigated by suitable state engineering and by loading them into optical tweezer arrays which prevent collisional decay and allow for tuning the interaction strength by changing the tweezer separation. The tweezer approach has gained traction over the last decade with proposed applications in quantum information processing and quantum simulation [13], [101].

An alternative to electric dipolar species are neutral atoms with a magnetic dipole in their ground state. The magnetic DDI is several orders of magnitude weaker but its

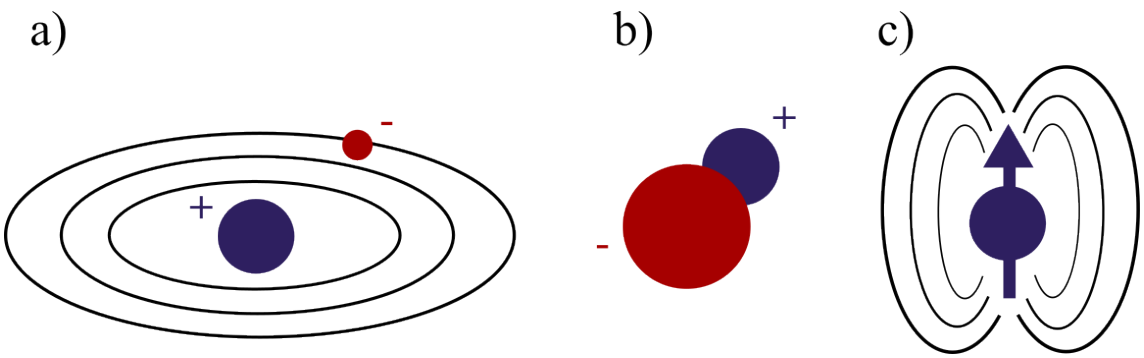


Figure 1.2: Dipolar species. a) Rydberg atoms, b) heteronuclear molecules and c) magnetic atoms are some of the most widely used species used for studying dipolar physics. This thesis concerns degenerate bosonic gases of erbium–an element with one of the highest known magnetic moments.

presence in the atomic ground state means that lifetimes are limited by other mechanisms and are, in general, much longer. The magnetic moment itself is a result of the intricate electronic structure of the atoms and requires the individual spin and orbital angular momenta to combine to give high values of total angular momentum J [91]. This substantially narrows down potential candidates in the periodic table to heavier elements with more valence electrons. Furthermore, the complex electronic structure implies less obvious cooling schemes compared to the alkalis but still relatively simple compared to molecules. Thanks to a focused effort, in 2005 the transition metal Chromium with its magnetic moment of $6\mu_B$ was the first dipolar species to be cooled to quantum degeneracy [102]. This was soon followed by the lanthanides dysprosium ($10\mu_B$) [103] and erbium ($7\mu_B$) [104] in 2011 and 2012 respectively and, more recently, by europium ($7\mu_B$) [105] in 2022. Despite the initial success of Chromium, the lanthanides eventually emerged as the workhorse of the strongly magnetic elements thanks to their favourable mass, scattering properties and simpler cooling schemes.

The production of degenerate lanthanide samples led to a multitude of theoretical and experimental achievements in the following years. For example, a minimum in the excitation spectrum of a dipolar Bose gas–also known as the *roton* minimum–which was first studied in liquid ^{4}He [106], [107] and which arises from the anisotropic interaction of the dipoles in a confined geometry, has been observed in Erbium [108], [109]. Increasing the depth of this minimum via tuning the contact interactions can lead to an instability and subsequent collapse of the atomic cloud. Under special circumstances, implosion can be prevented by the beyond-mean-field quantum fluctuations. In this case, the gas forms stable, self-bound *quantum droplets* of high density and well-defined volume [110]. Furthermore, careful choice of parameters can lead to an array of droplets partially submerged in a condensate. The condensate can then facilitate particle exchange between the droplets, allowing for both long range order and coherence across the system–a signature of a *supersolid* [111]. Both of these states have been recently observed in Erbium and Dysprosium [112]–[118] and they represent a direct manifestation of the dipolar nature of these gases. In general, the competition between the contact and long-range DDI interactions together with the sensitivity to trapping geometry induced by the anisotropy of

the DDI gives rise to many exotic phases. To name a few, the so-called labyrinthine and pumpkin phases [119] have been theoretically predicted to exist in quasi-2D geometries and the simulations of dipolar vortices have revealed interesting novel dynamics [120]. Some experiments have, indeed, shown a signature of these phases [121], but more thorough investigations are limited by the attainable densities and lifetimes.

The richness of ultracold atom physics can be further enhanced by mixing different species. From a practical point of view, mixing bosons and fermions allows for sympathetic cooling of the latter [122] whereas mixing a well known species with a new one can provide a benchmark for high precision measurements [123]. From a fundamental point of view, mixing different species opens up the possibility of studying impurity physics [124], mediated interactions [90] and heteronuclear molecules [125], as discussed above, to name a few. Impurity physics, in particular, is closely related to condensed matter systems. If the two mixed species are fermionic [126], [127], then the combined system resembles the Kondo problem [128] in which a magnetic impurity is immersed in a sea of electrons. However, if the background species is bosonic [129], [130], the overall situation is similar to an electron moving through a sea of phonons–a picture that is believed to be relevant to understanding colossal magnetoresistance [131] or high T_c superconductivity [132]. In both cases, the impurity creates a disturbance in the background gas which travels with the impurity–a form of an elementary excitation called a polaron [133]. The study of polarons and, in particular, of dipolar bose polarons is one of the end goals of the Oxford Er-K experiment.

In practice, mixing is achieved by either changing the internal state of a fraction of the trapped atoms or by loading different atomic species into the same trap. The former involves inducing a transition between two Zeeman sublevels using an RF field. Creating such a mixture is experimentally more feasible but the two species originate from the same element and therefore lack the characteristics of a 'true' mixture. The latter approach requires separate cooling stages for the two species which, in many cases, doubles the amount of optics and electronics needed. The mixing step itself is also more involved because the final trap needs to be sufficiently deep to hold both species whilst the interactions need to be tuned to support a miscible phase. Despite these challenges, using two atomic species allows for the study of 'true' mixtures where the disparity in mass, electronic structure and scattering properties gives rise to a plethora of new phenomena [134], [135]. The most common mixtures are between alkali and alkaline earth atoms with the first experiments dating back to early 2000s [122], [136]. However, lanthanides have also recently joined the fray with the first Er-Dy [137] and Dy-K [138] mixtures. These mixtures will be of particular interest to this thesis.

Hopefully by now, the reader can appreciate the impact and potential applications of ultracold atom experiments–in particular those involving dipolar species. In the following section we will introduce our experiment, describe its main goals and discuss how these goals align with the current efforts within the field, paying particular attention to the unique features of our experiment that set it apart from the rest. We will conclude this chapter by outlining the structure of this thesis and by describing how the work presented

in it contributes to the overall goals of the experiment as well as the field of ultracold atoms.

1.1 The Oxford Er-K experiment

There are several cold atom experiments involving dipolar species around the world. To name a few, we mention those conducted in Innsbruck [104], Stuttgart [139], Bonn [140], Paris [141], Florence [118], Hong Kong [142], Tokyo [105] and at Stanford [143], MIT [144] and Harvard [145]. Our experiment joins the ranks with a novel mixture of Erbium and Potassium with the aim of studying some of the interesting dipolar and impurity physics described above. The choice of Erbium is motivated by its high magnetic moment, by the existing knowledge of favourable cooling transitions of its bosonic isotopes thanks to the pioneering works [104], [146] and, last but not least, by the non-existence of other mixture experiments that involve this lanthanide and an alkali. Potassium, on the other hand, is a well researched species with a simple electronic structure, considerably lower mass, and accessible bosonic as well as fermionic isotopes. The combination of these two elements will allow us to study the interplay between the dipolar and contact interactions and their role in the formation of dipolar bose polarons [147], [148]. These are believed to differ from their non-dipolar counterparts in two ways. Firstly, the phonon background of Erbium that the impurity interacts with has an anisotropic dispersion relation. Secondly, the exotic roton excitations will also contribute to the dressing of the impurity, resulting in a complex polaronic structure that is heavily dependent on the geometry and the dipolar interaction strength. Our experiment is set to be the first to study these effects.

As we already discussed, trapping geometry governs the observable dipolar physics due to the anisotropy of the DDI. Magnetic quadrupole traps or focused laser beam optical dipole traps (ODTs) are the standard within the field and are widely used for the final stages of cooling. At low enough temperatures, they can be approximated by a harmonic potential defined by its trapping frequencies. For ODTs, these frequencies can be, to some extent, controlled by the shape of the beam or other optical components such as acousto-optic modulators [149]. Changing the trapping geometry of magnetic traps, on the other hand, is more challenging. Despite the possible tunability, the anisotropy of the resulting traps is still limited and more importantly the trapped gas is inhomogeneous because it preferentially occupies the regions at the bottom of the trap. This makes measuring density-dependent effects such as the polaron energy shift [150] difficult, if not impossible. Our experiment aims to overcome these limitations by using a novel box potential inspired by recent advancements in optical trapping [46], [151]. The planned box potential will be created by a combination of an attractive sheet beam and a repulsive hollow cylindrical beam produced using a spatial light modulator (SLM). This will result in a flat 'pancake' trap that displays both strong anisotropy and homogeneity in the radial direction, mimicking other condensed matter systems with translational symmetry and allowing for the study of novel 2D dipolar phases [117], [119], [152].

To have full control over the gas parameters, a strong enough magnetic field is required to tune the scattering length of the two species. For Erbium, suitable Feshbach resonances

exist below 4 G [153], however, for Potassium (and other alkalis in general) the region of interest is in 100s of G [154], increasing the requirements on the achievable magnetic field strength. For that purpose, we will employ two large water-cooled coils capable of creating homogeneous magnetic fields of strength up to 300 G. These fields will not only be sufficient for the individual species but we believe they will also cover the appropriate range for studying interspecies Feshbach resonances, based on previous experiments with Dy-K mixture and Erbium [138], [155], [156]. Additionally, a set of smaller fast coils will be used to rotate the Erbium dipoles on timescales much faster than the typical dynamics of the gas particles, effectively averaging the DDI without changing the scattering length [157], [158]. Doing so will gives us direct control over the DDI and hence the relative strength of the contact and dipolar interactions without significantly affecting the scattering properties and loss rate of the gas. This is in direct contrast to the majority of current experiments where tuning the s-wave scattering length is the only way of controlling the relative strength of the two interactions.

1.2 Thesis structure

Building a cold atom experiment is a complicated and lengthy process that entails many stages and spans over several years. For mixture experiments such as ours, this is doubly true. But even during the building phase, opportunities can arise for innovating and conducting interesting science. The work presented here covers the exciting period in the project's lifetime in which quantum degeneracy of Erbium was achieved and ultracold Potassium was introduced to the main chamber. Consequently, the thesis is split into two major and one minor section.

The first section focuses on Erbium. It starts by introducing its atomic properties in relation to laser cooling techniques and by discussing how the dipole-dipole interaction affects both the non-degenerate and degenerate phases. The following two chapters describe the experimental apparatus and the cooling sequence that leads to the production of an unprecedented large dipolar Bose Einstein condensate, focusing on optical dipole trapping, evaporative cooling (both numerically and experimentally) and on the possibility of atom transport using focus-tunable lenses. The last two chapters of this section then focus on two major scientific investigations which will soon result in publications. The first one studies the three-body loss mechanism in ^{166}Er, carefully mapping out the three-body loss coefficient L_3 between 0 G and 4 G, identifying new resonant features that are believed to be inherently three-body in nature and presenting a novel model of the heating mechanism that matches experimental data. The second chapter describes the first reported measurement of the shift of the critical BEC temperature due to the dipolar interaction. It outlines the existing theory, discusses the experimental method, including the measures taken to mitigate systematic errors, and finally presents the measured data.

The second major section is devoted to the addition of potassium. Once again, we start by describing the element itself, paying attention to the difference in electronic structure and consequently in the optical pumping cycles compared to erbium. We then proceed with detailing the optical and vacuum setup that has been built over the past year to

facilitate the introduction of the second species into the main vacuum chamber. Namely, we describe the design and implementation of a 2D+ MOT chamber [159] that serves as a source of cold K atoms as well as the necessary optics for cooling on the D1 and D2 lines [160]. The last chapter in this section discusses the performance and optimization of the 2D+ MOT.

The third and last section serves as a conclusion to the thesis and as a short teaser of the future of our mixture experiment. We first list the remaining steps necessary for the realization of the first ever Er-K ultracold mixture in a novel 2D trap. Finally, this leads to a discussion of possible experimental areas we might want to explore using our platform including dipolar polarons, roton physics and non-Markovian quantum reservoirs.

Overview and contributions

The work presented here is a culmination of three and a half years of concerted team effort that covers both the main erbium experiment and the potassium addition. The latter was the original focus of my project but through a mixture of unforeseen circumstances as well as deliberate decisions, I ended up being majorly involved with building, operating and utilizing the erbium experiment for scientific advancement. The experiment wouldn't exist if it wasn't for all the individual contributions made by my coworkers. Below, I will outline the contents of each chapter, highlighting the role of my colleagues as well as establishing my own contributions.

Chapter 2 puts erbium in the spotlight, describing in detail its atomic properties and the origin and role of dipole-dipole interactions (DDIs). It then goes on to introduce atomic scattering from a theoretical perspective, including a discussion of Feshbach resonances (FRs) and their practical use. The chapter concludes with outlining the theory of degenerate dipolar bosonic gases and its major predictions.

Chapter 3 introduces the Oxford Er-K experiment, including the vacuum hardware, optics and other supporting systems. It focuses on the first stages of laser cooling that allow us to reach the Doppler limit. The majority of work on the Zeeman slower and MOT systems was already conducted by Dr Milan Krstajić and Dr Anna Marchant. I was involved with their subsequent re-optimization, operation and minor upgrades. I also have to mention contributions from Dr Lucas Hofer who built the whole lab software infrastructure for data acquisition and analysis.

Chapter 4 describes, step-by-step, the rest of the experimental procedure that leads to the production of large ^{166}Er Bose-Einstein condensates (BECs). I was heavily involved with the optical dipole trap system which I partially built (after taking over from Dr Péter Juhász), characterized and prepared for the evaporation stage with the help of Milan. I then played a major role in optimizing the evaporation ramp, which eventually lead to our first production of an erbium BEC. The tunable lens stabilization system was designed by myself and a summer student, Meg Savage. The project was then taken over by Gavin Lamb who overhauled the system and did a tremendous amount of work on optimizing it and implementing it in the main experiment, whereas I remained involved with it on the theoretical side, simulating atomic transport and making the stabilization scheme more

robust.

Chapter 5 presents our measurements of the three-body loss spectrum in ^{166}Er. This became one of my major projects and the first experimental publication of our group. I was responsible for developing a refined theoretical model of the three-body loss process, analysing newly found loss features and comparing them with existing theory and taking a substantial portion of the data together with Milan and Gavin. Péter contributed with developing a fitting routine and analyzing one of the data sets. Milan, Peter and I (together with Rob) then prepared the manuscript for publication.

Chapter 6 details (to our knowledge) the first ever successful measurement of the critical temperature (T_c) shift due to the long-ranged, anisotropic dipole-dipole interactions. This was a challenging project that involved an exciting mixture of experimentation, careful data analysis and theoretical modelling. Together with Milan, I was heavily involved in the experimental part of the project and took the lead in calculating numerous temperature corrections necessary for accurate estimation of the T_c, some of which were based on the work of our summer student Joanne Roper. Lucas lay the foundation of our multi-stage fitting routine and Milan was responsible for data processing, analysis and setting up the theoretical framework. Together, we prepared a manuscript which will be submitted for review in the coming weeks.

Chapter 7 starts by describing important atomic properties of potassium, motivating our choice of the element as the impurity species. It then continues to outline the cooling stages that we have already implemented or plan to implement in order to produce an ultracold mixture of potassium and erbium. Special attention is paid to the the light preparation system which was originally designed and partially built by Lucas and then overtaken, upgraded and built by me.

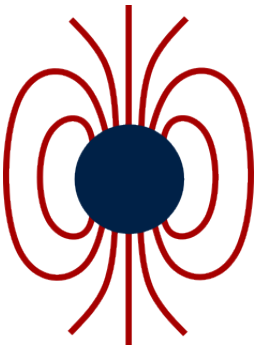
Chapter 8 provides a detailed account of the design, construction and performance of our K 2D+ MOT which serves as a source of ultracold potassium atoms and introduces them into the main experimental chamber. Lucas designed and commissioned the vacuum system and, together with Gavin, also designed the 3D printed oven. I took the lead in the actual assembly and, with Milan and Gavin's help, saw the whole system through baking and attachment to the main experiment. I was also responsible for designing and building the optics (both internal and external) which I did together with a Master's student Noah El Alami. Finally, once operational, we optimized the performance of the 2D+ MOT, making it suitable for loading into the 3D MOT.

Chapter 9 serves as a conclusion to the thesis, providing a brief summary of what has been achieved as well as outlining the next steps that are currently being taken towards the first realisation of an ultracold erbium-potassium mixture. The chapter, and hence the thesis, concludes with a discussion of possible scientific avenues that could be pursued with our novel experiment.

Part I

Erbium

2. Erbium–the dipolar star of the show



It is useful and informative to devote a section of an ultracold atom thesis to a detailed description of the atomic species at hand. In this chapter, we will do just that, focusing on the workhorse of our experiment–erbium. We first set the stage by informing the reader on its basic physical and chemical properties, providing some real world context to the importance of this lanthanide. We then enter the quantum domain to describe its electronic structure which is at the heart of what makes erbium an interesting subject of research. Namely, we discuss the atomic levels and the corresponding transitions which are relevant for laser cooling and we outline how the orbitals occupied by the valence electrons combine to give an unusually large magnetic dipole moment in the ground state. We then go on to describe the atomic interactions which arise as a combination of both the short-range, dispersive, electric dipole interactions and long-range, permanent, magnetic dipole interactions.

This discussion will prove useful in section 2.3.3 where we first focus on the scattering properies of erbium and the effect of the DDI on the scattering length. A brief section is then devoted to the phenomenon of Feshbach resonances and how they can be used to tune the scattering length and hence the relative strength of the dipole-dipole interactions (DDI) and the contact interactions. Finally, we use the example of erbium to present the theory of degenerate dipolar Bose gases. Initially, we concentrate on non-dipolar Bose-Einstein condensates and the mathematical techniques used to describe their macroscopic as well as dynamical properties only to later demonstrate how these change in the presence of the long-range, anisotropic dipole-dipole interaction.

2.1 The element

Erbium was discovered in 1843 in the Swedish mine of Ytterby to which it owes its name alongside the elements terbium, ytterbium and yttrium, all of which were unearthed from

Isotope	^{162}Er	^{164}Er	^{166}Er	^{167}Er	^{168}Er	^{170}Er
Statistics	boson	boson	boson	fermion	boson	boson
Abundance	0.14%	1.60%	33.5%	22.9%	27.0%	14.9%

Table 2.1: Stable isotopes of Erbium, their relative abundances and corresponding quantum statistics. This work and our experiment in general concerns with ^{166}Er. Data taken from [163].

the same mine. Erbium was found in a sample of gadolinite ore by Carl Gustaf Mosander [161], a prominent Swedish chemist and a discoverer of two other elements, lanthanum and terbium. With its atomic number of $Z = 68$, erbium is classified as a rare earth metal and located at the bottom of the periodic table along with other lanthanides such as dysprosium, holmium and europium. The average mass of $m = 167.26\,\text{amu}$ not only makes it one of the heaviest elements to have been cooled to quantum degeneracy but it also has direct implications for the relative energy scales of the spin-orbit and electron-electron interaction as we shall see below. In terms of its isotopes, erbium offers six stable ones, five of which are bosonic and one fermionic with a relatively high abundance–see table 2.1. This makes it particularly lucrative for experiments where quantum statistics [162] governs the behaviour of the system.

When it comes to physical properties, erbium appears as a grey metallic solid not dissimilar from silver. It is easily malleable and has a relatively high melting point of 1529 °C. At room temperature, it is paramagnetic and only becomes ferromagnetic when cooled below −254 °C [164]. When combined with hot water, it quickly forms erbium hydroxide and hydrogen gas, making it slightly more difficult to work with, especially in the context of ultracold atom experiments with a hot erbium source. In nature, erbium is always found in chemical combination with other elements and therefore in ores. The most common way of extracting it is then via ion exchange from salts formed by acidic etching of crushed ores.

Erbium and its ions find a variety of uses ranging from metallurgy to medicine. Pink in colour, erbium ions have useful optical properties. A transition at 1530 nm suitable for lasing is widely utilized for amplifying signals in erbium-doped optical fibres as well as in fibre lasers. The fluorescence of Er^{3+} at 2940 nm, on the other hand, finds use in laser surgery because light of this wavelength is readily absorbed by water, making the impact of the absorbed and re-emitted laser light on the surrounding tissue only superficial. Lastly, erbium itself can be used as an additive to change the physical properties of alloys. In combination with vanadium, it significantly lowers the stiffness of the metal and improves workability whereas erbium-nickel alloys are used in cryogenics due to their high heat capacity at low temperatures [165].

2.2 The atom

From a quantum physicist's perspective, erbium gets even more interesting on the atomic scale. Thanks to its electronic structure, it has one of the highest ground state magnetic dipole moments of all the elements. With $\mu = 7\mu_B$, erbium is only rivalled by other lanthanides dysprosium ($10\mu_B$), terbium ($10\mu_B$), holmium ($9\mu_B$) and europium ($7\mu_B$) as well as by the group VI element chromium ($6\mu_B$). However, as we will see below, it is not only the magnitude of the dipole moment but also the atomic mass that influences the relative strength of the dipole-dipole interaction (DDI). For that reason, despite being the first dipolar species to be cooled to quantum degeneracy [102], chromium with its mass of $m_{\mathrm{Cr}} = 52.0\,\mathrm{amu}$ has a weaker dipolar character.

2.2.1 Electronic structure

With 68 electrons, the internal structure of erbium is complex and affects many of its properties. Using the standard noble gas notation, its electron configuration can be written as

$$[\mathrm{Xe}]\ 4f^{12}6s^2. \tag{2.1}$$

The filling of the $6s$ orbital before the $4f$ orbital is an example of the so-called submerged shell configuration. The effect can be partially explained by taking into account the penetration of the $6s$ orbital into the lower shells, increasing the effective charge experienced by the electron and consequently lowering its energy relative to the less penetrative $4f$ orbital [166]. The two vacancies, or *electron holes*, in the high orbital angular momentum $4f$ state are directly responsible for the high total angular momentum of $J = 6$ of the ground state of erbium as we will see shortly.

To understand the electronic structure and the resulting terms and levels in more detail, we first invoke the semi-empirical Madelung rule [167] which states that orbitals are filled in order of increasing $n + l$, where n is the principal quantum number associated with shells and l is the orbital angular momentum quantum number associated with the usual labels s, p, d, f etc. In case that some orbitals are degenerate in $n + l$, the orbital with lower n is filled first. In this way, the $6s$ orbital in erbium with $n + l = 6$ gets filled before the $4f$ orbital with $n + l = 7$, leaving the latter with two electron vacancies.

The filling of the $4f$ state follows yet another semi-empirical set of rules–the Hund's rules [166]–which are based on the assumption that the electron-electron repulsion between the $4f$ electrons is stronger than their spin-orbit coupling. As a result of this assumption, the total spin and angular momentum quantum numbers associated with the operators $\hat{S} = \sum_{4f} \hat{s}_i$ and $\hat{L} = \sum_{4f} \hat{l}_i$ are considered 'good' and they couple together to give the total angular momentum $\hat{J} = \hat{L} + \hat{S}$. This is known as the LS coupling scheme [80] and its validity for erbium will be briefly discussed below.

Hund's first rule states that S is maximized for electrons in an unfilled orbital. Consequently, all the $2l + 1 = 7$ states designated by the m_l quantum number are first singly occupied by electrons with aligned spins before being filled with electrons of opposite spin.

This leaves the $4f$ orbital with two singly-occupied m_l states in the same $m_s = +1/2$ spin state such that $S = 1$. Hund's first rule is understood to arise from the fact that singly-occupied states are less screened from the nucleus, experiencing more of its electrostatic potential.

Hund's second rule is used to determine which m_l states are singly-occupied by stating that in the ground state, the electrons arrange to maximize the total orbital angular momentum $\hat{L}$. Consequently, the two unpaired $4f$ electrons occupy the $m_l = +2$ and $+3$ states, giving $L = 5$. Physically, the second rule arises from minimizing the electron-electron repulsion and can be classically interpreted by realizing that electrons orbiting in the same direction spend, on average, less time close to each other than electrons orbiting in opposite directions.

Finally, Hund's third and last rule dictates how S and L combine to give J. For a less than half-filled subshell, J is minimized, whereas for more than half-filled subshell it is maximized. Clearly, with only two electron holes, the $4f$ orbital in erbium is more than half-filled and so $J = L + S = 6$ (as opposed to $J = |L - S|$ as would be the case for less than half-filled subshell). The third rule originates from the spin orbit interaction in the LS coupling regime where the level energy shift can be expressed as $E_{\mathrm{SO}} \propto \langle \hat{L} \cdot \hat{S} \rangle \propto J(J+1) - L(L+1) - S(S+1)$. The constant of proportionality changes sign when the subshell becomes more than half-filled, lowering the energy of high J levels.

At this point it is interesting to point out that since erbium has an even number of protons (and hence electrons), all of its bosonic isotopes must have an even number of neutrons to give an overall integer spin. Furthermore, nuclei of atoms with an even number of protons and neutrons have no spin [168]. This means that none of the bosonic isotopes of erbium have nuclear spin and therefore have no hyperfine structure. The fermionic isotope ^{167}Er, on the other hand, has a nuclear spin of $I = 7/2$.

Having justified and detailed the ground state configuration of erbium and the individual orbitals involved, we can now describe how these combine to give the overall ground state level structure. In the case of light elements, the electron-electron repulsion between the valence orbitals is stronger than their individual spin-orbit (SO) interaction, coupling the individual orbital angular momenta $\hat{l}_i$ separately to the spin angular momenta $\hat{s}_i$ before combining them in the total angular momentum $\hat{J}$ in the usual LS coupling procedure. However, in heavier elements such as erbium, the high nuclear charge enhances the SO interaction, making it comparable or stronger than the electron-electron repulsion. Consequently, the SO interaction first couples the individual $\hat{l}_i$ and $\hat{s}_i$ into $\hat{j}_i = \hat{l}_i + \hat{s}_i$ before coupling the $\hat{j}_i$s into $\hat{J} = \sum \hat{j}_i$. This is called jj coupling. Erbium and most other lanthanides [169] and their excited states follow a special case of this scheme called J_1J_2 coupling [168] in which the individual orbitals (in our case $6s$ and $4f$) and their electrons follow LS coupling scheme but the resulting $\hat{J}_{6s}$ and $\hat{J}_{4f}$ couple together into the total $\hat{J} = \hat{J}_{6s} + \hat{J}_{4f}$ in the jj coupling fashion.

Applying this to the ground state of erbium, we have the filled $6s^2$ orbital with $L = 0$, $S = 0$ and hence $J_{6s} = 0$ which can also be written as $^1S_0$ using the standard spectroscopic notation. We also have the more than half-filled $4f^{12}$ orbital with $L = 5$, $S = 1$ and $J_{4f} = 6$

i.e. $^3H_6$. Combining these as described above using the $(J_1, J_2)_J$ notation yields the final coupled ground state

$$[\text{Xe}]\ 4f^{12}\ (^3H_6)\ 6s^2\ (^1S_0) = (6,0)_6\ . \tag{2.2}$$

Significant transitions

Given its large atomic number, it is not surprising that erbium displays a rich energy spectrum. Figure 2.1 shows the energy levels of erbium relative to its ground state, split based on their parity and total angular momentum J. When choosing a transition suitable for laser cooling, several considerations need to be made. Firstly, and more fundamentally, the selection rules only allow certain transitions [80]. In the case of ground state erbium which has even parity, the excited state needs to have odd parity and a total angular momentum that differs from the ground state by 1, i.e. $J = 5$ or 7.

Secondly, not all allowed transitions are practical. In order to achieve efficient cooling, ideally a closed optical cycle exists between the ground and excited state. The simplest example of this is a two level system in which laser light drives the transition one way and spontaneous emission the other. The existence of a third, metastable state into which the excited state can relax breaks the cycle. Atoms accumulate in this *dark*[1] state over time without a direct way of 'escaping' it, reducing the number of photon scattering events and hence the cooling efficiency. In real atoms with a multitude of energy levels, it can be impossible to avoid other decay channels. If that is the case, one can still close the optical cycle by using another laser field to drive the atoms from the third state back to the excited state. This is called optical *re-pumping* and it is commonly used in alkalis. We implement a re-pumping scheme in our experiment for cooling potassium and discuss it in detail in chapter 7.

Lastly, the physical parameters of the transition such as its linewidth and wavelength determine the capture velocity of atoms, photon recoil energy as well as the minimum achievable temperature known as the *Doppler temperature*. This will be expanded on in the next chapter where we describe the full cooling setup but for now, it is sufficient to point out that wider transitions are more useful for the early stages of cooling such as in the Zeeman slower [172] where the gas is still hot and its atoms have a wide range of velocities, whereas narrower transitions are suitable for magneto-optical traps (MOTs) [173] where the gas ideally approaches the Doppler limit.

Taking erbium as an example, it appears that, on one hand, a dense energy spectrum is more likely to yield fortuitous laser cooling transitions that tick all the boxes. On the other hand, a large number of energy levels also means a potentially large number of decay avenues (also known as branching ratios [174]) for the excited state which could break optical cycling. Luckily, a multitude of laser cooling transitions have been identified in erbium [175] that range from wide (30 MHz) to ultra narrow (2 Hz). Two transitions in particular have become the standard in ultracold erbium experiments–a broad (29.7 MHz)

[1] Such states are called dark because they don't interact with the laser light that is driving the primary transition.

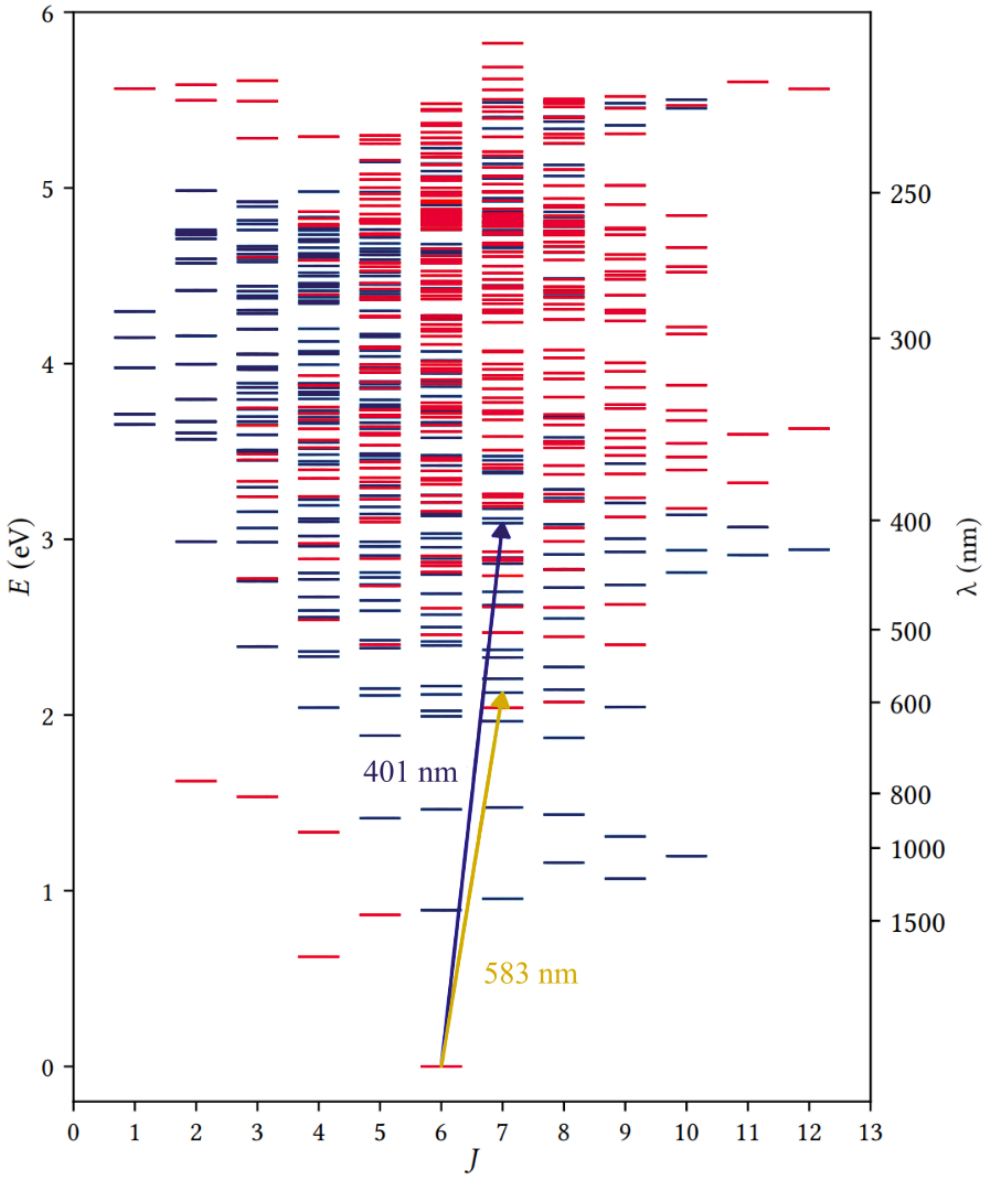


Figure 2.1: Energy levels of erbium. Even (odd) states are depicted in red (blue) and they are arranged based on their total angular momentum J. Two of the most prominent transitions are indicated with arrows–a blue transition at 401 nm which is used for Zeeman slowing and a yellow transition at 583 nm used in the magneto-optical trap. Data taken from [170], [171].

Wavelength (λ)	400.91 nm	582.84 nm
Color	Blue	Yellow
Linewidth ($\Gamma/2\pi$)	29.5 MHz	186 kHz
Doppler temperature ($T_D = \hbar\Gamma/2k_B$)	707 µK	4.46 µK
Recoil temperature ($T_R = \hbar^2k^2/2mk_B$)	0.36 µK	0.17 µK
Saturation intensity ($I_{\text{sat}} = \pi hc\Gamma/3\lambda^3$)	59.8 mW cm^{-2}	0.12 mW cm^{-2}

Table 2.2: Properties of erbium cooling transitions. The wide, blue transition is suitable for early stages of cooling where large stopping forces are needed whereas the narrow, yellow transition with its low Doppler temperature is ideal for later stages such as the magneto-optical trap. Data taken from [177].

transition at 401 nm widely used for initial Zeeman and molasses slowing [176] due to large scattering rates and recoil momenta and a narrow (190 kHz) transition at 583 nm used in MOTs [146] for its low Doppler temperature of 4.5 µK. Both of these are utilized in our experiment. We also note that another ultranarrow transition (8 kHz) at 841 nm has been recently successfully used which gives access to even colder Doppler temperatures [145].

Lets briefly discuss the properties of the two transitions utilized in our experiment as well as the electronic levels involved in them. Table 2.2 summarizes the physical parameters of both transitions. In terms of electronic states, both transitions correspond to a $6s$ electron being excited to the $6p$ orbital. In case of the blue transition at 401 nm, the two electrons in the $n = 6$ shell form the $^1P_1$ singlet state whereas for the narrow yellow transition at 583 nm they form the $^3P_1$ triplet state. In the J_1J_2 coupling scheme, the two excited states are then represented as

$$\begin{aligned} 401\,\text{nm} &: [\text{Xe}]\ 4f^{12}\ (^3H_6)\ 6s6p\ (^1P_1) = (6,1)_7\ , \\ 583\,\text{nm} &: [\text{Xe}]\ 4f^{12}\ (^3H_6)\ 6s6p\ (^3P_1) = (6,1)_7\ . \end{aligned} \tag{2.3}$$

As an aside, we note that the magnitude of the isotope shift [178] for two neighbouring bosonic species of erbium is of the order of 900 MHz. For more details on the specific shifts see [179], [180].

2.2.2 Magnetic properties

As mentioned before, lanthanides have some of the largest magnetic moments of all the elements. They are also ferromagnetic, albeit with low Curie temperature [92], [181], and in alloys with transition metals they can form very strong room temperature permanent *neodymium* magnets with magnetic field strengths of up to 1.4 T [182]. This is due to the $4f$ orbitals which carry the lanthanide's magnetic moments and which are contracted so close to the nuclei that they don't overlap with other surrounding orbitals, preventing bulk magnetic moment reduction via spin-flip hopping [183].

The large magnetic dipole moment of erbium ($7\mu_B$) also, and rather unsurprisingly, arises from the two electron holes in its $4f$ orbital. To see this, we first note that in

the limit of low magnetic fields relative to the strength of the spin-orbit interaction, the component of the magnetic moment along the quantisation axis is given by

$$\mu = m_J g_J \mu_B \ , \tag{2.4}$$

where m_j is the magnetic quantum number associated with the total angular momentum J, g_J is the Landé g-factor that encompasses the different contributions to the magnetic moment from spin and orbital motion and finally μ_B is the Bohr magneton[2]. For completeness, this 'low' magnetic field limit is valid for fields up to $\langle E_{\mathrm{SO}} \rangle / \mu_B \approx 4 \times 10^3\,\mathrm{T}$ [184], [185] which is several orders of magnitude larger than is practically attainable in experiments and so the use of equation 2.4 is justified.

In order to calculate the Landé g-factor g_J of the ground state as well as the excited states, we have to proceed in two steps. As mentioned in section 2.2.1, the electronic structure of erbium follows a special case of jj coupling called the $J_1 J_2$ coupling in which the two valence orbitals are treated separately in the LS coupling regime before being coupled together to give the total angular momentum J. In the LS regime in which L_i and S_i couple together to give J_i, the g factor is given by

$$g_{J_i} = 1 + (g_s - 1)\frac{J_i(J_i+1) - L_i(L_i+1) + S_i(S_i+1)}{2J_i(J_i+1)} \tag{2.5}$$

with $g_s \approx 2.00232$, the gyromagnetic ratio of the electron [186]. Once the individual g_{J_i} are obtained for the two orbitals, they can be coupled together to give the final g_J as

$$g_J = g_{J_1}\frac{J(J+1) + J_1(J_1+1) - J_2(J_2+1)}{2J(J+1)} + g_{J_2}\frac{J(J+1) + J_2(J_2+1) - J_1(J_1+1)}{2J(J+1)} \ . \tag{2.6}$$

In the ground state, the two electrons in the $6s$ orbital are in the ${}^1S_0$ state with $L = S = J = 0$. This significantly simplifies equation 2.6 and reduces it to $g_J = g_{4f}$ given by equation 2.5. The $4f$ electrons are in the ${}^3H_6$ state which, upon substitution, gives $g_J = 1.1670532$. This relatively simple treatment omits relativistic and diamagnetic effects as well as the deviation of the LS coupling scheme from reality. Compensating for these effects gives $g_J = 1.1637985$ [185] which is in close agreement with the measured value of $g_{J,\mathrm{exp}} = 1.163801(1)$ [185]. We can now calculate the magnetic moment of the ground state using equation 2.4 and by realizing that in the ground state $J = 6$ and so the lowest Zeeman sublevel will have $m_J = -6$

$$\mu_{\mathrm{Er}} = m_J g_J \mu_B = -6.982806(6)\mu_B \ . \tag{2.7}$$

We can repeat this process for the excited states involved in the 401 nm and 583 nm transitions. For these states, the electrons in the $n = 6$ shell are in the ${}^1P_1$ singlet and ${}^3P_1$ triplet state respectively (see 2.3). Substituting the appropriate quantum numbers into equation 2.6 gives the values $g_{J,401} = 1.140$ and $g_{J,583} = 1.212$ which match reasonably

[2]The Bohr magneton is defined in terms of the fundamental constants as $\mu_B = e\hbar/2m_e = 9.27 \times 10^{-24}\,\mathrm{J\,T^{-1}}$ and represents the typical scales of magnetic moments in atoms.

well with the experimental values $g_{J,401} = 1.160$ and $g_{J,583} = 1.195$ [171].

The nuclear moment $\hat{I}$ of the fermionic isotope (which is absent in the bosonic isotopes) couples to the angular momentum $\hat{J}$ to give the total angular momentum $\hat{F} = \hat{I} + \hat{J}$. The corresponding quantum number F takes on the values of 19/2 in the ground state which has a magnetic moment given by $\mu = m_F g_F \mu_B$ in correspondence with equation 2.4. The Landé g factor of $g_F = 0.735$ results in the same magnetic moment of $\mu = -6.982\mu_B$ in the ground state as we have previously seen in the bosonic isotopes. This is a direct consequence of weak coupling between the nuclear magnetic moment and the applied field.

However, despite the weak coupling (and owing to the quirky nature of quantum mechanics), the addition of one neutron to the nucleus that already contains 166 nucleons not only substantially changes the energy spacing of neighbouring Zeeman sublevels at a given B field but more importantly it completely changes the statistics and hence measurable macroscopic properties of cold ensembles of these atoms. For more detailed discussion of the fermionic isotope of erbium see reference [174].

Zeeman splitting

When a state with total angular momentum $\hat{J}$ is subject to an external magnetic field B, the $2J+1$ Zeeman sublevels denoted by the magnetic quantum number m_J split in energy according to

$$E_Z = m_J g_J \mu_B B \tag{2.8}$$

This expression is at the heart of magnetic field (anti)trapping since atoms in a particular m_J state experience a force proportional to the gradient of magnetic field magnitude $F \propto \nabla|\vec{B}|$. We note that the ground state of erbium with $m_J = -6$ and $g_J > 0$ is a *high-field seeking* state and therefore can't be trapped purely magnetically [187] due to the non-existence of global maxima in magnetic field magnitude (also known as Earnshaw's theorem [188]). Precise measurement of the Zeeman splitting of two adjacent m_J sublevels via radio-frequency spectroscopy can be used to calibrate the magnetic fields around the experimental chamber–a technique used frequently in our experimental routine and described in section 3.1.2.

Perhaps an even more important implication of the Zeeman shift, at least in the context of erbium, is the differential shift between the excited state $|J_e, m_e\rangle$ and the ground state $|J_g, m_g\rangle$

$$\Delta E_Z = (m_e g_e - m_g g_g)\mu_B B \ . \tag{2.9}$$

In this way, an applied magnetic field can detune the transition frequency and compensate for other frequency-shifting effects such as the Doppler shift or the Stark shift [80] as well as create spatially dependent radiation force–a mechanism central to the workings of magneto-optical traps [173]. Figure 2.2 depicts the uses of the Zeeman shift in atomic physics.

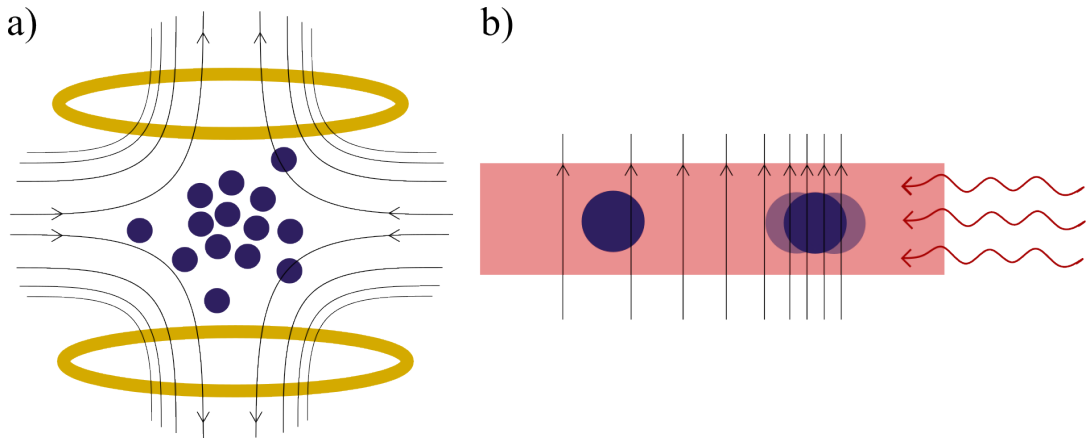


Figure 2.2: Utility of the Zeeman effect. a) Magnetic trapping–an atom in a suitable *low-field seeking* state can be spatially trapped in a minimum of an applied magnetic field. Gauss' law for magnetism, $\nabla \cdot \mathbf{B} = 0$, prohibits the existence of a local maximum in the magnitude of a magnetic field $|\mathbf{B}(\mathbf{r})|$ and so high-field seeking states such as the ground state of erbium are not suitable for magnetic trapping. b) The detuning of a laser field with respect to an atomic transition can be changed by applying an external magnetic field, provided that the two states involved in the transition have a different Zeeman shift. In this way, spatially dependent optical pressure can be exerted onto an atomic cloud–see section 3.2 for more detail.

2.3 Interactions

Having discussed in detail the atomic structure of individual erbium atoms, we can now focus on how these atoms interact when part of a larger ensemble. After all, it is precisely the mutual atom-atom interactions that are responsible for the near-impossibility of solving the underlying Schrödinger equation on one hand, and the richness of the resulting physics on the other.

2.3.1 Contact interaction

In the classical picture, atoms in a gas are thought of as *hard spheres* moving through space on straight lines and occasionally colliding in a similar fashion to the elastic collisions of billiard balls. Fundamentally, this picture can't be valid if only because atoms don't have hard boundaries and are instead more similar to dispersed probabilistic clouds of electrons with a dense, positively charged core in their center. When two such 'cloudy' atoms come in a close proximity, the electron wave functions are warped by the Coulomb force of the charge fluctuations present in the other atom. The closer the two atoms are, the stronger the Coulomb forces, and so their mutual interaction has a smooth rather than an abrupt hard-sphere character. At some point, the atoms will be so close that their electron clouds overlap and the resulting Coulomb and Pauli repulsion will push the atoms apart. The collision is complete.

We will see that despite the discrepancy between the classical and the quantum models, in dilute gases the 'hard sphere' character of the collisions is to some extent retained and the complexity of the quantum collision is encompassed in a single constant–the scattering

length. But for now, we will formalize the form of the neutral atom-atom interaction potential described above and will worry about any implications for scattering later in section 2.3.3.

Even in spherically symmetric atoms such as the alkalis, temporary fluctuations in the electron charge distribution result in formation of electric dipoles (and higher order multipoles). These temporary dipoles create an electric field around them that scales as $E_{\text{dip}} \propto p/r^3$ where p is the dipole magnitude and r is the distance from the dipole. If another atom enters the vicinity of the dipole, the electric field exerts a force on the atom's electron cloud, shifting the negative charge distribution and consequently inducing a dipole on the atom of magnitude $\vec{p}_{\text{ind}} = \alpha\vec{E}_{\text{dip}}$ where α is the polarizability of the atom which depends on the details of its electronic structure. The induced dipole interacts with the electric field and experiences a potential $U = -\vec{E}_{\text{dip}} \cdot \vec{p}_{\text{ind}} = -\alpha|E_{\text{dip}}|^2 \propto -1/r^6$.

This short-ranged, attractive interaction potential is also known as the Van der Waals potential [189] and it is customary to write it in the form

$$U_{\text{VdW}} = -\frac{C_6}{r^6} \tag{2.10}$$

where C_6 is the species-dependent dispersion coefficient that encompasses the quantum mechanical details of the interaction. We note that higher order n-multipoles, e.g. quadrupoles, that scale as $1/r^{4+n}$ also contribute to this expression but their coefficients are smaller and are usually omitted. It is clear that the Van der Waals (VdW) potential can't fully describe the atom-atom interaction because of its attractive divergence at $r = 0$. At much smaller nuclear separations, the Pauli repulsion between the electrons wins over the induced dipole attraction and the potential becomes repulsive. The full description of the interaction requires demanding quantum mechanical calculations but some semi-empirical models such as the extensively used Lennard-Jones potential [190] have a simple form and capture the underlying physics well [191]. Moreover, it will become clear when we discuss ultracold collisions that the exact details of the scattering potential are not important as long as it faithfully describes the long-range part of the interaction and results in the same scattering length. An interesting feature of the dispersive atomic potentials is the existence of a minimum due to the competition between the repulsion (Pauli) and attraction (VdW)–see figure 2.3. This minimum allows for the existence of bound molecular states which have direct implications for atomic scattering and the phenomenon of Feshbach resonances as we will see later in section 2.3.4.

In the case of erbium, the situation is more complicated due to its electronic structure. The two holes in the $4f$ orbital result in an anisotropic charge distribution and consequently, the dispersion potential is also anisotropic. Full quantum mechanical calculations [192] reveal a spread of C_6 coefficients, each coupling different m_j scattering channels, where m_j is the projection of the atom's total angular momentum J onto the collision axis [193]. Note that in the case of a spherically symmetric potential such as in the alkalis, collisions can't couple states of different m_j and so C_6 has a singular value as opposed to being a matrix. For erbium, the dispersion coefficient and its anisotropic contribution ΔC_6 have been calculated as $C_6 = 1723\,\text{au}$ and $\Delta C_6 = 350\,\text{au}$ [192]. Remarkably, due to

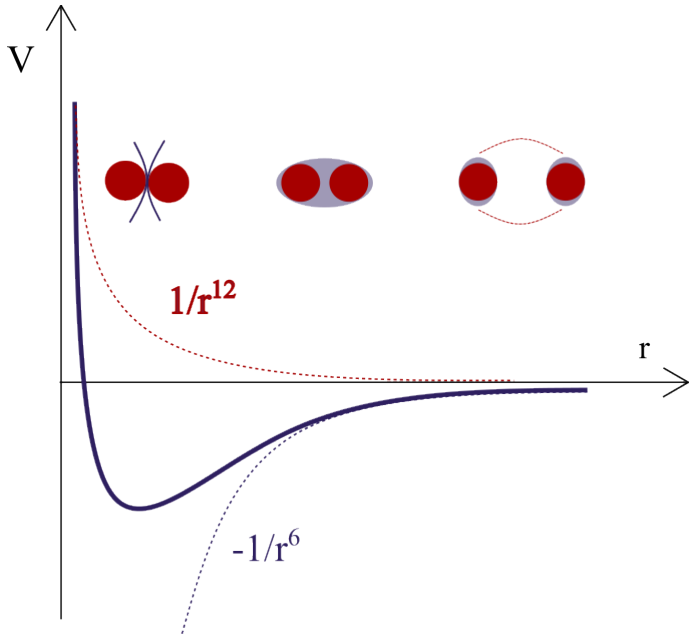


Figure 2.3: Lennard-Jones potential. Most commonly used potential form for describing dispersive interactions between neutral atoms. The attractive part of the potential that decays as $1/r^6$ comes from mutually-induced electric dipole-dipole interaction whereas the repulsive part of the potential is a result of Pauli exclusion. The stable minimum of the potential can, in general, support a bound state.

the short range character of the interaction, the effect of the anisotropic part can still be represented by an adjustment to the s-wave scattering length [194].

2.3.2 Dipole-dipole interaction

The dispersive contact interaction described in the previous section is, in one form or another, present in all neutral atoms. What sets erbium and other dipolar species apart is the presence of a permanent magnetic moment and the resulting dipole-dipole interaction (DDI) between the atoms. In general, two dipoles (be it magnetic or electric) interact via a potential of the form

$$U_{\text{dip}} = \frac{C_{dd}}{4\pi} \frac{\hat{e}_1 \cdot \hat{e}_2 - 3(\hat{e}_1 \cdot \hat{r})(\hat{e}_2 \cdot \hat{r})}{r^3} \tag{2.11}$$

where $\hat{e}_1$ and $\hat{e}_2$ are the unit vectors pointing in the direction of the dipoles and $\vec{r}$ is the vector separating the dipoles, defined by its direction $\hat{r}$ and magnitude r. The dipolar coupling constant C_{dd} depends on the nature of the interaction and the strength of the dipoles. For magnetic dipoles (e.g. lanthanides), it is given by $C_{dd,m} = \mu_0\mu_1\mu_2$, whereas for electric dipoles (e.g. heteronuclear molecules or Rydberg atoms), it is equal to $C_{dd,e} = p_1p_2/\varepsilon_0$. Notably, the ratio of the two coupling constants for $\mu \approx \mu_B$ and $p \approx ea_0$ is given by $C_{dd,m}/C_{dd,e} = \alpha^2/4$ where $\alpha = e^2/4\pi\varepsilon_0\hbar c \approx 1/137$ is the fine structure constant. Clearly, for typical atomic scales the electric DDI is much stronger than the magnetic one.

Typically in cold atom experiments, an external magnetic field is used to manipulate the atomic levels via the Zeeman effect and tune the s-wave scattering length via Feshbach

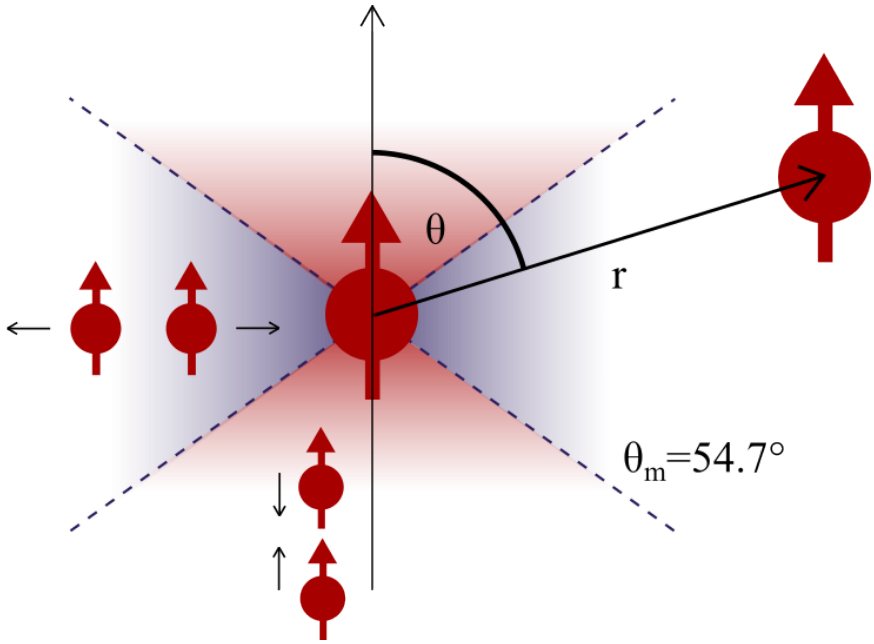


Figure 2.4: Geometry of the dipole-dipole interaction. Dipoles polarized along the same axis interact via a long ranged potential that scales as $1/r^3$ where r is the separation of the atoms. The interaction is either attractive or repulsive depending on their relative orientation given by angle θ. In a side-by-side configuration, the dipoles repel, whereas in a head-to-tail configuration they attract. At the magic angle $\theta_m \approx 54.7°$, the interaction vanishes. The range of the contact, Van der Waals interaction is much shorter than the range of the DDI and its effect on the gas is therefore independent of the trapping geometry as opposed to the DDI.

resonances–for more details, see sections 3.2 and 2.3.4 respectively. Such magnetic field polarizes the atoms and defines a quantization axis for the whole system. If we take the polarization axis to be along the $\hat{z}$ direction, the dipole-dipole potential of equation 2.11 simplifies to

$$U_{\text{dip}} = \frac{C_{dd}}{4\pi} \frac{1 - 3\ \cos^2\theta}{r^3} \tag{2.12}$$

with θ being the angle between the dipoles ($\hat{z}$ direction) and the separation vector $\vec{r}$. Figure 2.4 shows the geometry of the interaction.

The DDI potential has several notable features. First, its strength and sign depend on the angle of approach of the interacting dipoles meaning it is *anisotropic*. Secondly, for a range of angles $0 < \theta < \theta_m$, the interaction is attractive. This is known as the *head-to-tail* attraction. For $\theta_m < \theta < \pi - \theta_m$, the potential is repulsive, which is referred to as *side-by-side* repulsion. At the so-called *magic* angle $\theta_m \approx 54.7°$, the interaction vanishes completely. The angle-dependent term in equation 2.12 ranges from -2 to 1 and so the attraction is twice as strong as the repulsion. Moreover, integrating the potential over all space gives zero, meaning that the energy of a homogeneous dipolar gas is unchanged by the DDI in the bulk and it is only affected by boundary effects. Consequently, the anisotropy of the DDI is responsible for the dependence of the gas properties on the dimensionality of the system [195]. This motivates our use of a homogeneous 'pancake' trap for probing interesting phases and effects [119], [152] in our dipolar quantum gas. The

attractive part of the DDI, on the other hand, governs the peculiarities of the excitation spectrum (e.g. roton minimum [108]) and can cause collapse and formation of self-bound states [196], [197].

Comparing the form of the DDI potential (equation 2.12) with the Van der Waals contact potential (equation 2.10) reveals that the DDI with its $1/r^3$ scaling is long-ranged compared to the aptly-named contact interactions that fall off as $1/r^6$. In fact, the classification of potentials as either long- or short-ranged is quite ambiguous, nuanced and generally depends on the dimensions of the embedding space. For a more comprehensive overview of this problem in the context of the DDI, see reference [91]. Here, we only note that from a thermodynamic point of view, one can classify a potential as long-ranged if the macroscopic properties of the gas associated with atom-atom interactions, such as the chemical potential, are intensive i.e. they depend on the total particle number rather than solely on the local density. Mathematically, it can be shown that potentials $U(r) \propto 1/r^n$ for which $\int U(r) d^N r$ converges, are short range. This is true in N dimensions if $n > N$ [198]. Consequently, according to this classification the contact interaction is short-ranged in 1D, 2D and 3D whereas the DDI is short-ranged in 1D and 2D and long-ranged in 3D. Lastly, from the point of view of ultracold collisions (see below), long-ranged potentials, including the DDI, contribute with higher order partial waves with $l > 0$ whereas short-ranged potentials only contribute with spherically symmetric s-waves with $l = 0$.

We close this section by discussing the tunability of the DDI. Just like for the contact interactions, it is possible to define a parameter that describes the strength of the DDI in analogy with the scattering length a_s. This parameter, called the dipolar length, is defined as $a_{dd} = m\mu_0\mu^2/12\pi\hbar^2 \propto C_{dd}$ and it follows naturally from considering the energy scale of the DDI as we will see in section 2.3.3. Unlike the scattering length, a_{dd} can't be tuned directly via Feshbach resonances. Furthermore, the value of μ is fixed by the ground state properties. Luckily, in section 2.4 we will show that the properties of a dipolar quantum gas emerge from a competition between the contact interactions and DDI and, as such, depend only on a dimensionless parameter $\varepsilon_{dd} = a_{dd}/a_s$. As a result, one can tune the dipolar nature of the gas by simply changing a_s e.g. via Feshbach resonances. However, this widely used approach comes with a few challenges. Firstly, the scattering length governs the particle collision rate and hence determines the efficiency of evaporative cooling (more on this in section 4.3). In order to achieve degeneracy, one therefore has to start in the high a_s regime in which the dipolar character of the gas is suppressed. Entering the dipolar regime then requires ramping the magnetic fields at the end of the evaporation sequence. It is consequently more difficult to directly probe the thermal to degenerate dipolar transition. Secondly, and more importantly, approaching a Feshbach resonance enhances three-body losses (detailed measurements of this effect in ^{166}Er are presented in chapter 5). As a result, entering the dipolar regime via lowering a_s often incurs a cost in atom number, making studying interesting high-density phases such as quantum droplets [114] difficult.

The impossibility of directly tuning C_{dd} (and hence a_{dd}) can be fortunately bypassed by rapidly changing the dipole orientation [158]. In this way, the potential of two interacting

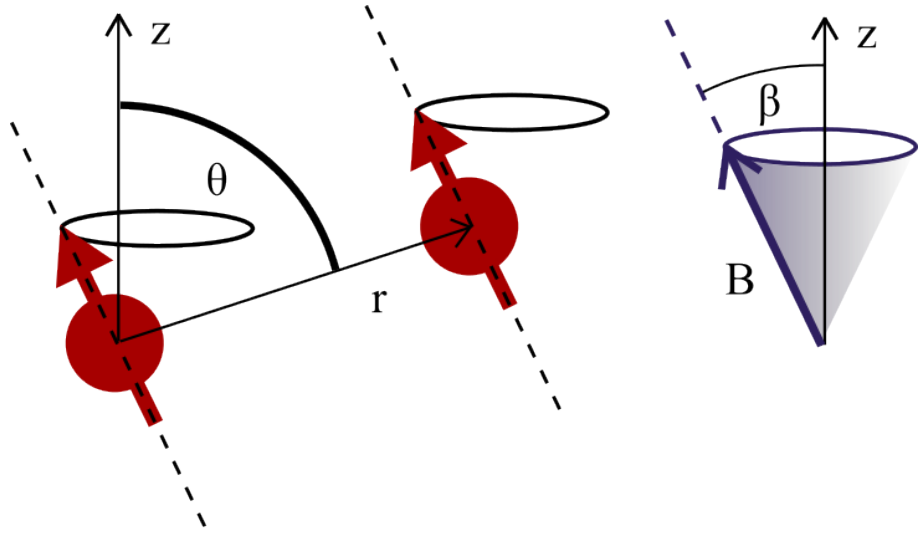


Figure 2.5: Controlling the DDI. The strength of the dipole-dipole interaction can be tuned directly without changing the s-wave scattering length a_s by quickly rotating the dipoles. If the polarizing field is precessing about an axis (z for clarity) at an angle β, the effective potential experienced by the two particles is modified by a factor of $(3\cos^2\beta - 1)/2$. Consequently, the DDI can be turned off or its sign reversed [158]. A set of coils was designed for the Oxford Er-K experiment to implement this technique [199].

particles (equation 2.12) is time averaged to give an effective $\tilde{C}_{dd}$. If the magnetic field rotates around the z axis at an angle β, the time averaged potential can be written as

$$U_{\text{dip}} = \frac{C_{dd}}{4\pi}\frac{1 - 3\ \cos^2\theta}{r^3}\ \frac{3\ \cos^2\beta - 1}{2}\ . \tag{2.13}$$

For $\beta = 0$, we recover the static field case of equation 2.12, as expected. As the field tilts away from the vertical axis, the averaged potential changes from repulsive to attractive. At $\beta = \beta_m \approx 54.7°$, the dipolar interaction vanishes irrespective of the relative position of the atoms. The relative geometry of the rotating field and dipoles is shown in figure 2.5. Equation 2.13 can also be understood as equation 2.12 with an effective dipolar coupling constant $\tilde{C}_{dd} = C_{dd}(3\cos^2\beta - 1)/2$. This means that the effective dipolar length $\tilde{a}_{dd} \propto \tilde{C}_{dd}$ can now be tuned by tilting the rotating field and the relative dipolar strength $\varepsilon_{dd} = \tilde{a}_{dd}/a_s$ can be varied independently of the scattering length and can even be made negative.

This technique is only possible because of separation of timescales. The rotating field needs to change much faster than the interparticle distance such that when averaging the DDI, we can assume r is constant. The typical timescales of the particle motion are on the order of the trapping frequencies and so we need $\omega_B \gg \bar{\omega}$. At the same time, we require the dipoles to be polarized along the rotating B field at all times i.e. the dipoles need to *adiabatically* follow the field. This only happens if the field changes much slower than the Larmor frequency $\omega_L = eB/m \gg \omega_B$ which is the characteristic frequency of dipole precession around an external field [79]. For a typical field strength of 1 G, the Larmor frequency equals $\omega_L \approx 18$ MHz. In an experiment, the field is generally rotated by applying an out-of-phase voltage wave to two Helmholtz pairs that are oriented perpendicular

to each other. The lower bound on the rotation frequency together with Feshbach requirements on the field magnitude make for a tricky set of constraints and so the coils at hand can't be neither too big nor too small. A suitable set of 'fast' and 'slow' coils was designed and manufactured for our experiment that will allow us to simultaneously tune the DDI and reach magnetic fields of up to 300 G in the science cell part of the experiment–for more details, see sections 3.1 and chapter 9.

This concludes our discussion of atomic interactions in dipolar gases. We have seen that on top of a mostly isotropic, short-ranged contact potential, there exists an anisotropic, long-ranged one due to the mutual magnetic dipole-dipole interactions. In the spirit of ultracold atom experiments, both of these can be tuned together, or independently, to change the properties of the gas. The effects of both types of interactions on the gas properties will be further elaborated on below when we discuss ultracold scattering and, later, the properties of dipolar Bose-Einstein condensates.

2.3.3 Ultracold scattering

Interactions between atoms greatly enrich the observable physics of ultracold gas systems. In the degenerate regime, they determine the shape and chemical potential of the condensate as well as its excitation spectrum and the dynamics of its time evolution. They also provide a direct link to other quantum systems, e.g. polarons [200], and are therefore at the heart of quantum simulation. As we will see below when we discuss the degenerate regime in section 2.4, interactions are also responsible for the non-linearity of the Gross-Pitaevskii equation and hence for phenomena such as solitons [201] or superfluid quantum vortices [202].

More fundamentally, interactions facilitate collisions between atoms. During a collision, energy is redistributed between particles and their external as well as internal state can change. Consequently, collisions determine the propagation speed of perturbations, the thermalization rate of the gas which is essential for evaporative cooling (see section 4.3) as well as the timescale of decoherence of quantum information in the system. Furthermore, inelastic collisions can lead to detrimental losses and heating by allowing for the flow of energy between the internal energy levels and the external motional states of atoms–chapter 5 discusses this in detail.

Quantum theory of scattering is a complicated, daunting topic with results and methods that seem rather unintuitive. This spans from the fundamental conflict between using the language of states and energy levels on one hand, and the language of discrete, time-dependent processes on the other, to describe the same phenomenon. Numerous books have been written on this topic and we point the reader to references [79], [203] for a comprehensive overview of quantum scattering theory. Here we only outline the main results and assumptions in order to show how this theory leads to a mean-field picture in which collisions contribute to a short-ranged interaction potential that is, rather remarkably, only described by a single parameter–the s-wave scattering length a_s. We will also discuss how the presence of the anisotropic, long-ranged DDI contributes to this picture.

s-wave scattering

Let's start by looking at a collision of two particles of equal mass interacting via a spherically symmetric potential $V(r)$ in a dilute gas. The diluteness condition allows us to neglect any higher order scattering events and it can be more rigorously formulated by requiring that the average interparticle spacing $d = n^{-1/3}$ is much larger than the range of the interaction potential r_V. The typical magnitude of r_V is $r_V \approx 10^2\,\mathrm{a}_0$ where a_0 is the Bohr radius[3] whilst the typical densities in ultracold gas experiments are on the order of $n \approx 10^{20}\,\mathrm{m}^{-3}$ and so the particle spacing $d \approx 4 \times 10^3\,\mathrm{a}_0 \gg r_V$ [204]. The assumption of spherical symmetry of the potential $V(r)$ is, strictly speaking, not necessary but it greatly simplifies some steps in the following calculations and, more importantly, the most common form of interactions–the dispersive contact ones (see section 2.3.1)–are predominantly spherically symmetric. Furthermore, even though we have seen that the contact interactions in erbium display anisotropy (see section 2.3.1), it turns out that the geometrical details of the short-ranged, contact potential are unimportant and the scattering still has a spherically symmetric, s-wave character [194].

Formally, the Hamiltonian of two interacting particles can be separated into the center-of-mass motion and the interaction part which is equivalent to a single particle of reduced mass $m_r = m_1 m_2/(m_1 + m_2)$ scattering from a stationary potential $V(r)$. Solving the interaction part of the Hamiltonian is the goal of scattering theory. We begin by looking for an eigenstate of the scattering Hamiltonian

$$(\hat{H}_k + \hat{V})|\psi\rangle = E_k|\psi\rangle \tag{2.14}$$

where $\hat{H}_k$ is the free particle Hamiltonian, $\hat{V}$ is the scattering potential operator and E_k is the energy of the free particle state $|\mathbf{k}\rangle$ such that $\hat{H}_k|\mathbf{k}\rangle = E_k|\mathbf{k}\rangle$. We look for solutions $|\psi\rangle$ such that $|\psi\rangle \to |\mathbf{k}\rangle$ as $\hat{V} \to 0$. Here we have implicitly assumed that the scattering is elastic and the incoming plane wave $|\mathbf{k}\rangle$ gets scattered into the state $|\psi\rangle$ by the potential without changing its energy.

For local potentials and at large distances, a self-consistent solution to equation 2.14 know as the Lippman-Schwinger equation can be found in the position basis which has the following form:

$$\begin{aligned}\langle \mathbf{x}|\psi\rangle &= \langle \mathbf{x}|\mathbf{k}\rangle - \frac{1}{4\pi}\frac{2m_r}{\hbar^2}\frac{e^{ikr}}{r}\int d^3x' e^{-i\mathbf{k}'\cdot\mathbf{x}'} V(\mathbf{x}')\langle \mathbf{x}'|\psi\rangle \\ &= \langle \mathbf{x}|\mathbf{k}\rangle + \frac{e^{ikr}}{r} f(\mathbf{k},\mathbf{k}')\ .\end{aligned} \tag{2.15}$$

We can see that the scattered wave consists of the incoming plane wave at wave vector $\mathbf{k}$ and an outgoing spherical wave modulated by a direction-dependent amplitude $f(\mathbf{k},\mathbf{k}')$ with $\mathbf{k}'$ being a vector of magnitude k that points in the direction of observation, $\mathbf{x}$. See figure 2.6 for an illustration of the scattering geometry. The self-consistency of equation 2.15 makes obtaining an explicit form of $f(\mathbf{k},\mathbf{k}')$ quite difficult. However, a few useful conclusions can still be drawn. Firstly, using the probability flux $\mathbf{j} = \frac{i\hbar}{2m}(\phi\nabla\phi^* - \phi^*\nabla\phi)$

[3] Bohr radius is defined as $a_0 = 4\pi\varepsilon_0\hbar/me^2 \approx 5.29 \times 10^{-11}\,\mathrm{m}$

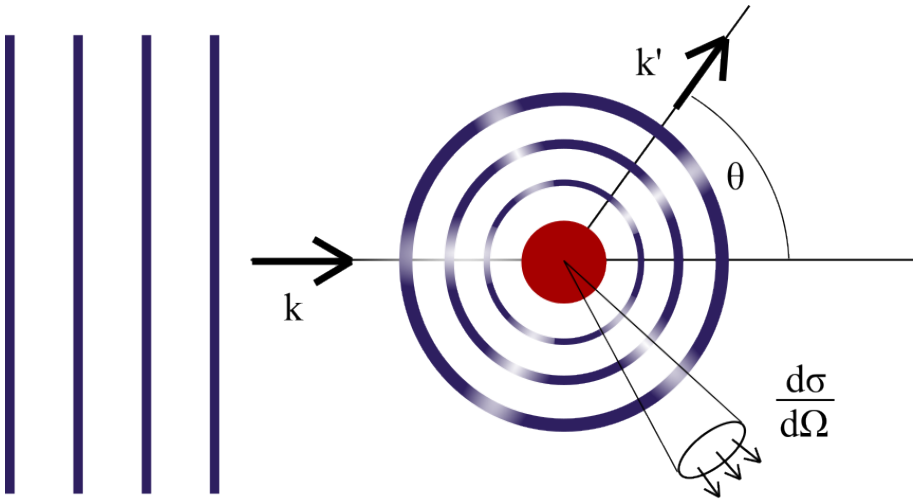


Figure 2.6: Scattering geometry. The scattered wave consists of the incoming plane wave of wave-vector $\mathbf{k}$ and the outgoing spherical waves modulated by the scattering amplitude $f(\mathbf{k}, \mathbf{k}')$. The square modulus of the scattering amplitude $|f(\mathbf{k}, \mathbf{k}')|^2$ can be interpreted as the differential scattering cross section $\frac{d\sigma}{d\Omega}$. For spherically symmetric potential, it is only the relative angle of $\mathbf{k}$ and $\mathbf{k}'$ denoted by θ that enters the expression for the scattering amplitude.

associated with wave-function $\phi(\mathbf{x})$, we can calculate the differential scattering cross-section defined as

$$\frac{d\sigma}{d\Omega} d\Omega = \frac{\text{flux scattered into solid angle } d\Omega}{\text{incoming flux}} = |f(\mathbf{k}, \mathbf{k}')|^2 d\Omega \ , \tag{2.16}$$

giving the amplitude f a physical meaning. Secondly, by defining the operator $\hat{T}$ such that $\hat{V}|\psi\rangle = \hat{T}|\mathbf{k}\rangle$, we can write the scattering amplitude as

$$\begin{aligned} f(\mathbf{k}, \mathbf{k}') &= -\frac{1}{4\pi} \frac{2m_r}{\hbar^2} \langle \mathbf{k}' | \hat{T} | \mathbf{k} \rangle \\ \hat{T} &= \hat{V} + \hat{V} \frac{1}{E - \hat{H}_k} \hat{V} + \hat{V} \frac{1}{E - \hat{H}_k} \hat{V} \frac{1}{E - \hat{H}_k} \hat{V} \ ... \end{aligned} \tag{2.17}$$

where the operator $\hat{T}$ has an iterative expansion in powers of $\hat{V}$. The origin of this recursion can also be seen by repeatedly re-inserting the expression for $\langle \mathbf{x}|\psi\rangle$ into the integral of equation 2.15. This might not seem that helpful because we replaced one problem of self-consistency with another problem of infinite recursion. However, if the potential is weak, we can replace $\hat{T}$ with $\hat{V}$ to first order. This is called the Born approximation. We immediately see that doing so simplifies $f(\mathbf{k}, \mathbf{k}')$ to a Fourier transform of the interaction potential. Furthermore, for spherically symmetric potentials, $f = f(\theta)$ is real and only depends on the angle θ between the incoming plane wave and the scattering direction (see figure 2.6). Notably, in the case of low energy[4] scattering for which $e^{i\mathbf{k}\cdot\mathbf{r}} \approx 1$, the scattering amplitude is independent of θ and tends to a constant value. We will keep this in mind when we discuss the concept of scattering length.

[4]This limit is usually defined in terms of the interaction potential range r_V as $E \ll \frac{\hbar^2}{m r_V^2}$.

Although the Born approximation is useful for understanding the basic physics of scattering, it might be hard to justify its use a-priori, given that interaction potentials cannot be considered weak at short distances. To make progress and ascertain more information about the scattering amplitude $f(\mathbf{k}, \mathbf{k}')$ in its most general form represented by equation 2.17, it is helpful to change basis. For problems with axial symmetry such as the one at hand, the spherical waves defined as the eigenstates of the angular momentum operators $\hat{L}^2$ and $\hat{L}_z$ with a definite energy E are naturally suitable. We denote them $|E, l, m\rangle$ such that $\hat{H}_k|E, l, m\rangle = E|E, l, m\rangle$ and the quantum numbers l and m have the usual meaning. Applying this transformation to equation 2.17 gives

$$\begin{aligned} f(\mathbf{k}, \mathbf{k}') &= -\frac{1}{4\pi}\frac{2m_r}{\hbar^2}\int_{E,E'}\sum_{l,l'}\sum_{m,m'}\langle\mathbf{k}'|E,l,m\rangle\langle E,l,m|\hat{T}|E',l',m'\rangle\langle E',l',m'|\mathbf{k}\rangle \\ &= -\frac{4\pi^2}{k}\sum_{l}\sum_{m}T_l(E_k)Y_l^m(\hat{\mathbf{k}}')Y_l^{*m}(\hat{\mathbf{k}}) \\ &= \sum_{l=0}^{\infty}(2l+1)f_l(k)P_l(\cos\ \theta) \end{aligned} \tag{2.18}$$

where going from the first to the second line we used

$$\langle E, l, m|\hat{T}|E', l', m'\rangle = T_l(E)\delta(E - E')\delta_{ll'}\delta_{mm'} \tag{2.19}$$

which follows from the Wigner-Eckart theorem and the fact that a spherically symmetric potential $\hat{V}(r)$, and consequently the Hamiltonian and the operator $\hat{T}$, commute with the angular momentum operators $\hat{L}^2$ and $\hat{L}_z$. Going from the second to the third line, we assumed without the loss of generality that $\mathbf{k}$ is pointing along the z axis, making only the $m = 0$ terms non-zero, and we used Legendre polynomials $P_l(y)$ to express the spherical harmonics Y_l^0. We also defined a new quantity $f_l(k) \equiv -\pi T_l(E_k)/k$.

At this point, it is useful to write out the whole scattered wave function in the new basis:

$$\langle\mathbf{x}|\psi\rangle = \sum_{l=0}^{\infty}(2l+1)\frac{P_l(\cos\ \theta)}{2ik}\left[(1+2ikf_l(k))\frac{e^{ikr}}{r} - \frac{e^{-i(kr-l\pi)}}{r}\right]. \tag{2.20}$$

This form makes it clear that the scattered wave consists of an incoming and outgoing spherical wave, the outgoing one only differing by a factor $S_l(k) = 1 + 2ikf_l(k)$. Slightly unintuitively, $|\psi\rangle$ is a stationary state of the system and so its probability density $|\psi(\mathbf{x})|^2$ doesn't change in time. Consequently, the probability flux of the incoming and outgoing spherical waves should be equal. Furthermore, due to conservation of angular momentum, this is independently true for each partial wave l. The equality of fluxes amounts to a condition on the factor $|S_l(k)| = 1$ and so we can can set $S_l(k) = e^{2i\delta_l(k)}$ with $\delta_l(k)$ a real parameter and derive a concise expression for the scattering amplitude and the total

scattering cross section

$$f(\mathbf{k},\mathbf{k}') = \frac{1}{k}\sum_{l=0}^{\infty}(2l+1)e^{i\delta_l}\sin\delta_l P_l(\cos\ \theta) \tag{2.21}$$

$$\sigma_{\text{tot}} = \int \frac{d\sigma}{d\Omega}d\Omega = \frac{4\pi}{k^2}\sum_{l=0}^{\infty}(2l+1)\sin^2\delta_l \tag{2.22}$$

which now only depend on a set of real parameters $\delta_l(k)$.

The exact values of these phases depend on the scattering potential and calculating them is often complicated. The general prescription starts by looking for the full solution of the Schrödinger equation both within and outside of the range of the scattering potential. The solution outside is potential-free and is therefore given by a linear combination of spherical waves $\langle\mathbf{x}|E,l,m\rangle$. This should also be equivalent to expression 2.20 valid for large r, providing a link between the phase shifts δ_l and the coefficients of $\langle\mathbf{x}|E,l,m\rangle$. Solving the Schrödinger equation within the range of the potential, either analytically or numerically, with the boundary condition $\psi(r=0)=0$ and matching it to the far-field solution determines the values of $\delta_l(k)$.

This procedure is, in most cases, not analytically solvable. However, it is possible [203] to derive a simple scaling relation in the low energy regime for which $kr_V \ll 1$ for potentials that scale as $1/r^n$. Under these conditions, $\delta_l \propto k^{2l+1}$ for $l < (n-3)/2$ and $\delta_l \propto k^{n-2}$ otherwise. The contact interaction has $n=6$ and so the s-wave ($l=0$) scattering channel dominates at low k. More quantitatively, we can look for the solution of the Schrödinger equation in the form $\psi(\mathbf{r}) = \sum_{m,l} R_l(r)Y_m^l$. Using $R_l(r) = u_l(r)/r$, each partial wave radial wave function has to satisfy

$$\frac{d^2u_l}{dr^2} + \left(k^2 - \frac{2m_r}{\hbar^2}V - \frac{l(l+1)}{r^2}\right)u_l = 0\ , \tag{2.23}$$

which is a 1D, Schrödinger-like equation with an effective potential $V_{\text{eff}} = V + l(l+1)/r^2$ with a centrifugal barrier term for $l > 0$–see figure 2.7. Focusing on the $l=0$ channel, we can take the low energy limit outside of the range of the potential such that $k \to 0$ and $V \to 0$. Equation 2.23 then has a simple solution of the form

$$u_0(r) = C(r-a)\ . \tag{2.24}$$

Comparing this with the $l=0$ term in expansion 2.20 which reads

$$u_0(r) = (1/k)e^{i\delta_0}\sin(kr+\delta_0), \tag{2.25}$$

we immediately identify

$$\frac{\delta_0}{k} = -a\ . \tag{2.26}$$

Because of the $\delta_l \propto k^{2l+1}$ scaling, only the s-wave channel contributes non-negligibly in

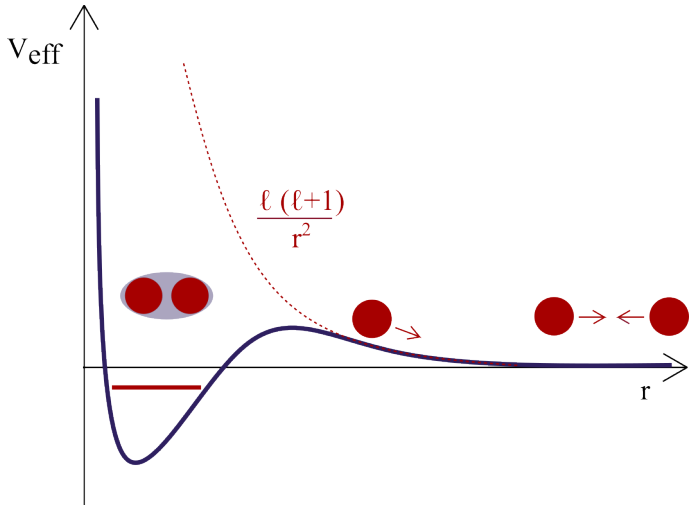


Figure 2.7: Effective scattering potential. The scattering potential experienced by each channel as given by equation 2.23. The centrifugal barrier prevents the atoms from fully experiencing the scattering potential $V(\mathbf{r})$. The minimum of the effective potential can support a bound state. If the energy of such bound state approaches the entrance channel energy, a scattering resonance can occur–for more detail see section 2.3.4

.

the low energy limit. The total scattering cross-section is then

$$\sigma_{\text{tot}} = \frac{4\pi}{k^2}\sum_{l=0}^{\infty}(2l+1)\sin^2\delta_l \approx 4\pi\frac{\delta_0^2}{k^2} = 4\pi a^2 \ . \tag{2.27}$$

Interestingly, this form is identical to the classical scattering cross section of hard sphere particles of radii a. However, we note that in real systems, a is much larger than the typical atomic size, reflecting the quantum nature of atomic scattering. The constant a is known as the s-wave scattering length. From now on, we will denote it as a_s to distinguish it from the dipolar scattering length a_{dd} which will be introduced in the next section. For ^{166}Er, the typical value is $a_s \approx 80\,\text{a}_0$ [153] which is on one hand much larger than the atomic size but also much smaller than the interparticle spacing, justifying our assumption of diluteness of the gas.

Remarkably, low energy scattering is isotropic and can be described by a single parameter a_s. This parameter does, indeed, depend on the form of the scattering potential but the detailed knowledge of it is no longer necessary and experimental determination of a_s (e.g. via cross-dimensional thermalization [153]) is all that is needed to fully understand the scattering of the species at hand. This result should be compared with the Born approximation discussed above which also predicts a single parameter

$$a_s = \frac{m_r}{2\pi\hbar^2}\int V(r)d^3r \tag{2.28}$$

governing the scattering but which, unlike our approach, operates withing the framework of perturbation theory and assumes V is small. The domination of the s-wave channel and the resulting isotropy of scattering can be partially understood by considering the

centrifugal term $l(l+1)/r^2$ in equation 2.23 which represents a long-ranged repulsive barrier for incoming channels with $l > 0$. Higher partial waves are therefore repelled from the origin before experiencing the scattering potential and don't contribute to the scattering process.

Clearly, there is an infinite number of potentials V that correspond to the same scattering length a_s and that exhibit the same low-energy scattering behaviour. We are therefore free to construct and use a new pseudopotential $U(\mathbf{r})$ which is much simpler to work with as long as it gives the same scattering length as the original potential. A natural choice is the zero-range contact interaction

$$U(\mathbf{r}) = g_s\delta(\mathbf{r}) = \frac{2\pi\hbar^2 a_s}{m_r}\delta(\mathbf{r}) \tag{2.29}$$

which reproduces correctly the long-range behaviour of the scattered wave function $\langle\mathbf{x}|\psi\rangle$ when substituted into the Schrödinger equation and which gives the correct scattering length under the Born approximation. We will appreciate the usefulness of this functional form when we discuss the properties of Bose-Einstein condensates in section 2.4 and for now we only note that $a_s < 0$ clearly corresponds to an attractive potential whereas $a_s > 0$ represents a repulsive one.

An important consideration was omitted when deriving the expression for the scattering cross section 2.27. Namely the fact that the scattered state $|\psi\rangle$ needs to be symmetrized (anti-symmetrized) for identical bosons (fermions). Symmetrizing $|\psi\rangle$ leads to an adjusted scattering amplitude

$$f(\mathbf{k},\mathbf{k}') \to \frac{f(\mathbf{k},\mathbf{k}') \pm f(\mathbf{k},-\mathbf{k}')}{\sqrt{2}} \ , \tag{2.30}$$

where the plus (minus) sign applies to bosons (fermions). Due to the symmetry of Legendre polynomials, only even (odd) terms contribute in the expansion 2.21 and so in the low energy limit, the scattering cross section for bosons is

$$\sigma_B = 8\pi a_s^2 \tag{2.31}$$

and for fermions

$$\sigma_F = 0 \ . \tag{2.32}$$

This is a striking conclusion because not only does quantum statistics enhance scattering of bosons by a factor of 2 but, more shockingly, it completely suppresses scattering of fermions. The absence of scattering in ultracold fermions is one of the main hurdles of reaching degeneracy in Fermi gases because it prohibits the use of evaporative cooling which requires collisions of atoms for thermalization and subsequent cooling. In the next section, we will see how the presence of the DDI bypasses this by allowing for low-energy scattering of higher order partial waves.

Dipolar scattering

So far, we have based our understanding of scattering on the assumption that the scattering potential is spherically symmetric. Even though this is commonly true for contact interactions e.g. Wan der Waals dispersive forces, it doesn't fully describe the scattering of dipolar atoms such as erbium. As previously discussed, the dipole-dipole interaction (DDI) is anisotropic and scales as $1/r^3$ with the distance r between the dipoles. Using the spherical wave formalism outlined in the previous section, we can still express the total scattering cross section as a sum of contributions from all the scattering channels. However, this time the anisotropy of the potential couples different scattering channels and so the scattering matrix T is no longer diagonal in l, m_l:

$$\sigma = \frac{4\pi}{k^2} \sum_{l,l'} \sum_{m,m'} |T_{lm}^{l'm'}|^2 \tag{2.33}$$

This makes calculating the exact value challenging [205], [206]. Fortunately, in the limit of low energies, the diagonal elements are still $T_{lm} \propto \delta_l(k)$. Recalling that in this regime, $\delta_l \propto k^{2l+1}$ for $l < (n-3)/2$ and $\delta_l \propto k^{n-2}$ otherwise [203], [204], we conclude that for the DDI, which has $n = 3$, all the phase shifts $\delta_l \propto k$ and so all collision channels contribute to the total scattering cross section. Consequently, the scattering cross-section for fermions no longer vanishes as $k \to 0$. This has profound implications for cooling of dipolar fermionic species as the presence of dipolar scattering enables the use of evaporative cooling to reach degeneracy [207].

The low energy regime also justifies the use of Born approximation because, due to the centrifugal barrier, incoming particles experience only a weak perturbation from the scattering potential [208]. Using this approximation, it is possible to derive an exact expression for the scattering cross-section of bosons and fermions [209], [210]

$$\sigma_B = \frac{8\pi}{5} a_{dd}^2 + 8\pi a_s^2 \tag{2.34}$$

$$\sigma_F = \frac{24\pi}{5} a_{dd}^2 \tag{2.35}$$

where we defined the dipolar length a_{dd} as

$$a_{dd} = \frac{m\mu_0\mu^2}{12\pi\hbar^2} \ . \tag{2.36}$$

This definition follows from a simple comparison of the typical dipolar energy $E_{dd} \propto C_{dd}/a_{dd}^3$ and the kinetic energy scale given by the uncertainty principle $E_k = \Delta p^2/2m = (\hbar/a_{dd})^2/2m$. The numerical prefactor was chosen such that a three-dimensional, homogeneous, dipolar condensate becomes unstable with respect to local density perturbations for $a_s < a_{dd}$ or equivalently for $\varepsilon_{dd} = a_{dd}/a_s > 1$ [196]. The significance of the dimensionless parameter ε_{dd} as a measure of the dipolar character of the given species will become clear once we discuss the properties of dipolar condensates in section 2.4. For ^{166}Er, the dipolar length $a_{dd} \approx 66\,\mathrm{a_0}$, and so even away from a Feshbach resonance $\varepsilon_{dd} \sim \mathcal{O}(1)$. In contrast,

^{52}Cr with $\mu_{\mathrm{Cr}} = 6\mu_B$, comparable to the magnetic moment of erbium, has $\varepsilon_{dd} \sim \mathcal{O}(0.1)$ which highlights the importance of atomic mass in dipolar physics.

Another remarkable feature of dipolar scattering is its universality at low energies [211]. Where a_s depends on the details of the scattering potential, a_{dd} only depends on the magnitude of the magnetic dipole and the mass of the particles. As a result, completely different dipolar systems will display the same scattering properties as long as they have the same product of the particle mass and the dipolar coupling constant C_{dd}. In fact, dipolar scattering shows some universal features even in the intermediate temperature range between the ultracold and semi-classical regimes [209].

As we did with the contact interactions, it is possible to formulate a pseudopotential for the atom-atom interaction in the presence of the DDI which is easier to work with but leads to the same physics [212]–[214]. Interestingly, the DDI not only introduces an anisotropic, long-range term but it also contributes to the hard-sphere like contact potential, adjusting the value of the s-wave scattering length [215], [216]. The full pseudopotential reads as

$$\begin{aligned} U(\mathbf{r}) &= \frac{4\pi\hbar^2}{m}\left(\tilde{a}_s\delta(\mathbf{r}) + \frac{3}{4\pi}a_{dd}\frac{1-3\cos^2\theta}{r^3}\right) \\ &= g\delta(\mathbf{r}) + U_{dd}(\mathbf{r}) \end{aligned} \tag{2.37}$$

where we used tilde to explicitly denote that the s-wave scattering length now has a contribution from both the contact, Van der Waals interaction and the DDI. From now on, we will just use a_s to denote the full scattering length including all contributions.

2.3.4 Feshbach resonances

The central role of scattering length in ultracold physics is further reinforced by the fact that its sign as well as magnitude can be tuned using scattering resonances. One can thus turn a weakly interacting gas into a strongly interacting one, opening up avenues for studying the BEC-BCS crossover [33], [35], [87] or the unitary regime [83], [84]. Remarkably, it is also possible to change the nature of the interaction from repulsive to attractive (and vice versa), allowing one to induce instability and collapse in Bose-Einstein condensates [85]. Furthermore, resonant behaviour can also be utilized to facilitate formation of weakly bound, diatomic molecules in highly excited states [94] which can be later transferred to their rovibronic ground state using adiabatic passage techniques [217], [218]. It is this tunability and versatility that makes ultracold atom experiments excellent candidates for quantum simulation.

Phenomenologically, scattering resonances occur when the energy of a scattering entrance channel is degenerate with the energy of a bound state of the system that is somehow coupled to the entrance channel. Under these circumstances, the channel's contribution to the total scattering cross section is greatly enhanced. An example of such process is the so-called *shape resonance* [79] in which, for a given channel l, there exists a resonant bound state in the effective potential of the channel (see equation 2.23 and figure 2.7).

An even more important example is the Fano-Feshbach resonance [219], or Feshbach resonance (FR) for short, which revolutionized the field of ultracold atoms. The theory of

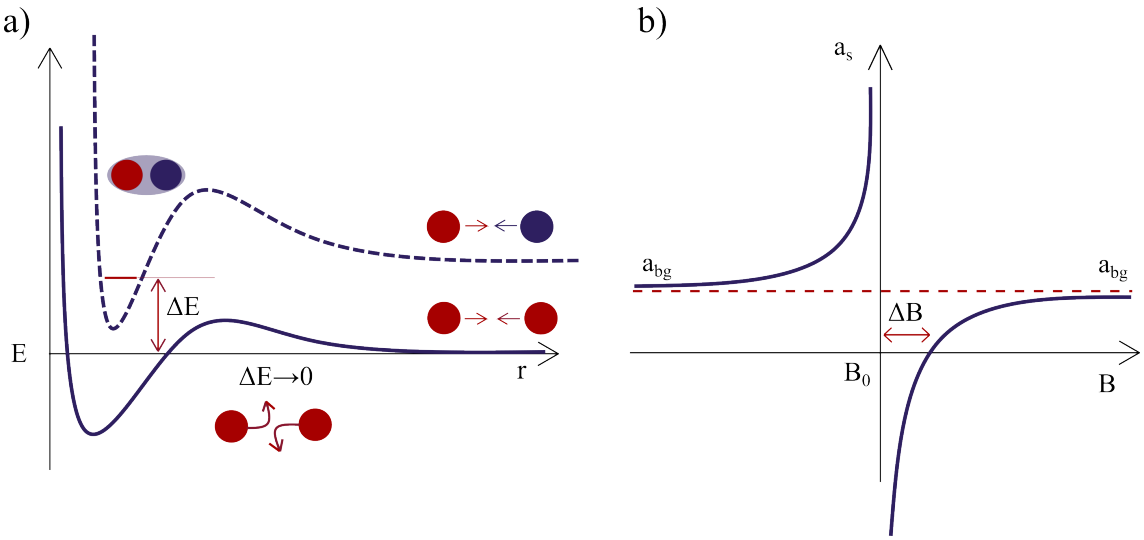


Figure 2.8: Feshbach resonance. a) Mechanism of a Feshbach resonance–when the energy of a bound state in a closed channel becomes comparable to the energy E of the entrance channel, a Feshbach resonance occurs which greatly enhances the scattering length of the interacting atoms. The energy difference ΔE can be tuned by applying an external magnetic field provided that the two channels involved in the process have different magnetic moment. b) Scattering length vs B. The scattering length diverges and changes sign in the vicinity of a FR. The width of the resonance ΔB is determined by the zero crossing whereas the background value corresponds to fields far away from the resonance.

FRs was developed by Fano and Feshbach in late 1950s [220], [221] and their first experimental detection in nuclear physics followed in 1970s [222], [223]. FRs gained considerable traction after the pioneering experiments with Bose-Einstein condensates in late 1990s demonstrated the possibility of tuning the interaction strength using FRs [82] by simply applying an external magnetic field. Since then, FRs have become the most widely used and sought after tool for tuning the atom-atom interaction in ultracold experiments.

As a concept, FRs appear in many areas of physics ranging from nuclear to molecular and chemical physics [219]. The basic mechanism can be described by considering atoms colliding with energy E in one of the energetically allowed channels i.e. open channels. Let there also be another channel which is energetically not allowed i.e. a closed channel. This can correspond to scattering of the same atoms but in a different internal state e.g. spin. In general, the effective potential of these two channels is different because the atoms in different internal states don't interact identically. A Feshbach resonance then occurs if there exists a bound state in the closed channel with energy comparable to E–see figure 2.8a.

Coupling of the open channel to the virtual bound state greatly enhances the scattering rate of that channel and hence the scattering length a_s. What makes this phenomenon so useful in experiments is the fact that internal energy levels of atoms can be quantum mechanically tuned by applying electric (e.g. Stark shift) or magnetic fields (e.g. Zeeman shift). If the two coupled channels respond differently to the applied field, for instance by having a different polarizability or magnetic moment, one can tune their relative energy

separation ΔE and hence the resonance strength by smoothly varying the field magnitude. The most common way of exploiting this is by simply superimposing a homogeneous magnetic field (using just two coils in the Helmholtz configuration) onto the interacting atoms. In that case, the scattering length around the resonance can be shown to behave as [219], [224]

$$a_s(B) = a_{bg}\left(1 - \frac{\Delta B}{B - B_0}\right) \tag{2.38}$$

where a_{bg} is the background value far away from the resonance, ΔB is the resonance width defined by the zero crossing (see figure 2.8b) and B_0 is the position of the resonance that satisfies the resonance condition $B_0\delta\mu = \Delta E$ for the differential magnetic moment of the open and closed channel $\delta\mu$. Figure 2.8b shows the typical behaviour of a_s around a Feshbach resonance. Notably, by sweeping through a resonance it is possible to flip the sign of the interaction as well as enter the unitary regime in which a_s diverges. In the presence of multiple resonances, the scattering length can be approximated by

$$a_s(B) = a_{bg}\prod_i\left(1 - \frac{\Delta B_i}{B - B_{0,i}}\right) \ . \tag{2.39}$$

It is worth mentioning that although magnetic fields are the standard for tuning the scattering length, it is also possible to induce resonances using optical fields [225], [226] which allow for a faster and more local control of the scattering length. We quantitatively describe this effect in chapter 5 when we investigate new resonant features found in ^{166}Er.

In order for a resonance to exist, there must be a bound state and coupling between it and the entrance channel. In case of shape resonances, the state is a meta-stable state trapped in the minimum of the effective potential of the same entrance channel. The coupling is then facilitated by tunneling between the asymptotic, far-field solution and this bound state. For Feshbach resonances, the picture is a bit more complicated because the bound state doesn't come from the same entrance scattering channel but from an entirely different closed channel. Depending on the complexity of the internal states of the interacting atoms, the number of such closed channels and the bound states supported by them can be large. This makes predicting the position of Feshbach resonances difficult and species-dependent, emphasizing the importance of experimental measurements.

For atoms with relatively simple electronic structure such as alkalis, where the bound states and their couplings arise from the hyperfine interaction, the methods for calculating the Feshbach spectrum are well established [227], [228]. In the case of lanthanides and their complex submerged shell structure, the calculations are more complicated. Taking bosonic erbium as an example, the hyperfine structure is missing, but due to the long-range nature of the DDI (see section 2.3.3), all higher-order partial waves contribute to low energy scattering. The anisotropy of both the DDI and the contact, Van der Waals interaction can then couple different rotational states l [229], [230], resulting in a very rich Feshbach spectrum [192]. It was shown that more than 40 channels need to be considered in order to reproduce the density of the Feshbach spectrum of magnetic atoms [155], demonstrating the complexity of the computational task.

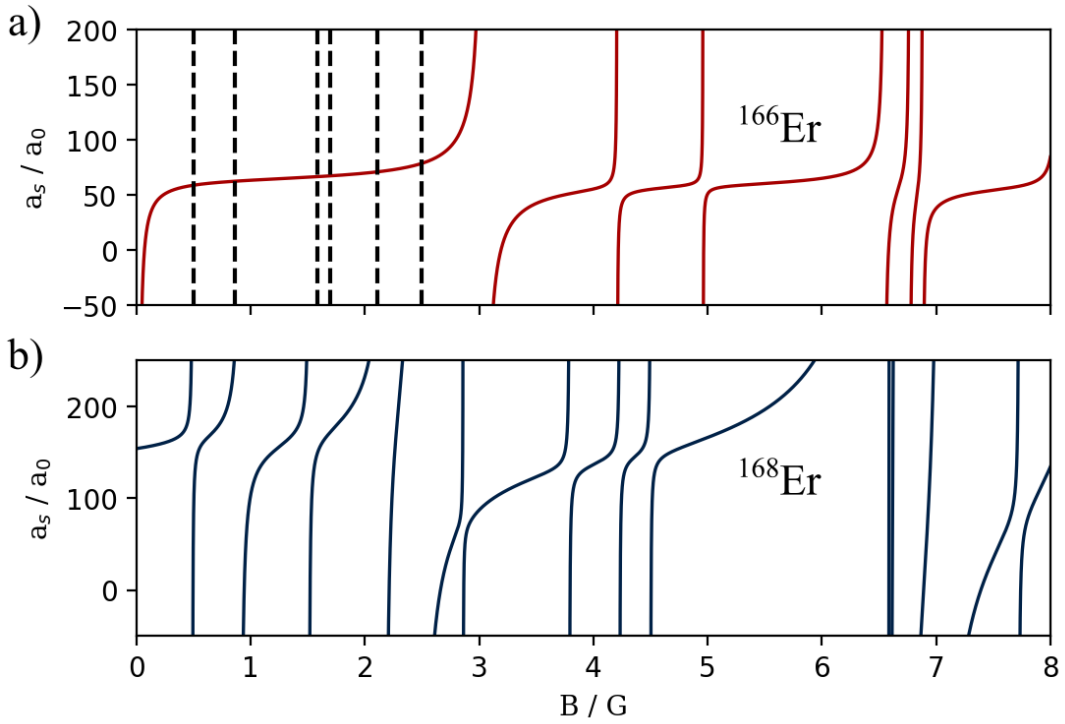


Figure 2.9: FRs in ^{166}Er (a) **and ^{168}Er** (b). The FR spectrum is dense due to the anisotropy of the DDI and shows numerous prominent features below 8 G. The positions of newly discovered features in ^{166}Er up to 4 G which are presented in chapter 5 are indicated by vertical dashed lines. Calculations were based on data from [153] and [155].

The experimental signature of a FR is usually observed as either an anomaly in the thermalization rate of the atomic cloud [210] or, more commonly, a pronounced increase in atomic loss, although other direct techniques of measuring a_s also exist [231]. Previous measurements of the Feshbach spectrum of ^{166}Er revealed a large number of resonances between 0 and 8 G [153] and beyond [155]. Similar results were also obtained for dysprosium [232]. The density of FRs in lanthanides $\approx 1\,\mathrm{G}^{-1}$ should be directly compared to that of alkalis $\approx 0.01\,\mathrm{G}^{-1}$, demonstrating the unique influence of the DDI on the properties of dipolar, quantum gases. Figure 2.9 shows the Feshbach spectrum of ^{166}Er and ^{168}Er based on the data from [153].

We conclude this section by noting that although Feshbach resonances are an extremely useful tool for tuning the s-wave scattering length a_s, they also enhance detrimental three-body losses. In other words, the tunability comes at a price. It can be shown [78] that the three-body loss coefficient L_3 scales as $L_3 \propto a_s^4$, and so interesting regimes are, in general, limited by the lifetime of the gas. In chapter 5, we present our measurement of the three-body loss in ^{166}Er and we identify several new unreported features that are narrow and show a strong temperature dependence. These features are also shown in figure 2.9.

2.4 Dipolar Bose-Einstein condensates

When a gas of particles is cooled to sufficiently low temperatures ($\approx 1 \times 10^{-7}\,\mathrm{K}$ in our Er system), their individual quantum character is no longer statistically suppressed because

populations of individual quantum states approach unity. As a result, large ensembles of particles start to display collective, coherent properties on a macroscopic scale. This quantum degenerate regime therefore offers an unprecedented view into the world of many-body quantum physics. The work presented here, and the Oxford Er-K experiment in general, aims to study the degenerate phases of bosonic ^{166}Er. This section will therefore focus on the phenomenon of Bose-Einstein condensation in dipolar gases. We begin by outlining the statistical origin of condensation and by deriving simple expressions governing its onset. We then go on to introduce the mathematical language used to describe the physics of dipolar condensates. Lastly, we present some of the main theoretical results and predictions, paying special attention to the role the dipole-dipole interaction (DDI) plays in influencing the stability and ground state properties of dipolar condensates.

Extensive literature has been written on the topic of Bose-Einstein condensates [77], [195], [204], [233]. In the following discussion, we mainly rely on the references [77], [204]. For readers interested in degenerate Fermi gases, we recommend references [234], [235].

2.4.1 Thermodynamics of non-interacting BECs

We have talked at length about the atomic interactions which are the main driving force behind many interesting phenomena. However, Bose-Einstein condensation itself is a process driven purely by quantum statistics and, as such, emerges from theory of non-interacting gases (although condensation in real systems is facilitated by interactions through thermalization; see our discussion of evaporative cooling in section 4.3).

We therefore start by considering a gas of non-interacting, bosonic particles moving in a general potential $U(\mathbf{r})$. The single-particle Hamiltonian $\hat{H} = \hat{p}^2/2m + U(\mathbf{r})$ supports a number of single-particle states ψ_i with energies ε_i. In thermal equilibrium at temperature T, the average occupation number of a state i is given by the Bose-Einstein distribution [162]

$$f_{\mathrm{BE}}(\varepsilon_i, T, \mu) = \frac{1}{e^{(\varepsilon_i - \mu)/k_B T} - 1} \, . \tag{2.40}$$

Here $\mu = \frac{\partial E}{\partial N}$ is the chemical potential which can be more practically thought of as a Lagrange multiplier fixing the total particle number N. As the temperature of the system changes so does μ in order to keep the total number of particles constant. The Bose-Einstein distribution shows a divergence for $\varepsilon_i = \mu$ and unphysical, negative population for $\varepsilon < \mu$. For that reason, if a system supports states of energies ε_i, the chemical potential is bound from above by the energy of the ground state ε_0. In a moment, we will see that this divergence lies at the heart of Bose-Einstein condensation.

Calculating μ for a given temperature T and particle number N turns into a simple counting problem where one needs to sum over all states and their average occupations and equate the result to the total particle number

$$N = \int f_{\mathrm{BE}}(\varepsilon, T, \mu) g(\varepsilon) d\varepsilon \tag{2.41}$$

where we define the density of states $g(\varepsilon)$ such that the number of states dN between

energy $\varepsilon, \varepsilon + d\varepsilon$ is $g(\varepsilon)d\varepsilon$. The from of $g(\varepsilon)$ is generally determined by the trapping potential $U(\mathbf{r})$.

Lets assume now, without the loss of generality, that $\varepsilon_0 = 0$. Increasing the temperature increases the average occupation number of higher lying energy states. In order to keep the particle number constant, the chemical potential μ reacts to this change by increasing its value. Therefore, for temperatures high above degeneracy when many energy levels are occupied, the chemical potential is negative and its absolute value is large. In other words, at high temperatures, the average occupation of each individual states is low, but the number of thermally excitable states is large and so the number of particles is constant.

As we begin to reduce the temperature, few and fewer states remain significantly occupied and the chemical potential has to increase to compensate for this. As mentioned above, it cannot increase indefinitely, though, and it only ever approaches the ground state energy to prevent the divergent behaviour of the Bose-Einstein distribution. At any given temperature T, the maximum number of particles in a thermal cloud is given by setting $\mu \to 0$ to get

$$N_c = \int_0^\infty \frac{g(\varepsilon)}{e^{\varepsilon/k_B T} - 1} d\varepsilon \ . \tag{2.42}$$

We denoted this number as N_c where c stands for *critical* to emphasize that, remarkably, quantum statistics and the geometry of the confining space only ever supports a finite number of thermal particles. If one somehow managed to put more particles into the system than the critical number, i.e. $N > N_c$, all the extra particles would aggregate in the ground state. This statistically-enforced, macroscopic population of a single quantum state is called *Bose-Einstein condensation*.

An alternative way of thinking about condensation is by keeping the particle number constant and reducing the temperature. Since the critical number is a function of temperature only, $N_c = N_c(T)$, there will be a point at which the total number of particles will equal to the critical number, $N = N_c(T)$. This naturally leads to the definition of the so called *critical temperature* $T_c(N)$ defined as $N_c(T_c) = N$.

The critical number given by equation 2.42 can be found analytically for particular geometries. In a homogeneous gas confined to a volume V, the density of states is

$$g_{3D}(\varepsilon) = \frac{V m^{3/2}}{\sqrt{2}\pi^2 \hbar^3} \sqrt{\varepsilon} \tag{2.43}$$

and so the critical number can be calculated as

$$N_{c,3D} = V \left(\frac{m k_B T}{2\pi\hbar^2} \right)^{3/2} \zeta\left(\frac{3}{2}\right) \ . \tag{2.44}$$

Here ζ is the Riemann zeta function[5] which takes on the value $\zeta\left(\frac{3}{2}\right) \approx 2.612$. Importantly, we see that that the critical density $n_c = N_c/V \propto T^{3/2}$. It is useful to define the phase-space density $\rho = n\lambda_{\mathrm{dB}}^3$ where $\lambda_{\mathrm{dB}} = h/\sqrt{2\pi m k_B T}$ is the thermal de Broglie wavelength.

[5]The zeta function is defined as $\zeta(s) = \sum_{n=1}^{\infty} \frac{1}{n^s} = \frac{1}{\Gamma(s)} \int_0^\infty \frac{x^{s-1}}{e^x - 1} dx$ with $\Gamma(s) = \int_0^\infty x^{s-1} e^{-x} = (s-1)!$ being the gamma function

The critical number condition 2.44 then simplifies to

$$\rho_c = n_c \lambda_{\mathrm{dB}}^3 = \zeta\left(\frac{3}{2}\right) \sim \mathcal{O}(1) \tag{2.45}$$

and it has an elegant physical interpretation–the onset of condensation happens when the interparticle spacing is comparable to their thermal de Broglie wavelength, at which point the quantum wavepackets begin to overlap to form the macroscopic condensate.

Similar result can be derived for a gas trapped in a harmonic potential of the form $U(\mathbf{r}) = \frac{1}{2}m\sum_i \omega_i^2 r_i^2$. Such potentials are ubiquitous in the field of ultracold atoms. Here, the density of states is given by

$$g_{\mathrm{HO}}(\varepsilon) = \frac{\varepsilon^2}{2(\hbar\bar{\omega})^3} \tag{2.46}$$

where we defined the geometric average of the trapping frequencies $\bar{\omega} = (\omega_x\omega_y\omega_z)^{1/3}$. Following a similar calculation [204], [236], it can be shown that the critical number is

$$N_{c,\mathrm{HO}} = \left(\frac{k_B T}{\hbar\bar{\omega}}\right)^3 \zeta(3) \tag{2.47}$$

with $\zeta(3) \approx 1.202$. We see that for a harmonically trapped gas, $N_c \propto T^3$. Interestingly, the critical condition for the peak phase-space density at the center of the trap is the same as in the homogeneous case, i.e. $\rho_{0,c} = n_{0,c}\lambda_{\mathrm{dB}}^3 = n_c(\mathbf{r}=0)\lambda_{\mathrm{dB}}^3 = \zeta(3/2)$.

The phase space density is therefore a useful universal measure of how close to degeneracy the gas is. Its dependence on density and temperature also reflects the experimental challenge of reaching degeneracy–low temperatures are necessary but so are high particle numbers. The process of evaporative cooling (see section 4.3), in which a trapped gas is cooled at the expense of losing particles, is therefore only efficient if the overall phase-space density increases. Lowering of the temperature alone is not sufficient. Furthermore, detrimental particle loss (discussed in detail in chapter 5 in the context of erbium) limits the attainable densities, making the Bose-Einstein condensate phase even more illusive.

We close this section with a few remarks. First, we reassert that the exact details and scaling relations linked to Bose-Einstein condensation depend heavily on the underlying geometry of the problem. As an example, we note that in two or one dimension, in which the density of states is given by $g_{2D} \propto \varepsilon^0$ and $g_{1D} \propto \varepsilon^{-1/2}$ respectively, the integral 2.44 diverges. In other words, the thermal cloud is always able to accommodate any number of particles by appropriately adjusting the chemical potential. Consequently, Bose-Einstein condensation doesn't occur in homogeneous systems of lower dimensions. In the case of harmonically trapped gases, condensation is allowed in two but not in one dimension [77].

Second, although the phenomenon of condensation follows directly from the theory of non-interacting particles, we will see in chapter 6 that the presence of interactions shifts the critical point of condensation and leads to a *non-saturation* effect in which the thermal cloud can support more particles than the non-interacting theory predicts.

2.4.2 Physics of weakly interacting, dipolar condensates

A Bose-Einstein condensate (BEC) is a many-body, quantum object in which a macroscopic number of particles occupy the same quantum state. It is therefore natural to try and describe it using the language of second quantization. We will utilize the field operators $\hat{\psi}(\mathbf{r})$ and $\hat{\psi}^\dagger(\mathbf{r})$ which correspondingly anihilate or create a particle at position $\mathbf{r}$ and which obey the usual bosonic commutation relations:

$$[\hat{\psi}(\mathbf{r}), \hat{\psi}^\dagger(\mathbf{r}')] = \delta(\mathbf{r}-\mathbf{r}'), \quad [\hat{\psi}(\mathbf{r}), \hat{\psi}(\mathbf{r}')] = [\hat{\psi}^\dagger(\mathbf{r}), \hat{\psi}^\dagger(\mathbf{r}')] = 0 \ . \tag{2.48}$$

If the system supports single-particle states $\phi_i(\mathbf{r})$, we can write the field operator in terms of the single-particle creation and annihilation operators $\hat{a}_i$ and $\hat{a}_i^\dagger$ by identifying

$$\hat{\psi}^\dagger(\mathbf{r})|0\rangle = |\mathbf{r}\rangle = \sum_i |\phi_i\rangle\langle\phi_i|\mathbf{r}\rangle = \sum_i \phi_i^*(\mathbf{r})\hat{a}_i^\dagger|0\rangle \ . \tag{2.49}$$

And so we can write the field operator as

$$\hat{\psi}(\mathbf{r}) = \hat{a}_0\phi_0(\mathbf{r}) + \sum_{i\neq 0} \phi_i(\mathbf{r})\hat{a}_i \ . \tag{2.50}$$

where we have specifically emphasized the role of the single-particle ground state denoted as ϕ_0. As we have shown in the previous section, when a gas of particles undergoes Bose-Einstein condensation, the ground state of the system becomes macroscopically occupied. Consequently, the expectation value $\langle\hat{a}_0^\dagger\hat{a}_0\rangle = N_0 \gg 1 = [\hat{a}_0^\dagger, \hat{a}_0]$ and we can approximate the operators $\hat{a}_0^\dagger \approx \hat{a}_0 \approx \sqrt{N_0}$ with an increasing degree of accuracy. This is called the *Bogoliubov approximation* and it essentially amounts to treating the ground state wavefunction as a classical field, similar to the emergence of classical electromagnetism from a high-photon-count limit of the quantum theory of light.

At very low temperatures and for weak interactions, the occupation of higher energy states can be neglected and the field operator can be identified with the so-called *condensate wavefunction* Ψ_0 which plays a role of an order parameter

$$\lim_{T\to 0}\lim_{N_0\to\infty} \hat{\psi}(\mathbf{r}) = \sqrt{N_0}\phi_0(\mathbf{r}) = \Psi_0(\mathbf{r}) \ . \tag{2.51}$$

The condensate wavefunction is, in general, a complex quantity. In a few moments, we will see that its modulus represents the density of the condensate whereas its phase is connected to the superfluid flow field.

It is natural to ask what the time evolution of the order parameter is. For that, let us consider the expectation value $\langle\hat{\psi}\rangle = \langle N|\hat{\psi}|N\rangle$ in an N-particle BEC. The rules of annihilation operator algebra tell us that $\langle\hat{\psi}\rangle = 0$ on one hand, but our establishment of the condensate wavefunction gives $\langle\hat{\psi}\rangle = \Psi_0$ on the other. In order to reconcile this discrepancy, we can take the expectation value $\langle\hat{\psi}\rangle \approx \langle N-1|\hat{\psi}|N\rangle$ to be between a condensate with N and $N-1$ particles. In the thermodynamic limit, these two states should be physically equivalent up to an error of the order $1/N$. If we then consider the

time evolution of these N-particle condensates, we conclude that

$$\Psi_0(\mathbf{r},t) = \Psi_0(\mathbf{r})e^{-i(E_N - E_{N-1})t/\hbar} = \Psi_0(\mathbf{r})e^{-i\mu t/\hbar} \tag{2.52}$$

where we have identified $E_N - E_{N-1} \approx \partial E/\partial N = \mu$ as the chemical potential. Interestingly, the condensate wave function evolves with the chemical potential and not with the ground state energy as is the case with actual wave functions. This underpins the central role of μ in the physics of BECs as well as the fact that the condensate wave-function is not a true wavefunction. Next, we will see that although Ψ_0 is not a solution of the Schrodinger equation, it is a solution of another non-linear, Schrodinger-like equation that governs the dynamics of BECs.

Let's consider the time evolution of the field operator $\hat{\psi}(\mathbf{r},t)$. The Hamiltonian of a trapped, dilute gas can be written in the language of second quantization as

$$\begin{aligned}\hat{H} = \int -\frac{\hbar^2}{2m}\nabla\hat{\psi}^\dagger(\mathbf{r})\nabla\hat{\psi}(\mathbf{r})d^3\mathbf{r} \; &+ \int \hat{\psi}^\dagger(\mathbf{r})V_{\text{ext}}(\mathbf{r})\hat{\psi}(\mathbf{r})d^3\mathbf{r} \\ &+ \int \hat{\psi}^\dagger(\mathbf{r})\hat{\psi}^\dagger(\mathbf{r}')V_{\text{int}}(\mathbf{r}'-\mathbf{r})\hat{\psi}(\mathbf{r})\hat{\psi}(\mathbf{r}')d^3\mathbf{r}d^3\mathbf{r}'\end{aligned} \tag{2.53}$$

where V_{ext} is the external trapping potential and V_{int} is the interaction potential. Due to the diluteness condition, we only considered pair-wise interaction between particles. In the Heisenberg picture, the field operator then evolves in time as

$$\begin{aligned}i\hbar\frac{\partial}{\partial t}\hat{\psi}(\mathbf{r},t) &= [\hat{\psi}(\mathbf{r},t), \hat{H}] \\ &= \left[-\frac{\hbar^2\nabla^2}{2m} + V_{\text{ext}}(\mathbf{r},t) + \int \hat{\psi}^\dagger(\mathbf{r}',t)V_{\text{int}}(\mathbf{r}'-\mathbf{r})\hat{\psi}(\mathbf{r}',t)d\mathbf{r}'\right]\hat{\psi}(\mathbf{r},t)\end{aligned} \tag{2.54}$$

where the commutation relations for the bosonic field operator given by equations 2.48 were used to simplify the expression. In the Bogoliubov approximation and at low temperatures, we can replace $\hat{\psi}(\mathbf{r},t)$ with $\Psi_0(\mathbf{r},t)$. Assuming the wave function changes negligibly over the length scales associated with the interaction potential, we can also use the pseudopotential formalism of equation 2.37 to substitute for V_{int} to finally arrive at

$$i\hbar\frac{\partial}{\partial t}\Psi_0(\mathbf{r},t) = \left[-\frac{\hbar^2\nabla^2}{2m} + V_{\text{ext}}(\mathbf{r},t) + g|\Psi_0(\mathbf{r},t)|^2 + \Phi_{dd}(\mathbf{r},t)\right]\Psi_0(\mathbf{r},t) \tag{2.55}$$

with $g = 4\pi\hbar^2 a_s/m$ as defined in previous section and the non-local potential $\Phi_{dd}(\mathbf{r},t) = \int |\Psi_0(\mathbf{r}',t)|^2 U_{dd}(\mathbf{r}'-\mathbf{r})d^3\mathbf{r}'$ arising from the long-ranged DDI. This is known as the time-dependent, dipolar Gross-Pitaevskii equation (dGPE) and it is one of the most powerful and widely used tools for modelling Bose-Einstein condensates [237]–[239].

For investigating the ground state under static conditions, it is helpful to use the time-independent form of the dGPE by utilizing the known time-evolution of the condensate wave function given by equation 2.52. Furthermore, assuming the trapping is strong and the interaction terms are large, it is possible to omit the kinetic energy contribution to

derive the *Thomas-Fermi* approximate form of the dGPE

$$\mu = V_{\text{ext}}(\mathbf{r}) + g|\Psi_0(\mathbf{r})|^2 + \Phi_{dd}(\Psi_0(\mathbf{r})) \tag{2.56}$$

Albeit much simpler than its time-dependent counterpart 2.55, this is still an integral equation that, in general, needs to be solved numerically due to the long-ranged dipolar term Φ_{dd} which is self-consistent in Ψ_0. However, in the absence of the DDI, the condensate wave function in the Thomas-Fermi (TF) approximation takes on a particularly simple form

$$|\Psi_{0,\text{TF}}(\mathbf{r})|^2 = \frac{1}{g}(\mu - V_{\text{ext}}(\mathbf{r})) \tag{2.57}$$

with its shape completely determined by the trapping potential. Using the definition of the density operator $\hat{n}(\mathbf{r}) = \hat{\psi}^\dagger(\mathbf{r})\hat{\psi}(\mathbf{r}) = |\Psi_0(\mathbf{r})|^2$, we identify $|\Psi_0(\mathbf{r})|^2$ as the density of the condensate and the normalization

$$N = \int \hat{\psi}^\dagger(\mathbf{r})\hat{\psi}(\mathbf{r})d^3\mathbf{r} = \int |\Psi_0(\mathbf{r})|^2 d^3\mathbf{r} \tag{2.58}$$

then fixes the value of the chemical potential μ. In the special case of harmonically trapped BECs, the density profile is parabolic

$$n_{\text{TF}}(\mathbf{r}) = \frac{15N}{8\pi R_x R_y R_z}\left(1 - \frac{x^2}{R_x^2} - \frac{y^2}{R_y^2} - \frac{z^2}{R_z^2}\right) \tag{2.59}$$

and vanishes at a radius

$$R_i = a_{\text{HO}}\left(15N\frac{a_s}{a_{\text{HO}}}\right)^{1/5}\frac{\bar{\omega}}{\omega_i} \tag{2.60}$$

with $a_{\text{HO}} = \sqrt{\hbar/m\bar{\omega}}$. Furthermore, the chemical potential in this scenario is given by

$$\mu_{\text{TF}} = \frac{\hbar\bar{\omega}}{2}\left(15N\frac{a_s}{\bar{a}_{\text{HO}}}\right)^{2/5}. \tag{2.61}$$

We will use these expression when we discuss the non-saturation of a thermal Bose gas and the critical temperature shift due to dipole-dipole interactions in chapter 6.

In the intermediate temperature range $0 < T < T_c$ for which there is a considerable condensate population, i.e. $N_0 \gg 1$, as well as thermal fraction, i.e. $N_c \gg 1$, the thermal cloud and the condensate coexist in the same trap. Under usual conditions, $R_{\text{TF}} < \sigma_T = \sqrt{k_B T/m\omega^2}$, and so the condensate is smaller than the thermal cloud. Consequently, when imaging ultracold atomic gases, the presence of a condensate is signified by a typical bimodal distribution with a broad, approximately Gaussian, thermal cloud superimposed on top of a narrow, parabolic one which corresponds to the condensate. We discuss our imaging setup in chapter 3.1.3 and our fitting routine for characterizing BECs in chapter 4.4.1. Remarkably, in the presence of the DDI and under the Thomas-Fermi approximation, the condensate still takes on a shape of a paraboloid, but this time with the Thomas-Fermi radii adjusted in response to the non-local potential term Φ_{dd}. We will prove this point more rigorously in chapter 6 when we describe our measurement of the

critical temperature (T_c) shift due to the dipole-dipole interaction.

As before, we conclude this section by making a few remarks about interesting properties of the condensate wavefunction. First of all, we note that the condensate wavefunction can be written as $\Psi_0(\mathbf{r},t) = \sqrt{n(\mathbf{r},t)}e^{iS(\mathbf{r},t)}$. Using the expression for probability current

$$\mathbf{j}_0 = -\frac{i\hbar}{2m}(\Psi_0^*\nabla\Psi_0 - \Psi_0\nabla\Psi_0^*) \ , \tag{2.62}$$

we can identify the gradient of the phase with the condensate velocity field

$$\mathbf{v}_0(\mathbf{r},t) = \frac{\mathbf{j_0}}{n} = \frac{\hbar}{m}\nabla S(\mathbf{r},t) \tag{2.63}$$

Clearly, the flow of the condensate is irrotational i.e. $\nabla \times \mathbf{v}_s = 0$ which is a signature of fluids with vanishing viscosity, hinting at superfluid properties of BECs [240].

Secondly, the time-independent version of the GPE (equation 2.55) permits different solutions. The solution that minimizes the total energy

$$E = \int \left(\frac{\hbar^2}{2m}|\nabla\Psi_0|^2 + V_{\text{ext}}(\mathbf{r})|\Psi_0|^2 + \frac{g}{2}|\Psi_0|^4 + \frac{1}{2}\Phi_{dd}|\Psi_0|^2\right) d^3\mathbf{r} \tag{2.64}$$

corresponds to the ground state and can be shown to be real by realizing that a non-uniform phase $S(\mathbf{r})$ always increases the energy. The excited solutions are, on the other hand, complex and display flow. This might at first seem contradictory given that these were assumed to be solutions of the time-independent GPE. However, a steady state flow is permissible as long as $\frac{\partial n}{\partial t} = -\nabla \cdot \mathbf{j}_0 = 0$. In fact, one of the most famous examples of an excited state supported by the GPE is the vortex line [241], [242] which forms in rotating BECs [41], [43]. This solution corresponds to a vortex of quantized circulation with $\nabla \times \mathbf{v}_0 \propto \delta(\mathbf{r})$. The condensate density must vanish at $\mathbf{r} = 0$ in order to keep the flow irrotational, creating a hollow vortex core in the condensate [42]. Other examples of excited states include dark [39], [243] and bright [244], [245] solitons and vortex rings [246], [247].

In the next section, we will develop an understanding of low energy excitations in dipolar condensates which will inevitably lead to discussions regarding the stability of dipolar condensates and their exotic supersolid phases.

2.4.3 Excitations

The solutions of the GPE correspond to stationary states that don't evolve in time. Even though all the solutions with energy higher than the ground state energy (as given by equation 2.64) are technically excited states, they should be contrasted with time-dependent, low-energy perturbations to the condensate i.e. excitations. For example, in a homogeneous classical gas, the equivalent excitations are sound waves whereas in a solid lattice they are known as phonons [92]. In a moment, similar treatment of degenerate bosonic gases will reveal the presence of phonon-like excitations with a characteristic dispersion relation governed by the particle interactions.

To see this, we begin by altering the expression for the field operator in the low

temperature limit (equation2.50) such that it now allows for small excitations beyond the ground state

$$\hat{\psi}(\mathbf{r},t) = (\Psi_0(r) + \delta\hat{\psi}(\mathbf{r},t))e^{-i\mu t/\hbar} \tag{2.65}$$

with $\delta\hat{\psi} \ll \Psi_0$. Using the language of normal modes and second quantization [248], we will look for oscillatory perturbations of the form

$$\delta\hat{\psi}(\mathbf{r},t) = \sum_i (u_i(\mathbf{r})\hat{b}_i e^{-i\omega_i t} + v_i^*(\mathbf{r})\hat{b}_i^\dagger e^{i\omega_i t}) \tag{2.66}$$

where $\hat{b}_i^\dagger$ and $\hat{b}_i$ are the creation and annihilation operators of an excitation with frequency ω_i. Inserting this ansatz into the time-dependent GPE (equation 2.55), grouping terms with the same frequency components and working only to first order in u_i and v_i yields a set of coupled equations that can be expressed in matrix form as

$$\begin{pmatrix} \hat{H} + \hat{X} - \mu & \hat{X} \\ -\hat{X} & -\hat{H} - \hat{X} + \mu \end{pmatrix} \begin{pmatrix} u_i \\ v_i \end{pmatrix} = \hbar\omega_i \begin{pmatrix} u_i \\ v_i \end{pmatrix} \ . \tag{2.67}$$

with $\hat{H}$ the Hamiltonian of the unperturbed ground state given (in its full form) by equation 2.53 and $\hat{X}$ the exchange operator whose action on a function $\theta(\mathbf{r})$ is defined as

$$\hat{X}\theta(\mathbf{r}) = \Psi_0(\mathbf{r}) \int \Psi_0(\mathbf{r}')V_{\text{int}}(\mathbf{r}-\mathbf{r}')\theta(\mathbf{r}')d^3\mathbf{r}' \ . \tag{2.68}$$

Equations 2.67 are known as the Bogoliubov–de Gennes (BdG) equations and they yield the energy spectrum of the condensate excitations. It can be shown that as long as the functions $u_i(\mathbf{r})$ and $v_i(\mathbf{r})$ satisfy the orthonormalization condition

$$\int [u_i^*(\mathbf{r})u_j(\mathbf{r}) - v_i^*(\mathbf{r})v_j(\mathbf{r})]d^3\mathbf{r} = \delta_{ij} \ , \tag{2.69}$$

the total energy of the system can be expressed as

$$E = E_0 + \sum_i \hbar\omega_i \langle \hat{b}_i^\dagger \hat{b}_i \rangle \tag{2.70}$$

with E_0 the energy of the unperturbed ground state. The excitations can therefore be described as a gas of independent quasi-particles occupying states of energy $\hbar\omega_i$ with occupation number $n_i = \langle \hat{b}_i^\dagger \hat{b}_i \rangle$. Notably, expression 2.70 omits the zero-point energy of the excitations which corresponds to the vacuum state defined by $\hat{b}_i|vac\rangle = 0$ in analogy with the quantum harmonic oscillator. The vacuum state is the zero temperature limit of the condensate-excitation system and it affects the condensate in a real, physical way by causing its quantum depletion [249] and altering the particle correlations [250].

In general, BdG equations need to be solved numerically but in some special cases, analytic solutions exist. One of the most insightful results is that of a homogeneous dipolar gas. The order parameter is simply given by $\Psi_0(\mathbf{r}) = \sqrt{n}$ with n the density of the gas.

A plane wave ansatz for the excitations then yields

$$\hbar\omega(\mathbf{k}) = \sqrt{\frac{\hbar^2 k^2}{2m}\left(\frac{\hbar^2 k^2}{2m} + 2n\tilde{V}_{\text{int}}(\mathbf{k})\right)} \tag{2.71}$$

where $\tilde{V}_{\text{int}}$ is the Fourier transform of the interaction potential. Using the pseudopotential in the presence of the long-range DDI (equation 2.37) results in the following dispersion relation for the excitations

$$\hbar\omega(\mathbf{k}) = \sqrt{\frac{\hbar^2 k^2}{2m}\left(\frac{\hbar^2 k^2}{2m} + 2gn(1 + \varepsilon_{dd}(3\ \cos^2(\theta_{\mathbf{k}}) - 1))\right)} \tag{2.72}$$

with $\theta_{\mathbf{k}}$ being the angle between the polarization of the atoms and the $\mathbf{k}$-vector of the excitation.

This result has several important features. Firstly, for a non-dipolar gas with $\varepsilon_{dd} = 0$, the dispersion is isotropic as would be expected based on the isotropic form of the interaction potential. Secondly, the dispersion displays two distinct regimes. For large wavelength oscillations i.e. small k, we obtain $\omega/k = \sqrt{gn/m}$ which defines a phase velocity for the perturbations in close correspondence with the speed of sound of phonon modes in solids. For large k, the dispersion reads as $\hbar\omega = \hbar^2 k^2/2m + gn$ which is simply a dispersion of a free particle with an extra energy gn due to the mean field contact interaction potential.

For a dipolar gas i.e. $\varepsilon_{dd} > 0$, the dispersion becomes anisotropic. The cosine term changes between 2 and -1 and so for $\varepsilon_{dd} > 1$, there exists a subset of wave-vectors k and angles $\theta_{\mathbf{k}}$ for which the energy of the excitations $\hbar\omega(\mathbf{k})$ becomes imaginary. This marks the onset of instability in the quantum gas as can be seen from the divergence of the ansatz 2.66. The emergence of instability for $\varepsilon_{dd} > 1$ justifies our definition of the dipolar length a_{dd} as defined in 2.36 and highlights the usefulness of ε_{dd} as a parameter describing the dipolarity of the gas.

Another class of important and analytically solvable problems are dipolar gases confined in a quasi-2D geometry i.e. a 'pancake' trap. Such gases have a Gaussian (or similar) profile in one tightly trapped direction and are uniform in the other two directions–not unlike the final trapping potential of the Oxford Er-K experiment (see chapter 9). These have sparked both theoretical [251]–[253] and experimental [108], [109], [254] interest because the excitation spectrum–which is given by [255]

$$\begin{aligned}\hbar\omega(k_r) &= \sqrt{\frac{\hbar^2 k_r^2}{2m}\left(\frac{\hbar^2 k_r^2}{2m} + 2gn_{2D}\tilde{V}_{2D}(k_r)\right)} \\ \tilde{V}_{2D}(k_r) &= \frac{g}{\sqrt{2\pi}l_z} + \frac{C_{dd}}{3\sqrt{2\pi}l_z}F\left(\frac{k_r l_z}{\sqrt{2}}\right)\end{aligned} \tag{2.73}$$

with n_{2D} the $2D$ density, $\tilde{V}_{2D}(k_r)$ the $2D$ Fourier transform of the interaction potential with the third direction integrated out, $l_z = \sqrt{\hbar/m\omega_z}$ the harmonic oscillator length along the tight direction and $F(x) = 2 - 3\sqrt{\pi}xe^{x^2}(1 - \text{erf}(x))$–displays a characteristic minimum

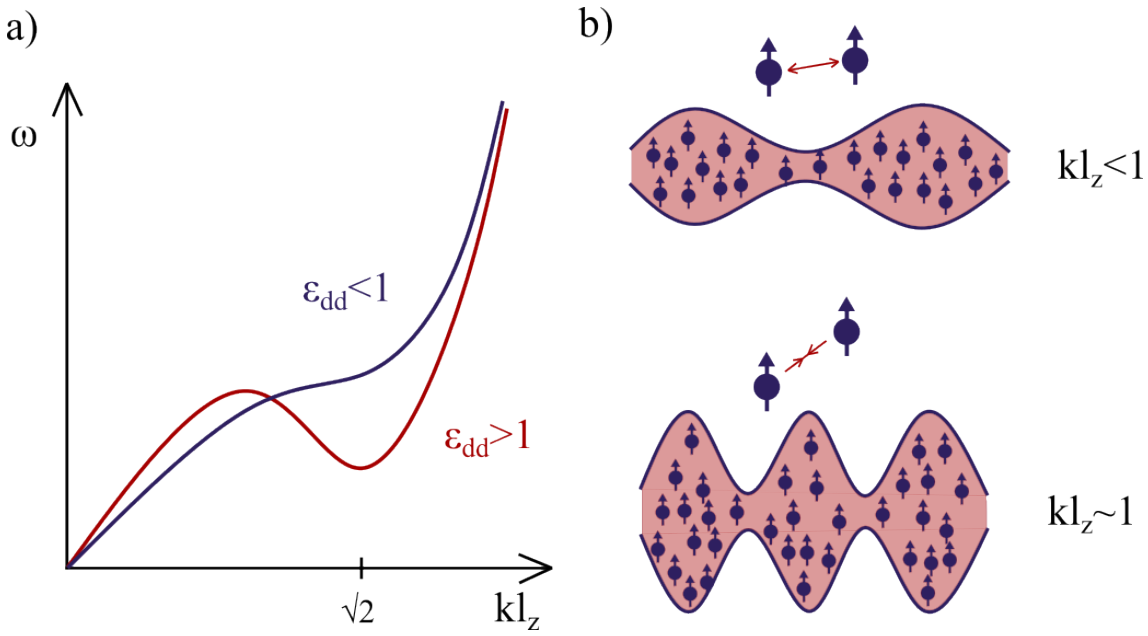


Figure 2.10: Roton-maxon spectrum. The elementary excitations of a quasi-2D dipolar gas show a peculiar feature known as the roton minimum. When the DDI is strong enough compared to the contact interactions, the energy of certain periodic perturbations is lowered due to the attractive part of the DDI. This happens for $k_r l_z \approx 1$, where l_z is the characteristic length scale in the transverse direction. For longer wave lengths, the repulsive part of the DDI dominates whereas for shorter wave lengths, it is the kinetic energy.

and maximum. This is known as the *roton-maxon* spectrum and a similar spectrum (although with a different microscopic origin) was first observed in liquid helium where it is believed to govern its superfluid properties [107], [256]. We note that the name *roton* is purely historical and doesn't refer to any rotation within the system.

Figure 2.10a shows a typical dispersion relation of a quasi-2D dipolar gas. For high enough ε_{dd} or density, the roton feature emerges at a wave-vector $k_{\mathrm{rot}} = \sqrt{2}/l_z$ [251]. The lowering of the excitation energy compared to the free-particle dispersion can be qualitatively understood in the following way. For small k_r, the modulation of the condensate density results in mostly repulsive interactions between two wave fronts where the density is enhanced. As a result, the low k_r regime corresponds to phonons with their phase velocity, i.e. speed of sound, enhanced by the contribution of the repulsive DDI. In this way, the DDI can, in fact, prevent the collapse of a BEC with attractive s-wave interactions ($a_s < 0$) which would otherwise be unstable. When the wavelength $\lambda \approx 1/k_r$ becomes comparable to the transversal dimension of the condensate (l_z), the interactions between two adjacent wave fronts become attractive, resulting in an overall lowering of the excitation energy–this is the origin of the roton minimum. At even higher k_r, kinetic energy dominates and the free particle dispersion is recovered. This mechanism is depicted in figure 2.10b.

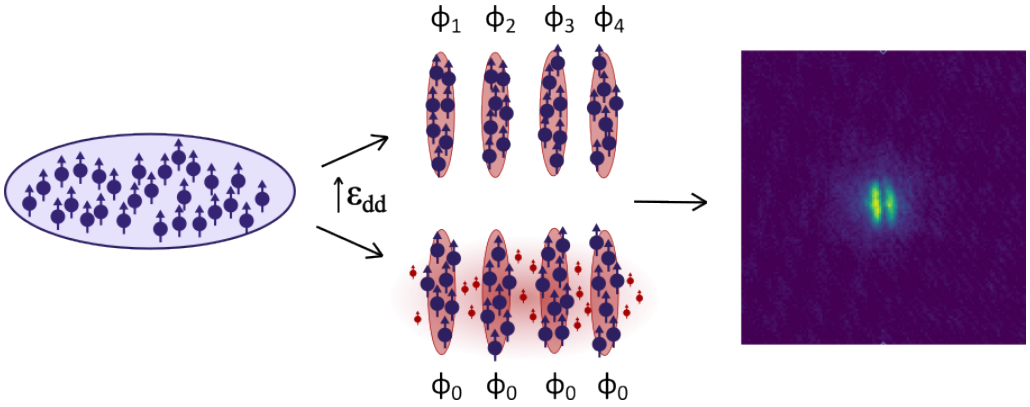


Figure 2.11: Quantum droplets and supersolids. When the dipolar scattering length becomes comparable to the s-wave scattering length such that $\varepsilon_{dd} \sim \mathcal{O}(1)$, the BEC becomes unstable against the formation of rotons and collapses to form dense, self-bound quantum droplets. These droplets are, in general, independent and phase incoherent. However, under special circumstances, droplets can exchange particles to become both spatially organized and phase coherent. These are signature properties of supersolids. In a time-of-flight experiment, droplets can be detected as characteristic matter wave interference patterns. The right image of interfering droplets was taken using our apparatus.

Collapse and supersolidity

The softening (lowering) of the roton minimum has several implications. Firstly, the critical superfluid velocity defined by the Landau criterion [257], [258] is lowered by the presence of roton excitations. In other words, it takes less energy to create excitations that would disturb the superfluid flow.

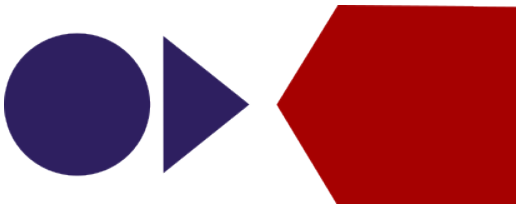
Secondly, when the energy of roton excitations vanishes, the gas becomes unstable. However, unlike in the case of e.g. attractive BECs and Bose novas [85], [259], the collapse isn't always catastrophic. Instead, the gas can undergo a phase transition to self-bound, dense, *quantum droplets* [112]–[115], [197]. The complete collapse is prevented by the presence of the so called *quantum fluctuations* (QFs) [260]. These are nothing more than fluctuations in the vacuum state of elementary excitations due to interactions as described by equation 2.70. We already mentioned that the vacuum state affects the condensate in a real way because of its zero-point energy. For a uniform dipolar gas, this QF contribution scales as $n^{3/2}$ [261], [262] and is repulsive in nature. Consequently, even though it is initially small compared to the chemical potential, it quickly grows as the gas collapses. At some point, the gas is so dense that the quantum fluctuation term balances out the attractive part of the mean field energy responsible for the collapse and a quantum droplet forms.

Larger atom numbers support the formation of multiple quantum droplets. The droplet-droplet interactions then lead to their spatial organization. If the phase coherence between adjacent droplets is retained–mainly through the exchange of particles–the system exhibits both superfluidity [263] and crystalline ordering as shown in figure 2.11. These are signatures of a state of matter called *supersolid* [264], [265]. Though also recently observed in other systems such as helium [266], high T_c superconductors [267], spin-orbit coupled BECs [268] or BECs in optical cavities [269], the epicenter of the study of super-

solids lies within the field of dipolar quantum gases [111], [139], both on the theoretical [144], [270] and the experimental side [115]–[118], [271]. However, the large densities associated with the droplet phase imply large three-body loss rates and short lifetimes, and so any experimental realisation of this phenomenon is challenging [272]. One of the long term goals of the Oxford Er-K experiment is to study supersolidity in two dimensions with large erbium BECs. The first two milestones on the way towards this goal have already been reached and are described in this work in chapters 4 and 5–these are namely the production of large atom number BECs of ^{166}Er and the characterization of its three-body loss landscape.

This concludes our discussion of erbium, its atomic properties and the role of dipole-dipole interactions in dipolar Bose-Einstein condensates. In the next two chapters, we will describe our experimental apparatus, paying special attention to the last stages of atomic cooling that lead to the production of large erbium BECs.

3. Experimental setup–reaching the Doppler limit



The task of cooling an atomic species to quantum degeneracy is challenging and the temperatures required to observe the effects of degeneracy are some of the coldest in the universe. The difficulty of the task is also accentuated by the fact that one often needs to heat up the atomic source first before cooling it in order to produce an atomic vapour. Furthermore, cooling by ten orders of magnitude from $\approx 1000\,\mathrm{K}$ to $\approx 100\,\mathrm{nK}$ cannot be achieved through simple means of refrigeration, if only because doing so would require the existence of an ultracold refrigerating medium in the first place. Luckily, laser cooling [11] techniques, first developed at the end of the previous century, allow us to bridge the gap, albeit at the cost of experimental complexity. A cold atom laboratory usually consists of tens of independent systems ranging from vacuum assemblies to lasers and electronic control devices. As such, it is difficult to design, operate, maintain and optimize. Consequently, relying on and furthering of existing knowledge is vital.

In this chapter, we provide a full description of the Oxford Er-K experiment. We start by detailing the vacuum assembly, magnetic field control and other auxiliary systems. We then focus on laser cooling–both theoretically and practically–which constitutes the first two stages of the experimental sequence. These stages allow us to approach the Doppler limit, marking a major milestone towards reaching quantum degeneracy.

3.1 Experimental overview

Our experiment was designed with several key features in mind–large atomic samples for access to exotic phases, precise magnetic control for exploring dipolar physics, excellent optical access for manipulation and probing of the degenerate gas and finally, second species addition for the study of impurity physics. It is these features that shaped the way the experiment evolved over several years of its existence. For a thorough account of the design process and the early building stages see [273]. Here, we provide an overview of the experimental setup and describe the purpose of each individual section, focusing in particular on the systems that I have been involved with throughout the course of my DPhil.

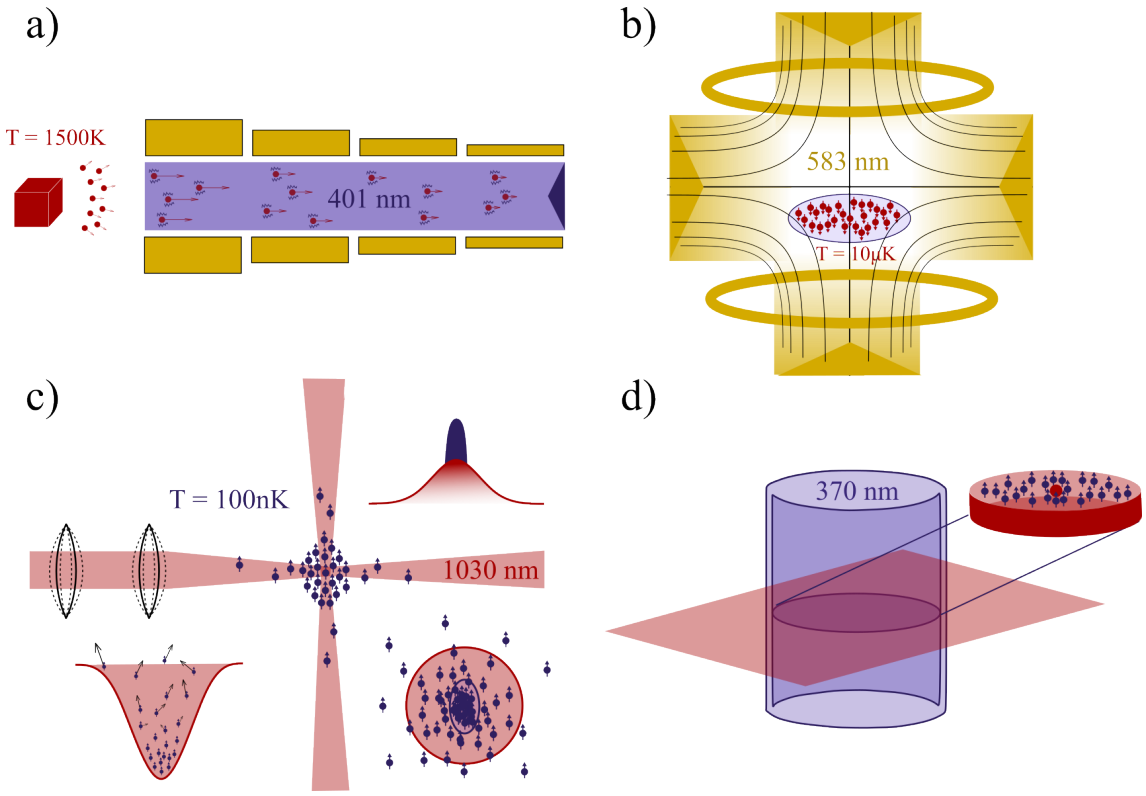


Figure 3.1: Experimental overview. (a) The journey of the atoms starts in an effusion cell oven. A stream of hot atoms emerging from the oven is first slowed using a Zeeman slower (ZS) stage operating at 401 nm. This creates a flux of slow atoms funneled into the main experimental chamber. (b) Six counter-propagating 583 nm beams overlapped with an anti-Helmholtz magnetic field gradient form a magneto-optical trap (MOT) for the atoms emerging from the ZS. The MOT cools the atoms down to $\approx 10\,\mu$K and prepares them for being loaded into an optical dipole trap. (c) Two crossed 1030 nm beams form a far-detuned optical dipole trap (ODT). Once the atoms are loaded into the ODT from the MOT, they undergo evaporative cooling to reach quantum degeneracy with 2.2×10^5 atoms in the BEC. A set of tunable lenses allows us to shift the focus of the main trapping beam and perform optical transport of the atoms from the MOT chamber to a transparent science cell. (d) With its superior optical access, the science cell will be used to trap the gas in a homogeneous pancake trap using a red-detuned sheet beam and a repulsive hollow cylindrical beam operating at 372 nm. This platform will be used to study dipolar physics in constrained geometries as well as mixture physics once the addition of potassium to the system is completed.

The journey of the atoms starts in an effusion cell oven. Here, a crystalline sample of erbium is heated up to 1250 °C in order to liberate some atoms from its surface. Atoms released in this way travel ballistically under the influence of gravity and, upon passing a series of irises, form a steady, hot jet. This jet is directed along a long, evacuated tube which serves as both a deceleration path and a differential pumping section that separates the oven from an ultra-high vacuum chamber. A 401 nm laser light is used to create a two-dimensional optical molasses [4] in the two directions perpendicular to the atomic beam. This step, referred to as *transverse cooling* (TC), collimates the jet by reducing the spread of atomic velocities in the transverse direction. The same light, in combination with magnetic coils wound around the differential tube, is used to implement a Zeeman slower (ZS) [172] along the direction of propagation. In this way, erbium atoms are slowed along the length of the ZS from velocities of $\approx 350\,\mathrm{m\,s^{-1}}$ down to $\approx 10\,\mathrm{m\,s^{-1}}$.

The atomic beam that emerges from the ZS tube into the main vacuum chamber is slow enough for a significant fraction of the atoms to be captured by a 3D magneto-optical trap (MOT) [80], [146], [173]. This is implemented with the use of six counter-propagating laser beams that operate at the 584 nm narrow transition and two anti-Helmholtz coils that provide a magnetic field gradient. Following a compressed MOT (cMOT) stage in which the atomic cloud, now consisting of $\approx 100 \times 10^6$ atoms, becomes denser and reaches temperatures of $\approx 10\,\mu\mathrm{K}$, the atoms are then loaded into a far-detuned optical dipole trap (ODT) [274].

The ODT itself is formed from a 1030 nm infra-red laser split into two beams that are focused down on the atomic cloud in a crossed beam configuration [275]. After a brief loading stage from the MOT, $\approx 1.8 \times 10^7$ atoms at $\approx 40\,\mu\mathrm{K}$ are trapped in the ODT. These are then evaporatively cooled to quantum degeneracy following a $\approx 8\,\mathrm{s}$ evaporation ramp. In this way, Bose-Einstein condensates of $> 200 \times 10^3$ erbium atoms are produced.

For increased optical access and hence experimental flexibility, a glass science cell maintained at ultra high vacuum ($< 10^{-11}$ mbar) is attached to the main vacuum chamber. Two focus-tunable lenses which form the main trapping beam of the ODT can be used to transfer the atoms from the MOT chamber to the science cell. Here, the atoms will then be be trapped in a homogeneous 'pancake' trap formed by an attractive 1064 nm sheet beam and a repulsive 372 nm hollow, cylindrical beam. This will allow us to study the interplay of dimensionality and dipolar physics in a nearly homogeneous system.

Lastly, in order to introduce a second atomic species–potassium–and study impurity and mixture physics, an additional vacuum chamber is attached to the main experiment that serves as a source of cold potassium atoms. In a similar manner to the ZS, a collimated atomic beam is produced with our implementation of a 2D+ MOT [159] operating at 767 nm (D2 line). This slow flux of K atoms is then used to load a 3D MOT in the main chamber which addresses both the D1 (770 nm) and D2 lines and which includes a grey molasses stage. When operated concurrently, the dual-species Er-K MOT will be a starting point for creating a degenerate, quasi-2D mixture in the manner described above.

Figure 3.1 provides an overview of the individual experimental stages. In the next section, we will describe our vacuum system, focusing on the erbium side of the experiment.

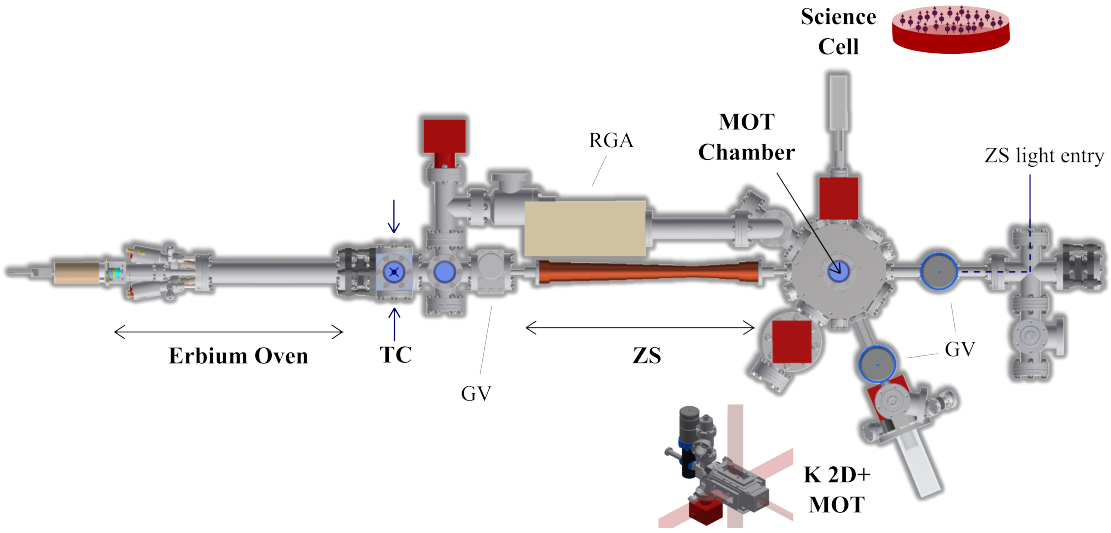


Figure 3.2: Vacuum assembly. Atoms emerge from the effusion cell oven and undergo transverse cooling before entering the Zeeman slower (ZS). The High Vacuum side is separated from the Ultra-High vacuum side of the MOT chamber with a gate valve (GV). The MOT chamber itself is connected to a glass Science Cell where most of our scientific pursuits will take place including the realization of a homogeneous pancake trap. The source of cold potassium in the form of a 2D+ MOT is connected to the main MOT chamber via a gate valve and directly feeds a cold atomic flux of potassium into the chamber. Lastly, a cross-junction where the ZS light enters the vacuum and reflects off a mirror is also separated from the rest of the system with a gate valve to allow for easy replacement of the mirror. A residual gas analyzer (RGA) can be used for assessing the quality of vacuum in the MOT chamber and for leak testing. Getter pumps shown in red maintain desired levels of vacuum throughout the whole experiment.

A full description of the potassium vacuum assembly is provided in section 8.1.1.

3.1.1 Vacuum

The requirement for a high temperature erbium source together with the deliberate decision of using a highly optically accessible science cell in addition to the central MOT chamber naturally lead to a 'three-chamber' vacuum design. This is depicted in figure 3.2. The majority of the metal parts are made of stainless steel with the MOT chamber specifically made of the 316LN type which has a particularly low magnetic susceptibility of $\mu_r \approx 1 \times 10^{-3}$ and is therefore suitable for experiments involving a high degree of magnetic field control. The parts themselves are a mixture of standard components and custom made pieces, including the MOT chamber, and they come from a number of manufacturers[1]. For a more detailed description of parts and materials, see [273].

HV section

The first section, also referred to as the High-Vacuum (HV) section, consists of the effusion cell erbium oven, a cube with viewports for transverse cooling, a cross with optical access for optional beam characterization and a vacuum pump connected to the cross.

[1]Prevalently Scanwel, Kurt J. Lesker and Vacom

The whole HV section is separated from the Ultra-High Vacuum (UHV) section, i.e. the MOT chamber, by a gate valve[2] which allows for pressurizing the HV section, e.g. for erbium source replacement (see below), without compromising the vacuum in the UHV section. Additionally, the two sections are also separated by a long differential pumping tube. This tube serves two purposes–firstly, it allows to maintain a hundred-fold pressure difference between the HV and UHV sections by working as a low–conductance connection in an equivalent circuit where pressures represent voltages and pumps represent current sources [273]. Such pressure difference is necessary because of the high oven temperatures on the HV side which cause outgassing of lighter elements–predominantly hydrogen–from the metal steel walls of the vacuum assembly. Secondly, the tube also serves as a Zeeman Slower–a cooling step which is necessary to decelerate atoms from their thermal velocity related to the oven temperature down to the capture velocity of the MOT (for more details on the two cooling steps, see section 3.2). As such, the diameter of the tube is an important parameter because it significantly affects the atomic flux but also the pressure difference between the two sections. Furthermore, it also changes the requirements on the coil winding for optimal ZS operation. A Monte Carlo atomic simulation in conjunction with an equivalent pressure circuit model was used to converge on a suitable value of 8 mm [273].

The pump operating in the HV section is a combined non-evaporable getter (NEG) and ion pump element[3] which was chosen, along with two other pumps of the same type attached to the UHV section, for its substantial pumping rate and its ability to efficiently pump all types of gases typically present in vacuum chambers, including molecular hydrogen.

The cube and the cross are equipped with four and three viewports[4] respectively for optical access. The cube viewports are used for transverse cooling (TC) whereas the cross viewports were historically used for performing spectroscopy on the atoms for the purpose of atomic beam characterization and laser locking. However, this became obsolete after we switched to using an external cavity as a reference for our 583 nm laser (see section 3.2.3). We note that a manufacturing fault in some of the viewports resulted in a sub-optimal performance of the TC setup. These have been replaced with new ones during our recent refilling of the erbium oven (more on this below).

The effusion cell oven[5], shown in figure 3.3, consists of a tantalum crucible with two apertures which split the crucible into two chambers. These are heated separately, allowing for independent control of their temperature. The first oven chamber houses an 8 g sample of erbium[6] broken into small pieces and is heated to 1100 °C in order to create high enough erbium vapour pressure. The first[7] aperture creates a collimated beam of erbium atoms that enters the second chamber. The second chamber is heated to 1200 °C to prevent build-up of material on the second aperture (known as the 'hot lip') which filters out

[2]UHV gate valve by VAT
[3]NEXTorr D 100-5 pump by SAES Getters
[4]Manufactured by Torr Scientific
[5]Dual Filament Cell (DFC-40-10-WK-2B-SHE) by CreaTec
[6]Distilled dendritic erbium by Alfa Aesar
[7]The melting point of erbium is 1529 °C

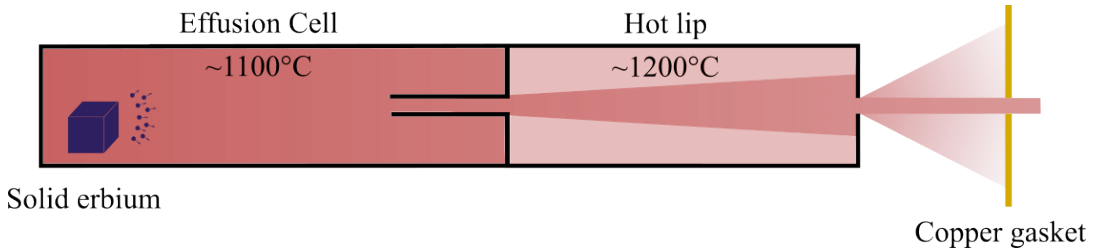


Figure 3.3: Effusion cell oven. The oven consists of a tantalum crucible with two chambers. The first chamber is the effusion cell itself which contains a solid sample of erbium (8 g) heated to 1100 °C. The second chamber (called the hot lip) is heated to 1200 °C to prevent the build-up of erbium. The apertures between the two chambers together with a copper gasket (which forms the third aperture) collimate the atomic beam. Figure adapted from [273].

divergent atoms. A third aperture made up of a bored copper gasket is placed after the oven to further collimate the atomic beam and direct it into the narrow Zeeman-slower (ZS) tube. The oven itself is mounted on a port aligner to allow for minor tilt corrections in case of missalignment or an uneven atomic beam. An electronically controllable shutter inside of the oven can interrupt the flux of atoms during later stages of the cooling sequence in order to prevent collisions of the hot flux with already cold atoms in the MOT and/or the ODT. We note that we only measured a noticeable difference in atomic lifetimes with and without the shutter when the oven was operated at elevated temperatures above the ones quoted in this paragraph.

To prevent build-up of heat on the experimental table and to increase the responsiveness of the oven temperatures to the control loop, the oven is water-cooled. The cooling system is built around a commercial water pump and a secondary loop that activates in case of a failure of the primary pump. This way, the temperature of the external casing of the oven is only slightly elevated above the room temperature. The choice of the operating temperatures for the oven was informed by numerical simulations [273] of the resulting atomic flux and the lifetime of the erbium sample. Too low a flux would hinder the performance of the MOT whereas too high a flux would result in short erbium lifetimes and a noticeable imbalance in the retroreflected TC beam due to excessive absorption. The control system of the oven allows us to cycle the temperature and hence reduce the depletion rate of the erbium source during experimental downtime. During a usual cycle, the oven is cooled from 1200 °C/1100 °C to 800 °C/700 °C over the course of two hours to prevent any sudden temperature change and the associated, and potentially catastrophic, expansion of the vacuum flanges.

We note that over the course of the five year operation of the experiment, we noticed a deterioration of the beam flux and consequently we decided to increase the operating temperature to 1150 °C and 1250 °C in the two oven chambers respectively. This decrease in flux eventually prompted us to replace the erbium source in the effusion cell oven. The procedure for doing this was relatively straightforward thanks to the design of our vacuum assembly. First, the gate valve was used to separate the UHV and HV sections. Second, the NEG pump in the HV section was turned off to prevent its exposure to atmospheric

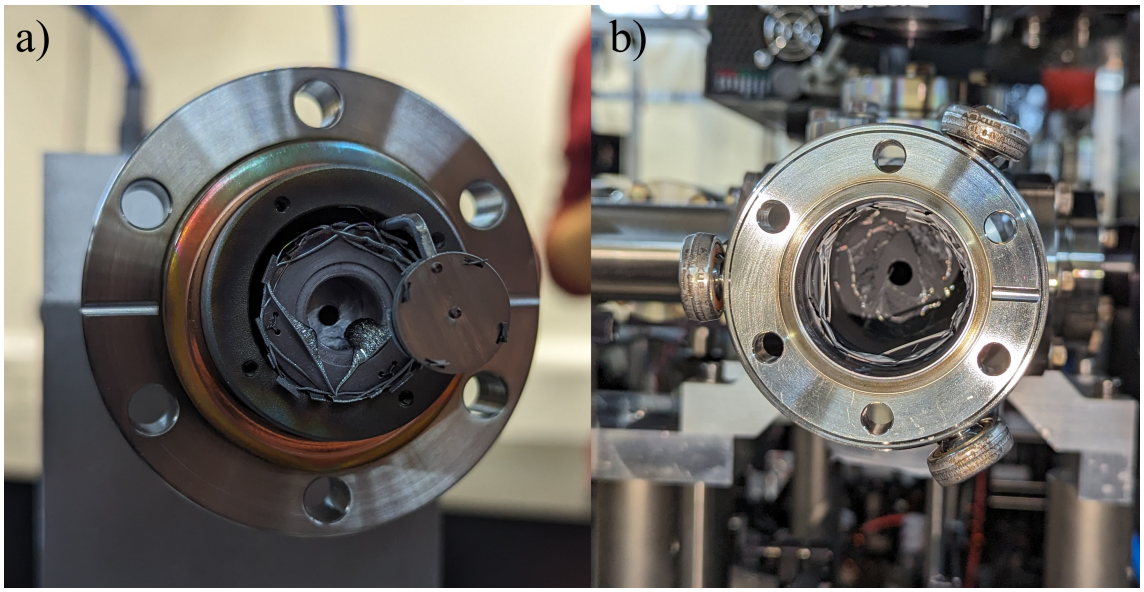


Figure 3.4: Erbium material build-up. Deposits of erbium after four years of operation at the entrance to the effusion cell oven (a) and around the last aperture (b). Note the controllable flap for blocking the beam in the left image.

pressure during operation[8]. The oven was then slowly ramped down and allowed to cool to ambient temperature. This step is imperative as hot erbium quickly reacts with water to form erbium hydroxide and hydrogen gas, which can potentially combust. Next, the HV section was slowly pressurized and simultaneously saturated with nitrogen gas which was let in through a valve connected to the cross via a T junction. This was done as a precaution against potential violent oxidization of residual erbium in the oven. Once the pressure reached the atmospheric level, the oven flange connected to the cube was opened. The replacement of the erbium source itself involves breaking down the crystalline sample into smaller pieces. This can be easily achieved with appropriate hand tools due to high brittleness of the dendritic erbium used as a source[9]. The tantalum crucible itself also needed to be replaced because deposits of hot erbium welded the crucible shut, preventing access to the effusion cell. Replenishing the oven was a suitable occasion for cleaning the last collimating aperture (the other two are replaced together with the crucible). Figure 3.4 shows the second (crucible end port) and the third (bored copper gasket) aperture after three year of use. The deposits of erbium form thread-like structures on the walls as well as on a piece of tantalum wire which fixes the crucible inside the oven and which was close enough to the oven opening. These structures have the potential to obstruct the atomic beam and negatively impact the experimental performance. For that reason, any surfaces that come in contact with the atomic beam should be minimized and extra care should be taken when cleaning and aligning the existing setup. After successfully refilling the crucible, the oven was reattached to the rest of the vacuum assembly and a turbo pump[10] connected to the cross was used to initiate pumping. At this point, the oven was

[8] Leaving the pump on could lead to irreversible damage of the active element inside
[9] Distilled dendritic erbium by Alfa Aesar
[10] HiPace 80 by Pfeiffer Vacuum

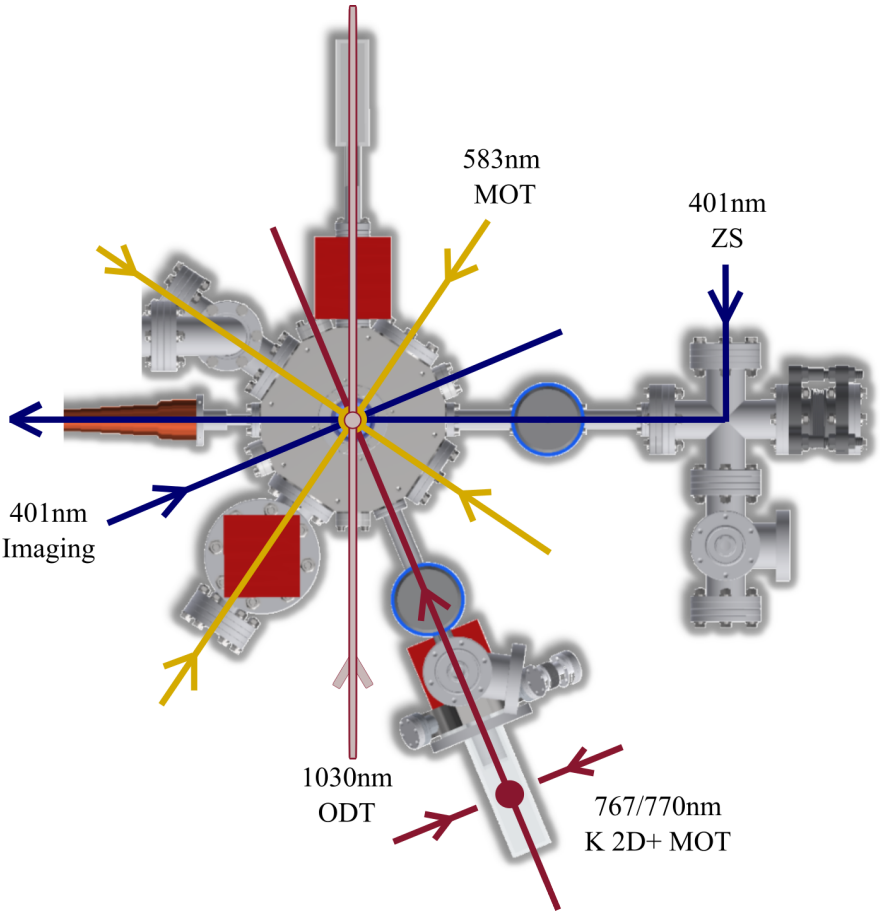


Figure 3.5: MOT chamber beam geometry. Blue–Zeeman slower and erbium imaging beams. Yellow–three pairs of counter-propagating erbium MOT beams. Red–potassium 2D+ MOT beams and a push beam (see chapter 8). Grey–optical dipole trap beams. Note that dots indicate beams coming in and/or out of page. The potassium 3D MOT beams will follow the same path as the yellow erbium MOT beams, forming a dichroic MOT. Optical 'congestion' of the main chamber prompted the 'three chamber' design of our vacuum system, including a glass cell for performing more involved, high-resolution measurements.

reignited again and the new crucible was left to outgas for an extended period of time two weeks. Finally, the NEG pump was engaged and, after the pressure stabilized, the gate valve was opened to reconnect the HV section to the MOT chamber.

UHV section

At the heart of the Ultra High-Vacuum (UHV) section, and in some sense at the heart of the whole experiment, lies the MOT chamber[11] which has 14 viewports[12]. Six have a larger 4 cm diameter and are used for the MOT beams. Six of the remaining eight smaller, 2 cm diameter viewports are used in radially opposing pairs for ZS, ODT and imaging. The last two are used for visual inspection and connection to the potassium chamber respectively (see section 8.1.1). Figure 3.5 depicts the MOT chamber geometry.

[11] A custom 316LN stainless steel chamber by Scanwel
[12] Manufactured by Torr Scientific

The ZS laser beam enters the vacuum through a viewport situated in a cross that is connected to the MOT chamber via a gate valve. The beam is reflected at 45° from a mirror[13] fixed to a port aligner inside the cross and hence under vacuum. The decision to reflect the beam from a mirror inside vacuum rather than shining it directly down the ZS tube through a viewport is based on the fact that the counterpropagating beam of erbium atoms would eventually deposit on the viewport and significantly reduce its transmissive properties. In this way, it is the mirror that gets coated instead but the metallic erbium coating doesn't significantly affect its reflectance [174], [194]. Should this become a problem in the future, a gate valve[14] allows us to replace the mirror without compromising the vacuum in the MOT chamber.

The glass science cell[15] is attached to the MOT chamber via a junction connected to another NEG pump[16]. The decision to include this pump in the design was made based on the requirement of achieving pressures of the order 1×10^{-11} mbar in the cell, allowing for very long atomic cloud lifetimes. We note that the inclusion of the pump slightly complicates atomic transport by increasing the distance to 33 cm but we believe the benefit of longer lifetimes will outweigh the potential atom loss due to longer transport. This pump, in combination with a third NEG pump[17] attached directly to the MOT chamber, is expected to maintain pressures of 3×10^{-11} mbar and 1×10^{-11} mbar in the MOT chamber and the science cell respectively [273]. The ion pump pressure gauges consistently maintain a reading below their detection level of 1×10^{-10} mbar, leading us to believe that the pumping system is performing as intended. Figure 3.13 shows the lifetime measurement of an atomic cloud of erbium trapped in the MOT which gives a value of $t_{\mathrm{MOT}} = 35\,\mathrm{s}$, indicating that the pressure in the MOT chamber is sufficiently low.

3.1.2 Magnetic fields

Application of external magnetic fields is an incredibly powerful tool in the arsenal of ultracold atom physicists. Due to the Zeeman splitting (see section 2.2.2), it allows for direct control of atomic energy levels. Consequently, magnetic fields can create spatially dependent trapping potentials–either conservative [6], [276] or in combination with optical fields [173] (more on this in section 3.2.3). Zeeman shift can also be used to compensate for the Doppler shift perceived by moving atoms, allowing for their resonant interaction with an incident laser field over several orders of magnitude in velocity without the need for tuning the laser frequency–this is the basic principle of a Zeeman slower (see section 3.2.2). Furthermore, probing the vicinity of a Feshbach resonance (see section 2.3.4) [219] via applying a magnetic field of a suitable strength leads to precise tuning of the interatomic contact interactions. In the case of dipolar atoms, an applied magnetic field also defines the polarization direction of the atomic magnetic moment. This in return

[13] A custom, solid aluminium mirror with a UV-enhanced, polished and coated (F01 UV Enhanced Aluminium) surface by Thorlabs

[14] UHV gate valve by VAT

[15] A 30 mm × 30 mm × 100 mm large cell with 2.5 mm thick walls, made from Borofloat glass by Precision Glassblowing

[16] NEXTorr D 100-5 by SAES Getters

[17] NEXTorr D 300-5 by SAES Getters

affects the magnitude and sign of the dipole-dipole interaction (DDI) of two dipolar atoms–see section 2.3.2. It is therefore important to have a high level of control over the magnetic field strength as well as direction across the whole experiment whilst maintaining precision to within 1 mG[18].

These requirements, together with spatial constraints around the experiment, lead to the design of magnetic field control system depicted in figure 3.6. For more technical details on the setup including coil windings and current to field conversion, see references [273], [277]. The first magnetic field encountered by atoms emerging from the oven is the ZS field. The importance and exact shape of the field will be discussed in section 3.2.2. Here we only note that the overall field along the ZS tube is generated by six coils–two profile coils with variable winding along the tube and a bias coils providing an offset to create the characteristic field shape, an extra coil to adjust the field at the end of the ZS and finally a pair of coils to compensate for any field 'leaking' into the MOT chamber from the rest of the ZS system. We note that we use these compensation coils in later stages of the experiment to finely adjust the magnetic field in the direction along the ZS, allowing us to move the position of the MOT and thus optimize loading from the MOT into the ODT.

Three pairs of coils are used to control the field in the MOT chamber. An anti-Helmholtz pair creates a field gradient in the center of the chamber in all three directions which is essential for the realization of our magneto-optic trap (see section 3.2.3). A Helmholtz pair provides a uniform bias field in the vertical direction, enabling us to shift the center position of the MOT as well as tune the contact interactions via FRs. Finally, an extra pair of low-current, Helmholtz coils allows for fine adjustments of the bias field.

Eleven coils form a compensation cage that encapsulates the whole UHV section, including the science cell. The cage was designed to provide a homogeneous field across the whole experiment and its role is three-fold. Firstly, it provides a polarizing field during transport between the MOT chamber and the science cell. This in return ensures that the atoms will never experience low field magnitude along the way and will thus avoid a loss-inducing Feshbach resonance at around 0 G [153], [155]. Secondly, the cage can compensate for any external fields–be it spurious ones from electronic infrastructure in the building and its vicinity or more stable fields, most notable of which is the Earth's magnetic field $B_E = (0,\ 0.19,\ 0.45)$G[19] with the laboratory frame axes defined in figure 3.6. Lastly, and similarly to the ZS and MOT compensation coils described above, the cage allows for fine adjustments to the MOT position which is beneficial for both the MOT and ODT loading phases (see section 4.2). The three coils that provide the field in the direction perpendicular to the ZS and to the vertical (also known as the Y cage) are particularly important because they are the only means of applying a uniform field in the Y direction. For more flexibility, a relay was installed that allows us to change the field direction along that axis.

Temporal stability of the applied fields is necessary to reduce the noise in atomic

[18]Such precision is desirable due to the large density of Feshbach resonances in erbium as well as due to the sensitivity of the MOT position to the applied bias field

[19]Data taken from https://www.ngdc.noaa.gov/

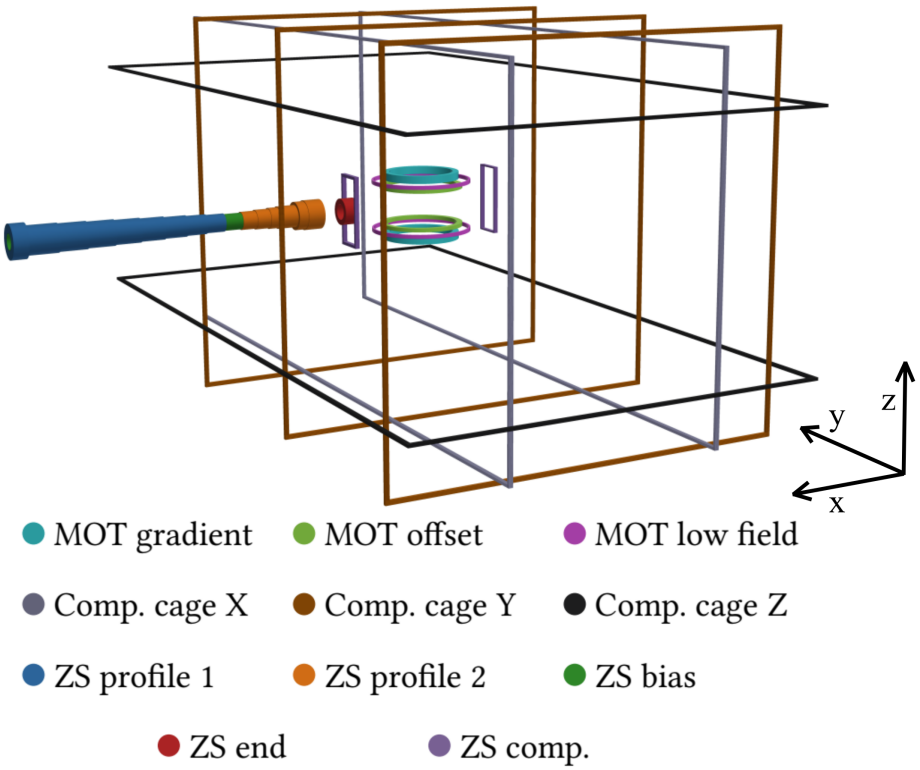


Figure 3.6: Magnetic field control. The ZS system consists of five coils. Three provide the characteristic 'square root' shape of the field discussed in section 3.2.2. The end coil and compensation coil both work to extend the ZS region into the MOT chamber and to remove any stray fields from the center of the chamber. The MOT coils come in three varieties. First, an anti-Helmholtz coil creates a field gradient in all three directions. An offset coil pair (also referred to as Feshbach coils) creates a homogeneous field for moving the center of the field gradient and for applying a uniform bias utilized in Feshbach spectroscopy. A third, fine coil pair is used for small adjustments to the bias. Finally, a large cage system encapsulates the whole experiment and is used for various purposes. Firstly, it can cancel Earth's magnetic field and has the potential to cancel any other stray fields coming from the outside. Secondly, it is used to rotate the atomic polarization axis to an arbitrary direction. Thirdly, it provides a nearly-uniform polarizing field between the MOT chamber and the science, allowing us to transport the atoms without crossing any loss-inducing Feshbach resonances. Note that the cage system also defines natural axes in the laboratory frame–for example, the ZS propagates along x whereas the main ODT transport beam (see section 4.1.4) propagates along y. Figure taken from [273].

positions and loading numbers as well as to prevent additional heating arising from a time-dependent driving force. To minimize the effects of spurious magnetization and eddy currents induced during ramping of the magnetic fields around the experiment, the MOT chamber was manufactured from 316L stainless steel with an exceptionally low relative magnetic permeability of $\mu_r - 1 \sim 1 \times 10^{-3}$. The breadboard[20] and the optical table on which the experiment was built are also made from non-magnetic materials (aluminium and 316L stainless steel respectively). We note that an observed instability in the MOT position arose suspicions regarding noise in the magnetic fields around the MOT chamber. This prompted us to construct a high precision magnetometer to measure, and potentially actively suppress, any spurious fields. Later it was revealed that this instability was caused by noise in the 583 nm laser frequency due to a sub-optimal locking procedure. The issue was resolved by implementing a locking scheme referenced to a high precision optical cavity (more details in section 3.2.3). The magnetometer might be used in the future to compensate for any time-dependent drifts of the magnetic fields, should the need arise, and its technical details are presented in appendix A.1.

Field calibration

The inability to access the center of the MOT chamber makes the task of calibrating and hence precisely knowing the fields applied to the atoms quite challenging. Luckily, the atoms themselves can serve as an excellent reference provided we know their magnetic moment. As discussed in section 2.2.2, an applied magnetic field B will lift the degeneracy of the Zeeman sublevels denoted by m_J, causing them to acquire an energy splitting given by

$$\Delta E_Z(m_J, m'_J) = (m_J - m'_J) g_g \mu_B B \ , \tag{3.1}$$

where $g_g = 1.163801(1)$ [185] is the ground state Landé g-factor. For a given magnetic field B, applying an oscillating electromagnetic field of frequency $\Delta E_Z(m_J, m_J+1)/\hbar$ will drive transitions between the m_J Zeeman sublevels. Consequently, an atomic cloud that starts in the polarized ground state $|J = 6, m_J = -6\rangle$ and that is subject to a magnetic field gradient during free fall will split into several clouds based on the m_J quantum number of the constituent atoms–a Stern-Gerlach like experiment [278]. By scanning through the frequency of an applied radio-frequency (RF) field and looking for a signature of this splitting, the magnetic field B can be measured precisely. A sample dataset and a typical image of atomic cloud splitting in our experiment is shown in figure 3.7. To produce the driving RF field, we use a single-loop coil of ≈ 4 cm diameter attached to the top of the MOT chamber. This coil is supplied with a sine wave pulse from an arbitrary wave generator amplified with an RF amplifier[21]. The RF pulse is applied just after the atoms are released from their trap while they are still experiencing the homogeneous field B subject to the measurement. The field gradient is applied during their fall under gravity. Calibrating the magnetic field this way allows us to know its magnitude

[20] The breadboard is essentially a large sheet of conductive material and as such it can create virtual charge images and strongly affect the fields around the experiment

[21] ZHL-3A-S+ by Mini Circuits

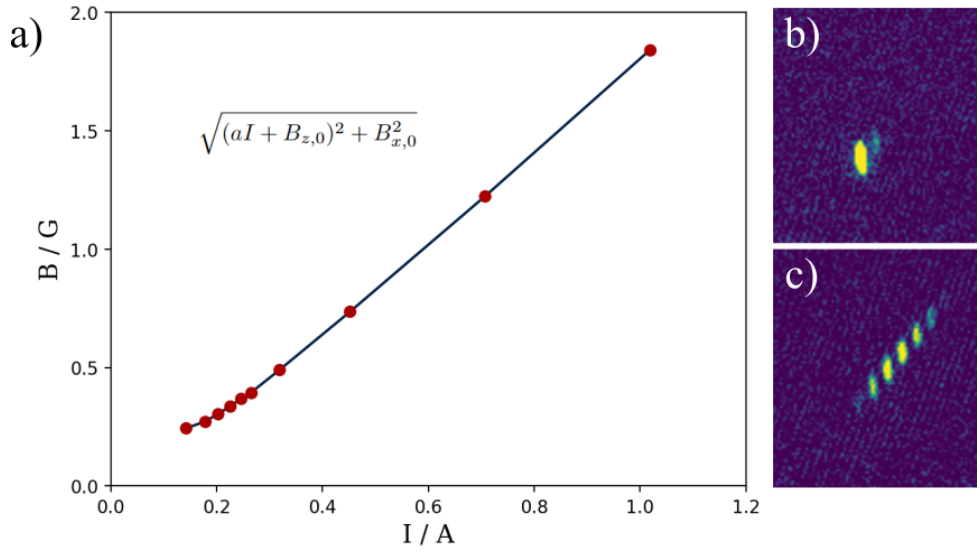


Figure 3.7: Magnetic field calibration. a) Typical calibration curve. By varying the RF field frequency and scanning the coil current, we can look for a resonance at which the field-dependent level splitting matches the driving field frequency. This way, we can map the magnetic field magnitude as a function of the coil current and find the calibration constant a that best fits the data with a model given by $B = \sqrt{(aI + B_{z,0})^2 + B_{x,0}^2}$, where $B_{i,0}$ are the residual fields in the i-th direction and the y field is assumed to be perfectly cancelled. b)-c) Typical experimental image of a Stern-Gerlach experiment. b) shows an atomic cloud driven off resonance whereas c) shows the cloud splitting into different m_J sublevels under the influence of a magnetic field gradient.

with $\sim 1\,\mathrm{mG}$ precision which proved crucial for thoroughly characterizing three-body loss features–known [153] as well as previously unreported–in ^{166}Er as discussed in chapter 5.

Future extension

To provide sufficient magnetic fields in the science cell, new system of coils was designed [199]. This includes three sets of smaller Helmholtz coils with limited field strength but capable of fast modulation and two sets of large, water-cooled coils[22] capable of generating field strengths of up to 300 G–see figure 3.8. The faster coils will be used to quickly rotate the polarization direction of erbium atoms, effectively time-averaging their dipole-dipole interactions allowing for separate tuning of the parameter ε_{dd} and the s-wave scattering length a_s–for more details on this technique see section 2.3.2 and reference [158]. The larger coils, on the other hand, will enable us to address prominent Feshbach resonances in ^{41}K and ^{39}K at 51.4 G [279] and 162.4 G [227] respectively at arbitrary rotation angles with respect to the vertical allowing for the study of strongly interacting impurities in a tunable dipolar condensate. We believe that this field range will also be more than sufficient for observing interspecies Er-K resonances which haven't been observed before and which are believed to lie in the $< 10\,\mathrm{G}$ region based on previous work with Dy and K mixtures [138].

[22] Manufactured by Oswald

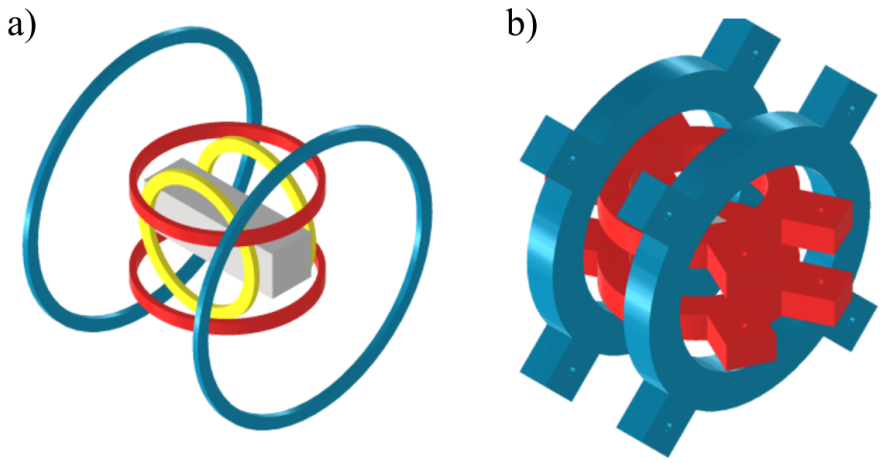


Figure 3.8: Field control around the science cell. A new set of coils was designed and manufactured to provide sufficient magnetic fields in the science cell region for Potassium and erbium-potassium Feshbach spectroscopy and erbium DDI control. a) Three pairs of smaller, faster coils will create a field that precesses around the vertical axis to create an effective time-averaged DDI between erbium atoms (see section 2.3.2). b) Two pairs of large, water-cooled coils will provide fields of up to 300 G at an arbitrary angle to the vertical to access potassium Feshbach resonances. Image taken from [199].

3.1.3 Imaging

Most of our measurements rely on imaging the atomic cloud and inferring its properties from the shape and density distribution. To obtain an image of the atoms, they are illuminated with resonant light which is then collected on a camera. One can either look at the shadow the atoms cast–*absorption* imaging–or collect the light that gets spontaneously re-emitted–*fluorescence* imaging. Our experiment has the capability of performing both types of imaging. Historically, fluorescence of the atoms emerging from the ZS and interacting with the ZS cooling beam was used to characterize the beam flux and its velocity distribution [273]. However, this method of imaging relies on long exposure times during which the atom cloud gets severely affected by its interaction with the imaging light. Consequently, unless the imaging light is also used as a means of cooling/trapping, the atom cloud is destroyed and the obtained image is essentially a distorted time series of this destruction i.e. its information content is limited.

Absorption imaging is also destructive, however, the short exposure times needed to create a sharp image mean that one gets a clear snapshot of the atomic cloud at a given point in time, before the atoms are blown away by the imaging light. For that reason, absorption imaging is the main tool used in our experiment–especially in later stages of cooling, i.e. evaporation, during which the atoms interact with non-resonant trapping light and are therefore not fluorescing.

Our absorption imaging setup consists of $\approx 10\,\mathrm{mW}$ of 401 nm light tuned close to resonance and collimated to a beam diameter of $\approx 24\,\mathrm{mm}$. The light is passed through a $\lambda/4$ waveplate which changes its polarization to $-\sigma$. After traversing the MOT chamber–for specific geometry see figure 3.5–the beam is incident on a confocal telescope consisting of 150 mm and 300 mm plano-convex lenses which project the image of the atomic shadow

on a CMOS camera[23] with 2× magnification, resulting in an apparent pixel size of ≈ 2.93 µm. Additionally, a pair of coils in near-Helmholtz configuration [280] provides a polarizing field along the beam direction, increasing the absorption rate by only allowing the $m_J = -6$ to $m_J = -7$ to be driven by the imaging field.

The intensity of a near-resonant beam of frequency ω passing through an absorbing medium of density $n(\mathbf{r})$ along the z axis is given by [80]

$$I(x, y, \omega) = I_0 e^{-\mathrm{OD}(x,y,\omega)} \tag{3.2}$$

with I_0 the incident intensity. The quantity $\mathrm{OD}(x, y, \omega)$ is known as the *optical density* and it is proportional to the reduced 2D density of the medium:

$$\mathrm{OD}(x, y, \omega) = \sigma(\omega) \int n(\mathbf{r}) dz \ . \tag{3.3}$$

The constant of proportionality σ is the *optical cross-section* which represents the scattering rate of incident photons and the illuminated atoms an so naturally depends on the light detuning δ and its intensity through

$$\sigma(\omega, I) = \left(\frac{3\lambda^2}{2\pi}\right) \frac{1}{1 + \left(\frac{2\delta}{\Gamma}\right)^2 + \frac{I}{I_{\mathrm{sat}}}} \ . \tag{3.4}$$

Since we are using resonant light ($\delta \approx 0$) of intensities much lower than the saturation intensity $I_{\mathrm{sat}} \approx 60\,\mathrm{mW\,cm^{-2}}$ (see section 2.2.1), we can safely assume $\sigma = 3\lambda^2/2\pi$ and so the optical density is a direct representation of the 2D density of the atomic cloud. From it, we can infer important quantities such as the total atom number and the cloud temperature.

In practice, the light intensity incident on the imaging camera contains not only the desired information about the atom cloud but also some background radiation. To get a clear image, we implement a three-shot sequence in quick succession. First, a 15 µs imaging pulse is used to record the light intensity in the presence of the atoms, I_a. Second, another pulse is used to record the imaging beam intensity without the atoms, effectively measuring I_0 in equation 3.2. Last, a background intensity shot I_b is taken in the absence of the imaging light. The optical density can then be simply reconstructed as

$$OD = -\ln\left(\frac{I_a - I_b}{I_0 - I_b}\right) \ . \tag{3.5}$$

We note that although this imaging sequence is specific to erbium, we use a similar sequence exploiting the strong D2 transition for imaging potassium atoms in the MOT chamber. For more details, see section 7.4. To achieve sub 3 µm resolution in the science cell for both erbium and potassium, more sophisticated imaging scheme is required that involves a trichroic objective as well as high spec camera[24]. Initial design of this new setup is outlined in references [199], [273] but it is yet to be implemented in the experiment.

[23] DCC3260M by Thorlabs
[24] C14440 by Hamamatsu

Time-of-flight expansion imaging

The optical density recovered from images of the atomic cloud using equation 3.5 can be converted to 2D density profile of the cloud. However, imaging a cloud essentially in-situ, i.e. right after it has been released from the trap, yields improper data because the cloud is still very dense and the imaging beam gets completely absorbed upon passing through it, resulting in 'saturation' of the shadow. Such saturated images underestimate the density because above certain density threshold, practically no light passes through and densities higher than the threshold are indistinguishable from it. It is therefore desirable to let the cloud expand during time-of-flight to reduce its density. That way, we can obtain accurate measurements of the atom number by integrating the density across the cloud. At the same time, by doing so we lose any information about the cloud's initial shape but we gain information about its initial velocity distribution and so temperature.

To see this in practice, lets assume that at time $t = 0$, i.e. before being released from the trap, the cloud has a density and momentum distribution given by $n_0(\mathbf{r})$ and $f_p(\mathbf{p})$. At some later time $t = t_{\text{tof}}$, the probability of finding an atom at position $\mathbf{r}$ is given by

$$P(\mathbf{r}, t_{\text{tof}}) = \int n_0(\mathbf{r}') f_p(m\frac{\mathbf{r} - \mathbf{r}'}{t_{\text{tof}}}) d^3\mathbf{r}' \ , \tag{3.6}$$

i.e. it is the probability that the atom was at position $\mathbf{r}'$ at $t = 0$ multiplied by the probability that it had momentum $\mathbf{p}/m = (\mathbf{r} - \mathbf{r}')/t_{\text{tof}}$ such that after time t_{tof} it would have propagated to position $\mathbf{r}$. Note that this approach assumes that the atoms move ballistically after being released from the trap and therefore neglects any atom-atom interactions. Above degeneracy, i.e. in the thermal phase, this is a sound assumption since the gas is generally very dilute. Under these conditions, the density and momentum distribution obey Maxwell-Boltzmann statistics with $n(\mathbf{r}) \propto \exp(-U(\mathbf{r})/k_B T)$ and $f_p \propto \exp(-\mathbf{p}^2/2mk_B T)$. In the case of harmonic trapping, the integral in equation 3.6 can be solved analytically to yield the cloud density after time-of-flight

$$n(\mathbf{r}, t) = N\bar{\omega}^3 \left(\frac{m}{2\pi k_B T}\right)^{\frac{3}{2}} \prod_i \frac{1}{\sqrt{1 + (\omega_i t)^2}} e^{-\frac{m}{2k_B T}\frac{\omega_i^2 r_i^2}{1+(\omega_i t)^2}} \ , \tag{3.7}$$

where the subscript i runs over the three axes x, y, z and ω_i are the trapping frequencies along these axes with $\bar{\omega} = (\omega_x \omega_y \omega_z)^{1/3}$. We see that the cloud remains Gaussian in shape with the characteristic sizes given by

$$\sigma_i^2(t) = \frac{k_B T}{m} \ \frac{1 + (\omega_i t)^2}{\omega_i^2}. \tag{3.8}$$

For long enough expansion times such that $\omega t \gg 1$, the cloud becomes isotropic with its size proportional to $\sqrt{T}$, independent of the original trapping geometry. In fact, as long as the initial momentum distribution is Maxwell-Boltzmann and independent of the initial density distribution as is the case for a thermal gas, in the long time-of-flight limit for which $t_{\text{tof}}\sqrt{k_B T/m} \gg \sigma_0$ with σ_0 the initial size of the cloud, equation 3.6 can be approximated by a Gaussian with standard deviation equal to $t_{\text{tof}}\sqrt{k_B T/m}$. In other

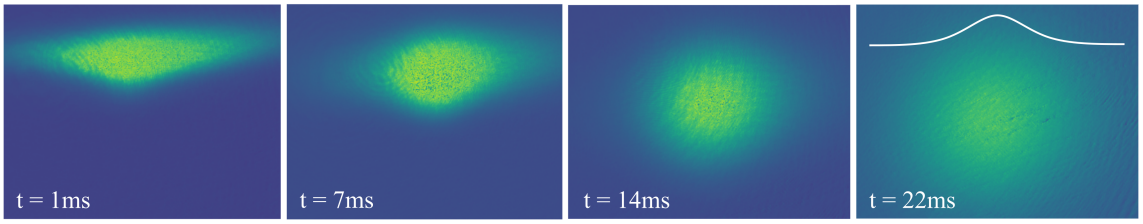


Figure 3.9: Time-of-flight MOT sequence. Images of the MOT cloud after increasing time-of-flight. Even though the density distribution is initially non-Gaussian and determined by the detailed balance of the laser beam intensities, detunings and magnetic field gradient, after a long ToF, the cloud becomes isotropic and Gaussian. By fitting the appropriate functional form to the density distribution, we can recover the temperature of the atoms according to equation 3.8.

words, the cloud becomes Gaussian and isotropic irrespective of its original shape. This can be seen in figure 3.9. In practice, we take a series of images at different t_{tof} and fit a line to σ^2 as a function of t_{tof}^2 to extract the temperature of the cloud.

Note that once the atoms approach degeneracy, their distribution deviates from Maxwell-Boltzmann statistics and needs to be replaced with the slightly more involved Bose-Einstein distribution. The treatment of a near-degenerate gas as well as of a dipolar BEC is presented in section 4.4.1.

3.1.4 Computer control and data acquisition

A cold atom laboratory is a complex ecosystem of optics, electronics and other peripheral devices. Moreover, the experimental sequence relies on concurrent, dynamical change of parameters with high precision and temporal resolution. Manual operation is therefore laborious and, in most cases, impossible. Consequently, a centralised, digital and programmable control system is required instead.

The Oxford experiment is controlled by Cicero Word Generator [281]–a computer software designed specifically for atomic physics experiments with the capability of creating multi-stage control sequences consisting of arbitrary analog waveforms and digital pulses, all through a graphical user interface (GUI). Cicero's functionality also offers integration with an FPGA chip[25], providing a variable time-base clock for the sequence.

The electronic signals themselves are provided by National Instruments (NI) analog and digital cards. The majority of the experiment is controlled by two analog[26] cards and one digital[27] card. This was later extended by the addition of an extra analog[28] and digital[29] card to allow for the control of potassium-related parts of the experiment. All cards are housed in a common chassis[30] and the digital cards are interfaced with the experiment through an optical isolator circuit (details of which can be found in [282]).

[25] XEM6001 by Opal Kelly
[26] NI PXIe-6733–8 Channel, 16-bit Analog Output Card and NI PXIe 6738–32 Channel, 16-bit Analog Output Card by National Instruments
[27] NI PXIe-6536–32 Channel Digital Output Card
[28] NI PXIe-6738
[29] NI PXIe-6536
[30] NI PXIe-1082 8-Slot PXI Express Chassis

We conclude this brief section by mentioning data handling. The main source of experimental data comes from the imaging system (see section 3.1.3). This data needs to be safely handled, stored and readily interpreted. A complex software infrastructure was built [280] that interfaces the image acquisition program with Cicero, stores the data in a MySQL database and, with the help of custom-built packages and a GUI, analyzes the data in real time. This robust dataflow ensures reliable, comprehensible storage architecture and facilitates smooth and dynamic operation of the experiment.

3.2 Laser cooling

The ultracold temperatures necessary for accessing quantum degeneracy wouldn't be attainable without laser cooling [11]. In the following section, we will introduce the theory of laser cooling and, using the examples of the 401 nm and 583 nm transitions implemented in our experiment based on pioneering works on erbium [104], [146], we will show how it is possible to cool a gas of erbium atoms from $\approx 1200\,\mathrm{K}$ to $\approx 10\,\mu\mathrm{K}$. To fully appreciate laser cooling which earned its inventors a Nobel prize [283] and which kick-started an entirely new field of experimental physics, we first need to understand how atoms interact with laser fields.

3.2.1 Light-scattering force

Electrons in an atom interact with an applied electric field $\mathbf{E}(t) = \mathbf{E_0}e^{-i\omega t}$ through a Hamiltonian of the form $\hat{\mathrm{H}} = -\mathbf{E}(t)\cdot\mathbf{p}$. This interaction can couple two internal states of the atom with energies E_g and E_e and a time-varying electric field can thus induce transitions between these states. The nature of the coupling is encompassed in two parameters– the *Rabi frequency* $\Omega = \langle g|\mathbf{p}\cdot\mathbf{E_0}|e\rangle/\hbar$, which reflects the strength of the applied field and its coupling to the two atomic states, and the *detuning* $\delta = \omega - \omega_0$ with $\omega_0 = (E_e - E_g)/\hbar$, which indicates how far off-resonance the driving field is. In this simple two-level picture, an atom that initially starts in the ground state $|g\rangle$ evolves coherently into a superposition of the two states and, after some time comparable to Ω^{-1}, comes back to its original state, undergoing the so-called *Rabi oscillations* [80], [284]. In the language of second quantization, a photon from of the applied field is absorbed and then some time later re-emitted into the same mode.

The picture gets more complicated when one takes into account the excited atom's interaction with the vacuum state of the electromagnetic-field. This interaction allows the atom to decay back to the ground state and emit a photon into an empty EM mode. The process is incoherent, random and happens on timescales of the order Γ^{-1} where Γ is known as the transition linewidth and it depends on the exact details of the two electronic levels involved in the transition. When an electric field with $\Omega \ll \Gamma$ is applied, atoms are continuously excited into the upper state by the driving field and de-excited through spontaneous emissions. This process results in an equilibrium population of the two states that depends on the detuning δ and the applied field strength.

By considering the steady state condition of the two-level system, it can be shown that

the excitation rate, i.e. the rate of photon scattering, for a single atom is given by [80]

$$R_{\text{scatt}} = \frac{\Gamma}{2}\frac{\frac{\Omega^2}{2}}{\delta^2 + \frac{\Omega^2}{2} + \frac{\Gamma^2}{4}} = \frac{\Gamma}{2}\frac{s}{1 + s + \left(\frac{2\delta}{\Gamma}\right)^2} , \tag{3.9}$$

where we have introduced the saturation parameter $s = I/I_s$ with I, the intensity of the incident laser light, and $I_s = \pi hc\Gamma/3\lambda^3$, the saturation intensity. The role of the saturation parameter can be understood in the following way. For low light intensities such that $s \ll 1$, the scattering rate is directly proportional to the applied intensity as one would expect by simply considering a 'target' atom in its ground state bombarded by an increasing number of photon 'projectiles'. For intensities $I \sim I_s$, the probability that the atom will be in the excited state during a potential collision is no longer negligible. Furthermore, an excited atom can't absorb any more photons and so the scattering rate is suppressed by a factor of s in the denominator for higher intensities. This is known as *saturation* of the transition. The highest scattering rate is still achieved for $s \to \infty$ and $\delta \to 0$ but, contrary to our naive intuition, the maximum rate approaches only half of the spontaneous emission rate Γ. This is because the transition saturates at equal population of the two levels. In other words, population inversion is not possible in a two-level system and the best we can do is to force the equilibrium to be half-way between the two levels.

Scattering of photons by atoms is the key to laser cooling. This is because photons not only carry energy $E = \hbar\omega$ but also momentum $\mathbf{p} = \hbar\mathbf{k}$. Consequently, during an absorption event, the atomic momentum changes by $\hbar k$. If the laser beam is oriented against the motion of the atom, the resulting momentum is smaller in magnitude and the atom slows down. The photon is later re-emitted, imposing recoil momentum on the atom. However, the direction of this recoil momentum is, in general, random and over many scattering events averages to zero. The same is not true for the absorbed momentum which is always directed along the laser beam. As a result, atoms in the laser beam experience a light-scattering force given by $\mathbf{F}_{\text{scatt}} = \hbar\mathbf{k}R_{\text{scatt}}$ which has a maximum magnitude $F_{\text{max}} \approx \hbar k\Gamma/2$ when the laser beam is intense and on resonance such that $s \gg 1$ and $\delta \to 0$. In practice, the detuning δ depends on several factors other than the driving frequency–most notably the atomic velocity through the Doppler effect. This somewhat complicates laser cooling procedures because effective cooling inevitably leads to a decrease in atomic velocities which leads to a change of detuning which finally leads to a reduction in cooling efficiency. Below, we will discuss how this effect can be mitigated and even embraced to cool a gas of erbium by eight orders of magnitude.

3.2.2 The Blue–401 nm

The first two stages of laser cooling of erbium rely on a prominent atomic transition at 401 nm. The relatively large linewidth of this transition, $\Gamma_{401} = 29.5\,\text{MHz}$, makes it particularly suitable for cooling hot samples due to the large magnitude of the resulting light-scattering force. A hot sample, on the other hand, is required because of the low vapour pressure of erbium at ambient temperature. Therefore, in order to produce high flux of cold atoms, the atomic beam has to be sufficiently collimated and slowed over a long

distance–for that reason, we implement a transverse cooling stage (TC) in combination with a standard Zeeman slower (ZS).

Transverse cooling–an optical molasses

As discussed above, the magnitude of the light scattering force is strongly dependent on the detuning of the laser light. Furthermore, slowing is only achieved when the beam is propagating in the opposite direction to the atomic velocity. A first step towards an omnidirectional cooling mechanism is to have pairs of counter-propagating, resonant laser beams. That way, maximal radiation pressure is exerted from all directions. However, this setup alone isn't sufficient for achieving efficient cooling because the scattering force is symmetric around zero detuning (see equation 3.9). An atom moving along the x axis with velocity v would experience equal push from the two beams propagating in the $+x$ and $-x$ directions because the square of the detuning for the two beams $\delta^2 = (kv)^2 = (-kv)^2$ due to the Doppler shift is identical.

A solution to this problem is to use beams which are slightly red detuned with respect to the atomic transition such that $\delta_0 < 0$. That way, the total detuning $\delta = \delta_0 + kv$ is only brought to resonance when the atom is moving against the beam–see figure 3.10a. In other words, the scattering force from the two counter-propagating beams is imbalanced for atoms with $v > 0$ and the resulting total force always points against the motion of the atom–see figure 3.10b. More mathematically, one can express the total force from two beams propagating along the $\pm$ x directions as

$$F_{\text{tot}} = -F(\delta_0 + kv_z) + F(\delta_0 - kv_z) \approx 4\hbar k^2 s \frac{2\delta_0/\Gamma}{\left(1 + (2\delta_0/\Gamma)^2\right)^2} v_z = -\alpha v_z \tag{3.10}$$

where we have assumed $s \ll 1$ and $kv_z \ll \Gamma$ i.e. small velocities and no saturation effects that could potentially couple the two beams. Equation 3.10 is effectively an equation of motion of a particle moving through a resistant, viscous medium with a characteristic damping time α^{-1} which is maximized for $\delta_0 = -\Gamma/2$. For that reason, this laser cooling technique is known as *optical molasses* [285].

The exponential decay implied by equation 3.10 is slightly deceptive because it might lead one to believe that in the limit of long cooling times, an arbitrarily low velocity (and hence temperature) is achievable with this technique. Even though the average component of the atomic momentum does tend to zero due to the random nature of spontaneous emission, the magnitude of the atom's momentum does not. This is because the recoil momentum from spontaneous emission is, in essence, a random walk and so while the cooling beams reduce the spread of momenta and energies along their direction, the random emissions cause isotropic, diffusive heating–see figure 3.10c. An equilibrium is reached when the heating and cooling rates balance each other out. This equilibrium corresponds to a certain average atomic energy or rather temperature which is known as the *Doppler temperature* and represents the cooling limit for optical molasses. For a 3D optical molasses under ideal conditions, the Doppler temperature is simply given by $k_B T_D = \hbar\Gamma/2$

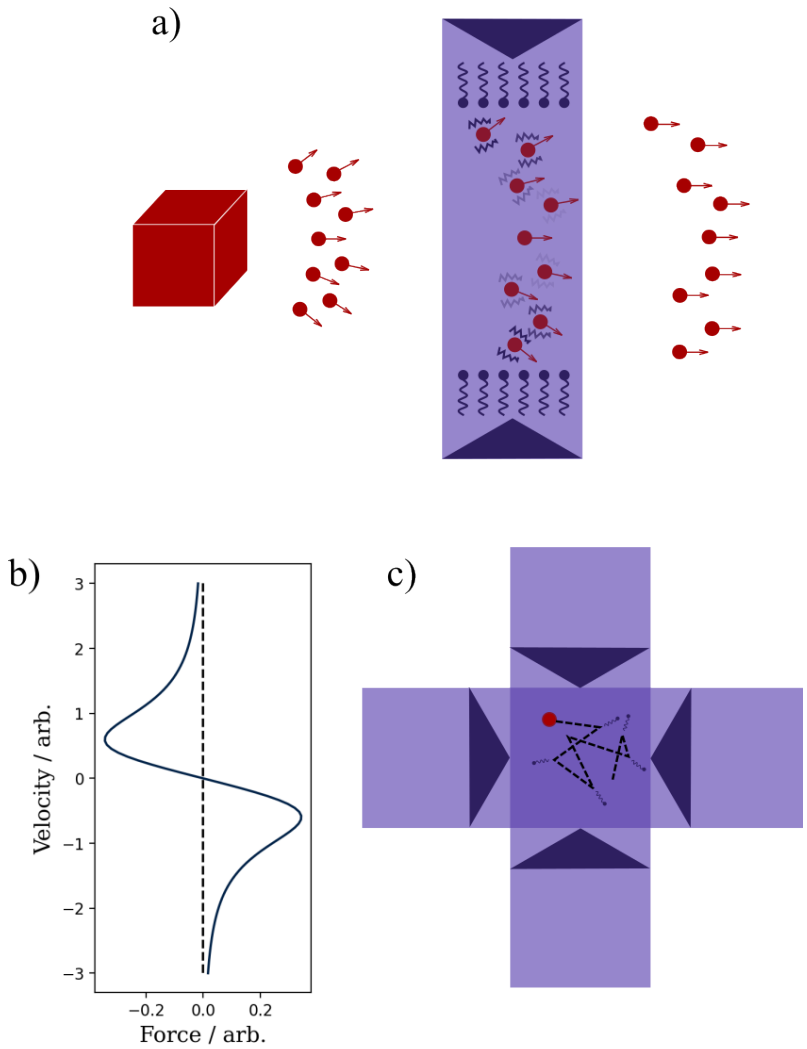


Figure 3.10: Optical molasses and the Doppler limit. (a) Two red-detuned, counter-propagating molasses beams can reduce the transverse velocities of a hot atomic beam, collimating it in the process. This is the principle of transverse cooling implemented in our experiment. (b) The light scattering force profile as a function of velocity for a 1D optical molasses. For small velocities, the force is linear in velocity and plays the role of damping. (c) Doppler cooling limit. For low enough velocities, the loss of energy thanks to the molasses force becomes comparable to the heating due to a random walk in momentum performed by the atom because of spontaneous emission events. The lowest achievable kinetic energy and hence temperature is known as the Doppler limit.

[12], [285] which depends only on the linewidth of the transition. Consequently, even though wider transitions are more suitable when large slowing forces are needed such as in the Zeeman slower (see next section), narrower transitions lead to lower Doppler temperatures and are therefore more suited for later cooling stages.

To collimate the hot atomic beam emerging from the erbium oven, we implement a transverse cooling (TC) stage operating on the 401 nm transition. This consists of two retro-reflected, circularly-polarized, elliptical laser beams of waists $17 \times 3\,\mathrm{mm}$[31] and total powers of $P_{TC} \approx 40\,\mathrm{mW}$ ($I/I_s \approx 0.8$). The TC stage is effectively a 2D molasses and so it helps to reduce the spread of transversal velocities in the atomic beam, thus enhancing the flux emerging from the ZS into the MOT chamber. With the TC light turned on, the number of atoms loaded into the MOT is enhanced by $\approx 50\%$, indicating the importance of this cooling step. We note that the experimental detuning was optimized to $\delta_0 = -2\pi \times 12.5\,\mathrm{MHz}$ which is slightly lower than the theoretical optimal value of $\delta_{\mathrm{opt}} = -\Gamma/2 = -2\pi \times 15.0\,\mathrm{MHz}$. We also note that the use of a retro-reflected beam as opposed to two separate beams can cause an imbalance in the transverse velocity distribution (and consequent deterioration of MOT loading) if the atomic absorption is strong or if the beam is attenuated before its second passing. The former issue can be addressed by increasing the power in the laser beams whereas the latter issue, which we encountered and discussed in section 3.1.1, can be mitigated with the use of appropriate optical coating.

Zeeman slower–fighting Doppler with magnets

Atoms emerging from the erbium oven ($\approx 1200\,^{\circ}\mathrm{C}$) have typical velocities of the order of $\approx 300\,\mathrm{m\,s^{-1}}$. The MOT, on the other hand, can only capture atoms with velocities $v \leq 10\,\mathrm{m\,s^{-1}}$. The light scattering force described in the previous section should, in principle, be able to provide enough deceleration if applied over long enough distance. However, the change in the Doppler shift over this range of velocities, $\Delta\omega = k\Delta v \approx 2\pi \times 700\,\mathrm{MHz} \gg \Gamma$, is too large, making a single-frequency slowing beam extremely inefficient on its own. Fortunately, the Zeeman effect can change the detuning of a transition by applying an external magnetic field (see section 2.2.2), negating the effect of the Doppler shift. If the profile of the field is chosen appropriately, the decelerating atoms always experience a resonant, slowing force–this is the working principle of a Zeeman slower (ZS) [172].

The problem can be described quantitatively by requiring that the atoms experience a constant slowing force $F(s,\delta) = \hbar k R(s,\delta)$ along their trajectory. Their velocity as a function of distance along the slower is then given by

$$v_0^2 - v^2(x) = \frac{2F}{m}x \tag{3.11}$$

where v_0 is their initial velocity. The atoms come to a near halt (subject to the Doppler

[31] The smaller waist matches the transversal dimension of the atomic beam

limit) after travelling over a distance

$$x_0 = \frac{mv_0^2}{2F} = \frac{mv_0^2}{\hbar k \Gamma s}\left(1 + s + \left(\frac{2\delta}{\Gamma}\right)^2\right) . \tag{3.12}$$

Conversely, for a given ZS length x_0, equation 3.12 defines the capture velocity v_0 above which the atoms won't be slowed by the ZS.

The total detuning δ which, together with the beam intensity, defines the magnitude of the slowing force encompasses several factors. It is a measure of how much the frequency of the laser light as perceived by the atoms deviates from the energy splitting of the two levels involved in the transition. As such, it is given by

$$\delta = \tilde{\omega} - \omega_0 = (\omega + kv) - \frac{1}{\hbar}\left(E_0 + \Delta\mu B\right) \tag{3.13}$$

where we have explicitly included the Zeeman shift of the electron energy levels $\Delta\mu B = (m_e g_e - m_g g_g)\mu_B B$. Clearly, under the assumption of negligible beam attenuation ($s \approx$ const.), the constant force condition corresponds to constant detuning along the slower. This yields the desired field strength profile as

$$B(x) = \frac{\hbar}{\Delta\mu}\left(\delta_0 - \delta + kv_0\sqrt{1 - \frac{x}{x_0}}\right) \tag{3.14}$$

where we defined the bare laser detuning from the unshifted transition as $\delta_0 = \omega - E_0/\hbar$. The field given by equation 3.14 has a square root profile with a constant offset and it can be realised by using coils of variable winding number along the beam path which gives the ZS its signature look of a copper-plated, cylindrical tube.

In our implementation of the ZS, we use two profile coils to generate the 'square root' shape and an additional bias coil to provide a constant offset. Technical parameters are provided in reference [273]. In practice, certain deviations from the ideal configuration given by equations 3.14 and 3.12 are necessary. Firstly, although zero total detuning $\delta = 0$ corresponds to maximum slowing and therefore shortest ZS, the system isn't robust against spread of velocities or fluctuations in the fields. If instead we choose $\delta < 0$, then atoms moving slower than the ideal velocity $v(x)$ (equation 3.11) will experience less slowing whereas atoms moving faster will experience more slowing, both eventually converging on the ideal value. For a given ZS length (constrained by the vacuum system), increasing the detuning therefore increases the robustness at the expense of lowering the capture velocity. Ideal parameters are discussed in references [174], [273]. Here we only provide the value of the raw detuning used in our experiment, $\delta_0 = -2\pi \times 540\,\mathrm{MHz}$.

In order to reduce the total field magnitudes and therefore the power load and volume of the ZS coils, our ZS operates in the 'spin-flip' configuration (see figure 3.11) which includes a zero-field crossing. This can potentially cause unwanted transitions to other m_J states when their energy splitting becomes negligible as $|B| \to 0$. However, a more quantitative analysis [273] reveals that optical pumping back into the $m_J = -7$ stretched state following the zero crossing is sufficient for our experimental parameters and the

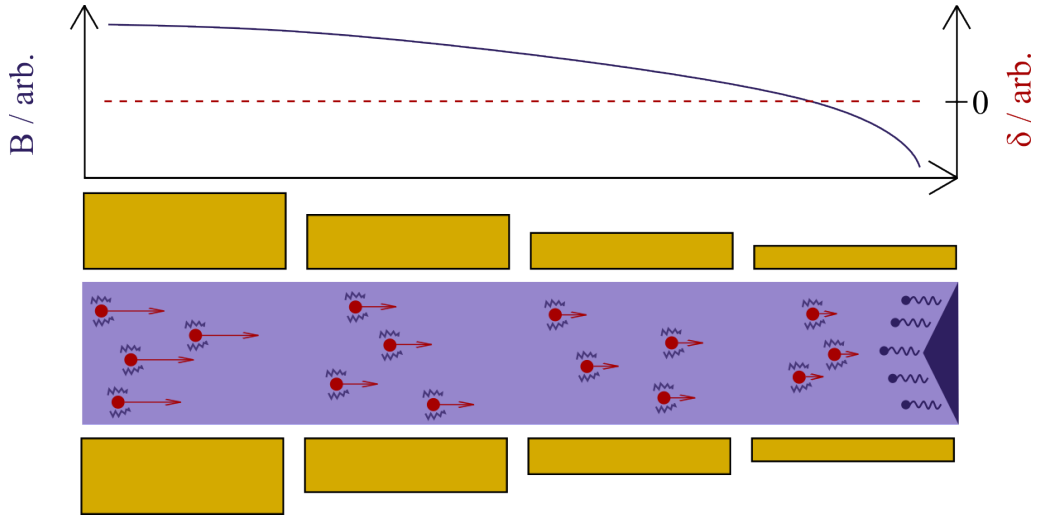


Figure 3.11: Principle of a Zeeman slower. Coils with variable winding and/or current provide a magnetic field profile which continuously brings the decelerating atoms into resonance with a counter-propagating beam. In this way, the atoms experience the maximum slowing force at all times, irrespective of their velocity.

practical benefits outweigh the negligible side effects.

Lastly, although efficient slowing is desirable across the whole path, it is also beneficial for the atoms to have non-zero velocity when they leave the ZS. This is because the center of the MOT is situated $\approx 10\,\mathrm{cm}$ away from the ZS tube which potentially gives them enough time to fall under gravity, spread out and miss the loading region. Furthermore, even though the beam is red-detuned for reasons discussed above, the stopping force at the end of the tube can still be strong enough to reverse the velocity of some of the atoms and consequently deteriorate loading. To achieve non-zero exit velocities of $\sim 10\,\mathrm{m\,s^{-1}}$ we therefore slightly increase the bias offset field. We also artificially extend the slowing region by applying a magnetic field between the end of the ZS tube and the center of the MOT chamber with the use of end coils–see figure 3.6.

With implementing these adjustments and using a circularly polarized, collimated beam of radius 3 mm and total power of $P_{ZS} \approx 110\,\mathrm{mW}$, our ZS is capable of producing an atomic flux of $5 \times 10^7\,\mathrm{s^{-1}}$ at velocities which are sufficiently low to be captured by the MOT. We conclude this section with a few experimental remarks. First, we note that the performance of the ZS is quite sensitive to the TC and ZS beam powers as well as to the overall alignment. The ZS beam alignment, in particular, is quite challenging because the target apertures, i.e. the ZS tube and the oven, aren't directly visible through any of the viewports in our setup. In the end, we found a suitable method that consisted of walking the beam with two mirrors and using the scattered light in the MOT chamber as one reference and the fluorescence of the atomic beam emerging from the oven as another. We also found that despite the 401 nm light being only weakly visible to human eye, it was very clear when imaged with a common web camera, allowing for in situ imaging of the fluorescence without the need for a complicated setup.

Light generation

For completeness, we provide a brief overview of the optical system that generates 401 nm light of the appropriate frequency and power for the TC, ZS and imaging systems. For a detailed description, see reference [273].

The primary laser beam is generated by a frequency-doubled[32] Ti-Sapphire laser[33] which is pumped by a solid state laser operating at 532 nm[34]. This setup is capable of outputting up to 2.0 W of 401 nm light. The beam is then gradually branched off using polarizing beam splitters into four separate branches. The first branch, which is derived directly from the main beam, is directed towards the ZS. The other three branches include, individually, an acousto-optic modulator (AOM)[35] operating at 270 MHz in a double pass configuration and are directed towards the spectroscopy, TC and imaging systems. This way, the ZS beam attains a detuning of ≈ -500 MHz with respect to the spectroscopy branch and consequently with respect to the resonance. The other branches operate close to resonance (remember that the optimal detuning for TC is $\approx -\Gamma/2$) and are individually tunable across several Γ thanks to their double pass AOMs. The light is transported from the optical preparation table with the laser system to the experimental table with the vacuum system with the use of appropriate optical fibres[36].

The frequency doubler in the laser as well as the laser etalon are locked using internal electronics. However, this locking on its own isn't sufficient to stabilize the laser frequency to a desirable level because of long term drifts associated with changes of temperature and pressure as well as sudden changes due to e.g. vibrations. We implement an active locking mechanism based on modulation transfer spectroscopy [286], [287] (MTS). In short, a hollow cathode lamp[37] (HCL) is used as an atomic reference. A pump beam is passed through an electro-optic modulator[38], acquiring two sidebands at ± 19 MHz, and then through the HCL. A weaker probe beam passes through the HCL in the opposite direction in the usual Doppler-free configuration. On resonance, a fraction of the sideband component of the pump beam is transferred to the probe beam via three-wave mixing mechanism [288]– hence the name *modulation transfer*. The two sideband frequencies produce a beating signal on the probe which can be demodulated and turned into an error signal suitable for locking.

As in the previous sections, to help with future troubleshooting, we discuss a few noteworthy experimental hurdles and how we overcame them. First, we note that a back reflection from the frequency doubler back into the SolsTiS system kept compromising the etalon lock. This was resolved by placing an optical isolator[39] between the two laser sections. Second, we noticed a steady drop in the attainable output power of the 532 nm pump laser over the course of several years. This has lately become a cause of concern

[32] ECD-X module by MSquared
[33] SolsTiS system by MSquared
[34] 15W Sprout G by Lighthouse Photonics
[35] AOMO 3270-125 by Gooch & Housego
[36] PMC-E-400Si-2.8-NA011-3-APC.EC-700-P by Schäfter+Kirchhoff
[37] Erbium HCL by Photron
[38] E0-30M3-VIS by Qubig
[39] IO-5-780-HP by Thorlabs

and so a 802 nm laser[40] was bought to replace the pump and SolsTiS and couple straight into the doubler. We also note that the overall performance of the MSquared laser system hasn't been optimal and required several realignment and general maintenance sessions. Lastly, the MTS locking scheme, although relatively easy to implement, has been one of the weakest points of the experiment when it comes to uninterrupted operation. In the future, we plan to explore an alternative that combines Doppler-free spectroscopy of potassium (see section 7.4.2) with a Fabry-Perot cavity for generating a lockable error signal.

3.2.3 The Yellow–532 nm

The steady flux of slow atoms coming from the ZS ($5 \times 10^7\,\mathrm{s}^{-1}$ at $v \sim 10\,\mathrm{m\,s}^{-1}$) is an excellent starting point. In order to reach quantum degeneracy though, the erbium gas still needs to undergo further cooling and density enhancement–remember that a good measure of proximity to degeneracy is the phase space density of the gas that scales as $\rho \propto nT^{-3/2}$ (see section 2.4.1). Fortunately and for practical reasons listed above, we haven't yet fully tapped into the power of Doppler cooling with the temperature of the atoms emerging from the ZS, $T_{ZS} \sim 1\,\mathrm{K}$, being orders of magnitude above the Doppler temperature limit of the 401 nm transition, $T_D = \hbar\Gamma_{401}/2k_B \approx 700\,\mu\mathrm{K}$. Below, we demonstrate how we produce ultracold clouds of $> 100 \times 10^6$ erbium atoms at around $\sim 10\,\mu\mathrm{K}$ using a narrow-line, magneto-optical trap (MOT) operating at 583 nm. The use of a narrow transition gives us access to much lower Doppler temperatures, $T_D = \hbar\Gamma_{583}/2k_B \approx 4.5\,\mu\mathrm{K}$, albeit at the expense of a lower capture velocity.

Magneto-Optical trap–approaching the Doppler limit

Although the optical molasses technique discussed in the previous section allows, in theory, for cooling all the way to the Doppler limit, the slowing force confines atoms only in momentum space. In other words, the damping coefficient α of equation 3.10 is independent of position and so is the light scattering force itself. Consequently, an atomic cloud in an optical molasses and without any additional trapping would eventually disperse. A magneto-optical trap [173] solves this issue by overlaying a magnetic field gradient on top of the optical molasses. With a suitably chosen field and a set of atomic states, an atom situated away from the center of the field gradient will be brought into resonance with a counter-propagating, red-detuned molasses beam by the magnetically induced Zeeman shift, thus creating a spatially dependent confining force.

In more mathematical terms, lets first consider a quadrupole magnetic field produced by a pair of anti-Helmholtz coils of the from

$$\mathbf{B}(x, y, z) = B'(-\frac{1}{2}x, -\frac{1}{2}y, z) \tag{3.15}$$

with $B' = |\frac{\partial B}{\partial z}|$. The polarization axis of an atom moving through the field will adiabatically follow the field lines. Additionally, the magnetic field will change the energy

[40] TA Pro Amplified Tunable Single-mode Laser System by Toptica (Output power up to 3 W)

$m_J \to m_{J'}$	$-6 \to -7$	$-6 \to -6$	$-6 \to -5$
transition	σ^-	π	σ^+
$\frac{\partial\delta/2\pi}{\partial B}\ \left[\frac{\text{MHz}}{\text{G}}\right]$	1.93	0.26	-1.41

Table 3.1: Change in detuning in response to the applied magnetic field for the three allowed transitions.

level splitting via the Zeeman effect, effectively changing the detuning of the incident molasses beams according to equation 3.13. Importantly, the magnitude and sign of the Zeeman splitting depends on the $m_{J'}$ quantum number of the excited state that is being addressed by the corresponding beam. In the ground state, we have $m_J = -6$. Since the excited state has $J' = 7$, selection rules for electric dipole transitions only allow $m_J = -6 \to m_{J'} = -7, -6, -5$ which can be driven by σ^-, π and σ^+ polarized beams respectively. The beam polarization is, in return, only defined relative to the polarization axis of the atoms and hence the magnetic field. Consequently, depending on the atom's position within the field gradient, some of the molasses beams will 'appear' as σ^- whereas others will appear as either π or σ^+ and their interaction with the atom will therefore be, in general, different. Table 3.1 shows the rate of change of the detuning with magnetic field for the three allowed Δm_J transitions. We see that for a red-detuned laser with $\delta_0 < 0$, the σ^- and π transitions are brought back into resonance by an external magnetic field whereas the σ^+ transition is further red detuned. Consequently, atoms moving away from the center of the gradient will preferentially interact with σ^- polarized beams (and to some extent with π polarized beams)–see figure 3.12a.

This is beneficial because in practice (and if possible), the purpose of the MOT stage is not only to cool the atoms but also to prepare them in a single Zeeman sublevel. Since the $m_{J'} = -7$ excited state can only decay back to the ground state with $m_J = -6$, the σ^- transition is preferable to the others as it is closed i.e. it avoids decay into the other Zeeman substates in the ground state manifold. As mentioned above, the light's designation as σ^+, σ^- or π depends on its propagation direction with respect to the quantization axis of the atoms. A left-hand circularly polarized EM field propagating *along* the quantization axis drives the σ^+ transition whereas the same light propagating in the *opposite* direction drives the σ^- transition. Consequently, for the anti-Helmholtz field configuration, its is desirable for the beams in the x-y plane to be right-handed and the z beams to be left-handed. In that way, an atom moving away from the center in any of the six directions will interact with a counter-propagating beam which the atom will perceive as σ^-. This interaction will push the atom back towards the center and it will preferentially pump the atom into the $m_J = -6$ state. Close to the center of the field gradient, the Zeeman splitting and hence the effect of the magnetic field becomes negligible and the MOT is essentially a simple molasses. Under these conditions, the atoms still preferentially interact with the counter-propagating beams because of their red-detuning. However, their polarization axis is no longer well defined and other Zeeman substates in the ground state manifold can become

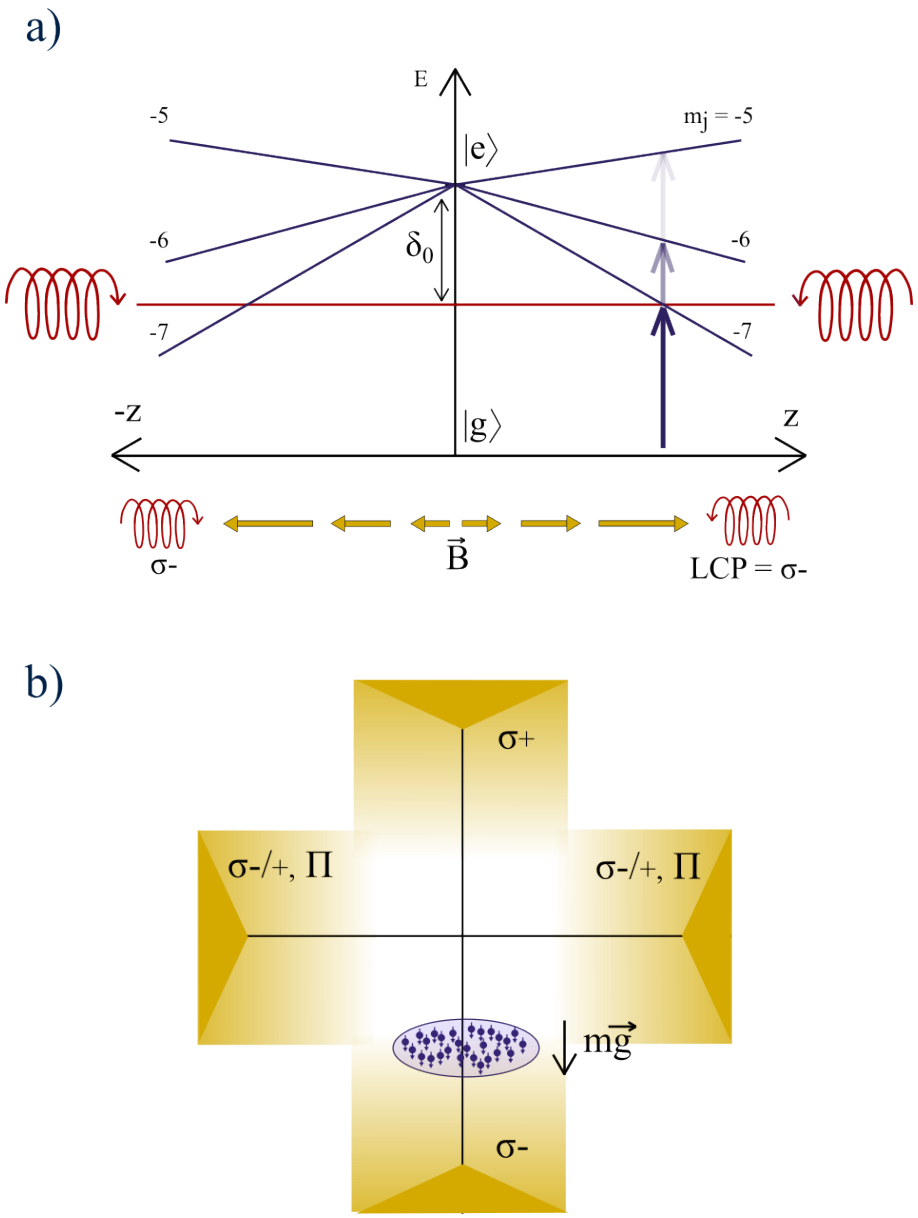


Figure 3.12: Principle of a magneto-optical trap. (a) An optical molasses with red-detuned, counter-propagating beams is overlapped with a magnetic field gradient. The gradient creates a Zeeman splitting in the excited state which is dependent on the distance from the center of the trap. If the beam's polarization is suitably chosen, they become resonant with the atoms as they move away from the center, creating a spatially dependent force field that pushes the atoms back to the center. (b) Due to the large mass of erbium atoms, the equilibrium position of the MOT 'sag' below the center. Consequently, it is mainly the bottom beam that provides the trapping and cooling because the transitions addressed by the other beams are too far detuned to be driven. As a result, the gas becomes polarized as it mainly operates on the closed $m_j - 6 \rightarrow -7$ transition.

populated.

In practice, the MOT stage is, on one hand, responsible for capturing atoms emerging from the ZS. As such, it needs to operate at high detunings and intensities to provide sufficient braking force for the still relatively fast atoms. On the other hand, it also ideally approaches the Doppler limit by working at low intensities to minimize the recoil energy from spontaneous emissions. The whole picture is further complicated by the action of gravity which breaks the symmetry of the problem and causes the atomic cloud to 'sag'. In our experiment, we implement a two stage MOT scheme based on reference [146] and fully described in [273].

Three pairs of counter-propagating beams of 33 mm diameter form the optical molasses and two pairs of coils–one in the anti-Helmholtz configuration responsible for the field gradient and the other in Helmholtz configuration to provide an offset–create the position-dependent detuning. In the first stage, the MOT is loaded from the ZS. In this stage, the detuning of the MOT beams is set to $\delta_0 \approx -70 \times \Gamma_{583}$ while the power in the beams is maximized to increase the capture velocity. Given our experimental constraints, the peak intensity of the horizontal beams optimized to $I/I_{\text{sat}} \approx 55$ whereas the top/bottom beams optimized to $I/I_{\text{sat}} \approx 20/30$ respectively. We believe the uneven power distribution is due to two effects. Firstly, it is the horizontal beams that are responsible for the initial slowing of the atoms emerging from the ZS and consequently, more power is required there. Secondly, the weaker the bottom beam, the further down the atomic cloud sags due to gravity. Too far and the atoms will experience reduced intensity due to the Gaussian profile of the MOT beams, too little and the MOT cloud will interact with the ZS beam, causing detrimental loss and drastically reducing the lifetime. Sagging has one more advantage, namely that away from the gradient center, the cloud preferentially interacts with the σ^- beam coming from the bottom, spontaneously pumping the atoms into the $m_J = -6$ ground state [289]–see figure 3.12b.

After loading the MOT for ≈ 12 s, the ZS light and coils are turned off and a waiting time of ~ 1 s is implemented to let the MOT shape and position equilibrate. In order to reduce the temperature, increase the density and bring the cloud closer to the center of the MOT chamber (to facilitate loading into the ODT), the atom cloud then undergoes a compressed MOT (cMOT) stage. The light intensity is reduced ($s \approx 0.2$) to approach the Doppler limit. However, on its own this would cause the cloud to sag further down due to the reduction in light-scattering force. To compensate for this effect, the detuning of the molasses beams is increased i.e. they are brought closer to resonance such that $\delta_0 \approx -15 \times \Gamma_{583}$. This step, which happens over ≈ 300 ms, simultaneously compresses and lifts the cloud. The details of the force balance and dynamics are nuanced and we point the reader to references [17], [290]. Here we only mention that the MOT cloud is bowl-shaped and bounded by an elliptical surface whose dimensions are determined by magnetic and optical fields. At the end, we capture about 100×10^6 spin-polarized atoms at 10 µK in a $1 \times 1 \times 0.5$ mm region of space.

We note that throughout both the loading and the compressed stages, the field gradient is held at $|\frac{\partial B}{\partial z}| = 8$ G/cm and the Helmholtz coils (also designated as Feshbach coils–see

section 3.1.2) are used to fine-tune the vertical position of the zero of the gradient. We also note that although the field gradient creates confinement for the gas by spatially modulating the light-scattering force, it also contributes with an anti-trapping force of magnitude $F_{AT} = -\mu\nabla|B(\mathbf{r})|$. For high-field-seeking states such as the ground state with $m_J = -6$, this force is directed radially out of the center of the gradient. Although considerably smaller in magnitude than the light-induced forces, this force can be used to spatially resolve atoms in different sublevels in a Stern-Gerlach manner during time-of-flight (see section 3.1.2 for notes on field calibration) or to excite oscillation modes in the ODT stages to measure trapping frequencies (see section 4.1.3).

The MOT is a complex physical system with many parameters influencing its cooling and capture efficiency. As such, its optimization is a challenging, high-dimensional problem. Below, we discuss several observations we made during the optimization process that could be beneficial to future researchers working with erbium MOTs. Despite the dominant role of the bottom beam in cooling and supporting the gas against gravity, we measure a $\approx 30\%$ decrease in atom number and a $\approx 10\%$ decrease in temperature when the top beam is completely covered. This is most likely because the top beam becomes relevant during the cMOT stage when the cloud is compressed and moves closer to the center of the gradient. As we will see later, loading into the ODT becomes saturated above certain MOT atom number, most likely because of density dependent losses induced by the cooling light and three-body collisions. Consequently, a drop in MOT atom number isn't necessarily detrimental to later stages of the experiment. Not using the top beam could therefore be acceptable if doing so allows for more optical access to the MOT chamber as has been demonstrated in reference [291].

The issue of light-assisted collisions [292], [293] not only limits the ODT loading efficiency but it also greatly reduces the lifetime of the cMOT. Figure 3.13 shows a lifetime measurement of the MOT and cMOT under operating conditions. Whilst the MOT lifetime, $\tau_{\mathrm{MOT}} \approx 35\,\mathrm{s}$, is considerably longer than the usual experimental sequence ($\sim 20\,\mathrm{s}$) and its decay can be modelled well by a one-body collision process with residual gas in the vacuum chamber (confirming the quality of our vacuum), the cMOT is short-lived, $\tau_{\mathrm{cMOT}} \approx 370\,\mathrm{ms}$, and shows a characteristic two-body decay rate. This greatly limits the length of the loading step into the ODT and consequently the transfer efficiency. We note that lowering the light intensity might, on one hand, increase the lifetime and reduce the temperature of the atoms but it would also necessitate bringing all six beams closer to resonance, inducing transitions into $m_J \neq -6$ states and depolarizing the gas. Another important factor is the quality of polarization as the light-scattering force in the presence of magnetic fields is polarization-dependent. We observed a deterioration of the polarization uniformity after the circularly-polarized beams were reflected off a dielectric mirror[41] at 45°. This can be partially mitigated by using $\lambda/2$ and $\lambda/4$ waveplates in tandem to create an arbitrary elliptical polarization of the incoming beam. However, a fully uniform, circular polarization could never be attained.

Lastly, we mention the positional stability of the cMOT. The equilibrium position of

[41] Fused silica, broadband dielectric mirror BB2-E02 by Thorlabs

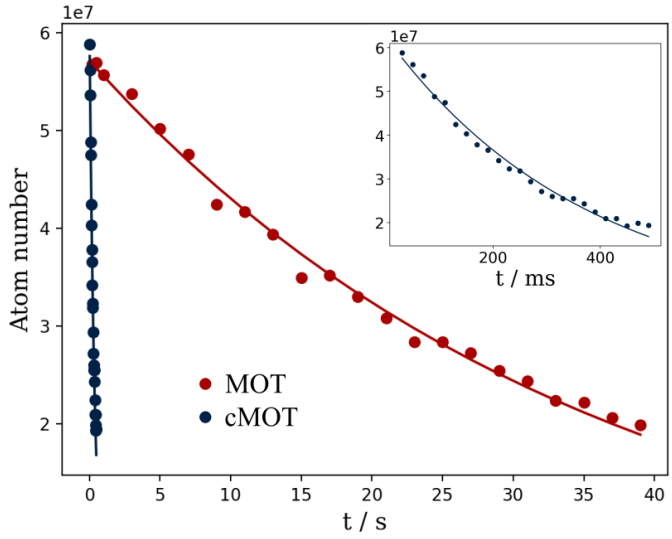


Figure 3.13: MOT and cMOT lifetime. Measurement of atom number decay of atoms trapped in the MOT (red) and cMOT (blue, inset) stages respectively. The datapoints were fitted with an exponential curve and the lifetimes of $\tau_{\mathrm{MOT}} \approx 35\,\mathrm{s}$ and $\tau_{\mathrm{cMOT}} \approx 370\,\mathrm{ms}$ were extracted. The long lifetime of the MOT stage points towards good quality of the vacuum in the main chamber. The much shorter lifetime of the cMOT, on the other hand, is believed to be caused by detrimental light-assisted collisions which significantly limits the overlap time with the ODT (see section 4.2).

the MOT is an interplay of light intensity and magnetic field strength. On its own, a shot-to-shot spread in the cMOT position isn't by any means catastrophic and is, to some extent, inevitable. However, it becomes problematic during loading into the ODT which essentially represents a small ($\approx 30 \times 30\,\mu\mathrm{m}$) 'target' that needs to be overlapped with the cMOT as well as possible for maximized transfer of atoms. Historically, we observed a large spread in the cMOT center position of the order of $\sim 200\,\mu\mathrm{m}$. This was later narrowed down to two factors. Firstly, an imperfection in some of the MOT steering mirrors which caused an instability in the polarization and hence the light-scattering force (reference [273] provides a full account of this). Secondly, insufficient frequency locking which caused the laser detuning to change shot-to-shot and affect the vertical position of the cloud. The former was simply resolved by replacing the set of mirrors whereas the later got addressed by implementing a locking scheme utilizing a high-finesses reference cavity and the Pound-Drever-Hall technique–see next section.

Light generation

As with the 401 nm light, we provide a brief overview of the 583 nm laser system which is primarily used for the MOT stage but will be used in the future to perform Bragg spectroscopy on the quasi-2D gas (see chapter 9). A detailed schematic of the optical setup is given in [273]. The light is generated by a diode laser with a frequency-doubling cavity and a tapered amplifier[42]. The total power delivered by the system is up to 700 mW which is more than sufficient given the low saturation intensity of the MOT transition,

[42] DL-TA-SHG-Pro by Toptica

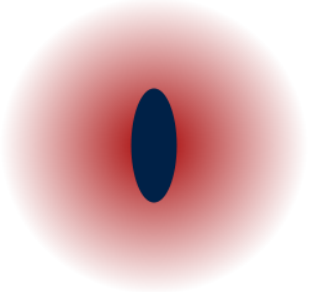
$I_s = 0.13\,\mathrm{mW\,cm^{-2}}$. A set of polarizing beam-splitters (PBSs) creates two branches, one containing a 80 MHz AOM[43] in a double pass configuration coupled into an optical fibre. This branch is guided to the experimental table and seeds the six MOT beams (the splitting there is achieved using a series of PBSs and $\lambda/2$ wave-plates for complete control over the power balance). The other branch is used as a reference for a wave-meter[44] to find the locking signal before the lock is engaged.

The narrow linewidth of the MOT transition, $\Gamma_{583} = 186\,\mathrm{kHz}$, together with the requirement on the positional and temperature stability of the MOT necessitate the use of a tight locking scheme. In the past, modulation transfer spectroscopy (MTS) was used, which proved insufficient with respect to the positional stability. Currently, an ultra-low expansion (ULE) optical cavity[45] serves as a frequency reference in a Pound-Drever-Hall [294], [295] (PDH) setup used to lock the pre-doubled (1166 nm) light. This locking scheme relies on the fact the reflected part of a beam coupled into an optical cavity is phase- and amplitude modulated with a characteristic frequency dependence. If the incoming beam is passed through an electro-optic modulator (EOM), it acquires two equally-spaced sidebands in frequency. These sidebands pick up different phase/amplitude modulation when reflected from the cavity. It can be shown [295] that the intensity of the reflected beam, i.e. the interference of the main beam and the sidebands, displays beating at the EOM modulation frequency. The amplitude of this beating can, in return, be used as an error signal because it has a zero crossing and a negative slope at the resonant frequency of the cavity. In our implementation of the PDH setup, we pick off the pre-doubled light and couple it into a fibre EOM[46] powered by an RF signal generator[47]. The light is then directed into the cavity and the reflection is collected by a photodiode[48]. The signal from the photodiode, i.e. the light intensity, is demodulated using a laser locking module[49] to extract the beating amplitude and hence the error signal. The cavity itself is temperature stabilized using built-in electric heaters, thermistors for temperature sensing and a PID module for feedback. The target temperature is set to 37 °C which corresponds to the zero-crossing of the coefficient of linear thermal expansion of the cavity spacer as provided by the manufacturer, reducing the overall drift in frequency to $\approx 10\,\mathrm{kHz/week}$. We note that unlike the 401 nm laser system, the 583 nm system hasn't shown any signs of deterioration and has been performing up to specifications.

In summary, our laser cooling stages which consist of a Zeeman slower operating at 401 nm and a magneto-optical trap operating at 583 nm allow us to produce and capture a cloud of $\approx 100 \times 10^6$ spin-polarized ^{166}Er atoms at $\approx 10\,\mu\mathrm{K}$. In the next chapter, we will describe the rest of our experimental sequence which allows us to bypass the Doppler limit and reach quantum degeneracy.

[43] AOMO 3080-125 by Gooch & Housego
[44] WS7 by HighFinesse
[45] By Stable Laser Systems
[46] NIR-MPX-LN-02-00-P-P-FA-FA by iXblue
[47] DSG815 by Rigol
[48] PDA05CF2 by Thorlabs
[49] DigiLock 110 by Toptica

4. Production of large ^{166}Er BECs



Reaching the Doppler limit is, in itself, a noteworthy achievement. However, from the point of view of Bose-Einstein condensation, we have only just made it to the Moon. Next station? Mars. Fortunately, the four orders of magnitude in phase-space density can be bridged using other optical techniques.

In this chapter, we describe the rest of our experimental procedure that results in the production of large BECs of erbium. A substantial part is devoted to evaporative cooling in a crossed-beam, optical dipole trap (ODT). This is the final cooling stage that leads directly to condensation and in which phase space density is increased at the expense of atom number. As such, optimization of this step is crucial for efficient BEC production. We discuss our optimization efforts from numerical as well as experimental perspective. Another section is concerned with the characterization of our erbium BEC and a discussion of experimental signatures of its dipolar character. Finally, a special part is devoted to our use of focus-tunable lenses as a tool for shaping the trapping potential (and hence the condensate itself) and performing atomic transport. In the spirit of an experimental DPhil thesis, in each section, we also try to provide an account of complications encountered on the way, their potential causes and, where possible, our countermeasures.

4.1 Optical dipole trapping

We have discussed at length the resonant interaction of an atom with a driving laser field and how it can be used to reduce its kinetic energy and transfer entropy from the atomic cloud into the electromagnetic field. The cooling efficiency of these techniques is limited by the shot noise in momentum introduced by the photon recoil energy. Fortunately, off-resonant atom-laser interactions can lead to strong, conservative trapping which can, in return, be used to perform evaporative cooling and reach quantum degeneracy. Below, we outline the theory of optical dipole trapping [274] and how we utilize it in our experiment to trap atoms in a crossed beam, near-harmonic trap, transport the atoms between the MOT chamber and the science cell and finally create a flat, radially symmetric, pancake trap for the study of homogeneous dipolar gases in reduced dimensions.

4.1.1 Polarizability

To understand the origin of the dipole force, we can consider a semi-classical interaction of an atom with an oscillating electric field of the form $\mathbf{E} = \mathbf{E_0}e^{-i\omega t} + c.c.$. Here, we assumed that the electric field is uniform across the atom which is valid for electromagnetic radiation with $\lambda \gg r_{\text{atom}}$ (also known as the *dipole approximation*). This electric field will induce an electric dipole on the atom given by $\mathbf{p} = \alpha(\omega)\mathbf{E}$ where $\alpha(\omega)$ is the *polarizability* of the atom which depends on its internal structure and the frequency of the oscillating field and can be, in general, complex. An induced dipole experiences a potential of the form $U_{\text{dip}} = -\frac{1}{2}\mathbf{p}\cdot\mathbf{E}$. Note that the factor of $\frac{1}{2}$ is a direct consequence of the fact that the dipole is induced by the field it interacts with. In case of a permanent dipole, the factor is equal to unity. To obtain the total potential experienced by the atom, we simply need to average in time

$$U_{\text{dip}} = -\frac{1}{2}\langle \mathbf{p}\cdot\mathbf{E}\rangle = -\frac{1}{2\varepsilon_0 c} Re(\alpha) I(r) \ . \tag{4.1}$$

Here, we expressed the the potential in terms of the intensity of the incoming EM wave, $I = 2\varepsilon_0 c|\mathbf{E_0}|^2$. This dependence of the dipole potential on the intensity of the incoming light is at the heart of optical dipole trapping. Note that for $Re(\alpha) > 0$, the resulting potential is attractive whereas for $Re(\alpha) < 0$ it is repulsive. The frequency dependence of α can be, to some extent, understood from a simple model of a driven harmonic oscillator. When the oscillator is driven below resonance, i.e. $\omega < \omega_0$, it moves in-phase with the driving field and so $Re(\alpha) > 0$. Above resonance, the oscillator shifts out of phase and $Re(\alpha) < 0$. In analogy, a red-detuned laser field with $\omega < \omega_0$ will create a trapping potential whereas a blue-detuned one with repel the atoms instead. Thus, the atomic polarizability $\alpha(\omega)$ plays a central role in optical trapping of neutral atoms and its frequency dependence allows for creating arbitrary potentials by overlapping red- and blue-detuned laser fields.

Staying with the semi-classical for a bit longer, we can also derive the rate of power dissipation by the induced dipole, $P_{\text{diss}} = \langle \dot{\mathbf{p}}\cdot\mathbf{E}\rangle$. In more quantum mechanical terms, the atom will absorb energy from the driving field in the form of photons at a rate

$$\Gamma_{\text{scat}} = \frac{P_{\text{diss}}}{\hbar\omega} = \frac{1}{\hbar\varepsilon_0 c} Im(\alpha) I(r) \ . \tag{4.2}$$

In practice, photon scattering by the trapping beam is undesirable as it deposits energy in the atom cloud and heats it up. Luckily, as we shall briefly see, the scattering rate is negligible for far-detuned trapping beams.

A more rigorous quantum mechanical treatment [204] that employs second-order, time-dependent perturbation theory [296] yields the polarizability

$$\alpha(\omega) = \sum_e \frac{2(E_e - E_g)|\langle e|\mathbf{p}\cdot\hat{\mathbf{e}}|g\rangle|^2}{(E_e - E_g)^2 - (\hbar\omega)^2} \tag{4.3}$$

with $\hat{\mathbf{e}}$ the unit vector of the driving field and the sum running over all the excited states $|e\rangle$. In the usual perturbation theory fashion, the driving field couples the ground state and all the excited states and thus shifts the ground state energy. The amount of this

shift depends not only on how well the two levels are coupled via the electric dipole matrix element, $\langle e|\mathbf{p}\cdot\hat{\mathbf{e}}|g\rangle$, but also on how close the driving field frequency is to the resonant frequency $\omega_0 = (E_e - E_g)/\hbar$. Assuming a complex energy of the excited state of the form $E_e = E_e^0 - i\hbar\Gamma_e/2$, i.e. assuming the excited state has a finite lifetime given by Γ_e^{-1}, one can derive expressions for the real and imaginary part of $\alpha(\omega)$ which reveal typical scalings in the limit of large detunings, $Re(\alpha_i) \propto 1/\delta_i$ and $Im(\alpha_i) \propto \Gamma_i/\delta_i^2$. Here, we have specifically used index i to denote the contribution of the i-th excited state to the real and imaginary part of the polarizability with its corresponding lifetime and detuning. Clearly, as the driving frequency moves away from resonance, the photon scattering rate decays faster than the trapping potential. Consequently, there most likely exists a region in the frequency space where the trapping is sufficient while the heating from off-resonant scattering events is low enough to allow for long lifetimes, making optical dipole trapping a powerful tool in cold atom physics.

Even though it is relatively easy to measure the atomic polarizability e.g. by characterizing trapping frequencies (see section 4.1.3), mapping the polarizability as a function of frequency this way isn't practically possible due to our inability to continuously tune the laser frequencies over large ranges. Fortunately, using equation 4.3 in combination with spectroscopic and/or numerical data, it is possible to calculate $\alpha(\omega)$ directly. For anisotropic atoms such as erbium, the dipole matrix element $\langle e|\mathbf{p}\cdot\hat{\mathbf{e}}|g\rangle$ and hence the polarizability acquire a tensorial character and, in general, depend on the light polarization and propagation direction relative to the polarization axis of the atoms. More quantitatively, following references [297], [298], the polarizability can be written as

$$\alpha(\omega) = \alpha_{\text{scal}}(\omega) + \epsilon\cos\theta_k \frac{m_J}{2J}\alpha_{\text{vec}}(\omega) + \frac{3m_J^2 - J(J+1)}{J(2J-1)}\frac{3\ \cos^2\theta_p - 1}{2}\alpha_{\text{tens}}(\omega) \qquad (4.4)$$

where $(J, m_J) = (6, -6)$ for the ground state of erbium and ϵ is the ellipticity of the light polarization. The two angles θ_k and θ_p are, respectively, defined as the angle between the atomic polarization and the direction of light propagation $\hat{\mathbf{k}}$ and the angle between the atomic polarization and the light polarization. For clarity, these angles are depicted in figure 4.1.

The expression for the scalar, vector and tensor parts of the polarizability are given in reference [297]. Here we only note that for a linearly polarized trapping light (as is the case in our experiment), the vector contribution to the polarizability vanishes because the ellipticity parameter $\epsilon = 0$. The total polarizability then oscillates between its maximal and minimal value based on the angle θ_p between the light polarization and the quantization axis of the atoms as defined by an external magnetic field. In practice, the tensor part α_{tens} is smaller than the scalar part α_{scal} and so the overall trapping is affected only weakly by changing the light polarization.

Using data from [299] and equation 4.4, we calculated the complex atomic polarizability of ^{166}Er for the case of trapping light linearly polarized at and angle $\theta_p = 90°$ to the atomic quantization axis and for a range of wavelengths. Both the real and the imaginary parts are plotted in figure 4.1. For the wavelength of our optical dipole trap (ODT),

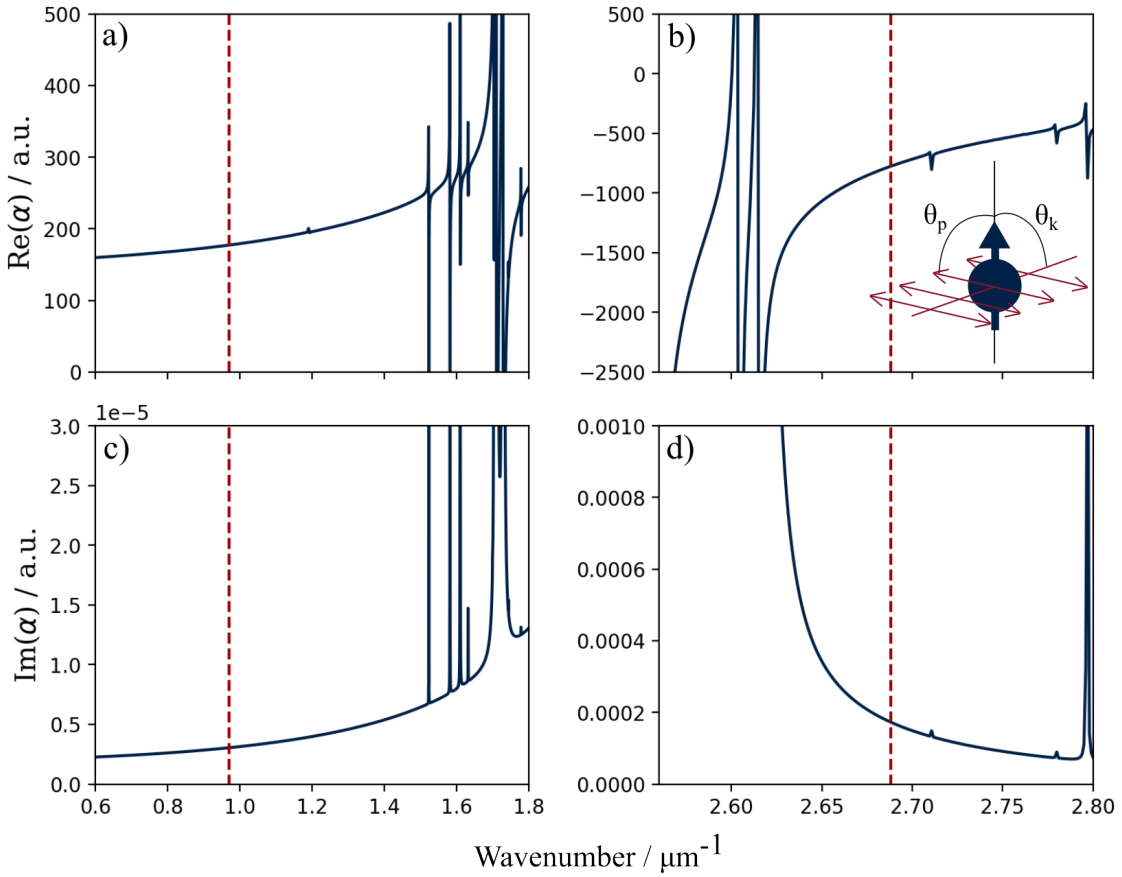


Figure 4.1: Polarizability of ^{166}Er. a) Real part of the complex polarizability around the main trapping wavelength of 1030 nm indicated by the red dashed line. The sharp features mark transitions at which the polarizability diverges and changes sign. b) Same quantity but this time around the repulsive wavelength of 372 nm which will be used to create the walls of our box potential. Note that the value is negative implying that the resulting potential is repulsive. The inset shows the two angles θ_k and θ_p which determine the polarizability of anisotropic atoms according to equation 4.4. c-d) Equivalent plots of the imaginary part of the complex polarizability which is related to the off-resonant photon scattering rate via equation 4.2. Stronger trapping is inherently accompanied by higher heating rates due to off-resonant scattering.

$\lambda_{\mathrm{ODT}} = 1030\,\mathrm{nm}$, the real polarizability $Re(\alpha_{1030}) = 177.27\,\mathrm{au}$[1] and the resulting potential is attractive. We also plan to use a laser with $\lambda_{\mathrm{sheet}} = 1064\,\mathrm{nm}$ to create a confining planar sheet beam potential and another laser with $\lambda_{\mathrm{cyl}} = 372\,\mathrm{nm}$ to create a repulsive hollow cylindrical beam. These will be overlapped to produce the final 'pancake' trap. The values of the real part of the polarizability at these two wavelengths are $Re(\alpha_{1064}) = 175.29\,\mathrm{au}$ and $Re(\alpha_{372}) = -775.95\,\mathrm{au}$. We note that the imaginary polarizability at 1030 nm yields (for our ODT1 beam with a waist of $\approx 30\times30\,\mu\mathrm{m}$) a photon scattering rate of $0.15\,\mathrm{s}^{-1}\,\mathrm{W}^{-1}$ or equivalently a heating rate of $5\,\mathrm{nK\,s}^{-1}\,\mathrm{W}^{-1}$ which is sufficiently low at the powers and timescales used in the experiment that it can be neglected.

4.1.2 Trapping potential

The most common way of trapping atoms using optical potentials is to use a combination of focused Gaussian laser beams. The intensity profile of a Gaussian beam propagating along the z direction is given by [300]

$$I(x,y,z) = \frac{2P}{\pi w_x(z) w_y(z)} \exp\left[-2\left(\frac{x^2}{w_x^2(z)} + \frac{y^2}{w_y^2(z)}\right)\right] \tag{4.5}$$

where P is the total power in the beam, $w_i(z) = w_{0,i}\sqrt{1+(z/z_{R,i})^2}$ is the waist of the beam along the i-th direction, $w_{0,i}$ is the waist at the focus and $z_{R,i} = \pi w_{0,i}^2/\lambda$ is the Rayleigh range of the beam which determines how tight the trap is along the beam's direction (i.e. z axis). Note that we assumed the beam is focused at $z = 0$.

The expression for the trapping potential 4.1 can be expanded around the minimum at $\mathbf{r} = (0,0,0)$ to obtain a harmonic approximation of the form $U_{\mathrm{harm}} = m/2(\omega_x^2 x^2 + \omega_y^2 y^2 + \omega_z^2 z^2)$ with the trapping frequencies given by

$$\begin{aligned}
\omega_x &= \sqrt{\frac{\alpha}{\varepsilon_0 mc}\,\frac{4P}{\pi w_{0,y} w_{0,x}^3}} \\
\omega_y &= \sqrt{\frac{\alpha}{\varepsilon_0 mc}\,\frac{4P}{\pi w_{0,x} w_{0,y}^3}} \\
\omega_z &= \sqrt{\frac{\alpha\lambda^2}{\varepsilon_0 mc}\,\frac{P(w_{0,x}^4 + w_{0,y}^4)}{\pi^3 w_{0,x}^5 w_{0,y}^5}}\ .
\end{aligned} \tag{4.6}$$

Here we used α to denote the real part of the polarizability. The total depth of the trap sets the maximum energy of trapped particles and its expression is simply given by the magnitude of the dipole potential at the focal position

$$U_d = \frac{\alpha}{\varepsilon_0 c}\,\frac{P}{\pi w_{0,x} w_{0,y}}\ . \tag{4.7}$$

In practice, the harmonic approximation is good as long as the temperature of the atoms is much smaller than the trap depth, $k_B T \ll U_d$. For single beam traps, the

[1] The conversion between atomic units of polarizability and SI is defined as follows: $1\,\mathrm{au} = 4\pi\varepsilon_0 a_0^3$ with a_0, the Bohr radius

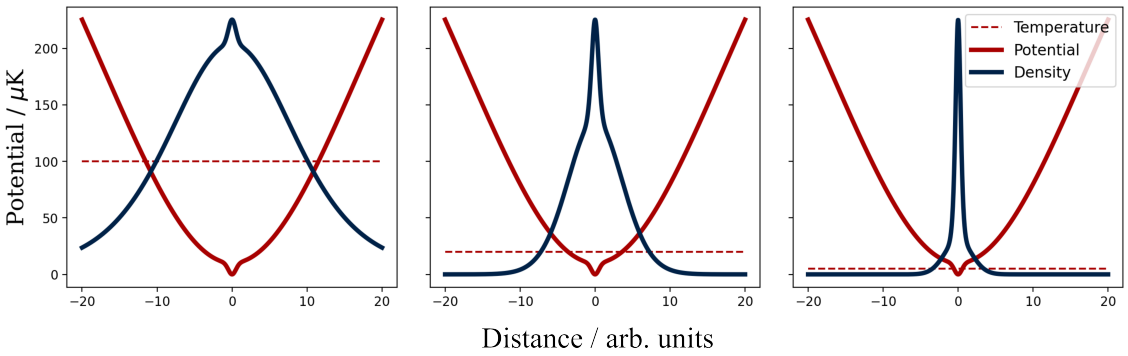


Figure 4.2: Effects of a dimple the density. As the temperature (dashed line) of the cloud decreases, the role of the dimple becomes more pronounced. Initially, the cloud has a Gaussian shape determined by the main trapping beam. In the intermediate regime, the second beam creates a region of enhanced density which facilitates faster evaporation and the density distribution acquires characteristic 'wings' along the main trapping beam. When the depth of the dimple is larger than the temperature of the cloud, most of the atoms converge to the crossing and the density takes on a Gaussian shape. This time determined by the trapping frequencies of both beams.

cloud usually thermalizes through evaporation (see section 4.3) to temperatures that give $\nu = U_d/k_BT \approx 6$–10 and so the trap is essentially harmonic. For crossed beam setups such as the one in our experiment (see below), the picture is a bit more complicated because one beam creates a 'dimple' [275], [301] in the potential of the other beam. The depth of this dimple governs how well the trap can be described as harmonic. Deep dimples lead to harmonic trapping and a Gaussian cloud density whereas shallow dimples result in density 'wings' forming along the other beam–this is depicted in figure 4.2. The cross-over of harmonic and non-harmonic regimes in crossed beam traps makes their numerical modelling challenging and, in general, analytically unsolvable. We touch on this in section 4.5.2 and in appendix C when we discuss optical transport in our system and modelling evaporation.

Dithering

An optical dipole trap is easy to implement because in its simplest form it is just a single focused beam (albeit a high-power one which comes with its own challenges). Moreover, the generally small trap volume of an ODT is responsible for high atomic densities and efficient initial stages of evaporation. However, its simplicity is, in some sense, also its shortcoming because once the beam is shaped using optical elements, the only easily controllable variable is the total power. Both the trap depth and the trapping frequencies are controlled by this parameter and are thus coupled. Lowering the trap depth during forced evaporation results in lowering of the trap frequencies, making the cloud less dense and slower to rethermalize. Furthermore, the size of the trap is fixed by the beam's waists and one has to find a balance between having a large trap with good overlap with the MOT for optimal loading and a small trap with enhanced densities for fast evaporation.

In our experiment, we implement two techniques to increase the flexibility of our ODT. The first technique relies on the use of two focus-tunable lenses (TLs) in tandem to produce

a beam of controllable waist size and focal position. This can be used to dynamically change the trap shape during evaporation and to move the atom cloud by changing the position of the focus [149]. The details of this setup are discussed in section 4.1.4. The second technique relies on fast modulation of the beam's position using an acousto-optic modulator[2] (AOM) to produce a time-averaged potential. If the modulation frequency is much larger than the timescales associated with atomic motion given by the average trapping frequency $\bar{\omega} = (\omega_x \omega_y \omega_z)^{1/3}$, the atoms can't react fast enough to the change in potential and experience its time-average instead.

In an AOM, a piezoelectric transducer is driven by a radio-frequency (RF) field to create sound waves in an optical crystal. These sound waves periodically modulate the refractive index of the crystal and so when a laser beam is incident on it, it refracts into several peaks akin to diffraction off a grating. The deflection angle is given by the Bragg condition [302]

$$\sin\theta_d \approx \theta_d = \frac{\lambda f_{\mathrm{AOM}}}{2v_s} \tag{4.8}$$

where v_s is the speed of sound in the crystal, f_{AOM} is the driving frequency of the AOM and λ is the wavelength of the incident light. If the beam is then passed through a lens, a change in the deflection angle results in a translation of the beam in the plane perpendicular to its direction of propagation. Consequently, a fast modulation of the driving frequency leads to fast lateral displacement, e.g. 'dithering', of the beam.

For a periodic displacement $x_D(t)$ of a Gaussian beam in a direction along one of the principal axes, we can write the time averaged potential at the focus as

$$U(x,y) = \frac{U_d}{T} e^{-\frac{2y^2}{w_y}} \int_0^T e^{-\frac{2(x-x_D(t))^2}{w_x}} dt \ , \tag{4.9}$$

with U_d the depth of an undithered trap and T the period of the displacement. Ideally, the time averaged potential should still remain Gaussian, albeit with a different width and trap depth. An analytic solution to 4.9 doesn't exist but a dithering function of the form [303]

$$x_D(t) = \begin{cases} \frac{2A}{\pi} \arcsin\left(\frac{4t}{T} - 1\right) & 0 \le t \le \frac{T}{2} \\ -\frac{2A}{\pi} \arcsin\left(\frac{4t}{T} - 3\right) & \frac{T}{2} \le t \le T \end{cases} \tag{4.10}$$

with amplitude A approximates a Gaussian reasonably well as is shown in figure 4.3. The approximation is particularly good for dithering amplitudes smaller than the initial waist size, $A < w_x$. To employ this technique, we generate an electronic signal with the desired frequency and waveform given by equation 4.10 using the arbitrary waveform generation functionality of a Red Pitaya micro-controller[3]. This signal is then amplified and added on top of a constant offset voltage using an in-house built circuit which gives us the ability to move the beam laterally to a certain position and then dither it around that position.

In theory, the dithering frequency is irrelevant as long as it is much higher than the trapping frequencies to prevent parametric heating of the cloud [304], [305]. However, in

[2] AOMO 3080-199 by Gooch & Housego
[3] STEMlab 125-14 by Red Pitaya

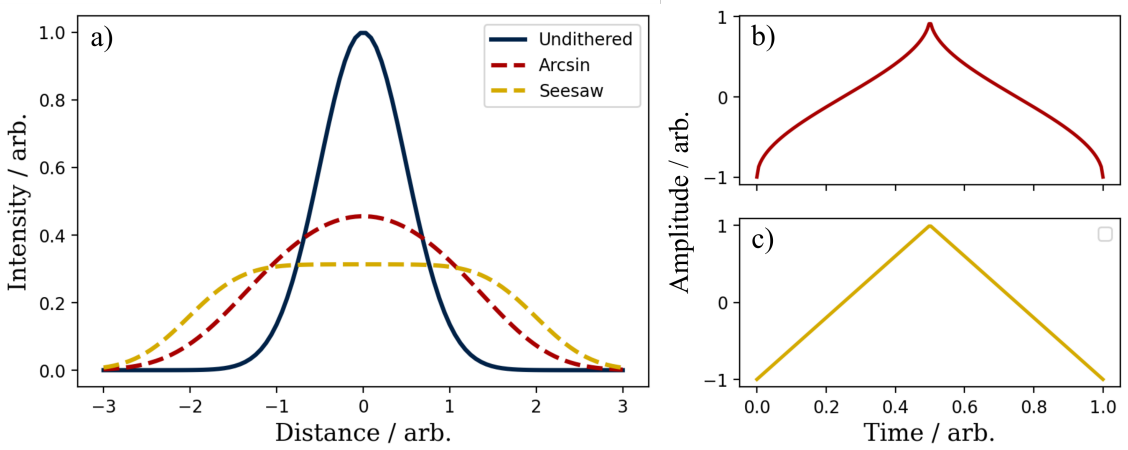


Figure 4.3: Dithering. (Left) The intensity profile of an undithered Gaussian beam (blue) and of the same beam dithered using an Arcsin waveform (equation 4.10) and a Seesaw waveform. Both waveforms result in a widened beam and a shallower trap. The Arcsin closely replicates a Gaussian shape whereas the Seesaw is flat in the center. For loading, the shape of the trap isn't important but at later stages, it becomes crucial for interpreting measurements. (Left) Arcsin (red) and Seesaw (yellow) dithering waveforms.

practice, the response of the AOM driver to a change in the modulation frequency has a finite bandwidth. Consequently, if the dithering waveform is changing too fast, the driver is not able to follow and the waveform is skewed, resulting in a smaller effective dithering amplitude. For that reason, we also tested a 'see-saw' waveform which is similar in shape to the 'arcsin' but changes more slowly around the maxima. The resulting time-averaged potential is shown in figure 4.3. Because the beam moves at a constant rate between the extrema, the potential is essentially a series of superimposed Gaussians with equal weights and so it is flat in the central region. Furthermore, the beam spends, on average, more time at the extrema, making the potential wider than in the case of the 'arcsin' waveform. This is beneficial during the loading stage when the overlap with the MOT needs to be maximized and the exact functional form of the potential isn't important.

Indeed, a 'see-saw' waveform gave marginally better results in terms of loading numbers, with the added benefit of being easily generated by an ordinary function generator. Using the dithering technique, we can enhance our loading numbers by $\approx 50\%$ whilst also reducing the cloud temperature immediately after loading from 70 µK to 40 µK because of the lowering of the trap depth that comes naturally with dithering. This point will be further clarified when we discuss the loading procedure in section 4.2. After the loading stage, the dithering amplitude is ramped down to increase the atom density and thus enhance evaporation. We note that the dithering frequency used in our setup is 60 kHz. We also note that despite the 'see-saw' waveform being simpler and slightly better during loading, the benefit of the 'arcsin' is its near-harmonicity. As we shall see in section 4.3.1 and chapter 5, it is beneficial to employ dithering once again in the last stages of evaporation to deliberately reduce the density and consequently the three-body loss rate. At that point, the atom cloud is nearly or even completely degenerate and it is therefore convenient to use an analytically tractable potential for easier data interpretation.

Lastly, we mention that other techniques–most notably the ones employing spatial light modulators [14] or digital micro-mirror devices [15], [16]–can be used to shape laser beams with an almost arbitrary degree of freedom. We are planning to employ such techniques in the science cell to create and study the quasi-2D dipolar gas. For an overview, see chapter 9 and reference [273].

4.1.3 Characterizing the trap

The trapping frequencies are integral parameters. They determine the shape and density of both the thermal cloud and the BEC (see section 2.4). They also set the characteristic timescale of motion in the trap and so knowledge of them is essential for interpreting data and inferring physical quantities from time-of-flight images. However, in practice, they are not straightforward to measure. Below, we outline several techniques we use to estimate the trapping frequencies of our single and crossed-beam ODT.

Waist measurement

A seemingly straightforward way of determining the trapping frequencies is to use equations 4.6. This relies on the direct knowledge of the scalar polarizability α, the total power in the beam and, crucially, the waists at the focus. The polarizability can be calculated as outlined in section 4.1.1 with the error on the order of at most a few percent coming from the lack of complete spectroscopic data. The measurement of the waist at the focus can be done by imaging the beam at its tightest spot and fitting a 2D Gaussian to the image. A sample image and the fitted Gaussian curves are shown in figure 4.4.

Measuring the trapping frequencies this way is sufficient as a crude estimate. However, in reality, the beam won't take on a perfect Gaussian shape as can be seen from figure 4.4. The error introduced by the imperfections can be large and can change the estimate of the trapping frequencies by tens of percent. As an alternative, one can directly fit a quadratic around the maximum of intensity. This yields frequencies in the transverse directions which are robust against beam imperfections. However, in order to obtain the trapping frequency along the beam, one has to gather intensity data at several points along the beam which makes the measurement slightly more demanding. A sample dataset is shown in figure 4.4 along with the fitted frequency which differ non-negligibly from the ones obtained from simply using the measured waists and equation 4.6.

One way of reconciling the two methods is to calculate the fraction of the power that is lost to the non-Gaussian part of the beam. This can be done by directly summing the total power per pixel over the whole image and comparing it with the integrated power of the fitted Gaussian. The ratio of these two gives us a conversion factor ('power fudge') that can then be used to adjust the power in equation 4.6 to account for the losses. We note that in our experiment, using either the harmonic fit method or the power-adjusted waist method yields sufficiently accurate estimates of the trapping frequencies.

A possible downside of this technique is the fact that one needs to be able to access the focus of the beam with a camera which is not possible inside the vacuum chamber. A setup that mirrors the optical path of the beam needs to be built instead, possibly

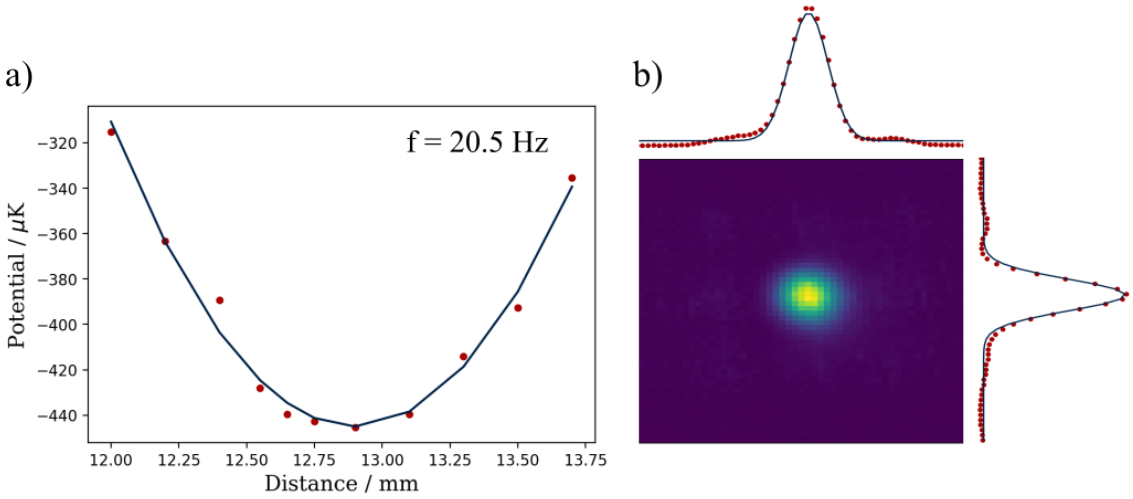


Figure 4.4: Beam characterization. a) Measurement of the longitudinal trapping frequency. By extracting the intensity along the beam, converting it to the potential via polarizability and fitting a quadratic to the data, the frequency can be obtained. Notably, using the fitted waist values and equation 4.6 yields a considerably larger value of $f = 24.0\,\mathrm{Hz}$. b) Direct image of the ODT1 beam. Summing the pixel intensity along the two axes and fitting a Gaussian can be used to directly obtain the waists of the beam. However, due to imperfections (non-Gaussianity) in the beam, the real trapping frequencies are generally lower. A better way of measuring them is to directly fit a quadratic to the maximum pixel intensity around the focus.

using a pick off prism. Additionally, it is impossible to accurately determine the trapping frequencies in the crossed-trap this way because the exact overlap of the two beams in the vacuum chamber is unknown and a mirror setup can't therefore reliably mimic the potential experienced by the atoms.

Atom cloud excitation

A more robust way of measuring the trapping frequencies is to directly probe center-of-mass (COM) dynamics of the atomic cloud in the trap. That way, we let go of any assumptions about the potential except for one–namely that the trapping is harmonic– and we can also perform the measurements in situ. Exciting COM motion in a particular direction and extracting the period of oscillations yields the trapping frequency along that direction. The biggest challenge here is to find a way of probing all three orthogonal directions and resolving the COM motion.

For measuring vertical trapping frequencies, we exploit the fact that the atoms sag under gravity. Consequently, quickly increasing the power in the beam responsible for vertical trapping suddenly changes the equilibrium position of the atoms and excites their oscillations. For the direction perpendicular to our main trapping beam (ODT1), we suddenly change the driving frequency of the AOM used to modulate the beam which shifts the beam laterally (see the discussion above) and once again excites COM motion. The last direction i.e. along ODT1, is the most challenging. Firstly because the trapping along that direction is weak and the oscillations are heavily damped. Secondly because we can't

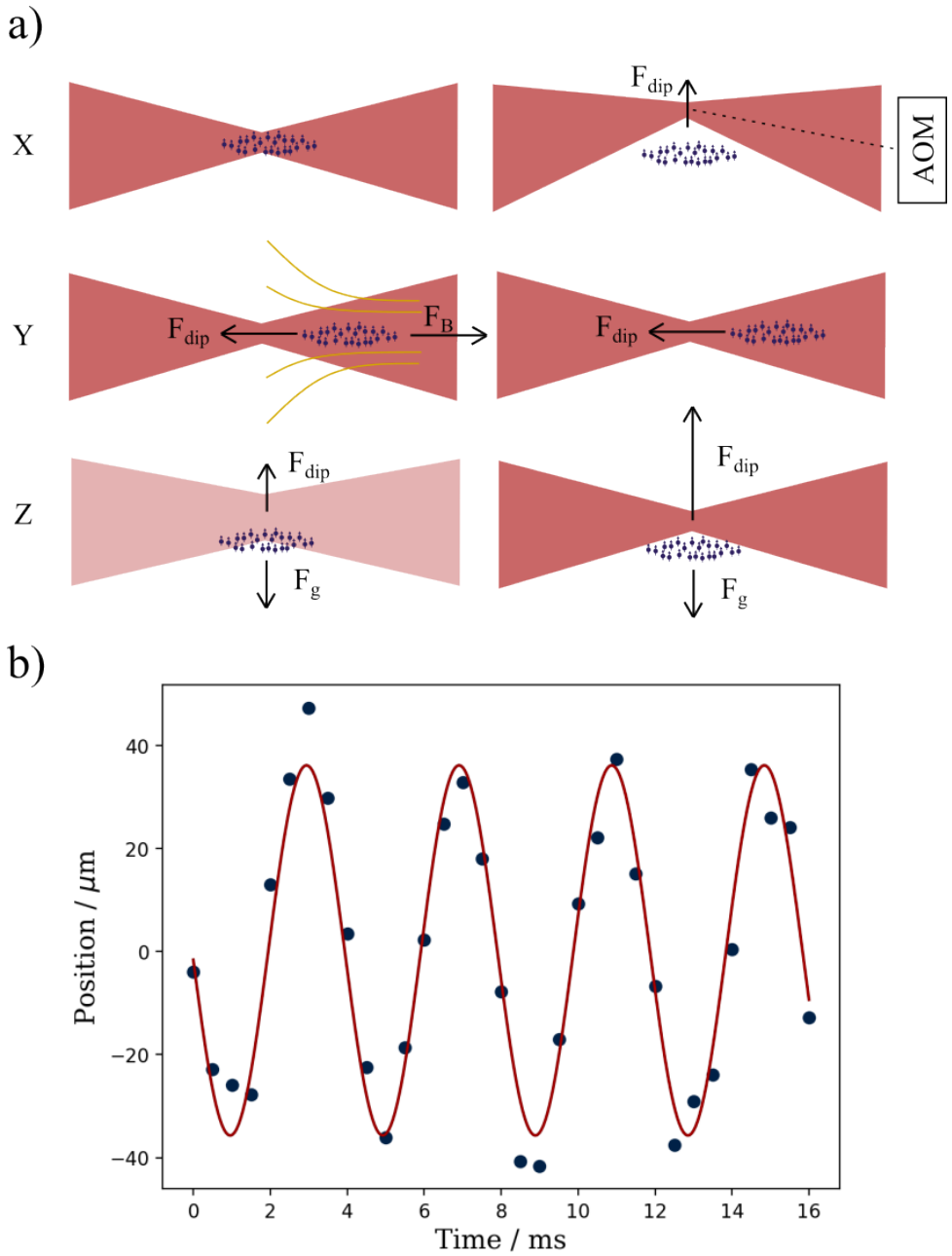


Figure 4.5: Center-of-mass oscillations. (a) Methods for exciting COM motion in the three directions. X–the trap is suddenly displaced in the x direction using an AOM. Y–a magnetic field gradient is used to push the cloud off the center. Suddenly turning off the magnetic field initiates oscillations. Z–quick ramp in the power of the trapping beam causes the atoms to oscillate vertically thanks to their initial gravitational sag in a weakened trap. (b) Sample dataset of the cloud position as a function of time held in the trap before being released. The relevant trapping frequency can be simply extracted by fitting a sine curve to the data.

use standard optical techniques. Luckily, the magnetic field gradient used for the MOT stage exerts a non-negligible force on the atoms along ODT1 and so we can temporarily turn it on to shift the atoms from their equilibrium position. An alternative method is to introduce a sudden but small change in the focal power of one of our tunable lenses. This effectively moves the focus of ODT1 along its direction of propagation, displacing the atoms from equilibrium. The methods for all three axes are summarized in figure 4.5a.

A sample dataset is shown in figure 4.5b together with a fitted sine curve. Interestingly, what we image in time-of-flight isn't technically the spatial oscillation of the cloud but rather its oscillation in velocity. Consequently, increasing the free-fall time improves the resolution by allowing the cloud to travel further given an initial (non-zero) velocity. We note that in order to observe all three directions, the imaging beam must not coincide with one of the principal directions. We also note that exciting the cloud too vigorously could cause it to experience anharmonic parts of the potential, resulting in a slightly lower estimate of the frequency. Using these techniques, we can measure the trapping frequencies with an uncertainty of $\leq 3\%$.

An alternative to COM oscillations is to measure the so called *breathing modes* of the dipolar BEC. These are collective excitation modes in the degenerate dipolar phase with their frequency depending on the trapping frequencies as well as on the polarization axis of the atoms relative to the principal axes of the trap [306]. Although we can use the same techniques as the ones described above to excite these oscillation modes, the subsequent mapping between their frequency and the trapping frequency isn't straightforward and so for practical reasons we don't employ this technique.

Parametric heating

Perhaps the easiest method of measuring the trapping frequencies is to periodically drive the power in the trapping beam. It can be shown [274], [304], [305] that when the driving frequency coincides with twice the trapping frequency, the beam starts resonantly depositing energy into the cloud. Consequently, the cloud heats up and it gradually evaporates from the trap. Thus, scanning the driving frequency over a wide range and recording the atom loss can reveal loss features at twice the trapping frequencies.

Figure 4.6 shows a typical dataset including Gaussian fits to extract the peak positions. On one hand, this technique is easy to implement, it is robust against beam imperfections (i.e. it is only sensitive to the real trapping frequencies) and importantly gives access to all three trapping frequencies by modulating just a single parameter. Moreover, since the measured quantity is atom number and/or temperature, the technique works irrespective of the imaging axis. On the other hand, the features of interest are broad, resulting in lower accuracy and possible overlap of close-lying peaks (which is likely for nearly circular Gaussian beams). For that reason, we prefer to use the slightly more involved but also more accurate COM oscillation measurements.

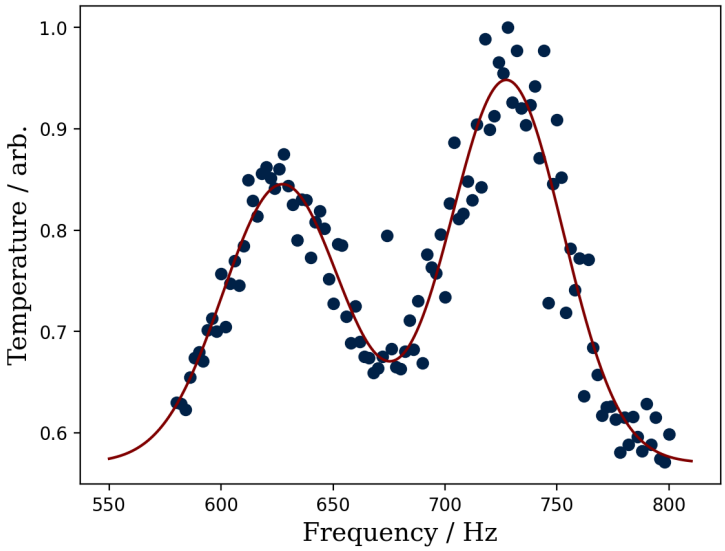


Figure 4.6: Parametric heating. Driving the power of the trapping beam with a periodic signal results in heating of the atomic cloud. When the driving frequency coincides with twice the trapping frequency, the cloud is driven resonantly, resulting in a peak in transferred energy and hence in temperature. Data set above shows two peaks which correspond to the two (nearly identical) transverse trapping frequencies. The width of the peaks and relatively large noise in the data makes this method less accurate than determining the trapping frequencies from COM excitations of the cloud.

4.1.4 Optical system

In this section, we will describe our experimental setup used to create an optical dipole trap (ODT). The main purpose of the ODT is to load cold atoms ($\approx 10\,\mu K$) directly from the MOT and proceed with forced evaporation (see section 4.3) until degeneracy is reached. To increase the atomic density and hence the efficiency of evaporation, we divert a portion of the power in the main ODT beam (ODT1) to a second trapping beam (ODT2) and overlap them in the usual crossed-beam configuration [275]. Furthermore, to eventually transport the atoms from the MOT chamber into a glass science cell over a distance $d \approx 30\,cm$, we employ a pair of tunable lenses (TLs) which allow us to move the focus of ODT1 while keeping a constant waist.

Figure 4.7 shows a diagram of the optical setup. The light originates from a single infrared (IR) laser[4] operating at 1030 nm and with a maximum output power of 45 W. The wavelength was chosen based on the availability of commercial lasers and on the large distance from any transitions (see figure 4.1). Additionally, this wavelength is suitable for trapping both erbium and potassium [123]. The linearly polarized output beam is focused down using a telescope and passed through an AOM[5]. This AOM serves three purposes. First, it splits the beam into the main trapping branch (ODT1) and the secondary crossed beam (ODT2). Secondly, it allows us to continuously control the total power in the ODT1 branch. Lastly, by changing the driving frequency of the AOM, we can rapidly change the position of ODT1, resulting in a time-averaged, wider potential (see dithering section

[4] Azurlight Systems
[5] AOMO 3080-199 by Gooch & Housego

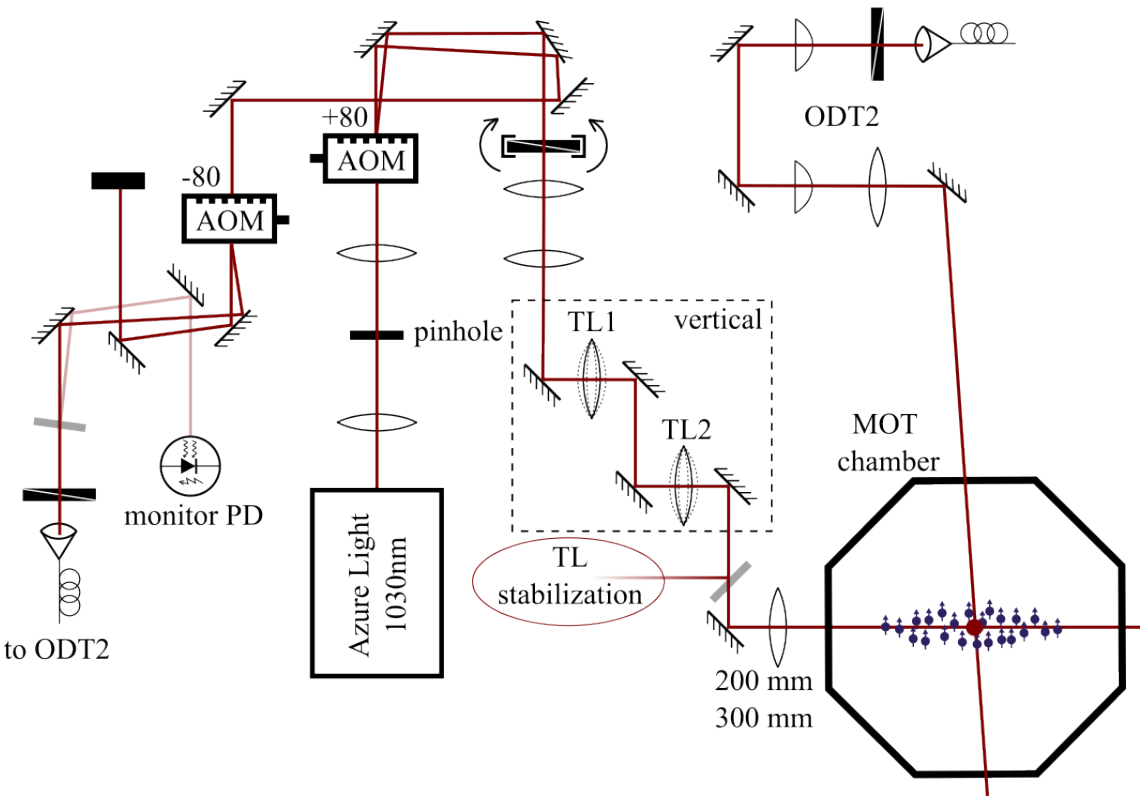


Figure 4.7: ODT optical setup. The optical path is described in detail in the text. Here we only point out a few important features. Firstly, a pinhole is used to block out undesirable EM mode residuals emitted by the laser. This greatly improves the beam quality [307]. The AOMs used to control the ODT1/2 beam intensities shift the frequency in opposite directions (± 80 MHz), suppressing interference effects. A monitor photo diode in the ODT2 branch is used for limiting the maximum power coupled into the ODT2 fibre. A motorized $\lambda/2$ waveplate allows us to finely control the polarization of the ODT1 beam. The tunable lens (TL) section is suspended on a vertical breadboard to minimize gravitational distortions (and consequent aberrations) of the lens membrane. Prior to entering the experimental chamber, a pick-off mirror diverts a portion of the beam into the optical setup used for active stabilization of the TLs–see section 4.5.

above). The zeroth order maximum is passed through a second AOM[6] for intensity control and coupled into a high power optical fibre[7]. The fibre guides the light to the top of the MOT chamber. Here, the outcoupled beam is shaped using a series of lenses and focused in the center of the MOT chamber to its final waist of $30 \times 140\,\mu m$.

The ODT1 beam, i.e. the first order maximum of the first AOM, is passed through an electronically-controllable $\lambda/2$ wave-plate, allowing us to dynamically change the polarization at different stages of the experiment. This is beneficial during sequences when we rotate the dipole orientation of the trapped atoms because we can compensate for the change in the tensorial polarizability by keeping the angle θ_p constant (see equation 4.4). We can also finely tune the relative polarization of the two crossed beams and prevent interference effects when necessary. The controllable mount[8] is interfaced with our digital control system through an in-house built circuit.

After passing through the $\lambda/2$ waveplate, the beam is expanded using a telescope and then continues through a pair of tunable lenses (TLs). The details of this setup are discussed in section 4.5. Here, we only note that the TLs introduced noise and long-term drifts into the system. Such drifts made data from longer experimental sequences unreliable. For that reason, we decided to temporarily replace them with a single fixed lens of 750 mm focal length. The data presented in chapters 5 and 6 was collected using this fixed lens setup. A stabilization scheme designed to combat these drifts is discussed in section 4.5.1. In combination with the last fixed focusing lens[9], the beam is focused down to a waist of $\approx 25 \times 25\,\mu m$ in the center of the MOT chamber. The beam penetrates the chamber in the horizontal plane and then continues its propagation through the science cell before being stopped by a beam dump.

The geometry of the crossing is shown in figure 4.8. Note that ODT2 propagates in the plane orthogonal to ODT1 and at an angle $\theta = 15°$ to the vertical. Its weaker trapping axis (waist of $130\,\mu m$) and its polarization coincide with the propagation direction of ODT1. That way, the polarizations of the two beams are mostly orthogonal at all times, suppressing interference. In practice, crossing the two beams is challenging given their small waists and the inaccessibility of the crossing point from outside of the chamber. Once the atoms are loaded into ODT1 and cooled to sufficiently low temperatures, we carefully scan the angle θ and look for an enhancement in the atomic density along ODT1. Once partial crossing is achieved, we maximize the overlap by finely scanning the horizontal position of ODT1 via changing the driving frequency of the dithering AOM.

Under normal operating conditions, the approximate power splitting between ODT1 and ODT2 is 21 W/2.5 W respectively. These powers are independently controlled by changing the amplitude of the respective AOM driving signals. Furthermore, each beam has its own active power stabilization using a PID feedback loop with pick-off glass slides aligned as close to normal incidence as possible to minimize the effects of polarization change. As an interesting aside and possible warning for future researchers, we note that

[6] AOMO 3080-199 by Gooch & Housego
[7] PMC-E-980-10 5-NA009-3-APC by Schäfter & Kirchhoff
[8] ELL14 by Thorlabs
[9] AC254-200-B-ML achromatic doublet lens by Thorlabs

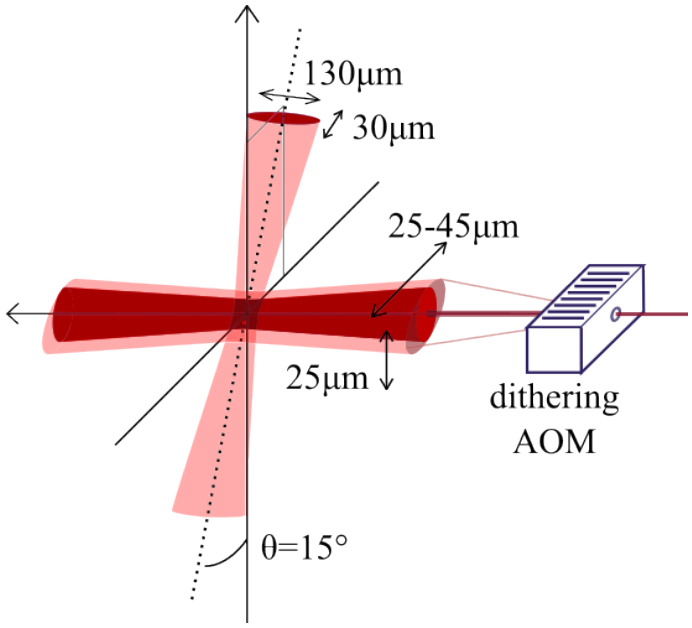


Figure 4.8: ODT crossing geometry. ODT1 enters the experimental chamber in the horizontal plane. Quick lateral displacement of the beam ('dithering'; see section 4.1.2) effectively enlarges the waist by up to a factor of 2. ODT2 beam enters the chamber at 15° to the vertical and in the plane perpendicular to ODT1. Its wider waist is aligned along ODT1 and creates a dimple in the potential–see figure 4.2.

despite using a polarization-maintaining fibre for ODT2 and despite detuning the two beams by $\approx 160\,\text{MHz}$ via the two AOMs, we still observe high sensitivity of the system to small changes in input polarization into the ODT2 fibre which manifest as heating and atom loss. We also note that the quality of the ODT1 trapping beam was greatly improved when a high-power AOM was used in place of a low-power equivalent.

4.2 Loading

After the ZS and MOT stages, the ODT system assumes a central role in the experiment with loading being the first of several steps towards degeneracy and, eventually, exploration of novel physics. In its essence, the loading stage simply consists of overlapping the trapping potential of the ODT with the compressed MOT cloud. The end of loading then serves as the starting point for the evaporation procedure. As such, the goal of loading isn't necessarily to only maximize the number of transferred atoms but also to potentially maximize the phase-space density (PSD; see section 2.4.1) by limiting the heating of the cloud which is inevitably associated with the loading dynamics.

The loading sequence in our experiment is as follows. First, the newly-formed compressed MOT cloud is allowed to equilibrate for 20 ms to reduce loading noise from transient dynamics of the MOT. Next, the dithered (see section 4.1.2) ODT1 beam at 21 W is suddenly turned on, instantly overlapping with the MOT cloud. Given the small size of the focus ($\approx 25 \times 25\,\mu\text{m}$), the loading efficiency is very sensitive to the positioning of the MOT cloud in the plane transverse to the beam (along the beam, the typical length scale is given by the Rayleigh range $z_R \approx 2.7\,\text{mm}$ and so that direction is less sensitive).

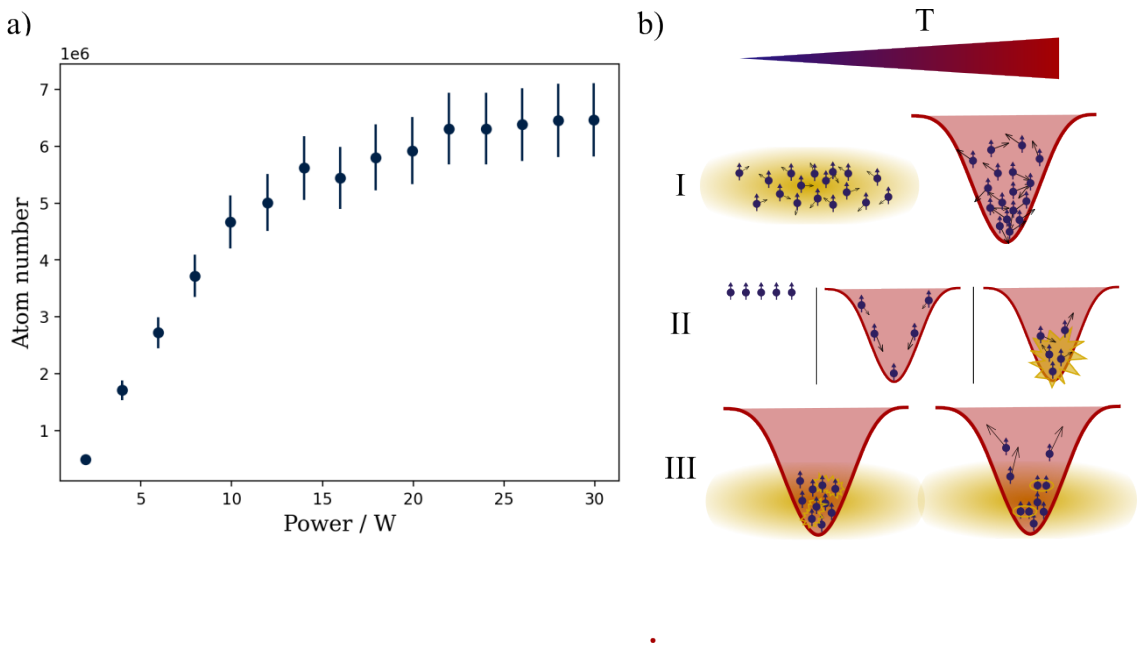


Figure 4.9: Loading saturation. a) The number of loaded atoms into the ODT saturates at higher beam powers despite stronger trapping. Light-assisted, inelastic collisions are believed to be the cause of this behaviour. b) Mechanisms describing the increase of temperature after loading. I–the volume of the ODT is much smaller than the MOT, resulting in gas compression and heating; II–atoms gain kinetic energy as they rush toward the focus of the trapping beam. This is later converted into heat via elastic collisions; III–the MOT light induces inelastic, two-body losses in the dense regions of the ODT, heating up the cloud in the process.

It is impractical to steer the beam itself if only because the process can't be automated without the use of motorized mirror mounts. Instead, we finely adjust the position of the MOT to optimize the overlap. This is done using a combination of bias fields to shift the center of the MOT (see section 3.1.2) as well as by changing the detuning of the MOT beams which shifts the equilibrium position of the MOT cloud in the vertical direction.

As mentioned in section 4.1.2, dithering of the beam increases the volume of the trap at the expense of reducing its depth. We find that dithering enhances loading numbers by $\approx 50\%$ whilst reducing the temperature of the cloud prior to evaporation from 70 µK to 40 µK. We also note that ODT2 has no measurable effect on loading and therefore remains off until later evaporation stages. This is mainly due to the low trap depth of ODT2 (≈ 20 µK) relative to ODT1 (≈ 700 µK) and to the temperature of loaded atoms (≈ 40 µK). Additionally, dithering shifts the focus of ODT1 away from ODT2, reducing the overlap of the MOT cloud with ODT2.

The overlap of ODT1 and MOT lasts for 80 ms, after which $\approx 1.8 \times 10^7$ atoms are loaded with a typical temperature of 40 µK. The overlap time is relatively short as it is limited by the cMOT lifetime (see figure 3.13). Furthermore, we found that above certain MOT atom number and/or ODT1 loading power, the number of loaded atoms remains constant i.e. it saturates as can be seen in figure 4.9a. We believe this to be due to inelastic, light-assisted collisions between the MOT atoms and the atoms trapped in the ODT, which induce density-dependent losses and heating.

The elevated temperature of loaded atoms as compared to the cMOT temperature ($\approx 10\,\mu K$) can be explained by three orthogonal effects. Firstly, given the small volume of the ODT compared to the cMOT, the gas is essentially compressed upon loading, resulting in an equivalent increase in temperature. Secondly, even though the optical dipole potential is conservative, its sudden turning on is not. As a result, some atoms find themselves instantaneously on the slope of the (very steep) potential and they gain kinetic energy as they rush towards the focus. This energy is later redistributed into the cloud as heat via collisions. Consequently, even though higher trapping powers result, in general, in higher loading numbers, they also indirectly contribute to heating via this effect. Lastly, the aforementioned light-assisted collisions deposit energy into the cloud, increasing its temperature. All three effects are summarized in figure 4.9b.

Unfortunately, the MOT molasses beams cannot be used for simultaneous cooling of the atoms because the light shift from the ODT1 beam detunes the ground state from the main transition by $\approx 15\,MHz$ (assuming the excited state doesn't shift). Interestingly, we attempted to implement a 'blinking' scheme in which the ODT1 beam was periodically turned on and off to facilitate molasses cooling during the dipole trap's downtime. This, however, didn't result in any improvement and later it was realized that dithering inherently results in a similar 'blinking' pattern from the point of view of the atoms.

To conclude this section, we mention a few experimental observations and planned optimization avenues. Firstly, we note that we observed a strong dependence of the loading efficiency on the polarization of ODT1. Although we are yet to understand the origin of this behaviour we, at least, have full control over the polarization thanks to a motorized waveplate implemented in the optical path (see section 4.1.4). This allows us to independently optimize loading and the crossed beam evaporation stage where the relative polarization of the two beams is crucial to prevent interference. In the future, we plan to explore possible ways of utilizing the focus-tunable lenses for enhancing loading. These include, for example, dynamically changing the shape of the trap to better match the geometry of the MOT cloud and scanning the focal position during the overlap to effectively 'dither' the trap in the longitudinal direction.

4.3 Evaporative cooling

At the end of the loading stage, the phase-space density of the atoms in the ODT is on the order of $\rho \approx 1 \times 10^{-4}$. Although a remarkable enhancement has been achieved compared to an ambient, room temperature gas with $\rho \approx 1 \times 10^{-8}$, the onset of degeneracy in a harmonic trap happens when $\rho = \zeta(3/2) \approx 2.612$ and so on a logarithmic scale, we have only just reached the midpoint of our journey towards Bose-Einstein condensation. Fortunately, this seemingly elusive endpoint can be reached with the use of evaporative cooling [308], [309].

The main principle behind this technique is simple and intuitive as it mirrors our everyday experience with cooling a cup of tea or our bodies via perspiration[10]. As a

[10]Disclaimer: DO NOT try to cool your body to quantum degeneracy!

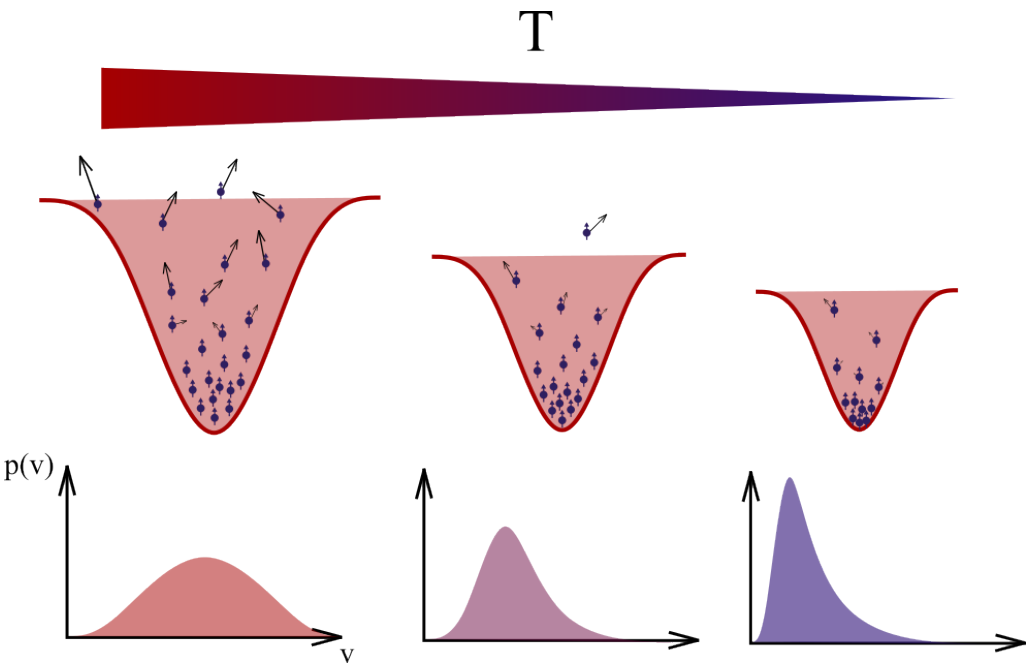


Figure 4.10: Evaporative cooling. As high energy particles leave the trap, the rest of the cloud rethermalizes to a lower temperature. This way, particle loss is converted into energy loss and cooling. By continuously lowering the trap depth, more evaporation is facilitated and the process is maintained at a steady rate. Reduction in temperature is accompanied by narrowing of the velocity distribution which can be detected in time-of-flight measurements.

starting point, let's consider an ensemble of atoms confined in a trap of finite depth. These atoms frequently collide and redistribute energy in the system, e.g. they *thermalize*, to form a well defined velocity and density distribution that depends on the temperature and, in general, on the trap geometry. At any time, there is a finite, non-zero probability that there exists an atom within the ensemble that has enough energy to escape the trap. If the trap is deep enough such that the required energy is larger than the average energy of atoms in the trap, an atom lost in this way carries away more than its 'share' of energy. Consequently, when the remaining atoms re-thermalize via collisions, they assume a distribution with lower average energy or, equivalently, lower temperature. In this way, the atomic cloud is cooled down at the expense of loosing atoms. Figure 4.10 summarizes this process.

To understand it a bit more quantitatively, we can take the example of atoms trapped in a harmonic trap. By equipartition, the average energy per atom is $3k_BT$. If the trap depth is given by ηk_BT with η a free parameter, we can approximately assume that any atom that escaped the trap must have had energy $E_{\text{esc}} \approx \eta k_BT$. Consequently, after dN atoms leave the trap, the cloud re-thermalizes to a new temperature $T + dT$ such that

$$\begin{aligned} 3k_B(T+dT)(N+dN) &= 3Nk_BT + \eta k_BTdN \iff \\ \frac{dT}{T} &= \frac{\eta-3}{3}\frac{dN}{N} \iff \\ T &\propto N^{(\eta-3)/3} . \end{aligned} \tag{4.11}$$

Clearly, in order to achieve cooling, we require $\eta > 3$, i.e. the energy cut-off needs to be larger than the average energy. However, cooling in itself is not sufficient for enhancing the phase-space density (PSD). In a harmonic trap, $\rho \propto NT^{-3} \propto N^{4-\eta}$ and so we might require $\eta > 4$. In fact, in this simple model, the optimal energy cut-off diverges, i.e. $\eta \to \infty$, because we can simply wait for a fortuitous (and infinitely unlikely) event in which one particle happens to carry away all of the energy of the cloud, leaving behind a pure BEC. In real life, we need to consider the lifetime of the atomic cloud[11] which is limited by the vacuum quality, stability of trapping lasers and loss-inducing three-body collisions.

Furthermore, in our derivation we omitted the fact that for a static trap, the parameter $\eta = \eta(T)$ depends on the temperature of the cloud. The colder the cloud gets, the harder it is for any atoms to escape the trap. In practice, the trap depth is lowered simultaneously with the temperature and atom number. This widely used technique is known as *forced evaporation* [308]. The main challenge here is to figure out how quickly to lower the trap–too slow and the evaporation will die out and succumb to losses; too fast and even the low energy atoms will be able to escape, reducing the cooling effect. Our optimized evaporation ramp is described in section 4.3.1.

There are two main ways in which evaporative cooling is performed in ultracold atom experiments. Historically first to be implemented is the radio-frequency (RF) knife technique [7], [310] in which atoms are placed in a magnetic trap in a low-field-seeking state. An RF field is used to induce transition between this state and a high-field-seeking state that gets expelled from the trap. The frequency of the radiation is tunable and chosen such that it is only resonant with atoms that reach certain depth within the trap. If atoms have enough energy to reach this depth, they are instantly expelled. In this way, the RF field cuts through the trap like a knife and gradually 'chops off' more and more of it as the frequency is tuned, lowering the trap depth in the process. The second method, which is also used in our experiment, utilizes the trapping potential of an ODT to perform evaporation [140], [275], [311] by lowering the optical power in the beam.

There are several differences between these methods. Whilst the magnetic evaporation is heavily state dependent (it needs a low-field-seeking state), the optical method is not and allows for trapping of mixtures of states. Furthermore, application of an external magnetic field can enhance the atomic scattering rate via Feshbach resonances (see section 2.3.4) which is considerably easier to achieve in the case of optical traps. However, the all-optical method suffers from the lack of confinement of the atoms along the axis of the trapping beam (this can be fixed by utilizing the crossed-beam geometry [301], [312]). Furthermore, as the power of the beam is lowered, the shape and characteristic frequencies of the trap change, making runaway evaporation [313] very hard to achieve. This is not the case for magnetic trapping where the shape is conserved and only the trap depth is tuned.

It is clear that despite its simple physical explanation, evaporation in its full glory is anything but simple. Although we are already armed with sufficient intuition to understand the details of our experimental implementation of evaporative cooling presented in

[11] Or the lifetime of an average PhD student. Whichever is shorter.

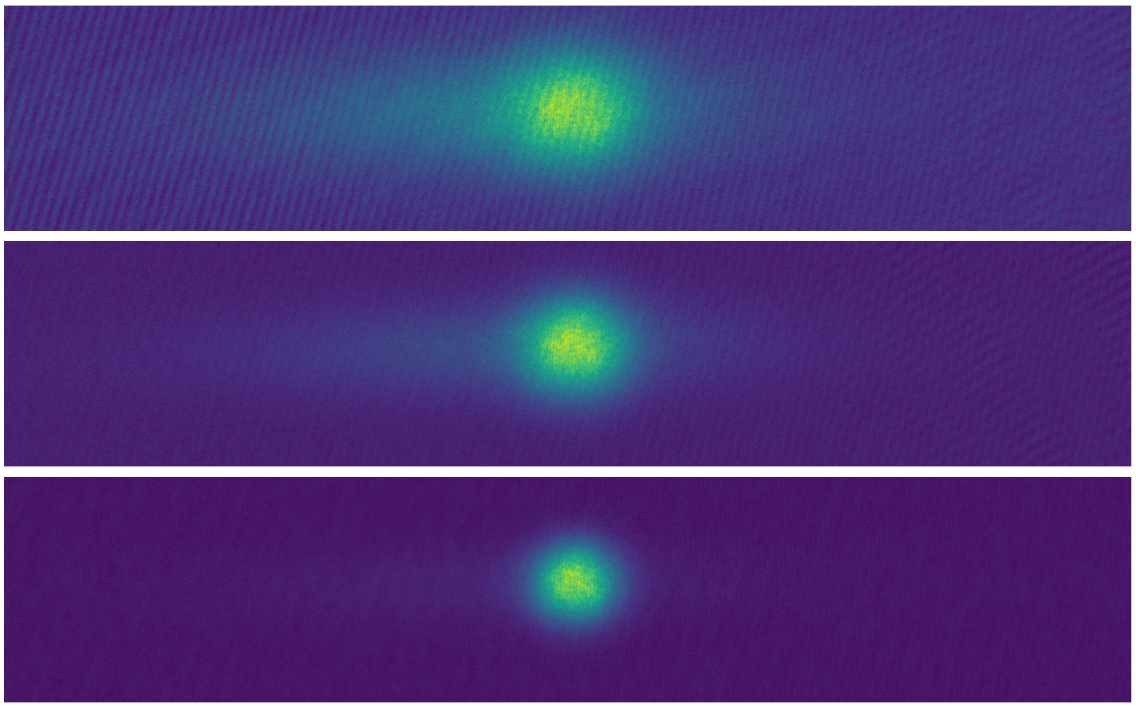


Figure 4.11: Crossing formation. Time-of-flight absorption images of the trapped cloud during the second evaporation stage. As the evaporation proceeds and the depth of the dimple becomes comparable to the temperature, the cloud converges to the beam crossing.

the next section, appendix C provides the reader with additional theoretical background. It also describes the mathematical tools we use to simulate the evaporation process and to benchmark our dynamic DSMC simulations of atomic transport described in section 4.5.2.

4.3.1 Evaporation procedure

To recapitulate, at the start of our evaporation procedure, i.e. right after loading from the cMOT, we have $\approx 1.8 \times 10^7$ atoms at $\approx 40\,\mu\text{K}$ loaded in a spatially dithered, single beam ODT at 21 W. The evaporation procedure that follows thereafter can be split into three stages. During the first stage, the dithering amplitude of ODT1 is ramped down to enhance the atomic density and facilitate faster, more efficient evaporation (remember that evaporation rate scales as the square of atomic density). However, by doing so, we inevitably increase the depth of the trap which exponentially suppresses evaporation. Therefore, to keep the $\eta = \varepsilon_t/k_B T$ parameter roughly constant and maintain high evaporation rates, we have to simultaneously reduce the power in the beam to $\approx 9\,\text{W}$. This is done over the course of a 1.1 s time step.

In the second stage, ODT2 is turned on at 2.5 W to form the high-density crossing region. Initially, only a small fraction of the atoms gets trapped in the 'dimple' [301], [314], [315] but as the atomic cloud cools down, more atoms gradually fill the crossing as shown in figure 4.11. At some point, the dimple depth–which is governed by the power of ODT2–becomes a relevant evaporation parameter. Consequently, during the second stage

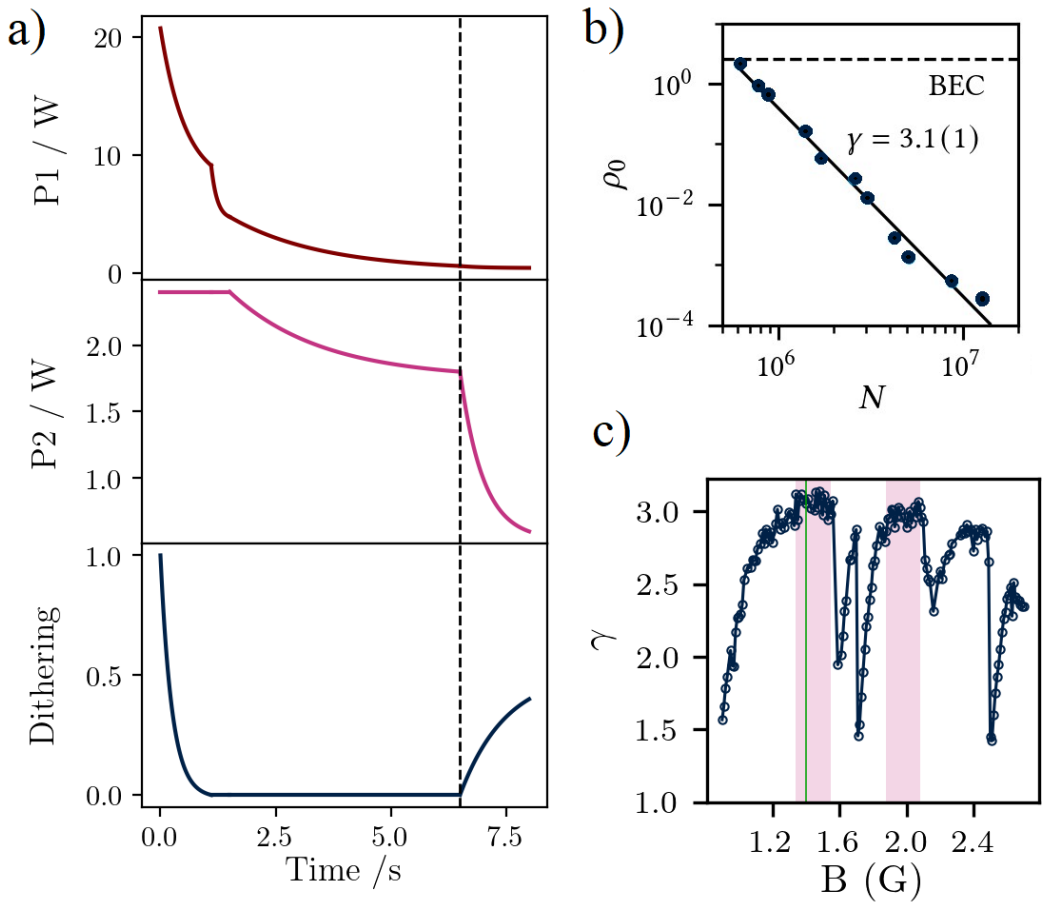


Figure 4.12: Evaporation procedure. (a) The ramps in powers of the two trapping beams and the magnitude of dithering over the course of the evaporation sequence. Vertical line denotes the onset of condensation. (b) The phase space density ρ as a function of particle number N. The evaporation efficiency γ is steady throughout the process. (c) Evaporation efficiency for different magnetic fields B. Two red-shaded regions correspond to the most optimal magnetic fields. These are intricately connected to the three body loss rate discussed in chapter 5. Our evaporation is performed at $B = 1.4\,\mathrm{G}$.

we simultaneously ramp down the power in both beams. By the end of this stage, which lasts for $\approx 5.5\,\mathrm{s}$, the atom cloud is completely confined to the crossing and is at the brink of degeneracy with $N \approx 6.2 \times 10^5$ atoms at $T \approx 530\,\mathrm{nK}$ which corresponds to a peak PSD of $\rho \approx 2.61$.

The parameters of the third and last stage are influenced by our investigation of the three-body losses which is presented in chapter 5. Once a BEC starts forming, the atomic density is so high that the loss rate becomes comparable to the evaporation rate. Given that the three-body losses scale as density cubed whereas evaporation rate is proportional to density squared, it is beneficial at this point to relax the trap and reduce the overall density. We do this by simultaneously lowering the power in both beams and slightly dithering the ODT1 beam. After a relatively short $\approx 1.5\,\mathrm{s}$ ramp, we are able to produce nearly-pure dipolar BECs of 2.2×10^5 atoms which are almost twice as large as the largest reported condensates used to study the roton regime [271]. The full evaporation ramp is shown in figure 4.12a.

To quantify the efficiency of our evaporation procedure, it is customary to define the efficiency parameter γ as

$$\gamma = -\frac{d\ \ln(\rho)}{d\ \ln(N)}\ , \tag{4.12}$$

which essentially signifies how many orders of magnitude in PSD are gained per order of magnitude reduction in the particle number. We measured γ throughout the evaporation ramp using the know temperature, particle number and the trapping frequencies in combination with the peak phase space density given by (for a harmonic trap) $\rho_0 = N(\hbar\bar{\omega}/k_B T)^3$. The data is presented in figure 4.12b all the way up to degeneracy which corresponds to the end of the second evaporation stage. Note that once degeneracy is reached, the peak PSD of the thermal gas stays constant and γ is no longer a suitable parameter. We see that throughout the process, we maintain a steady efficiency of $\gamma = 3.1$ which signifies a well optimized evaporation ramp.

So far, we have omitted the discussion of magnetic fields. These can affect evaporation in two major ways. Firstly, by utilizing Feshbach resonances (see section 2.3.4), magnetic fields can be used to increase the s-wave scattering length and hence the scattering cross section which, in return, enhances the rate of evaporation. On the other hand, the three-body loss coefficient $L_3(B)$ depends on the magnitude of the applied field and, in general, is amplified close to resonances. The dependence of L_3 on B is thoroughly investigated in chapter 5. This nuanced interplay of losses and atomic scattering results in the existence of optimal regions in the magnetic field space. We have investigated this experimentally by comparing the evaporation efficiency γ at different magnetic fields. Our results are shown in figure 4.12c. We identify two 'safe' regions within the 0-4 G range–one in the vicinity of 1.4 G and the other close to 2 G. The temperature dependence (also thoroughly discussed in chapter 5) of newly discovered loss features which manifest as pronounced dips in figure 4.12c informed our decision to evaporate at 1.4 G where $a_s = 72a_0$. This choice of field proved crucial in producing large erbium BECs.

4.4 Degenerate dipolar gas

We have reached the end of the journey of our atoms (for now!) and can start performing experiments with erbium Bose-Einstein condensates (BECs). These could involve looking at the roton minimum in the excitation spectrum of the dipolar BEC [107]–[109], at the formation of quantum droplets [114], [115] and supersolids [117], [270], [271] or at other exotic phases in constrained geometries where the anisotropy of the dipole-dipole interaction (DDI) governs the structural properties of the condensate [119], [152]. In chapter 6 we present our measurements of the critical BEC temperature shift and of the non-saturation effect of the thermal fraction due to its interaction with the dipolar BEC. In the following short section we won't be going into detail about any of these possible experimental avenues. Instead, we will describe how we detect and characterize our erbium BECs which show a strong dipolar character in certain regimes.

4.4.1 Characterizing erbium BECs

As described in section 3.1.3, most of our experimental data comes from absorption imaging. An image taken this way is essentially a snapshot of the 2D density distribution of the gas. Using the time-of-flight technique (also described in section 3.1.3), we can not only extract the total atom number but also the temperature of the cloud.

For a harmonically trapped gas which is considerably hotter than the BEC critical temperature, $T \gg T_c$, the initial 3D density distribution is Gaussian and it can be shown (see equation 3.7) that after time-of-flight, the distribution remains Gaussian with its standard deviation depending on the temperature of the gas. The fact that the atomic density follows a normal distribution is rooted in our assumption that the energy distribution function of the atoms is well approximated by the Maxwell-Boltzmann (MB) distribution, i.e. $f_{\mathrm{mb}}(\epsilon, \mu, \beta) \propto e^{-\beta(\epsilon-\mu)}$ where μ is the chemical potential of the gas and $\beta = 1/k_B T$. At or near degeneracy, the value of the chemical potential is no longer large and negative and we need to consider the full Bose-Einstein distribution instead:

$$f_{\mathrm{BE}}(\epsilon, \mu) = \frac{1}{e^{\beta(\epsilon-\mu)} + 1} = \sum_{n=1}^{\infty} e^{-n\beta(\epsilon-\mu)} = \sum_{n=1}^{\infty} f_{\mathrm{mb}}(\epsilon, \mu, n\beta) \ . \tag{4.13}$$

We can then calculate the density distribution by taking a semi-classical approach in which the density is assumed to change slowly compared to the de Broglie wavelength of the atoms. In this case, we can write the density of momentum states in a small volume of real space ΔV as $g(k) = \Delta V/(2\pi)^3$. To get the spatial density, we can simply integrate over all the momentum states multiplied by their occupation probability given by 4.13 to get

$$n_{\mathrm{BE}}(\mathbf{r}) = \int \frac{d^3\mathbf{p}}{(2\pi\hbar)^3} \frac{1}{e^{\beta(\mathbf{p}^2/2m + U(\mathbf{r}) - \mu)} + 1} = \frac{1}{\Lambda^3} g_{3/2}\left[e^{\beta(\mu - U(\mathbf{r}))}\right] \tag{4.14}$$

where Λ is the thermal de Broglie wavelength[12], $U(\mathbf{r}) = \frac{m}{2}\sum_i \omega_i^2 r_i^2$ is the harmonic trapping potential and finally $g_s(z)$ is the polylogarithmic function[13]. Near degeneracy, we can take $\mu \approx 0$ and compare this expression with the corresponding non-degenerate, Gaussian expression 3.7. This is shown in figure 4.13. The proper density distribution given by equation 4.14, also known as the *Bose-enhanced* distribution, is narrower and shows a pronounced increase in density near the bottom of the trap. Note that in deriving expression 4.14, we neglected any interatomic interactions. For more accurate determination of the density profile and particle number, they need to be taken into account. This is discussed in chapter 6 which is concerned with determining the shift of the critical temperature due to the DDI.

As was the case for a Gaussian cloud, it turns out that during-time-of (ToF) flight the 3D density distribution remains polylogarithmic. We can understand this by realizing that according to equation 4.13, the BE distribution is a linear combination of MB Gaussian distributions and so individually these normal distributions undergo a self-similar transformation during ToF and remain normal and hence the total distribution remains

[12] $\Lambda = \sqrt{\frac{2\pi\hbar^2}{mk_BT}}$

[13] $g_s(z) = \sum_{n=1}^{\infty} \frac{z^n}{n^s} = \frac{1}{\Gamma(s)} \int_0^{\infty} \frac{x^{s-1}}{e^x/z - 1} dx$ with Γ the Gamma function

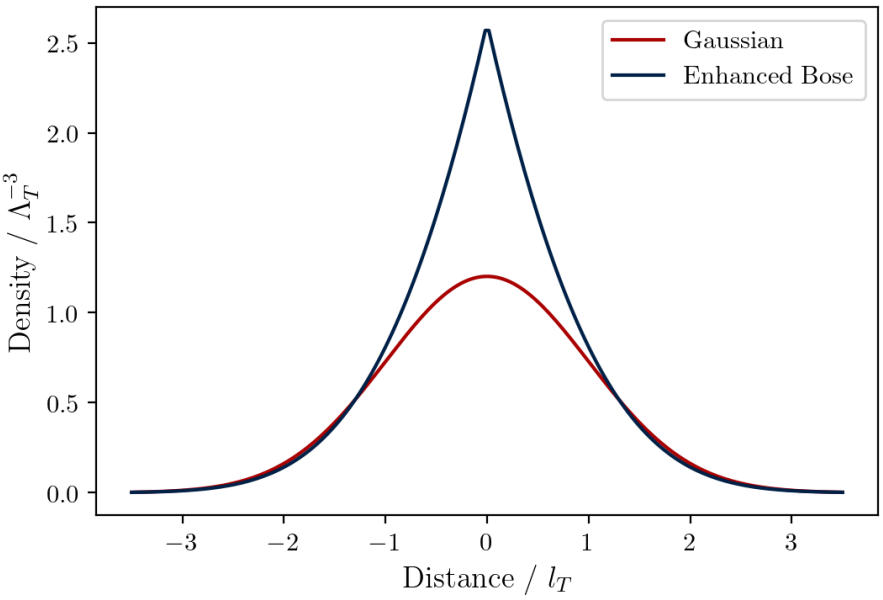


Figure 4.13: Gaussian vs Enhanced Bose density distribution. A cut through the 3D density distributions along one axis. The enhanced Bose distribution is sharply peaked at the bottom of the trap. Here $l_T = \sqrt{k_B T/m\omega^2}$ is the thermal size of a harmonically trapped cloud.

polylogarithmic. By performing a similar calculation to 3.6 and integrating along the z axis, we can derive an expression for the 2D density distributions of the Bose-enhanced thermal cloud after ToF:

$$n_{2D}(\mathbf{r},t) = \frac{1}{\Lambda^3}\left(\frac{2\pi k_B T}{m\omega_z^2}\right)^{\frac{1}{2}} \prod_{i=x,y} \frac{1}{\sqrt{1+(\omega_i t)^2}}\, g_2\left(e^{\beta\mu} \prod_{i=x,y} e^{-\frac{m}{2k_B T}\frac{\omega_i^2 r_i^2}{1+(\omega_i t)^2}}\right) . \quad (4.15)$$

Note that the base of the polylog function is different from the 3D case of equation 4.14. Also note that the characteristic size of the distribution still evolves according to 3.8.

So far, we have only discussed the near-degenerate thermal gas. Once a BEC starts forming, the situation gets more complicated. As detailed in section 2.4, atoms in the condensate occupy the ground state of the trap which has, in general, a much narrower density distribution compared to the thermal cloud. Consequently, when the cloud is partially condensed such that the two phases coexist in the trap, a signature bimodal density distribution is detected in absorption images that contains both the Bose-enhanced thermal cloud and the narrow peak from the BEC. This is shown in figure 4.14 for a progressively larger condensed fraction.

In the Thomas-Fermi approximation (see section 2.4.2), the shape of a BEC interacting via contact interactions is simply given by the shape of the trapping potential, i.e. parabolic in the case of harmonic trapping [233]. This turns out to be true even for dipolar BECs as will be discussed in chapter 6 [316]. Furthermore, during ballistic expansion, a parabolic condensate remains parabolic, albeit with its size changing in time [317]. Consequently, we can write the density distribution of a dipolar BEC during ToF

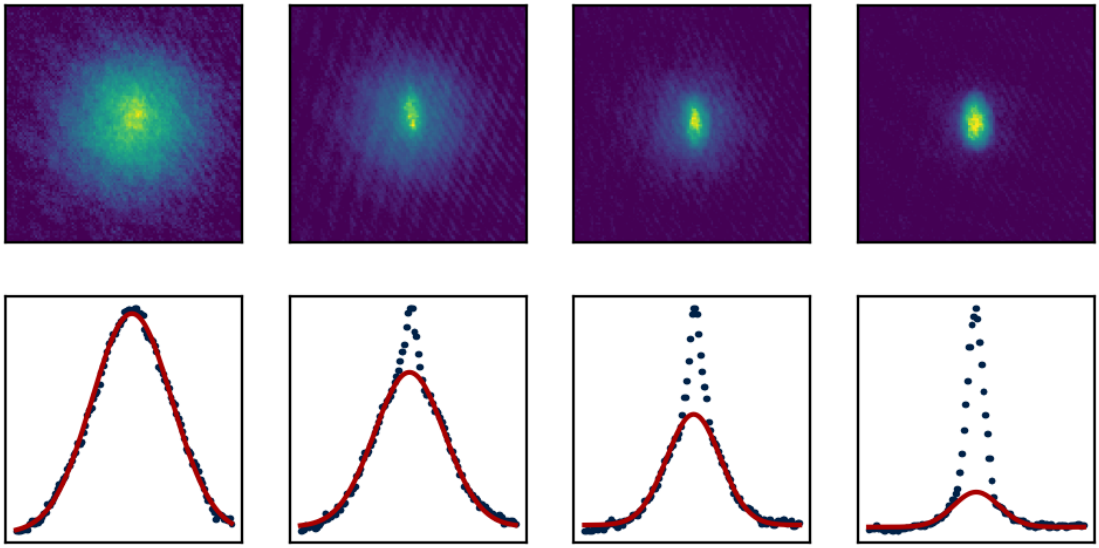


Figure 4.14: Typical BEC sequence. Top row–absorption images of a progressively more condensed atomic cloud of ^{166}Er produced by gradually reducing the depth of the final trap. A typical bimodal feature appears, reflecting the saturation of the excited thermal fraction and macroscopic population of the ground state. Bottom row–1D pixel sums along the vertical axis. A crude Gaussian fit (red) represents the thermal cloud. A sharp Thomas-Fermi peak appears at the center of the cloud signifying the onset of condensation.

as:

$$\tilde{n}_{3D}(\mathbf{r},t) = n_0 \left(1 - \frac{x^2}{R_x^2(t)} - \frac{y^2}{R_y^2(t)} - \frac{z^2}{R_z^2(t)}\right) \tag{4.16}$$

with $n_0 = 15N_0/8\pi R_x R_y R_z$ given by the normalization condition on the BEC atom number N_0. The corresponding 2D density (relevant for imaging) is then

$$\tilde{n}_{2D}(\mathbf{r},t) = \frac{4}{3} n_0 \left(1 - \frac{x^2}{R_x^2(t)} - \frac{y^2}{R_y^2(t)}\right)^{\frac{3}{2}} \tag{4.17}$$

So in order to analyze images containing a BEC, we need to fit them with a bimodal distribution which consists of a sum of the Bose-enhanced thermal distribution given by equation 4.15 and the BEC parabolic distribution given by 4.17. In practice, rather than fitting both distributions at the same time, it is desirable to mask out specific regions of the image and only ever fit the thermal or condensed fraction at a time. This way, parameter redundancy is avoided at the expense of a more complex fitting routine. Our general routine and methods are described in detail in reference [280] and section 6.3.2 discusses the specific fitting procedure used to measure the dipolar critical temperature shift.

We note that interactions between the BEC and the thermal cloud slightly alter the density distribution of the thermal cloud. Furthermore, thermal-thermal and thermal-BEC interactions also change the ToF expansion of the thermal cloud. The first effect is responsible for the so-called non-saturation of the thermal fraction whereas the second

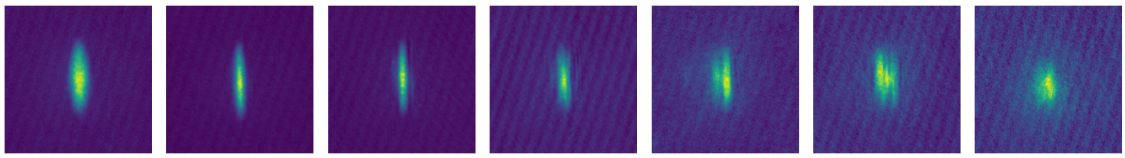


Figure 4.15: Dynamic quench into a quantum droplet. Time evolution of BEC density after a quench of the magnetic field magnitude. Formation of quantum droplets leads to the appearance of interference fringes and subsequent decay of atom number and contrast.

effect changes the apparent temperatures we measure using the ToF technique. Both of these effects are, in general, small and are discussed in detail in chapter 6.

4.4.2 Quantum droplets and supersolidity

As a short conclusion to this section and a teaser for the future of our experiment, we present evidence of the dipolar nature of erbium BECs. Reiterating on some of the points made in section 2.4, the anisotropy of the DDI combined with its simultaneous attractive and repulsive character leads to unusual properties of dipolar BECs. For example, the excitation spectrum shows a distinct non-monotonic feature known as the roton minimum [108], [109] which corresponds to an effective lowering of the excitation energy. The depth of this minimum depends on the geometry of the system as well as on the strength of the DDI relative to the contact interactions.

When the energy cost of creating these roton excitations vanishes, the gas becomes unstable and undergoes a phase transition, forming quantum droplets [112]–[114], [197]. These can be characterized as self-bound hyper-dense objects which are supported against collapse by quantum fluctuations [261], [262]. The number of droplets formed depends on the details of the trap and, importantly, on the atom number. With appropriate resolution, droplets can be detected in-situ as distinct peaks. Our current experimental resolution doesn't allow us to do that well enough and so we have to resort to time-of-flight imaging instead.

When a multitude of droplets are released from their trap, they begin to expand and interfere with each other in a matter-wave fashion. After a long ToF, they can be detected as distinct interference patterns in the images. The shot-to-shot phase of the fringes is, in general, random as long as the droplets aren't phase coherent. However, under special conditions, droplets can become phase coherent by exchanging particles, forming a supersolid instead [115], [116], [118], [270]. The signature of a supersolid is then a well defined phase difference between the droplets which results in a consistent interference pattern across different measurements.

Figure 4.15 shows an experimental signature of the quantum droplet phase. The series of images depicts the time evolution of the BEC density profile after a fast quench of the magnetic field magnitude into the droplet regime ($\varepsilon_{dd} > 1$). Elongation of the BEC and gradual appearance of fringes points to interesting dynamics. Our future experiments will aim to shed more light on these processes. However, enhanced densities associated with

the formation of quantum droplets mean that any steady state analysis is challenging due to three-body losses. To map the loss landscape in order to inform our future experimental design, we performed a series of detailed measurements of three-body loss in ^{166}Er. These are presented in the following chapter.

4.5 Tunable lenses

Our planned use of a glass science cell for performing more involved experiments that require superior optical access comes with its drawbacks. The major one being the fact that we need to transport cold atomic sample from the MOT chamber into the cell, i.e. approximately 33 cm, without incurring substantial losses or heating. There are several commonly used solutions to the problem of atomic transport. In the case of magnetically trappable species, it is possible to create a moving magnetic potential using a series of overlapping coils [318] or a single pair of coils on a moving stage [319]. Unfortunately, since erbium in its ground state is a high field seeker, i.e. not magnetically trappable, we have to resort to optical methods of which there are several. One can, for instance, use a travelling optical lattice [320], [321] by overlapping two beams of controllable phase difference. Alternatively, the dipole trap can be moved by changing the position of the focus either via a moving stage [322] or with the use of tunable lenses [323], [324]. We decided to implement the latter in our experiment to avoid vibrations introduced by a motorized stage.

To create a transportable ODT, we use a three lens scheme [324] where the first two lenses[14] have a tunable focal length and the last lens focuses the beam on the atomic sample. In principle, a single tunable lens would be sufficient to dynamically move the focus of the beam by simply increasing the focal length of the lens. However, doing so would inevitably lead to an increase of the beam waist and consequently 'loosening' of the trap. The weaker the trapping in the direction of motion, the slower the transport needs to be in order to prevent atoms from spilling from the trap. A two lens setup, on the other hand, allows one to transport the focus while keeping the waist constant along the way. A simple calculation using the thin lens equation[15] reveals that if a lens (TL2) of variable focal length f_2 is placed a distance f from a fixed lens of focal length f, then the divergence of the beam after the fixed lens is given by $\theta = d/f$, where d is the size of the beam incident on the tunable lens. This setup is shown in figure 4.16a. Since the divergence of the beam determines the waist at the focus and since it is independent of f_2, we can change the focal position by changing f_2 while keeping the waist constant.

By putting another tunable lens (TL1) before this pair, we can also independently change the input beam size incident on TL2 and thus change the resulting beam divergence and waist. Figure 4.16b shows the 'two-TLs one-fixed lens' scheme employed in our experiment. Using the standard ray transfer matrix analysis [325], we can calculate the

[14] EL-16-40-TC-VIS-5D by Optotune

[15] This is usually expressed as $\frac{1}{f} = \frac{1}{a} + \frac{1}{b}$ where f is the focal length of the lens, a is the distance of the object from the lens and b is the distance of the image

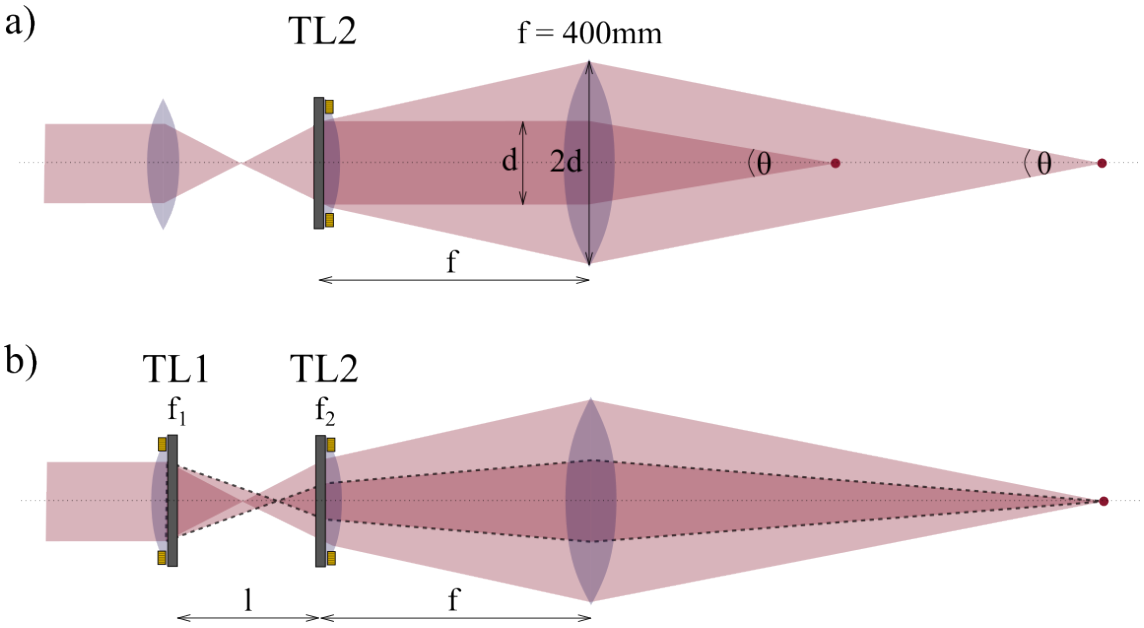


Figure 4.16: Tunable lens setup for transport at constant waist. (a) Two lens setup with a single tunable lens and a fixed lens. When the tunable lens (TL2) is placed focal length away from the fixed lens, the beam's divergence $\theta = d/f$ is independent of f_2. By changing f_2, the focus can be moved whilst maintaining constant beam waist. (b) Three-lens setup implemented in our experiment. Another tunable lens (TL1) can be used to change the input beam size incident on TL2. This way, we can independently tune the beam waist and the focal position whilst still transporting at constant waist by changing f_2. Figure adapted from [324].

waist size and focal position directly as

$$w_f = \frac{f|f_1|w\lambda}{\sqrt{(f_1 - l)^2(\pi w^2)^2 + (f_1 \lambda l)^2}}, \tag{4.18}$$

$$x_f = f - f^2 \left(\frac{1}{f_2} + \frac{(f_1 - l)(\pi w^2)^2 - f_1^2 \lambda^2 l}{(f_1 - l)^2(\pi w^2)^2 + (f_1 \lambda l)^2} \right), \tag{4.19}$$

where $f_{1/2}$ is the focal length of TL1/TL2, l is the distance between the two TLs and w is the waist of the incoming beam which is assumed to be collimated ($w = 4\,\text{mm}$ in our experiment). As expected, the waist is independent of f_2 and the focal position closely follows the thin lens prediction $\tilde{x}_f = f(f_2 - f)/f_2$ with a small correction term due to the physics of Gaussian beam propagation.

Initially, the system was designed with the intention of using a 400 mm fixed lens. However, later we decided to use a 200 mm one instead to reduce the trap waist and thus enhance the atomic density. This meant that TL2 was no longer distance f away from the fixed lens due to experimental constraints. The two degrees of freedom provided by the TLs are still enough to perform transport at constant waist but this time, both f_1 and f_2 need to be tuned simultaneously and the exact analytic expression for the waist size and the focal position is more complicated. Furthermore, a more tightly focusing lens prohibits us from transporting the atoms all the way to the science cell because the beam incident on the fixed lens becomes bigger than the aperture of the lens. For that reason, we eventually

replaced the 200 mm lens with a 300 mm one. This choice represents a compromise between having a tight enough trap for efficient evaporation and fast transport and a 'weak' enough lens to allow us to transport the atoms over ≈ 33 cm.

The operating principle of the TLs used in our experiment is based on the dynamical tunability of their curvature. A fluid of known refractive index is enclosed between two elastic membranes. An electromagnetic actuator powered by electric current exerts pressure on the membrane which, in return, changes its shape. This way, one can tune the focal power of the lens between -2 and 3 dpt by simply changing the magnitude and direction of the current. A controllable current driver was provided by the manufacturer which proved unsuitable for our application. This was because the driver displayed digitized behaviour where the focal power of the lens would only change in discretized steps rather than continuously. Consequently, small drifts in control voltage resulted in random 'jumps' of the focal position which, in return, deteriorated the stability of loading and evaporation. Furthermore, transporting the atoms in this stepped fashion would result in extensive heating and loss. To solve this issue, a controllable and stable current source was built which closely matches the input requirements of the lens. Details of the circuit are provided in appendix A.2.

Our use of the focus-tunable lenses comes with its challenges. Firstly, due to gravitational sag of the membranes and the fluid enclosed within them, the plane of the lenses needs to be horizontal at all times to prevent aberrations. For that reason, a section of our optical system depicted in figure 4.7 is mounted on a vertical breadboard, making the alignment less straightforward. Secondly, the soft nature of the membranes and the optical fluid makes the lenses more susceptible to thermal drifts and thermal lensing effects. This is especially problematic given the high power of the ODT1 beam passing through them (up to ≈ 30 W). Figure 4.17 shows the change in beam shape, focal position and trapping frequencies after exposing the lenses to high power (≈ 30 W) for an extended period of time. During a standard evaporation sequence, the lenses are subject to considerable powers for $t \approx 0.5$ s and so these short-term drifts can have a detrimental effects on the evaporation efficiency. Moreover, they can also negatively influence transport stability, necessitating a brief pre-cooling stage before commencing transport at lowered powers.

In addition to the beam quality deterioration and short term fluctuations, we have also recorded significant drifts in the focal position on the timescales of several hours which we believe to be due to thermal drifts of the actuator resistance and the refractive index of the optical fluid. To combat these undesirable properties of the TLs, we have designed an active stabilization system for future use of the TLs in loading and optical transport. This will be discussed in the next section.

4.5.1 Stabilization

Our stabilization system is based on reference [326] with added flexibility and the possibility of atomic transport. Unlike beam power stabilization, which is usually achieved with a simple photo-diode and a PID controller, positional stabilization is more challenging. For long-term drifts, it is sufficient to directly image the beam, fit an appropriate function to

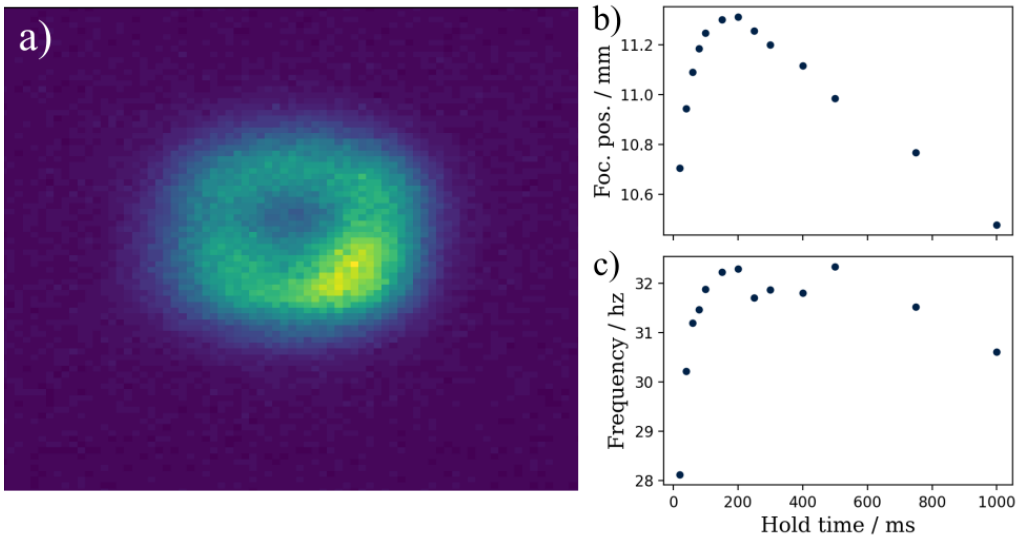


Figure 4.17: Thermal drifts of tunable lenses. a) Extreme case of beam quality deterioration far away from focus when the TL system was exposed to a 30 W beam for 1 s. We note that the beam quality closer to the focus isn't perturbed as severely but the properties of the trap are still affected non-negligibly. b)-c) Drifts in the focal position (b) and longitudinal trapping frequency (c) as a function of exposure time of the TL system to a high power beam (30 W).

the intensity profile, extract the beam's position and finally apply a suitable correction. For fast changes, though, image analysis is too slow.

In an alternative approach, one can use a quadrant photo-diode to keep track of the lateral position by comparing the changes in the quadrant intensity signals. In our case, the drift is in the focal position and so predominantly along the beam direction i.e. not lateral but longitudinal. Consequently, such drift can't be detected by simply projecting the beam onto a quadrant photodiode which is only sensitive to lateral motion.

An elegant solution to this problem presented in [326] uses a cylindrical lens rotated by 45° with respect to the axes of a quadrant photo-diode to transform changes in focal position to changes in ellipticity of the projected beam. Figure 4.18 shows the principle of operation of this scheme. In our setup, a small fraction of the trapping beam is picked off right after the last focusing lens (see figure 4.16). A collimating lens of focal length f_{col} is placed a distance $d = f_{\text{col}}$ behind the focal position of the beam–this focus mimics the position of the real focus in the MOT chamber. In this configuration, the collimating lens creates a collimated beam which is then incident on a cylindrical lens of focal length f_{cyl}. The cylindrical lens is rotated by 45° with respect to the vertical and focuses the beam along one of its principal axes. Finally, a quadrant photo-diode (QPD)[16] is placed a distance $d' = 2f_{\text{cyl}}$ behind the cylindrical lens and has its quadrant axes aligned with the natural axes of the lab/optical table.

When the trap focus is at a distance $d = f_{\text{col}}$ from the collimating lens, the input beam to the cylindrical lens is collimated. Consequently, the beam is focused along one axis a distance f_{cyl} away from the cylindrical lens and by the time it reaches the QPD,

[16] G6849 by Hamamatsu

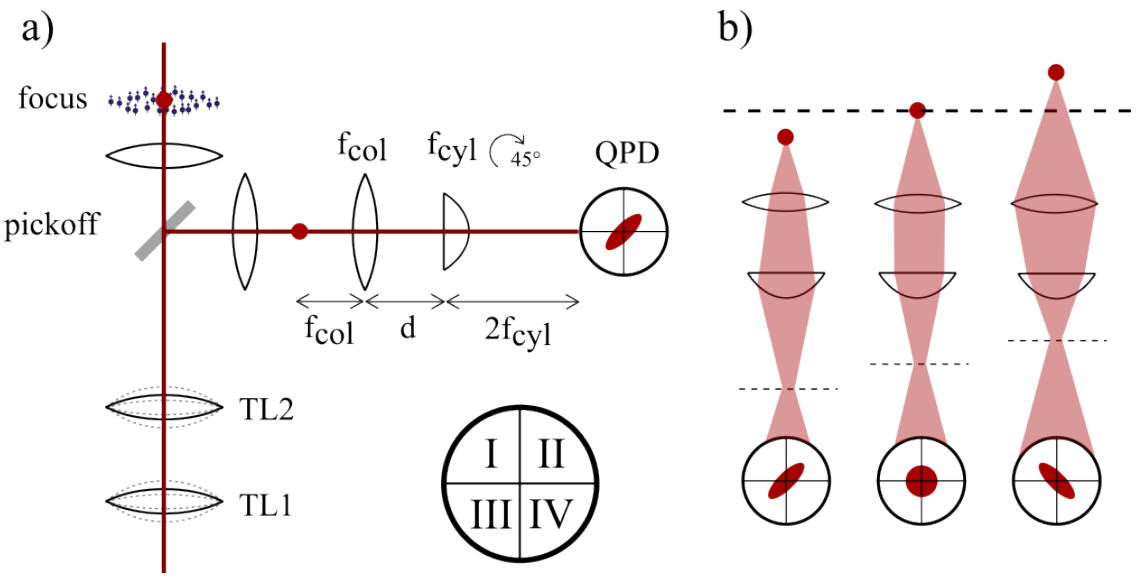


Figure 4.18: Quadrant photo-diode stabilization scheme. a) Optical setup for stabilizing the focal position. After the beam passes through the last, fixed lens and before it hits the atomic cloud, a small portion of it is diverted to the stabilization branch. Here, the beam is collimated using a lens with focal length f_{coll} and passed through a cylindrical lens (focal length f_{cyl}) with its principal axis tilted by 45° with respect to vertical direction. After propagating over a distance $2f_{\text{cyl}}$, the beam is projected on a quadrant photo diode (QPD). b) When the focus of the trapping beam is exactly f_{col} away from the collimating lens, the beam on the QPD is circular. However, any deviation from this position results in a change in ellipticity which can be detected through an appropriate combination of the four QPD signals.

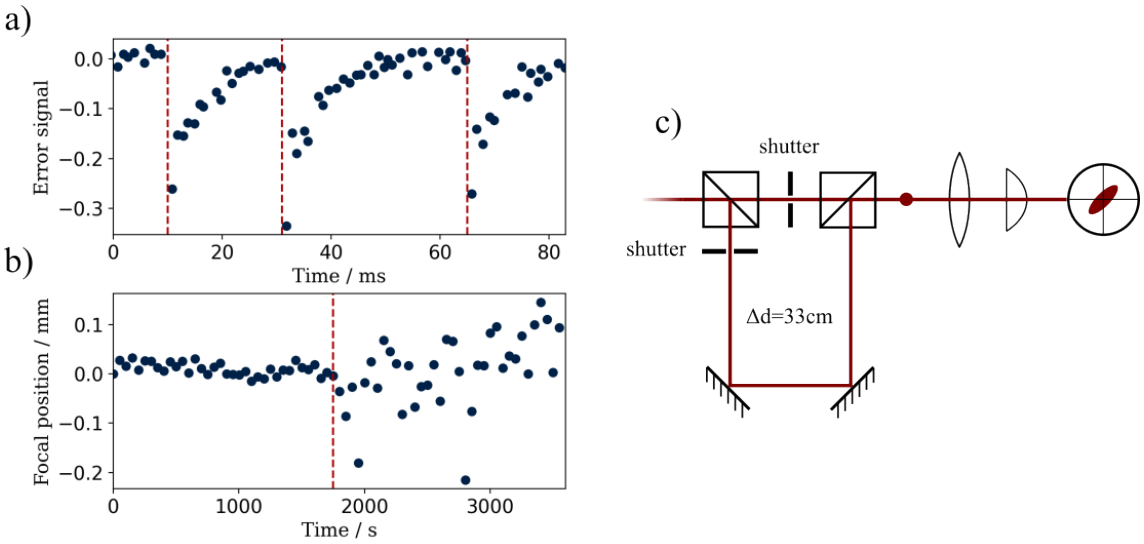


Figure 4.19: TL stabilization in action. (a) Response of the error signal given by equation 4.20 to sudden changes in lens voltage. The PID restores the signal back to its setpoint within $\approx 25\,\text{ms}$, showing both short response time and robust stabilization. Vertical lines denote a sudden change in control voltage. (b) Drift of the focal position with ($t < 1750\,\text{ms}$) and without ($t > 1750\,\text{ms}$) active stabilization. Data taken by Gavin Lamb. (c) Simple optical scheme that allows for activate stabilization prior to and after transport by selectively extending the optical path by the transport distance, $\Delta d = 33\,\text{cm}$.

it is exactly circular again. However, if the trap focus deviates from its 'ideal' position, the input to the cylindrical lens is uncollimated and so the focus of the beam after the cylindrical lens is no longer exactly half-way between it and the QPD. Consequently, the QPD now detects an elliptical beam with its ellipticity changing sign as the focus passes through its 'ideal' position.

This change in ellipticity can be directly converted into an electronic error signal by taking the following combination of the QPD voltages with their roman numeral designations defined in figure 4.18a

$$E = \frac{(V_{II} + V_{III}) - (V_I + V_{IV})}{V_I + V_{II} + V_{III} + V_{IV}}\,, \tag{4.20}$$

where the numerator is essentially difference in intensity between the two diagonals and the denominator serves as a normalisation to make the error signal insensitive to power fluctuations and limited to the range $(-1, 1)$.

We use an Arduino micro-controller[17] to read off the QPD voltages, combine them and perform a PID calculation based on a controllable setpoint. The output of the Arduino is then added on top of the voltage used to control the current in TL2 (which is mainly responsible for the focal position), creating a closed feedback loop. Figure 4.19a shows response of the error signal to sudden changes in the TL2 control current. Clearly, the error signal quickly stabilizes to its setpoint value on a time scale $\approx 25\,\text{ms}$ which is comparable to the settling time of the lens $\approx 12.5\,\text{ms}$[18]. Figure 4.19b shows the focal position over

[17] Arduino DUE
[18] EL-16-40-TC-VIS-5D data sheet by Optotune

a long period of time with the PID engaged for the first 1750 s. The onset of instability after this period points to a positive effect of the PID on the system. This preliminary data is promising and the scheme is now implemented in the main experiment to assess its performance with respect to loading and evaporation stability. We note that the scheme is insensitive to the source of the drift in focal position (i.e. electronic, thermal etc.) and as such its more universal than other techniques [327].

In principle, choosing any error signal value E as a set point for a feedback circuit gives us the ability to move the trap focus around and lock it in place. In practice, the slope of the error signal, i.e. its response to fluctuations in the focal position, and therefore its sensitivity decays when the trap focus is displaced far away from its ideal $E = 0$ position. Furthermore, the elliptical beam becomes bigger than the active region of the QPD. Both of these effects limit the suitability of this technique for long distance optical transport. For that reason, we plan to only use the active stabilization for the two endpoints of the transport path which are crucial for optimal loading and unloading of the atoms and perform the transport itself without any stabilization. To avoid needing separate QPDs for the two endpoints, we designed a two-path setup which will allow us to switch between the two regimes by simply switching between two optical paths with a path difference $\Delta d = d_{\text{transport}} \approx 33\,\text{cm}$ with the use of shutters. The schematic of this setup is shown in figure 4.19c and it will be implemented in the main experiment in the near future.

As an interesting conclusion to this section and to motivate our choice of optical elements, we briefly analyze the dependence of the error signal on the geometry of the setup. This will allow us to make informed decision on the focal length of the collimating and cylindrical lenses, f_{col} and f_{cyl}, as well as on their spacing d. Given an elliptical, Gaussian beam incident on the QPD, the error signal given by equation 4.20 can be expressed in integral form as

$$E = \frac{4(I_1 - I_2)}{P_{\text{tot}}}\ , \tag{4.21}$$

where P_{tot} is the total power in the beam and the integrals I_1 and I_2 are given by

$$\begin{aligned} I_1 &= \frac{P_{\text{tot}}}{2\pi\sigma_x\sigma_y}\int_0^\infty\int_0^x e^{-\frac{x^2}{2\sigma_x^2}} e^{-\frac{y^2}{2\sigma_y^2}}\,dxdy \\ I_2 &= \frac{P_{\text{tot}}}{2\pi\sigma_x\sigma_y}\int_0^\infty\int_0^y e^{-\frac{x^2}{2\sigma_x^2}} e^{-\frac{y^2}{2\sigma_y^2}}\,dxdy \end{aligned} \tag{4.22}$$

with the parameters σ_x and σ_y defining the ellipticity of the beam. The integrals, in general, don't have a simple analytic form. However, in the case of a nearly circular beam with $\sigma_x/\sigma_y = 1 + \varepsilon$ and $\varepsilon \ll 1$, the error signal can be shown to be $E \propto \varepsilon = \frac{1}{2}(\sigma_x/\sigma_y - \sigma_y/\sigma_x)$. If we denote the trap focal position as u, we are interested in quantifying the sensitivity S of the error signal to changes in u, i.e. $S = \frac{dE}{du}$. Working to first order in ε, it is easy to show that $S \propto \frac{d\sigma_x}{du}\frac{1}{\sigma_x} - \frac{d\sigma_y}{du}\frac{1}{\sigma_y}$.

The dependence of σ_x and σ_y on u can, in return, be derived by considering ray propagation and assuming thin lens approximation. Here, we only present the final result

for the sensitivity

$$S = \frac{dE}{du} = \frac{8}{\pi}\frac{f_{\text{cyl}}}{f_{\text{coll}}^2}\left(1 + \frac{2\delta}{f_{\text{col}}}\left(\frac{d}{f_{\text{col}}} - 1\right) + \mathcal{O}(\delta^2)\right) \tag{4.23}$$

where we defined $\delta = u - f_{\text{col}}$ as the deviation of the trap focus position from its ideal position $u = f_{\text{col}}$. Equation 4.23 suggests that highest sensitivity is achieved for large f_{cyl} and small f_{col}. Furthermore, away from the ideal position ($\delta \neq 0$), the sensitivity increases on one side of the focus and decreases on the other, depending on the spacing d of the two lenses. In practice, limitations on the available lenses and the difficulty of alignment define a set of appropriate focal lengths f_{col} and f_{cyl}. In our setup, we use $f_{\text{col}} = 50\,\text{mm}$ and $f_{\text{cyl}} = 75\,\text{mm}$. Full calculations of the error signal sensitivity are presented in appendix B.1.

As well as maximizing the error signal's sensitivity to focal position change, we also want to minimize its sensitivity to lateral displacements of the beam due to vibrations. To do that, we can try and investigates what happens to the error signal if the beam is displaced laterally by a vector (δ_x, δ_y) where $\delta_{x/y} \ll w$ with w the beam waist. By considering the symmetry of the problem, it is possible to derive that

$$E(\delta_x, \delta_y) = E_0 + \alpha\delta_x\delta_y + \beta(\delta_x^2 + \delta_y^2) \tag{4.24}$$

where E_0 is the unperturbed error signal and α, β are constants. Given that we have access to the four quadrant signals, we can construct two other quantities that represent the vertical and horizontal displacements as $U = (V_I + V_{II}) - (V_{III} + V_{IV}) \propto \delta_y$ and $R = (V_{II} + V_{IV}) - (V_I + V_{III}) \propto \delta_x$. To make the error signal robust against lateral displacement, we then simply subtract an appropriately weighted linear combination of $U \times R$ and $U^2 + L^2$ from the raw error signal.

For a circular beam (which arises in the ideal case of perfect alignment and trap focus at the desired location), it can be shown that the appropriate weights for the two terms are equal to $1/\sum V_i$ and 0 respectively. We apply this correction in our stabilization scheme together with an empirically chosen weight for the $U^2 + R^2$ term to account for imperfections in alignment. For detailed derivation of these relations see appendix B.2.

4.5.2 Transport

In parallel with designing and building the TL setup, we numerically analyzed the optimal transport parameters. When it comes to the transport ramp, i.e. $y_T(t)$ where y_T is the position of the focus along the beam, one needs to decided on its functional form as well as on the duration of the ramp. Ultimately, an optimal transport ramp minimizes the losses and heating along the way while also minimizing the transport time to reduce the experimental duty cycle and to prevent excessive heating of the TLs. Additionally, given our ability to perform efficient evaporative cooling in the MOT chamber as well as in the science cell, we also need to decide whether to transport at higher temperatures (making the heating due to the transport ramp less relevant) or at lower temperatures (reducing the ODT1 laser power needed for transport and thus protecting the TLs from overheating).

To assess the heating caused by the movement of the trap, we can first consider an analytically solvable model of non-interacting particles moving in a harmonic trap with time-dependent position. The 3D equations of motion of a single particle are decoupled i.e. the three directions behave as independent harmonically oscillating systems. If we take y as being the transport direction, then the y equation of motion reads as

$$\begin{aligned} \ddot{y} &= -\omega_y^2(y - y_T(t)) \iff \\ \ddot{y} + \omega_y^2\, y &= \omega_y^2\, y_T(t) \iff \\ \hat{L}y &= \omega_y^2\, y_T(t) \end{aligned} \tag{4.25}$$

with $y_T(t)$ the time-dependent trap position and $\hat{L} = \frac{d^2}{dt^2} + \omega_y^2$ a linear operator. The solution to equation 4.25 consists of the particular solution to $\hat{L}y = 0$ which is just simple harmonic motion with initial conditions $y(0) = y_0$ and $\dot{y}(0) = v_0$, and the complementary solution to $\hat{L}y = F(t) = \omega_y^2\, y_T(t)$. The complementary solution can be found using Green's functions [328] and combined with the particular solution to get

$$y(t) = y_0 \cos(\omega t) + \frac{v_0}{\omega} \sin(\omega t) + \omega \int_0^t \sin(\omega(t - t'))y_T(t')dt' \ . \tag{4.26}$$

Here, we dropped the subscript y from the trapping frequency for clarity. We can now try and calculate the increase in temperature due to the driving term $F(t) = \omega_y^2\, y_T(t)$ after the transport. To do this, we first assume that the cloud is initially in thermal equilibrium at temperature T such that the initial position and velocity follow a Gaussian distribution. We can then simply calculate the total energy of an 'average' particle long time after the transport as

$$\begin{aligned} \lim_{t\to\infty} \langle E_{\text{tot}}(t)\rangle &= \lim_{t\to\infty} \frac{1}{2}m\langle \dot{y}^2(t)\rangle + \frac{1}{2}m\omega^2\langle y^2(t)\rangle \\ &= k_B T + \lim_{t\to\infty} \frac{1}{2}m\omega^4 \left| \int_0^t e^{-i\omega t'} y_T(t')dt' \right|^2 \ , \end{aligned} \tag{4.27}$$

where the average is taken over the ensemble of particles (not time!) and we used $\langle y_0\rangle = \langle v_0\rangle = \langle y_0 v_0\rangle = 0$ and $\frac{1}{2}m\omega^2\langle y_0^2\rangle = \frac{1}{2}m\langle v_0^2\rangle = \frac{1}{2}k_B T$. Given the average initial energy in the y degrees of freedom is $k_B T$ by equipartition theorem, the second term on the second line of equation 4.27 represents the increase in temperature $k_B \Delta T$. To calculate this, we first note that the term is essential the square magnitude of the Fourier component of the ramp at frequency ω. If the ramp starts at $t = 0$ such that $y_t(t) = 0$ for $t < 0$ and if it ends after time t_R at position $y_T(t_R) = D$, we can write the extra term as

$$\begin{aligned} k_B \Delta T &= \lim_{t\to\infty} \frac{1}{2}m\omega^4 \left| \int_0^t e^{-i\omega t'} y_T(t')dt' \right|^2 \\ &= \frac{1}{2}m\omega^4 \left| \int_0^{t_R} e^{-i\omega t'} y_T(t')dt' + \lim_{t\to\infty} D \int_{t_R}^t e^{-i\omega t'} dt' \right|^2 \\ &= \frac{1}{2}m\omega^4 \left| \int_0^{t_R} e^{-i\omega t'} y_T(t')dt' + \frac{De^{-i\omega t_R}}{i\omega} \right|^2 \ , \end{aligned} \tag{4.28}$$

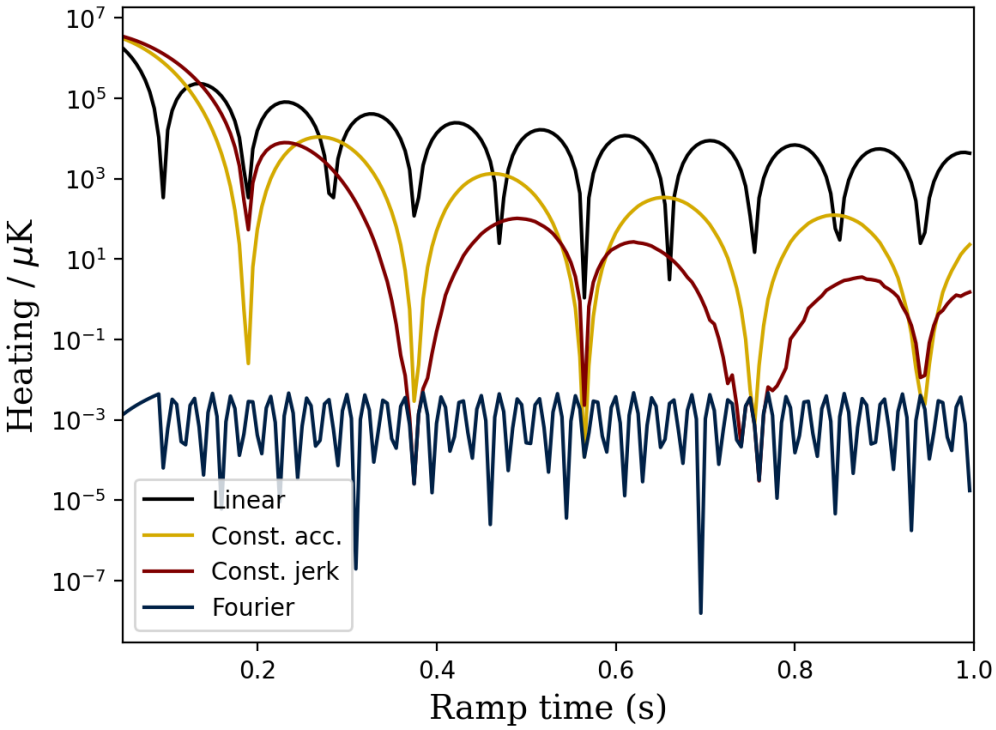


Figure 4.20: Heating of non-interacting particles in a transported harmonic trap. Clearly, the Fourier ramp outperforms the other ramps and results in negligible heating on the order or 1 nK. Constant Jerk ramp with $\dddot{y}_T = const.$ reaches acceptable levels of heating for longer ramp times as does the constant acceleration ramp. Linear ramp shows excessive heating across the whole range of feasible transport times. Notice that the constant acceleration and jerk ramps, in particular, show favourable transport times with close to no heating which correspond to anti-resonant modes of motion in the trap. In practice, particle collisions and experimental drifts make these 'sweet spots' less sweet and harder to maintain. The Fourier ramp seems to be a more robust solution from this point of view.

where the last line, we used the known Fourier transform of the Heaviside step function. Armed with this expression, we can calculate heating for different ramp types and different ramp speeds given the distance we need to cover $D = 33\,\text{cm}$ and assuming we transport in a $30 \times 30\,\mu\text{m}$ waist trap with total power $P = 12\,\text{W}$. Figure 4.20 shows the average heating as a function of ramp time for four different types of ramp–linear ($\dot{y}_T = const.$), constant acceleration ($\ddot{y}_T = const.$), constant jerk ($\dddot{y}_T = const.$) [329] and a filtered Fourier ramp which filters out the ω component from the Fourier transform of $y_T(t)$ [330]. The ramp forms are included in appendix C.1. Clearly the higher order ramps and in particular the filtered Fourier ramp outperform the other ramps in terms of heating and achievable speeds. Interestingly, all the ramps show periodically spaced 'sweet spots' where the heating is suppressed. However, as we will briefly see, these sweet spots vanish in real systems due to collisions and noise.

Despite giving important insight and pointing us towards optimal solutions, the simple harmonic model deviates from the real experiment in two major ways–it fails to take into account the anharmonicity of the trap and its finite depth which can result in losses should

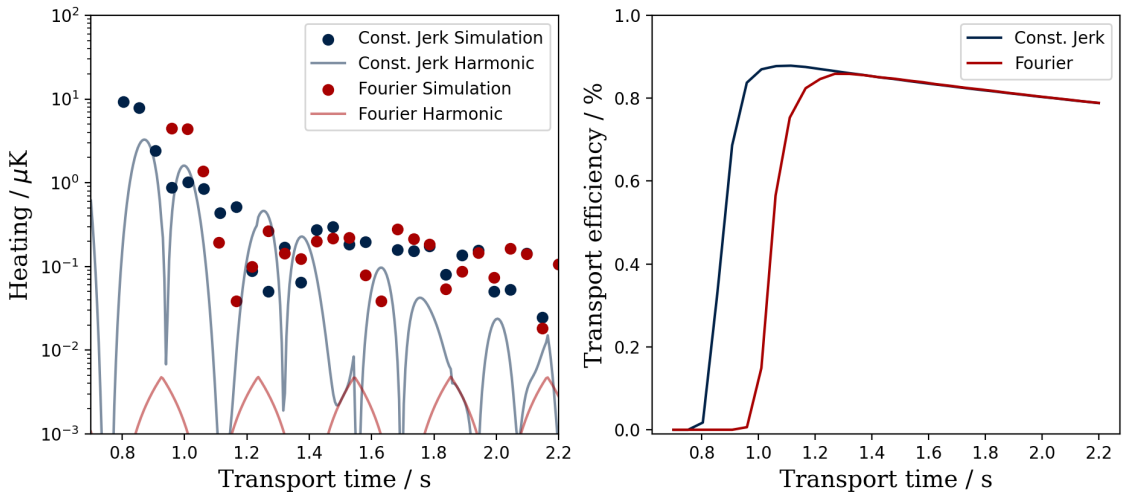


Figure 4.21: Atomic transport simulated with DSMC. (Left) The heating of the cloud as a function of the transport time for the two most promising ramps–the constant jerk and the filtered Fourier ramp. Full curves correspond to the analytic prediction that assumes perfect harmonic trapping and no collisions. DSMC simulations deviate from the ideal transport, indicating the importance of collisions and anharmonicity. (Right) Efficiency of the two transport ramps defined as the ratio of the transported and initial atom number. Constant jerk ramp allows for faster transport but both ramps gradually drop in efficiency as the one- and three-body loss processes kick in.

the ramp exceed a threshold speed, and it neglects particle collisions which redistribute energy in the cloud and, in general, dampen the harmonic motion. To fully account for these effects, a dynamic simulation was written in Python that utilizes the DSMC method [331], [332] to model particle collisions without the need for checking all the individual pairs of particles at each simulation step. The details of our implementation are presented in appendix C together with a benchmark test of evaporative cooling simulation methods.

Each simulation starts by initializing $N = 1 \times 10^4$ test particles at a particular temperature in a 12 W, single beam trap. The real particle number and temperature are set to 4.2×10^6 and 12 µK respectively which correspond to our standard experimental values. The particles are initialized from a Gaussian distribution and are left to equilibrate in the (slightly) non-harmonic trap for 100 ms. The focus of the beam is then translated according to the particular ramp. At the end of the ramp, the test particles are left to equilibrate for another 100 ms after which their temperature is measured based on the average kinetic energy.

Figure 4.21 shows plots of average heating and transport efficiency against ramp duration for the two superior ramps, i.e. the filtered Fourier and constant jerk ramps, and compares them with the analytic results for an infinitely deep harmonic trap. Both ramps deviate from the harmonic model and show comparable amounts of heating–contrary to the analytic result which predicts that the Fourier ramp should be almost two orders of magnitude better in this regard. Upon closer inspection, we still notice some form of periodic modulation, pointing to the existence of ideal 'sweet spots' in the transport time which minimize the heating. However, these features are much less pronounced than

in the case of non-interacting, harmonic transport. Clearly, particle collisions and trap anharmonicity play a significant role in the transport process. The transport efficiency (defined as the ratio of the particle number after and before transport) peaks at around 85% and then decays due to one- and three-body loss processes. Interestingly, the constant jerk ramp supports faster transport due to its lower peak acceleration (see appendix C.1) and performs equally well in terms of heating compared to the Fourier ramp. Our results suggest that transporting in $\approx 1.3\,\mathrm{s}$ using the constant jerk ramp should lead to sub $0.1\,\mu\mathrm{K}$ heating whilst maximizing the particle number and minimize the experimental sequence time.

To assess whether it is beneficial to transport at lower or higher temperatures, the constant jerk ramp with $t_{\mathrm{trans}} = 1.27\,\mathrm{s}$ and $P = 12\,\mathrm{W}$ was used with clouds initialized at different temperatures and atom numbers to mimic the evaporation process prior to transport. The exact initial values were chosen by assuming a constant evaporation efficiency of 3 as defined by equation 4.12 and choosing a range of initial atom numbers. Technically, this approach yields phase-space densities (PSDs) and not temperatures. We can use the expression for the peak PSD of a harmonically trapped gas, $\rho = N(\hbar\bar{\omega}/k_B T)^3$, together with the knowledge that the trap frequencies scale with the beam powers as $\bar{\omega} \propto \sqrt{P}$ and that the temperature of the gas in equilibrium is mostly defined by the trap depth such that $T \propto U_d \propto P$, to convert between PSD and initial beam power. Using reference experimental values of $N = 4.2 \times 10^6$, $T = 6.5\,\mu\mathrm{K}$ and $P = 4\,\mathrm{W}$, we can easily produce the other parameters for our choice of N. All that is left to do is to ramp the power in the beam to its transport value of $12\,\mathrm{W}$. If we assume this process is adiabatic, it is possible to show that $T \propto \bar{\omega} \propto \sqrt{P}$ and so we can quickly derive the temperatures at the beginning of transport for different N.

Armed with different initial conditions corresponding to different degrees of evaporation, we can run the simulation and measure the heating of the cloud after transport. However, heating itself is not the best metric because we are comparing clouds of different sizes. Instead, we can try and assess which of the transported atomic clouds puts us in the best position to produce as large BEC as possible. Once again, we will assume that our evaporation efficiency after transport is constant. The onset of condensation starts when the peak PSD reaches its critical value of $\rho_{\mathrm{c}} = \zeta(3/2)$ (see section 2.4.1). Using the expression for evaporation efficiency 4.12, we can derive

$$\frac{\rho_{\mathrm{c}}}{\rho_i} = \left(\frac{N_i}{N_{\mathrm{c}}}\right)^3 . \tag{4.29}$$

By setting $\rho_{\mathrm{c}} = \zeta(3/2)$, we can express the number of atoms at the onset of condensation as

$$N_{\mathrm{c}} = N_i \left(\frac{\rho_i}{\zeta(3/2)}\right)^{1/3} . \tag{4.30}$$

This number gives us a good metric for assessing which initial pre-transport conditions are optimal. All we have to do is calculate the number of atoms at the end of the transport, N_i, and the PSD of the cloud at that point, ρ_i.

Figure 4.22 shows a plot of N_{c} vs the initial (pre-transport) cloud temperature. The

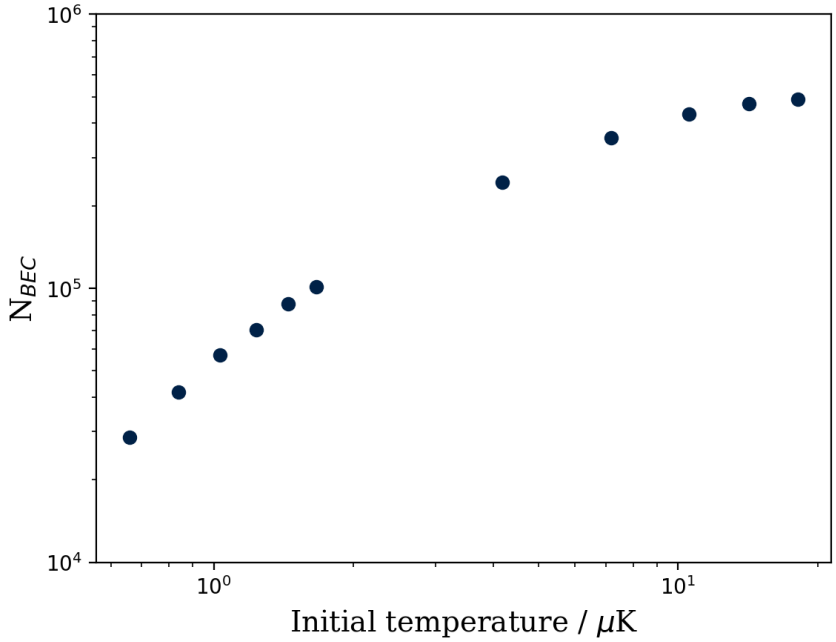
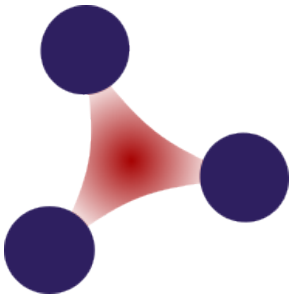


Figure 4.22: Benefits of transporting at a higher T. The predicted atom number at the onset of condensation, N_{BEC}, as a function of the atomic cloud temperature prior to transport performed with a fixed beam power $P = 12\,\mathrm{W}$ and ramp duration $t_{\mathrm{trans}} = 1.27\,\mathrm{s}$. Due to density-dependent losses and higher relative heating, it is beneficial to transport at as high temperature as possible without compromising the quality of the trap.

results suggest that it is beneficial to transport at as high temperature as possible to reduce the amount of relative heating and particle loss associated with ramping up the power to 12 W and thus increasing the density. Some of the losses at low temperatures could be mitigated by transporting in a weaker trap. However, this would have to be accompanied by an increase in transport time, prolonging the sequence. In practice, we are limited by the maximum power we can use during transport and by the performance of the tunable lenses. Higher powers give us access to bigger, hotter clouds but at the expense of compromising the shape of the trap and ramp. The above results also suggest that the gains in atom number eventually saturate, pointing to a compromise between trap quality and atom number at the onset of condensation in the $\approx 10\,\mu\mathrm{K}$ region. Using this temperature as the starting point, our most recent transport and evaporation attempts in the science cell lead to successful condensation with $\approx 300 \times 10^3$ atoms at its onset– consistent with the numerical results presented above and subject to further optimization in the near future.

To conclude, in this chapter, we described how we use a crossed-beam optical dipole trap to evaporatively cool ^{166}Er down to quantum degeneracy. Our optimized evaporation procedure that utilizes a dynamically adjustable trapping potential and detailed knowledge of the three-body loss landscape leads to the production of large BECs with $> 2.0 \times 10^5$ atoms. We have also demonstrated a functional tunable lens setup with active stabilization suitable for atomic transport to the science cell. The next two chapters describe two major scientific contributions made with our new Er machine.

5. Three-body loss in ^{166}Er



One of the main advantages of cold atom experiments is the ability to finely tune the interaction strength between atoms. This is achieved by exploiting the phenomenon of *Feshbach resonance* in which an external magnetic field can be used to change the magnitude and sign of the scattering length [154], [219], [333]. For a gas with purely contact Wan der Waals interactions such as the alkalis, this level of control allows for investigation of interesting regimes and phases. For example, at a resonance, the scattering length diverges and the gas enters a *unitary* regime which exhibits scale invariance and universality [83], [84], [334]. Moreover, negative scattering lengths which correspond to effective attraction between the atoms can lead to instabilities and collapse in case of bosons [85], [335] or Cooper-pairing and BEC-BCS crossover in case of fermions [87].

Systems exhibiting long-range interactions such as dipolar atoms or heteronuclear polar molecules [91], [336] still benefit from the versatility of Feshbach resonances but have an added layer of complexity. This is because the scattering length is no longer the only parameter that controls interatomic interactions. Instead, the contact interaction competes with the long-ranged, anisotropic dipole-dipole interaction (DDI), yielding a rich phase landscape that depends on the atom number, dimensionality, dipole orientation and the relative strength of the two interactions [117], [196], [212], [271]. The latter, usually denoted as $\varepsilon_{dd} = a_{dd}/a_s$ where $a_{dd} = m\mu_0\mu_a^2/12\pi\hbar^2$ is the dipolar length and a_s is the s-wave scattering length, can be tuned by changing a_s using a Feshbach resonance.

A prime example of an extensively studied and sought-after exotic dipolar phase is the *quantum droplet* [113], [114] in which the collapse of the condensate due to the dipolar attraction is balanced out by the beyond mean-field repulsion, leading to a stable, self-bound droplet of superfluid atoms. Under certain conditions, an array of droplets can form a *supersolid* [115], [271], [337], exhibiting global phase order (superfluid) as well as spatial order (solid). Theoretical studies have also predicted the existence of a plethora of spatially ordered phases in 2D, ranging from honeycomb to labyrinthine patterns [119], [121], [152]. Probing these exotic regimes requires direct control over ε_{dd} and consequently, it requires a precise knowledge of the Feshbach resonance landscape. Luckily, the anisotropy of the DDI and the Wan der Waals interactions in magnetic lanthanides allows for coupling between many scattering channels [155], [230], [338], resulting in a dense Feshbach spectrum with as

many as $1\mathrm{G}^{-1}$ resonances. This should be contrasted with alkalis where the low resonance densities ($0.1\mathrm{G}^{-1}$ to $0.01\mathrm{G}^{-1}$ [154], [227], [339], [340]) mean that higher magnetic field strengths are often required.

Apart from ground state engineering, tuning the scattering length serves another important purpose. The rate of elastic two-body collisions is directly proportional to the scattering cross section and hence to the square of the scattering length. These collisions are responsible for the rethermalization of the gas and, crucially, for evaporative processes in which fast particles are scattered out of the trap, carrying away excess energy and cooling the rest of the gas (see section 4.3). Rather intuitively, the rate of n-body collisions ($n > 2$) also increases with the scattering length. The higher the number of particles involved in the collision, the less likely it is to occur, and so naturally the next significant collision process is the three-body one with its rate determined by the magnetic field- and temperature-dependent three-body coefficient $L_3(B, T)$. Vitally, in a three-body collision, the conservation of energy and momentum no longer prohibits the formation of bound states. Consequently, some of the three-body collisions will result in the formation of a dimer and a free particle. The binding energy of the dimer ($E_{\mathrm{bind}} \approx \hbar^2/ma_s^2 \sim k_B \times 100\mu K$ [203]) is turned into kinetic energy of the colliding particles, allowing them to escape the trap. This process is known as three-body recombination and it is one of the main sources of detrimental atom loss in ultracold gases [78], [341].

For dense enough gases (usually close to degeneracy), three-body loss throttles the efficiency of evaporative cooling and determines the maximum achievable atom number. So far, attainable atom numbers have been the largest limiting factor for the study of the many interesting phases in dipolar gases. Moreover, in the droplet and similar regimes the atomic densities are enhanced, greatly limiting the lifetime and observable dynamics of the system. The precise knowledge of the loss landscape as a function of the magnetic field strength is therefore of paramount importance.

Previous studies of ^{166}Er below 4 G reported wide Feshbach resonances at 0.02 G, 3.04 G and 4.028 G [153]. In this chapter, we present our measurements of the three-body loss rate in the range 0–4 G, revealing six new narrow features at 498 mG, 861 mG, 1574 mG, 1702 mG, 2102 mG and 2493 mG. We describe the observed temperature and laser-intensity dependence of these resonances and compare it to existing theory [342]–[344]. Furthermore, we discuss the optimal field configuration for studies of gases in the highly dipolar regime.

The chapter is organized as follows. First, we describe our method for measuring the three-body loss coefficient L_3, covering both the experimental sequence and our data analysis. We then present the results of our measurements, discussing the various properties of the newly-identified resonances, comparing them with existing theory and using our knowledge to inform the reader on optimal field configurations for future studies. We conclude the chapter by outlining a new theoretical model of the three-body loss process in trapped ultracold gases that accounts for secondary collision effects and extra heating observed in the experiment.

5.1 Measuring three-body loss

In the following section, we will describe the experimental procedure for performing the three-body loss measurement in ^{166}Er. First, we focus on the experimental sequence itself, including some technical details regarding the trapping and the magnetic fields. We will then outline our fitting routine and briefly discuss its validity in light of the model presented in section 5.3.

5.1.1 The experiment

A starting point of any loss measurement is a time series of the atom number $N(t)$ and the accompanying temperature of the atomic cloud $T(t)$ taken over an extended period of time over which the atom number decays considerably. To this end, we prepare an atomic sample by loading the atoms from a compressed MOT (cMOT) stage into a crossed beam optical dipole trap (ODT)–both of these stages are described in detail in chapters 3 and 4. We then proceed with a forced evaporation sequence which is deliberately interrupted at a specific time to prepare a sample of a desired temperature T and a corresponding atom number N. To prevent further evaporation and the associated particle number and temperature change, we increase the intensity of the ODT beam(s) over 100 ms, effectively deepening the trap and increasing the temperature due to adiabatic compression. Note that, by design, η still increases in the process. Finally, the magnetic field strength is quenched to its final value at which we want to probe the loss coefficient $L_3(B, T)$.

The large coils around our experiment (see section 3.1.2) allow us to control the magnitude and the direction of the magnetic field[1] as well as to compensate for the magnetic field of the Earth. This is particularly useful when dealing with dipolar species such as Er because many of the physical processes depend on the relative polarization of the atoms and the trapping light or the trapping axes (see section 4.1.1 and [91], [117], [271]). In the specific case of three-body losses, we used the flexibility of our setup to try and measure any angular dependence of L_3. The results of this investigation are discussed in section 5.2. Where relevant, the rotation of the dipoles was performed after evaporation but before trap ramp up. Additionally, the change in atomic polarizability (see section 4.1.1) due to field rotation was accounted for by appropriately changing the laser beam power to keep the trapping frequencies fixed. The field strength was quenched last, as described above. It is worth noting that whenever fields above 3 G were probed, the evaporation was done at 3.8 G, whereas for fields below 3 G it was done at 1.4 G. This was to prevent sweeping through the wide Feshbach resonance at 3 G [153] during the field quench.

After preparing the sample at the desired B and T, the atoms were held in the trap for a variable time t before being released and absorption-imaged. The particle number $N(t)$ was extracted from the optical density and the temperature $T(t)$ from the time-of-flight size of the cloud (see section 3.1.3 for more details on the procedure). Typical $N(t)$ and $T(t)$ series are shown in figure 5.1. Such series are the starting point for our fitting

[1] All fields were calibrated using a Stern-Gerlach experiment and an RF source as described in section 3.1.2

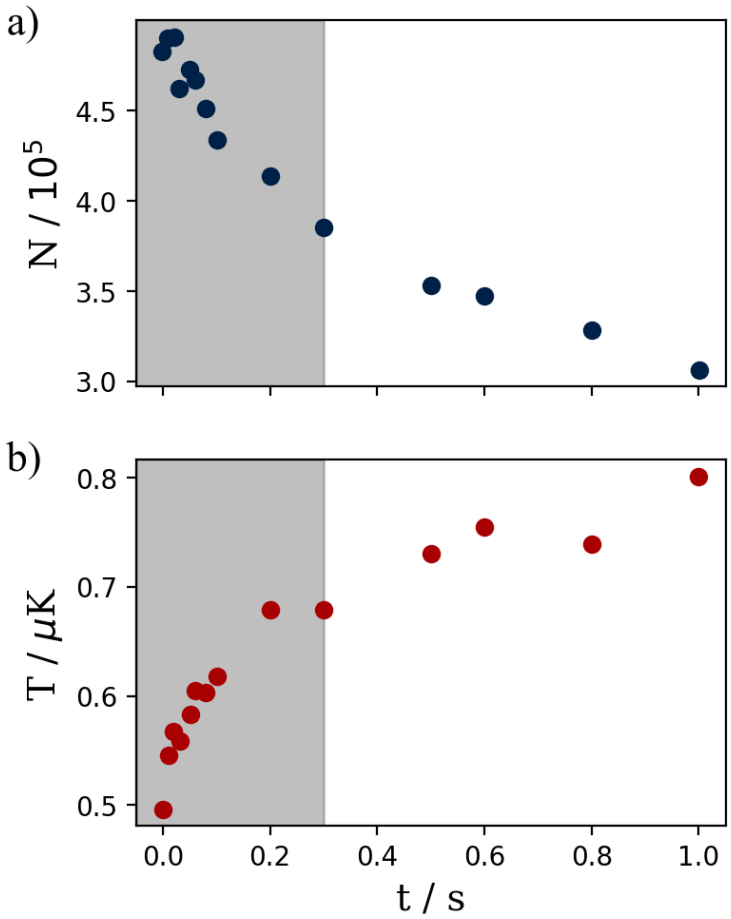


Figure 5.1: Typical three-body loss dataset. a) The particle number and b) the cloud temperature as a function of hold time. These quantities are fitted to equations 5.7 to obtain the three-body loss coefficient L_3. To minimize the effect of changing temperature on the fitted value, we decided to use only those data points for which the measured temperature was within 40% of the initial temperature. This is shown as the shaded region.

procedure.

5.1.2 Fitting procedure

A rigorous derivation of the particle number and temperature time evolution is given below in section 5.3. Here we only note that for a general one- and three-body loss process, the gas density evolves as

$$\dot{n}(\mathbf{r}) = -\frac{n(\mathbf{r})}{\tau} - L_3 n^3(\mathbf{r}) \tag{5.1}$$

with τ the one-body lifetime and L_3 the three-body loss coefficient (which we are trying to measure). For a thermal gas in a harmonic trap, the particle number then evolves as

$$\dot{N} = -\frac{N}{\tau} - L_3 \bar{\omega}^6 \left(\frac{\beta m}{2\sqrt{3}\pi}\right)^3 N^3 = -\frac{N}{\tau} - \gamma(T, \vec{\omega}) \frac{N^3}{T^3} \tag{5.2}$$

where $\beta = 1/k_B T$ and $\bar{\omega} = (\omega_x \omega_y \omega_z)^{1/3}$.

In a three-body recombination process, two of the three particles form a bound dimer. The binding energy is released as excess kinetic energy of the particles participating in the collision, ejecting them from the trap and resulting in particle loss. The simple loss model described by equation 5.1 captures this process well. However, it fails to account for secondary collisions of the ejected particles with the rest of the atomic cloud. These will inevitably lead to more losses and potentially heating. We can estimate the contribution of this process by considering the rate of collisions between a fast particle with velocity v and a cloud of average density $\langle n \rangle$. If the scattering cross section for the process is σ, the rate of collisions is $\langle n \rangle \sigma v$. The average time the 'projectile' particle spends in the cloud is simply $\langle r \rangle / v$ where $\langle r \rangle$ is the average size of the cloud. If we assume that each collision leads to further particle loss, we can write

$$\dot{N}_{3B} = -\gamma(T, \vec{\omega}) \frac{N^3}{T^3} \left(1 + \frac{1}{3} \langle n \rangle \langle r \rangle (\sigma + \tilde{\sigma}) \right) \tag{5.3}$$

where the factor of $\frac{1}{3}$ accounts for the fact that each three-body event happens at a rate which is $\frac{1}{3}$ lower than the corresponding original particle loss rate and where $\tilde{\sigma}$ is used to denote the collision cross section between a Feshbach dimer and a normal gas particle. Calculating the averaged quantities using the harmonic approximation and accounting for any numeric factors (geometric or other) that we have neglected yields

$$\dot{N} = -\frac{N}{\tau} - \gamma(T, \vec{\omega}) \frac{N^3}{T^3} \left(1 + G \frac{m \bar{\omega}^2 N}{k_B T} (\sigma + \tilde{\sigma}) \right) . \tag{5.4}$$

Here G is a numerical factor of $\sim \mathcal{O}(1)$ which is more rigorously estimated in section 5.3.4.

As can be seen in figure 5.1, the loss process also leads to considerable heating of the cloud. In the simple model, this can be understood by realizing that due to the cubic scaling of the loss rate with density, i.e. $\dot{n}_{3B} \propto n^3$, it is preferentially particles from the dense regions at the bottom of the trap that are lost. These particles carry less energy than the average $3k_BT$ prescribed by equipartition. Consequently, their removal leads to 'anti-evaporation' and an overall increase in temperature. A quick calculation outlined in section 5.3 gives the heating rate as

$$\dot{T} = \frac{1}{3} \gamma(T, \vec{\omega}) \frac{N^2}{T^2} . \tag{5.5}$$

Particle loss due to secondary collisions will naturally lead to a similar 'anti-evaporation' effect. Additionally, some of the collision energy can get deposited into the atomic cloud, further increasing the temperature. Taking both of these effects into account results in the following adjusted equation for the heating rate (see section 5.3.4)

$$\dot{T} = \frac{1}{3} \gamma(T, \vec{\omega}) \frac{N^2}{T^2} \left(1 + \frac{m \bar{\omega}^2}{k_B} (\sigma + \tilde{\sigma}) \left(G' \frac{N}{T} + G'' \frac{N}{T^2} \right) \right) \tag{5.6}$$

with G' and G'' yet another set of numerical factors which are more rigorously derived at the end of this chapter.

Therefore, when it comes to fitting the experimental data with a model, we have several options. Equations 5.4 and 5.6 give the time evolution of both the particle number and the temperature as

$$\begin{aligned}\dot{N} &= -\frac{N}{\tau} - \gamma(\omega)\frac{N^3}{T^3}\left(1 + \Theta\frac{N}{T}\right) \\ \dot{T} &= \gamma(\omega)\frac{N^2}{3T^2}\left(1 + \Theta A\frac{N}{T} + \Theta B\frac{N}{T^2}\right)\end{aligned} \tag{5.7}$$

where we combined common quantities into a fitting parameter Θ and we introduced two new parameters A and B. This is a system of two coupled differential equations that need to be solved concurrently and, in general, numerically. With each additional term, the equations grow in complexity and in the number of fitting parameters. When deciding which form of the equations to use or, in other words, which terms to omit, we need to consider the experimental regime and the size of the dataset because each term dropped makes the fitting more robust and removes redundancy in the parameter space at the cost of potentially losing physical accuracy. Additionally, we also have the option of solving only for $N(t)$ using the experimentally measured temperatures (suitably extrapolated between data points if necessary).

Ultimately, two factors affected our decision. First, the primary aim of our investigation was measuring the three-body loss coefficient L_3, making the fitting parameter $\gamma(\omega)$ the most important one. Secondly, we realized that $L_3(T)$ is an unknown function of temperature (see section 5.2.2 for full discussion) and so the solutions to equations 5.7 are only approximately valid for short time evolutions for which T doesn't change significantly. Furthermore, any change in L_3 due to a change in T would non-trivially affect all the fitting parameters (which assume that L_3 is constant), making the extracted values inaccurate and harder to interpret. To reduce the effects of this temperature dependence, for each decay series we used only those data points for which the measured temperature was within 40% of the initial temperature (shaded region in figure 5.1). This increased the validity of the fitted L_3 values at the cost of reducing the size of the dataset, making multi-parameter models ill-defined. Consequently, for our main measurement presented in section 5.2, we decided to use the simplest version of the loss model given by equation 5.2 which only has one fitting parameter γ and which doesn't take into account the secondary collision effects. Since the main goal was to characterize the particle decay and not the heating, we also decided to use the measured temperatures instead of solving for $T(t)$. This allowed us to extract γ with the minimum number of assumptions and the most robust fitting procedure.

To solve the equation, τ was determined to be 33.2 s based on an exponential fit to a long timescale decay measurement of a low density sample for which the three-body losses are negligible. Furthermore, the trapping frequencies (necessary to extract L_3 from γ) were measured by exciting center-of-mass oscillations along the three trapping directions– more details on the experimental procedure are in section 4.1.3. We note that the scaling of $L_3 \propto \bar{\omega}^{-6}$ makes the uncertainty in the trapping frequencies the dominant source of error in the final L_3 values.

Irrespective of the model used, the general fitting procedure minimized the χ^2 function defined as

$$\chi^2 = \sum_{D=N,T} \sum_i \frac{(D_i^{sol} - D_i^{meas})^2}{\sigma_{D,i}^2}, \tag{5.8}$$

where D corresponds to either N or T or both, D_i^{meas} denotes the measured quantity and D_i^{sol} denotes the corresponding numerical solution at time t_i. For the case of using the measured temperatures instead of solving for $T(t)$, we have $\chi^2 = \chi_N^2$ i.e. $D = N$, whereas for the case of solving the two equations concurrently, we have $\chi^2 = \chi_N^2 + \chi_T^2$ i.e. $D = N,\ T$. This places the N and T datasets on equal footing which is justified by the fact that they are both the output of the same model. The uncertainties $\sigma_{D,i}$ were both determined to be $\sigma_N/N \approx \sigma_T/T \approx 3\%$ from repeated measurements of the corresponding quantities. The upper (lower) error in the fitting parameters was determined by increasing (decreasing) the parameter to a point where χ^2 increased by 1 whilst optimizing the other remaining parameters.

5.2 Results

In this section, we present our results for the measurement of L_3 in the 0–4 G range. We identify three already reported resonances as well as six new features. We discuss the temperature dependence of these features and quantify the peak width and position as a function of temperature. Finally, we report on the intensity dependence of these resonances, pointing to a light shift in the two channels forming the resonance.

5.2.1 The loss spectrum

Figure 5.2 shows the measured L_3 coefficient as a function of the magnetic field strength B for three different initial temperatures $0.5\mu K$, $1.5\mu K$ and $4\mu K$ corresponding to blue, pink and yellow data points respectively. The L_3 coefficient was extracted from particle decay series performed at a specific magnetic field strength B and cloud temperature T using the procedure outlined in section 5.1.2.

We observe regions of enhanced loss in the vicinity of the previously reported Feshbach resonances at 0 G, 3 G and 4 G [153]. The three-body loss coefficient L_3 increases by more than two orders of magnitude in these regions relative to its minimal background value of $L_3^{(\mathrm{bg})} \approx 0.5 \times 10^{-41}\,\mathrm{m}^6/\mathrm{s}$. We note that this background value is in excellent agreement with values reported in literature [114] but that it is also subject to potential systematic offset due to uncertainty in $\bar{\omega}$.

In addition, we identify six new narrow features in the 0–3 G region at 498 mG, 861 mG, 1574 mG, 1702 mG, 2102 mG and 2493 mG. Upon closer inspection, these features show a temperature dependence of the peak width and position, shifting to the right and broadening as the temperature increases. Furthermore, the peak value also responds to the change in temperature. We discuss our observations in more detail in the following section.

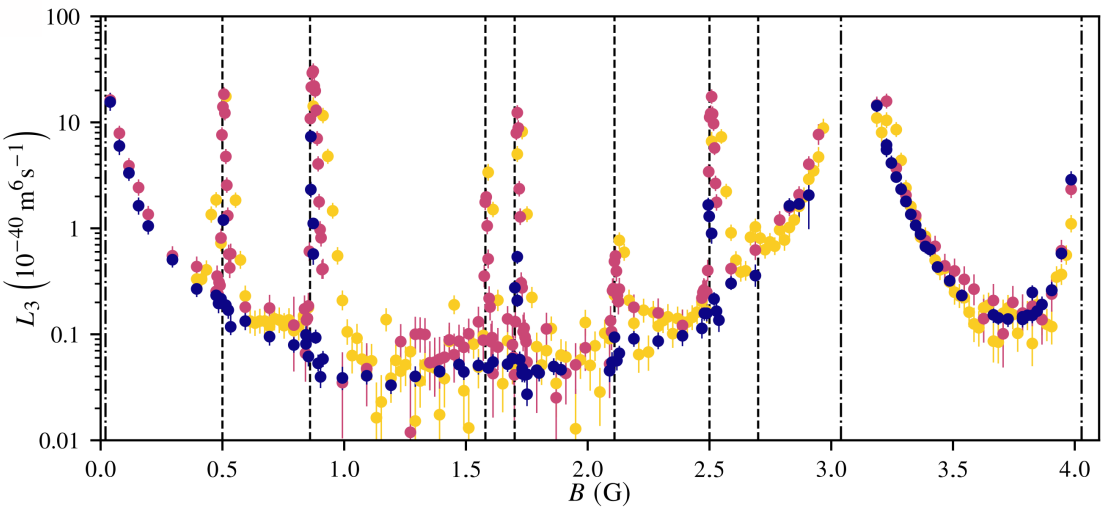


Figure 5.2: Three-body loss in ^{166}Er. Extracted three-body loss coefficients L_3 and their standard errors as a function of the magnetic field strength B. L_3 was measured at three initial cloud temperatures of $0.5\mu K$, $1.5\mu K$ and $4\mu K$ corresponding to blue, pink and yellow data points respectively. Six new narrow features were identified (dashed lines) on top of the previously described wide resonances (dash-dotted lines). As the temperature increases, the new features shift to higher B values and their widths increase. We quantify this in section 5.2.2.

5.2.2 Temperature dependence and light shift

To probe the temperature dependence of these narrow resonances, we focused on the feature at 0.9G. Once again, we measured the L_3 coefficient for several cloud temperatures using the same procedure as described above. The peaks were fitted with a skewed Gaussian curve of the form

$$L_3(B) = Ae^{\frac{-(B-\tilde{B})^2}{2\sigma^2}} \left(1 + erf\left(\frac{\alpha(B-\tilde{B})}{\sqrt{2}\sigma}\right)\right) + C, \tag{5.9}$$

where $\tilde{B}$, σ, α, A and C are fitting parameters. From the fits, we extracted the peak position and the width which was taken as twice the variance. Sample curves as well as the peak width and position as a function of temperature are shown in figure 5.3 (a, b, c). We note that the quoted temperatures are calculated as the average temperature of the corresponding decay series at a particular magnetic field strength B to reflect the fact that the cloud heated up.

Our data shows a linear increase in the peak width and position with temperature as well as a decay of the peak height subject to experimental uncertainty. The slope of the width and position trend lines are 6.2 mG/µK and 2.0 mG/µK respectively. Additionally, we realised that the peak position depended not only on temperature but also on the trap used for the measurement. The general mechanism behind a Feshbach resonance relies on matching the energy of the incoming scattering channel with the energy of a bound state in the outgoing channel by changing the magnetic field strength (see section 2.3.3). This is only possible if the two channels have a differential magnetic moment. However, there

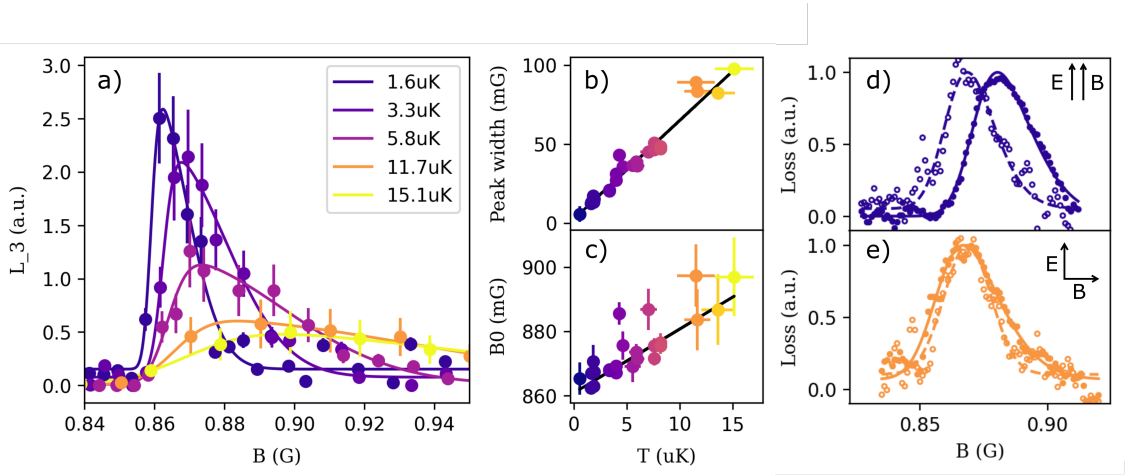


Figure 5.3: Temperature and intensity dependence of the three-body loss feature at 0.9 G. a) Sample features measured for clouds with several different initial temperatures. The features shift to higher B fields and get wider as the temperature increases. The data was fitted with equation 5.9. b-c) Width and peak position of the loss feature as a function of temperature. The data is well fitted by a linear trend which was used to extrapolate and find the peak position at $T = 0\,\mathrm{K}$ (see table 5.1). The slopes of the two lines are 6.2 mG/µK and 2.0 mG/µK respectively. d-e) Shift of the loss feature due to light intensity for two dipole orientations. Full (empty) circles represent a single beam trap at 8 W (1.9 W). Top (bottom) plot d (e) is for dipoles oriented along (perpendicular to) the trapping light polarization. There is a clear light shift for dipoles oriented along the trapping field. Note that data in a-c) has already been compensated for this light shift as different temperature sets corresponded to different intensity traps.

is another way of changing the energy of a state–namely via the AC stark shift, or Light shift (see section 4.1). The existence of a differential light shift between the two scattering channels should, in principle, result in a light intensity-dependent shift of the resonance position.

To test this, we performed a series of loss measurements in which a thermal cloud was prepared at 2 µK in a single-beam ODT at two different powers. By measuring the relative atom loss at different B fields, we were able to observe a shift in the loss feature position based on the beam power. Moreover, we performed the same measurement for two different atomic dipole orientations with respect to the trapping light polarization. The data for 0° ($E \parallel B$) and 90° ($E \perp B$) in the vicinity of 0.9 G is shown in figure 5.3d and e respectively. The measured light shift for the two polarizations is different, which is consistent with the fact that the atomic polarizability of magnetic atoms depends, in general, on the relative orientation of the magnetic field and the polarization of the trapping light (see section 4.1.1).

We extracted the constant of proportionality between the light intensity and the shift of the peak for all six features. Furthermore, we compensated for this light shift in our original dataset for the temperature dependence shown in figure 5.3a. When applying the correction, one needs to take into account the fact that atoms move around in the trap and experience an average light intensity rather than the maximum value. For a harmonic potential $U(r) = \alpha(I(0) - I(r))$ where $I(0)$ is the peak intensity at the bottom of the trap and α is a constant of proportionality, we can calculate the average $\langle I \rangle = I(0) - \frac{3}{2}\frac{k_B T}{\alpha}$ and the variance $\langle I^2 \rangle - \langle I \rangle^2 = \frac{3}{2}\left(\frac{k_B T}{\alpha}\right)^2$. We can then use these values to correct the peak position and width respectively.

5.2.3 Comparison with theory

Although we mainly looked at the new resonances from the loss perspective, they can also reveal some information about the states involved in the scattering process. We devote the rest of this chapter to a brief discussion of our measurements in the context of existing theoretical models. Following on from references [342]–[344], in the 'resonant trimer' model, three free particles in an entrance channel can temporarily form a bound trimer at a rate $\Gamma(E_3)$ that scales with a certain power of the collision energy E_3 [345]. This trimer is short lived and decays at a rate Γ_{br} into a dimer and an atom. The associated loss coefficient can then be written in terms of the trimer collision energy E_3 and the magnetic field strength B as

$$L_3(E_3, B) = \frac{48\pi^2\hbar^5}{\mu_3^3 E_3^2} \frac{(2\lambda+1)\Gamma(E_3)\Gamma_{\mathrm{br}}}{\left(E_3 - \mu(B - B_0)\right)^2 + \Gamma_{\mathrm{tot}}^2(E_3)/4}, \tag{5.10}$$

where $\Gamma(E_3) = A_\lambda E_3^{\lambda+2}$, Γ_{br}, μ and B_0 are the entrance channel energy width, the trimer decay rate, the relative magnetic moment of the trimer and the entrance channel, and the position of the resonance at $T = 0K$, respectively. Furthermore, $\mu_3 = m/\sqrt{3}$ is the collisional reduced mass, $\Gamma_{\mathrm{tot}} = \Gamma(E_3) + \Gamma_{\mathrm{br}}$ and λ is a non-negative integer associated with the relative orbital angular momentum of the collision. The two least repulsive centrifugal

barriers (and therefore the most likely collisional channels) correspond to values $\lambda = 0$ and $\lambda = 2$ [342]. At a particular temperature $T > T_c$, the collision energy E_3 (from now referred to as E for clarity) is sampled from the Boltzmann distribution. And so the measured L_3 is an average value

$$L_3(T, B) = \frac{1}{2(k_B T)^3} \int_0^\infty E^2 L_3(E, B) e^{-E/k_B T} dE \tag{5.11}$$

This thermal sampling is the origin of the temperature dependence of the loss features. Equation 5.11 has a fairly complicated integral form and, in general, needs to be solved numerically but one can still derive exact expressions for the peak width, position and height scaling in particular regimes.

For low T such that $k_B T \ll \Gamma_{\rm br}$, the exponential factor suppresses anything but very low energies. In that case, any energy-dependent terms in the denominator can be neglected and the integral turns into a standard gamma function. The three-body coefficient is then proportional to

$$L_3(B, T) \propto \frac{(k_B T)^\lambda}{\mu^2 (B - B_0)^2 + (\Gamma_{\rm br}/2)^2} \ , \tag{5.12}$$

i.e. a Lorentzian shape with width determined by $\frac{\Gamma_{\rm br}}{\mu}$, maximum at B_0 and peak height scaling with T^λ. This means that the feature should vanish at $T = 0\,\mathrm{K}$ for any resonance with $\lambda > 0$. We performed a series of decay measurements with an almost pure BEC in the B field regions where considerable loss was expected but detected no loss features, suggesting that the newly-found resonances involve scattering with $\lambda > 0$. However, we note that the feature could have been narrower than our field resolution.

In the intermediate temperature regime where $k_B T \gg \Gamma_{\rm br} \gg A(k_B T)^{\lambda+2}$, the Lorentzian described by the denominator is sharply peaked at $E = \mu(B - B_0)$ compared to the function in the numerator. In that case, integrating over energies gives $L_3(B, T) \propto (k_B T)^{\lambda-1} \theta^{\lambda+2} e^{-\theta}$, where $\theta = \frac{\mu}{k_B T}(B - B_0)$. This function has a maximum at $\theta_{\rm max} = \frac{\mu}{k_B T}(B_{\rm max} - B_0) = \lambda + 2$ and so clearly the maximum value scales as $L_3^{max} \propto T^{\lambda-1}$ and the peak position shifts with temperature according to $\frac{dB_{\rm max}}{dT} = \frac{k_B}{\mu}(\lambda + 2)$. Furthermore, from twice the variance we can recover the temperature dependence of the peak width $\Delta = \frac{2k_B T}{\mu}\sqrt{\lambda + 3}$ and accordingly $\frac{d\Delta}{dT}$. This regime is consistent with our data in the sense that both the peak position and width show a linear trend with temperature. However, there are a few discrepancies. Firstly, the peak height seems to reduce with temperature which is only consistent with $\lambda = 0$. However, the lack of a loss feature in the degenerate regime suggests otherwise. Secondly, taking the ratio of $\frac{d\Delta}{dT}$ to $\frac{dB_{\rm max}}{dT}$ should give $\frac{2\sqrt{\lambda+3}}{\lambda+2}$, providing a novel way of measuring λ without having to know other parameters of the collision. This is a monotonically decreasing function with a maximum value of $\sqrt{3} \approx 1.73$ at $\lambda = 0$. Our data predicts this ratio to be 3.1(5), inconsistent with any allowed values of λ. This puzzling discrepancy between the experiment and the theory will be the subject of future studies.

	B_0	$\frac{dB_{\max}}{dT}$	$\frac{d\Delta}{dT}$	$\frac{dB_{\max}}{dI}\|_{\theta=0}$	$\frac{dB_{\max}}{dI}\|_{\theta=\pi/2}$
	mG	$\mathrm{mG}/\mu K$	$\mathrm{mG}/\mu K$	$\mathrm{G}\mu m^2/W$	$\mathrm{G}\mu m^2/W$
1	498(1)	3.0(5)	8.6(2.2)	1.5(3)	-0.5(2)
2	860.8(1.1)	2.0(3)	6.2(3)	1.7(5)	-0.2(2)
3	1574(2)	3.9(9)	4.6(1.5)	0.7(2)	0.1(3)
4	1702(2)	3.7(8)	5.3(1.0)	1.2(6)	-0.1(3)
5	2102(3)	5.5(7)	7.8(8)	2.6(9)	0.1(9)
6	2493(4)	5.4(1.6)	6.1(5)	1.9(3)	0.0(4)

Table 5.1: Newly detected resonant features and their properties. The position of the resonance B_0 at $T = 0K$ and the rate of change of the peaks' position $dB_{\max}/dT$ and width $d\Delta/dT$ with temperature was obtained by linear extrapolation from the finite-temperature datasets. The rate of change of $B_{\max}$ due to the differential light shift $dB_{\max}/dI$ is also tabulated, for dipoles aligned along ($\theta = 0$) and perpendicular ($\theta = \pi/2$) to the trapping field polarization.

5.2.4 Conclusion

Table 5.1 shows our data for the newly detected resonances, including (extrapolated) peak position at $T = 0\,\mathrm{K}$, shift of peak width and position with temperature and the rate of change of peak position with light intensity for the two orientations. This newly gained knowledge of the loss landscape helped us establish the most optimal magnetic field for evaporative cooling which we believe to be at around 1.4G. Here, the three-body loss coefficient is minimized whilst maintaining a high scattering length for efficient evaporation [153]. Furthermore, at this field we are sufficiently far away to the right of the 0.9 G resonance to avoid crossing it at high temperatures. The value of L_3 also informed us on the relative importance of three-body losses for each stage of the evaporation process, prompting an improvement to the experimental sequence at the onset of degeneracy via beam dithering (see section 4.3.1).

It is worth mentioning that even though we measured a difference in resonance properties (namely the light shift) depending on the relative orientation of the dipoles and the light polarization, we did not observe any difference when it comes to the orientation of the dipoles with respect to the trapping axes. This could come as a surprise given that many other properties of dipolar gases do depend on the trapping geometry and its interplay with the anisotropy of the DDI [196], [210], [346]. A possible explanation is that despite the anisotropic cigar shape of our trap, the gas is not in a quasi 1D regime and so from the point of view of the relatively localized collisions, the trap is locally homogeneous and isotropic. Furthermore, any energy shifts due to the mean-field DDI affects all the colliding particles in the same way and so have no effect. This is not the case in the degenerate regime where the collective nature of the gas results in long-ranged correlations which are no longer insensitive to the trap anisotropy.

One of the main controllable parameters of dipolar gases is the relative strength of the

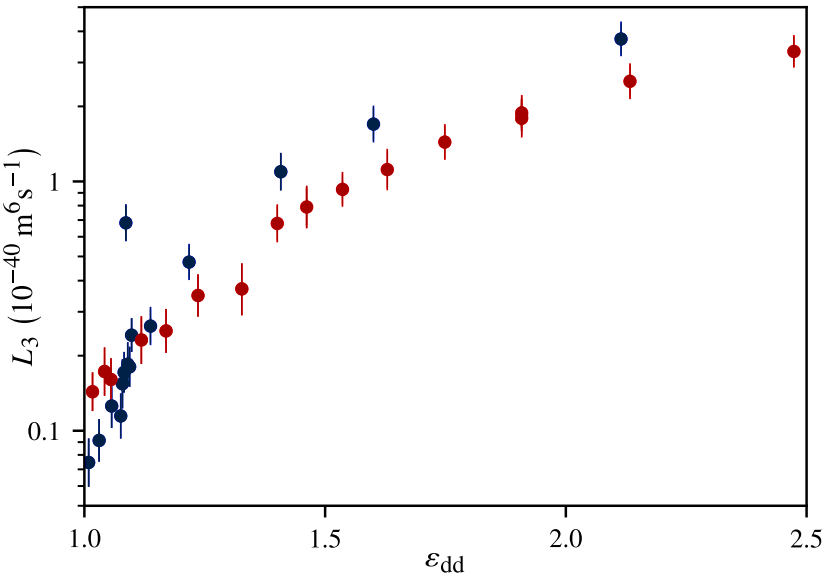


Figure 5.4: L_3 as a function of ε_{dd}. The figure shows the three-body loss coefficient L_3 as the B field approaches a wide Feshbach resonance from the right. The 0 G (3 G) resonance is shown in blue (red). The difference isn't significant but the data suggests that the 0 G resonance is more suitable for evaporation (low ε_{dd}) whereas the 3 G resonance might be better for studying highly dipolar samples (high ε_{dd}) for longer times.

DDI and the contact interactions $\varepsilon_{dd} = a_{dd}/a_s$ which can be adjusted by tuning a_s via a Feshbach resonance. As long as the resonance is wide enough to allow for a good resolution of a_s, it should be fit for the purpose. However, since some highly dipolar exotic states such as quantum droplets or supersolids [113], [114], [117] show density enhancement via dipolar collapse, three-body losses greatly limit their the lifetimes. It is therefore natural to try and compare wide resonances in terms of the three-body loss rate in their vicinity. Fig 5.4 shows L_3 as a function of ε_{dd} for the resonance at 0 G (blue) and 3 G (red). We observe no significant difference between the two resonances but we note that 3 G seems to be slightly more suitable for dipolar studies due to a lower L_3 for higher ε_{dd}.

5.3 Extended loss model

In the last section of this chapter, we present our extended thermodynamical model of the three-body loss process in trapped ultracold gases. The model takes into account secondary collisions of fast particles–products of three-body recombination events–with the rest of the trapped cloud. These collisions result in further atom loss and heating.

5.3.1 General m-body loss

Before fully focusing on three-body collisions, it is helpful and instructive to first consider the case of a general m-body process. By that we mean a process in which m gas particles have to come together in order for the process to happen. Since the gas density $n(r)$ is proportional to the probability of finding a particle at position r, the rate of any such m-body process is proportional to $n^m(r)$. In case of a loss process i.e. one in which some

or all of the m particles disappear from the trap (the validity of this assumption will be discussed below), we can express the rate of change of the atomic density as

$$\frac{dn(r)}{dt} = -L_m n^m(r), \tag{5.13}$$

here L_m is a general m-body loss coefficient which can depend on other thermodynamical quantities (in some cases on $n(r)$ itself). A loss of particles from the system also inherently causes a loss of energy. In some cases, as we will see below, this energy loss is different from the average energy of the particles in the atomic cloud and as such will change the temperature of the gas. In general, the rate of change of the energy density is given by

$$\frac{d\epsilon(r)}{dt} = \frac{dn(r)}{dt}E(r) = -L_m n^m(r)\left(\frac{3}{2}k_B T + U(r)\right), \tag{5.14}$$

where $E(r)$ is the energy per particle at position r and $U(r)$ is the potential energy per particle. We assumed that the gas is three-dimensional and far from degeneracy such that the average kinetic energy per particle is $\frac{3}{2}k_B T$. In this thermodynamic regime and for a cloud with N particles, we can define the particle density as $n(r) = \frac{N}{\alpha}e^{-\beta U(r)}$ where the normalization constant α

$$\alpha(\beta, \vec{\omega}) = \int e^{-\beta U(r)} dV \tag{5.15}$$

generally depends on the temperature and trap parameters through $\beta = 1/k_B T$ and the trap frequencies $\vec{\omega}$ respectively. In the special case of harmonic trapping, α can be evaluated explicitly to give

$$\alpha_{\mathrm{ho}}(\beta, \vec{\omega}) = \left(\frac{2\pi}{\beta m}\right)^{3/2} \frac{1}{\bar{\omega}^3} = \beta^{-3/2}\Theta(\vec{\omega}), \tag{5.16}$$

with $\bar{\omega} = (\omega_x \omega_y \omega_z)^{\frac{1}{3}}$.

This will allow us to evaluate the particle and energy loss rate directly by integrating equations 5.13 and 5.14 over the trap volume. Using the notation introduced in equation 5.15, we can write the characteristic integrals as

$$\begin{aligned} I_n^{(m)}(N, \beta, \vec{\omega}) &= \int n^m(r) dV = \left(\frac{N}{\alpha(\beta, \vec{\omega})}\right)^m \int e^{-m\beta U(r)} dV \\ &= \left(\frac{N}{\alpha(\beta, \vec{\omega})}\right)^m \alpha(m\beta, \vec{\omega}), \end{aligned} \tag{5.17}$$

and similarly for the potential energy density integral

$$\begin{aligned} I_E^{(m)}(N, \beta, \vec{\omega}) &= \int n^m(r) U(r) dV = \left(\frac{N}{\alpha(\beta, \vec{\omega})}\right)^m \int e^{-m\beta U(r)} U(r) dV \\ &= \left(\frac{N}{\alpha(\beta, \vec{\omega})}\right)^m \left(-\frac{1}{m}\right) \frac{\partial}{\partial \beta} \int e^{-m\beta U(r)} dV \\ &= \left(-\frac{1}{m}\right) \frac{\partial ln\left(\alpha(m\beta, \vec{\omega})\right)}{\partial \beta} I_n^{(m)}, \end{aligned} \tag{5.18}$$

where we used subscripts n and E to denote the particle and energy density integrals respectively. Combining equations 5.13, 5.14, 5.17 and 5.18 we can write the rate of change of the particle number and energy as

$$\begin{aligned}\dot{N}_m &= -L_m I_n^{(m)} \\ \dot{E}_m &= -L_m I_n^{(m)} \left(\frac{3}{2}k_B T - \frac{1}{m}\frac{\partial ln\left(\alpha(m\beta,\vec{\omega})\right)}{\partial\beta}\right) \\ &= \dot{N}_m \left(\frac{3}{2}k_B T - \frac{1}{m}\frac{\partial ln\left(\alpha(m\beta,\vec{\omega})\right)}{\partial\beta}\right)\end{aligned} \tag{5.19}$$

For a gas of non-interacting particles, the total energy is given by $E_{\text{tot}} = N\left(\frac{3}{2}k_B T + \bar{U}\right)$ where $\bar{U} = \frac{1}{N}\int n(r)U(r)dV = -\frac{\partial ln(\alpha(\beta,\vec{\omega}))}{\partial\beta}$ is the average potential energy. Differentiating this expression w.r.t time and assuming constant trap (i.e. $\dot{\vec{\omega}} = 0$) gives a general equation for the temperature time evolution

$$\begin{aligned}Nk_B\dot{T}\left(\frac{3}{2} + \beta^2\frac{\partial^2 ln(\alpha(\beta))}{\partial^2\beta}\right) &= \dot{E} - \frac{\dot{N}}{\beta}\left(\frac{3}{2} - \beta\frac{\partial ln(\alpha)}{\partial\beta}\right) \\ Nk_B\dot{T}\left(\frac{3}{2} + \beta^2\frac{\partial^2 ln(\alpha(\beta))}{\partial^2\beta}\right) &= \sum_m \dot{N}_m\left(\frac{\partial ln(\alpha(\beta))}{\partial\beta} - \frac{1}{m}\frac{\partial ln(\alpha(m\beta))}{\partial\beta}\right)\end{aligned} \tag{5.20}$$

Note that all the derivations so far are completely general and do not depend on the trapping potential or the nature of the loss process. Furthermore, first line of equation 5.20 is universally valid even for cases where $\dot{E} = \sum\dot{E}_i$ and $\dot{N} = \sum\dot{N}_i$ have contributions from different effects (e.g. m-body, off-resonant scattering, evaporation etc.) whereas the second line assumes contribution from m-body processes only.

For a gas trapped in an off-resonant Gaussian beam at temperatures $k_B T \ll U_{\text{depth}}$, the potential is well described using the harmonic approximation $U(r) = \frac{1}{2}m\sum_i \omega_i^2 r_i^2$. Under these conditions, equations 5.19 and 5.20 take on a simpler form

$$\begin{aligned}\dot{N}_m^{ho} &= -L_m m^{-3/2}\frac{N^m\beta^{3(m-1)/2}}{\Theta^{m-1}(\vec{\omega})} \\ \dot{E}_m^{ho} &= 3k_B T\dot{N}_m^{ho}\left(\frac{1}{2} + \frac{1}{2m}\right) \\ \dot{T}^{ho} &= T\frac{\dot{N}_m}{N}\left(\frac{1}{2m} - \frac{1}{2}\right),\end{aligned} \tag{5.21}$$

with $E_{\text{tot}} = 3Nk_B T$ following from the equipartition theorem and $\Theta(\vec{\omega})$ defined in equation 5.16. We will now briefly discuss the particular cases of one- and three-body loss processes which are relevant to our experiment.

We note that in general, two-body processes can also result in particle loss when the corresponding collisions are inelastic i.e. the particles change their internal state during the collision. An example of such a process is *spin relaxation* [347] in which the colliding particles change their spin state, leading to release of energy, heating and losses. These can occur when the atoms are prepared in an excited stated (perhaps due to favourable Feshbach resonances) as opposed to the ground state. Another example of a two-body loss

process are light-assisted collisions [292], [293] where a resonant field facilitates temporary mutual attraction between an atom in a ground state and an atom in an excited state. As the atoms accelerate towards each other, they gain kinetic energy which can get later deposited into the trapped cloud, once again leading to heating and losses. Fortunately, our cooling and trapping scheme for ^{166}Er only involves the ground state and so we don't observe spin relaxation effects. However, we believe that light assisted collisions are one of the main factors limiting the efficiency of loading atoms from the MOT into the ODT (see section 4.2 for full discussion). Once the atoms are in the ODT, the trapping light is off-resonant and so the light-assisted collisions are suppressed.

5.3.2 One-body loss

One body loss is widely encountered in cold atom experiments and it arises from collisions of the trapped atoms with background residual gas of the imperfect vacuum. Classically, the rate at which a trapped particle encounters a background gas atom is given by $\Gamma_{1B} = n_{\mathrm{bg}}\sigma_{\mathrm{bg}}v_{\mathrm{rel}} \approx n_{\mathrm{bg}}\sigma_{\mathrm{bg}}v_{\mathrm{bg}}$ where n_{bg} is the background gas density (directly proportional to the background pressure), σ_{bg} is the collision cross section and we assumed that the velocity of background particles is much larger than the velocity of the trapped particles such that $v_{\mathrm{rel}} \approx v_{\mathrm{bg}}$. This approximation is justified because the background is in thermal contact with the vacuum chamber and hence, to a good approximation, at room temperature whereas the trapped atoms are (hopefully) eight orders of magnitude colder. This is also the reason why such a collision always results in the loss of the trapped atom. Since these collisions involve only one particle of the trapped gas, they are effectively a one-body process and the particle decay rate is simply

$$\dot{N} = -\Gamma_{1B}N \tag{5.22}$$

i.e. an exponential decay with time constant $\tau = 1/\Gamma_{1B}$. Looking at the temperature evolution in equation 5.20 for the case $m = 1$ reveals that one-body loss has no effect on the gas temperature irrespective of the trapping potential. This can be understood by realizing that each trapped particle has an equal probability of undergoing a collision with the background gas (i.e. the process is density independent) and so the average energy lost in such process is equal to the average energy of the trapped gas, resulting in no heating. In practice, one-body collisions limit the lifetimes of ultracold atomic samples to tens of seconds and they are responsible for high requirements on the vacuum quality.

5.3.3 Three-body loss

As mentioned above, in a three-body collision, two of the participating particles can form a dimer, turning its binding energy into the kinetic energy colliding particles. If we assume this additional energy is large compared to the trap depth and that the ejected particles don't scatter further, we can simply treat the ejected particles and their original energy as being lost from the trap without a trace. Under these assumptions, we can use equation

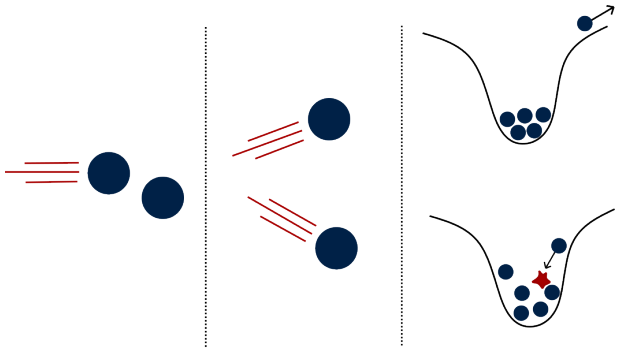


Figure 5.5: Secondary collision effects. A fast particle–product of a three-body recombination–can collide with other cloud particles on its way out of the trap. These collisions can result in further particle loss and/or deposition of thermal energy into the cloud.

5.21 to write for a harmonically trapped gas

$$\begin{aligned} \dot{N}_{3B} &= -L_3 \bar{\omega}^6 \left(\frac{\beta m}{2\sqrt{3}\pi} \right)^3 N^3 = -\gamma(T, \vec{\omega}) \frac{N^3}{T^3} \\ \dot{T} &= \frac{1}{3} \gamma(T, \vec{\omega}) \frac{N^2}{T^2} \end{aligned} \tag{5.23}$$

Note that the temperature always increases. This effect is known as anti-evaporation and it is a direct consequence of the fact that due to the n^3 scaling of the loss rate, particles are preferentially removed from high density regions at the bottom of the trap. Furthermore, particles at the bottom have, on average, less energy than the rest of the cloud and so their removal increases the average energy of the cloud, leading to heating. The set of equations 5.23 is the most common mathematical description of three-body particle loss and the related heating. They can be used individually or in tandem to fit to experimental data and extract the three-body loss coefficient L_3 (see section 5.1.2). However, this simple model is only valid under the assumptions that the ejected particles don't scatter further and that the binding energy of the dimer is large compared to the trap depth. In the following section, we outline a model that takes into account secondary collisions, yielding first order corrections to the model presented above.

5.3.4 Secondary collisions

To calculate the effect of secondary collisions (see figure 5.5), we first need to calculate the probability that a fast particle hits another cloud particle on its way out of the trap. Then, we need to look at the energetics of such collision and decide whether the collision products stay in the trap (causing heating) or leave the trap (leading to loss and possible secondary anti-evaporation). Finally, we can use this knowledge to formulate the rate equations for particle loss and heating.

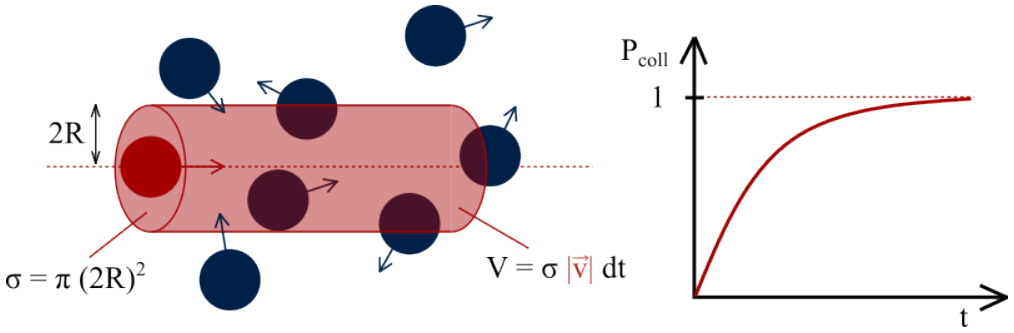


Figure 5.6: Collision probability. A projectile moving through a gas of density n collides with $nV = n\sigma v_r dt$ gas particles in a short time dt, where v_r is the average relative velocity of the projectile and the gas particles and $V = \sigma v_r dt$ is the collisional volume. The probability of colliding with a particle after time t exponentially approaches 1 such that $P_{\text{coll}} = 1 - e^{-n\sigma v_r t}$.

Escape probability

The aim of this section is to derive an expression for the probability $P_{\text{esc}} = P_{\text{esc}}(\vec{r}, \vec{\omega}, T)$ that a particle starting at position $\vec{r}$ manages to leave the cloud without colliding with other particles on its way. This probability will, in general, depend on the trapping potential and temperature of the cloud.

Lets start with the usual classical picture of a 'projectile' particle moving through a space filled with 'targets' of number density $n(r)$ as shown in figure 5.6. In time dt, the probability that the projectile will have hit a target on its way is given by $P_{\text{col}} = \sigma n v_r dt$ where σ is the collision cross section and v_r is the average relative velocity of the projectile and the targets. After a long time τ, the probability of escaping is given by a product of individual probabilities of escaping in small time intervals Δt_i such that:

$$P_{\text{esc}} = \prod_i (1 - \sigma n v_r \Delta t_i) = \lim_{\Delta t \to 0} (1 - \sigma n v \Delta t)^{\frac{\tau}{\Delta t}} = e^{-n\sigma v_r \tau} \tag{5.24}$$

The difference between this simple picture and the real case of a particle escaping from a trapped cloud is that a) as the particle travels through the potential, its velocity will change and b) the density of surrounding targets will also change. Fortunately, given that the energy of the projectile particle is generally much larger than the trap depth, we can assume that the motion of the particle is not perturbed by the potential i.e. the particle moves *ballistically* on a straight line. This assumption of large velocity also allows us to use $v_{\text{rel}} \approx v_{\text{proj}}$ i.e. from the point of view of the projectile, all the other gas particles are stationary. From now on we will drop the 'projectile' subscript when referring to velocity unless stated otherwise.

To address point b), we can partition the trajectory of the particle into time segments. During each time segment, the particle moves through a slightly different density of targets. In order to find out the total probability of escaping, we simply multiply the probabilities of escaping through each time segment:

$$P_{\text{esc}} = \prod_i e^{-\sigma v n(t_i)\Delta t_i} = e^{-\sigma v \sum n(t_i)\Delta t_i} = e^{-\sigma v \int n(t)dt} \tag{5.25}$$

We define $n(\vec{r}) = \frac{N}{\alpha} e^{-\beta U(\vec{r})}$ with $U(\vec{r}) = \frac{1}{2} m \sum_i {r_i}^2 {\omega_i}^2$ (see section 5.3.1 for the definition of α). Provided the ballistic motion assumption holds, we can also write $\vec{r}(t) = \vec{r_0} + \vec{v}t$ which will allow us to analytically solve equation 5.25. One can rewrite the equation as $P_{\text{esc}} = \exp(-\frac{\sigma v N}{\alpha} I)$ with $I = \int_0^\infty exp\left(-\frac{\beta m}{2} \sum {\omega_i}^2 (r_{0i} + v_i t)^2\right) dt$. The integral can be solved by completing the square to yield:

$$\begin{aligned} I &= e^{-\beta U(\vec{r_0})} e^{\frac{\beta m}{2} \frac{\Phi^2}{\chi}} \sqrt{\frac{\pi}{2\beta m \chi}} \left(1 - erf\left(\sqrt{\frac{\beta m}{2\chi}} \Phi\right)\right), \\ \chi &= \sum {\omega_i}^2 v_i^2, \\ \Phi &= \sum {\omega_i}^2 r_{i0} v_i. \end{aligned} \tag{5.26}$$

If we assume that all initial velocities are equally likely, then we have $\langle \Phi \rangle = 0$ and $\langle \chi \rangle = \frac{1}{3} \langle v^2 \rangle \sum {\omega_i}^2$. Substituting these into equation 5.26 gives

$$\begin{aligned} \langle I \rangle &= exp\left(-\beta U(\vec{r_0})\right) exp\left(\frac{\beta m}{2} \frac{\sum {\omega_i}^4 {r_{i0}}^2}{\sum {\omega_i}^2}\right) \sqrt{\frac{3\pi}{2\beta m v^2 \sum {\omega_i}^2}} \\ &= exp\left\{-\beta \left(U(\vec{r_0}) - \tilde{U}(\vec{r_0})\right)\right\} \sqrt{\frac{3\pi}{2\beta m v^2 \sum {\omega_i}^2}}, \end{aligned} \tag{5.27}$$

where we have defined an adjusted harmonic potential $\tilde{U}(r) = \frac{1}{2} m \frac{\sum {\omega_i}^4 {r_i}^2}{\sum {\omega_i}^2}$. Note that the assumption of velocity isotropy might be broken for a gas of polarized atoms with anisotropic interactions. Combining this with equation 5.25 and substituting in for α finally gives the expression for the probability of escape

$$P_{\text{esc}}(\vec{r}, \vec{\omega}, T) = exp\left(-\sigma n(r) \sqrt{\frac{3\pi}{2m\beta \sum {\omega_i}^2}} e^{\beta \tilde{U}(r)}\right). \tag{5.28}$$

Notice that the escape probability is independent of the projectile velocity. As long as the particle is fast enough to move on a straight line, the higher rate of encountering the targets is perfectly cancelled out by the shorter time the particle spends in the cloud.

Collision outcomes

Having calculated the probability of secondary collisions, we can now analyze all the possible outcomes of a three body collision. Namely the case when both the formed molecule and the single particle escape the trap and the cases when either of them undergo secondary collisions–see figure 5.7. In all of the subsequent calculations, we assume that $P_{\text{esc}} \approx 1$ (see equation 5.28) such that $P_{\text{col}} = 1 - P_{\text{esc}} \ll 1$ and we can neglect terms of order $\sim \mathcal{O}(P_{\text{col}}^2)$.

Consider a small cell of volume ΔV and particle number N_{cell} at a position r_0. Let

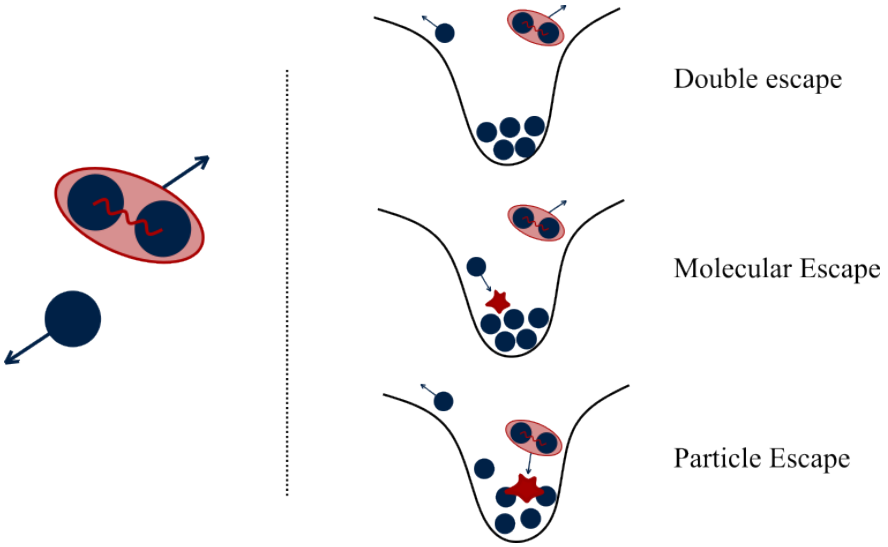


Figure 5.7: Three-body collision outcomes. After a three-body recombination event, the fast particle and molecule can either both escape the trap, or one of them can collide with other trapped particles on the way out and deposit its energy. Note that wo collision processes are neglected.

$P_{3B}(n)$ be the the probability that a three-body collision happens per particle per unit time. Then the number of three-body events in time Δt is given by $N_{3B} = P_{3B} N_{\text{cell}} \Delta t$. This is the starting point for all the subsequent calculations. We now describe all the possible outcomes of such a three-body event.

Double escape

The first and easiest case to consider is when both the molecule and the singular particle created in the process escape the cloud without perturbing it. We will use tilde to distinguish between quantities that relate to the particle and the molecule respectively because in general $\sigma \neq \sigma_{\text{mol}} = \tilde{\sigma}$ (similarly for the mass).

The probability of such 'double escape' event (per particle per unit time) is the product of the probability of a three body collision happening and a probability that both the particle and the molecule escape:

$$\begin{aligned} P_{\text{DE}} &= P_{3B} P_{\text{esc}} \tilde{P}_{\text{esc}} = P_{3B}(1 - P_{\text{col}})(1 - \tilde{P}_{\text{col}}) \\ &\approx P_{3B}(1 - P_{\text{col}} - \tilde{P}_{\text{col}}). \end{aligned} \tag{5.29}$$

Note that all the quantities depend on the properties of the particular cell such as its position r_0 in the cloud and the local density $n(r_0)$. Since all three particles escape the trap, the corresponding particle loss in time Δt from the cell is

$$\Delta N_{\text{DE}} = -3 N_{\text{cell}} P_{\text{DE}} \Delta t \tag{5.30}$$

and the energy lost from the cell

$$\Delta E_{\text{DE}} = -3 N_{\text{cell}} \bar{E}(r_0) P_{\text{DE}} \Delta t, \tag{5.31}$$

where $\bar{E}(r_0)$ is the average particle energy at the position of the cell.

Collision on the way out

The remaining two cases mirror each other so we will only describe one of the processes. Namely either the Feshbach molecule or the singular particle undergoes a collision on its way out while the other leaves without colliding. Note that the probability of both colliding is $\sim \mathcal{O}(P_{\text{col}}^2)$ and so assumed negligible.

For the case of the single particle collision and molecular escape, we have for the probability of the whole process

$$\begin{aligned} P_{\text{ME}} &= P_{3B} P_{\text{col}} \tilde{P}_{\text{esc}} = P_{3B} P_{\text{col}} (1 - \tilde{P}_{\text{coll}}) \\ &\approx P_{3B} P_{\text{col}} \end{aligned} \tag{5.32}$$

The subscript ME stands for 'molecular escape' and we will use PE for the equivalent case of 'particle escape' and molecular collision. The effect of the collision on particle number and energy of the cloud needs some careful thought. If we assume that the particles undergo elastic collisions, there are three possible outcomes of a collision of the singular 'projectile' particle with a slow particle of the cloud:

1. The projectile transfers some of its energy to the target particle, turning it effectively into a projectile while itself remaining ballistic in nature

2. The projectile grazes the target particle, giving it a bit of energy but not enough to knock it out. In this case, the target stays in the cloud and heats it up

3. The projectile hits the other particle head on, transferring most of its energy such that the projectile becomes slow and stays in the cloud and the target particle becomes a projectile and leaves the cloud. In this case, the original projectile stays behind and heats up the cloud with the excess energy it has left

These are depicted in figure 5.8. We denote the probabilities of these processes respectively as P_{KO} where KO stands for 'knock-out', P_{LE} where LE means 'low energy' transfer and finally P_{HE} where HE stands for 'high energy' transfer. For a very fast bullet and essentially stationary target of equal mass, we have $P_{\text{LE}}, P_{\text{HE}} \ll 1$ and $P_{\text{KO}} \approx 1$. Without going into detailed expressions for these probabilities (more on that in the next section), we can now write the particle and energy loss from a cell due to these processes

$$\begin{aligned} \Delta N_{\text{ME}} &= -N_{\text{cell}} P_{\text{ME}}(r_0) \{4 P_{\text{KO}} P_{\text{esc}}^2(r_1) + 3 P_{\text{LE}} P_{\text{esc}}(r_1) + 3 P_{\text{HE}} P_{\text{esc}}(r_1)\} \Delta t \\ &\approx -4 N_{\text{cell}} P_{3B} P_{\text{col}}(r_0) \Delta t, \end{aligned} \tag{5.33}$$

where we only kept the terms to first order in P_{col}, P_{HE}, P_{LE} and $1 - P_{\text{KO}}$. The numerical factors of 3 and 4 reflect how many particles are lost in each of the respective processes. We explicitly stated the dependence of the individual probabilities on position with r_0 being the position of the cell and r_1 the position of the secondary collision. Similarly, for

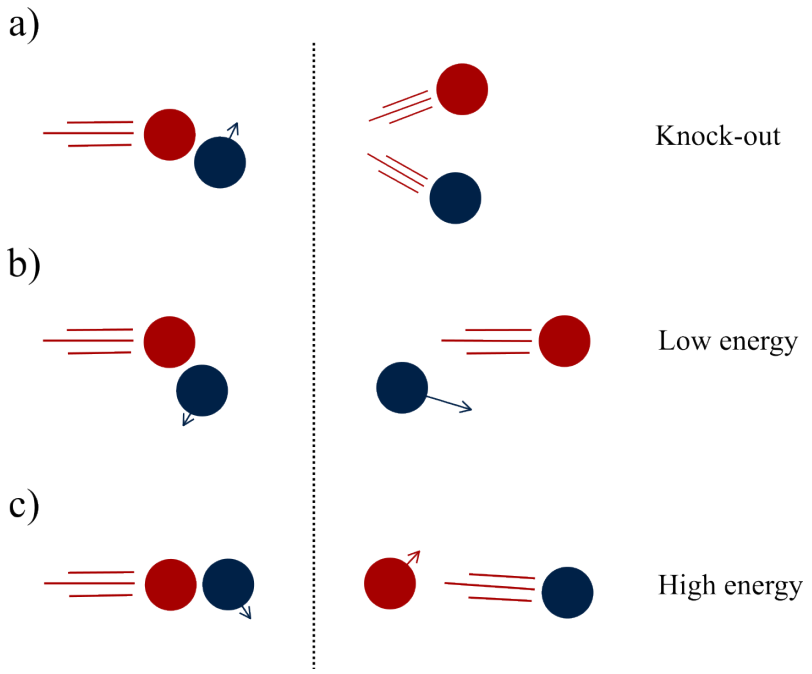


Figure 5.8: Secondary collision outcomes. The projectile can a) share some of its energy with a collision target, turning it effectively into another projectile; b) deposit a fraction of its energy into the target, heating it up; c) transfer most of its energy, turning the target into a projectile whilst staying behind and heating up the rest of the cloud.

the energy we can write

$$\begin{aligned}\Delta E_{\mathrm{ME}} =& - N_{\mathrm{cell}} P_{\mathrm{ME}} \{ P_{\mathrm{KO}} P_{\mathrm{esc}}^2(r_1)(3\bar{E}(r_0) + \bar{E}(r_1)) \\ &+ P_{\mathrm{LE}} P_{\mathrm{esc}}(r_1)(3\bar{E}(r_0) - E_{\mathrm{LE}}) \\ &+ P_{\mathrm{HE}} P_{\mathrm{esc}}(r_1)(2\bar{E}(r_0) + \bar{E}(r_1) - E_{\mathrm{HE}}) \} \Delta t \\ \approx& - N_{\mathrm{cell}} P_{\mathrm{ME}} \{ (3\bar{E}(r_0) + \bar{E}(r_1)) \\ &+ P_{\mathrm{LE}}(3\bar{E}(r_0) - E_{\mathrm{LE}}) + P_{\mathrm{HE}}(2\bar{E}(r_0) + \bar{E}(r_1) - E_{\mathrm{HE}}) \} \Delta t.\end{aligned} \tag{5.34}$$

Let's briefly discuss each term in the curly brackets. The first one corresponds to the most likely event in which both the projectile and the target particle leave the trap without a trace. In this case, the total energy removed from the trap is the average energy of the three collided particles at the position of the cell i.e. $3\bar{E}(r_0)$ summed together with the average energy of the target particle at the location of the secondary collision $\bar{E}(r_1)$.

The second term corresponds to a low-energy collision in which the target particle stays in the trap and redistributes the energy of the collision E_{LE} as heat into the cloud. The original molecule and projectile particles are still lost.

Lastly, when the projectile particle transfers most of its energy to the target particle, it redistributes its remaining energy E_{HE} into the cloud. The original molecular energy $2\bar{E}(r_0)$ and the target particle energy $\bar{E}(r_1)$ are lost.

Following this logic, one can easily obtain equivalent expressions for the case of single

particle escape and molecular collision:

$$\begin{aligned} P_{\mathrm{PE}} &\approx P_{3B}\tilde{P}_{\mathrm{col}}(r_0) \\ \Delta N_{\mathrm{PE}} &\approx -4N_{\mathrm{cell}}P_{3B}\tilde{P}_{\mathrm{coll}}\Delta t \\ \Delta E_{\mathrm{PE}} &\approx -N_{\mathrm{cell}}P_{\mathrm{PE}}\{(3\bar{E}(r_0)+\bar{\tilde{E}}(r_1)) \\ &\quad + \tilde{P}_{\mathrm{LE}}(3\bar{E}(r_0)-\tilde{E}_{\mathrm{LE}}) + \tilde{P}_{\mathrm{HE}}(\bar{E}(r_0)+\bar{\tilde{E}}(r_1)-\tilde{E}_{\mathrm{HE}})\}\Delta t, \end{aligned} \tag{5.35}$$

where we used tilde to denote quantities that depend on the nature of the projectile–for example, the collision probability of a molecule is different from the collision probability of a single particle. Equally, the average energies and probabilities of the high/low energy transfer collisions differ between the two cases.

Combined particle decay

We can now use equations 5.29-5.35 to express the rate of change of particle number. First, we can divide the expression for total particle loss from a cell $\Delta N_{\mathrm{cell}} = \Delta N_{\mathrm{DE}} + \Delta N_{\mathrm{ME}} + \Delta N_{\mathrm{PE}}$ by the cell volume and Δt to obtain the rate of change of density

$$\frac{dn}{dt} = -3nP_{3B} - nP_{3B}(P_{\mathrm{col}} + \tilde{P}_{\mathrm{col}}) \tag{5.36}$$

With reference to equation 5.13, we realise that without the last term, we recover the simple three-body decay equation by setting $P_{3B} = \frac{1}{3}L_3n^2$ to get

$$\frac{dn}{dt} = -L_3n^3\left(1 + \frac{1}{3}(P_{\mathrm{col}}(r) + \tilde{P}_{\mathrm{col}}(r))\right) \tag{5.37}$$

This is a first-order correction to the three-body decay equation. We can make more progress by realizing that for $P_{\mathrm{col}} \ll 1$, we can use equation 5.28 to write

$$\begin{aligned} P_{\mathrm{col}} = 1 - P_{\mathrm{esc}} = 1 - e^{-\delta} &\approx \delta = \sigma n(r)\sqrt{\frac{3\pi}{2m\beta\sum {\omega_i}^2}}e^{\beta\tilde{U}(r)} \\ &= \Lambda(T,\vec{\omega})n(r)e^{\beta\tilde{U}(r)} \end{aligned} \tag{5.38}$$

Integrating equation 5.37 over all space gives the particle decay rate

$$\begin{aligned} \dot{N} &= -L_3\int n^3 dV - \frac{L_3}{3}\left(\Lambda+\tilde{\Lambda}\right)\int n^4 e^{\beta\tilde{U}}dV \\ &= \dot{N}^0_{3B}\left(1 + \frac{\Lambda+\tilde{\Lambda}}{3}\frac{N}{\alpha(\beta,\vec{\omega})}\frac{\alpha(\beta,\vec{\Omega})}{\alpha(3\beta,\vec{\omega})}\right) \\ &= \dot{N}^0_{3B}\left(1 + \frac{3}{4\pi}(\sigma+\tilde{\sigma})\frac{Nm}{k_BT}\frac{\bar{\omega}^6}{\bar{\Omega}^3}\frac{1}{\sqrt{\sum\omega_i^2}}\right), \end{aligned} \tag{5.39}$$

where $\dot{N}^0_{3B}$ is the decay rate in the simplest model described in section 5.3.3 in which all products of the three-body collision escape the trap without interacting with the cloud. We have also defined $\Omega_i^2 = 4\omega_i^2 - \frac{\omega_i^4}{\sum\omega_j^2} > 0$. We see that the particle decay rate is

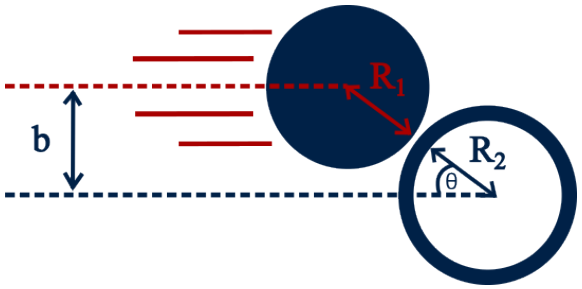


Figure 5.9: Classical collision parameters. In our simplified secondary collision model, we assume the particles behave as hard spheres of radii R_1 and R_2. The energy transfer is determined by the masses and radii as well as by the impact parameter b as described by equation 5.40.

enhanced due to secondary collisions and depends on the collisional cross section of the particle-particle and particle-molecule interaction as well as on the trap geometry.

Secondary collision energetics

Before we can move forward with evaluating the energy loss rate, we need to quantify the terms in equations 5.34 and 5.35 that describe a product of a low- or high- energy transfer collision. These terms involve the probabilities of such collisions $P_{\mathrm{LE/HE}}$ and the average energy left behind $E_{\mathrm{LE/HE}}$. To calculate these, we assume a classical hard-sphere collision model governed by the impact parameter b and the radii of the two colliding particles (see figure 5.9).

If one assumes random initial relative velocity of the two colliding particles such that $\langle \vec{p}_{\mathrm{proj}} \cdot \vec{p}_{\mathrm{targ}} \rangle = 0$ and that $E_{\mathrm{proj}} \gg E_{\mathrm{targ}}$ i.e. the target particle is effectively stationary w.r.t to the projectile, the energy transferred to the target particle is

$$\begin{aligned} \Delta E_{\mathrm{targ}} &= E_{\mathrm{proj}} \frac{4Mm}{(m+M)^2} cos^2(\theta) \\ &= E_{\mathrm{proj}} \underbrace{\frac{4Mm}{(m+M)^2}}_{\mu} \left(1 - \left(\frac{b}{R_{\mathrm{proj}} + R_{\mathrm{targ}}}\right)^2\right), \end{aligned} \tag{5.40}$$

where we have assumed a general mass M of the projectile (either a single particle or a molecule). For a uniform 'flux' of projectile particles, the probability of the impact parameter to be in the range $(b, b+db)$ is given by $P(b)db = \frac{2\pi b}{\sigma} db$ where we defined the collisional cross-section as $\sigma = \pi(R_{\mathrm{proj}} + R_{\mathrm{targ}})^2$ with R the classical radii of the the particles (see figure 5.9).

To advance with the calculations, we need to define what is meant by a high/low energy collision. In general, a particle at position r_1 after a collision with a projectile will need at least $E = E_k + U(r_1) + \Delta E_{\mathrm{targ}} > U_d$ energy to leave the trap. In most cases, the trap depth $U_d \geq 10 k_B T > E_k + U(r_1) \sim \mathcal{O}(3 k_B T)$ is roughly an order of magnitude larger than the average particle energy and so we can choose the cut-off transfer energy $\Delta E_{\mathrm{targ}} = U_d$ above which the target particle will leave the trap. We can also define the corresponding critical impact factor b_c^{LE}. If ΔE_{targ} is too large, the projectile might be

left behind after the collision with not enough energy to escape the trap. In this case, we have $E_{\text{proj}} - \Delta E_{\text{targ}} < U_d$ which defines a lower cut-off for the impact parameter b_c^{HE} below which the bullet will stay behind and heat the cloud.

For the case of particle-particle collision (as opposed to particle-molecule), $\mu = 1$ and using equation 5.40 we have

$$\begin{aligned} P_{\text{LE}} &= \int_{b_c^{LE}}^{b_{\max}=\sqrt{\frac{\sigma}{\pi}}} \frac{2\pi b}{\sigma} db = \frac{U_d}{E_{\text{proj}}} \\ \bar{E}_{\text{LE}} &= \int_{b_c^{LE}}^{b_{\max}} \frac{2\pi b}{\sigma} \Delta E_{\text{targ}}(b) db = \frac{1}{2}\frac{U_d^2}{E_{\text{proj}}} \\ P_{\text{HE}} &= \int_0^{b_c^{HE}} \frac{2\pi b}{\sigma} db = \frac{U_d}{E_{\text{proj}}} \\ \bar{E}_{\text{HE}} &= \int_0^{b_c^{HE}} \frac{2\pi b}{\sigma} (E_{\text{proj}} - \Delta E_{\text{targ}}(b)) db = \frac{1}{2}\frac{U_d^2}{E_{\text{proj}}} \end{aligned} \tag{5.41}$$

Similar expressions can be derived for the case of $M = 2m$ or equivalently $\mu = \frac{8}{9}$ which corresponds to a collision between a fast molecule and a single particle. Expressions for $\bar{P}_{\text{LE}}$ and $\bar{E}_{\text{LE}}$ are simply enhanced by a factor of $\frac{1}{\mu}$ compared to the expression in equations 5.41 and the general scaling remains the same. Interestingly and following from equation 5.40, the lowest energy the molecule can end up with after the collision is $\frac{1}{9}E_{\text{proj}}$ i.e. a little over 10% of its original energy which, given our ballistic assumption $E_{\text{proj}} \gg U_d$, would still most likely leave it with enough energy to escape the trap. As a consequence, we can take $\tilde{P}_{\text{HE}} \approx 0$. In other words, we discard the events in which the projectile molecule is left behind and heats the cloud.

Trap regimes

Knowledge of the collision statistics and the relative energy scales allows us to further simplify the expression for the energy loss and hence the temperature time-evolution. Even though we *always* assume that the projectile energy is much larger than the trap depth (and so the projectiles move approximately on straight lines), the trap depth itself affects what happens to the products of the secondary collisions. Inspecting equations 5.34 and 5.35 and denoting $\frac{U_d}{E_{\text{proj}}} = \kappa \ll 1$ reveals the order of magnitude of each contribution:

$$\ldots \{\underbrace{(3\bar{E}(r_0) + \bar{E}(r_1))}_{\mathcal{O}(4\cdot 3k_BT)} + \underbrace{P_{\text{LE}}(3\bar{E}(r_0) - E_{\text{LE}})}_{\mathcal{O}(\kappa(3\cdot 3k_BT))-\mathcal{O}(\kappa U_d)} + \underbrace{P_{\text{HE}}(2\bar{E}(r_0) + \bar{E}(r_1) - E_{\text{HE}})}_{\mathcal{O}(\kappa(3\cdot 3k_BT))-\mathcal{O}(\kappa U_d)}\} \tag{5.42}$$

where we assumed $\bar{E}(r_1) \approx 3k_BT$ which will be discussed further below. In case of a medium depth trap where the trap depth $U_d > k_BT$ is large enough to avoid severe atom loss but the ratio $\eta = U_d/k_BT$ is of the order 10 to maintain optimal evaporation [348], [349], the second and third terms in the above expression are suppressed by a factor of κ and are therefore negligible. In this case, the correction to the temperature evolution is solely due to second-order anti-evaporation i.e. particle loss with no direct heating.

However, if the trap depth becomes large, the heating terms of the order $\mathcal{O}(\kappa U_d)$ in

the above expression become non-negligible. Note that even though this requires $\eta = U_d/k_BT \gg 1$ we still need $\kappa \ll 1$ to preserve the ballistic motion of the bullets. For higher U_d for which $\kappa \sim \mathcal{O}(1)$ i.e. the non-ballistic regime where all the products of a three-body collision stay trapped, a different model is required.

Tying things together

As we did with particle evolution in equation 5.36, we can combine all the contributions to the change in energy $\Delta E_{\text{cell}} = \Delta E_{\text{DE}} + \Delta E_{\text{ME}} + \Delta E_{\text{PE}}$, drop negligible terms as discussed in section 5.3.4 and integrate over the whole cloud to get

$$\begin{aligned}\dot{E} =& -L_3 \int n^3 \bar{E}(r) dV - \frac{L_3}{3} \int n^3 \left(P_{\text{col}}(r) + \tilde{P}_{\text{col}}(r)\right) \bar{E}(r_1) dV \\ &+ \frac{L_3}{3} \int n^3 U_d^2 \left(\frac{P_{\text{col}}}{E_{\text{proj}}} + \frac{\tilde{P}_{\text{col}}}{2\mu \tilde{E}_{\text{proj}}}\right) dV,\end{aligned} \tag{5.43}$$

where the first term is due to the zeroth-order anti-evaporation, the second term due to secondary anti-evaporation and the third term is due to heating from low-energy-transfer collisions between the projectiles and the atomic cloud. An alert reader will notice that the second term contains an expression for the average energy of particles at the point of secondary collision, $\bar{E}(r_1)$. This is, in general, not the same as the average energy at the point of the three-body collision, $\bar{E}(r)$, and it needs to be calculated.

To do so, we can start from the probability of a bullet colliding with background gas in a small time interval dt given by $P_{\text{col}}(t)dt = P_{\text{esc}}(t) n\sigma v dt$ where $P_{\text{esc}}(t) = exp\left(-\sigma v \int_0^t n(t')dt'\right)$ is the probability of no collision before time t as developed in section 5.3.4. Clearly, $P_{\text{col}}(t, t+dt) = -\frac{dP_{\text{esc}}(t)}{dt}$. We can use this expression to find the average energy of particles in the region of the collision

$$\begin{aligned}\bar{E}(r_1) &= \int_0^\infty P_{\text{col}}(t) \bar{E}(r(t)) dt \\ &= \int_0^\infty n(t) \sigma v e^{-\sigma v \int_0^t n(t')dt'} \left(\frac{3}{2} k_B T + U(r(t))\right) dt \\ &= \underbrace{\frac{3}{2} k_B T + U(r_0)}_{E(r_0)} + \frac{1}{2} k_B T - \tilde{U}(r_0),\end{aligned} \tag{5.44}$$

with $r(t) = r_0 + vt$ and $\tilde{U}(r) = \frac{1}{2} m \frac{\sum {\omega_i}^4 {r_i}^2}{\sum {\omega_i}^2}$ as defined in section 5.3.4. Unsurprisingly, the energy $\bar{E}(r_1)$ is comparable to the energy $E(r_0)$, but not exactly the same.

Now we are ready to simplify equation 5.43. Luckily, many of the steps in the calculation closely mirror the ones used to obtain the expression for the particle time-evolution

$$\begin{aligned}\dot{N} &= \dot{N}^0_{3B} \left(1 + \frac{3}{4\pi}(\sigma + \tilde{\sigma}) \frac{Nm}{k_B T} \frac{\bar{\omega}^6}{\bar{\Omega}^3} \frac{1}{\sqrt{\sum \omega_i^2}}\right) \\ &= \dot{N}^0_{3B} \left(1 + \Theta(\sigma, \vec{\omega}) \frac{N}{T}\right)\end{aligned} \tag{5.45}$$

Using the above formalism and the variable Θ, the final expression for energy time-evolution is:

$$\dot{E} = 2k_B T \dot{N}^0_{3B} \left(1 + \Theta \frac{N}{T} \left(\frac{5}{2} - \frac{3}{2} \sum \frac{\omega_i^2}{\Omega_i^2} - \frac{U_d^2}{2k_B T} \left(\frac{\sigma}{E_{\text{proj}}} + \frac{\tilde{\sigma}}{2\mu \tilde{E}_{\text{proj}}}\right)\left(\frac{1}{\sigma} + \frac{1}{\tilde{\sigma}}\right)\right)\right) \tag{5.46}$$

and consequently for the temperature time-evolution

$$\begin{aligned} \dot{T} &= \frac{\dot{E} - 3k_B T \dot{N}}{3Nk_B} \\ &= \underbrace{\frac{L_3 N^2}{3T^2}}_{\dot{T}_0} \left(1 + \Theta \frac{N}{T} \left(1 - 3\left(1 - \sum \frac{\omega_i^2}{\Omega_i^2}\right)\right) + \Theta \frac{N}{T} \frac{U_d^2}{k_B T} \left(\frac{\sigma}{E_{\text{bullet}}} + \frac{\tilde{\sigma}}{2\mu \tilde{E}_{\text{bullet}}}\right)\left(\frac{1}{\sigma} + \frac{1}{\tilde{\sigma}}\right)\right), \end{aligned} \tag{5.47}$$

with $\Omega_i^2 = 4\omega_i^2 - \frac{\omega_i^4}{\sum \omega_j^2}$.

In a typical time-of-flight experiment, the accessible quantities are the particle number N and cloud size which is a proxy for the cloud temperature T. By holding the atoms in a trap for a variable amount of time and measuring both N and T, one can obtain the value of the three-body recombination coefficient L_3 by fitting the data to the numerical solutions of the following equations:

$$\begin{aligned} \dot{N} &= \underbrace{-\frac{N}{\tau}}_{\dot{N}_{1B}} \underbrace{-\gamma \frac{N^3}{T^3}}_{\dot{N}^0_{3B}} \left(1 + \Theta \frac{N}{T}\right) \\ \dot{T} &= \underbrace{\gamma \frac{N^2}{3T^2}}_{\dot{T}^0_{3B}} \left(1 + \Theta A \frac{N}{T} + \Theta B \frac{N}{T^2}\right), \end{aligned} \tag{5.48}$$

where γ, Θ, A and B are fitting parameters and $\gamma = L_3 \bar{\omega}^6 \left(\frac{m}{2\sqrt{3}\pi k_B}\right)^3$. These fitting parameters are not independent and also not completely unknown but their knowledge is conditioned by our knowledge of σ, $\tilde{\sigma}$, E_{proj} and $\tilde{E}_{\text{proj}}$ which are experimentally hard to measure–especially the molecular quantities. In fact, a careful measurement of the loss and heating rate could, in principle, give an estimate on these values. We note that $A = 1 - 3(1 - \sum \frac{\omega_i^2}{\Omega_i^2})$ is, in practice, determined by the trapping frequencies and can potentially be supplied to the fitting routine as a constant. We have explicitly labelled the zeroth-order terms to highlight that the non-unity terms in the brackets are assumed to be small and in case they are negligible, we recover the original expressions of equations 5.23. Additionally, we also included the omnipresent one-body loss which needs to be taken into account in real experiments. We note that depending on the trap regime, temperature, and particle density, some of the additional terms can be neglected to a varying degree of accuracy. To conclude this chapter, we will briefly discuss the feasibility of the secondary collision model in light of our three-body loss measurements in ^{166}Er.

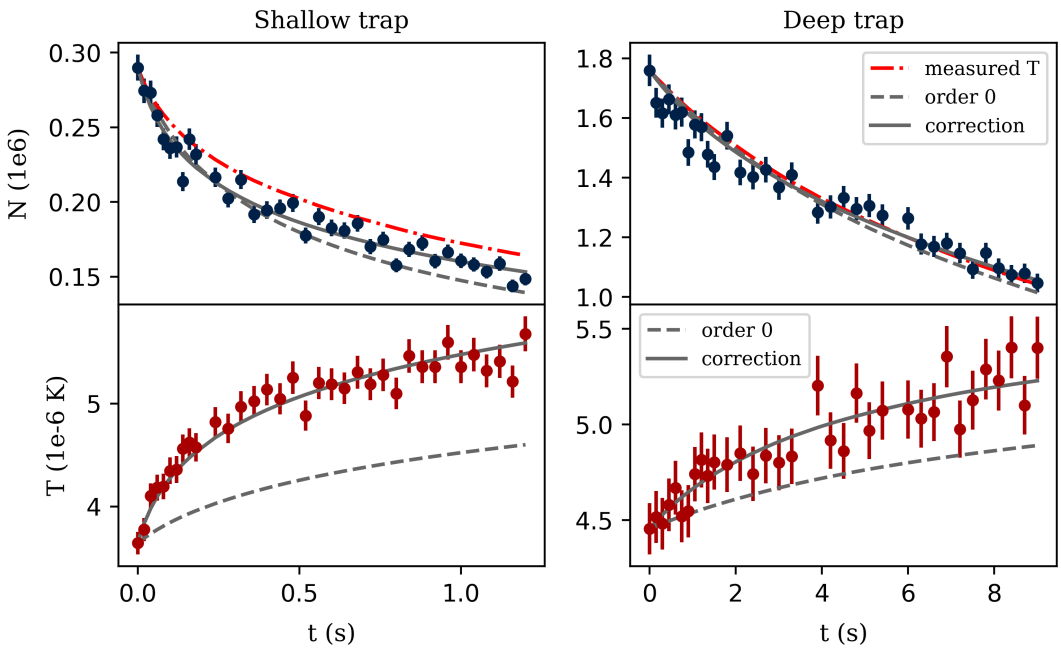


Figure 5.10: Typical data set and fitting model comparison. The figure shows particle number and temperature time evolution at 2.9 G for two different traps. The left column shows measurements done in a 'shallow' crossed beam trap of total depth $\approx 20\mu K$ whereas the right column shows data taken in a deep single beam trap of depth $\approx 130\mu K$. The data was fitted by numerically solving equations 5.48 without the secondary collision effects ('0th order', grey dashed curve), with the trap depth correction ('correction', grey full curve) and finally using measured temperatures to solve the particle number equation only ('measured T', red dash-dotted curve). The heating correction is necessary to fully describe the temperature time evolution whereas the particle decay is mainly encompassed in the zeroth order three-body recombination term.

5.3.5 Experimental comparison

To assess our model, we performed a loss measurement with a high number of data points at 2.9 G. This is a region of considerable loss, allowing us to perform the measurements in short time to avoid any other long time scale losses and heating whilst improving our signal to noise ratio. It is also away from any temperature dependent loss features that we identified (see section 5.2.2). We used two different traps–a crossed beam trap with a depth of $\approx 20\,\mu$K and a single beam trap of depth $\approx 130\,\mu$K–in order to see any trap depth effects. The data is shown in figure 5.10.

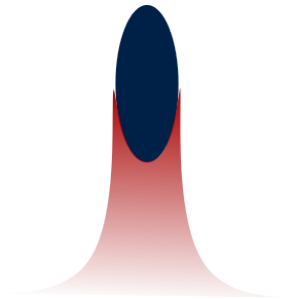
We fitted the data with several models. First, we used the simple 'zeroth order' three-body loss equation 5.23 including the one-body loss term (grey dashed lines). Clearly, the model captures well the particle number decay but fails to fully account for the heating of the cloud. A natural extension would be to include the first order correction as shown in equation 5.48 which accounts for the secondary anti-evaporation effect. This potentially introduces two new fitting parameters A and Θ, where A is a purely geometric factor and Θ contains information about the three-body collision. However, A can be determined from the trapping frequencies and so we performed a fitting routine on γ and Θ only. Doing this revealed two things. The fitted values of Θ was extremely small, resulting in

fits that almost perfectly overlapped with the zeroth order model (and hence we omitted these plots from the figure for clarity). This is not surprising given that even the simple model is sufficient to describe the particle number evolution, forcing Θ to be small. Once Θ is fixed, the temperature dependence is fully determined by the combination with A (also fixed). We therefore conclude that a) the fist-order correction to the particle number decay rate is small, validating our assumptions in its derivation and b) secondary anti-evaporation can't explain the observed heating.

Finally, we added the extra 'trap depth' correction term as shown in equation 5.48 while keeping A fixed. This is shown as full grey lines in the figure. The addition of this term greatly improves the temperature fits whilst marginally improving the particle number fits. This is not surprising given that we have essentially added an additional fitting parameter to the temperature differential equation and hence more flexibility to the fitting routine. There are several points to raise here. First, based on these results the role of the extra heating mechanism (in addition to anti-evaporation) is dominant. Second, the temperature evolution is well captured by the addition of a term of the form $C\frac{N}{T^2}$ where C is a constant. Interestingly, despite the fact that the extra term was derived for the case of a deep trap, it seems to be vital regardless of the trap depth. This might point to other unaccounted for mechanisms and prompt revisiting our model–especially approximations made in equation 5.42.

To conclude, we investigated the particle number decay and heating due to three-body collisions using several models that account for progressively more physical effects. Regardless of the model, the particle decay rate is dominated by the primary three-body recombination events as described by the coefficient L_3 (equation 5.23) and the variation of the fitted L_3 across all models was minimal ($\pm 8\%$) compared to the range of L_3 values in the 0–4 G region. This justifies our use of the simple model with measured temperatures for measuring L_3 in ^{166}Er (see section 5.2). Red dash-dotted curves in figure 5.10 show such fit of the data. Furthermore, the heating of the cloud can't be accounted for solely by the anti-evaporation effect. An extra term of the form $C\frac{N}{T^2}$ fits the trend well. The constant C most likely encompasses information about the collision dynamics and its origin was partially explained in section 5.3.4. However, our data points to some further sources of heating, prompting us to, for instance, measure how C depends on the trap and applied field in the future. The remaining uncertainty in the heating mechanism further justifies our use of the measured temperatures when solving the particle number differential equation instead of solving it concurrently with the temperature evolution equation.

6. Dipolar T_C shift



The dipole-dipole interaction (DDI) not only affects the ground state properties and the excitation spectrum of the BEC (see section 2.4.2), but it also changes the statistical distribution of the thermal gas. In the local density approximation, we can treat the gas at each point as homogeneous with local density $n(\mathbf{r})$. For a homogeneous gas, the condition for condensation is given by equation 2.44 which is equivalent to the phase-space density $\rho = n\Lambda^3$ reaching a critical value of $\zeta(3/2)$. In a harmonically trapped gas where density varies with position, condensation begins when the peak density (which is at the bottom of the trap) reaches this critical value, i.e. $n(\mathbf{0})\Lambda^3 = \zeta(3/2)$.

For a given trap and total particle number, as the temperature is reduced, the density profile of the thermal gas becomes sharper and taller. At some point, the peak density reaches the critical value. If we slowly turn on the interatomic interactions - for simplicity, lets consider only repulsive contact interactions–the gas expands, reducing the peak density. Consequently, condensation is delayed and further reduction in temperature is necessary in order to reach it. The interactions have thus caused a *shift* in the critical temperature. Equivalently, we could have added more particles to reach the critical density. From this alternative point of view, it is the critical particle number that is adjusted by the interactions.

This chapter is concerned with our measurement of the critical temperature (T_c) shift due to the long-ranged DDI present in erbium. To our knowledge, this is the first ever measurement of the dipolar T_c shift. The chapter is organized as follows. First we, present the relevant theory, starting with purely contact interactions and extending it to the anisotropic dipole-dipole interactions. We discuss the phenomenon of Bose gas saturation and how it is affected by the presence of the BEC. Next, we detail the design of our experimental sequence, focusing on the BEC and thermal atom number measurement which involves a multi-stage fitting procedure as well as on temperature measurements which need to be corrected for various dynamical processes that happen during time-of-flight. Lastly, we present our results, demonstrating a clear shift in the critical number (and hence temperature) that depends on the dipole polarization direction.

6.1 Theory

As discussed in section 2.4.1, Bose-Einstein condensation is an inherently statistical phenomenon which happens when the number of particles in the system exceeds the number of thermal excitations that can be supported by the quantum states constituting that system. The number of thermal excitations is maximized when the chemical potential approaches the ground state energy. We denote this maximum number as N_c where c stands for critical. Note that $N_c = N_c(T)$ is a function of temperature so for a given particle number N, we can equivalently define the critical temperature T_c such that $N_c(T_c) = N$.

Equation 2.47 gives the critical number for a non-interacting, harmonically-trapped gas. In deriving this expression, we assumed that $\mu \to 0$ i.e. that the ground state energy is zero (since μ cannot exceed the minimum energy of the system). However, in a quantum harmonic oscillator, the ground state energy is given by $\epsilon_0 = \hbar(\omega_x + \omega_y + \omega_z)/2 > 0$. We have also implicitly treated the trap as infinitely deep and perfectly harmonic, both of which aren't true in an optical dipole trap created by a Gaussian laser beam as discussed in section 4.1. Lastly (and most interestingly!), in the mean field picture, interactions between atoms create an effective potential on top of the trapping potential, changing the character of the quantum states occupied by the particles. All of these effects will shift the critical number N_c relative to its ideal value $N_c^0 = \zeta(3)(k_B T/\hbar\bar{\omega})^3$.

To the first order, we can express this shift as a sum of all the individual effects

$$\Delta N_c = \Delta N_{c,\mathrm{fs}} + \Delta N_{c,\mathrm{trap}} + \Delta N_{c,\mathrm{CI}} + \Delta N_{c,\mathrm{DDI}} \tag{6.1}$$

where the first term (denoted 'fs' for 'finite size') corresponds to the shift due to zero point energy and finite atom number, the second term encompasses trap imperfections such as its anharmonicity and finite depth, the third term is due to contact interactions and, finally, the last term is due to dipole-dipole interactions. It is precisely the effects of this last term that we are trying to measure.

Mathematically, the relative critical number shift due to dipole-dipole interactions in a highly-anisotropic, cylindrically symmetric, cigar trap (as is the case for our ODT) can be written as [350], [351]

$$\frac{\Delta N_{c,\mathrm{DDI}}(\theta)}{N_c^0} \approx -10.278 \frac{a_{dd}}{\Lambda} \frac{3\cos\theta - 1}{4} \tag{6.2}$$

with θ the angle between the dipole orientation and the weak trapping axis and Λ the thermal de Broglie wavelength. In order to demonstrate this shift, all we need to do is perform a differential measurement of N_c for the two extremal dipole orientations, i.e. $\theta = 0°$ and $90°$, and compare the two critical numbers. This way, we avoid having to distinguish and individually measure the different contributions of equation 6.1.

For completeness, in the next few sections, we will describe in detail the origin of each of these contributions to the critical number shift but table 6.1 provides a quick summary of the relevant expressions and their relative magnitudes. At this point, an eager reader might want to skip to section 6.3 which describes our experimental procedure for measuring the

Contribution	Expression $\left(\frac{\Delta N_c}{N_c^0}\right)$	Magnitude	Section
Finite size	$2.052\ \frac{\hbar\omega_{\rm avg}}{k_B T_c^0}$	+5%	6.1.1
Trap imperfection	Not analytic	+1.5%	6.1.2
Contact interactions	$10.278\ \frac{a_s}{\Lambda}$	+10%	6.1.3
Dipole interactions	$-10.278 \frac{a_{dd}}{\Lambda} f\left(\frac{\omega_\parallel}{\omega_\perp}\right) \frac{3\cos\theta - 1}{4}$	$-6/+3$%	6.1.4

Table 6.1: Contributions to the N_c shift. Each of these contributions are discussed in detailed in the sections listed. Their approximate magnitudes were calculated at $T = 250\,\text{nK}$ and for parameters $\omega = (290, 14, 233)\text{Hz}$, $a_s = 72\,\text{a}_0$. The aim of this work is to measure the shift due to the long-ranged, dipole-dipole interactions which depends on the trap geometry and the dipole orientation.

dipolar critical point shift and to section 6.4 which presents our results that demonstrate a successful measurement of this effect. In addition, section 6.2 introduces the phenomenon of non-saturation which we use to our advantage to estimate N_c.

As an aside, in this chapter, we will use the shift in critical particle number ΔN_c and the shift in critical temperature ΔT_c somewhat interchangeably. This is because for a small shift in either quantity, we can write quite generally $N_c(T) = N_c^0(T) + \Delta N_c(T)$ and $T_c(N) = T_c^0(N) + \Delta T_c(N)$. By definition, for a given particle number N we have

$$\begin{aligned} N_c(T_c) &= N \\ N_c^0(T_c^0 + \Delta T_c) + \Delta N_c(T_c^0) &= N \\ N_c^0(T_c^0) + \left.\frac{dN_c^0}{dT}\right|_{T_c^0} \Delta T_c + \Delta N_c(T_c^0) &= N \end{aligned} \tag{6.3}$$

where we only kept terms to first order in the shifts denoted by Δ. Using the expression for N_c^0 and the fact that $N_c^0(T_c^0) = N$, one can easily derive the following equation

$$\frac{\Delta N_c}{N_c^0} = -3\frac{\Delta T_c}{T_c^0} \tag{6.4}$$

which links the two shifts and allows us to derive one from the other. As we shall shortly see, using our experimental procedure, it is easier to determine ΔN_c and convert it to ΔT_c.

6.1.1 Finite size correction

The total number of thermal excitations can be obtained by integrating the 3D Bose-enhanced density profile given by equation 4.14. This is a very general approach that holds for any form of trapping potential $U(\mathbf{r})$ (including mean-field interaction potentials) as long as we can treat the gas using the semi-classical approximation in which the density varies negligibly over length scales comparable to the thermal De Broglie wavelength. For

a harmonically trapped gas, the integration yields

$$N_{\text{th}} = \left(\frac{k_B T}{\hbar\bar{\omega}}\right)^3 g_3[e^{\mu/k_B T}] \tag{6.5}$$

which reduces to the ideal result given by equation 2.47 in the limit $\mu \to 0$. Due to the divergent behaviour of the Bose-Einstein distribution (equation 2.40) when $\mu = \varepsilon_i$, the value of the chemical potential is bounded from above by the minimum energy present in the system i.e. the energy of the grounds state ε_0. In a 3D harmonically trapped gas, the zero point energy shifts ε_0 above zero

$$\varepsilon_0 = \frac{\hbar}{2}(\omega_x + \omega_y + \omega_z) = \frac{3}{2}\hbar\omega_{\text{avg}} \tag{6.6}$$

where we defined the algebraic average of the trapping frequencies ω_{avg}. As a result of the zero point energy, the chemical potential that maximizes the number of thermal excitations (and hence the one that corresponds to the critical number N_c) is shifted by $\Delta\mu = \varepsilon_0 \neq 0$.

Treating the change in μ and the critical temperature T_c as a small quantities and fixing the total particle number N_{th}, we can expand the total differential of $N_{\text{th}}(\mu, T)$ around the critical point

$$dN_{\text{th}} = \left.\frac{\partial N_{\text{th}}}{\partial\mu}\right|_{\mu=0} \Delta\mu + \left.\frac{\partial N_{\text{th}}}{\partial T}\right|_{T=T_c^0} \Delta T_c = 0 \tag{6.7}$$

Differentiating equation 6.5 with respect to μ and T and using the property of the polylog function $\frac{\partial g_i(z)}{\partial z} = \frac{g_{i-1}(z)}{z}$, we have $\frac{\partial N_{\text{th}}}{\partial\mu} = \frac{\zeta(2)}{\zeta(3)}\frac{N_c^0}{k_B T_c^0}$ and $\frac{\partial N_{\text{th}}}{\partial T} = \frac{3N_c^0}{T_c^0}$ and so we can write for the shift in critical temperature ΔT_c

$$\frac{\Delta T_c}{T_c^0} = -\frac{\hbar\bar{\omega}}{k_B T}\frac{\zeta(2)}{\zeta(3)}\frac{\omega_{\text{avg}}}{2\bar{\omega}} = -\frac{\zeta(2)}{\zeta(3)^{2/3}}\frac{\omega_{\text{avg}}}{2\bar{\omega}}\frac{1}{\sqrt[3]{N_c^0}} \tag{6.8}$$

where we used the expression for N_c^0 given by equation 2.47. Note that for systems with large number of particles, this correction tends to zero and it is therefore also know as the *finite size shift*. Interestingly, for very elongated cigar-shaped traps, the ratio of the two frequency averages can be large and the finite size shift becomes dominant. For our usual experimental parameters, the relative critical temperature shift is approximately 2%.

6.1.2 Trap geometry

Optical dipole traps formed by focused laser beams are only approximately harmonic as can be seen in figure 6.1. Their full profile is Gaussian in shape and given by equations 4.1 and 4.5. Furthermore, the trap has a finite depth and so the momentum distribution at each position withing the trap has to be truncated to account for the escape of particles that have sufficient kinetic energy [313], [352], [353]. Where the first effect increases the volume of the trap and hence the number of supported states, the second effect cuts off states with high energy and thereby reduces N_c. It is therefore not entirely obvious what the magnitude and sign of ΔN_c is.

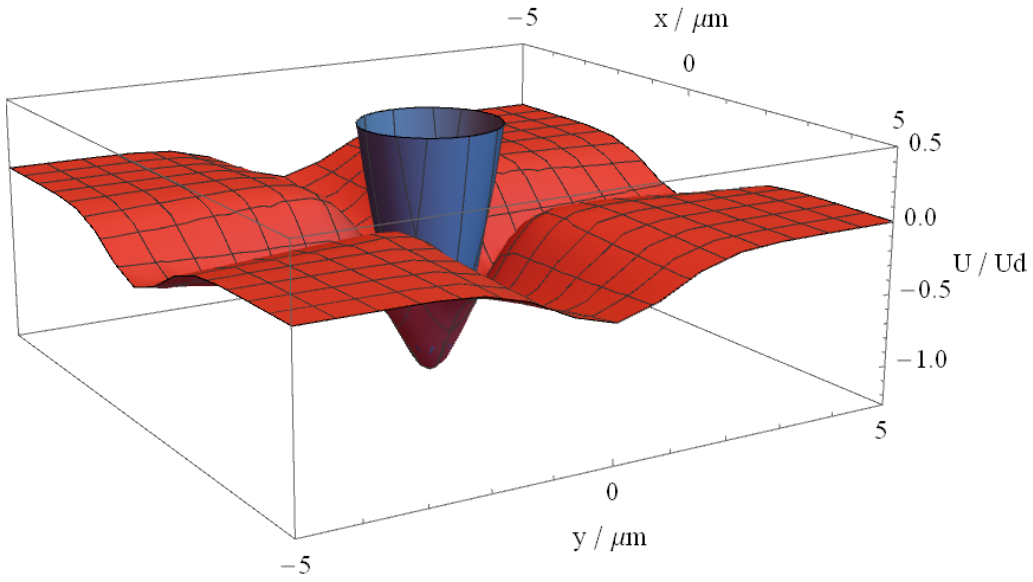


Figure 6.1: Harmonic approximation.3D rendering of the real crossed-beam optical dipole trap (red) and its harmonic approximation (blue). When the temperature is low compared to the trap depth, i.e. $U_d/k_BT \ll 1$, the approximation is good for qualitative understanding. However, in order to accurately determine thermodynamic quantities such as the critical atom number N_c for the BEC transition to within a few percent, the full Gaussian beam trap needs to be considered instead.

The answer depends on the exact trap parameters and can be obtained by evaluating

$$N_{\text{th}} = \frac{1}{(2\pi\hbar)^3} \int\int \frac{1}{e^{\varepsilon(\mathbf{r},\mathbf{p})/k_BT} - 1} \, d^3\mathbf{p} \, d^3\mathbf{r} \tag{6.9}$$

with $\varepsilon(\mathbf{r}, \mathbf{p}) = U(\mathbf{r}) + p^2/2m$ using the full Gaussian form of the trapping potential $U(\mathbf{r})$ and subject to the local constraint in momentum space $p^2/2m < U_d - U(\mathbf{r})$. This constraint is equivalent to limiting the total energy of the particle to be no greater than the trap depth U_d given by equation 4.7.

This six dimensional integral can be simplified by integrating over the angular momentum coordinates. By setting $q = p^2/2mk_BT$, $\gamma(\mathbf{r}) = U(\mathbf{r})/k_BT$ and $\eta = U_d/k_BT$, we obtain

$$N_{\text{th}} = \frac{2}{\sqrt{\pi}\Lambda^3} \int d^3\mathbf{r} \int_0^{\eta-\gamma(\mathbf{r})} \frac{q^{1/2}}{e^{\gamma(\mathbf{r})}e^q - 1} dq \tag{6.10}$$

with Λ the thermal De Broglie wavelength. This integral has to be evaluated numerically and for our typical experimental parameters yield a relative shift in the critical temperature $\Delta T_c/T_c^0 \sim \mathcal{O}(0.5\%)$.

6.1.3 Contact interactions

Even though interactions are not a necessary prerequisite for Bose-Einstein condensation, they not only facilitate it by allowing particles to reach thermal equilibrium via collisions but they also directly affect the critical parameters describing its onset. Within the mean-field Hartree-Fock approximation [233], interactions between particles result in an effective

potential. For contact interactions described by the first term of equation 2.37, the effective interaction potential is given by [204]

$$V_{\rm int}(\mathbf{r}) = 2gn(\mathbf{r}) \tag{6.11}$$

with $g = 4\pi\hbar^2 a_s/m$. This means that in the semi-classical (locally homogeneous) picture, a single particle state in a trapping potential $U(\mathbf{r})$ has energy

$$\varepsilon(\mathbf{r},\mathbf{p}) = \frac{p^2}{2m} + U(\mathbf{r}) + 2gn(\mathbf{r}) \tag{6.12}$$

which depends on the local density. Consequently, when interactions are included, the gas density (described by equation 4.14 for the non-interacting gas) is given by a self-consistent relation

$$n(\mathbf{r}) = \frac{1}{\Lambda^3} g_{3/2}\left[e^{(\mu - U(\mathbf{r}) - 2gn(\mathbf{r}))/k_B T}\right] . \tag{6.13}$$

The effective interaction potential (which itself depends on density) distorts the density distribution. As a result, the critical atom number obtained by integrating equation 6.13 is different from the ideal result 2.47 denoted by N_c^0.

When the size of the thermal cloud is much larger than the extent of the ground state of the harmonic trap, i.e. when $\sqrt{k_B T/m\omega_i^2} \gg \sqrt{\hbar/m\omega_i}$, the energy of the ground state is shifted by the interaction potential at the bottom of the trap such that

$$\varepsilon_0 = \frac{3}{2}\hbar\omega_{\rm avg} + 2gn(\mathbf{0}) . \tag{6.14}$$

The chemical potential μ will tend to this value as the critical point is approached. There are therefore two effects that are responsible for the shift in critical temperature ΔT_c. Similarly to the finite size correction discussed in section 6.1.1, there is a shift due to the change in chemical potential but there is also a shift associated with the distortion of the density distribution.

To quantify these effects, we can once again fix the total atom number and expand it around the non-interacting critical point corresponding to $\mu = 0$, $T = T_c^0$ and $g = 0$, similar to equation 6.7. This time, we will also have to include the effect of the interaction potential $V_{\rm int}(\mathbf{r}) = 2gn(\mathbf{r})$ which will be treated as small in the parameter g such that

$$dN_{\rm th} = \left.\frac{\partial N_{\rm th}}{\partial \mu}\right|_{\mu=0} \Delta\mu + \left.\frac{\partial N_{\rm th}}{\partial T}\right|_{T=T_c^0} \Delta T_c + \left.\frac{\partial N_{\rm th}}{\partial g}\right|_{g=0} g = 0 . \tag{6.15}$$

The first two terms were already derived in section 6.1.1 with the only difference being that $\Delta\mu$ is now given by the interacting ground state energy 6.14. The last term can be written as

$$\left.\frac{\partial N_{\rm th}}{\partial g}\right|_{g=0} g = \int g \left.\frac{\partial n(\mathbf{r})}{\partial g}\right|_{g=0} d^3\mathbf{r} = -\frac{2g\beta_0}{\Lambda^6}\int g_{1/2}[e^{-\beta_0 U(\mathbf{r})}] g_{3/2}[e^{-\beta_0 U(\mathbf{r})}] \tag{6.16}$$

where we used the general expression for density given by 6.13 and we defined $\beta_0 = 1/k_B T_c^0$. The integral on the right hand side of equation 6.16 can be easily evaluated since

$U(\mathbf{r})$ is a harmonic potential

$$\begin{aligned}\int g_{1/2}[e^{-\beta_0 U(\mathbf{r})}]g_{3/2}[e^{-\beta_0 U(\mathbf{r})}]d^3\mathbf{r} &= \sum_{j=1}^{\infty}\sum_{k=1}^{\infty}\frac{1}{j^{1/2}}\frac{1}{k^{3/2}}\int e^{-(j+k)\beta_0 U(\mathbf{r})}d^3\mathbf{r} \\ &= \Lambda^3\left(\frac{k_B T_c^0}{\hbar\bar{\omega}}\right)^3\sum_{j=1}^{\infty}\sum_{k=1}^{\infty}\frac{1}{j^{1/2}}\frac{1}{k^{3/2}}\frac{1}{(j+k)^{3/2}} \\ &= \Lambda^3 N_c^0\frac{S}{\zeta(3)}\end{aligned} \tag{6.17}$$

where the numerical constant S is defined as

$$S = \sum_{j=1}^{\infty}\sum_{k=1}^{\infty}\frac{1}{j^{1/2}}\frac{1}{k^{3/2}}\frac{1}{(j+k)^{3/2}} \approx 1.208\ . \tag{6.18}$$

Combining all the terms in equation 6.15 and expressing the relative shift in the critical temperature yields

$$\begin{aligned}\frac{\Delta T_c}{T_c^0} &= -\frac{\hbar\bar{\omega}}{k_B T}\frac{\zeta(2)}{\zeta(3)}\frac{\omega_{\text{avg}}}{2\bar{\omega}} - \frac{4}{3}\frac{1}{\zeta(3)}\left[\zeta(2)\zeta(3/2) - S\right]\frac{a_s}{\Lambda} \\ &\approx -0.684\frac{\hbar\omega_{\text{avg}}}{k_B T_c^0} - 3.426\frac{a_s}{\Lambda}\end{aligned} \tag{6.19}$$

where we identify the first term as the finite size correction derived in section 6.1.1 and the second term as the contribution from contact interactions. We see that repulsive interactions ($a_s > 0$) tend to reduce the critical temperature or equivalently increase the critical atom number because they 'inflate' the gas and allow for more thermally excited particles to exist in it before the critical density at the center of the trap is reached. This expression was first derived by Giorgini *et al.* [354] and since then has been experimentally confirmed [353], [355]. For our typical experimental parameters of $T = 250\,\text{nK}$ and $a_s = 72\,\text{a}_0$, the relative shift of the critical temperature due to contact interactions is $\approx 4\%$.

As an interesting aside, in a homogeneous system, the mean field correction vanishes because the chemical potential at the critical point and the interaction potential are both constant and equal and so the critical density obtained by inserting $\mu = 2gn$ into equation 6.13 is the same as the non-interacting value $n_c^0 = \zeta(3/2)/\Lambda^3$. However, beyond mean-field corrections due to long-ranged particle correlations [356] do shift the critical temperature by an amount equal to $\Delta T_c/T_c^0 \approx 1.8(a_s/\Lambda)$ [357], [358] which is comparable in magnitude to result 6.19 valid for a harmonically trapped gas. The shift is in the opposite directions though since correlations between particles work to establish coherence and allow for the existence of the condensate at higher temperatures. Similar beyond mean-field corrections in a harmonically trapped gas are of a higher order in a_s/Λ and therefore negligible compared to the mean-field correction derived above [354]. This is because at the critical point, the region that undergoes the phase transition and therefore experiences the effect of correlations is vanishingly small, suppressing their long-range nature.

6.1.4 Dipole-dipole interactions

Similarly to the contact interactions, the DDI also shifts the critical temperature. However, due to its anisotropic nature, the T_c shift will, in general, depend on the polarization direction of the dipoles relative to the trapping axes. In the mean field picture, the effective dipolar interaction potential experienced by the atoms is once again density-dependent, but its form is defined through an integral equation

$$\Phi_{dd}(\mathbf{r}) = \int U_{dd}(\mathbf{r}-\mathbf{r}')n(\mathbf{r}')d^3\mathbf{r}' = \int \frac{C_{dd}}{4\pi}\frac{1-\cos^2\theta}{|\mathbf{r}-\mathbf{r}'|^3}\, n(\mathbf{r}')d^3\mathbf{r}' \tag{6.20}$$

with the dipolar interparticle interaction potential U_{dd} defined by equation 2.37 and discussed in section 2.3.3. Both the angular and the $1/r^3$ dependence of U_{dd} make the potential (and in return the T_c shift) difficult to calculate.

The only analytic result was derived by Glaum *et al.* [350] for the case of a cylindrically symmetric, harmonic cigar trap of the form

$$U(x,y,z) = \frac{1}{2}m\left[\omega_\perp(x^2+y^2)+\omega_\parallel z^2\right] \tag{6.21}$$

The relative dipolar critical temperature shift for this trap geometry is given by [350], [351]

$$\frac{\Delta T_c}{T_c^0} \approx 3.426\frac{a_{dd}}{\Lambda} f\left(\frac{\omega_\parallel}{\omega_\perp}\right)\frac{3\cos\theta-1}{4} \tag{6.22}$$

with a_{dd} the dipolar length defined in 2.36, θ the angle between the dipole polarization and the symmetry axis of the trap and $f(\kappa)$ a function defined as

$$f(\kappa) = \frac{1+2\kappa^2}{1-\kappa^2} - \frac{3\kappa^2}{(1-\kappa^2)^{3/2}}\tanh^{-1}\sqrt{1-\kappa^2}\ . \tag{6.23}$$

and plotted in figure 6.2. In the limit of $\omega_\parallel/\omega_\perp \to 0$, i.e. for a highly anisotropic cigar trap, the total critical temperature shift due to both contact and dipole-dipole interactions takes on a simple, polarization angle dependent form

$$\frac{\Delta T_c}{T_c^0} \approx 3.426\frac{a_s}{\Lambda}\left(\varepsilon_{dd}\frac{3\cos\theta-1}{4}-1\right)\ . \tag{6.24}$$

Initial measurements with chromium [351] dated almost twenty years back failed to reveal the dipolar contribution to the critical temperature shift. This is because of the low relative dipolar strength ε_{dd} of chromium (despite its high magnetic dipole moment of $6\mu_B$!). With our erbium experiment, we have access to a wide range of ε_{dd} values on the order of $\sim\mathcal{O}(1)$ thanks to erbium's favourable Feshbach resonance spectrum (see section 2.3.4 and chapter 5), high atomic mass and large magnetic dipole moment. This allows us to measure the dipolar contribution to the critical temperature shift using a combination of experimental techniques and utilizing the phenomenon of non-saturation.

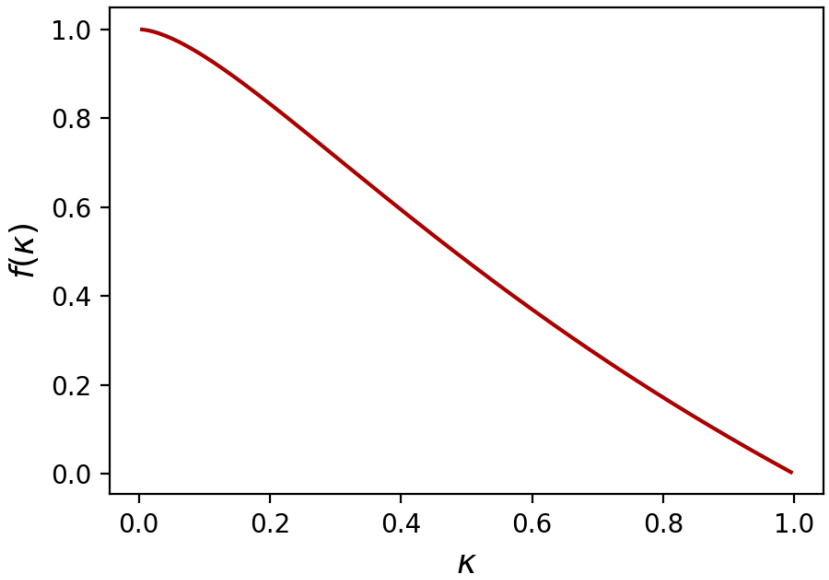


Figure 6.2: Dipolar shift scaling function. The function f enters the expression for the dipolar T_c shift as a scaling factor with its argument given by the ratio of the longitudinal and transverse trapping frequencies, $\kappa = \omega_{\parallel}/\omega_{\perp}$. Note that according to equation 6.22, in an isotropic trap (i.e. $\kappa = 1$), the dipolar shift completely vanishes as opposed to just becoming independent of θ.

6.2 Non-saturation

Lets change our perspective for a moment and instead of investigating a system with a fixed particle number and a variable temperature and trapping potential, we will look at a system in a static trap and at a fixed temperature T with variable particle number N. For a non-interacting gas, these conditions unambiguously fix and define the critical number of thermal excitations supported by the system, $N_c^0 = \zeta(3)(k_B T/\hbar\bar{\omega})^3$.

If the total particle number is below the critical number, i.e. $N < N_c^0$, all the atoms are thermally distributed in the available quantum states according to the Bose-Einstein distribution (equation 2.40). If we add more particles to the system, qualitatively nothing changes as long as $N \leq N_c^0$. Above the critical point though, any more particles added are forced to condense in the ground state of the system and form a BEC. The number of thermal excitations *saturates* at the critical value N_c^0 and the total particle number obeys $N = N_c^0 + N_0$ with N_0 the number of atoms in the condensate. This ideal saturation behaviour is depicted in figure 6.3. In practice, increasing the particle number at a constant temperature is difficult [359]. What is easier though is losing them due to inelastic processes (see chapter 5). With a suitably chosen trap, the phase transition can be crossed in reverse. We discuss our experimental realisation of this fixed temperature traversal in section 6.3.

If we now turn on the interactions, based on our previous discussion we know that the critical number will shift by several percent. What we haven't considered, though, is what happens to the critical number as more particles are added! In other words, we only considered the self interaction of the thermal gas and its effect on the critical point but

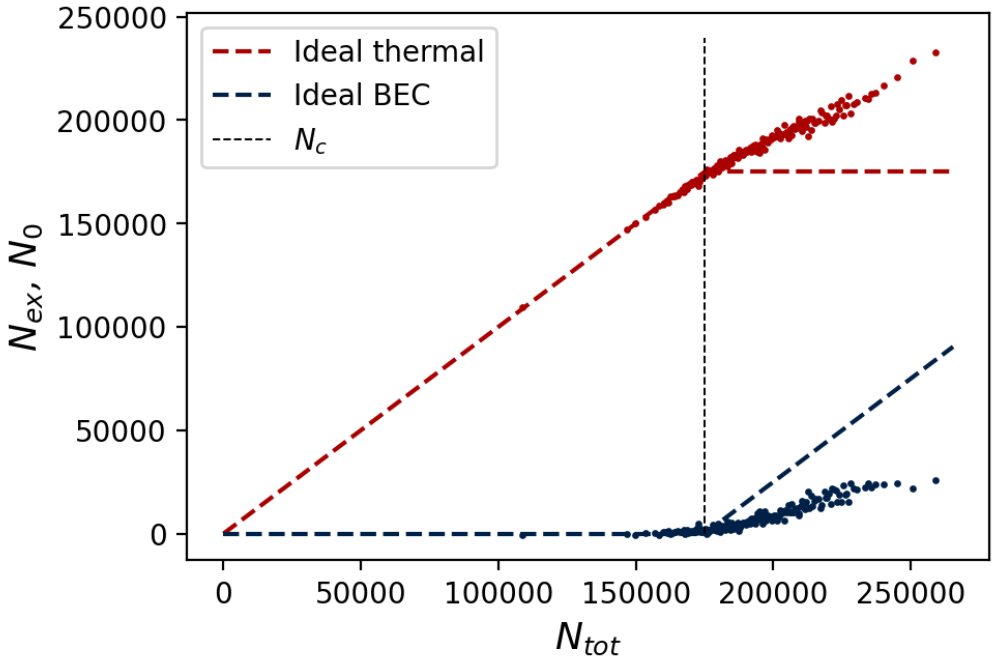


Figure 6.3: Non-saturation of the thermal cloud. Experimental measurement of the BEC atom number N_0 (blue dots) and the thermally excited atom number N_{ex} (red dots) performed at constant temperature ($\approx 235\,\text{nK}$) and for a varying total atom number $N_{\text{tot}} = N_0 + N_{\text{ex}}$. Dashed lines indicated the ideal (non-interacting) behaviour according to which the thermal fraction saturates at the critical number N_c while the BEC continues to grow as we add more atoms. In a real, interacting system, the thermal fraction doesn't saturate and continues to grow at the expense of the BEC.

we omitted the influence of the newly formed BEC. Figure 6.3 shows our experimental measurement of the thermal atom number and the BEC atom number as a function of the total atom number, clearly displaying a deviation from the ideal saturation.

To quantify this effect, we can once again work in the Hartree-Fock approximation in which the effective potential experienced by the thermal gas is given by

$$V_{\text{eff}}(\mathbf{r}) = U(\mathbf{r}) + 2g(n(\mathbf{r}) + n_0(\mathbf{r})) \tag{6.25}$$

where $n(\mathbf{r})$ is the density of the thermal gas and $n_0(\mathbf{r})$ is the density of the BEC. If we neglect the effect of the thermal gas on the BEC and use the Thomas-Fermi approximation discussed in section 2.4.2, the BEC density profile is given by equation 2.59 which can alternatively be written as $n_0(\mathbf{r}) = (\mu_0 - U(\mathbf{r}))/g$. Furthermore, if we also neglect the self interaction of the thermal gas which is considerably less dense than the BEC, the effective potential simplifies to

$$V_{\text{eff}}(\mathbf{r}) = U(\mathbf{r}) + 2gn_0(\mathbf{r}) = |U(\mathbf{r}) - \mu_0| + \mu_0 \tag{6.26}$$

since the BEC only extends in the region defined by $\mu_0 - U(\mathbf{r}) > 0$. Note that neglecting the thermal-thermal interactions amounts to turning a blind eye to the (relatively small) critical number shift at the onset of condensation given by equation 6.19. The shape of the effective potential is shown in figure 6.4 together with its effect on the thermal gas density distribution.

Using the potential of equation 6.26 together with the general expression for thermal gas density 4.14 (with V_{eff} in place of U) and the Thomas-Fermi chemical potential 2.61, we can calculate the total number of thermally excited states as

$$N_c(N_0) = \int n(\mathbf{r}) d^3\mathbf{r} = \frac{1}{\Lambda^3} \int g_{3/2} \left[e^{(\mu_0 - V_{\text{eff}}(\mathbf{r}))/k_B T} \right] d^3\mathbf{r} \ . \tag{6.27}$$

If the atoms in the overlap region with the BEC are neglected [233], [353], the effective potential is just the trapping potential and we can rewrite the integral 6.27 in the following way

$$N_c(N_0) \approx 4\pi \left(\frac{R_{\text{th}}}{\Lambda} \right)^3 \int_{\sqrt{2\alpha_0}}^{\infty} \rho^2 g_{3/2} \left[e^{-(\rho^2/2 - \alpha_0)} \right] d\rho \tag{6.28}$$

where we defined

$$\alpha_0 = \frac{\mu_0}{k_B T}, \quad R_{\text{th}} = \sqrt{\frac{k_B T}{m\bar{\omega}^2}}, \quad \rho = \frac{r}{R_{\text{th}}} \ . \tag{6.29}$$

Substituting

$$\frac{Q^2}{2} = \frac{\rho^2}{2} - \alpha_0 \tag{6.30}$$

and working to first order in α_0 which is equivalent to the condition $\mu_0 \ll k_B T$ valid for low BEC numbers, we get

$$N_c(N_0) \approx 4\pi \left(\frac{R_{\text{th}}}{\Lambda} \right)^3 \int_0^{\infty} (Q^2 + \alpha_0) \ g_{3/2}[e^{-Q^2/2}] \ dQ \ . \tag{6.31}$$

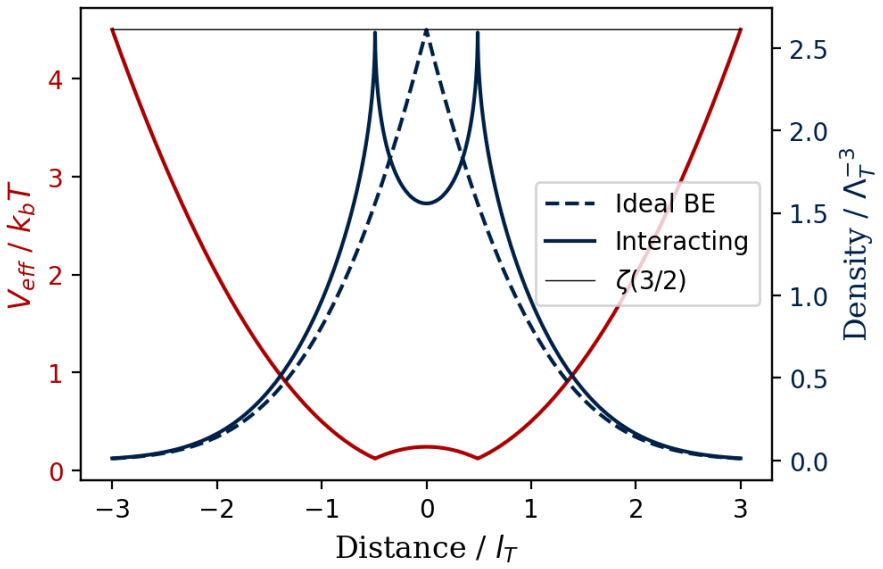


Figure 6.4: Effective potential. The presence of the BEC at the bottom of the trap creates a repulsive barrier. On the surface of the BEC, the total effective potential is equal to the chemical potential and the density $n(\mathbf{r}) \propto g_{3/2}(e^{-(V_{\text{eff}}-\mu)/k_BT})$ reaches its maximal value there equal to $\zeta(3/2)\Lambda^{-3}$. Despite the lowering of density in the overlap region, the total number of thermally excitable states, N_c, increases compared to the non-interacting case because of the density enhancement on the BEC surface accompanied by a shift in chemical potential which increases the density even in the non-overlapping region of the trap.

Expanding the polylog function and performing the (analytic) Gaussian integrals finally yields

$$N_c(N_0) \approx N_c^0 + \frac{\zeta(2)}{2}\left(\frac{k_BT}{\hbar\bar{\omega}}\right)^2\left(\frac{15a_s}{\bar{a}_{\text{ho}}}\right)^{2/5} N_0^{2/5} \ . \tag{6.32}$$

The critical thermal atom number is therefore larger than the ideal saturated value N_c^0 and scales as $N_0^{2/5}$. In principle, by measuring N_c, i.e. the thermal atom number for $T < T_c$, and plotting it against $N_0^{2/5}$, the value of the critical number at the transition point, $N_c(0)$, can be obtained from the intercept. This method is at the heart of our measurement of the dipolar T_c shift and it is further elaborated on in section 6.3.

At a first glance, result 6.32 is surprising given that we have actually excluded a somewhat dense region at the bottom of the trap when we integrated the density. Furthermore, in the region that we did integrate over, the effective potential is identical to the trapping potential so how do we end up with more particles compared to the ideal result N_c^0? The answer lies in the chemical potential $\mu_0 > 0$ which enhances the density even outside of the overlap region compared to the non-interacting case with $\mu_0 = 0$. This can be seen in figure 6.4 which shows both the ideal Bose-enhanced and the BEC-distorted density profiles. For small BEC numbers, the excluded region is small and contributes negligibly to the total thermal atom number. However, for higher BEC numbers, the critical number deviates from the $N_0^{2/5}$ scaling and both the excluded region and particle correlations from the edge of the excluded region need to be considered to fully account for the non-saturation effect [353].

6.2.1 Dipolar non-saturation

Given the complicated functional form of the effective dipolar potential (equation 6.20), it is by no means obvious whether the non-saturation of the thermal gas should follow the same scaling with BEC atom number, i.e. $N_c \propto N_0^{2/5}$, when the long-ranged DDI is taken into account. There are two ways in which the DDI enters the expression for the critical atom number. Firstly, it changes the condensate wavefunction and the associated chemical potential. The shape of the condensate, in return, determines the integration region in equation 6.28 whereas the shift in the chemical potential affects the density profile across the whole cloud. Secondly, the effective potential outside of the condensate is now different from the trapping potential because even in the mean-filed picture the DDI extends outside of the condensate. This is to be contrasted with purely contact interactions which are bound by the density profile of the condensate.

Previous theoretical investigations [360], [361] of the ground state properties of harmonically trapped, dipolar BECs in the Thomas-Fermi limit revealed a surprising result– namely that the dipolar condensate still retains its typical parabolic profile, albeit with adjusted Thomas-Fermi radii. With this knowledge, it is also possible to derive the magnetic dipole potential outside of a polarized BEC ellipsoid [360]. Here, we present a brief overview of these results and how we use them to investigate non-saturation in the presence of the DDI.

In the Thomas-Fermi limit (see section 2.4.2), the dipolar BEC density satisfies

$$U(\mathbf{r}) + gn_0(\mathbf{r}) + \Phi_{dd}(n_0(\mathbf{r})) = \mu \tag{6.33}$$

with Φ_{dd}, the mean-field dipolar potential, defined in equation 6.20. Using the identity

$$\frac{\delta_{ij} - 3r_i r_j}{r^3} = -\nabla_i \nabla_j \frac{1}{r} - \frac{4\pi}{3}\delta_{ij}\delta(\mathbf{r}) \ , \tag{6.34}$$

the dipolar mean field potential can be rewritten as

$$\Phi_{dd}(\mathbf{r}) = -C_{dd}\hat{e}_i\hat{e}_j \left(\nabla_i \nabla_j \phi(\mathbf{r}) + \frac{2\delta_{ij}}{3} n_0(\mathbf{r}) \right) \tag{6.35}$$

where the Einstein summation convention is assumed, $\hat{e}_i$ is the i-th component of the unit vector pointing along the dipole polarization direction and $\phi(\mathbf{r})$ is a potential that satisfies Poisson's equation

$$\phi(\mathbf{r}) = \frac{1}{4\pi} \int \frac{n(\mathbf{r}')}{|\mathbf{r} - \mathbf{r}'|} d^3\mathbf{r}' \iff \nabla^2\phi(\mathbf{r}) = -n(\mathbf{r}) \ . \tag{6.36}$$

Upon closer inspection of equation 6.33, it is clear that a parabolic Thomas-Fermi (TF) solution of the form

$$n_0(\mathbf{r}) = \rho_0 \left(1 - \frac{x^2}{R_x^2} - \frac{y^2}{R_y^2} - \frac{z^2}{R_z^2} \right) \tag{6.37}$$

will be possible if $\phi(\mathbf{r})$ only contains terms proportional to r_i^2 and $r_i^2\ r_j^2$ which we denote

ϕ_i and ϕ_{ij} respectively. Note that in general, the TF ellipsoid can be rotated with respect to the trapping axes, particularly when the dipole polarization is at an arbitrary angle. We can account for this by working in the natural frame of the ellipsoid and rotating the trapping potential instead such that

$$U(\mathbf{r}) = \frac{m}{2}\mathbf{r^T R^{-1}} \begin{pmatrix} \omega_x^2 & 0 & 0 \\ 0 & \omega_y^2 & 0 \\ 0 & 0 & \omega_z^2 \end{pmatrix} \mathbf{Rr} \tag{6.38}$$

where we defined the associated rotation matrix $\mathbf{R}$. Using the TF ansatz and considering 'charged' elliptical homeoid shells [362], it is possible to show that the coefficients of the $\phi(\mathbf{r})$ potential are given by

$$\phi_i = \frac{\mathcal{N}}{2}\frac{\partial}{\partial R_i^2} I \tag{6.39}$$

$$\phi_{ij} = \begin{cases} \dfrac{\mathcal{N}}{6}\dfrac{\partial^2}{\partial^2 R_i^2} I & i = j \\ \mathcal{N}\dfrac{\partial^2}{\partial R_i^2 \partial R_j^2} I & i \neq j \end{cases} \tag{6.40}$$

where $\mathcal{N} = \rho_0 R_x R_y R_z = 15N_0/8\pi$ and I is defined via the following integral equation

$$I(R_x, R_y, R_z) = \int_0^\infty \frac{d\sigma}{\sqrt{(R_x^2+\sigma)(R_y^2+\sigma)(R_z^2+\sigma)}} \, . \tag{6.41}$$

Plugging these coefficients into equation 6.35 and requiring that the chemical potential of equation 6.33 has no spatial dependence leads to an equation for the TF radii R_i as well as for the components of the rotation matrix $\mathbf{R}$. These are, in general, not analytic although for the special case of a cylindrically symmetric, cigar trap with dipoles oriented along the symmetry axis, an analytic solution exists and is presented in reference [360]. Interestingly, regardless of the dipole orientation and the trap shape, the radii scale as $N_0^{1/5}$ i.e. identically to the pure contact interaction result 2.60

As for the potential outside of the BEC ellipsoid, equations 6.35, 6.39 and 6.40 still hold (with $n_0(\mathbf{r}) = 0$). However, integral 6.41 has to be adjusted to account for the lack of charged 'shells' outside of the BEC

$$I(R_x, R_y, R_z, \lambda) = \int_{\lambda(\mathbf{r})}^\infty \frac{d\sigma}{\sqrt{(R_x^2+\sigma)(R_y^2+\sigma)(R_z^2+\sigma)}} \, . \tag{6.42}$$

with λ defined by the elliptical surface passing through the point $\mathbf{r} = (x, y, z)$ and confocal with the elliptical BEC

$$\frac{x^2}{R_x^2+\lambda} + \frac{y^2}{R_y^2+\lambda} + \frac{z^2}{R_z^2+\lambda} = 1 \, . \tag{6.43}$$

Within the Hartree-Fock approximation, the effective potential experienced by the

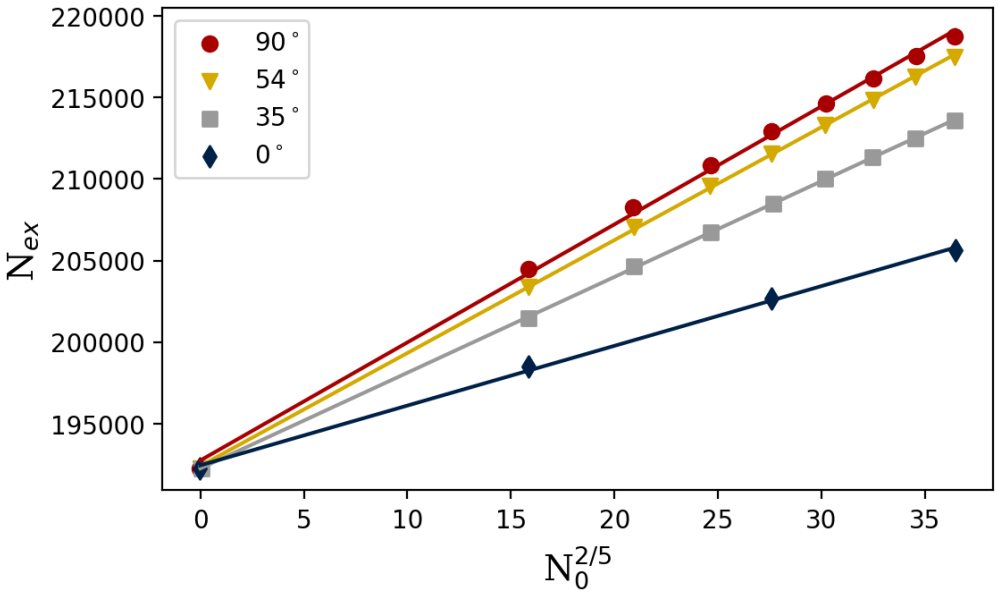


Figure 6.5: Dipolar non-saturation. Numerically calculated number of thermal excitations, N_{ex}, plotted against the BEC atom number to the power of two fifths, $N_0^{2/5}$, for various dipole polarization angles in the $z-y$ plane with respect to the z axis. We see that the linear trend of equation 6.32 is preserved even after the addition of the long-ranged, anisotropic DDI. Numerical calculations were performed with following trap parameters– $\boldsymbol{\omega} = 2\pi \times (333,\ 42.3,\ 257)\ \text{rad}\,\text{s}^{-1}$, $a_s = 72.5\,\text{a}_0$.

thermal gas then reads as

$$V_{\text{eff}}(\mathbf{r}) = U(\mathbf{r}) + 2gn_0(\mathbf{r}) + \Phi_{dd}(\mathbf{r}, 2n_0(\mathbf{r})) \tag{6.44}$$

where we explicitly included the dependence of the mean field dipolar potential Φ_{dd} on the density distribution of the dipolar BEC and we have included a factor of 2 arising from bosonic exchange symmetry (much like in the case of contact interactions). When substituted into equation 6.27, the effective potential together with the adjusted chemical potential and TF radii can be used to numerically calculate the number of thermally excited states.

My colleague Dr Milan Krstajić performed calculations of the critical thermal atom number in the presence of the DDI for various BEC atom numbers, trap shapes and dipole polarization angles. Figure 6.5 shows a subset of these calculations for $a_s = 72.5\,\text{a}_0$ and $\boldsymbol{\omega} = 2\pi \times (333,\ 42.3,\ 257)\ \text{rad}\,\text{s}^{-1}$. The number of excited thermal states N_{ex} is plotted against the BEC atom number raised to the power of two fifths, $N_0^{2/5}$, and a linear trend is recovered as is the case for purely contact interactions (equation 6.32). These results confirm that the non-saturation in the presence of the DDI still follows the same scaling but now with an angle-dependent constant of proportionality, allowing us to extract the critical atom number N_c at the transition point from linear fits to our data.

6.3 Experimental design

Measuring the critical temperature and/or atom number shift directly is difficult for two reasons. Firstly, there are several sources of instability in the experiment, ranging from temperature, pressure and polarization drifts to electronic noise and vibrations. Combined, these make it particularly hard to repeatedly and reproducibly prepare an atomic sample exactly at the critical point. Secondly, in typical absorption image measurements, the onset of condensation is heralded by the formation of a bimodal density distribution. For small BEC atom numbers, i.e. near the critical point, the BEC density distribution is screened by the thermal cloud, making it difficult to detect and therefore recognize criticality.

What we can do instead is to measure the (non-saturated) thermal atom number for various BEC sizes and extrapolate its $N_0^{2/5}$ dependence demonstrated in section 6.2 to $N_0 = 0$ to obtain the value of the critical atom number $N_c(N_0 = 0)$. That way, we reduce the experimental uncertainty by effectively averaging over a much larger set of data points, most of which don't actually correspond to the critical number but carry the information about its value nonetheless.

A disadvantage of this technique is the fact that all measurements should be performed at a particular temperature and in a fixed trap, both of which need to stay constant throughout the measurement series. Only then is the scaling of N_c linear in $N_0^{2/5}$ (see equation 6.32 and figure 6.5). As alluded to in the previous section, changing the BEC atom number at will is not an easy task and even less so while trying to keep the temperature and the trap unchanged. Fortunately, rather than gradually increasing the condensed fraction e.g. by evaporating to lower trap depths, we can instead utilize (density-dependent) losses (see chapter 5) to lower the BEC atom number by simply holding the partially condensed gas in a fixed trap for variable amount of time.

This approach to crossing the critical point comes with a small caveat. The losses that help us vary the BEC atom number also heat up the trapped gas, invalidating our assumption of constant temperature. To overcome this last hurdle, we empirically choose the final trap parameters in such a way that the residual cooling from evaporation perfectly cancels the heating from inelastic losses. In summary, all we have to do is prepare a partially condensed sample in a suitably chosen trap. We then wait for long enough time such that the BEC completely disappears to make sure that we cross the critical point. Finally, we record the BEC and thermal cloud atom numbers along the way as well as the temperature of the sample and recover the critical atom number $N_c(0)$ from a linear fit of $N_c(N_0)$ to $N_0^{2/5}$.

In this section, we will first briefly describe the experimental sequence for performing the dipolar T_c shift measurements. We will then outline our procedure for fitting absorption images used to extract the thermal gas and BEC atom numbers and temperatures. Lastly, we will discuss the importance of accurate temperature measurements and how we correct for systematic errors introduced by interparticle interactions.

6.3.1 The Sequence

The majority of the sequence follows the same steps as described in section 4.3.1. During the last stage of forced evaporation in our crossed-beam optical dipole trap (ODT), the ramp down of the trapping beam power is suddenly stopped. At this point, we usually have $N_0 \approx 2.5 \times 10^4$ atoms in the condensate and $N_{\text{ex}} \approx 2.3 \times 10^5$ thermally excited atoms at a temperature of $T \approx 200\,\text{nK}$ with the dipoles oriented along the vertical z axis.

Next, the dipoles are rotated in the zy-plane to make an angle $\pi/2 - \theta$ with the vertical z axis. Note that the y direction is along the ODT1 beam and corresponds to the weakest trapping axis. An experimentally determined scaling factor is applied to the powers of the two trapping beams to account for the change in polarizability (and hence trap frequencies) caused by different relative orientation of the dipoles and the laser field (see section 4.1.1). After that, the powers in the two beams are simultaneously ramped to their final values. In a typical scenario, these would be $P_1 = 0.37\,\text{W}$ and $P_2 = 1.0\,\text{W}$ respectively, which result in measured trapping frequencies of $\boldsymbol{\omega} = 2\pi \times (293,\ 14.0,\ 233)\ \text{rad}\,\text{s}^{-1}$. The final trap powers are fine-tuned to give no change in temperature over several seconds of hold time. The coil currents are then also ramped to their final value, preserving the polarization angle θ and only changing the magnitude of the total magnetic field $|B|$ which determines the strength of the contact interactions through a_s (see section 2.3.4 and figure 2.9).

Finally, the atoms are held in the trap for a variable amount of time t_h, after which they are released and allowed to expand for 18 ms in the usual time-of-flight (ToF) fashion before they are imaged using our absorption imaging setup (see section 3.1.3). The hold time t_h ranges between zero and a maximum value chosen such that the BEC has entirely disappeared from the images, guaranteeing a passage through the critical point.

The entire dataset consists of BEC decay time series, each with 100+ data points and performed at several tilt angles and scattering lengths in the range $(50, 100)\ a_0$. Each data point therefore corresponds to a particular hold time t_h, BEC atom number N_0, thermal atom number N_{ex} and temperature T as well as a dipole tilt angle θ and a scattering length a_s. A typical time series for $\theta = 90°$ and $a_s = 72\,\text{a}_0$ is shown in figure 6.6.

6.3.2 Image fitting procedure

Absorption images of the atomic cloud after ToF are our main source of information and we use them to extract the relevant atom numbers as well as the temperature. Neglecting the effect of interactions for now, during ToF, the thermal cloud at or below the critical point retains its polylogarithmic shape given by equation 4.15 with the characteristic cloud size evolving according to 3.8. Moreover, the BEC too retains its shape and stays parabolic (see equation 6.37), albeit with a time-dependent aspect ratio [363].

In order to obtain accurate atom number estimates for both phases, we need to reliably extract the two distributions from an image of their overlap. Although a single bimodal fit consisting of an integrated parabola summed with a polylogarithm of a Gaussian should, in principle, match the data, in practice, such fit suffers from coupling between fitting parameters which can lead to inaccurate results. For that reason, we devised a multi-stage fitting routine based on reference [353] which treats the two phases separately by

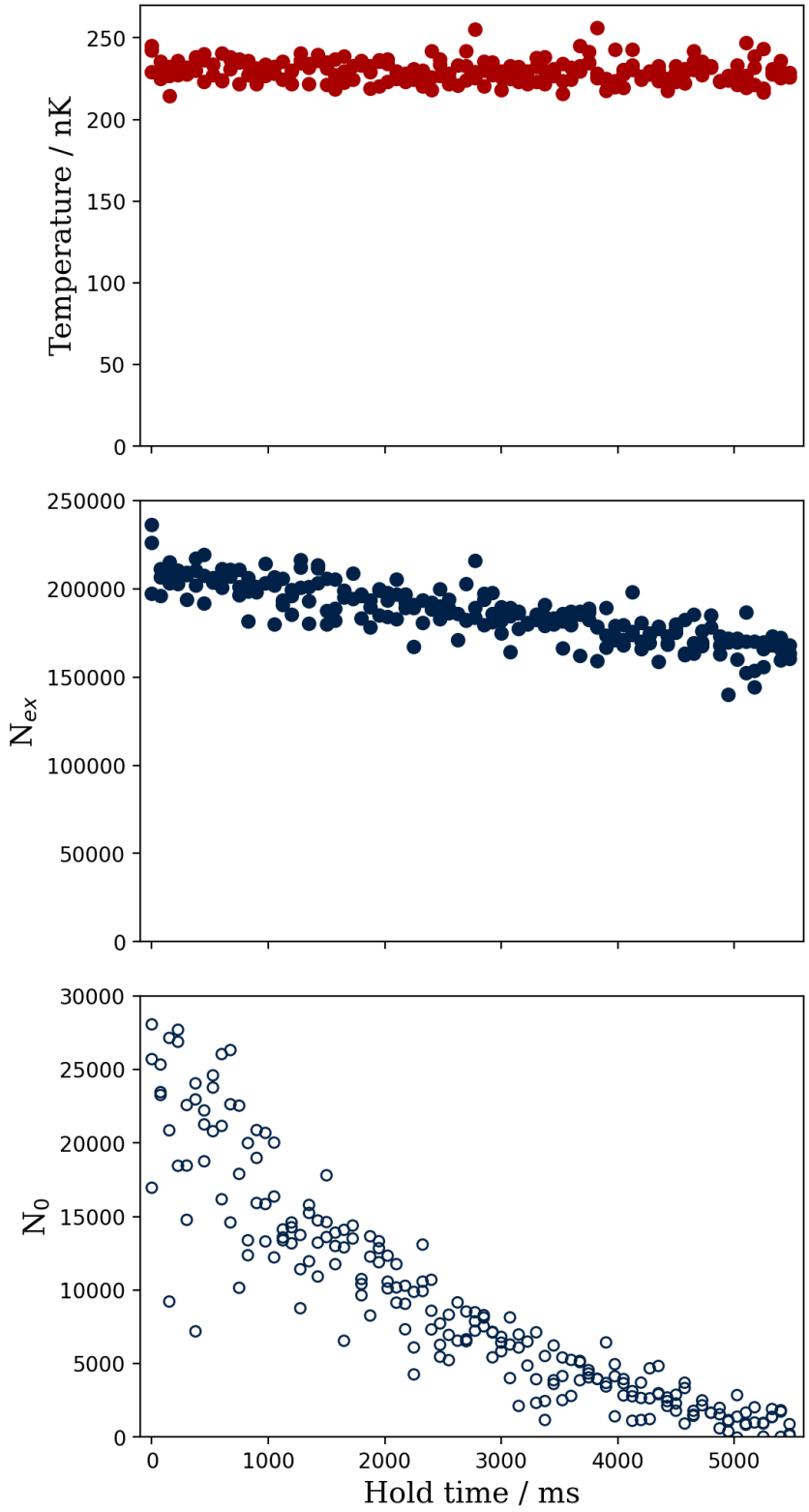


Figure 6.6: Typical dataset. T, N and N_0 as a function of the final hold time. Note that by design, the temperature remains nearly constant. The thermal atom number decreases together with the BEC atom number despite the fixed trapping potential and temperature–a clear sign of non-saturation.

masking out the relevant regions of the image. The routine itself was implemented by Dr Lucas Hofer in Python using a custom-made GPU fitting package. For more technical details, see [280]. Below, we outline the main features of the different fitting stages and discuss the rationale behind using them.

Before being subject to any fitting, the images are first cropped to a size of 300×300 pixels and processed using a fringe removal algorithm [364] to reduce fitting noise. Any obvious outliers, i.e. blank shots due to experimental failure, are manually removed. After this pre-processing stage, all images are analyzed using the following fitting routine:

1D Gaussian fits: The pixel intensity is summed along the two axes separately and each 1D profile is fitted with a simple Gaussian. The parameters of the two Gaussians are used to estimate the center of the atom cloud and the size of the thermal component.

Thermal fit–no BEC: Using the center coordinates extracted from the previous fit, we create a fixed circular mask of radius $\approx 30\,\mu\text{m}$ centered on the BEC which excludes even the largest BEC samples. We then fit an integrated 2D Bose-Enhanced density distribution given by a reduced form of equation 4.15 (see next section) to the image data outside of the masked region. Integrating the density yields a good estimate of the thermal atom number N_{ex}. Note that in this fit, we set the chemical potential μ to zero.

Thermal fit–no BEC, more tails: Once again, we mask out the BEC in the central region with a fixed mask. This time, however, the mask has a radius comparable to the characteristic size of the Bose-enhanced distribution after time-of-flight, $\sigma_{\text{th}} = t_{\text{tof}}\sqrt{k_B T/m}$. This way, we remove any bias to the fit caused by distortions of the thermal cloud close to the BEC and we recover the best possible estimate for the cloud size which is a proxy for the temperature T.

BEC fit–no Thermal: Finally, we use a similar thermal fit to the previous two stages with a variable mask depending on the BEC size. We then subtract this thermal fit from the image and sum up the remaining atoms in the center within a tighter mask, yielding an estimate of the BEC atom number N_0 (see figure 6.7).

At this point, any clear outliers in thermal or BEC atom number are filtered out by removing images that significantly deviate from a trend line fitted to the particular time series. Extra care is taken to remove clouds with zero or negative BEC atom number where the fitting routine struggled to identify a BEC density profile withing the thermal cloud. This fitting routine gives us accurate estimates of both the BEC and thermal atom numbers. As discussed in sections 3.1.3 and 4.4, in the long time-of-flight limit, the size of the cloud σ_i can be used to directly estimate the temperature as $T = m\sigma_i^2/k_B t_{\text{tof}}^2$. However, given that we are trying to measure the relative critical temperature shift on the order of a few percent, this temperature estimate isn't accurate enough and the initial size of the cloud needs to be taken into account. Furthermore, interactions between particles during ToF will distort the cloud, effectively changing the measured value as well. Since the ideal critical number $N_c^0 \propto T^3$ is proportional to the cube of the temperature, any

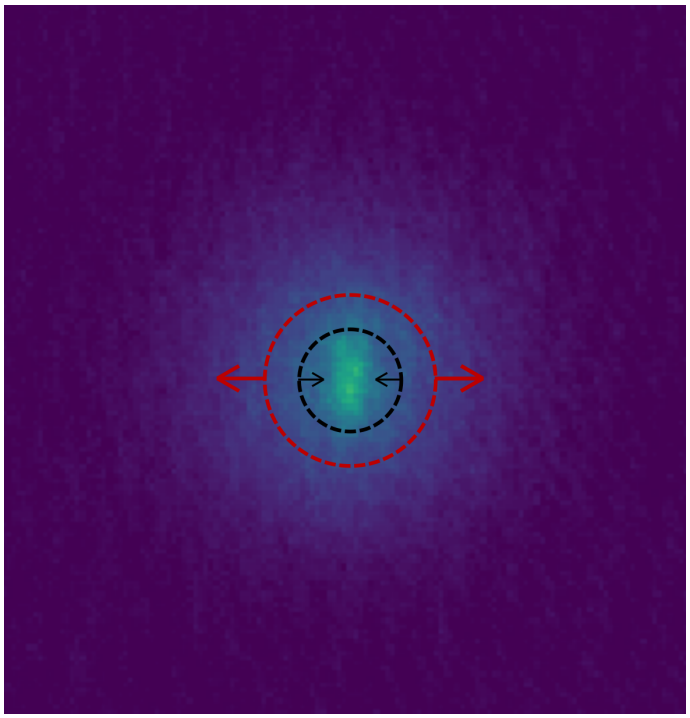


Figure 6.7: Fitting regions. To extract the thermal atom number and temperature, a 2D fit is performed on a region of the atomic cloud outside of a circular mask centered on the BEC (red dashed line). The size of the mask differs between the fits used to extract N_{ex} and T (see text). After subtracting the thermal cloud, a tighter mask (black dashed line) is used to sum up the remaining atoms which constitute the BEC to obtain N_0.

changes to the value of the relative shift $\Delta N_c/N_c^0$ due to temperature errors are tripled, stressing out the importance of the temperature measurement. In the next section, we describe how we compensate for various systematic effects to obtain the most accurate estimate of the temperature of the system.

6.3.3 Temperature corrections

In a non-interacting, harmonically trapped gas at or past the critical point, the characteristic size of the cloud evolves during time-of-flight as

$$\sigma_i^2(t) = \sigma_{0,i}^2 + \frac{k_B T}{m} t^2 \tag{6.45}$$

with the initial size $\sigma_{0,i}^2 = k_B T/m\omega_i^2$. The corresponding 2D density distribution is then given by equation 4.15 which can be further simplified for the purpose of fitting to

$$n_{2D}(x,y) = n_0 g_2 \left[e^{-\frac{x^2}{2\sigma_x^2(t)} - \frac{y^2}{2\sigma_y^2(t)}} \right] , \tag{6.46}$$

yielding the characteristic size $\sigma_i(t)$. Compared to the usual single-point time-of-flight temperature measurements where the initial size σ_0 is neglected and the temperature is simply obtained from equation 6.45 as $T = m\sigma_i^2/k_B t^2$, we can go a step further and account for σ_0. The relative magnitude of the correction to temperature obtained this way is

$\Delta T/T = (\omega_i t)^{-2}$ and ranges between 0.5% to 20% depending on the strength of trapping along the particular axis–the stronger the trapping, the less relevant the correction becomes. The correction is conditioned on our knowledge of the trapping frequencies which we know to within 3% of their actual value i.e. with a sufficient degree of accuracy (see section 4.1.3).

When interactions are taken into account, the whole picture becomes considerably more complicated. The initial density distribution is now defined self-consistently (see equation 6.13) and deviates from the ideal polylogarithmic Gaussian form so it can't be easily described by a single set of parameters $\sigma_{i,0}$. Furthermore, the non-interacting results 3.6 and 6.45 for the density distribution after expansion no longer apply because mean field forces and scattering between particles result in redistribution of momentum during ToF. Fully solving this problem i.e. mapping the final density distribution to an initial temperature is computationally demanding and would have to be done for every single data point. What we can do instead is to treat these effects as perturbations to the non-interacting regime, calculate their contributions separately and finally add them together with the knowledge that the correction obtained in this way will only be accurate to the first order in the (hopefully small) individual contributions.

We begin by rewriting equation 6.45 in terms of the initial momentum distribution as

$$\sigma_i^2(t) = \sigma_{0,i}^2 + \frac{\langle p_{0,i}^2 \rangle}{m^2} t^2 \ , \tag{6.47}$$

where we used the classical equipartition result $mk_BT = \langle p_{0,i}^2 \rangle$. Strictly speaking, in a degenerate, Bose-enhanced gas, the average momentum squared is actually given by $\langle p_{0,i}^2 \rangle = \frac{\zeta(4)}{\zeta(3)} mk_BT \approx 0.9\ mk_BT$. Equally, the second moment of the density distribution is different from the fitting parameter σ of equation 4.13 by the same factor. By fitting an integrated 2D polylogarithm (equation 4.15) directly to our data and using σ as a proxy for the second moment, we effectively account for this factor. In doing so, we introduce a 5% error to any corrections to the second moment that may arise from interaction effects. However, as we shall shortly see, these quantities are already quite small and on the order of a single percent so we can safely neglect this error.

By taking into account changes to the initial density distribution as well as dynamical effects during the expansion, we can write

$$\sigma_i^2(t) = \sigma_{0,i}^2 + \Delta\sigma_i^2 + \frac{\langle p_{0,i}^2 \rangle}{m^2} t^2 + \frac{\Delta\langle p_i^2 \rangle}{m^2} t^2 \ . \tag{6.48}$$

Equation 6.48 has a simple interpretation–the cloud starts from an initial size $\sigma_{0,i}$ and expands ballistically with velocity $v_i = \sqrt{p_{0,i}/m}$. However, due to interactions, the second moment of the initial density distribution is distorted by $\Delta\sigma_i^2$. Furthermore, interactions during the first, dense stage of the expansion redistribute momentum and convert potential energy into kinetic energy, changing the second moment of the momentum distribution by $\Delta\langle p_i^2 \rangle$. Here, we implicitly assume that interactions only affect the momentum distribution during a short period of time, after which the cloud expands in the ballistic, low-density regime in which interactions can be safely neglected.

Both correction terms in equation 6.48 can be further split into two terms–one originating from the self-interaction of the thermal gas and the other one from its interaction with the BEC. We will now consider these terms individually, starting from the momentum correction due to self-interaction.

Momentum correction–self-interaction

We closely follow reference [143] in which the authors derive the correction term for a harmonically trapped, dipolar gas above the critical point, well approximated by a Gaussian density and momentum profile. The correction can be written as

$$\Delta\langle p_i^2\rangle = \langle p_i^2\rangle_{\mathrm{MF}} + \langle p_i^2\rangle_{\mathrm{HD}} \tag{6.49}$$

The first term represents the effect of the mean-field, interaction potential on the momentum distribution, essentially describing the conversion of potential energy into kinetic energy. The authors write the term as

$$\Delta\langle p_i^2\rangle_{\mathrm{MF}} = 2N\frac{\hbar^2\bar{\omega}^3 m^{3/2}}{(k_B T)^{3/2}}\left(a_s H^{(i)} + a_{dd}H_d^{(i)} + a_s F^{(i)} + a_{dd}F_d^{(i)}\right) \tag{6.50}$$

where H, H_d, F and F_d are dimensionless constants defined by integral equations listed in appendix D that represent the contact and dipolar Hartree and Fock corrections.

The second term, designated as HD for 'hydrodynamic', arises from two-body collisions which transfer energy from 'hotter' axes to 'colder' axes. The full term is given by

$$\begin{aligned}\Delta\langle p_i^2\rangle_{\mathrm{HD}} = \; 2Nm^2a_{dd}^2\bar{\omega}^2 \Bigg\{ &\left[A_0^{(i)} + A_1^{(i)}\left(\frac{a_s}{a_{dd}}\right) + A_2^{(i)}\left(\frac{a_s}{a_{dd}}\right)^2\right] \\ &+ N\left(\frac{\hbar\bar{\omega}}{k_B T}\right)^3\left[B_0^{(i)} + B_1^{(i)}\left(\frac{a_s}{a_{dd}}\right) + B_2^{(i)}\left(\frac{a_s}{a_{dd}}\right)^2\right]\end{aligned} \tag{6.51}$$

with A_j and B_j being, once again, dimensionless constants that only depend on the trapping geometry and the dipole orientation (see appendix D).

We calculate the constant factors in equations 6.50 and 6.51 numerically using our experimental parameters. Furthermore, to account for the effects of Bose enhancement near criticality which were assumed negligible in the original manuscript, we replace all instances of $\bar{\omega}$ in equations 6.50 and 6.51 with an adjusted frequency $\tilde{\omega}$. The role of this adjusted frequency is to scale the peak phase-space density of the Gaussian distribution to its (correct) critical value, $\rho_c = \zeta(3/2)$. In other words, we chose $\tilde{\omega}$ such that, for a given (measured) particle number $N \approx N_c^0$, we have

$$\zeta\left(\frac{3}{2}\right) = N\left(\frac{\hbar\tilde{\omega}}{k_B T}\right)^3 \approx \zeta(3)\left(\frac{\tilde{\omega}}{\bar{\omega}}\right)^3 . \tag{6.52}$$

This approach is essentially equivalent to increasing the density of the gas on the account of Bose enhancement, emphasizing the central role of density (as opposed to the cloud shape) in both the mean-field effects and two-body collisions.

Momentum correction–BEC

The second correction to the momentum distribution comes from the interaction between the thermal gas and the BEC. Rather than trying to derive a semi-analytic expression, we use the effective potential 6.44 experienced by the thermal gas to simulate its expansion dynamics during ToF in the presence of a BEC.

In a single simulation run, 10 000 test particles are initialized in a harmonic trap with their positions and momenta sampled from the respective Gaussian distributions at an initial temperature T_0. For a given scattering length a_s, dipolar tilt angle $\theta = 0°$ or $90°$ and BEC number N_0, the initial Thomas-Fermi radii $R_{0,i}$ are calculated. The system is then numerically propagated in time using the velocity Verlet algorithm [365] with forces given by the gradient of the effective potential. The potential is, in return, fully defined by the shape and size of the BEC.

However, the BEC itself changes shape during its free-space expansion and so the potential has to be recalculated at each time-step. Following references [195] and [363], the time-dependence of the TF radii can be written as

$$R_i(t) = R_{0,i} b_i(t) \tag{6.53}$$

with $b_i(0) = 1$ and $\dot{b}_i(0) = 0$, i.e. the condensate remains parabolic but its aspect ratio changes during the expansion. For purely contact interactions, the coefficients $b_i(t)$ evolve in time according to [195]

$$\ddot{b}_i(t) = \frac{\omega_i^2}{b_i b_x b_y b_z} \ . \tag{6.54}$$

For a dipolar gas, a similar analytic expression exists if the dipoles are aligned along the x axis and it is given by [363]

$$\ddot{b}_i(t) = \frac{\tilde{\omega}_i^2}{b_i b_x b_y b_z} \left[1 - \varepsilon_{dd} \Omega(R_{0,x}, R_{0,y}, R_{0,z}, b_x, b_y, b_z)\right] \tag{6.55}$$

with $\tilde{\omega}_i^2 = 15 N_0 \hbar^2 a_s / (m^2 R_{0,i}^2 R_{0,x} R_{0,y} R_{0,z})$ and $\Omega(\vec{R_0}, \vec{b})$ an analytic function involving elliptic integrals of the first and second kind and their first derivatives. Numerically solving this set of three coupled differential equations yields the BEC radii at an arbitrary point in time and hence the full effective potential. We note that since equation(s) 6.55 only apply to the case of dipoles polarized along the x axis, we can only use it to simulate expansion of the BEC for $\theta = 0°$ or $90°$ (after appropriate relabeling of the axes). This is sufficient for measuring the maximum differential dipolar T_c shift $\Delta T_c/T_c^0|_{\theta=0°} - \Delta T_c/T_c^0|_{\theta=90°}$ but more numerical work will have to be done to expand the temperature correction to intermediate angles θ.

To obtain the correction $\Delta\langle p_i^2\rangle_{\mathrm{BEC}}$ to the momentum distribution, we evolve the simulated particles for a time $t = t_{\mathrm{tof}}$, after which we numerically calculate the second moment of their momentum distribution in the three orthogonal directions, $\langle p_i^2(t)\rangle$, and subtract it from the same quantity calculated right after their initialization, i.e. $\langle p_i^2(0)\rangle$. We perform the simulation for a range of BEC atom numbers $N_0 \in (0, 50\,000)$, for the two dipole ori-

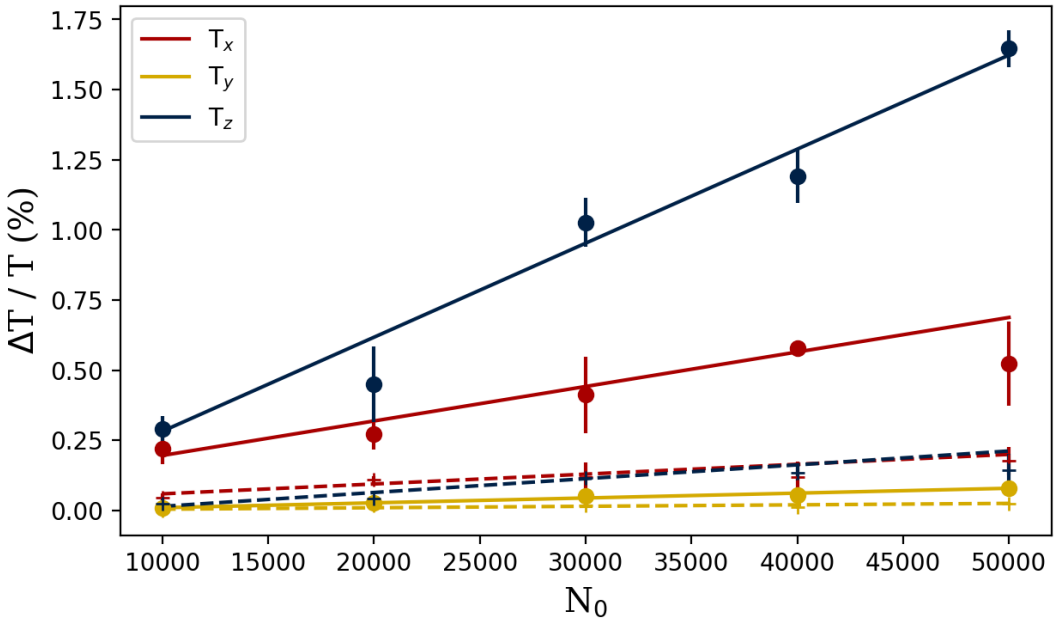


Figure 6.8: Effect of a BEC on thermal cloud expansion. Relative temperature increase along the three orthogonal directions due to the BEC-thermal interaction as measured from the momentum spread after time-of-flight. In this regime, the temperature grows approximately linearly with the BEC atom number and affects mostly the strong trapping axes (x and z). Data taken at $a_s = 72\,\mathrm{a_0}$ and $\theta = 90°$ (full lines) and $\theta = 0°$ (dashed lines).

entations $\theta = 0°,\ 90°$ and for a range of scattering lengths $a_s \in (70, 130)a_0$. Additionally, for each set of parameters N_0, θ and a_s, the simulation is performed 10 times and the result is averaged to mitigate the error introduced by random initialization of the simulated particles.

The results for $\theta = 0,\ 90°$, $a_s = 72\,\mathrm{a_0}$ and for a range of BEC atom numbers N_0 are shown in figure 6.8. The data suggests a linear trend with BEC atom number which was consistent across all the scattering lengths and polarization angles used in our simulations (albeit with variable slopes). We therefore extracted the linear fitting parameters for different a_s and θ and extrapolated between those values to apply the momentum correction across our whole experimental dataset.

Initial size corrections

Mutual interactions between the thermally excited atoms as well as their interactions with the BEC will distort the initial density distribution. Considering only contact interactions for the moment, their effect will be two-fold. Firstly, the self interaction of the thermal cloud will inevitably lead to its inflation. The peak phase-space density will remain constant, matching the local condensation criterion 2.45, but the distribution will become broader [353] such that $\Delta\sigma^2 > 0$. After all, this is precisely the same effect that increases the critical atom number N_c compared to the non-interacting value, N_c^0, given by equation 2.47.

Secondly, the addition of the BEC will, on one hand, push the atoms away from the

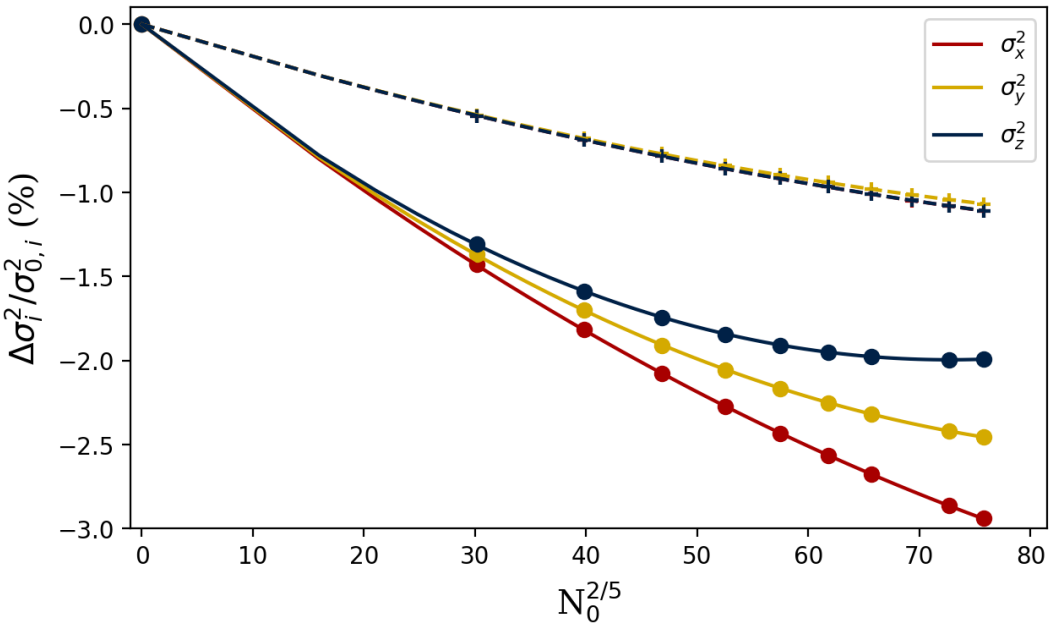


Figure 6.9: Effect of a BEC on initial size. The relative change of the second moment of the thermal cloud density distribution in the three orthogonal directions as a function of the BEC atom number raised to two fifths. For small BECs, the thermal cloud slightly contracts since the high density region (corresponding to $V_{\text{eff}} - \mu = 0$) is mainly concentrated around the bottom of the trap. As the BEC grows, this region (i.e. the edge of the BEC) gets pushed out, increasing the second moment. Data taken at $a_s = 72\,\text{a}_0$ and $\theta = 90°$ (full lines) and $\theta = 0°$ (dashed lines). Note that the data is well fitted by a curve of the functional form $aN_0^{2/5} + bN_0^{4/5}$ i.e. quadratic in $N_0^{2/5}$.

overlap region but, on the other hand, it will also create a large surface at its boundary corresponding to the condensation condition $V_{\text{eff}} - \mu = 0$. Consequently, for intermediate size BECs, thermal atoms actually aggregate close to the bottom of the trap, reducing the thermal cloud width, i.e. $\Delta\sigma^2 < 0$. As we add more atoms to the BEC, the TF radii become comparable or larger than the non-interacting equilibrium extent of the cloud, σ_0, resulting in an actual increase in size $\Delta\sigma^2 > 0$. Since we only ever prepare atomic samples close to the critical point, we usually operate in the small to intermediate BEC regime where the thermal cloud size is reduced compared to the non-interacting case. This is also confirmed by our calculations (see below).

Utilizing our previous calculations of the full effective potential including the DDI, we numerically estimate the relative change of the second moment of the density distribution, $\Delta\sigma^2/\sigma_0^2$, due to the presence of the BEC for various BEC sizes, dipole polarization angles and scattering lengths. A sample dataset for $a_s = 72\,\text{a}_0$ and for both dipole orientations is shown in figure 6.9. We clearly see the reduction in size for small to intermediate BECs, followed by a gradual increase as discussed above.

Performing similar calculations to account for the thermal gas self-interaction is more involved because the mean field potential of a magnetized Gaussian and/or Bose-enhanced cloud lacks a semi-analytic form. Instead, we reason that applying *any* corrections to the initial size due to interactions (be it self-interactions or the thermal-BEC ones) is

unnecessary and only results in second order adjustments. Firstly, this is because the two contributions, i.e. self-interactions and thermal-BEC interactions, have opposite effects and work to cancel each other out. Given that the magnitude of the latter contribution is on the order of a single percent as confirmed by our calculations, their difference will most likely be even smaller.

Secondly and more importantly, as discussed at the beginning of this section, the effects of the initial size on the measured temperature are suppressed by a factor of $(\omega_i t_{\mathrm{tof}})^{-2}$. For the weak trapping axis, this factor is already quite small and equal to ≈ 0.2 whereas for the strong trapping axes, it can be as low as ≈ 0.005. With this in mind, we decided to use the cloud size along the strong trapping axis (z) to estimate the initial temperature for all our data points.

We do this by using the measured value $\sigma_z(t)$ in combination with equation 6.48 and the two corrections to the momentum distribution as discussed above but omitting any alterations to the initial size $\Delta\sigma_z^2$. Note that because the momentum corrections themselves are a function of temperature, we need to solve equation 6.48 numerically to obtain the best estimate for the initial temperature T. We are aware that in applying these corrections, we neglect any scattering between the thermally excited atoms and the BEC and only taken into account mean field interactions. However, as supported by our data, we believe this to have negligible effect on the measured temperature.

6.4 Results

Armed with accurate estimates of the thermal atom number N_{ex}, BEC atom number N_0 and temperature T of the thermal cloud at different stages of condensation, we can finally measure the effect of the anisotropic DDI on the critical point.

We do this by plotting N_{ex}/N_c^0 against $(N_0/N_c^0)^{2/5}$ where $N_{\mathrm{ex}} = N_c(N_0)$ is the non-saturated thermal atom number. The normalization by the ideal critical value N_c^0 ensures that the y intercept of the fitted line is equal to $1 + \Delta N_c/N_c^0$ i.e. to the the relative shift in the critical atom number. Furthermore, it follows from equation 6.32 that the slope of the normalized trend line is proportional to $(T/\bar{\omega})^{1/5}$ and so any fluctuations in trap parameters and/or temperature reflect only minimally on the extracted parameters of the fit.

Additionally, to combat any long term drifts inherently present in such large datasets taken over several hours or even days, we designated a reference dataset corresponding to parameters $a_s = 72\,\mathrm{a_0}$, $\theta = 90°$. For each time series at a given a_s and θ, a calibration dataset with $a_s = 72\,\mathrm{a_0}$ and $\theta = 90°$ was taken at the same time. The results of this calibration measurement were compared with the original reference dataset and the accompanying (a_s, θ) time series was calibrated accordingly. In doing so, we compensate for temporal drifts in the trap and/or imaging parameters (subject to any uncertainties present in the reference dataset).

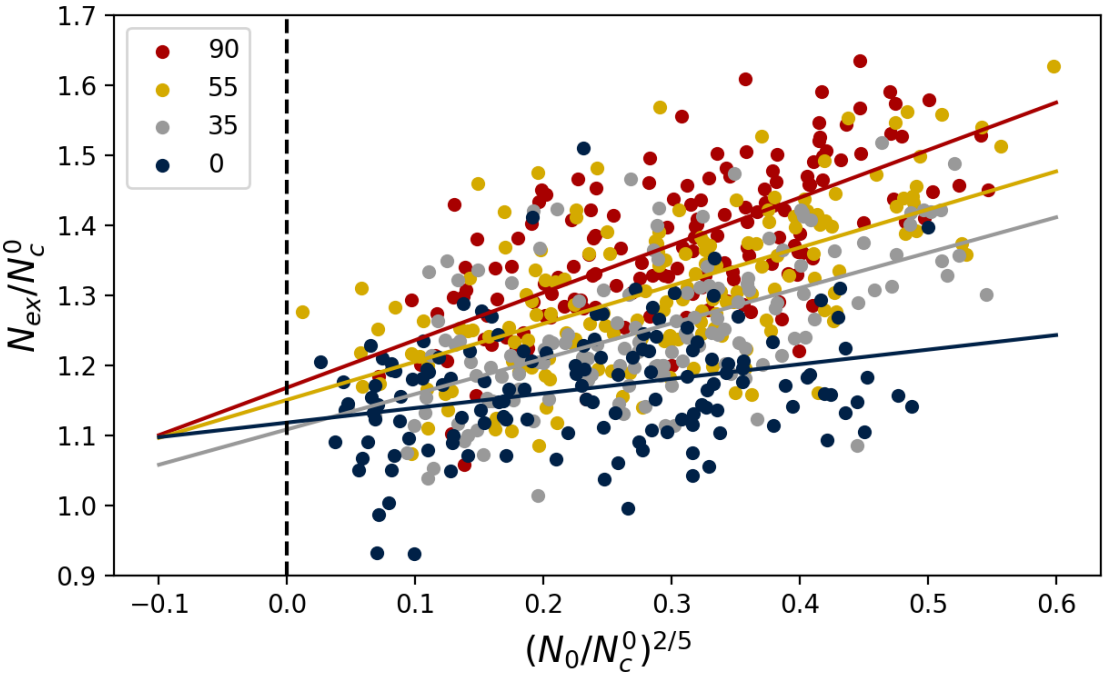


Figure 6.10: Non-saturation and N_c shift for different θ. Normalized non-saturated thermal atom number plotted against normalized BEC atom number raised to 2/5 for different dipole tilt angles with respect to the weak trapping axis of our cigar-shaped trap. Extrapolating the linear trend to $N_0 = 0$ allows us to estimate the critical atom number N_c and its shift with respect to the ideal value N_c^0. Data corresponds to $a_s = 72\,a_0$.

6.4.1 Dipolar T_c shift and non-saturation

Figure 6.10 shows the reference dataset with $a_s = 72\,a_0$ plotted in this way for several dipole tilt angles θ. A difference in the y intercepts points to a critical number shift that depends on θ–a distinct feature of the dipolar T_c shift as predicted by equation 6.24. Keeping in mind the conversion between the relative shift in critical temperature and atom number (equation 6.4) and neglecting the finite size correction and trap imperfections (see sections 6.1.1 and 6.1.2), the theoretical y intercepts are given by

$$\frac{\Delta N_c(\theta)}{N_c^0} \approx 10.278 \frac{1}{\Lambda}\left(a_s - a_{dd}\frac{3\cos\theta - 1}{4}\right) \tag{6.56}$$

where we assumed that our trap is highly anisotropic such that $f(\omega_\parallel/\omega_\perp) \approx 1$.

For a given scattering length, the differential shift between $\theta = 0°$ and $\theta = 90°$ is independent of a_s and given by

$$\frac{\Delta N_c(90°) - \Delta N_c(0°)}{N_c^0} = \delta N_c^{(90,0)} \approx 7.709\frac{a_{dd}}{\Lambda} \tag{6.57}$$

which, for the specific case of the dataset depicted in figure 6.10, evaluates to $\delta N_c^{(90,0)} \approx 9.5\%$. The experimental value extracted from the fitted intercepts is equal to $\delta N_{c,\mathrm{fit}}^{(90,0)} = 5.0 \pm 2.3\%$ which is plausibly close to the theoretical one, albeit suffering from considerable uncertainty. Additionally, we observe a clear separation of the datasets corresponding to

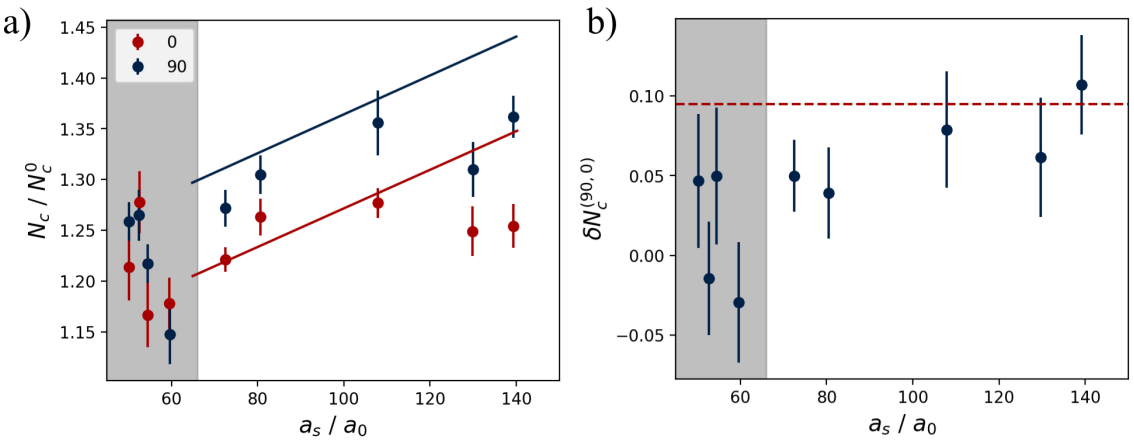


Figure 6.11: Critical point shift vs a_s. a) Normalized critical number N_c as a function of the s-wave scattering length. Despite deviating from the theoretical trend lines (full lines), the data shows a clear dependence of the critical number on the dipole polarization angle. b) Differential dipolar critical number shift vs a_s. For $\varepsilon_{dd} < 1$, the data is consistent with the predicted constant value of $\approx 9.5\,\%$ (red dashed line). However, for $\varepsilon_{dd} > 1$ (shaded region), the data deviates.

different values of θ and their approximate linear scaling, demonstrating that the non-saturation of the thermal gas and its dependence on the tilt angle is in close correspondence with the numerical and theoretical results discussed in sections 6.2 and 6.2.1.

6.4.2 Dependence on contact interactions

We can extend our analysis to other datasets corresponding to different values of the scattering length, a_s. Equation 6.56 predicts that plotting the normalized critical number N_c/N_c^0 against the scattering length for $\theta = 0°$ and $\theta = 90°$ should result in two parallel lines with their slope equal to $10.278/\Lambda$ and separated by $\delta N_c^{(90,0)} \approx 9.5\%$. Figure 6.11a shows this plot for our data in the range $a_s = (50, 140)a_0$. We see a clear separation corresponding to the two values of θ and an increasing trend in accordance with the predicted slope. We note that for high values of a_s, the contact interaction shift is expected to deviate from expression 6.19 and become lower [77], [355]. Similarly, the theoretical result 6.22 for the dipolar shift is not applicable for $\varepsilon_{dd} > 1$ or equally for $a_s < a_{dd} \approx 66\,a_0$ (gray shaded region). Both of these facts partially explain the deviation of our data from the expected lines. Another source of systematic error comes from our lack of knowledge of the so called 'fudge factor' related to the calibration of our imaging system. This essentially amounts to scaling the measured atom number by a constant (unknown) factor which is usually in the range 1.0–1.5.

The differential dipolar shift $\delta N_{c,\mathrm{fit}}^{(90,0)}$ can be easily extracted from the data and is plotted against a_s in figure 6.11b. Our measurements are consistent with the predicted constant value of $9.5\,\%$ (red dashed line) in the $\varepsilon_{dd} < 1$ region. For highly dipolar gases with $\varepsilon_{dd} > 1$, the shift seems to vanish. A natural next step would be to further investigate this highly dipolar regime in which quantum droplets are predicted to form and to shed more light on how their structure and spatial organization affects the non-saturation of

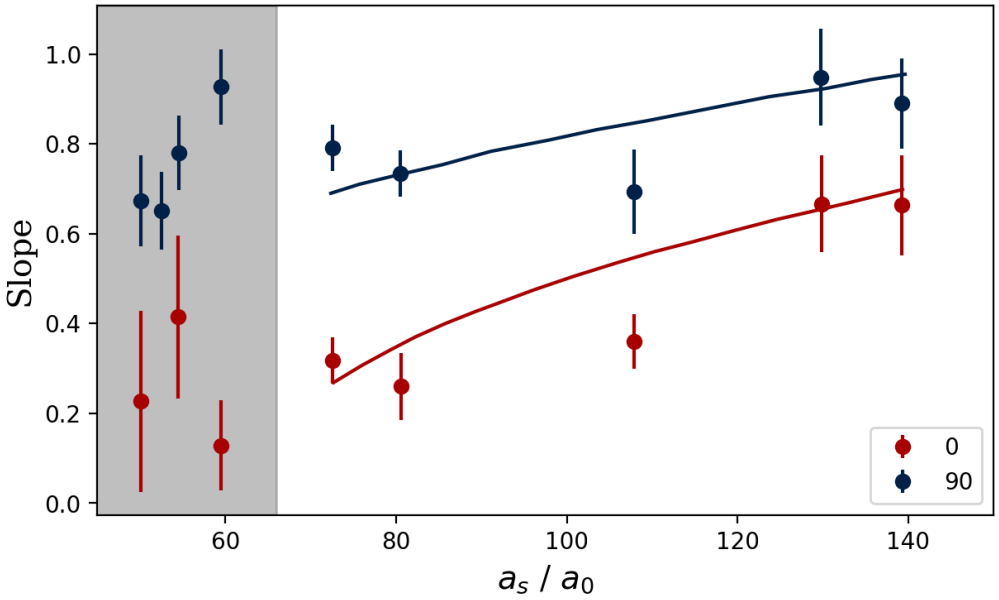


Figure 6.12: Non-saturation slopes vs a_s. The slopes of the lines fitted to the N_{ex} vs $N_0^{2/5}$ plots (see figure 6.10) for different scattering lengths and for the two extremal dipole tilt angles. The data agrees well with numerical simulations (full lines) outside of the strongly dipolar regime (grey region) in which the simulations are no longer valid.

the thermal gas.

Additionally, we can compare the extracted slopes of the non-saturation lines (see figure 6.10) with the ones predicted using our numerical calculations (see section 6.2.1 and figure 6.5) for different scattering lengths and tilt angles. This is shown in figure 6.12. Once again, our data replicates the predicted trends for $\varepsilon_{dd} < 1$ and shows a clear dependence of the thermal gas non-saturation on the dipolar angle.

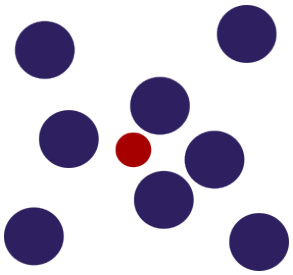
6.4.3 Conclusion

In this chapter, we demonstrated our successful measurement of the critical number (and hence temperature) shift in ^{166}Er due to the long-ranged, anisotropic dipole-dipole interactions. Our measurements are consistent with the existing theory [350], [351] and with our numerical calculations for the dipolar non-saturation effect. The data is in good agreement across a range of scattering lengths and only deviates from predictions when $\varepsilon_{dd} > 1$, i.e. when the gas enters a strongly dipolar regime, opening up possible avenues for future research. Higher resolution measurements will be needed to confirm the cosine dependence of the shift on the dipole tilt angle. Other trap geometries could also be explored to study the influence of constrained dimensionality on this phenomenon.

Part II

Potassium

7. Potassium–an impurity



One of the ultimate goals of the Oxford experiment is to study mixture physics, focusing predominantly on impurities submerged in a dipolar condensate. As was outlined in the introduction to this thesis, ultracold mixtures can be realized in several ways. The slightly simpler approach that doesn't necessitate use of much additional equipment and experimental techniques utilizes the internal states of an already trapped and cooled gas to create a quantum mixture of atoms in different spin states. Although suitable for studying various phenomena such as spin relaxation, correlations, thermalization dynamics or topology [366], this approach lacks the characteristic features of a true mixture such as mass imbalance or distinct quantum statistics of the two species. In order to create a true mixture, one has to (not surprisingly) mix two different atomic species. Due to considerable differences in their electronic structure, this often requires two completely separate cooling routines which naturally comes with its set of challenges. Nevertheless, this is the approach adopted in our group.

The role of the impurity in the Oxford experiment is played by potassium (K). This part of the thesis focuses on the early stages of introducing potassium to the main vacuum chamber and producing first erbium-potassium mixtures. This chapter describes atomic properties of potassium and our motivation behind choosing it as the impurity species. It outlines the laser cooling techniques that are needed to create ultracold clouds of potassium prior to mixing with erbium and details our optical setup used to produce light of appropriate wavelengths and powers. The second chapter in this part then focuses on our implementation of a 2D+ MOT [159], [367] which serves as a steady source of cold potassium atoms. These can then be loaded into a 3D MOT in the main vacuum chamber and mixed with erbium in a dual species dipole trap. Subsequent evaporation and transport will finally lead to a quasi-2D, homogeneously trapped erbium BEC with low-density potassium content–an ideal platform for studying impurities submerged in a dipolar bath. For more details on our planned impurity experiments see section 9.1.2.

Isotope	^{39}K	^{40}K	^{41}K
Statistics	boson	fermion	boson
Abundance	93.26%	0.01%	6.73%

Table 7.1: Stable isotopes of potassium. Relative abundances and corresponding quantum statistics of the stable isotopes of potassium. This work and the Oxford experiment in general concerns with ^{41}K (and potentially ^{39}K).

7.1 Why potassium? Everyone likes vanilla

Before we can discuss any technical details of the cooling procedure, it is beneficial to review the atomic properties of potassium. As we will shortly see, its relatively simple, hydrogen-like electronic structure makes the search for suitable cooling transitions easier than in the case of lanthanides (see section 2.2.1). However, that is not to say that the cooling scheme itself is simpler too. In fact, the small hyperfine splitting of potassium levels and the absence of closed transitions necessitates the use of additional repumping beams, doubling the amount of optics and laser light needed to reach ultracold temperatures.

Despite this added complexity, alkalis have been at the forefront of the field since its conception. The first degenerate phases were those of rubidium [7] and cesium [8] and they paved the way for two decades of discoveries made with alkali species. Inevitably, this also lead to a build-up of experimental know-how related to the group I elements.

Our choice of potassium as the impurity is partially motivated by its well established role in the cold atom community combined with our prior experience with working with this element. Another practical consideration that played a role in the decision process was the lack of space on the experimental table which disqualified any species that require Zeeman slowing as the first cooling stage. Fortunately, potassium has a relatively high vapour pressure at slightly elevated temperatures and it can therefore be loaded into a magneto-optical trap straight from a background vapour. Additionally, it has a rich Feshbach resonance spectrum [154], [368], allowing for flexibility in tuning the K-K scattering properties and pointing towards suitable Er-K interspecies resonances [156] that could be utilized to tune the bath-impurity interactions.

Lastly, potassium has two stable bosonic isotopes–^{39}K and ^{41}K–and one stable fermionic isotope–^{40}K–as can be seen in table 7.1. All of these isotopes have been previously cooled to quantum degeneracy [369]–[371] using a range of techniques. Our initial plan is to work with ^{41}K due to its favourable scattering properties at low magnetic fields [154], [368], but the optical system has been designed to allow for straightforward switching to ^{39}K should the need arise.

7.2 The atom

In its pure form, potassium is a pale, silvery metal that is easy to cut with a knife. When exposed to air, it readily reacts with oxygen to form white potassium peroxide. When combined with water, potassium forms potassium hydroxide in an exothermic reaction

which can subsequently ignite the hydrogen gas that forms as a byproduct of this reaction[1]. Consequently, in nature, it only occurs in ionic salts or as a constituent of other minerals.

The name potassium derives from the words 'pot ash' since the primary method of extracting potassium in the past was to use water to dissolve potassium salts left over after burning plants. In the modern days, potassium is predominantly obtained from mining salt deposits from the bottom of ancient seabeds and lakes. As the original method of extraction suggests, potassium (together with its sister element sodium) plays an important role in living organisms, serving as a signal carrier in nerve cells and pathways. Even though classified as a stable isotope, ^{40}K is the most common radioactive isotope in human body.

7.2.1 Electronic structure

From a physical point of view, potassium with its atomic number $Z = 19$ is classified as an alkali metal element. These, together with hydrogen, form the group I elements of the periodic table and share the same hydrogen-like electronic structure with only one valence electron. Using the noble gas notation, the electron configuration of potassium can be written as

$$[Ar]\ 4s^1. \tag{7.1}$$

The fact that potassium has only one valence electron greatly simplifies its level structure. In the ground state, the valence electron occupies the $4s$ orbital with corresponding total orbital angular momentum of $L = 0$. Being a spin 1/2 particle, it also naturally follows that the total spin angular momentum is $S = 1/2$. Spin-orbit interaction couples the orbital and spin angular momenta into the total angular momentum $J = L + S$, giving the fine structure level of the ground state as $^2S_{1/2}$, where we used the standard spectroscopic notation $^{2S+1}L_J$.

When it comes to excited states, the most relevant ones correspond to the $4s$ to $4p$ transition. The single electron in the $4p$ orbital has orbital angular momentum of $L = 1$ and it retains its spin of $S = 1/2$. This results in two fine structure levels $^2P_{3/2}$ and $2P_{1/2}$ with the former being higher in energy than the latter according to Hund's third rule (see section 2.2.1). The transition from the ground state to the lower of the two excited states ($^2S_{1/2} \rightarrow 2P_{1/2}$) corresponds to a wavelength of $\lambda_{D1} = 770\,\text{nm}$ and is known as the D1 line. The other transition ($^2S_{1/2} \rightarrow 2P_{3/2}$) with $\lambda_{D2} = 767\,\text{nm}$ is know as the D2 line. Note that thanks to their shared electronic structure, D1 and D2 lines are common to all group I elements (albeit with different wavelengths).

Unlike in the case of erbium, the two bosonic isotopes of potassium, ^{39}K and ^{41}K, have nuclear spin of $I = 3/2$. Consequently, both isotopes have hyperfine structure and so the fine structure levels split further according to their total angular momentum $F = J + I$ as a result of the electron spin - nuclear spin interaction. The ground state and the $2P_{1/2}$ excited state therefore split into two hyperfine levels with $F = 1, 2$ whereas the $2P_{3/2}$ state

[1] It is highly advisable to keep potassium away from any source of water! In fact, even long exposure to air moisture is sufficient to produce detectable amounts of heat as experienced first hand from handling old potassium vials.

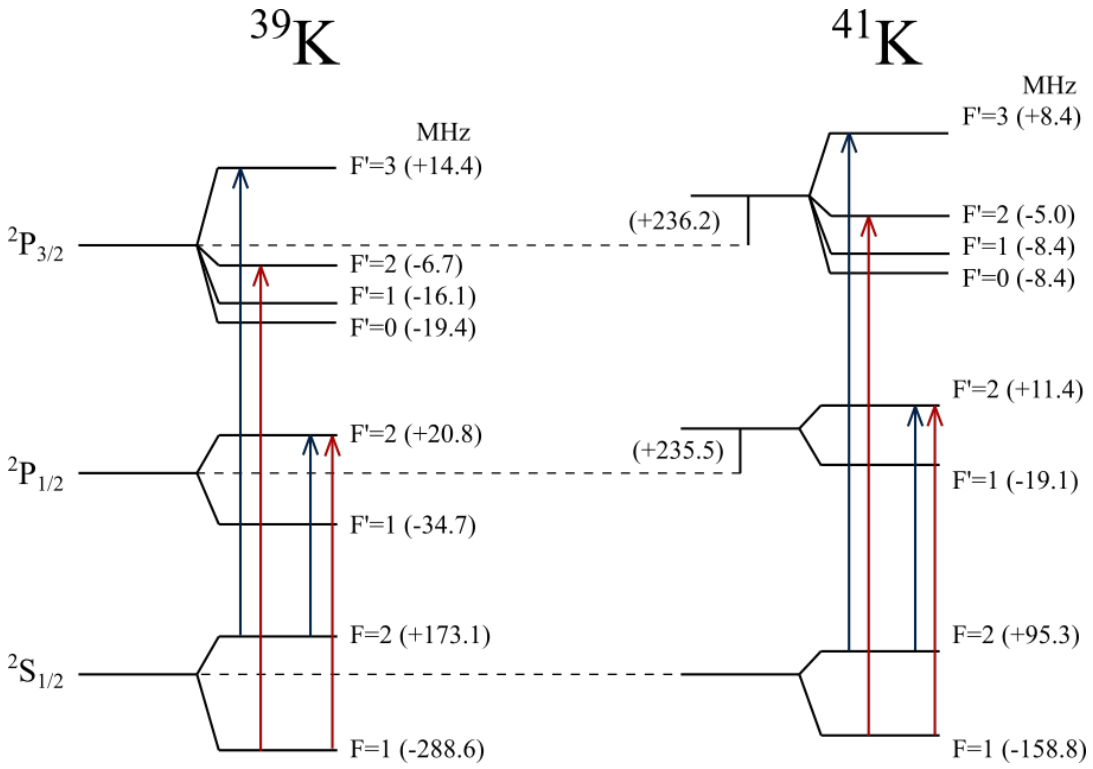


Figure 7.1: Energy level structure of ^{39}K and ^{41}K. The D2 line ($^2S_{1/2} \rightarrow 2P_{3/2}$) is used for initial cooling stages i.e. 2D+ MOT and the 3D MOT, whereas the D1 line ($^2S_{1/2} \rightarrow 2P_{1/2}$) is used for the 3D MOT and Grey molasses stage. The dark blue and red arrows indicate the cooling and re-pump transitions respectively. For more details of the cooling procedure see section 7.3. The isotope shift is sufficiently small and can be compensated for using regular AOMs.

splits into four levels with $F = 0, 1, 2, 3$. The hyperfine splitting of the $2P_{3/2}$ level can be as small as 3 MHz, making it difficult to address individual substates within the manifold which can limit the laser cooling efficiency of any schemes operating on this line.

The energy level structure for both bosonic isotopes of potassium is shown in figure 7.1. Due to its high abundance, ^{39}K is more suitable for being used as the main spectroscopic reference for locking our lasers (see section 7.4.2). However, our primary goal is to cool ^{41}K thanks to its favourable scattering properties at low magnetic fields. Luckily, the relative shift of the D1 and D2 lines with respect to the ground state is only ≈ 236 MHz higher in ^{41}K compared to the same splitting in ^{39}K. As a result, it is possible to lock the lasers to the (stronger) ^{39}K features and then shift the frequency using an appropriate combination of AOMs. The full optical setup is discussed in detail in section 7.4.

7.3 Cooling of potassium

As alluded to in the previous section, the D1 and D2 lines are the standard transitions used to laser cool potassium to ultracold temperatures. Table 7.2 lists the relevant properties of the two transitions. Although very similar, as we will see shortly, the hyperfine level structure of the D1 line allows for the implementation of the so called *grey molasses* cooling stage which can lead to sub-Doppler temperatures. For that reason, D1 light is used at

	D1	D2
Wavelength (λ)	770.108 nm	766.700 nm
Color	Red	Red
Linewidth ($\Gamma/2\pi$)	5.96 MHz	6.04 MHz
Doppler temperature ($T_D = \hbar\Gamma/2k_B$)	145 µK	145 µK
Recoil temperature ($T_R = \hbar^2k^2/2mk_B$)	0.41 µK	0.41 µK
Saturation intensity ($I_{\text{sat}} = \pi hc\Gamma/3\lambda^3$)	1.75 mW cm^{-2}	1.75 mW cm^{-2}

Table 7.2: Properties of ^{41}K cooling transitions. Although very similar, the D1 line is suitable for gray molasses cooling due to its favourable hyperfine level structure and so it is used in later cooling stages during the 3D MOT. The D2 line, on the other hand, is used in the initial 2D+ MOT stage and then later during the first part of the 3D MOT. Data taken from [160].

the end of the 3D MOT when the gas is cold enough to undergo grey-molasses cooling whereas D2 light is utilized in the 2D+ MOT and 3D MOT to provide both confinement and cooling.

Closed optical cycling is an essential prerequisite of efficient laser cooling. In its absence, atoms can accumulate in a dark state and forgo any further cooling. The hyperfine structure of the ground state and the excited states of potassium makes closed optical cycling slightly more challenging than in the case of erbium because once the atom is excited by the cooling light, it can decay to different sublevels in the hyperfine manifold. For that reason, it is necessary to implement a re-pump beam that depopulates other potential decay channels and pumps the atoms back into the original ground state.

For the D1 transition, the cooling light operates between the $F = 2 \rightarrow F' = 2$ sublevels. Here we used prime to denote a level belonging to the excited state. Following on from electric dipole transition selection rules, an atom in the $F' = 2$ level can decay to either of $F = 1, 2$ ground state levels. If it decays to $F = 1$, it is no longer addressed by the cooling light and remains there indefinitely–unless another re-pump beam operating between $F = 1 \rightarrow F' = 2$ is used to close the cycle.

Similarly, for the D2 transition, the primary cooling light operates between $F = 2 \rightarrow F' = 3$ sublevels. On its own, this would be a closed cycle since the $F' = 3$ can only decay to the $F = 2$ ground state. However, the small hyperfine splitting of the $^2P_{3/2}$ level is comparable to the linewidth of the transition and so occasionally a $F = 2 \rightarrow F' = 1, 2$ transition will be driven instead (albeit with a lower, off-resonant probability). These excited sublevels can decay to the $F = 1$ ground state level. As a result, a re-pump beam is once again necessary to pump atoms out of the $F = 1$ level to the $F' = 2$ level.

Both cooling and re-pump frequencies for the two lines are shown in figure 7.1. In the rest of this section, we will described how we plan to utilize these transitions to cool potassium to ultracold temperatures in four stages which include the 2D+ and 3D MOT, grey molasses and, finally, forced evaporation in a dual species Er-K optical dipole trap. We note that since potassium is primarily intended as an impurity in our experiment, we do not require particularly high atom numbers. Nevertheless, our design follows state-of-

the art techniques and procedures [372]–[375] so it should, in principle, allow us to produce standalone potassium BECs.

7.3.1 2D+ MOT

Due to its relatively high vapour pressure at temperatures only slightly above room temperature, it is possible to load a MOT directly from a background vapour. At the same time, high vapour pressure prevents the use of such procedure in the main MOT chamber where ultra-high vacuum ($\approx 1\times10^{-11}$ mbar) needs to be maintained to minimize scattering with background gas and hence maximize the lifetime of a trapped atomic cloud.

Based on these considerations, we decided to implement a two-dimensional magneto-optical trap (2D MOT) as a source of cold potassium atoms [159], [367]. This is done in a separate vacuum section consisting of a glass cell connected to the main vacuum chamber via a differential pumping tube to maintain a constant pressure difference between the two sections. The full details of the 2D+ MOT section including vacuum chamber design, optics, assembly procedure and the cooling performance are presented in chapter 8. Here we only outline the working principle of the 2D+ MOT.

Just like a regular 3D MOT, the 2D+ MOT consists of a combination of red-detuned molasses beams and a magnetic field gradient to provide spatial confinement. However, as the name suggests, the gradient and therefore the trapping force is only created in two (out of three) perpendicular directions by overlapping two anti-Helmholtz coil pairs with two pairs of beams. In this way an elongated cloud of cold K atoms is created.

A fifth laser beam is directed along the non-trapping axis and it is reflected from a linear polarizer-mirror tandem situated at the entrance to the differential pumping section. This beam plays the role of optical molasses (without trapping) along the third direction– hence the '+' designation in '2D+ MOT'. The power of the retroreflection can be tuned by changing the polarization of the incoming beam thanks to the linear polarizer. An imbalance in powers results in a net flux of cold atoms along the non-trapping direction. The flux is directed towards the differential pumping section and funneled through it into the main vacuum chamber where it is later captured in a 3D MOT. Additionally, a blue-detuned *push beam* can be aimed through the differential tube to enhance the flux. Figure 7.2 shows a schematic depiction of a 2D+ MOT with all the relevant beams, coils, optical elements and their relative geometry.

7.3.2 3D MOT

Much like the erbium MOT, the potassium 3D MOT will be formed in the main vacuum chamber by six counter-propagating, red-detuned beams of 23 mm in diameter and by a magnetic quadrupole field gradient created by the same anti-Helmholtz coil pair. The MOT will be loaded directly from the cold potassium flux entering the chamber from the 2D+ MOT section described above.

Initially, the light in the 3D MOT will operate on the D2 line, similarly to the 2D+ MOT. This ensures high capture velocity at the expense of increased temperature (several millikelvin [373], [374]) and reduced density. To cool the cloud further, the MOT will enter

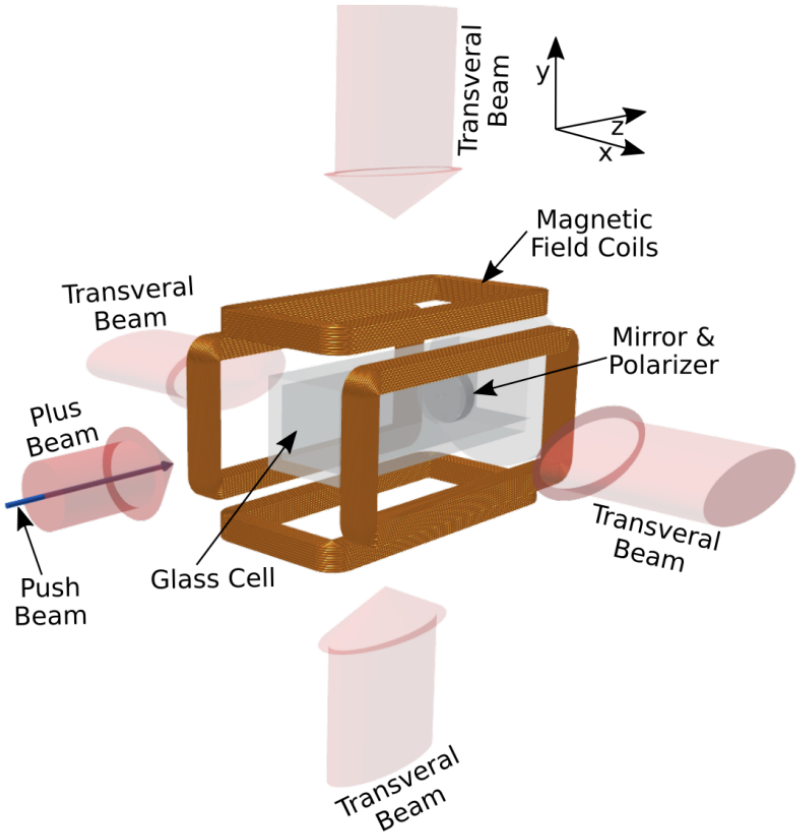


Figure 7.2: Schematic of a 2D+ MOT. A magneto-optical trapping potential is established in the x-y plane in a similar way to a conventional MOT (see section 3.2.3), creating an elongated cloud of K atoms in an evacuated glass cell. Another beam is directed along the z axis and retroreflected from a mirror/polarizer tandem situated at the end of the glass cell. This beam provides extra cooling but no confinement. The mirror/polarizer pair has a hole in the center that leads to main vacuum chamber through a differential pumping tube. The lack of confinement and imbalance of powers creates a flux of atoms in the z direction directed at the hole. An additional blue-detuned beam can be used to actively push the atoms through the hole to increase the atomic flux. Figure taken from [280].

a hybrid D1-D2 compressed stage (cMOT) in which the D2 cooling light is turned off while the re-pump remains and provides trapping. Additionally, blue-detuned D1 cooling beam is turned on and the field gradient is ramped up. This combination of optical and magnetic fields results in simultaneous compression and partial sub-Doppler cooling of the cloud to $\sim 400\,\mu K$ [374]. We note that compression is necessary for efficient loading of potassium atoms into the tight, dual-species optical dipole trap prior to evaporation.

An important thing to remember is that the main vacuum chamber also needs to support the erbium MOT. Due to the limited number of viewports and other experimental constraints, we will operate a dichroic MOT with the six counter-propagating yellow (Er) and red (K) beams overlapped prior to entering the chamber using dichroic mirrors. As was explained in section 3.2.3, the narrow-line erbium MOT sags under the influence of gravity. This will lead to spatial separation of the two MOTs during the loading phase. In order to trap both clouds in the same ODT, they will have to be eventually moved to the same location. This can be done during the compression step using suitable offset field and beam detunings.

However, the potassium MOT stage requires field gradient which is larger than the one required for erbium [138]. Using a high gradient in the erbium MOT phase would result in too high densities and light-induced losses (see section 3.2.3). Additionally, the grey molasses stage is done in the absence of any fields. Consequently, the two MOT clouds will have to be formed and loaded into the ODT sequentially. Given that our primary goal is an erbium BEC with potassium impurities, we might first load potassium into the ODT and hold it there while we form and load the erbium MOT. This will inherently lead to losses of K atoms from the ODT due to inelastic processes but it will allow us to optimize the experiment for erbium atom numbers.

7.3.3 Grey molasses

The last laser cooling step after the 3D MOT stage and prior to evaporation in the ODT is the so-called grey molasses [376], [377]. Due to the poorly resolved hyperfine structure of the $^2P_{3/2}$ excited state, the Doppler temperature of potassium ($\approx 150\,\mu K$) is quite hard to achieve using the conventional MOT operating on the D2 line. At the same time, we would like to avoid mixing hot potassium with cold erbium ($40\,\mu K$; see section 4.2) during loading of the dual-species ODT. Fortunately, the grey molasses stage involves a sub-Doppler cooling mechanism which allows us to bypass the Doppler limit and reach temperatures comparable to erbium.

As the name suggest, during this stage the magnetic field is turned off and the counter-propagating beams form a simple molasses which operates on the D1 line instead of the D2 line. Both the cooling and re-pump beams are tuned close to and above resonance i.e. they are slightly blue-detuned. This is in stark contrasts with the usual 'bright' molasses where the beams are red-detuned to provide Doppler-shift-dependent damping force. Over the course of several milliseconds, the power in the beam is reduced below saturation and the gas should reach temperatures on the order of $50\,\mu K$ [373], [374], well below the Doppler limit. The cooling is extremely efficient and so a few milliseconds of

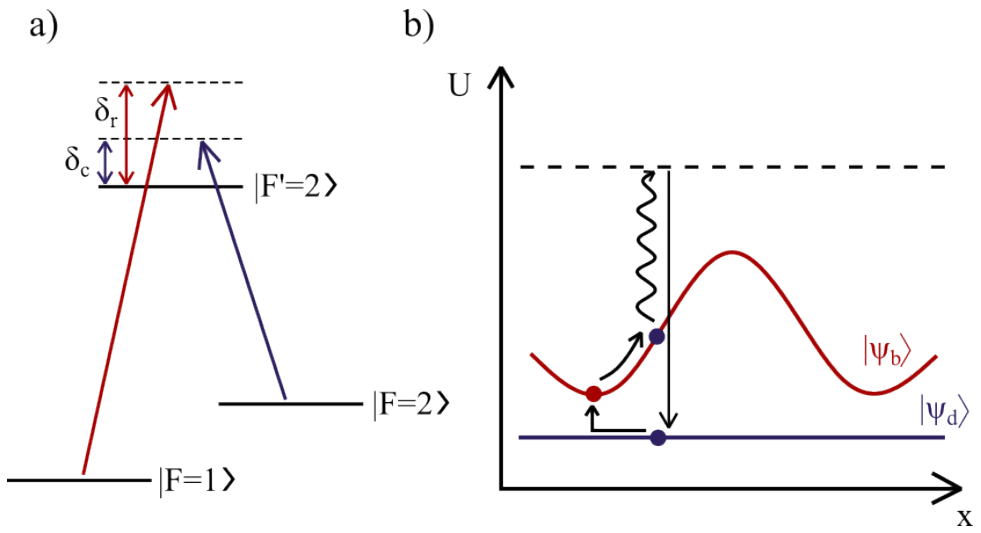


Figure 7.3: Mechanism of grey molasses. a) Two ground states coupled to an excited state of the D1 transition via two laser fields. The Raman condition $\delta_r = \delta_c$ leads to the formation of bright and dark states. b) Atoms in the bright state move in the optical potential created by the molasses beams. As they climb up the potential hills, they lose kinetic energy. During an absorption and subsequent decay into the dark state, this energy is irreversibly lost and the cloud cools down. Atoms in the dark state can transition to the bright state and thus re-enter the cooling cycle. This happens preferentially in the potential valleys at a rate proportional to the atomic velocity.

grey molasses should be sufficient to proceed with loading into the ODT. In fact, in a recent dysprosium-potassium experiment [138], it was demonstrated that grey molasses cooling can be achieved while the gas is already trapped in the ODT by appropriately adjusting the detunings of the molasses beams to counteract the light shift induced by the ODT [373]. This is beneficial because grey molasses on its own doesn't provide any spatial trapping (magnetic fields are turned off) and without the confining force of the ODT, the cloud would eventually become too dispersed to be efficiently loaded.

The sub-Doppler cooling mechanism of grey molasses relies on two effects–Sisyphus cooling [21], [378] and velocity-selective coherent-population transfer (VSCPT) [379]. To understand it, consider a system with two ground states coupled to an excited state via two laser beams of detunings δ_r and δ_c with respect to the excited state as depicted in figure 7.3a. Note that this is precisely the case of the D1 transition with the cooling and repump beams. The Raman condition $\delta_r = \delta_c$ leads to the creation of two coherent dressed states which are a linear combination of the two ground states [380], [381]. One of these states interacts with the laser fields in the usual way and is known as the 'bright' state. The other state doesn't interact with the fields and is therefore known as the 'dark state'. The resonant Raman condition needs to be corrected for the Doppler shift experienced by the atom such that $\delta_r - \delta_c = \delta_d(v)$, where $\delta_d(v)$ is the velocity-dependent Doppler shift. Clearly, only certain velocity groups form these bright and dark states. This is at the heart of VSCPT. If we tune $\delta_r \approx \delta_c$, only the coldest atoms with $v \approx 0$ will undergo the coherent population transfer into these states.

Much like in Sisyphus cooling, we now have a picture in which the bright states move in

the periodic potential created by the counter-propagating, blue-detuned molasses beams. As the atoms climb the potential hills, they loose kinetic energy. Regularly, they absorb a photon and get excited to the $|F' = 2\rangle$ state. From there, they can radiatively decay to either the bright or the dark state. Since the dark state doesn't interact with the light, its potential landscape is flat and so any kinetic energy expended on climbing a potential hill is irreversibly lost, resulting in overall cooling. Atoms in the dark state can re-enter the bright state via motional coupling or optical excitation at a rate proportional to their velocity [382]. Consequently, slow atoms preferentially remain in the dark state whereas hot atoms re-enter the cycle and get further cooled until they are trapped in the dark state as well. This way, the velocity distribution of the cloud is gradually narrowed down to sub-Doppler temperatures [376]. A schematic of this process is shown in figure 7.3b.

7.3.4 Evaporation

Once both species are loaded into the ODT, we can proceed with forced evaporative cooling. The polarizability of potassium at 1064 nm is ≈ 600 a u [123], [383] which is almost four times that of erbium at the same wavelength (see section 4.1.1). Consequently, the dipole trap experienced by potassium atoms will be four times as deep and twice as tight. Given that the rate of evaporation scales as e^{-U_d/k_BT} where U_d is the depth of the trap, evaporation of potassium will be heavily suppressed as long as we prioritize efficient evaporation of erbium. Fortunately, interactions between the two species will lead to their mutual thermalization and sympathetic cooling of potassium [138], [384]. The favourable scaling of the critical BEC number with mass and trap parameters (see section 2.4.1) also means that $N_c^{Er} > N_c^K$ and so, should we ever decide to pursue this research direction, simultaneous condensation of the two components is possible despite the lower potassium atom numbers.

7.4 Light preparation

To supply all the different cooling stages described in the previous section with the appropriate laser powers and frequencies, a relatively involved optical setup is required which should be both stable and tunable. Its complexity is further increased by our requirement to be able to switch between the two bosonic isotopes, ^{39}K and ^{41}K. Fortunately, the wavelengths corresponding to the D1 and D2 transitions can be generated using affordable diode lasers and frequency and intensity control can be achieved with a combination of acousto-optic modulators (AOMs). In the following section, we will describe our optical system which was designed [280] based on beam detunings and powers listed in literature [374], [385] and gradually built over the last two years in preparation for attaching the potassium vaccum section described in chapter 8.

7.4.1 Table optics

The light for the D1 and D2 lines is seeded from two separate diode lasers[2] which are independently frequency-stabilized to a potassium vapour cell reference (for more details on the locking scheme, see section 7.4.2). Each of these laser beams needs to be split and appropriately frequency-shifted to address the cooling and re-pump transitions. As the output power of the diode lasers at $\lambda = 770/767\,\text{nm}$ is only $60/45\,\text{mW}$ respectively, the light needs to be further amplified. We decided to opt in for a cost-efficient design that involves only one tapered amplifier[3] (TA) which amplifies both the D1 and D2 lines simultaneously. Consequently, the two beams need to be somehow combined before being inputted to the TA. In our case this is done by overlapping the two beams on a polarizing beam splitter (PBS) and then matching their polarization to the preferred input polarization of the TA using a dichroic half-waveplate[4]. After passing through the TA which can amplify the beams to up to 3 W of combined power, they are split to the 2D+ MOT and 3D MOT branches and finally coupled to two spliceless arrays which transfer the light to the experimental table and which evenly distribute the total power between the four and six MOT beams respectively (this is discussed in section 7.4.3).

The full optical setup is shown in figure 7.4. The D1 and D2 paths mirror each other except for the relevant frequency shifts and so in the description below we will only follow the D2 line. Once the beam leaves the seed laser, it is collimated using a two-lens cylindrical telescope. This was introduced after we noticed considerable divergence of the beam along one of the axes, the detrimental effect of which was further enhanced by the long optical path of the beam. After the initial beam shaping, a portion of the beam ($\approx 2\,\text{mW}$) is diverted to the spectroscopy branch using a PBS. There, it is passed through a 200 MHz AOM[5] before being sent to a potassium vapour cell for saturated absorption spectroscopy (see section 7.4.2). The role of the AOM is to shift the frequency of the seed laser beam (and any beams derived from it) by $-200\,\text{MHz}$ with respect to the locking feature.

The main laser beam is then split into two branches–one for the cooling transition and one for the re-pump. In each branch, the beam is first focused down using a telescope before being passed through an AOM in a double-pass configuration. Focusing the beam this way maximizes the diffraction efficiency of the AOM and therefore minimizes the power loss. With most of our AOMs, we can reach a double-pass efficiency of $\approx$ 70-80%. The difference in frequency shift of the AOMs in the two branches corresponds to the difference between the cooling and re-pump transitions. The AOMs also serve as independent intensity control of the cooling and re-pump beams. Note that a section of the optical table is reserved for a pair of AOMs that mirror the cooling/re-pump AOMs described above but that are designed for cooling of ^{39}K (see shaded region in figure 7.4). In the future, we will be able to switch between the two isotopes using an optical switch [386]. The two branches are recombined on a PBS and a portion of the light is

[2] DL Pro by Toptica
[3] BoosTA Pro by Toptica
[4] By Lens optics
[5] All AOMs in the potassium setup are from the AOMO 12X series by Gooche and Housego

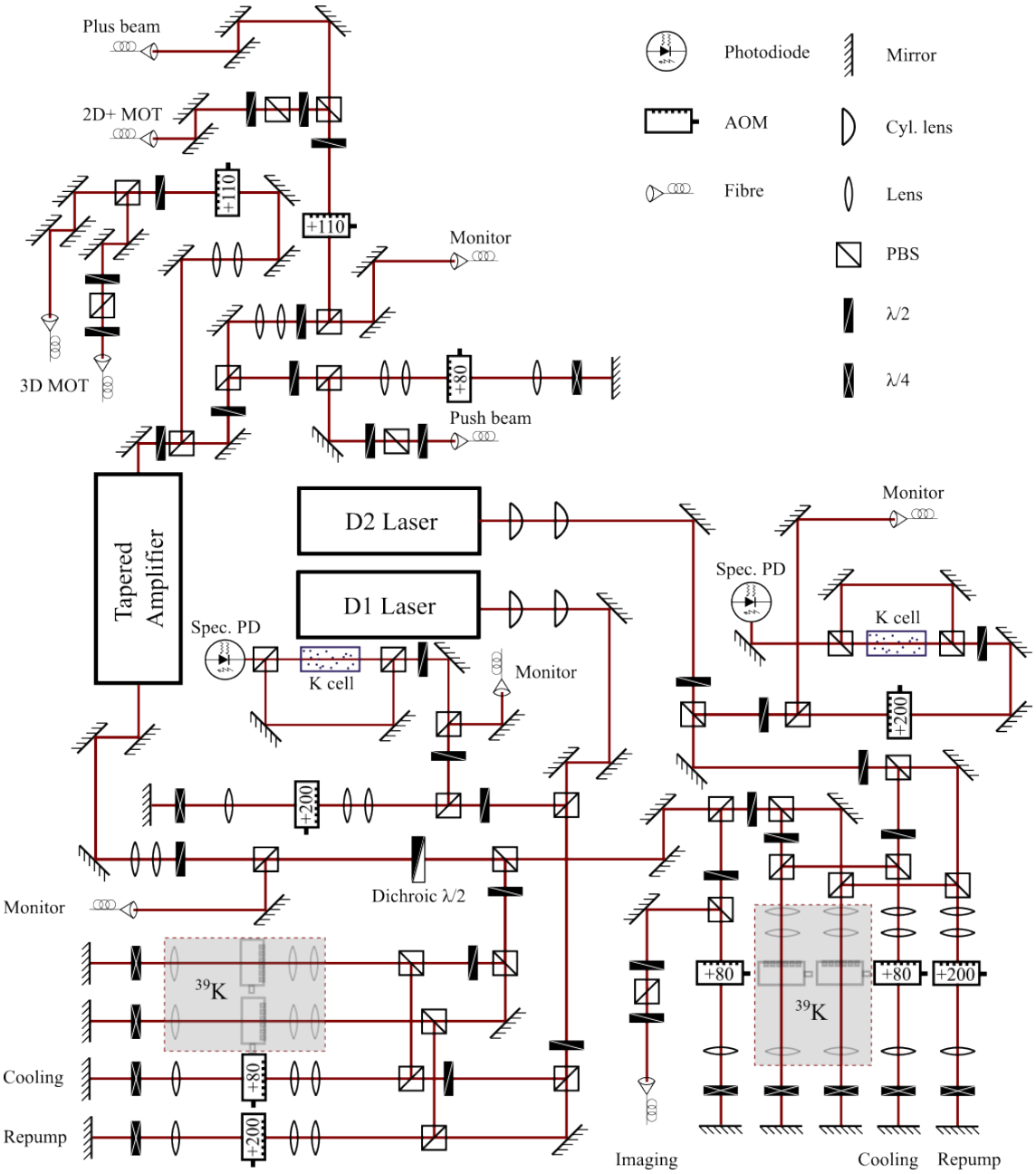


Figure 7.4: K optical setup. Two lasers generate light to address the D1 and D2 transitions respectively. After several frequency shifting stages, the two beams are combined on a PBS and polarization-aligned using a dichroic $\lambda/2$ wave plate. The combined beam is coupled into a TA. The output of the TA is split into the 2D+ and 3D MOT branches and the 2D+ MOT push beam. Shaded regions mark a portion of the D1 and D2 optical paths reserved for optics designed to address the other bosonic isotope of potassium, ^{39}K. This will be done by mirroring the cooling and repump double-pass AOM branches with suitably chosen frequencies, allowing for easy switching between the two isotopes by simply turning the two additional AOMs on and off.

diverted to the imaging branch where another AOM allows for fine tuning of the imaging light frequency. Combining the two branches this way is relatively simple but results in orthogonal polarizations and subsequent power loss when incident on the imaging PBS. Similar loss is incurred in the D1 branch prior to overlapping the two lines.

The two lines are overlapped on a PBS and a dichroic waveplate is used afterwards to rotate the polarization of the D1 light to match it to the polarization of D2 light. This way, both lines can be coupled into the TA without any further losses associated with preferred input polarization of the TA. The combined beams are shaped to the desired waist using a telescope and coupled into the TA using the standard double mirror configuration. Once amplified, the single beam (now containing four frequency components) is split into the 3D MOT and 2D+ MOT branches. In the 3D MOT branch, the light is frequency-shifted for the last time and then coupled into two inputs of a spliceless array which distributes the total power evenly into six outputs and transfers the light to the experimental table. The 2D+ MOT branch is split into the push beam and transverse MOT beams branch. The former is blue-detuned using a 80 MHz double-pass AOM to provide a repulsive force that enhances the atomic flux through the differential pumping section (see 7.3.1 and chapter 8). The latter, much like in the 3D MOT branch, passes through a 110 MHz AOM for intensity control and a final frequency shift. It is then coupled into a fibre designated for the '+' beam which cools along the non-trapping direction of the 2D+ MOT and into a single input port of a spliceless array that splits the power evenly into four outputs–one for each transverse beam.

7.4.2 Locking

The two seed lasers are frequency-locked to their respective potassium vapour cell references using Doppler-free saturated absorption spectroscopy [80], [387]. Due to the large relative abundance of ^{39}K compared to ^{41}K (93% vs 7%), we decided to lock both lasers to ^{39}K absorption features and then compensate for the isotope shift with AOMs. Our spectroscopy setup follows a standard scheme in which a relatively strong pump beam ($\approx 1\,\mathrm{mW}$) is directed through a vapour of the reference element. On its own, the absorption feature of the pump beam is broadened by various effects–most notably by the Doppler shift of different velocity groups present in the vapour, resulting in frequency broadening $\Delta f \propto f_0\sqrt{k_B T/mc^2} \gg \Gamma$, where f_0 is the central frequency of the feature and Γ is the natural linewidth of the corresponding transition. Locking to such broadened features results in unstable locks.

However, a weaker probe beam propagating in the opposite direction can be used to produce absorption features that are broadening-free. This is because the pump beam saturates the excited level population of atoms with velocities such that $\delta_{\mathrm{laser}}+\delta_{\mathrm{Doppler}}(v) = 0$. Once saturated, any extra light addressing the same atoms will not get absorbed. If the probe is incident on the atomic vapour from the opposite direction, it addresses atoms with velocities equal and opposite to the atoms addressed by the pump beam. Consequently, due to its low power, most of the probe beam can be absorbed. The situation is very different when the pump beam approaches the center of the broadened absorption feature

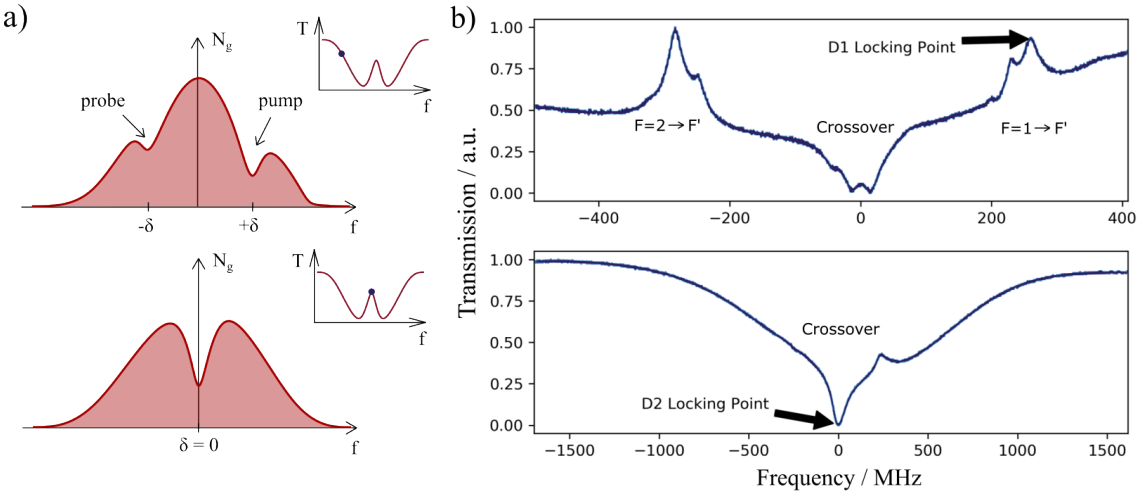


Figure 7.5: Saturated absorption spectroscopy of potassium. a) Principle of SAS. When the laser beam frequency is off resonance i.e. the detuning is non-zero, the probe and pump beams address different velocity groups with $\delta \pm kv = 0$. Consequently, the probe is partially absorbed by the atoms and the transmission drops. When $\delta = 0$, the pump and probe address the same atoms. Since the pump is strong, it saturates the excited level and no more absorption occurs. As a result, the probe passes through the vapour and its transmission shows a narrow peak which can be used as a reference for locking. b) Lock points of the D1 and D2 lines used in our spectroscopy setup.

i.e. when it addresses atoms with velocities close to zero. In that case, both beams address the same atoms and due to the saturation caused by the pump, the probe just passes through the sample. This results in a peak in intensity which has a width comparable to Γ and which is therefore suitable for locking. Figure 7.5a shows a cartoon of this process.

In our setup, the pump and probe beams are enlarged to address as many atoms as possible. The vapour cell itself is heated up to $\approx 50\,^{\circ}\mathrm{C}$ using a twisted pair of copper wires. This is to increase the vapour pressure and prevent potassium from sticking to the walls of the cell which greatly reduces the transmission of the beams. The probe is collected on a photodiode and the electronic signal is fed to the DL PRO controller which provides an interface for frequency scanning and lock-point selection. In terms of the relevant absorption features, the D1 laser is locked to the $F = 1 \rightarrow F' = 2$ transition peak whereas the D2 laser is locked to a large crossover feature which results from a combination of several crossover features of the poorly-resolved hyperfine transitions $F = 1 \rightarrow F' = 0, 1, 2$ and $F = 2 \rightarrow F' = 1, 2, 3$ and which is detuned from the $F = 1 \rightarrow F'$ transition by 226.1 MHz [386], [388]. Both locking features are shown in figure 7.5b.

7.4.3 Spliceless arrays

Omitting the push beam and the plus beam which are coupled directly to a fibre[6], the rest of the 2D+ MOT and 3D MOT light needs to be split evenly into four and six beams respectively. To establish stable splitting with minimum alignment and polarization optics, we decided to use spliceless arrays instead[7] [385]. These operate based on the evanescent

[6] P3-630PM-FC by Thorlabs
[7] By Evanescent optics

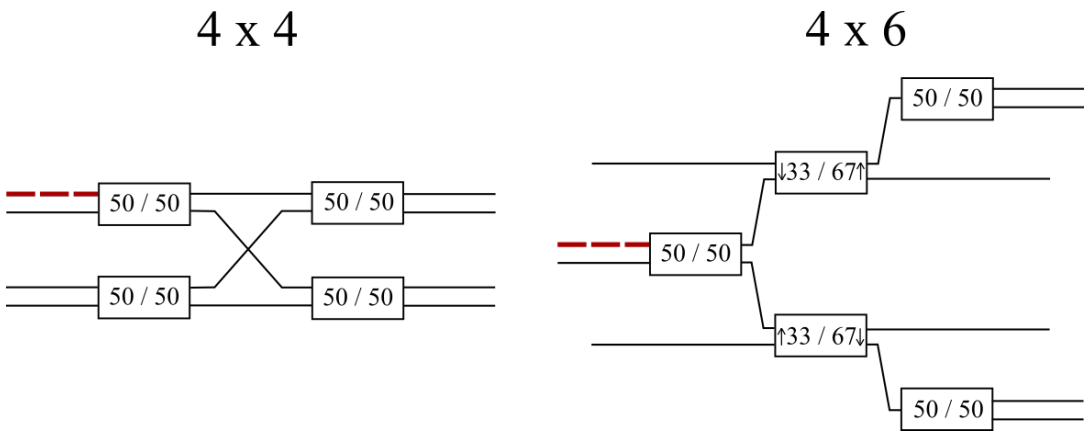


Figure 7.6: Spliceless array branching. The input channels used in our experiment are denoted by a red, dashed line. Note that interference effects during mixing prevent us from using more than one input in either of the arrays.

field phenomenon in which a waveguide transfers a (well-defined) portion of the guided field's energy into another waveguide in close proximity. This way, the laser field can be coupled between fibres with a fixed splitting ratio.

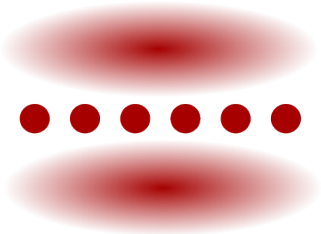
The arrays come in several branching configurations and our initial choice of the respective 2D+ MOT and 3D MOT arrays was based on the fact that each branching point can only handle a limited amount of input power (up to 750 mW[8]). From the available configurations, we therefore decided to use a 4×4 array for the 2D+ MOT and a 4×6 array for the 3D MOT with the intention of only using two of the four inputs for each array. The branching scheme for both arrays are shown in figure 7.6.

Later we realised that two inputs to the same splitter interfere with each other, resulting in large amplitude oscillations in the output on the timescale of several seconds. Consequently, we had to resort to using a single input for both of the arrays (indicated by red, dashed lines in figure 7.6). This limits the total power per transverse 2D+ MOT beam to ≈ 187 mW and per 3D MOT beam to ≈ 125 mW which we nevertheless believe to be sufficient for our application. In retrospect, a simple 1×4 array would have been a simpler, better choice with identical functionality. Once the light is coupled in with the appropriate polarization, the performance of the arrays is stable and reasonably good with all the outputs within $\pm 5\%$ of the mean.

To conclude, in this chapter, we discussed atomic properties of potassium and the various strategies used to cool it below the Doppler limit starting from a warm background vapour. We have also described our optical setup for generating light of appropriate frequencies and intensities necessary for the laser cooling stages. Next chapter is devoted to the first of these stages–a 2D+ MOT.

[8]Based on personal correspondence with Evanescent Optics

8. Building a source of cold K



In the following chapter we will describe our latest efforts towards introducing cold potassium into the main vacuum chamber using a 2D+ MOT as the source. This marks a major milestone on the way to creating the first mixture of erbium and potassium. The chapter is structured as following. First, we describe the overall design of the apparatus, focusing on the vacuum assembly and optics as well as on components specific to the 2D+ MOT setup. We then give an account of the construction process of each section, providing relevant technical data and our solutions to some of the challenges we faced. Finally, we conclude the chapter with characterization of the performance of our 2D+ MOT as a source of cold potassium atoms, presenting optimized experimental parameters and the resulting atomic flux and temperature.

8.1 Design

Given its sufficiently high vapour pressure at around 70 °C, potassium can, in fact, be loaded directly into a MOT from a background vapour. However, this needs to be done in a separate chamber so as not to compromise vacuum quality in the main chamber, necessitating the introduction of a pre-cooling stage similar to a Zeeman slower (see section 3.2.2). As described in section 7.3.1, the 2D+ MOT fulfils this role by producing a steady stream of potassium atoms fed directly into the main vacuum chamber through a combination of three-dimensional cooling and two-dimensional trapping. As such, the 2D+ MOT section needs to meet several criteria. Firstly, it needs to maintain a steady pressure differential between it and the main chamber. It also needs to have sufficient optical access to realize MOT cooling in four out of six directions and molasses cooling in the remaining two. Lastly, it has to be kept at an elevated temperature and connected directly to a solid source of potassium. Our 2D+ MOT setup was designed with these criteria in mind.

8.1.1 Vacuum

The 2D+ MOT vacuum assembly consists of several interconnected parts. At the heart of the system is a custom vacuum chamber made out of non-magnetic 316L stainless steel.

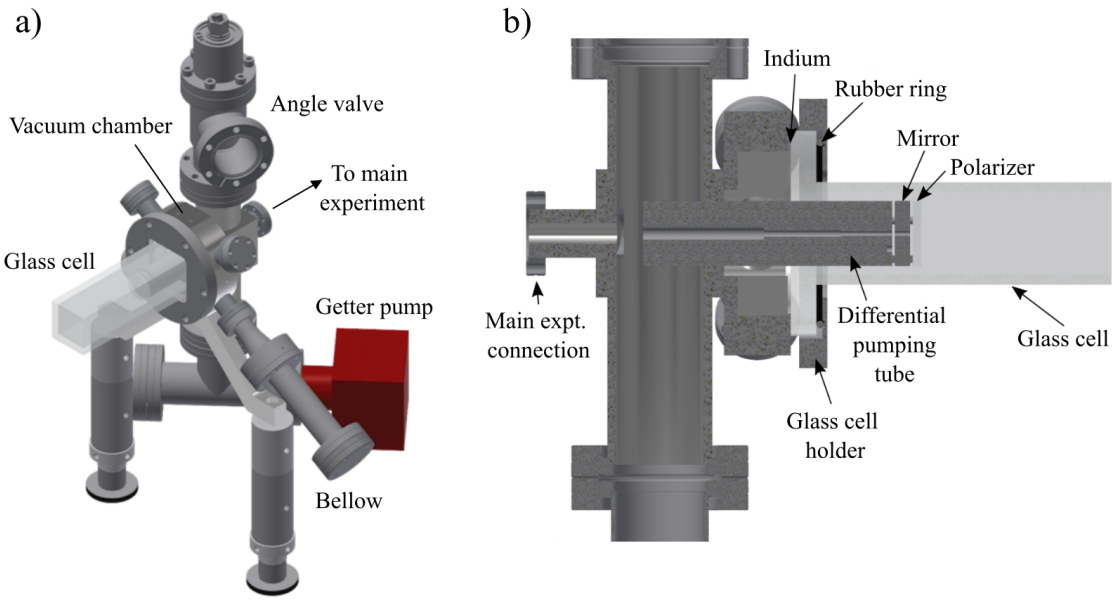


Figure 8.1: Vacuum design. a) 3D rendering of the whole system consisting of the vacuum chamber connected to the glass cell and a bellow with a potassium ampoule as a source. The chamber is connected to a four-way tee section via a differential pumping tube to maintain a pressure difference. The four-way tee, in return, connects the 2D+ MOT chamber to a getter pump, an angle valve used to attach a turbo pump or a helium detector for leak checking and to the main experiment. b) Cross-section of the system. The glass cell is attached to the vacuum chamber using a metal holder piece that pushes the cell against a flat circular flange. The seal between the metal chamber and the cell is created by an indium wire. A rubber ring is placed between the holder piece and the cell to evenly distribute the pressure and prevent cracking. A mirror and a linear polarizer are glued to the MOT chamber end of the differential pumping tube to allow for retro-reflection and intensity tuning of the '+' molasses beam. Figure adapted from [280].

This plays the role of a central hub and connects to all the other elements. Its front face has a flat, circular opening which connects directly to a rectangular glass cell. Together, the chamber and the cell form an enclosed volume which will contain the 2D+ MOT atomic cloud. The chamber is equipped with four CF16 flanges on its outer diameter. Three of these are blanked off and the last one is used to introduce potassium vapour into the space enclosed by the glass cell and the bulk of the chamber via a bellow. The connection between the bellow and the chamber is high-conductance, allowing for fast diffusion of potassium from its solid source to the glass cell. Both the glass cell and the source of potassium are discussed in more detail below. The unused CF16 flanges can be utilized in the future to introduce a source of enriched ^{40}K for the study of fermionic impurities. A 3D rendering of the whole setup is shown in figure 8.1a.

An important feature of the vacuum chamber is a 105 mm long differential pumping tube that connects the bulk of the chamber (and hence the 2D+ MOT region) to a four-way tee section. The tube itself extends into the glass cell and its end is terminated with a flat surface used to mount optics (see section 8.1.4). A small hole runs through the center of the tube and gradually increases in size from 2 mm on the glass cell side to 5 mm in the

four-way tee. A cross section of the whole system is shown in figure 8.1b.

The tube serves several purposes. Firstly and most importantly, due to its small cross section, it has a very low conductance ($\approx 0.02\,\mathrm{L\,s^{-1}}$) and it therefore helps to maintain a steady pressure differential between the ultra-high vacuum (UHV) in the main experimental chamber and the potassium vapour in the 2D+ MOT chamber. Rather obviously, the tube also provides a path for the atomic beam formed in the 2D+ MOT chamber to reach the 3D MOT in the main chamber. Finally, it serves as an indirect low-pass filter of slow atoms [367]. This is because it only lets through atoms that are sufficiently collimated. Such atoms that must have spent enough time in the 2D MOT region and so they have been exposed to the molasses damping force for longer.

The four-way tee at the end of the differential pumping tube connects to a gate valve (see section 3.1.1 for the erbium vacuum assembly) which itself separates the potassium section from the main experiment. Two CF40 flanges are part of the four-way tee and they are perpendicular to the differential pumping tube. One of them is connected to a tee junction which contains an ion-getter dual pump[1] used to maintain the steady pressure differential during normal operation. The other flange is attached to an angle valve[2] which connects the vacuum chamber to an external turbo pump used for the initial pumping during the assembly and the bake-out process (more details in section 8.2.3). The geometry of the four-way tee is shown in figure 8.1a.

The background vapour pressure of potassium at 50 °C is $\sim 1 \times 10^{-7}$ mbar whilst the pressure required in the main experimental chamber is $\sim 1 \times 10^{-12}$ mbar. Using this potassium vapour pressure as the steady-state value, the known pumping rates and the conductances of the vacuum parts, an equivalent circuit calculation confirmed that the desired pressures should be maintainable throughout the experiment i.e. both in the main chamber and in the science cell. For more details on pressure calculations, see [280].

Glass cell

The 2D+ MOT needs good optical access from five directions–four transverse directions for the counter-propagating MOT beams and one direction for the molasses '+' beam (and the blue-detuned push beam). Although it would have been possible to design a chamber with sufficient number of viewports, we decided to use a glass cell instead which gives superb optical access and minimizes the number of metal to glass seals. These are known to degrade in the presence of (corrosive) potassium[3], leading to potentially catastrophic leaks.

Due to experimental constraints, a custom glass cell had to be manufactured[4]. Its rectangular part has dimensions of $40 \times 40 \times 130$ mm whereas the circular flange has a thickness of 10 mm and an outer diameter of 80 mm as can be seen in figure 8.2a. The cell is AR coated[5] to reduce back reflections and power loss. The glass flange rests against

[1] NEXTorr D 100-5 by SAES
[2] Easy Close All-metal Angle Valve 54132-GE02 by VAT
[3] Based on consultation with Hadzibabic group in Cambridge
[4] Manufactured by Japan Cell
[5] 767-770 nm

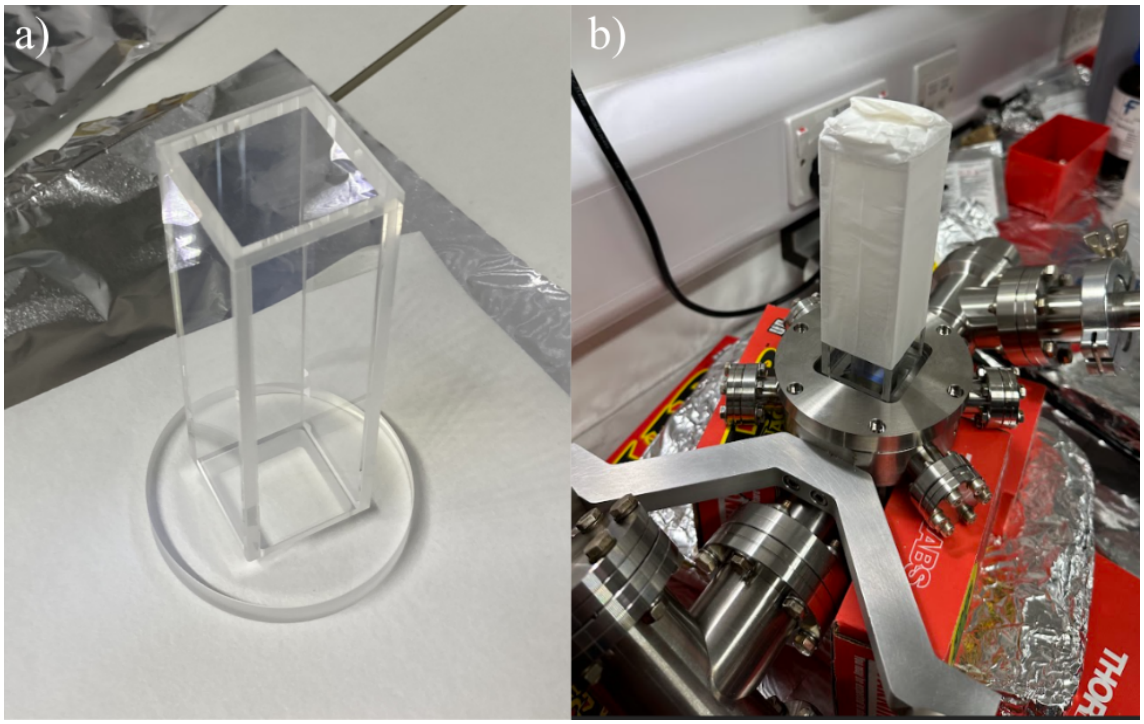


Figure 8.2: Glass cell. a) Glass cell manufactured by Japan Cell used to create enclosed and optically accessible volume for the 2D+ MOT. The circular part of the cell pushes against the front face of the steel vacuum chamber to create an air-tight seal using an indium wire sandwiched between the two parts. b) The cell is held in place and pushed against the chamber using a metal holder piece with six M5 screws.

the flat, circular face of the vacuum chamber. To seal the connection, we decided to use indium wire[6]. The decision was based on the fact that indium is resistant to potassium corrosion, extremely malleable and hence suitable as a sealant. However, its low melting point of 150 °C [389] limits the temperature of the bake-out procedure and extends its duration.

To help with placement of the wire, a circular groove 1.0 mm wide and 0.7 mm deep was cut into the face of the vacuum chamber. Given its cross section is smaller than the cross section of the wire, it holds the wire in place but allows for enough of the material to stick out and form the seal. The groove filled with indium wire can be seen in figure 8.5a. To press the glass cell against the surface and secure it in place, a steel holder piece was designed. This has a square cut to allow for the cell to pass through and six M5 holes through which the piece (and hence the cell) is attached to the chamber via screws–see figure 8.2b.

Potassium source

As mentioned above, one of the CF16 flanges on the vacuum chamber connects to the source of potassium vapour. In our experiment, the source is a CF25 bellow which contains a 5 mg ampoule of potassium. After the bake-out process, the ampoule is broken by simply bending the bellow, exposing the vacuum to the solid sample of potassium. To increase

[6] 1.6 mm diameter indium wire by Oxford Instruments

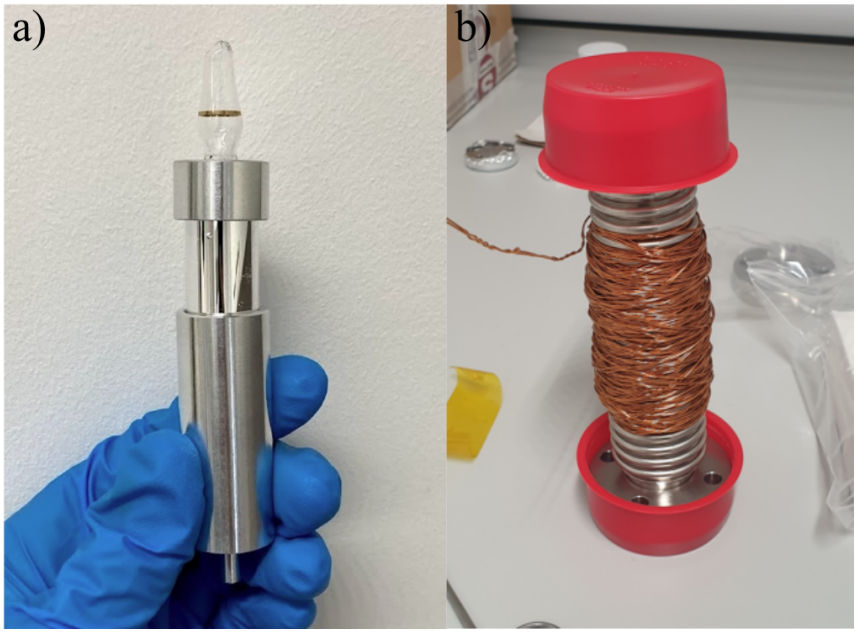


Figure 8.3: Potassium source. a) Glass ampoule filled with 5 g of potassium. The ampoule is glued to two aluminium holder pieces which allow for more efficient torque transfer between the bellow and the ampoule. b) Steel bellow used to house the potassium ampoule. After the bake-out procedure, the potassium ampoule will be broken by bending the bellow. The bellow will then be heated to $\approx 60\,^{\circ}\mathrm{C}$ with copper wire to increase the vapour pressure and hence the MOT cloud density.

the vapour pressure and hence density of the 2D+ MOT cloud, the bellow is heated by a twisted pair of copper wires to a temperature of $\approx 60\,^{\circ}\mathrm{C}$.

The inner diameter of the bellow is approximately 1 cm larger than the diameter of the potassium ampoule and so on its own, the bellow would require substantial bending to exert enough torque on the ampoule and break it. For that reason, a two-piece aluminium ampoule holder was designed to better match the diameter of the bellow. The holder also brings the ampoule closer to the middle of the bellow where maximum bending curvature can be achieved. Both the ampoule (mounted inside the aluminium holders) and the below are shown in figure 8.3.

8.1.2 Oven

Potassium vapour tends to coat the surface of its container when kept at room temperature. This greatly reduces the transmission coefficient of any transparent elements such as the glass cell. To prevent this from happening and to increase the vapour pressure and thus enhance loading, an oven was designed that encloses the glass cell and keeps it at slightly elevated temperatures ($\approx 50\,^{\circ}\mathrm{C}$) using heating elements.

Given the close proximity of the oven to the 2D+ MOT region, it needs to be non-magnetic. Furthermore, it needs to preserve the excellent optical access provided by the glass cell. With these constraints in mind, we decided to 3D print the oven as opposed to having it fabricated from non-magnetic steel. This significantly reduced the cost with the added benefit of making the oven non-magnetic, non-conductive and easily prototypable.

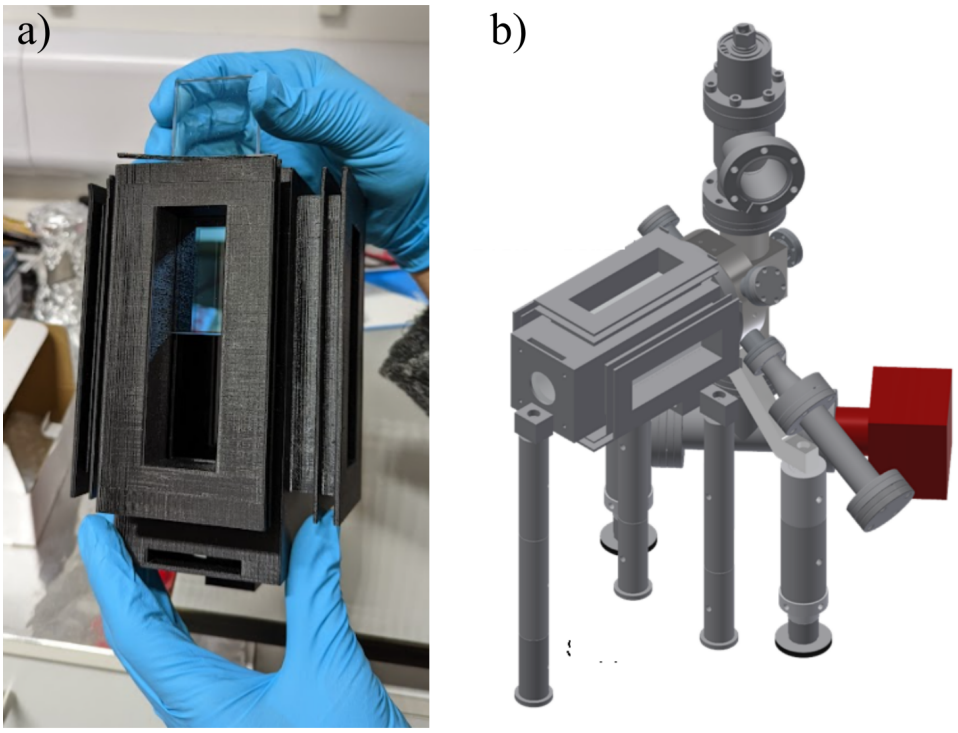


Figure 8.4: Glass cell oven. a) A 3D printed oven used to enclose the glass cell and keep it at an elevated temperature ($\approx 50\,^{\circ}\mathrm{C}$) to prevent coating of the cell walls with potassium. The oven has five viewports with AR coated windows to retain good optical access for the MOT beams. It also serves as a mount for the coils that provide the necessary gradient field. b) 3D rendering of the system with the oven enclosing the glass cell. This should be compared with figure 8.1 which shows the system without the oven. The oven is supported by its own posts and rests against the glass cell holder piece without touching the cell itself. That way, warm air is trapped in the cavity between the cell and the oven without causing any mechanical strain on the vacuum system.

The bulk of the oven was made out of CPE+ which has great structural properties and can withstand temperatures of up to $100\,^{\circ}\mathrm{C}$–way above our requirements. A water-soluble material[7] was used for internal support of any overhanging sections. The 3D printed oven is shown in figure 8.4.

To preserve the optical access, the oven features five viewports. These are filled with AR coated windows[8]–four rectangular windows for the transverse beams ($115 \times 40 \times 5\,\mathrm{mm}$) and one square window for the '+' and push beam ($40 \times 40 \times 5\,\mathrm{mm}$). The windows are slotted into the body of the oven and held there by friction and 3D-printed wedges.

The oven itself is supported by posts and slides onto the glass cell. It rests against the glass cell holder metal piece, creating a sufficient seal for maintaining the 30° temperature differential between the inside and the outside. A 7 mm gap between the cell and the oven walls allows for the placement of heating elements along the inner edges and around the square viewport. These are responsible for creating a uniform temperature profile along the glass cell. The oven also serves as a holder for the coils providing the trapping fields.

[7] AquaSys 120 by Infinite Materials Solutions
[8] Manufactured by Japan Cell

8.1.3 Coils

Unlike the 3D MOT, the 2D+ MOT requires a magnetic field gradient along only two axes. This is provided by two pairs of anti-Helmholtz coils with their axes perpendicular to each other and pointed along the transverse beam directions. Based on literature [159], [374], the coils were designed to produce field gradients of up to 13 G/cm with 3 A of current.

Two more pairs of Helmholtz coils sitting on top of the anti-Helmholtz coils create a uniform field in the transverse directions. This allows us to shift the center of the field gradient and thus the center of the 2D+ MOT cloud by up to 0.5 cm, giving us the ability to align the atomic beam with the differential pumping tube in a highly controllable fashion. All four pairs of coils are mounted directly on the 3D-printed oven described above. For more details on the fields and parameters of the coils, see [280].

8.1.4 Optics

The laser light generated on the optical table and split into individual beams using the spliceless array (see section 7.4) still needs to be shaped and appropriately polarized. From the optical point of view, the 2D+ MOT consists of four identical transverse beams and a combination of two overlapped axial beams–one that is retro-reflected and provides molasses cooling and another one which is blue-detuned and pushes the atomic cloud through the differential pumping tube.

Internal optics

Given that one of the six directions is inaccessible simply by the nature of the setup (the 2D+ MOT must be physically connected to the main experiment), the axial '+' beam needs to be retro-reflected off a mirror situated inside the vacuum chamber and attached to the differential pumping tube. In addition, a linear polarizer is mounted on top of the mirror which allows us to control the intensity of the reflected beam by rotating the incoming linear polarization (see [386]).

To allow the atomic beam to enter the differential pumping tube and leave the glass cell, both optical elements need to have a (minimum) 2 mm diameter hole drilled through their center. Furthermore, to minimize the contact surface between the two elements and the differential pumping tube which could potentially trap air, we decided to use two triplets of small cylindrical aluminium spacers (3 mm in diameter and 1 mm thick) which are glued on the outer edge of the circular surfaces and separate the mirror from the tube as well as the polarizer from the mirror. Figure 8.5 shows the optical elements attached to the differential pumping tube. Section 8.2 describes the gluing and drilling procedure as well as the exact components used and their performance after the bake-out. We also note that to prolong the lifetime of the polarizer, which is the first component hit by the atomic flux, it was coated with a 100 nm layer of SiO_2 resistant to the corrosive effect of potassium.

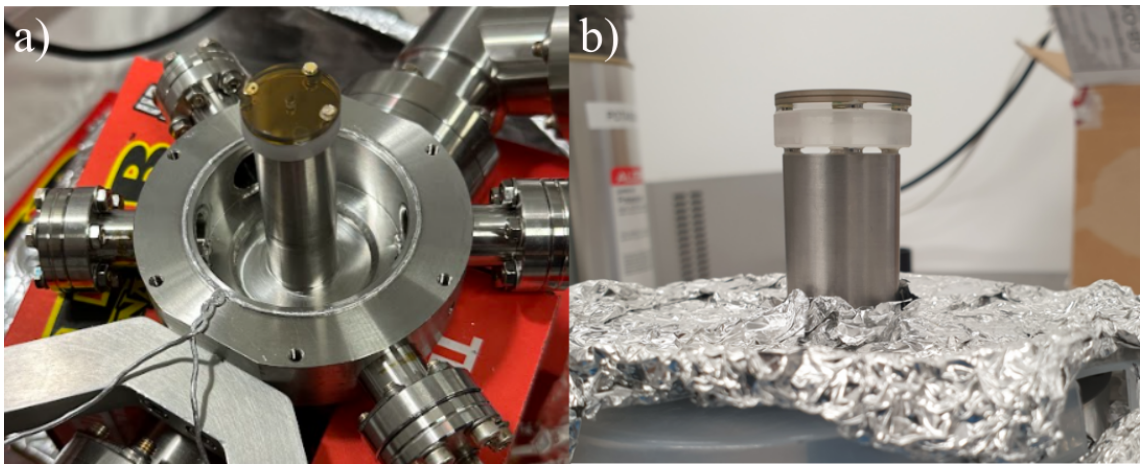


Figure 8.5: Internal optics. a) A gold mirror and a linear polarizer are glued to the end of the differential pumping tube. A 2 mm diameter hole had to be drilled through both elements. The drilling procedure is described in section 8.2.1. Notice the indium wire and its two ends that have been braided and flattened. b) Aluminium spacers were used to separate the optical elements and the metal surface in order to prevent trapping of air.

Beam shaping

Two separate setups are required to shape the four transverse MOT beams and the '+'/push beam. The transverse beams are identical (except for the handedness of their polarization) and need to be elliptical in order to match the dimensions of the glass cell (40×130 mm). Figure 8.6 shows a diagram of the optical system used to shape the transverse beams. After outcoupling from one of the four spliceless array outputs, the beam is collimated and passed through a polarizing beam-splitter (PBS) to remove residual polarization. It is then expanded using two telescopes–one circular and one cylindrical–to its final size of 18×54 mm in waist. Two mirrors at 45° provide enough degrees of freedom to align the beam through the cell. However, given that the light needs to be circularly polarized, the mirrors introduce polarization imperfections across the wavefront (a similar issue has been discussed in section 3.2.3). This can be partially mitigated by using a half- and a quarter-waveplate in tandem to pre-compensate for this distortion before the beam reflects off the mirrors.

The '+' and push beams, on the other hand, need to be circular in shape and linearly polarized such that the polarizer situated inside the vacuum chamber can be used to control the intensity of the retro-reflected '+' beam. Furthermore, while the '+' beam should match the dimensions of the cell and the optical elements inside (1 inch in diameter), the push beam has to pass through the differential pumping tube without clipping and so has to be focused down to < 2 mm in diameter. Additionally, the two beams enter the cell from the same side and therefore have to be overlapped beforehand. Figure 8.7 shows our optical setup designed to meet these requirements. Note that both beams need to be expanded together after the overlap due to the small size of the PBS. The final size of the '+' and push beams is 5.7 mm and 0.47 mm in waist respectively, matching well the our requirements.

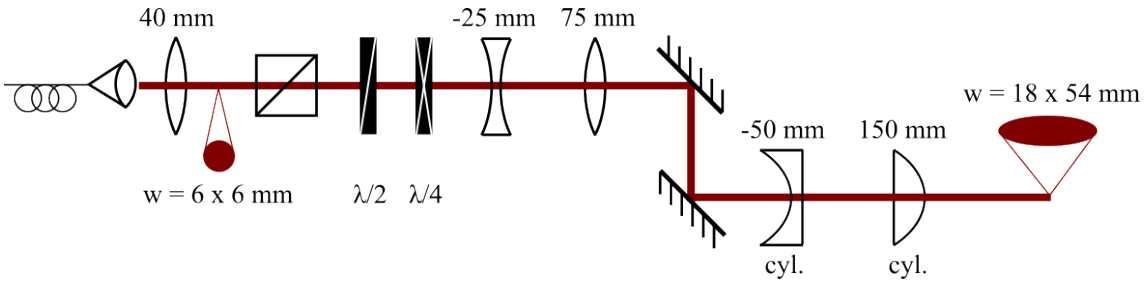


Figure 8.6: 2D+ MOT transverse beam optics. The light is outcoupled from one of the four spliceless array outputs and collimated to a waist of 6 mm. The polarization is cleaned using a PBS and the beam is then expanded to its final waists of 18 mm and 54 mm using a circular and a cylindrical telescope. Two mirrors are used to align the beam through the glass cell and a half- and a quarter-waveplate combination is used to correct for imperfections in circular polarization caused by reflection off the mirrors.

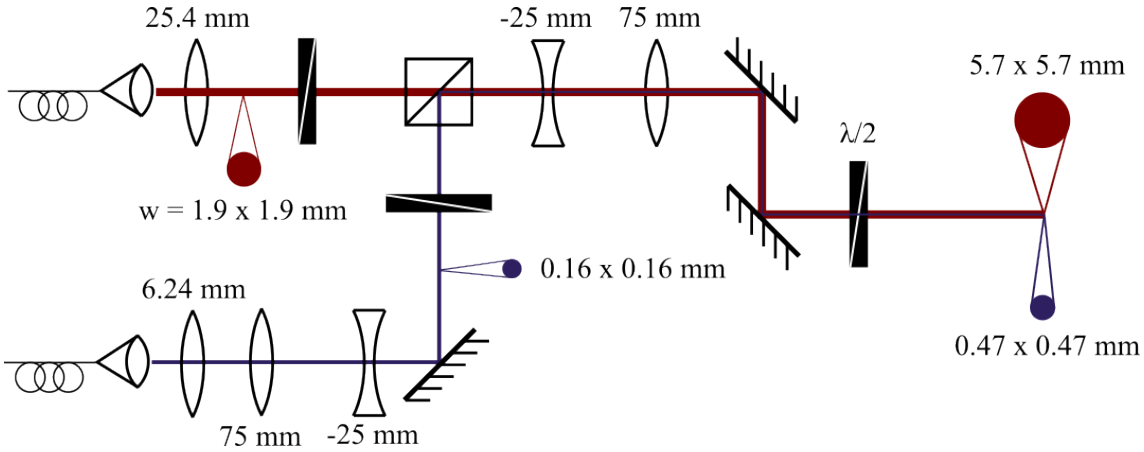


Figure 8.7: Push and '+' beam optics. Due to the small size of the PBS used for overlapping the two beams, they both need to be expanded together after the overlap such that the '+' beam reaches its desired final waist of 5.7 mm. To counteract this expansion and keep the push beam smaller than the differential pumping tube, it has to be focused down before the overlap. Two mirrors at 45° provide enough degrees of freedom to align the push beam through the tube into the main experimental chamber.

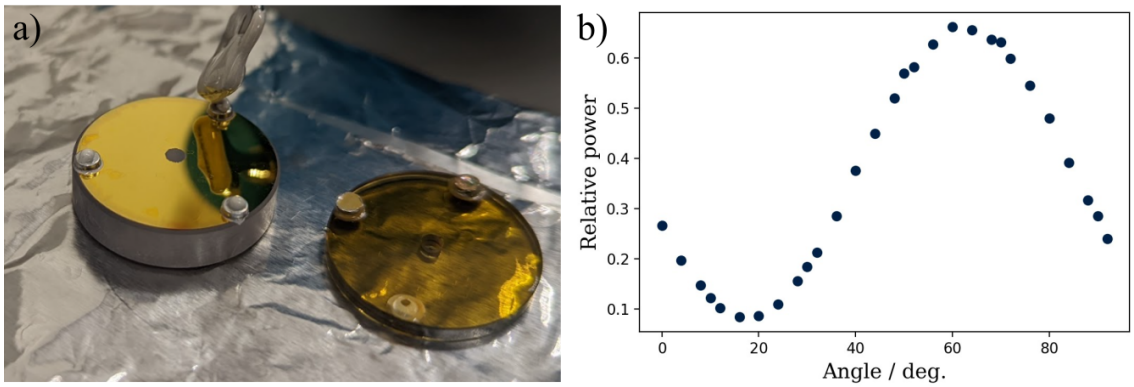


Figure 8.8: Gluing and optics performance. a) The epoxy glue was applied in small quantities using a metal spatula. Only three spacers were used per layer to minimize the amount of glue and the enclosed surface area. b) Performance of the polarizer/mirror tandem after the curing procedure. A linearly polarized beam was reflected off the optics and collected on a photodiode for a range of polarization angles. Using this setup, we can control the power of the reflected beam relative to the incoming beam in the $(0.1, 0.7)$ range.

8.2 Construction

In the following section, we give an account of the construction process of the 2D+ MOT vacuum section and the associated optics. We will particularly focus on some of the more technically demanding and non-standard steps such as the glass cell attachment and gluing of optical elements inside the chamber. Our hope is that this section can serve as a useful reference for future researchers constructing similar set-ups.

8.2.1 Gluing and drilling

As outlined in section 8.1.4, the optical molasses along the longitudinal direction is realized by retro-reflecting a red-detuned '+' beam from a linear polarizer/mirror pair situated inside the vacuum chamber on top of the differential pumping tube. Prior to sealing off the vacuum and pumping out the air, these optical elements needed to be drilled and attached to the chamber.

Initially, it was suggested that a sonic drill was used to drill a 2 mm diameter hole through both elements. Although partially successful, this method resulted in breaking of the polarizer due to its small thickness and in chipping of the optical material around the point of entry of the drill bit. Having learnt from this first attempt, we decided to drill the elements using a standard pillar drill and a diamond-coated drill bit. Furthermore, to prevent chipping and to support the material against breakage, we sandwiched each optical element between two spare N-BK7 mirrors separated from the element with lens tissue to guard against scratching. This sandwiching technique proved successful and, with very slow ($\approx 1\,\mathrm{mm\,min^{-1}}$) drill lowering speed, resulted in clean holes and minimal chipping. We note that during the drilling, a constant stream of distilled water was applied to the drilling region to carry away excess material and heat. The drilled components can be seen in figures 8.5 and 8.8a.

When it comes to the choice of glue, there are several requirements. Firstly, the glue has to work well with the materials involved i.e. N-BK7 glass, steel and aluminium (spacers). Secondly, it has to be suitable for vacuum applications which in practice means it must have a low outgassing rate. Lastly, its curing temperature needs to be below the damage threshold of the optical elements. Based on our previous communication with the author of reference [386], we first decided to use a two-component epoxy glue[9] with a brief (30 min) desiccation step preceding the application of the glue. Later it was discovered that this glue didn't provide sufficient binding between the optical elements and the aluminium spacers and the optics came loose. A different two-component epoxy was therefore used[10] which worked well and didn't require a desiccation step.

The glue was applied in small quantities to the aluminium spacers using a metal spatula. The whole system was then assembled layer by layer, starting with three spacers applied to the differential pumping tube, followed by the mirror, three more spacers and finally the linear polarizer[11]. The role of the spacers is to minimize the contact surface area between the components which could trap air. The glue application can be seen in figure 8.8 (left) and the effect of the spacers is shown in figure 8.5 (right). A 2 mm allen key was inserted into the hole in the optics and the differential pressure tube to keep the components aligned during the curing process.

Although the glue permits curing at room temperature (albeit for prolonged times), we decided to cure it at 100 °C which is a temperature comparable to the target bake-out temperature (see section 8.2.3). This way, we could also test whether the optics can withstand the temperatures of the bake. Initially, a fused silica dielectric mirror[12] was used but its reflective surface cracked and peeled off during the cure so we opted in for a gold mirror instead[13]. After successful gluing, we tested the optics with 767 nm light by collecting the reflected beam on a photodiode and plotting the power as a function of incoming linear polarization angle. The results are shown in figure 8.8 (right) for an input power of 11 mW, indicating that we can achieve reflections with relative power in the range $(0.1, 0.7)$ which covers the values used in literature [367], [374].

The potassium ampoule holder was glued to the ampoule in a similar fashion. Two small doses were applied to the top and bottom piece respectively (see figure 8.3). The components were then assembled and cured at 100 °C for 2 hours. We note that the aluminium holder pieces (as well as the spacers used for the vacuum optics) were put in an acetone sonic bath for 20 minutes to remove excess oil and dirt left over from the fabrication process. Once glued, the composite components were inserted into the bellow which was secured against bending using metal pieces to prevent accidental breakage of the ampoule prior to the bake-out.

As an interesting aside, we note that during our first curing attempt, a plastic flange cover was left attached to the vacuum chamber. This resulted in the plastic melting and covering the inside of the chamber. Fortunately, using a combination of metal and wooden

[9] Epotek 920 by Epoxy Technology
[10] Torr Seal by Agilent
[11] LPVIS100 by Thorlabs
[12] BB1 E03 by Thorlabs
[13] Unprotected gold mirror PF10-03-M03 by Thorlabs

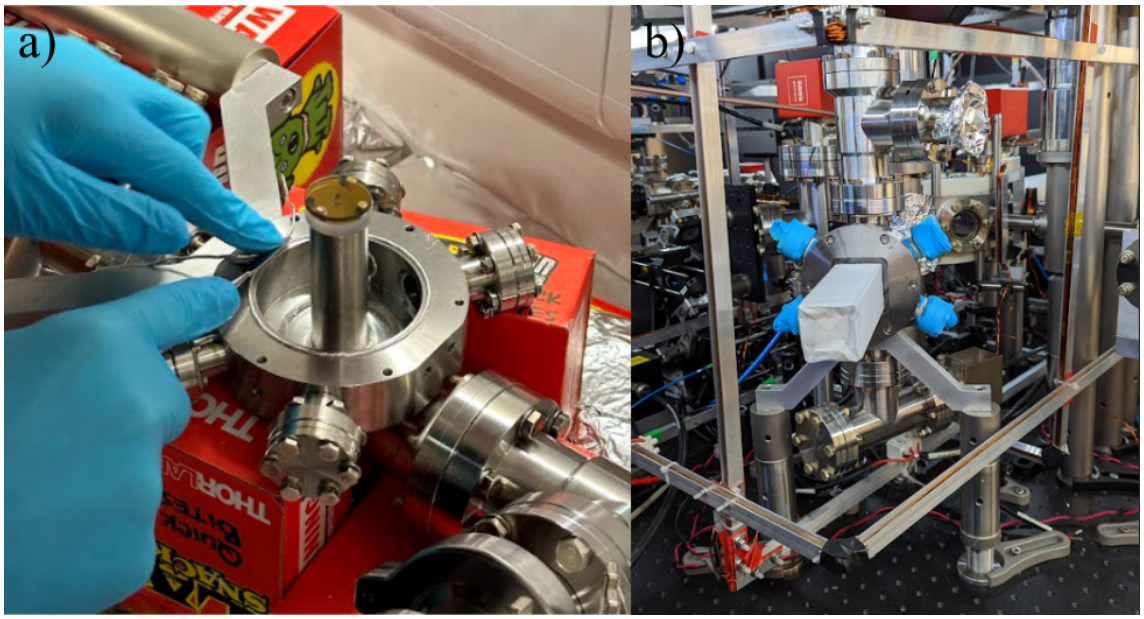


Figure 8.9: Assembly. a) Excess indium wire was cut off to retain the circular symmetry of the seal and hence distribute the pressure as evenly as possible. b) The potassium vacuum system attached to the main experiment. Note that the bellow was removed for better manoeuvrability. The blue rubber material was used to enclose some of the flanges, allowing us to localize vacuum leaks more efficiently.

tools (wood was used to prevent damaging the flanges), most of the plastic was removed. To remove any left over residues, toluene at slightly elevated temperature (50°) was left in the chamber for 3 hrs. This made the plastic more brittle and therefore easier to remove. After this incident, we didn't notice any deterioration of the vacuum quality.

8.2.2 Assembly and the glass cell

Before the potassium vacuum section is connected to the main experiment through the gate valve, the glass cell needs to be attached. This is best done when the 2D+ MOT vacuum chamber (and hence the glass cell flange) is horizontal to prevent any uneven pressure distribution alongside the indium seal during the initial tightening.

Prior to applying the indium wire to the flange, all surfaces were wiped with methanol using lint-free wipes. The indium wire itself was submerged in a 10% solution of HCl for 10 minutes in order to remove the top layer of indium oxide, ensuring better binding to the steel chamber and the glass cell. After cleaning the wire, it was gently pressed into the circular grove running along the flat flange surface. The two meeting ends of the wire were twisted several times and the resulting braid was flattened against the flange surface to the same thickness as the rest of the wire (see figure 8.5). This way, the pressure wouldn't concentrate around the braid but would be evenly distribute instead. Excess braid material was cut off using a razor blade to achieve a symmetric, circular application of indium to the flange. This process is shown in figure 8.9a.

Next, the glass cell was gently placed on top of the wire and centered in both directions. Finally, the metal holder piece (see section 8.1.1) was put over the cell, sandwiching the

metal flange between it and the vacuum chamber. In our initial design, there was a piece of teflon inserted between the holder and the cell to provide cushioning and distribute the pressure more evenly. However, during our first tightening attempt, the cell cracked. We believe this to be partially due to the stiffness of the teflon piece as well as due to overtightening. In the second (and this time successful) iteration, a rubber O ring was used in place of the teflon sheet. The diameter of the ring was chosen to match the diameter of groove holding the indium wire.

With the holder piece in place, we began tightening the six screws on its circumference responsible for closing the seal. After learning from our first failed attempt, we decided to use a torque wrench[14] which enabled us to tighten the screws in a more controlled and quantifiable manner. Since indium is highly malleable and sticky, it doesn't provide enough restoring (elastic) force on the holder piece. Consequently, all the screws feel quite loose even when the seal is complete. We therefore proceeded with great caution and only verticalized the chamber once the gap between the cell and the steel flange was visibly small and the torque on the screws approached the maximum threshold of the gauge.

Once verticalized, the chamber was connected to a helium detector (with its own pump) via the angle valve to test the quality of the seal. Bottled helium was sprayed around critical sections of the vacuum assembly to detect any leaks and several more rounds of tightening were performed before the seal was deemed sufficient. After that, the whole 2D+ MOT chamber was moved to the experimental table and attached to the main vacuum chamber via the gate valve–see figure 8.9b. Extra care was taken to match the height of the two vacuum assemblies to avoid any torque being exerted on the gate valve. In fact, we detected a sudden increase of pressure in the main vacuum chamber when we first attached the potassium section (note that at that point, the gate valve was still closed). This was quickly resolved by adjusting the height of the central post without causing any permanent damage but the incident could have had catastrophic effects if left unnoticed. A last round of leak checking was performed before the assembly was connected to a turbo pump (in place of the helium detector) to begin the initial pump-down before the bake-out procedure.

8.2.3 Bake-out

One of the major factors limiting the attainable quality of vacuum in stainless steel chambers is outgassing of material from the walls of the chamber. This is predominantly caused by hydrogen which gets trapped inside steel during the initial phases of production and fabrication [390]. To mitigate this, it is customary to perform a bake-out procedure in which the vacuum assembly is simultaneously heated up and pumped down over a long period of time. The increased temperature encourages outgassing of lighter compounds such as hydrogen whilst the continuous pumping ensures that the equilibrium concentration is shifted to lower values. In general, the higher the bake-out temperature, the faster the equilibrium can be approached. In practice, the temperature is limited either by the performance of the heating elements or by the damage threshold of the least resilient

[14] TD24 by Thorlabs

components.

We performed a week-long bake out of the potassium assembly at around 100 °C. The temperature was mainly limited by the the low melting point of indium (150 °C [389]) and the damage threshold of the linear polarizer (≈ 130 °C). Given the pivotal role the indium wire plays in maintaining the vacuum and our uncertainty regarding its mechanical properties at elevated temperatures, we decided to limit the bake to 100 °C and extended it over a week.

Four sections of the vacuum assembly–the glass cell, the bellow, the getter pump tee and the angle valve–we wrapped in individual heating tapes[15] controlled by variac transformers[16]. The whole systems was then wrapped in one layer of insulating material and several layers of aluminium foil. Six thermocouples and five digital thermometers[17] were distributed around the whole apparatus for monitoring. A pump down was performed using a turbo pump[18] connected to the system via the angle valve and an initial pressure of 4.6×10^{-8} mbar was reached.

With the turbo pump switched on, the temperature was gradually increased ($\approx 10\,^{\circ}\mathrm{C\,h^{-1}}$) in two steps up to ≈ 100 °C. After a three-day dwell period, the getter pump went through a conditioning cycle. This expelled material and caused a temporary spike in pressure but the system returned back to its state over the course of an hour. The assembly was baked for another four days after which the the power of the heating elements was lowered in two steps until the system reached room temperature. Towards the end of the cooling ramp, the getter pump was removed from the conditioning mode and the potassium ampoule was broken by bending the bellow. The reason behind switching off the conditioning mode is to protect the pump from an inevitable release of residual fumes trapped in the potassium ampoule. After one hour, the pressure returned to its original (pre-breakage) value. As the final step, the getter pump was cycled through the conditioning stage for the last time to prepare it for HV operation. Furthermore, the turbo pump was valved off using the angle valve and the ion pump in the four-way tee section was turned on, marking the end of the bake-out and pump-down procedure with the final ion pump and turbo pump pressure stabilizing at 3×10^{-10} mbar and 1×10^{-9} mbar respectively. Note that at this point, the K vacuum section was still separated from the main experiment using the gate valve. Full connection was only achieved once the 2D+ MOT was established (see section 8.3).

Temperatures and pressures were recorded throughout the whole bake-out procedure and are shown in figure 8.10. The temperature from the digital thermometers was read by an Arduino Uno micro-controller and sent to the central PC via a serial connection together with pressure readings from the ion pump controller. A logging program originally written by Dr Krstajić and adapted by me was used to query the two devices for readings and plot them in real time–see appendix A.3. It is clear that the bake-out procedure fulfilled its purpose, lowering the pressure in the K vacuum assembly by a factor of ∼ 50.

[15] 379-750 by RS Components
[16] MBV 2E-1 by RS Components
[17] Waterproof DS18B20
[18] HiPace 80 by Pfeiffer Vacuum

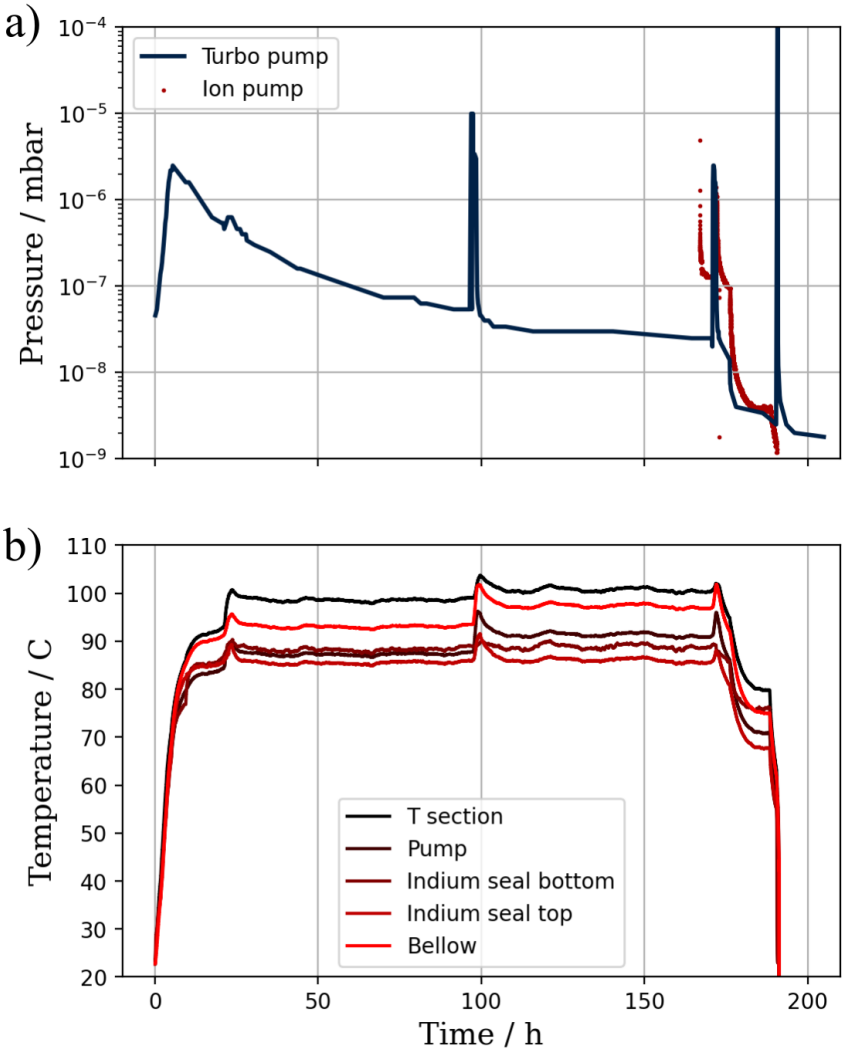


Figure 8.10: Bake-out procedure. a) Pressure and b) temperature readings recorded during the bake-out procedure of the potassium 2D+ MOT vacuum assembly. Note that the spikes in pressure correspond to the getter pump entering the conditioning mode (2×) and the breakage of the potassium ampoule (1×) respectively. Temperature probes were placed at five different points around the assembly to monitor (and minimize) temperature gradients.

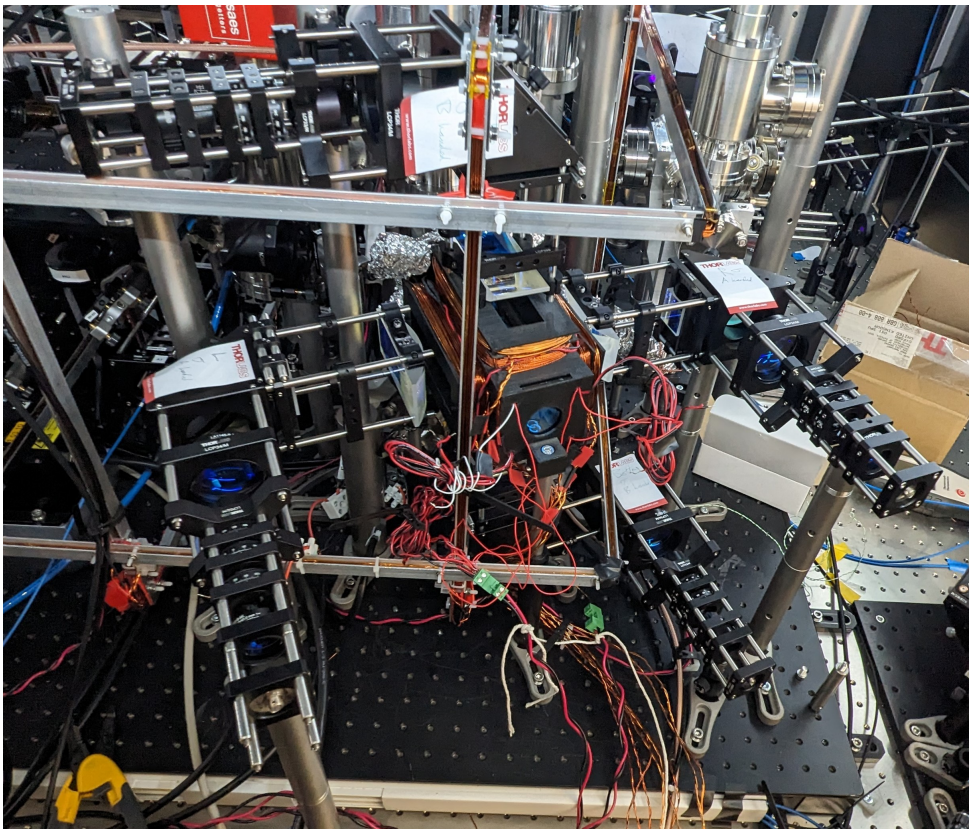


Figure 8.11: Assembled 2D+ MOT setup. The 3D-printed oven covers the glass cell and houses four pairs of coils. Four long optical 'arms' shape and direct the transverse MOT beams onto the cell. Note that the last optical system responsible for preparing the push and '+' beams is not present in the photo.

8.2.4 The full setup

Once the bake-out was finished and the vacuum assembly unwrapped, the glass cell was covered by the 3D-printed oven (see section 8.1.2). The heating elements in the oven and around the bellow were used to increase their temperature to 40 °C and 45 °C respectively. Finally, the 2D+ MOT optics described in section 8.1.4 was installed around the cell, addressing the potassium vapour trapped inside it from five directions. Figure 8.11 shows a photo of the full setup in place.

8.3 2D+ MOT

In this section, we demonstrate the realisation of a functional 2D+ MOT of ^{41}K. More optimization will be done in the near future using the (recently established) 3D MOT as a reference which will allow us to measure the loading rate and atomic flux produced by the 2D+ MOT. Nevertheless, we can still provide a useful account of our procedure and of the relevant experimental parameters.

Parameter	Literature	Oxford
Cooling detuning [Γ]	$(-5, -2.5)$	-3
Re-pump detuning [Γ]	$(-5, -2)$	-1.5
Push detuning [Γ]	$(2, 6)$	3.5
$P_{\text{cool}}/P_{\text{repump}}$	$(1.5, 2)$	1.6
I_{trans} $[I_s]$	$(5, 21)$	$(10, 25)$
I_+ $[I_s]$	$(1, 5)$	4
I_{push} $[I_s]$	$(10, 60)$	23
dB/dr [G/cm^{-1}]	$(11, 22)$	14.2

Table 8.1: 2D MOT parameters. Round brackets indicate a range of values. Note that for the D2 line, $\Gamma = 2\pi \times 6\,\text{MHz}$ and $I_s = 1.75\,\text{mW cm}^{-2}$. We quote a range for the transverse beam intensity because our setup gives us the ability to continuously tune the transverse beam waist.

8.3.1 Optimal parameters

Two-dimensional MOTs are a frequent occurrence within the field of ultracold physics. Consequently, there exists a lot of literature that covers their construction, optimization and performance [159], [374], [385], [386]. Each experiment is, of course, unique and not entirely reproducible. However, certain patterns arising from the nature of 2D MOTs and the physics behind them emerge and can be used as general guides for choosing the right experimental values.

As discussed in chapter 7, the potassium 2D MOT operates on the D2 line and uses a cooling ($F = 2 \rightarrow F' = 3$) and a re-pump ($F = 1 \rightarrow F' = 2$) frequency to ensure closed optical cycling. Both components need to be red-detuned to provide molasses-like cooling (see section 3.2). The usual literature values range from -2Γ to -5Γ with the re-pump beam usually tuned closer to resonance than the cooling beam. The power ratio of the two components tends to be around $8:5$, making the re-pump comparable in strength to the cooler. In terms of beam intensities, the higher the better with $I > I_s = 1.75\,\text{mW cm}^{-2}$ a sufficient condition for observing weak trapping.

The '+' beam acts as an additional molasses along the non-trapping direction and it is therefore identical in composition to the transverse beams. The push beam, on the other hand, should accelerate atoms out of the 2D MOT region and into the main chamber. As such, it should be blue-detuned with the detuning governing the final velocity of atoms along the beam's direction of propagation. The typical detuning values range between 0 and 5Γ and the intensities stay above the saturation level. Table 8.1 summarizes typical experimental parameters collected from literature as well as our own. We note that the total optical power diverted to the 2D MOT branch is, in our case, limited by the maximum input of the spliceless array used to evenly distribute power between the transverse beams (see section 7.4.3) and corresponds to a value of $\approx 150\,\text{mW}$ per beam.

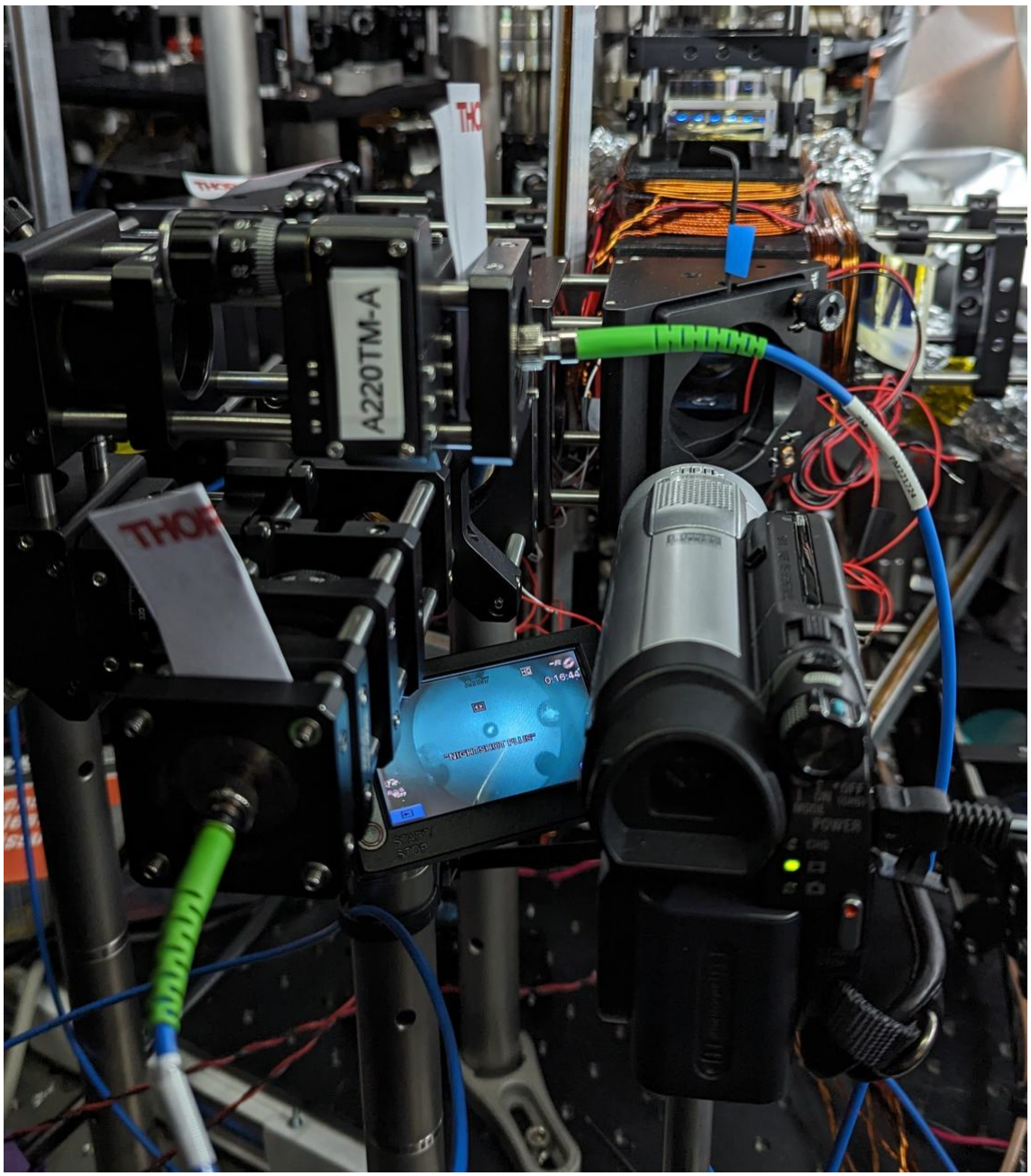


Figure 8.12: Ghostbusters camera. A digital camera was used to image the fluorescence from the 2D MOT in real time, speeding up the optimization process. The MOT is visible as a bright spot in the center of the hole drilled through the mirror/polarizer glued to the end of the differential pumping tube. Note that in order to get sufficient optical access, one of the mirrors directing the push and '+' beams into the chamber had to be removed, preventing us from directly imaging the MOT in the 2D+ configuration. The 2D+ configuration therefore had to be optimized separately using a fluorescence signal from the main experimental chamber.

8.3.2 Searching procedure–who you gonna call?

An initial MOT signal was obtained by setting the experimental parameters to the centers of the relevant ranges and by scanning the laser frequency using its internal piezo voltage and looking for florescence in the glass cell. For this purpose, the '+' and push beam optics was temporarily removed to allow access to the front viewport. Even though the Doppler-broadened florescence of the thermal gas was visible to the naked eye (under low background light conditions), the florescence from the 2D MOT was not. Fortunately, the group owns a digital camera[19] which is highly sensitive to red and infrared light and is therefore a perfect tool for hunting for the ghost MOT in real time as can be seen in figure 8.12.

Once a high-density, cigar-shaped region in the center of the glass cell approximately 1 mm in diameter was established (see figure 8.13), the '+' and push beams were put in place. All the experimental parameters were then optimized by using the atomic florescence signal collected in the main chamber and induced by an intense ($\approx 6I_s$), resonant imaging beam. The imaging beam was directed perpendicular to the atomic flux to minimize signal loss due to Doppler broadening. We note that the magnitude of the flux was highly sensitive to the alignment of the magnetic field gradient with respect to the differential pumping tube. However, we were able to compensate for minor imperfections using the offset field coils and the power balance in the transverse beams.

We observed a four-fold florescence signal enhancement when the push beam was enabled. Similarly, a three-fold enhancement was achieved with the longitudinal molasses '+' beam. The power ratio between the incoming and reflected '+' beam optimized to $\approx 4:1$ by rotating the linear polarization of the incoming beam and reflecting it off the polarizer/mirror tandem glued inside the chamber.

Using the imaging probe beam directed at an angle $\theta = 33.75°$ to the path of the atoms, we measured the velocity distribution of the atomic flux by changing the frequency detuning of the probe and recording the fluorescence signal. The magnitude of the signal can be approximated as

$$\Phi(\delta) = \eta \int \frac{F(v)}{v} \frac{\Gamma}{2} \frac{s}{1 + s + \left(\frac{2(\delta - \mathbf{k}\cdot\mathbf{v})}{\Gamma}\right)^2} dv \tag{8.1}$$

where η is a calibration constant, $s = I_{\text{probe}}/I_s$, $v = |\mathbf{v}|$ and $F(v)$ is the longitudinal velocity distribution of the atomic flux. Note that the $1/v$ factor reflects the fact that fast atoms spend shorter time in the probe beam interaction region and therefore contribute less to the fluorescence.

The intensity of the probe beam for this purpose was lowered such that $s \approx 1$. If we assume that the velocity distribution $F(v)$ is much wider than the resonance feature such that $k\Delta v \cos\theta \gg \Gamma$, the fluorescence signal is approximately proportional to the velocity distribution

$$\Phi(\delta) \propto \frac{F\left(\frac{\delta}{k\cos\theta}\right)}{\frac{\delta}{k\cos\theta}} \tag{8.2}$$

[19] Which was sold on eBay as a "Ghostbusters" camera

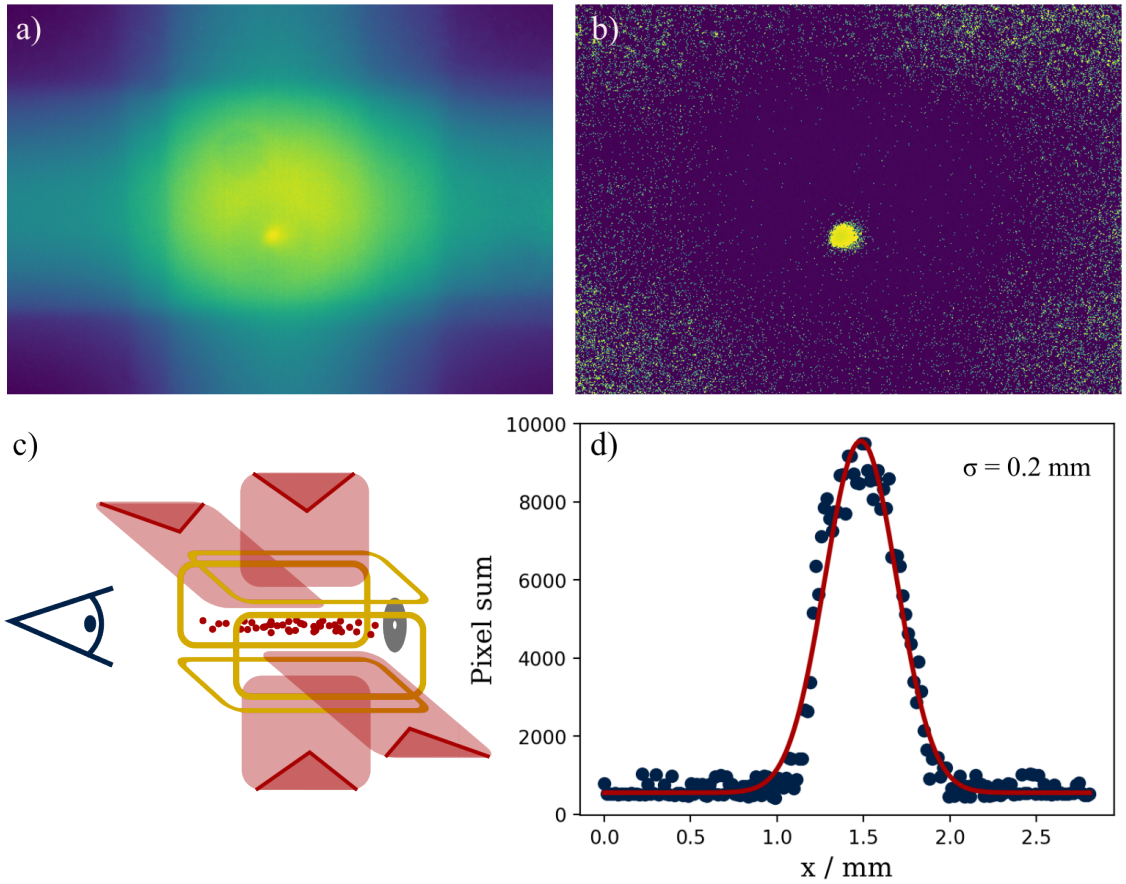


Figure 8.13: 2D MOT fluorescence. a) Atomic fluorescence in the center of the 2D MOT chamber. The dense region in the middle indicates a successful creation of a 2D MOT. The darker circular background around the dense region is the (out-of-focus) circular aperture of the drilled mirror/differential pumping tube. b) Image of the 2D MOT obtained by subtracting the background fluorescence of the thermal gas filling the glass cell. c) Imaging geometry with the four transverse cooling beams in red, quadruple coils in yellow and the mirror/differential tube in gray. d) A Gaussian fit of the 2D MOT transverse density. The estimated diameter is considerably smaller than the diameter of the differential pumping tube ($\approx 2\,\mathrm{mm}$), implying that an efficient transfer of atoms into the main experimental chamber should be possible.

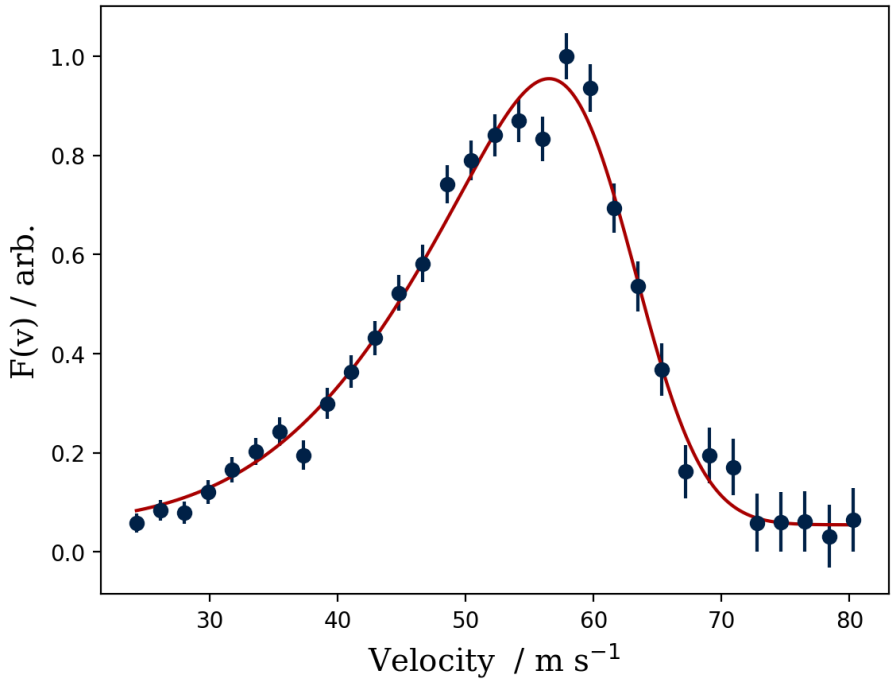


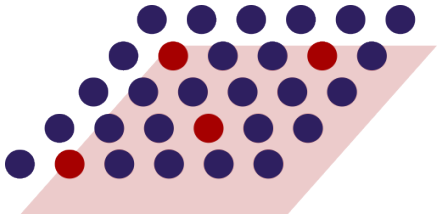
Figure 8.14: 2D MOT longitudinal velocity distribution. The velocity spectrum $F(v)$ of the atomic flux emerging from the 2D MOT section was obtained by measuring the atomic fluorescence as a function of the imaging beam detuning. The peak velocity $v_m \approx 55\,\mathrm{m\,s^{-1}}$ should lead to successful loading of the 3D MOT. Note that the fitted curve is solely a guide for the eye and implies no physical significance.

and we can recover it from our data. Figure 8.14 shows our measurement of the velocity distribution using this technique. The peak velocity $v_m \approx 55\,\mathrm{m\,s^{-1}}$ is consistent with literature values [159], [385] and should be slow enough to be captured by the 3D MOT, marking a major step towards an ultracold Er-K mixture.

Part III

The Mixture

9. Conclusion and Outlook



This thesis provides a comprehensive summary of the current state of the Oxford dipolar experiment, focusing on the progress made towards realising a first ultracold erbium-potassium mixture as well as on two major scientific contributions made with our erbium machine.

The first section, devoted to the erbium part of the experiment, begins by discussing key properties of dipolar quantum gases and, most importantly, of erbium in the context of ultracold atomic physics. The next two chapters then go into detail and describes our experimental sequence that leads to the production of large Bose-Einstein condensates ($> 2.2 \times 10^5$ atoms) of ^{166}Er. Special attention is given to the optical dipole trapping system, focusing on its utilization in efficient evaporative cooling and on its implementation using focus-tunable lenses which will allow for optical transport in the future.

The fifth chapter presents our investigation of three-body losses in ^{166}Er. We reveal six new features which show strong temperature dependence, hinting at their higher partial wave character. We also measure a light intensity-dependent shift in their position and compare our results with existing theories. The chapter concludes with the development of an extended model of the three-body loss process that accounts for additional heating of the atomic cloud observed in the experiment. We note that the knowledge of the position and the temperature dependence of the loss features allowed us to optimize our evaporation sequence and achieve large erbium Bose-Einstein condensates (BECs).

The last chapter of this section is devoted to the first measurement of the BEC critical temperature shift due to the anisotropic, long-ranged dipole-dipole interactions (DDIs). It starts by outlining the relevant theory, focusing first on contact interactions and then extending the theory to DDIs. It then goes on to detail our experimental procedure which involves complex image analysis and careful systematic error removal. The results presented in the chapter clearly demonstrate a shift in the critical temperature which is dependent on the dipole polarization angle, consistent with theory and numerical calculations.

The second major section of the thesis is concerned with the impurity species, potassium. Mirroring the structure of the first section, we begin by introducing potassium on the atomic level. We use this knowledge to discuss the laser cooling stages necessary to bring potassium close to degeneracy and mix it with an ultracold sample of erbium. The rest of the chapter then describes our optical setup designed and built for this purpose.

Finally, the second chapter of the potassium section and the last substantial chapter of this thesis details the design, construction process and performance of our 2D+ magneto-optical trap. The trap serves as a steady source of cold potassium atoms which are introduced to the main experimental chamber.

The work described in this thesis puts us at the doorstep of realising the first erbium-potassium ultracold mixture. We will conclude by outlining the immediate steps that are currently being taken to achieve this goal as well several potential scientific avenues for our novel Er-K platform.

9.1 The future of our experiment

Two major features distinguish the Oxford dipolar experiment from other similar experiments around the world. Firstly, it is the homogeneous pancake geometry of the final trap implemented using an optical box potential [46], [151] which will gives us access to regimes where the interplay of constrained geometry and the anisotropic DDI results in exotic states of matter [117], [119], [152].

Secondly, the addition of a second, non-dipolar species will enable us to study impurity physics in an environment where the reservoir particles interact anisotropically and over long ranges and where the reservoir-impurity interactions are fully controllable.

Below, we will consider each feature individually, discussing the immediate steps necessary for its implementation and the physical phenomena it will allow us to study.

9.1.1 Box potential

At the time of writing, the upgraded tunable lens (TL) stabilization system described in section 4.5 has been implemented in the main experiment and shows promising results with regards to the dipole trap loading stability. With it in place, we have performed successful transport of atoms from the main chamber into the science cell.

The sheet beam which provides planar confinement in the final 2D box trap has been overlapped with the transport beam, allowing us to perform efficient evaporation and reach degeneracy in the science cell (see figure 9.1a). The cylindrical walls of the box are formed from a blue-detuned (and hence repulsive) 372 nm beam reflected off a spatial light modulator (SLM) which imprints a phase pattern on the wavefront. The beam is then projected into a Fourier plane using series of lenses [45] to produce the final hollow cylindrical intensity pattern [391]. The pattern has been successfully created and its first signs have been detected on the atomic cloud–see figure 9.1b, c.

To have access to high-field Feshbach resonances of potassium [227], [279] and hence control the impurity-impurity interaction strength, a set of coils was designed by Gavin Lamb [199] that can produce uniform fields of up to 250 G at an arbitrary angle relative to the axis of the box trap. Additionally, another set of smaller, faster coils will allow us to quickly rotate the dipoles and effectively average out the DDI [158]. The coils have been fabricated but still need to be positioned around the science cell.

Future extensions of the experiment will include a digital micro-mirror device (DMD)

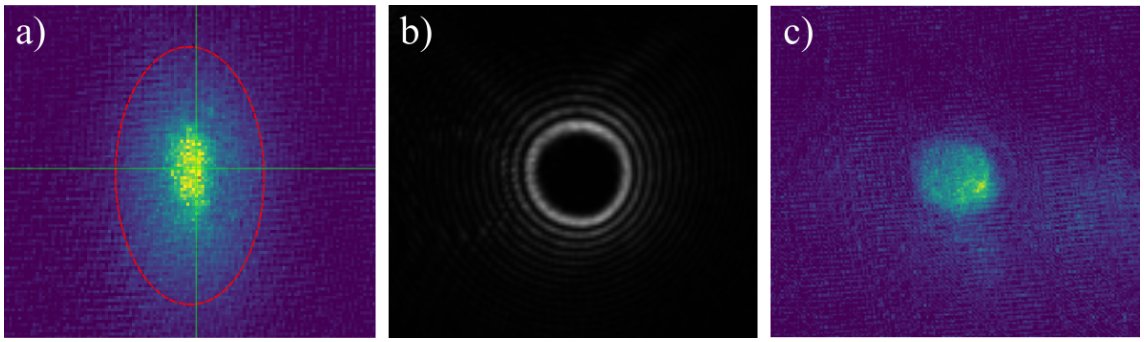


Figure 9.1: Pancake trap. a) A Bose-Einstein condensate produced in the science cell using the transport beam and the planar sheet beam. b) Hollow cylindrical intensity pattern produced by a spatial light modulator (SLM) which is overlapped with a horizontal sheet beam to create a 2D pancake trap. Image taken by Master's student Eugene Kim. c) Image of atoms confined to the cylindrical beam.

[392] for realizing Bragg spectroscopy [393] and probing the roton excitation spectrum [109], [394] of a 2D dipolar gas. Another planned upgrade involves the installation of a trichroic objective which will be used to enhance the imaging resolution for both erbium (blue) and potassium (red) as well as project Bragg beams (yellow) onto the atomic sample. An initial design of the setup was made by our Master's student Yuqing Wang and was further refined and prepared for final implementation by Gavin.

Once the last technical hurdles are overcome, the platform will be used for investigating a range of physical phenomena, some of which are listed below.

Roton physics

As discussed in section 2.4.3, a dipolar BEC confined to two dimensions shows a peculiar feature in its excitation spectrum. The feature, also known as the roton minimum, manifests as a pronounced dip in the excitation energy compared to the typical Bogoliubov dispersion [204]. The depth of the dip depends on the strength of the DDI, ε_{dd}, relative to the strength of the contact interactions.

The existence of the minimum should lead to lowering of the superfluid critical velocity as given by the Landau criterion [77]–this is depicted in figure 9.2a. Lowering the minimum even further by increasing ε_{dd} eventually leads to collapse and formation of quantum droplets [112]–[115], [197] or, under certain circumstances, of a supersolid [115]–[118], [271]. Our two-dimensional platform will allow us to probe the excitation spectrum either directly by utilizing Bragg spectroscopy or indirectly by measuring the superfluid critical velocity using a beam-stirring technique [395], [396] and a DMD. Comparing the results could shed more light on the role of vortex excitations in the collapse of a dipolar quantum gas.

Phase transition dynamics

When the critical temperature T_c of a thermal gas is crossed and a BEC begins to form, the condensate wave function ψ_0 evolves continuously from zero whereas its phase as-

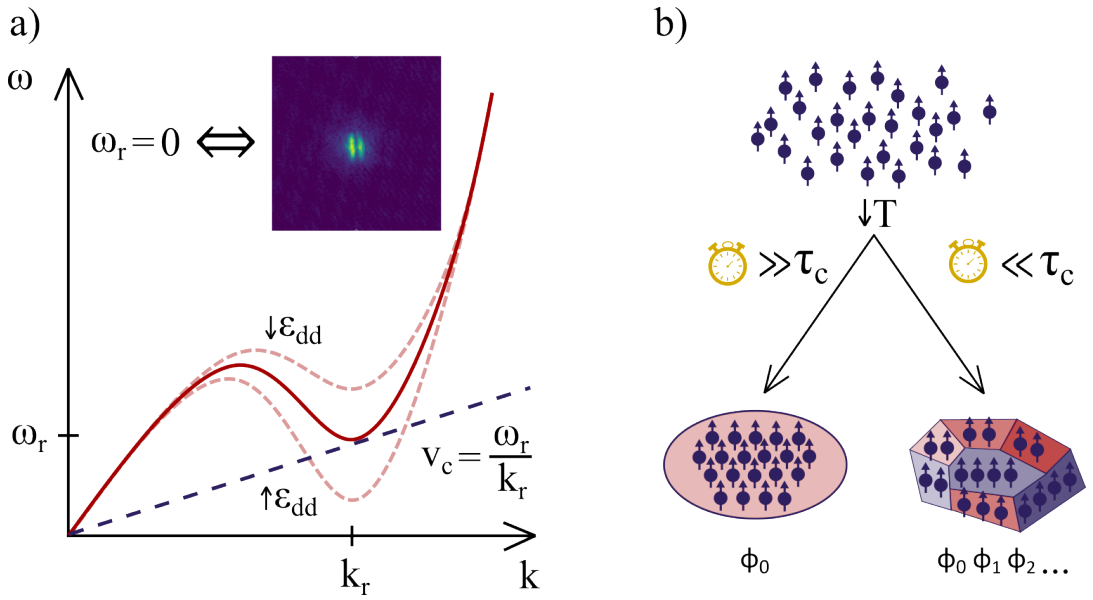


Figure 9.2: Future experiments. a) Roton minimum in the excitation spectrum of a 2D dipolar gas leads to lowering of the critical superfluid velocity v_c. The minimum becomes more pronounced as the dipolar strength ε_{dd} increases. Zero crossing leads to the collapse and formation of quantum droplets. b) BEC transition dynamics. According to Kibble-Zurek theory, crossing the BEC critical point at a finite rate comparable to, or smaller than the correlation propagation time τ_c results in the formation of condensate subdomains with different phases. The long-ranged DDI should affect the type of universal scaling followed by the system.

sumes a specific, finite value. The continuity of the order parameter ψ_0 accompanied by spontaneous symmetry breaking in the form of a non-zero, global phase are characteristic features of a second-order phase transition. However, this picture only holds if the critical point is crossed slowly, e.g. adiabatically.

If, instead, the transition happens faster than the typical timescale of correlation propagation in the system, subdomains with different order parameter values form. In other words, correlations *freeze out* before they can spread throughout the whole system and enforce a global phase, resulting in formation of smaller sub-regions that didn't have enough time to 'communicate' and match their phases–see figure 9.2b. This mechanism is described by Kibble-Zurek theory [397] which predicts a universal power law scaling of the correlation length, order parameter and other thermodynamic quantities with temperature, irrespective of the microscopic properties of the system [398].

The high degree of tunability combined with a range of accessible critical phenomena such as the BEC transition make cold atom experiments excellent platforms for testing these theories. Homogeneous systems are particularly well-suited for this purpose [36], [37], [399] since the whole sample undergoes the transition at the same time and the observable physics is thus no longer limited by the size of the system but rather governed by its correlations. With our homogeneous 'pancake' trap, we can investigate the effect of the long-ranged DDI on correlation propagation and hence on the critical exponents of the BEC transition. Furthermore, we can extend our investigation to the supersolid [400] and quantum droplet phases in search for an underlying difference in the transition dynamics.

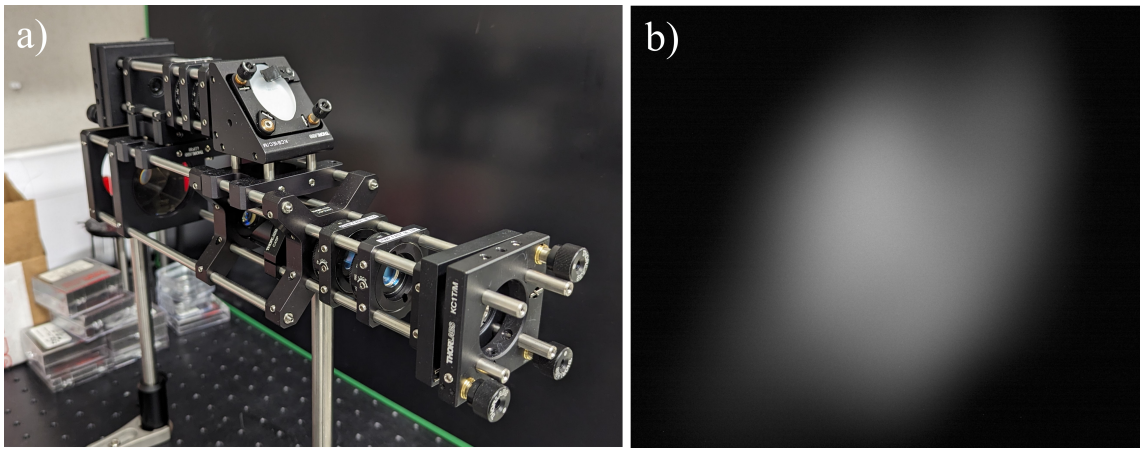


Figure 9.3: Dichroic MOT optics and ^{41}K 3D MOT. a) An optical assembly for combining and shaping the 583 nm and 767 nm MOT beams for simultaneous cooling of erbium and potassium. b) Fluorescence image of a 3D MOT of ^{41}K forming in the main experimental chamber.

9.1.2 Mixture physics

Having successfully built a source of cold potassium atoms (see chapter 8), the next step is to combine the two species in the main experimental chamber. As discussed in section 7.3, this will be done in two stages. First, both erbium and potassium will undergo cooling in a dichroic 3D MOT loaded from their respective sources. Second, the two MOT clouds will be overlapped and transferred into a single ODT, forming an ultracold Er-K mixture.

Due to the limited number of viewports in the main vacuum chamber, the erbium (yellow) and potassium (red) MOT light beams have to be overlapped prior to entering the chamber. This is done using a dichroic mirror and a compact cage system which is responsible for shaping and polarizing both beams–see figure 9.3a. At the time of writing, all of the original 3D MOT beams have been replaced with their dichroic equivalents and a 3D MOT of ^{41}K with $\sim 200 \times 10^6$ atoms has been established in the main chamber (figure 9.3b), awaiting further optimization.

All the necessary light preparation has already been done (see section 7.4) so the dual-species 3D MOT should be quickly attainable. The exact loading sequence will require careful consideration due to the difference in field gradient requirements for the two species but loading into the ODT should, in principle, be straightforward given the favourable polarizability of K at 1064 nm [123], [383]. Once the two species are mixed, we can start probing the properties of the mixture in various ways, some of which are described below.

Interspecies Feshbach resonances

Before we can investigate the nuances of impurity physics, we need to expand our already extensive experimental toolkit for the ability to control the reservoir-impurity interactions. Much like in single species experiments, this will be done using Feshbach resonances. However, due to the lack of data on Er-K resonances, we will first need to locate them before we can utilize them. Other experiments with Dy-K mixtures [138], [156], [401]

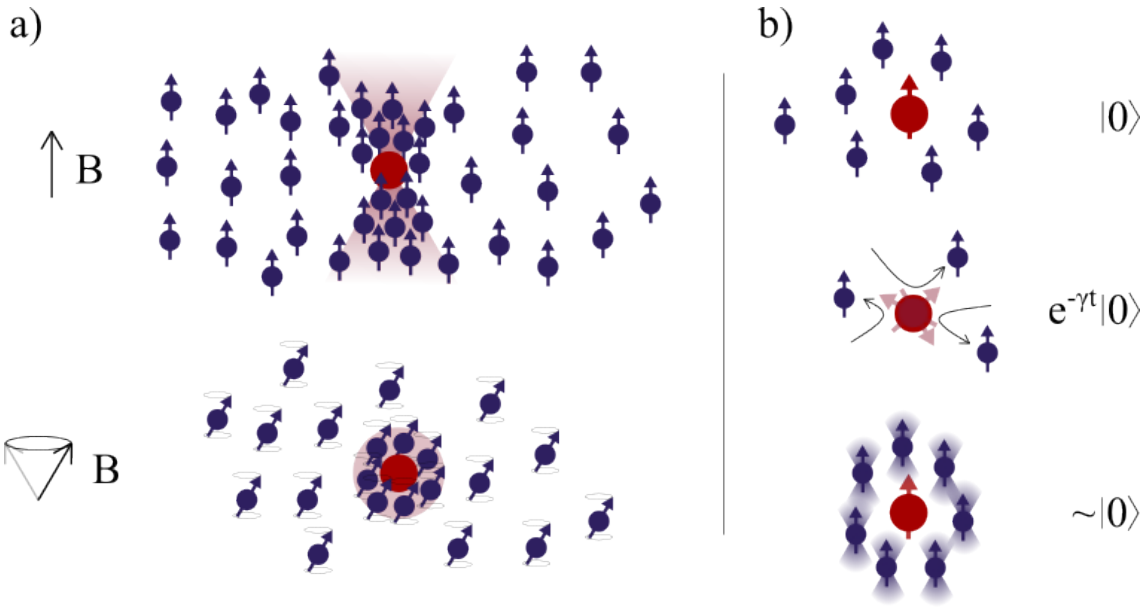


Figure 9.4: Mixture Physics cartoon. a) Dipolar Bose polarons. The dipole-dipole interaction between the atoms of the erbium bath will lead to anisotropic properties of the polarons formed around potassium impurities. We can tune the dipolarity of the system by quickly rotating the polarizing magnetic field. b) Non-Markovian reservoir. A qubit immersed in a dipolar condensate is expected to undergo coherence loss and subsequent revival due to the long-ranged nature of the DDI.

indicate that the resonances should be low-field, similar to resonances of erbium (see section 2.3.4), making them accessible within the main MOT chamber in the dual species ODT stage i.e. prior to transport to the science cell.

We can locate the resonances by looking for loss features of both Er and K when scanning the magnetic field magnitude B–a similar process is thoroughly described in chapter 5. However, in order to fully control the interaction strength, we need to measure the scattering length itself as a function of B. This can be done using, for example, cross-dimensional rethermalization [153], [401].

Dipolar Bose polarons

An impurity immersed in a background bath of atoms creates a disturbance in the atomic cloud. This disturbance is inherently tied to the impurity and, in some sense, it combines with it to form a new quasi-particle. These are known as polarons [133], [402] and they are believed to play a crucial role in a multitude of condensed matter phenomena ranging from colossal magnetoresistance [131] to high T_c superconductivity [132]. Although Bose polarons in ultracold atom mixtures have been previously realized and studied [129], [130], the case of an impurity immersed in a dipolar bath remains largely unexplored [148], [403]. The added long-ranged and anisotropic interaction between the reservoir atoms should affect the energy as well as mobility of the polaron. Our experimental platform with its high degree of tunability–both in terms of interaction strength and geometry–should be well suited for studying this phenomenon.

By rotating the polarizing field, we can change the polaron's effective mass and even

completely 'turn off' its dipolar character [157]–see figure 9.4a. By applying species-selective optical dipole potentials, we will be able to manipulate the impurities and measure their mobility as a function of the impurity-bath interaction strength. Finally, the homogeneity of our trap will not only lead to cleaner data bereft of density averaging but it will also provide for a more direct link to analogous problems in condense matter physics [131]–[133].

Non-Markovian reservoir

A quantum state–possibly a qubit encoded in an atom–immersed in a reservoir becomes progressively more entangled with particles of the reservoir through mutual interactions that are randomly and independently distributed in time. This large scale entanglement leads to a gradual loss of localized information stored within the qubit–a process that is often referred to as irreversible decoherence [404].

If, instead, the interaction events are somehow correlated, possibly through suitable engineering of reservoir particle interactions, the coherence of the qubit can evolve non-monotonously in time. In other words, the information can flow back into the qubit from the bath as shown in figure 9.4b. Such a reservoir is called non-Markovian [405]. Recent proposals [406], [407] suggest that an impurity coupled to a dipolar bath displays non-Markovian behaviour that is strongly dependent on the details of the impurity-bath interactions and that is facilitated by the roton excitations of the bath. We can test these proposals with our system by encoding information within the internal hyperfine states of the potassium impurities and tuning the Er-K and Er-Er interactions, the dipolar character of which is further enhanced by the reduced dimensionality of our trap.

Part IV

Appendix

A. Electronic circuits

A.1 Magnetometer

A high precision magnetometer was constructed to investigate magnetic field fluctuations in the MOT chamber. It consists of an HMC2003 3-axis magnetic sensor and a potential divider stage which appropriately scales the signal from the three axes and feeds it directly into an Arduino Due micro controller. The Arduino averages tens of samples per millisecond and sends the data via serial connection to a PC for analysis. The schematic of the circuit is shown in figure A.1.

The sensitivity of the sensor is 1 G/V which, after being scaled by the divider stage and digitized by the Arduino with 12-bit sampling rate, yields a final magnetic field resolution of 1.2 mG which is smaller than the typical fields we use during our cooling sequence (see section 3.1.2) and than the characteristic extent of three-body loss features in ^{166}Er. Additionally, digital control of the Arduino allows for synchronisation of the data acquisition with the rest of the experiment, enabling us to debug different stages with precision and potentially implement and active field stabilization scheme should the need arise.

A.2 Tunable lens driver

Although the original current driver for the tunable lenses (TLs) provided by Optotune came with a dedicated software, GUI and the option to control the focal power with an analog voltage, it was later discovered that the analog control is first converted to a digital signal which is then converted into a driving current corresponding to a specific focal power. This intermediate digitization step resulted in a non-negligible digitization error on the focal power. Furthermore, small drifts in the control voltage could result in sudden 'steps' in the focal position, exciting the atomic cloud and causing considerable heating and losses in later cooling stages.

For this reason, a stable voltage-controlled current source was built that would allow us to continuously control the current running through the membrane coils of the TLs and thus smoothly vary the membrane curvature and focal power. The current source consists of an instrumentation amplifier and a stable voltage reference which shift our experimental control voltage from the $(0, 10)$V to the $(-5, 5)$V range. This voltage is then mapped onto current using a high current gain operational amplifier (OPA547) and a stable 20 Ω resistance reference (VPR221ZT) to supply the tunable lens with $(-250, 250)$mA current which covers its full focal power range of $(-2, 3)$dpt. The schematic of the circuit is shown in figure A.2.

The current drivers proved to be invaluable for realizing reliable loading and atomic transport. However, despite its adequate stability and precision, additional active stabilization had to be implemented to combat temperature and other drifts affecting the

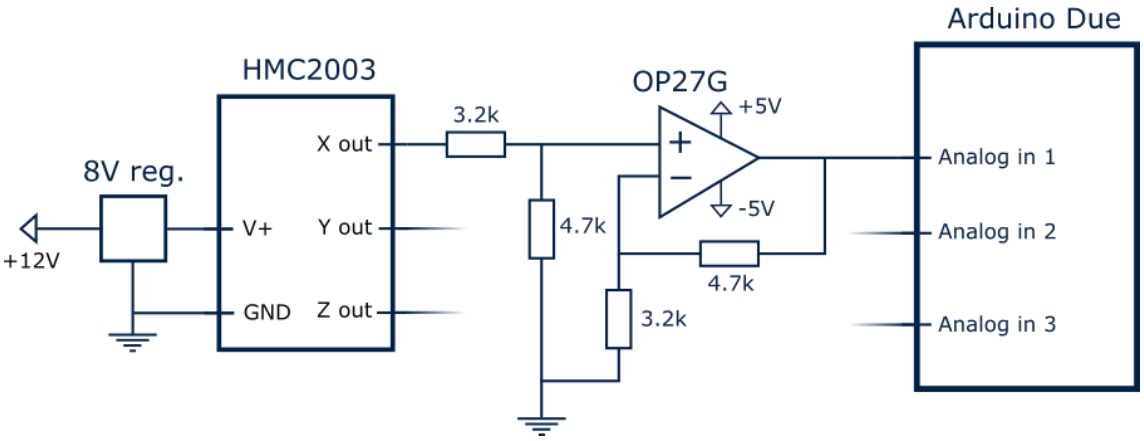


Figure A.1: Magnetometer circuit. A schematic of a magnetometer circuit used in our experiment for detecting and potentially compensating for magnetic field drifts around the MOT chamber. Note that an identical potential divider stage (middle section) is implemented for each magnetometer axis separately but only one is shown for clarity.

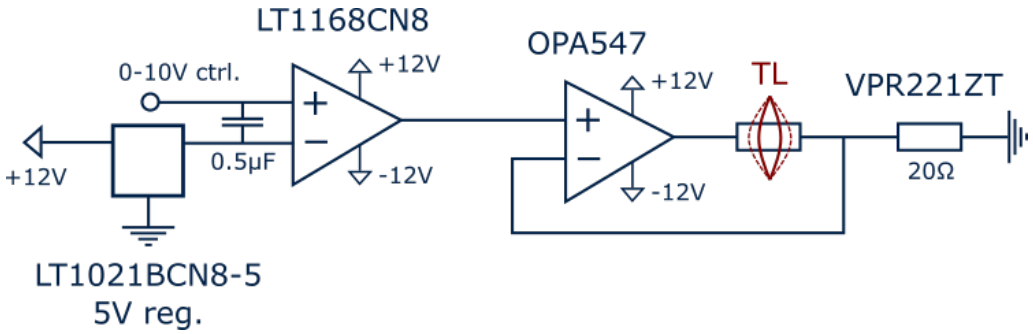


Figure A.2: Tunable lens current driver. The driver consists of a voltage shifting stage which maps the positive control voltage onto a symmetric range around 0. A high current gain op-amp is then used to supply the lens membrane coils with current given simply by $V_{\text{in}}/R_{\text{ref}}$ where V_{in} is the input op-amp voltage and R_{ref} is a stable 20 Ω reference resistor.

tunable lenses. This was done by measuring the focal position of the trapping beam using a quadrant photo diode and a cylindrical lens and converting any drifts into an electronic error signal fed back into the lens current drivers (see section 4.5).

A.3 Bake-out temperature and pressure logging

To monitor the temperature in different parts of the 2D+ MOT vacuum assembly during the bake-out procedure, a five-channel digital thermometer based on the Arduino Uno micro controller was built. The digital temperature sensors (DS18B20) have a sub-degree resolution and can work in a temperature range of $(-55, 125)°\mathrm{C}$ which is suitable for our intended bake-out temperature of $T < 110\,°\mathrm{C}$. The sensors communicate with the controller using the One Wire protocol, making it particularly easy to add or remove more sensors if necessary. Additionally, the Arduino has the ability to read off an analog voltage from a Pfeiffer gauge installed on the main turbo pump and convert the voltage to a pressure reading.

To monitor the values in real time, a program originally developed by Milan was adjusted to communicate with the Arduino via a serial port. The program periodically queries the Arduino for readings, records them and displays them on a graph. It also has the capability of directly communicating with an SAES ion pump and obtain its pressure readings. We used this capability in the later stages of the bake-out process after the ion and getter pumps were activated. For a full summary of the bake-out data, see figure 8.10.

The logging program and the arduino code is available at `https://github.com/Mogthar/temperature-logger-arduino.git`

B. Tunable lens stabilization

B.1 Error signal sensitivity

If we assume an elliptical Gaussian beam of sizes σ_x and σ_y, the error signal defined by equation 4.20 can be written in integral form as

$$E = \frac{4(I_1 - I_2)}{P_{\text{tot}}} \ , \tag{B.1}$$

where P_{tot} is the total power in the beam and the integrals I_1 and I_2 represent the powers in the top half and bottom half of the first quadrant as depicted in figure B.1. Mathematically, they are given by

$$\begin{aligned} I_1 &= \frac{P_{\text{tot}}}{2\pi\sigma_x\sigma_y}\int_0^\infty\int_0^x e^{-\frac{x^2}{2\sigma_x^2}}e^{-\frac{y^2}{2\sigma_y^2}}dxdy \\ I_2 &= \frac{P_{\text{tot}}}{2\pi\sigma_x\sigma_y}\int_0^\infty\int_0^y e^{-\frac{x^2}{2\sigma_x^2}}e^{-\frac{y^2}{2\sigma_y^2}}dxdy \end{aligned} \tag{B.2}$$

which can be rewritten in terms of the *error function* as

$$\begin{aligned} I_1 &= \frac{1}{2}\frac{P_{\text{tot}}}{\sqrt{2\pi}}\int_0^\infty \text{erf}\left(\frac{\sigma_x}{\sigma_y}\frac{\chi}{\sqrt{2}}\right)e^{-\frac{\chi^2}{2}}d\chi \\ I_2 &= \frac{1}{2}\frac{P_{\text{tot}}}{\sqrt{2\pi}}\int_0^\infty \text{erf}\left(\frac{\sigma_y}{\sigma_x}\frac{\chi}{\sqrt{2}}\right)e^{-\frac{\chi^2}{2}}d\chi \ . \end{aligned} \tag{B.3}$$

In the limit of a nearly circular beam, i.e. when the focus of the trapping beam is close to its ideal location, we can take $\frac{\sigma_x}{\sigma_y} \approx 1+\varepsilon$ and $\frac{\sigma_y}{\sigma_x} \approx 1-\varepsilon$ with $\varepsilon \ll 1$. Furthermore, we can use the Taylor series of the error function

$$\text{erf}(x) = \frac{2}{\sqrt{\pi}}\sum_{n=0}^{\infty}\frac{(-1)^n x^{2n+1}}{n!(2n+1)} \tag{B.4}$$

to write the integral in equation B.3 as

$$\begin{aligned} &\int_0^\infty \text{erf}\left(\frac{\sigma_x}{\sigma_y}\frac{\chi}{\sqrt{2}}\right)e^{-\frac{\chi^2}{2}}d\chi \\ &= \frac{2}{\sqrt{\pi}}\sum_{n=0}^{\infty}\frac{(-1)^n(1+\varepsilon)^{2n+1}}{n!(2n+1)2^{n+1/2}}\int_0^\infty \chi^{2n+1}e^{-\frac{\chi^2}{2}}d\chi \\ &= \frac{2}{\sqrt{2\pi}}\sum_{n=0}^{\infty}\frac{(-1)^n(1+\varepsilon)^{2n+1}}{(2n+1)} = \frac{2}{\sqrt{2\pi}}\arctan(1+\varepsilon) \end{aligned} \tag{B.5}$$

where on the second line we used the substitution $\frac{\chi^2}{2} = \theta$ and the known factorial result of the Gamma function integral to simplify the integral term to $2^n n!$. For small ε, we can

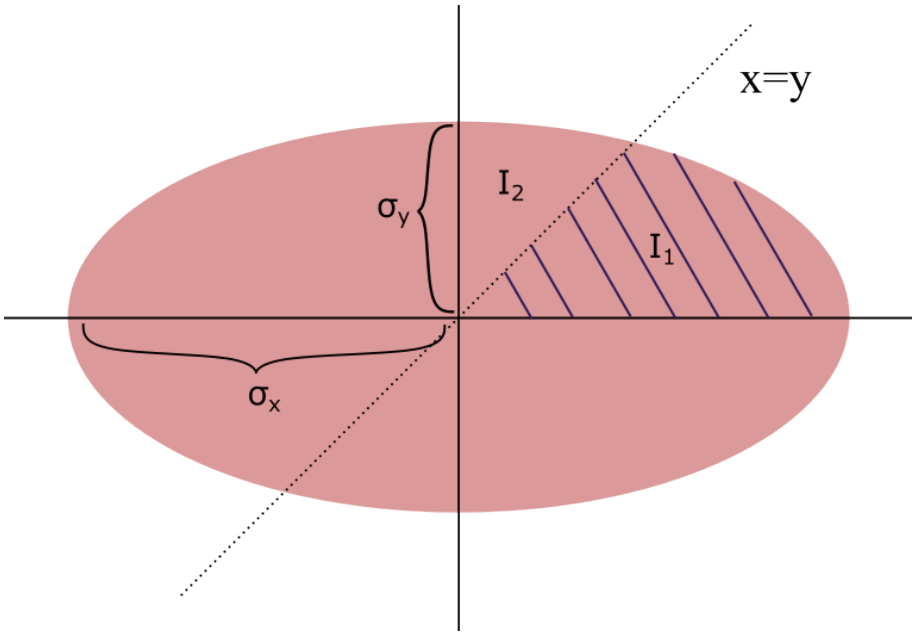


Figure B.1: Error signal integral. Relevant regions of an elliptical Gaussian beam defined by orthogonal sizes σ_x and σ_y. The error signal derived from our cylindrical lens setup is proportional to the difference in power incident onto the lower and upper half of the first quadrant denoted by I_1 and I_2 respectively.

take $\arctan(1+\varepsilon) \approx \pi/4 + \varepsilon/2$ and so the error signal B.1 can be written as

$$\begin{aligned} E &= \frac{2}{\pi}\left(\arctan(1+\varepsilon) - \arctan(1-\varepsilon)\right) \\ &= \frac{2\varepsilon}{\pi} = \frac{1}{\pi}\left(\frac{\sigma_x}{\sigma_y} - \frac{\sigma_y}{\sigma_x}\right) \end{aligned} \tag{B.6}$$

In practice, we are interested in how the error signal responds to small changes in the focal position. In other words, we want to calculate the sensitivity $\left|\frac{dE}{du}\right|$ and maximize it by choosing suitable optical elements. We therefore need to find out how the beam sizes σ_x and σ_y vary as a function of the focal position u. Luckily, we can use simple ray geometry to figure that out!

Figure B.2 shows the ray path for the two orthogonal directions. Most notably, because of the cylindrical lens, only the y dimension becomes focused and defocused before being incident on the quadrant photo diode. Using trigonometry, we can easily derive the expressions for the beam sizes σ_x and σ_y as a function of the focal position u from the collimating lens after propagating through the system

$$\begin{aligned} \sigma_x &= w\left(1 + \left(\frac{f_{\text{coll}}}{u} - 1\right)\left(\frac{d + 2f_{\text{cyl}}}{f_{\text{coll}}}\right)\right) \\ \sigma_y &= w\left(\frac{2f_{\text{cyl}} - d}{u} + \frac{d - 2f_{\text{cyl}}}{f_{\text{coll}}} - 1\right) \end{aligned} \tag{B.7}$$

As a sanity check, if the trapping beam is focused in the correct position such that $u = f_{\text{coll}}$, the two sizes are equal to w as expected. We can now differentiate equation B.6

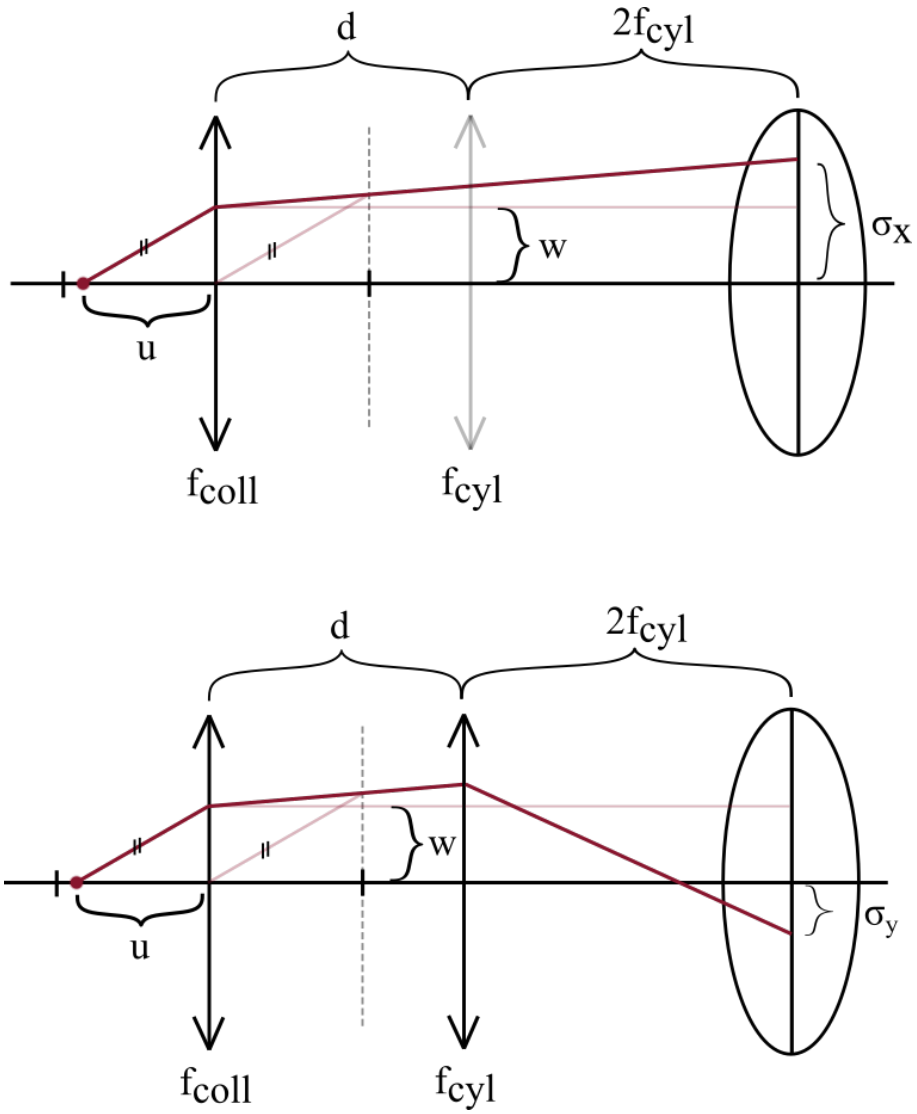


Figure B.2: Beam propagation in the lens stabilization system. The rays originate in the trapping beam focus which is distance u away from a collimating lens. In one direction, the beam is simply collimated by the collimating lens and projected onto the quadrant photo diode (QPD). In the other direction, the beam is further focused and defocused by a cylindrical lens. The sizes of the beam incident on the QPD given by σ_x and σ_y can be derived using simple trigonometry, the known focal powers, distances and the input waist w.

with respect to u and use $\frac{\sigma_x}{\sigma_y} = 1 + \varepsilon$ and $\left(\frac{\sigma_x}{\sigma_y}\right)^2 = 1 + 2\varepsilon$ to get

$$E = \frac{2}{\pi}\left(\frac{1}{\sigma_x}\frac{d\sigma_x}{du} - \frac{1}{\sigma_y}\frac{d\sigma_y}{du}\right) \tag{B.8}$$

For small perturbations of u around f_{coll} such that $u = f_{\text{coll}} + \delta$, we can finally differentiate the beam sizes given by equations B.7 to yield the error signal sensitivity

$$\frac{dE}{du} = \frac{8}{\pi}\frac{f_{\text{cyl}}}{f_{\text{coll}}^2}\left(1 + \frac{2\delta}{f_{\text{coll}}}\left(\frac{d}{f_{\text{coll}} - 1}\right) + O\left(\left(\frac{\delta}{f_{\text{coll}}}\right)^2\right)\right) \tag{B.9}$$

Clearly around the ideal position ($\delta = 0$), the sensitivity is given simply by $\frac{8 f_{\text{cyl}}}{\pi f_{\text{coll}}^2}$ and so shorter collimating lens and longer cylindrical lens are desirable.

B.2 Vibration compensation

In order to make the stabilization scheme more reliable, it is desirable to make the error signal E robust to small displacements of the beam $\delta = (\delta_x, \delta_y)$ which can arise from vibrations of the optical table or from Poynting fluctuations of the trapping beam.

We first need to assess the influence of such displacement on the error signal given by 4.20. In other words, we need to find out the change in power in all four quadrants as a function of $\delta = (\delta_x, \delta_y)$. Luckily, working to second order in $\delta_{x/y}/w_{x/y}$ where $w_{x/y}$ are the waists of the beam and exploiting the symmetries of the problem allows us to derive an elegant expression as we shall see bellow.

Lets first consider the top right quadrant denoted by roman numeral II. Note that results for the remaining three quadrants will follow by symmetry. Figure B.3 shows the additional power incident on quadrant II after the elliptical beam (tilted by 45° w.r.t. the x axis) is displaced by $\delta = (\delta_x, \delta_y)$. We can calculate it to second order in the displacement by considering the power in the trapezoids and approximating the change in intensity along the height by taking the average of intensities at the top and bottom base. Mathematically, we can write for the total power in quadrant II

$$A_{II} = A_{II,0} + \delta_x \int_0^\infty \frac{I(0,y) + I(-\delta_x, y - \delta_y)}{2} dy + \delta_y \int_0^\infty \frac{I(x,0) + I(x - \delta_x, -\delta_y)}{2} dx \tag{B.10}$$

where we defined $A_{II,0}$ as the unperturbed power (also equal to $A_{III,0}$ by symmetry) and where we explicitly work in a coordinate system centered on the ellipse. Exploiting the symmetry of the intensity profile in the native coordinates in which $I(x,y) = I(y,x)$ and $\frac{\partial I}{\partial y}(x,0) = -\frac{\partial I}{\partial y}(-x,0)$, we can expand equation B.10 to second order in δ

$$A_{II} = A_{II,0} + a(\delta_x + \delta_y) - \frac{b}{2}(\delta_x^2 + \delta_y^2) + \delta_x \delta_y I(0,0) \tag{B.11}$$

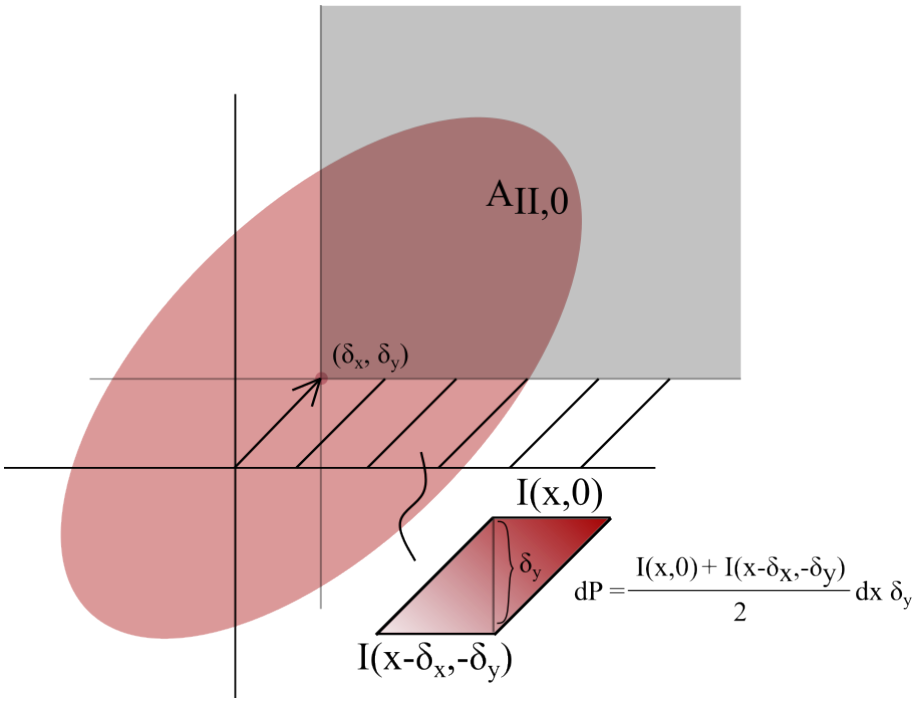


Figure B.3: Quadrant power change. After a lateral displacement $\delta = (\delta_x, \delta_y)$ of the incident elliptical beam, the power distribution on the quadrant photo diode changes. This causes a distortion to the error signal which can be falsely interpreted as a change in the focal position. We can approximate the shift in power by considering how the intensity changes between the original and new x axis after the shift.

where we defined the constants a and b as follows

$$\begin{aligned} a &= \int_0^\infty I(0,y)dy = \int_0^\infty I(x,0)dx \\ b &= \int_0^\infty \frac{\partial I}{\partial y}(x,0)dx = \int_0^\infty \frac{\partial I}{\partial x}(0,y)dy \end{aligned} \tag{B.12}$$

Using the symmetry of the problem, we can relatively easily find similar expressions for the powers in the other three quadrants

$$\begin{aligned} A_I &= A_{I,0} + a(-\delta_x + \delta_y) + \frac{b}{2}(\delta_x^2 + \delta_y^2) - \delta_x\delta_y I(0,0) \\ A_{III} &= A_{III,0} + a(-\delta_x - \delta_y) - \frac{b}{2}(\delta_x^2 + \delta_y^2) + \delta_x\delta_y I(0,0) \\ A_{IV} &= A_{IV,0} + a(\delta_x - \delta_y) + \frac{b}{2}(\delta_x^2 + \delta_y^2) - \delta_x\delta_y I(0,0) \end{aligned} \tag{B.13}$$

As a sanity check, we notice that the total power $P_{\text{tot}} = A_I + A_{II} + A_{III} + A_{IV} = A_{I,0} + A_{II,0} + A_{III,0} + A_{IV,0}$ remains unchanged as expected from a lateral translation.

We can now find out the effect on the error signal E by subtracting the power in the diagonals and normalizing the result by the total power to get

$$E = \frac{(A_{II} + A_{III}) - (A_I + A_{IV})}{P_{\text{tot}}} = E_0 + \frac{4\delta_x\delta_y I(0,0)}{P_{\text{tot}}} - \frac{2b(\delta_x^2 + \delta_y^2)}{P_{\text{tot}}} \tag{B.14}$$

where E_0 is the unperturbed error signal. Clearly, lateral displacement of the beam affects the error signal value and it therefore changes the "apparent" position of the beam's focus. To counteract this, we can come up with a suitable compensation term to subtract from the measured error signal and cancel out the two extra terms in equation B.14.

Fortunately, we have access to all four quadrants individually and so we can construct two more quantities that will help us keep track of the lateral displacement. Namely, we can define U and R which stand for 'up' and 'right' as

$$\begin{aligned} U &= \frac{(A_I + A_{II}) - (A_{III} + A_{IV})}{P_{\text{tot}}} = \frac{4a\delta_y}{P_{\text{tot}}} \\ R &= \frac{(A_{II} + A_{IV}) - (A_I + A_{III})}{P_{\text{tot}}} = \frac{4a\delta_x}{P_{\text{tot}}} \end{aligned} \tag{B.15}$$

We can then subtract appropriately weighted combination of $U \times R$ and $U^2 + R^2$ from the measured error signal to get its unbiased value E_0. All we need to do now is figure out the weights by calculating the constants a and b for a general tilted Gaussian beam.

The intensity profile of such a beam is given by

$$I(x, y) = \frac{2P_{\text{tot}}}{\pi w_x w_y} e^{-\mathbf{x}^T \mathbf{H} \mathbf{x}} \tag{B.16}$$

with the matrix $\mathbf{H}$ defined as

$$\begin{pmatrix} \frac{1}{w_x^2} + \frac{1}{w_y^2} & \frac{1}{w_x^2} - \frac{1}{w_y^2} \\ \frac{1}{w_x^2} - \frac{1}{w_y^2} & \frac{1}{w_x^2} + \frac{1}{w_y^2} \end{pmatrix} = \begin{pmatrix} D & \Theta \\ \Theta & D \end{pmatrix} \tag{B.17}$$

Armed with these expressions, we can now calculate a and b

$$\begin{aligned} a &= \frac{2P_{\text{tot}}}{\pi w_x w_y} \int_0^\infty e^{-Dx^2} dx = \frac{P_{\text{tot}}}{\sqrt{\pi}} \frac{1}{\sqrt{w_x^2 + w_y^2}} \\ b &= -\frac{2P_{\text{tot}}}{\pi w_x w_y} \int_0^\infty 2\Theta x e^{-Dx^2} dx = \frac{2P_{\text{tot}}}{\pi w_x w_y} \frac{w_x^2 - w_y^2}{w_x^2 + w_y^2} \end{aligned} \tag{B.18}$$

which, in return, allows us to write the error signal in terms of E_0, U and R as

$$E = E_0 + (U \times R) \frac{w_x^2 + w_y^2}{2w_x w_y} + (U^2 + R^2) \frac{w_x^2 - w_y^2}{4w_x w_y} \tag{B.19}$$

If we know the waists w_x and w_y, we can fully compensate for the error introduced by lateral displacement of the trapping beam. In a circular configuration, i.e. when the focus of the beam is close to its ideal position, we have $w_x \approx w_y$ and the compensation term becomes simply $U \times R$.

C. Simulating atomic transport and evaporation

C.1 Transport ramps

Mathematical forms of relevant transport ramps used in simulating atomic transport in our experiment. Where possible, the initial and final velocities and accelerations were set to 0 to prevent sudden spikes in force exerted on the atoms. In all cases, L denotes the transport distance and T the total transport time

Linear

The most basic of ramps of the form:

$$y(t) = \begin{cases} y = 0 & t < 0 \\ y = L\frac{t}{T} & 0 < t < T \\ y = L & t > T \end{cases} \tag{C.1}$$

Quadratic

Also known as constant acceleration ramp ($\ddot{y} = \text{const.}$):

$$y(t) = \begin{cases} y = 0 & t < 0 \\ y = 2L\left(\frac{t}{T}\right)^2 & 0 < t < \frac{T}{2} \\ y = L - 2L\left(\frac{t-T}{T}\right)^2 & \frac{T}{2} < t < T \\ y = L & t > T \end{cases} \tag{C.2}$$

Cubic

Also known as constant jerk ramp ($\dddot{y} = \text{const.}$):

$$y(t) = \begin{cases} y = 0 & t < 0 \\ y = \frac{16}{3}L\left(\frac{t}{T}\right)^3 & 0 < t < \frac{T}{4} \\ y = -\frac{16}{3}L\left(\frac{t}{T}\right)^3 + 8L\left(\frac{t}{T}\right)^2 - 2L\frac{t}{T} + \frac{L}{6} & \frac{T}{4} < t < \frac{3T}{4} \\ y = L + \frac{16}{3}L\left(\frac{t-T}{T}\right)^3 & \frac{3T}{4} < t < T \\ y = L & t > T \end{cases} \tag{C.3}$$

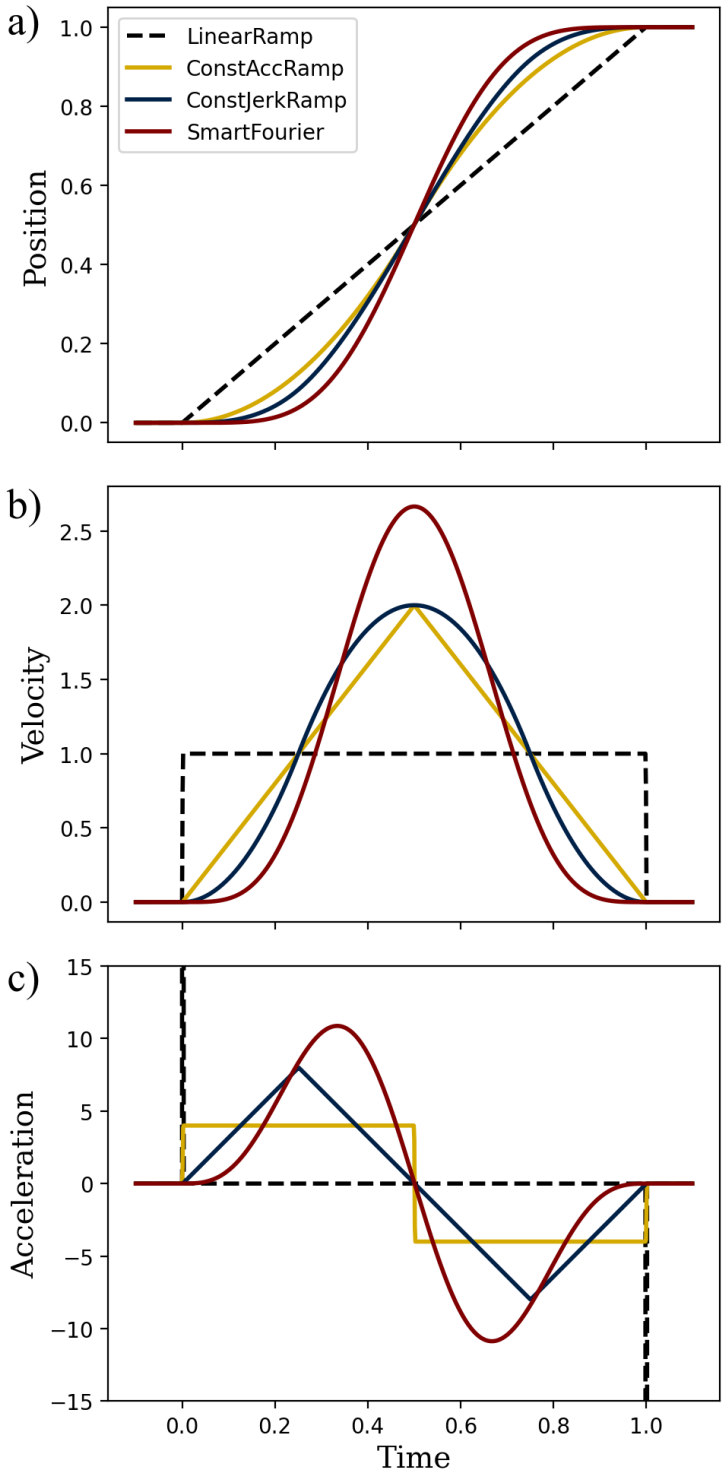


Figure C.1: Transport ramp profiles. a) Focal position, b) velocity and c) acceleration as a function of time for the four ramps that were numerically tested to assess optimal transport schemes in our experiment. Note that both the spatial and time coordinates are normalized for clarity.

Fourier

The frequency component of the ramp around the longitudinal trapping frequency ω_y is filtered out to prevent resonant heating [330]:

$$y(t) = \begin{cases} y = 0 & t < 0 \\ y = L\left(\frac{t}{T} - \frac{7}{12\pi} - \frac{8\pi}{3(\omega_y T)^2}\sin\left(2\pi\frac{t}{T}\right) - -\frac{4\pi}{3(\omega_y T)^2}\sin\left(4\pi\frac{t}{T}\right)\right) & 0 < t < T \\ y = L & t > T \end{cases} \quad \text{(C.4)}$$

Ramp overview

Figure C.1 shows a plot of the focal position, velocity and acceleration as a function of time for all four ramps using scaled dimensions for clarity. In the future, we plan to test ramps with non-symmetric acceleration profile such that the atoms spend less time in the first half of the transport path. This is because our initial transport data points to position-dependent losses that preferentially happen in the first half of the transport ramp.

C.2 DSMC

For simulating the dynamics of particles trapped in an optical dipole trap (either static or moving), we implement a version of the direct simulation Monte Carlo (DSMC) method introduced in reference [331].

The movement of the particles is treated using a simple velocity Verlet algorithm [408] where the positions and momenta at the next time step are calculated as follows

$$\begin{aligned} \mathbf{r}(t+\Delta t) &= \mathbf{r}(t) + \mathbf{v}(t)\Delta t + \frac{1}{2}\frac{\mathbf{F}(\mathbf{x}(t),t)}{m}\Delta t^2 \\ \mathbf{v}(t+\Delta t) &= \mathbf{v}(t) + \frac{\mathbf{F}(\mathbf{x}(t+\Delta t),t+\Delta t) + \mathbf{F}(\mathbf{x}(t),t)}{2m}\Delta t \end{aligned} \quad \text{(C.5)}$$

where we emphasized that the force acting on a particle of mass m depends on the particle's position as well as on time. The force can be easily obtained by analytically calculating the gradient of the trapping potential given by equations 4.1 and 4.5 and using this analytic form and the particle's position as an input.

For transport simulations, the potential itself moves in time which has to be accounted for when calculating the increment in velocity as expressed in equation C.5. Same applies to evaporation simulations where the power in the beam and hence the potential also changes in time.

Since real atomic clouds consist of millions of particles, it becomes progressively difficult to simulate them all, especially when collisions are taken into account. The DSMC method provides an alternative approach in which we only simulate the motion of N_s particles with each representing α real particles with $\alpha \gg 1$. In our simulations, we typically use $N_s = 10\,000$.

But even with this number reduction, full treatment of two-body collisions is computationally costly since it scales as N_s^2. In DSMC, instead of evaluating collisions on a pair-wise basis across the whole cloud, the simulation volume is first divided into small cells. Within each cell, a number of test collisions, N_{coll}, and a collision probability, P_coll, are calculated based on the local density. Finally, N_{coll} pairs of particles are randomly picked from the cell and their momenta are randomized with probability P_coll (whilst conserving their total momentum and energy) to mimic a real collision process. This way, we only have to loop through particles to assign them to cells ($\mathcal{O}(N_s)$) and then loop through occupied cells ($\mathcal{O}(N_c) \ll \mathcal{O}(N_s)$) to perform random collisions on a much smaller subset of particles.

In quantitative terms, once the number of simulated particles N_{cell} in a cell of volume ΔV is known, we first calculate the total number of pairs $N_{\text{pairs}} = N_{\text{cell}}(N_{\text{cell}} - 1)/2$. We then calculate the number of test collisions as

$$N_{\text{coll}} = \text{ceil}\left(\alpha N_{\text{pairs}} \frac{\sigma v_{\text{rel}} \Delta t}{\Delta V}\right) \tag{C.6}$$

where 'ceil' is the ceiling rounding function, σ is the collision cross section and v_{rel} is the maximum relative velocity of particles in the cell [331]. In the next step, we draw N_{coll} random pairs and collide the particles with probability

$$P_{\text{coll}} = \frac{\alpha N_{\text{pairs}}}{N_{\text{coll}}} \frac{\sigma v_{\text{rel}} \Delta t}{\Delta V} \ . \tag{C.7}$$

Finally, in case of a collision, the momenta of the two particles are randomized as follows

$$\begin{aligned} \mathbf{p}_{\text{com}} &= \frac{\mathbf{p}_1 + \mathbf{p}_2}{2} \\ \mathbf{p}_{\text{rel}} &= \mathbf{p}_1 - \mathbf{p}_2 \\ \mathbf{p}_{\text{rand}} &= |\mathbf{p}_{\text{rel}}| \hat{\mathbf{r}} \\ \mathbf{p}_1' &= \mathbf{p}_{\text{com}} + \frac{\mathbf{p}_{\text{rand}}}{2} \\ \mathbf{p}_2' &= \mathbf{p}_{\text{com}} - \frac{\mathbf{p}_{\text{rand}}}{2} \end{aligned} \tag{C.8}$$

with $\hat{\mathbf{r}}$ a random vector from the unit sphere.

An important parameter is the cell size ΔV. Too large and the captured dynamics could result in unphysical collisions between distant particles. Too small and the partitioning becomes too granular, resulting in no collisions. In our simulations, we use cubic cells of size $\Delta x = 0.01\lambda_{MFP}$ where $\lambda_{MFP} = 1/\bar{n}\sigma$ is the mean free path of the particles and $\bar{n}$ is the average density which is easily obtainable from the individual cell occupation numbers. Note that particles that leave the simulation box (defined as a multiple of the beam waists and/or of the Rayleigh range) are permanently removed.

To speed up the simulation, we use two different time steps. A shorter one defined as a fraction of the mean oscillation time within the dipole trap, $\Delta t_{\text{osc}} = 0.005/\bar{\omega}$, and a longer one defined as a fraction of the mean collision time, $\Delta t_{\text{coll}} = 0.1\lambda_{MFP}/\bar{v}_{\text{rel}}$. The Verlet dynamical evolution of the particle positions and momenta is performed with a period of

Δt_{osc}. The collision calculations, on the other hand, are performed only once Δt_{coll} time has passed since the last calculation. Furthermore, as the trap and particle number change during the simulation, we continuously recalculate the two time step sizes.

Lastly, to account for one-body losses, we slowly decay α in time according to $\Delta\alpha = -\alpha\Delta t_{\text{osc}}/\tau_{1B}$ with τ_{1B} the characteristic one-body decay time. Similarly, we also account for particle loss due to three-body collisions (see chapter 5). However, as this loss is density dependent, we have to evaluate it for each cell independently based on the local density n_{cell}. This is done by keeping track of the number of real particles lost to three-body recombination within each cell, $\Delta N_{3B} = -L_3 n_{\text{cell}}^3 \Delta t$. Once the cumulative loss becomes larger than α, we remove $N_R = \text{floor}(N_{3B}/\alpha)$ simulated particles from the cell at the end of the collision step. We note that heating due to off-resonant photon scattering with the trapping beam is neglected in our simulations.

C.3 Evaporation theory

Given that in atomic evaporation the system at hand, i.e. the atomic cloud and the trap, is closed and consists of a relatively large number of particles, it is convenient to formulate the problem in the language of statistical physics and thermodynamical quantities. The question we are trying to answer is the following–given an initial trap, atom number and temperature, what is the time evolution of the latter two quantities, $N(t)$ and $T(t)$, provided that the trap parameters change in time as $P(t)$ (here P can mean the beam power/trap depth/trapping frequencies)? Once we have an answer to this question, we can also easily find the peak phase-space density $\rho_0 \propto n_0 T^{-3/2}$ where n_0 is the peak atomic density which depends on the trap, atom number and temperature.

We can begin by writing the total differential of the system energy as a function of the three pivotal parameters N, T and P as $dE = \frac{\partial E}{\partial T}dT + \frac{\partial E}{\partial N}dN + \frac{\partial E}{\partial P}dP$. Dividing by dt and rearranging the expression gives the time derivative of temperature

$$\dot{T} = \frac{\dot{E} - \mu\dot{N} - Q\dot{P}}{C} \tag{C.9}$$

where we identify the heat capacity $C = \frac{\partial E}{\partial T}$, the chemical potential $\mu = \frac{\partial E}{\partial N}$ and the contribution from trap changes $Q = \frac{\partial E}{\partial P}$. Note that in general, the parameter P can encompass several trap parameters such as the trap depth ε_t, the trapping frequencies ω or the beam power.

Total energy can be generally written as $E = \int \epsilon\rho(\epsilon)f(\epsilon)d\epsilon$ where $\rho(\epsilon)$ is the density of states in the trap and $f(\epsilon)$ is the occupation probability distribution. In a non-degenerate, thermal gas we would expect $f(\epsilon) \propto e^{-\beta\epsilon}$ to follow the usual Maxwell-Boltzmann distribution with $\beta = 1/k_B T$. In our case though, the finite trap depth means that $f(\epsilon > \varepsilon_t)$ will be heavily suppressed. To make more progress, it is convenient to use the following approximation

$$f(\epsilon) \propto e^{-\beta\epsilon}\Theta(\varepsilon_t - \epsilon) \tag{C.10}$$

where Θ is the Heaviside step function such that $f(\epsilon)$ is now a *truncated Boltzmann*

distribution [352]. The validity of this assumption relies on the diluteness of the gas[1] far from degeneracy and it has been tested numerically [313]. For a similar treatment of nearly-degenerate gases, we point the reader to reference [409]. Employing the truncated distribution leads to the following expression for total energy

$$E(N,T,P) = \frac{N}{\zeta(T,P)} \int_0^{\varepsilon_t} \epsilon \rho(\epsilon,P) e^{-\beta\epsilon} d\epsilon \ . \tag{C.11}$$

Here, we emphasized the dependence of certain quantities on N, T and P. We also defined the partition function $\zeta(T,P) = \int \rho(\epsilon,P) e^{-\beta\epsilon} \Theta(\varepsilon_t - \epsilon) d\epsilon$ which determines the constant of proportionality in equation C.10 via the particle number normalization condition. Armed with this expression, we can calculate the heat capacity C and chemical potential μ with appropriate differentiation. The trap-related quantity Q depends on how we parametrize the trap. In the case of RF knife magnetic traps, it is only the trap depth that changes and so $P = \varepsilon_t$. For an optical dipole trap, the trap depth changes in parallel with the trapping frequencies and so we can write $\frac{\partial E}{\partial P}\dot{P} = \frac{\partial E}{\partial \varepsilon_t}\dot{\varepsilon}_t + \frac{\partial E}{\partial \bar{\omega}}\dot{\bar{\omega}}$, where the time derivatives depend on the time derivative of the power in the beam as well as on the beam's geometry.

The last ingredient to figuring out the change in temperature are the rates of change of particle number and total energy, $\dot{E}$ and $\dot{N}$. In deriving expression 4.11 in section 4.3, we essentially undertook the same steps that lead us to the 'proper' equation C.9 but we made a few strong assumptions and simplifications on the way. For example, we neglected any changes to the trap. We also assumed the truncation of the Boltzmann distribution has no effect on the heat capacity and chemical potential and so we simply used the values for a harmonically trapped gas, $C = 3Nk_B$ and $\mu = 3k_BT$. Furthermore, we proposed that the particle loss due to evaporation, dN_{ev}, results in a loss in energy equal to $dE_{\mathrm{ev}} = dN_{\mathrm{ev}}\varepsilon_t$, i.e. we assumed that the energy lost per evaporated particle is simply equal to the trap depth. Finally, we also neglected any other loss or heating mechanisms such as the three-body recombination or off-resonant scattering with the trapping laser. In the following paragraphs, we will consider all these contributions one by one to build a full understanding of the processes in play.

Taking evaporation as our first example, proper thermodynamical treatment needs to account for the dynamical nature of the process in which particles continuously scatter into different energy states via collisions. Some occasionally end up with $\epsilon > \varepsilon_t$ and are assumed to be instantly lost. The rate of particle loss is then essential a sum over all the occupied states, multiplied by the rate of scattering from the original state into a state with $\epsilon > \varepsilon_t$. Appropriate averaging of the energies above the cut-off threshold then yields the average energy lost per evaporated particle. Reference [313] outlines the full derivation and here we only present the rather complicated final results for the rate of particle and

[1] Also known as the Knudsen regime in which the mean free path is larger than the size of the gas cloud

energy loss due to evaporation:

$$\dot{N}_{\mathrm{ev}} = -\int_{\varepsilon_t}^{\infty} \rho\left(\epsilon\right) \dot{f}\left(\epsilon\right) d\epsilon = \dot{N}_{\mathrm{ev}} = -n_0^2 \sigma \bar{v} e^{-\eta} V_{\mathrm{ev}} \tag{C.12}$$

$$\dot{E}_{\mathrm{ev}} = -\int_{\varepsilon_t}^{\infty} \epsilon\rho\left(\epsilon\right) \dot{f}\left(\epsilon\right) d\epsilon = \dot{N}_{\mathrm{ev}} \left\{\varepsilon_t + \frac{V_{\mathrm{ev}} - X_{\mathrm{ev}}}{V_{\mathrm{ev}}} k_B T\right\} \tag{C.13}$$

$$V_{\mathrm{ev}} = \frac{\Lambda^3}{k_B T} \int_0^{\varepsilon_t} \rho(\epsilon) \left[\left(\varepsilon_t - \epsilon - kT\right) e^{-\beta\epsilon} + k_B T e^{-\eta}\right] d\epsilon \tag{C.14}$$

$$X_{\mathrm{ev}} = \frac{\Lambda^3}{k_B T} \int_0^{\varepsilon_t} \rho(\epsilon) \left[k_B T e^{-\beta\epsilon} - \left(\varepsilon_t - \epsilon + k_B T\right) e^{-\eta}\right] d\epsilon \tag{C.15}$$

here σ is the s-wave scattering cross section, $\bar{v} = (8kT/\pi m)^{1/2}$ is the characteristic velocity of an atom in the cloud, Λ is the thermal de Broglie wavelength, $\eta = \beta\varepsilon_t$ and finally n_0 is the pseudo- peak density defined by the relation $n_0\Lambda^3 = N/\zeta$. The main takeaway here is that the evaporation rate scales as density squared and is directly proportional to the scattering cross section. Furthermore, it gets suppressed by the factor $e^{-\eta}$ i.e. it decays exponentially with trap depth. The average energy lost per particle is larger than the trap depth ε_t as can be expected given that any particle with energy equal to or *greater* than ε_t is lost.

One of the major factors limiting evaporation efficiency are particle losses that are not associated with simultaneous cooling and are, in fact, in many cases responsible for heating of the gas instead. In the case of erbium, two such processes are the one- and three-body collisional losses. The rate of change of particle number and energy for an m-body process can be generally written as

$$\dot{N}_{\mathrm{mb}} = -L_m \int n^m(\mathbf{r}) d^3\mathbf{r} \tag{C.16}$$

$$\dot{E}_{\mathrm{mb}} = -L_m \int n^m(\mathbf{r}) \bar{E}(\mathbf{r}) d^3\mathbf{r} \tag{C.17}$$

where L_m is a constant m-body loss coefficient and $\bar{E}(\mathbf{r})$ is the average energy per particle at position $\mathbf{r}$. Chapter 5 presents a full discussion of m-body loss processes and develops the mathematical tools used to describe them. Here we only note that one body loss is essentially an exponential decay with a lifetime independent of the density of the gas. Furthermore, it can be shown that the one-body contributions to equation C.9 cancel out, resulting in no heating. Three-body losses, on the other hand, scale with density and are particularly enhanced at or near degeneracy where the PSD is high. They also cause detrimental heating through 'anti-evaporation' (see section 5.3.3).

Although the trapping light creates a conservative potential through the dipole force, from time to time, an off-resonant photon can scatter with a trapped particle. By doing so, it transfers an energy equal to $E_r = 2\frac{(\hbar k)^2}{2m}$ to the atom (the factor of 2 comes from considering absorption and subsequent emission). The off-resonant scattering rate is proportional to intensity $I(\mathbf{r})$ of the trapping beam and so we can write for the total increase in energy

$$\dot{E}_\Gamma = C_\Gamma \frac{(\hbar k)^2}{m} \int I(\mathbf{r}) n(\mathbf{r}) d^3\mathbf{r} \tag{C.18}$$

with C_Γ a constant that is related to the imaginary part of the atomic polarizability such that $C_\Gamma I(\mathbf{r}) = \Gamma_{\text{scat}}$ (see section 4.1.1). In practice, this heating term is relatively small given the extreme detunings of optical dipole traps and only becomes relevant in the degenerate phase.

Lastly, we need to figure out the particle and energy loss rate due to changes of the trap. As the trap depth is lowered, occupied states at the edge of the trap are inevitably lost. This effect is called *spilling* and the associated changes in particle number and energy can be intuitively expressed as

$$\dot{N}_s = f(\varepsilon_t)\rho(\varepsilon_t)\dot{\varepsilon}_t = \frac{N}{\zeta} e^{-\beta\varepsilon_t}\rho(\varepsilon_t)\dot{\varepsilon}_t \tag{C.19}$$

$$\dot{E}_s = \dot{N}_s\varepsilon_t \ . \tag{C.20}$$

Spilling, just like one-body loss, doesn't directly contribute to temperature change because the corresponding terms in equation C.9 cancel out. This can be understood by realizing that moving the truncation cutoff of the Boltzmann distribution doesn't change the distribution of particles that are left in the trap and so temperature remains the same. Spilling, however, does contribute to particle loss and is one of the main mechanisms disfavouring fast evaporation ramps.

As mentioned before, optical dipole traps (ODTs) relax (their trapping frequencies weaken) as the power is reduced during a forced evaporation ramp. In our approach, we view it as an adiabatic decompression of the gas. By writing the entropy as $S = \frac{E-F}{T}$, where $F = -kTln(\frac{\zeta^N}{N!})$ is the Helmholtz free energy, taking the total differential and setting $dS = 0$ (adiabatic) and $dN = 0$ (no particle loss), we can derive the rate of change of energy due to this compression

$$\dot{E}_P = -k_B T \frac{N}{\zeta}\dot{P}\int e^{-\beta\epsilon}\frac{\partial\rho}{\partial P}d\epsilon \ . \tag{C.21}$$

The parameter P can be any trap parameter and in our calculations we take it to be the harmonic average of the trapping frequencies, $\bar{\omega}$. We note that our method was in quantitative agreement with an alternative approach presented in [352].

By combining all the different contributions to the change in energy and particle number, $\dot{E} = \dot{E}_{\text{ev}} + \dot{E}_{1b} + \dot{E}_{3b} + \dot{E}_\Gamma + \dot{E}_s + \dot{E}_P$ and $\dot{N} = \dot{N}_{\text{ev}} + \dot{N}_{1b} + \dot{N}_{3b} + \dot{N}_s$, and inserting them into equation C.9, we get a master differential equation for the temperature and particle number which can be solved numerically for a given ramp $P(t)$.

Although mathematically heavy, hopefully this section shed some light on the inner complexities of evaporative cooling and on why its optimization is a difficult, multidimensional problem. In the next section, we will further develop these methods and demonstrate how we can use them to simulate evaporative cooling.

C.4 Simulating evaporation

A comprehensive overview of the theory behind evaporative cooling was provided above in section C.3. Here, we further develop all the relevant mathematical expressions used in practice for simulating the evaporation process following references [313], [410].

The two central quantities in all of our calculations are the truncated Boltzmann distribution

$$f(\epsilon) = n_0 \Lambda^3 e^{-\epsilon/kT} \Theta\left(\varepsilon_t - \epsilon\right) \tag{C.22}$$

and the density of states in the trap

$$\rho(\epsilon) \equiv (2\pi\hbar)^{-3} \int d^3r d^3p \delta\left(\epsilon - U(\mathbf{r}) - p^2/2m\right) = \frac{2\pi(2m)^{3/2}}{(2\pi\hbar)^3} \int_{U(\mathbf{r})\leq\epsilon} d^3r \sqrt{\epsilon - U(\mathbf{r})} \tag{C.23}$$

The former is a result of our assumption that the gas is deep within the thermal regime, i.e. far from degeneracy, and that any states with energy larger than the trap depth $\epsilon > \varepsilon_t$ are not supported. The latter is a general expression that holds for any trapping potential $U(\mathbf{r})$. From these two quantities, we can derive all the terms in the equation for temperature time evolution

$$\dot{T} = \frac{\dot{E} - \mu\dot{N} - Q\dot{P}}{C} \tag{C.24}$$

such as the total energy

$$E(N,T,P) = \frac{N}{\zeta(T,P)} \int_0^{\varepsilon_t} \epsilon\rho(\epsilon,P) e^{-\beta\epsilon} d\epsilon \tag{C.25}$$

the partition function

$$\zeta(T,P) = \int_0^{\varepsilon_t} \rho(\epsilon,P) e^{-\beta\epsilon} d\epsilon \tag{C.26}$$

or any of its derivatives such as the heat capacity $C = \frac{\partial E}{\partial T}$ and the chemical potential $\mu = \frac{\partial E}{\partial N}$. In all of the above expressions, we included an explicit dependence of the quantities on trap parameters P. In practice, we can either parametrize the trap using its depth ε_t and trapping frequencies ω_i or simply by its total power P_t. In either case, we can write the corresponding change in energy as $\dot{E} = \frac{\partial E}{\partial P}\dot{P} = Q\dot{P} = \frac{\partial E}{\partial \varepsilon_t}\dot{\varepsilon}_t + \frac{\partial E}{\partial \bar{\omega}}\dot{\bar{\omega}} = \frac{\partial E}{\partial P_t}\dot{P}_t$.

These in combination with the particle and energy change due to evaporation (equations C.12), one- and three-body losses (equations C.16) and spilling (equations C.19) as well as heating due to off resonant scattering (equation C.18) and work done on the gas by the trap (equation C.21) give us the full time evolution of the particle number and temperature–two central thermodynamic quantities in cold atom systems.

In general, these coupled differential equations need to be solved numerically. However, many of the terms involved can be calculated with varying degree of efficiency depending on the approximations used. Most notably, one can either assume a completely general form of the trapping potential $U(\mathbf{r})$ or use the harmonic approximation valid for $k_B T \ll \varepsilon_t$. The former is computationally more expensive but allows for the treatment of intermediate

regimes where the density distribution doesn't have a well defined functional form (e.g. in crossed beam traps; see section 4.2). The latter leads to analytic expressions for quantities such as the density of states, heat capacity or chemical potential and is thus much faster but its applicability is limited. Below, we will outline important results and shortcuts that can be used to implement and boost the efficiency of both methods.

C.4.1 Full treatment

Even in the case of a generic trapping potential $U(\mathbf{r})$, certain degree of mathematical analysis can still be applied to simplify expressions that would otherwise have to be derived by the means of numerical differentiation.

To start with, the atom density $n(\mathbf{r})$ can be obtained by simply integrating the truncated Boltzmann distribution using the semi-classical local density of momentum states given by $(2\pi\hbar)^{-3}$ and the per-state energy $\varepsilon = U(\mathbf{r}) + p^2/2m$ subject to the local constraint on momentum $p^2/2m < \varepsilon_t - U(\mathbf{r})$. This yields

$$n(\mathbf{r}) = \int^{|p|<p_c} \frac{d^3\mathbf{p}}{(2\pi\hbar)^3}\, e^{-\beta(U(\mathbf{r})+p^2/2m)} = n_0 e^{-\beta U(\mathbf{r})} P(3/2, \kappa) \tag{C.27}$$

where $p_c = \sqrt{2m(\varepsilon_t - U(\mathbf{r}))}$, $\kappa = \beta(\epsilon_t - U(\mathbf{r}))$ and $P(a, \nu)$ is the incomplete gamma function defined as

$$P(a, \nu) \equiv \frac{1}{\Gamma(a)} \int_0^\nu dt t^{a-1} e^{-t} \tag{C.28}$$

Note that $P(a, \infty) \to 1$ and so for an infinitely deep trap, the result C.27 simplifies to the usual Boltzmann distribution. Interestingly, the cut-off in energy introduced by the finite trap depth lowers the peak density by a factor of $P(3/2, \eta)$ with the truncation parameter $\eta = \varepsilon_t / k_B T$. The parameter n_0 can be figured out from the normalization condition on the total number of atoms which yields $n_0 \Lambda^3 = N/\zeta$ and so the knowledge of $U(\mathbf{r})$ and the partition function ζ gives us easy access to the density.

The knowledge of density, in return, allows us to calculate the one- and three-body loss and heating rates and the off-resonant scattering heating rates given by equations C.16 and C.18 by integrating over the volume of the trap. To figure out the average energy lost per particle, we can once again invoke the truncated Boltzmann distribution and the semiclassical approximation in which

$$\bar{E}(r) = \frac{\int (U(\mathbf{r}) + \frac{p^2}{2m}) f(\mathbf{r}, \mathbf{p}) d^3\mathbf{p}}{\int f(\mathbf{r}, \mathbf{p}) d^3\mathbf{p}} = U(\mathbf{r}) + \frac{3}{2} kT \frac{P(5/2, \kappa)}{P(3/2, \kappa)} \tag{C.29}$$

which, once again, simplifies to the usual result $\bar{E} = U + \frac{3}{2} k_B T$ in the infinitely deep trap limit.

To progress further, we need to calculate the density of states $\rho(\epsilon)$. In this general approach, this is done by numerically integrating equation C.23 for different values of ϵ and is thus one of the more 'costly' steps in the calculation pipeline. Nevertheless, once $\rho(\epsilon)$ is known for a range of ϵ values, we can proceed with calculating the partition function ζ (equation C.26) and all the derived quantities.

Since we have access to the trap parameters as a function of time–after all, that's what defines the evaporation trajectory that we are trying to simulate–we can easily calculate the spilling and evaporation terms (equations C.19 and C.12) as well as the heat capacity and chemical potential using integrals of the form

$$\int_0^{\varepsilon_t} \epsilon^n \rho(\varepsilon) e^{-\beta\epsilon} d\epsilon \tag{C.30}$$

What is left to calculate are the terms related to the change in trap parameters (other than spilling) given by equation C.21 and the quantity $Q = \frac{\partial E}{\partial P}$. Due to the lack of an analytic expression for the density of states $\rho(\epsilon)$, any derivatives of the form $\frac{\partial \rho}{\partial P}$ need to be calculated numerically by incrementing the trap parameters P and recalculating ρ while keeping all the other parameters such as T constant. This is another costly but unavoidable step. We now have all the ingredients to numerically integrate $\dot{T}$ and $\dot{N}$ in time, recalculating ρ at each time step.

C.4.2 Harmonic approximation

In this section, we will list all the relevant analytical results which are only usable when we assume a perfectly harmonic trapping potential, albeit with a finite depth ε_t. For a potential of the form

$$U(\mathbf{r}) = \frac{1}{2} m(\omega_x^2 x^2 + \omega_y^2 y^2 + \omega_z^2 z^2) \tag{C.31}$$

with $\bar{\omega} = (\omega_x \omega_y \omega_z)^{1/3}$, the relevant analytic expressions are as follows

$$\rho(\epsilon) = \frac{\epsilon^2}{2(\hbar\bar{\omega})^3} \tag{C.32}$$

$$\zeta = \left(\frac{k_B T}{\hbar\bar{\omega}}\right)^3 P(3,\eta) \tag{C.33}$$

$$\mu = 3k_B T \frac{P(4,\eta)}{P(3,\eta)} \tag{C.34}$$

$$C = 3Nk_B \left(4\frac{P(5,\eta)}{P(3,\eta)} - 3\left(\frac{P(4,\eta)}{P(3,\eta)}\right)^2\right) \tag{C.35}$$

$$Q = N\frac{\eta^2 e^{-\eta}}{P(3,\eta)}\left(\frac{\eta}{2} - \frac{3}{2}\frac{P(4,\eta)}{P(3,\eta)}\right) \tag{C.36}$$

$$\dot{N}_{\text{ev}} = -\frac{N^2\sigma\bar{v}}{\Lambda^3\zeta} e^{-\eta}\left(\eta + \frac{\eta^3 e^{-\eta}}{6P(3,\eta)} - 3\frac{P(4,\eta)}{P(3,\eta)} - 1\right) \tag{C.37}$$

$$\dot{E}_{\text{ev}} = \dot{N}_{\text{ev}} k_B T \left(\eta + \frac{\eta - 3\frac{P(4,\eta)}{P(3,\eta)} - 2 + \frac{\eta^3 e^{-\eta}}{3P(3,\eta)}\left(1 + \frac{\eta}{8}\right)}{\eta - 3\frac{P(4,\eta)}{P(3,\eta)} - 1 + \frac{\eta^3 e^{-\eta}}{6P(3,\eta)}}\right) \tag{C.38}$$

$$\dot{N}_s = \frac{N e^{-\eta}}{2P(3,\eta)} \frac{\varepsilon_t^2 \dot{\varepsilon}_t}{(k_B T)^3} \tag{C.39}$$

$$\dot{E}_s = \dot{N}_s \varepsilon_t \tag{C.40}$$

$$\dot{E}_P = 3Nk_B T \frac{\dot{\bar{\omega}}}{\bar{\omega}} \tag{C.41}$$

The expressions for the one-body particle and energy loss are independent of the trap and are simply given by

$$\dot{N}_{1B} = -\frac{N}{\tau} \tag{C.42}$$

$$\dot{E}_{1B} = -\frac{E}{\tau} = -\frac{N\mu}{\tau} \tag{C.43}$$

The equivalent expressions for the three-body loss, on the other hand, don't have an analytic form. At least not for the truncated harmonic potential. However, to a good degree of approximation, we can treat the trap as infinitely deep in which case results derived in chapter 5 can be used and they read as

$$\begin{aligned} \dot{N}_{3B} &= -L_3 N^3 \left(\frac{m}{2\pi k_B T\sqrt{3}}\right)^3 \bar{\omega}^6 \\ \dot{E}_3 &= 2k_B T \dot{N}_{3B} \end{aligned} \tag{C.44}$$

Similarly for the heating due to off resonant scattering, no analytic expression exists but we can use the fact that the trapping potential is proportional to the light intensity, $U(\mathbf{r}) = \varepsilon_t - (Re(\alpha)/2\varepsilon_0 c)I(\mathbf{r})$, that the off resonant scattering rate is given by $\Gamma = (Im(\alpha)/\hbar\varepsilon_0 c)I(\mathbf{r})$ and that the average potential energy of an atom is approximately $(3/2)k_B T$ in the infinitely deep trap regime to derive

$$\dot{E}_\Gamma = \frac{2N}{\hbar}\frac{Im(\alpha)}{Re(\alpha)}\frac{(\hbar k)^2}{m}\left(\varepsilon_t - \frac{3}{2}k_B T\right) \tag{C.45}$$

where α is the atomic polarizability and $Re(\alpha)$ and $Im(\alpha)$ are its real and imaginary parts respectively. The above set of equations allows us to numerically solve for the particle number and temperature as a function of time, given specific ramps in $\varepsilon_t(t)$ and $\bar{\omega}(t)$, without the need for performing costly three-dimensional integrals of density and density of states.

C.4.3 Method comparison

In this brief section we present the comparison of the two semi-analytical methods and the DSMC dynamical method when used to simulate forced evaporative cooling in a single-beam Gaussian ODT. For this comparison, we use an exponential ramp in beam power starting at 4 W and finishing at 0.5 W with the characteristic decay time $\tau = 0.3$ s. The ramp was performed over 3 s and 1 s to compare how the different approaches handle situations that might deviate from thermodynamic equilibrium.

The initial conditions for the atom number $N = 3.2 \times 10^6$ and temperature $T = 6\,\mu$K correspond to standard experimental values. The DSMC simulation was performed using the full Gaussian potential of the trapping beam as well as a truncated harmonic potential with the same trapping frequencies to contrast it directly with the analytic harmonic treatment discussed above. Figure C.2 shows the result of the four simulations for the two ramp times. Note that the atomic samples were held in the final trap for 250 ms to let

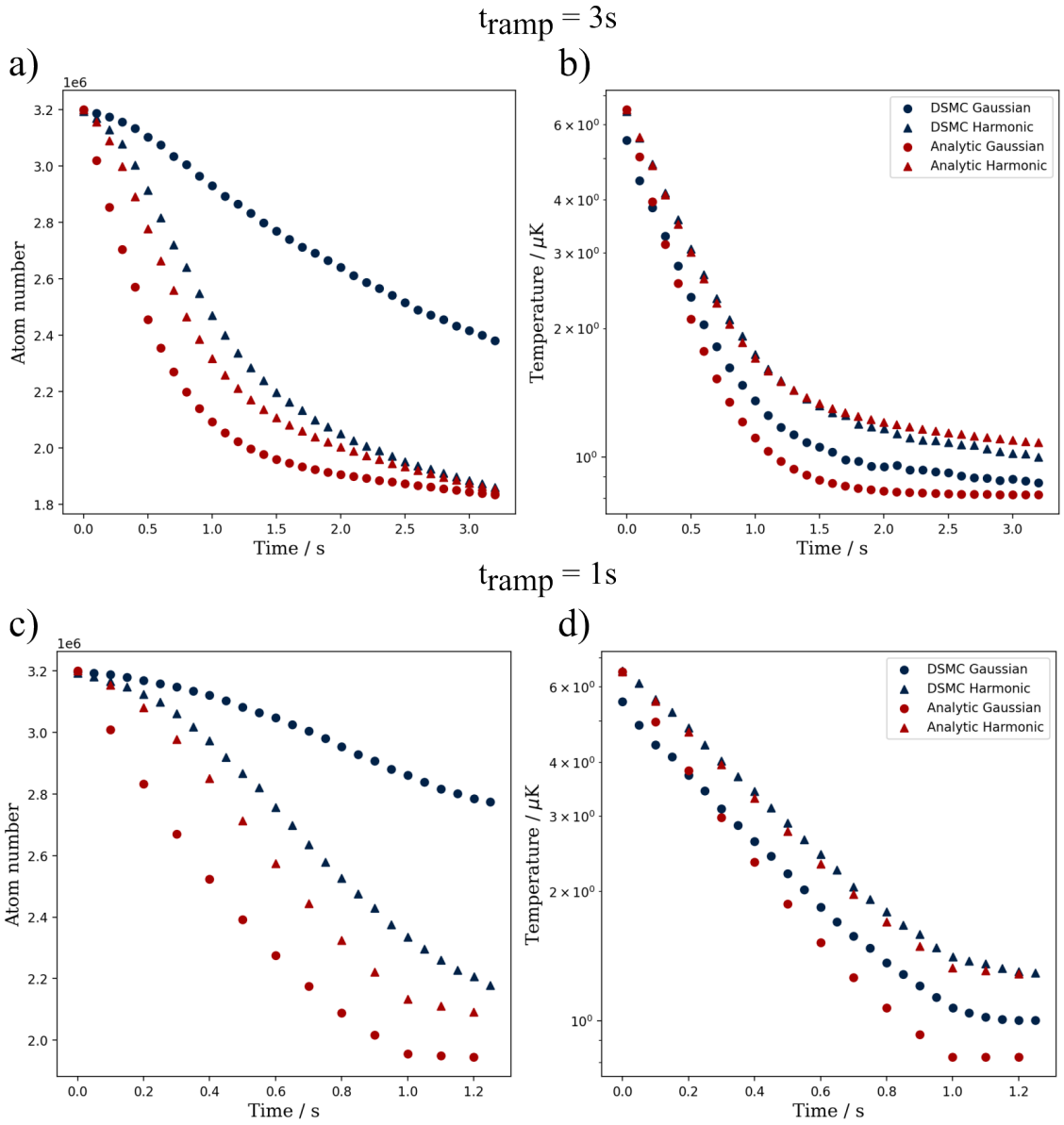


Figure C.2: Comparison of simulation methods. a)-b) Atom number (a) and temperature (b) of an atomic cloud undergoing a 3 s forced evaporation ramp as simulated using four methods–DSMC assuming a real Gaussian beam potential as well as a truncated harmonic potential and two corresponding analytic approaches as described in this appendix. c)-d) Equivalent simulation results for a faster evaporation ramp (1 s).

them move towards equilibrium.

Perhaps the most striking difference is between the Gaussian DSMC and the other three simulations when it comes to particle number. The explanation is most likely related to the fact that due to the large volume of the Gaussian trap compared to the corresponding harmonic trap, particles at the edge of the cloud are not in perfect thermal equilibrium with the center of the cloud. This is because it takes long time for particles to travel all the way to the edge of the cloud, collide with other particles there and redistribute their energy. Consequently, the analytic methods (which assume complete thermal equilibrium) overestimate particle loss due to spilling of states at the edge of the trap (see section C.3).

Second observation is related to temperatures. These are remarkably robust across all simulations, with the Gaussian simulations falling slightly lower than the harmonic simulations. It seems like in this regime, the temperature is mainly determined by the trap depth and the relaxation of the gas. The latter being responsible for the lower temperatures of the Gaussian simulations due to the higher volume of the Gaussian trap.

Thirdly, the DSMC simulation of the harmonic trap is in good agreement with the corresponding analytic calculations. This validates our implementation of the DSMC method and allows us to use it to simulate atomic transport (see section 4.5.2).

Lastly, in the case of the fast ramp, the discrepancy in the particle number is further enhanced which is compatible with our first conclusion i.e. that the discrepancy is caused by the lack of equilibrium in the system. The temperatures, on the other hand, remain robust and converge to similar values as for the case of the slow ramp.

When it comes to computational speed and simulation capabilities, the harmonic analytic method is by far the fastest and only takes about 50 ms[2] to compute the 1 s evaporation ramp. The DSMC method with 10 000 simulated particles takes approximately 3 min whereas our implementation of the full analytic treatment using a 3D grid takes 9 min and is thus inferior. As mentioned before, both analytic methods are based on the assumption of thermal equilibrium which might not always be valid and is certainly not the case in more dynamical scenarios such as atomic transport. The DSMC, on the other hand, is well suited for this purpose. Additionally, the harmonic analytic approach breaks down in dimple traps at intermediate temperatures when the density distribution deviates strongly from the ideal Gaussian distribution (see section 4.3.1).

[2]The simulations were run on a system with 16GB or RAM and a 3.2 GHz Intel Core i7–8700 CPU

D. Temperature corrections after ToF expansion

In section 6.3.3, we discussed the corrections that need to be applied to our measurement of the cloud temperature from time-of-flight images. One of the leading terms originates from the thermal cloud self interaction which includes both the short-ranged contacts interactions and the long-ranged, anisotropic dipole-dipole interactions.

Reference [143] derives an analytic form for these corrections which take into account collisions and mean-field forces. We use these in the form of equations 6.50 and 6.51 with the numerically calculated constants H, F, A and B defined below:

$$H_d^{(i)} = \frac{3}{2^4\pi^{3/2}} \int d^2\hat{p} \frac{\hat{p}_i^2}{\left(\sum_j \hat{p}_j^2 \frac{\bar{\omega}^2}{\omega_j^2}\right)^{3/2}} \left[(\hat{p}\cdot\hat{\epsilon})^2 - \frac{1}{3}\right] \tag{D.1}$$

$$H^{(i)} = \frac{1}{2^4\pi^{3/2}} \int d^2\hat{p} \frac{\hat{p}_i^2}{\left(\sum_j \hat{p}_j^2 \frac{\bar{\omega}^2}{\omega_j^2}\right)^{3/2}} \tag{D.2}$$

$$F_d^{(i)} = \frac{3}{2^4\pi^{3/2}} \int d^2\hat{p} \frac{\sqrt{\left(\sum_j \frac{\omega_j^2\hat{p}_j^2}{\omega_i^2}\right) - 1} - \arccos\left[\sqrt{\frac{\omega_i^2}{\sum_j \hat{p}_j^2\omega_j^2}}\right]}{\left[\left(\sum_j \frac{\omega_j^2\hat{p}_j^2}{\omega_i^2}\right) - 1\right]^{3/2}} \left[(\hat{p}\cdot\hat{\epsilon})^2 - \frac{1}{3}\right] \tag{D.3}$$

$$F^{(i)} = \frac{1}{2^4\pi^{3/2}} \int d^2\hat{p} \frac{\sqrt{\left(\sum_j \frac{\omega_j^2\hat{p}_j^2}{\omega_i^2}\right) - 1} - \arccos\left[\sqrt{\frac{\omega_i^2}{\sum_j \hat{p}_j^2\omega_j^2}}\right]}{\left[\left(\sum_j \frac{\omega_j^2\hat{p}_j^2}{\omega_i^2}\right) - 1\right]^{3/2}} \tag{D.4}$$

$$\tag{D.5}$$

$$A_0^{(i)} = \frac{3}{2^6\pi^2}\int d^2\hat{p}\int d^2\hat{p}'\frac{\left(\hat{p}_i'^2-\hat{p}_i^2\right)\left[\frac{(\hat{p}'\cdot\hat{\epsilon})^2+(\hat{p}\cdot\hat{\epsilon})^2-2(\hat{p}'\cdot\hat{\epsilon})(\hat{p}\cdot\hat{\epsilon})(\hat{p}'\cdot\hat{p})}{1-(\hat{p}\cdot\hat{p}')^2}-\frac{2}{3}\right]^2}{\sqrt{\sum_j \hat{p}_j^2\frac{\omega_j^2}{\bar{\omega}^2}}} \tag{D.6}$$

$$A_1^{(i)} = \frac{1}{2^4\pi^2}\int d^2\hat{p}\int d^2\hat{p}'\frac{\left(\hat{p}_i'^2-\hat{p}_i^2\right)\left[\frac{(\hat{p}'\cdot\hat{\epsilon})^2+(\hat{p}\cdot\hat{\epsilon})^2-2(\hat{p}'\cdot\hat{\epsilon})(\hat{p}\cdot\hat{\epsilon})(\hat{p}'\cdot\hat{p})}{1-(\hat{p}\cdot\hat{p}')^2}-\frac{2}{3}\right]}{\sqrt{\sum_j \hat{p}_j^2\frac{\omega_j^2}{\bar{\omega}^2}}} \tag{D.7}$$

$$A_2^{(i)} = \frac{1}{48\pi^2}\int d^2\hat{p}\int d^2\hat{p}'\frac{\left(\hat{p}_i'^2-\hat{p}_i^2\right)}{\sqrt{\sum_j \hat{p}_j^2\frac{\omega_j^2}{\bar{\omega}^2}}} \tag{D.8}$$

$$B_0^{(i)} = \frac{3}{2^7\pi^2}\int d^2\hat{p}\int d^2\hat{p}'\frac{\left(\hat{p}_i'^2-\hat{p}_i^2\right)\left[\frac{(\hat{p}'\cdot\hat{\epsilon})^2+(\hat{p}\cdot\hat{\epsilon})^2-2(\hat{p}'\cdot\hat{\epsilon})(\hat{p}\cdot\hat{\epsilon})(\hat{p}'\cdot\hat{p})}{1-(\hat{p}\cdot\hat{p}')^2}-\frac{2}{3}\right]^2}{\sqrt{\sum_j \left(3\hat{p}_j^2+\hat{p}_j'^2\right)\frac{\omega_j^2}{\bar{\omega}^2}}} \tag{D.9}$$

$$B_1^{(i)} = \frac{1}{2^5\pi^2}\int d^2\hat{p}\int d^2\hat{p}'\frac{\left(\hat{p}_i'^2-\hat{p}_i^2\right)\left[\frac{(\hat{p}'\cdot\hat{\epsilon})^2+(\hat{p}\cdot\hat{\epsilon})^2-2(\hat{p}'\cdot\hat{\epsilon})(\hat{p}\cdot\hat{\epsilon})(\hat{p}'\cdot\hat{p})}{1-(\hat{p}\cdot\hat{p}')^2}-\frac{2}{3}\right]}{\sqrt{\sum_j \left(3\hat{p}_j^2+\hat{p}_j'^2\right)\frac{\omega_j^2}{\bar{\omega}^2}}} \tag{D.10}$$

$$B_2^{(i)} = \frac{1}{96\pi^2}\int d^2\hat{p}\int d^2\hat{p}'\frac{\left(\hat{p}_i'^2-\hat{p}_i^2\right)}{\sqrt{\sum_j \left(3\hat{p}_j^2+\hat{p}_j'^2\right)\frac{\omega_j^2}{\bar{\omega}^2}}} \tag{D.11}$$

with

$$\hat{p} = (\sin\theta\cos\phi, \sin\theta\sin\phi, \cos\theta) \tag{D.12}$$

and

$$\int d^2\hat{p} = \int_0^{\pi}\sin\theta d\theta\int_0^{2\pi} d\phi \tag{D.13}$$

Note that some numerical prefactors differ by $\frac{2}{3}$ or $\frac{4}{9}$ from the ones listed in [143] because of a difference in the definition of a_{dd}–see equation 2.36 for our definition which is compatible with equations 6.50 and 6.51.

E. Lab BINGO

Does it hit the cage?	Maybe we can borrow it from the Foot or Kuhn group	Try restarting the Sacher box	Blue's gone	When did we last change the coolant?
It's probably the time to restart the SLM PC ...	Is the IR on?	Any new Thorlabs order coming in? (salivating)	The lenses have drifted	Yeah, that shouldn't take too long
Is it even a Gaussian??	Adds one more piece of rubbish to the pile	M^2	Where is the 5 mm ball driver?	Lets keep the lab book tidy
I got an email from Dave sharp	Guys, we need to tidy up the lab	We should have potassium by the end of the week	Hang on!	Has anyone seen the IR card?
Let's leave it like this for now (never returns to fix it)	Where is the fibre pen?	We should be able to squeeze out a bit more out of ...	What's that smell?	But what actually is a Feshbach resonance?

Table E.1: Lab BINGO

Bibliography

[1] X.-M. Hu, Y. Guo, B.-H. Liu, C.-F. Li, and G.-C. Guo, "Progress in quantum teleportation," *Nature Reviews Physics*, vol. 5, no. 6, pp. 339–353, 2023.

[2] B. J. Dalton, J. Jeffers, and S. M. Barnett, *Phase Space Methods for Degenerate Quantum Gases*. Oxford University Press, 2014.

[3] A. Einstein, "Quantum theory of the monatomic ideal gas," *Sitzungsberichte der Preussischen Akademie der Wissenschaften, Physikalisch-mathematische Klasse*, vol. 261, 1924.

[4] S. Chu, L. Hollberg, J. E. Bjorkholm, A. Cable, and A. Ashkin, "Three-dimensional viscous confinement and cooling of atoms by resonance radiation pressure," *Physical Review Letters*, vol. 55, pp. 48–51, 1 1985.

[5] S. Chu, J. E. Bjorkholm, A. Ashkin, and A. Cable, "Experimental observation of optically trapped atoms," *Physical Review Letters*, vol. 57, pp. 314–317, 3 1986.

[6] A. L. Migdall, J. V. Prodan, W. D. Phillips, T. H. Bergeman, and H. J. Metcalf, "First observation of magnetically trapped neutral atoms," *Physical Review Letters*, vol. 54, pp. 2596–2599, 24 1985.

[7] M. H. Anderson, J. R. Ensher, M. R. Matthews, C. E. Wieman, and E. A. Cornell, "Observation of Bose-Einstein condensation in a dilute atomic vapor," *Science*, vol. 269, no. 5221, pp. 198–201, 1995.

[8] K. B. Davis, M. .-. Mewes, M. R. Andrews, *et al.*, "Bose-Einstein condensation in a gas of sodium atoms," *Phys. Rev. Lett.*, vol. 75, pp. 3969–3973, 22 1995.

[9] B. DeMarco and D. S. Jin, "Onset of Fermi degeneracy in a trapped atomic gas," *Science*, vol. 285, no. 5434, pp. 1703–1706, 1999.

[10] I. Georgescu, "25 years of BEC," *Nature Reviews Physics*, vol. 2, no. 8, pp. 396–396, 2020.

[11] F. Schreck and K. v. Druten, "Laser cooling for quantum gases," *Nature Physics*, vol. 17, no. 12, pp. 1296–1304, 2021.

[12] H. J. Metcalf and P. Van der Straten, "Laser cooling and trapping of neutral atoms," *The Optics Encyclopedia*, 2007.

[13] A. M. Kaufman and K.-K. Ni, "Quantum science with optical tweezer arrays of ultracold atoms and molecules," *Nature Physics*, vol. 17, no. 12, pp. 1324–1333, 2021.

[14] D. McGloin, G. C. Spalding, H. Melville, W. Sibbett, and K. Dholakia, "Applications of spatial light modulators in atom optics," *Optics Express*, vol. 11, no. 2, pp. 158–166, 2003.

[15] D. Stuart and A. Kuhn, "Single-atom trapping and transport in DMD-controlled optical tweezers," *New Journal of Physics*, vol. 20, no. 2, p. 023 013, 2018.

[16] G. Gauthier, I. Lenton, N. M. Parry, *et al.*, "Direct imaging of a digital-micromirror device for configurable microscopic optical potentials," *Optica*, vol. 3, no. 10, pp. 1136–1143, 2016.

[17] T. H. Loftus, T. Ido, M. M. Boyd, A. D. Ludlow, and J. Ye, "Narrow line cooling and momentum-space crystals," *Physical review A*, vol. 70, p. 063 413, 6 2004.

[18] E. A. Curtis, C. W. Oates, and L. Hollberg, "Quenched narrow-line second-and third-stage laser cooling of ^{40}Ca," *J. Opt. Soc. Am. B*, vol. 20, no. 5, pp. 977–984, 2003.

[19] F. Sievers, N. Kretzschmar, D. R. Fernandes, *et al.*, "Simultaneous sub-Doppler laser cooling of fermionic ^{6}Li and ^{40}K on the d1 line: Theory and experiment," *Physical review A*, vol. 91, no. 2, p. 023 426, 2015.

[20] M. A. Norcia, J. R. Cline, J. P. Bartolotta, M. J. Holland, and J. K. Thompson, "Narrow-line laser cooling by adiabatic transfer," *New Journal of Physics*, vol. 20, no. 2, p. 023 021, 2018.

[21] P. D. Lett, R. N. Watts, C. I. Westbrook, W. D. Phillips, P. L. Gould, and H. J. Metcalf, "Observation of atoms laser cooled below the Doppler limit," *Physical Review Letters*, vol. 61, no. 2, pp. 169–172, 1988.

[22] L. Anderegg, B. L. Augenbraun, Y. Bao, *et al.*, "Laser cooling of optically trapped molecules," *Nature Physics*, vol. 14, no. 9, pp. 890–893, 2018.

[23] M. Tarbutt, "Laser cooling of molecules," *Contemporary Physics*, vol. 59, no. 4, pp. 356–376, 2019.

[24] L. D. Carr, D. DeMille, R. V. Krems, and J. Ye, "Cold and ultracold molecules: Science, technology and applications," *New Journal of Physics*, vol. 11, no. 5, p. 055 049, 2009.

[25] R. P. Feynman, "Simulating physics with computers," *Int. J. Theor. Phys.*, vol. 21, pp. 467–488, 1982.

[26] I. Bloch, J. Dalibard, and S. Nascimbene, "Quantum simulations with ultracold quantum gases," *Nature Physics*, vol. 8, no. 4, pp. 267–276, 2012.

[27] Q.-Z. Zhu and B. Wu, "Superfluidity of Bose–Einstein condensates in ultracold atomic gases," *Chinese Physics B*, vol. 24, no. 5, p. 050 507, 2015.

[28] O. Marago, S. Hopkins, J. Arlt, E. Hodby, G. Hechenblaikner, and C. Foot, "Observation of the scissors mode and evidence for superfluidity of a trapped Bose-Einstein condensed gas," *Physical Review Letters*, vol. 84, no. 10, pp. 2056–2059, 2000.

[29] S. Levy, E. Lahoud, I. Shomroni, and J. Steinhauer, "The a.c. and d.c. Josephson effects in a Bose–Einstein condensate," *Nature*, vol. 449, no. 7162, pp. 579–583, 2007.

[30] F. S. Cataliotti, S. Burger, C. Fort, *et al.*, "Josephson junction arrays with Bose–Einstein condensates," *Science*, vol. 293, no. 5531, pp. 843–846, 2001.

[31] M. Albiez, R. Gati, J. Fölling, S. Hunsmann, M. Cristiani, and M. K. Oberthaler, "Direct observation of tunneling and nonlinear self-trapping in a single bosonic Josephson junction," *Physical Review Letters*, vol. 95, no. 1, p. 010 402, 2005.

[32] A. Smerzi, S. Fantoni, S. Giovanazzi, and S. Shenoy, "Quantum coherent atomic tunneling between two trapped Bose–Einstein condensates," *Physical Review Letters*, vol. 79, no. 25, pp. 4950–4953, 1997.

[33] C. Regal and D. Jin, "Experimental realization of the BCS–BEC crossover with a Fermi gas of atoms," *Advances In Atomic, Molecular, and Optical Physics*, vol. 54, pp. 1–79, 2007.

[34] M. Ries, A. Wenz, G. Zürn, *et al.*, "Observation of pair condensation in the quasi-2D BEC–BCS crossover," *Physical Review Letters*, vol. 114, no. 23, p. 230 401, 2015.

[35] M. Bartenstein, A. Altmeyer, S. Riedl, *et al.*, "Crossover from a molecular Bose–Einstein condensate to a degenerate Fermi gas," *Physical Review Letters*, vol. 92, no. 12, p. 120 401, 2004.

[36] N. Navon, A. L. Gaunt, R. P. Smith, and Z. Hadzibabic, "Critical dynamics of spontaneous symmetry breaking in a homogeneous Bose gas," *Science*, vol. 347, no. 6218, pp. 167–170, 2015.

[37] L. Corman, L. Chomaz, T. Bienaimé, *et al.*, "Quench-induced supercurrents in an annular Bose gas," *Physical Review Letters*, vol. 113, no. 13, p. 135 302, 2014.

[38] A. Keesling, A. Omran, H. Levine, *et al.*, "Quantum Kibble–Zurek mechanism and critical dynamics on a programmable Rydberg simulator," *Nature*, vol. 568, no. 7751, pp. 207–211, 2019.

[39] D. Frantzeskakis, "Dark solitons in atomic Bose–Einstein condensates: From theory to experiments," *Journal of Physics A: Mathematical and Theoretical*, vol. 43, no. 21, p. 213 001, 2010.

[40] S. Burger, K. Bongs, S. Dettmer, *et al.*, "Dark solitons in Bose-Einstein condensates," *Physical Review Letters*, vol. 83, no. 25, p. 5198, 1999.

[41] M. R. Matthews, B. P. Anderson, P. Haljan, D. Hall, C. Wieman, and E. A. Cornell, "Vortices in a Bose-Einstein condensate," *Physical Review Letters*, vol. 83, no. 13, p. 2498, 1999.

[42] J. R. Abo-Shaeer, C. Raman, J. M. Vogels, and W. Ketterle, "Observation of vortex lattices in Bose-Einstein condensates," *Science*, vol. 292, no. 5516, pp. 476–479, 2001.

[43] M. Gajda, M. Lewenstein, K. Sengstock, G. Birkl, W. Ertmer, *et al.*, "Optical generation of vortices in trapped Bose-Einstein condensates," *Physical Review A*, vol. 60, no. 5, R3381, 1999.

[44] L. M. Pismen, *Vortices in nonlinear fields: from liquid crystals to superfluids, from non-equilibrium patterns to cosmic strings*. Oxford University Press, 1999, vol. 100.

[45] A. L. Gaunt, T. F. Schmidutz, I. Gotlibovych, R. P. Smith, and Z. Hadzibabic, "Bose-Einstein condensation of atoms in a uniform potential," *Physical Review Letters*, vol. 110, no. 20, p. 200 406, 2013.

[46] N. Navon, R. P. Smith, and Z. Hadzibabic, "Quantum gases in optical boxes," *Nature Physics*, vol. 17, no. 12, pp. 1334–1341, 2021.

[47] C. Eigen, A. L. Gaunt, A. Suleymanzade, N. Navon, Z. Hadzibabic, and R. P. Smith, "Observation of weak collapse in a Bose-Einstein condensate," *Physical Review X*, vol. 6, no. 4, p. 041 058, 2016.

[48] N. Navon, A. L. Gaunt, R. P. Smith, and Z. Hadzibabic, "Emergence of a turbulent cascade in a quantum gas," *Nature*, vol. 539, no. 7627, pp. 72–75, 2016.

[49] M. Lewenstein, A. Sanpera, V. Ahufinger, B. Damski, A. Sen, and U. Sen, "Ultracold atomic gases in optical lattices: Mimicking condensed matter physics and beyond," *Advances in Physics*, vol. 56, no. 2, pp. 243–379, 2007.

[50] M. Greiner, O. Mandel, T. Esslinger, T. W. Hänsch, and I. Bloch, "Quantum phase transition from a superfluid to a Mott insulator in a gas of ultracold atoms," *nature*, vol. 415, no. 6867, pp. 39–44, 2002.

[51] D. Greif, T. Uehlinger, G. Jotzu, L. Tarruell, and T. Esslinger, "Short-range quantum magnetism of ultracold fermions in an optical lattice," *Science*, vol. 340, no. 6138, pp. 1307–1310, 2013.

[52] F. Jendrzejewski, A. Bernard, K. Mueller, *et al.*, "Three-dimensional localization of ultracold atoms in an optical disordered potential," *Nature Physics*, vol. 8, no. 5, pp. 398–403, 2012.

[53] L. Fallani, J. Lye, V. Guarrera, C. Fort, and M. Inguscio, "Ultracold atoms in a disordered crystal of light: Towards a Bose glass," *Physical Review Letters*, vol. 98, no. 13, p. 130 404, 2007.

[54] G. Jotzu, M. Messer, R. Desbuquois, *et al.*, "Experimental realization of the topological Haldane model with ultracold fermions," *Nature*, vol. 515, no. 7526, pp. 237–240, 2014.

[55] M. Aidelsburger, M. Atala, M. Lohse, J. T. Barreiro, B. Paredes, and I. Bloch, "Realization of the Hofstadter Hamiltonian with ultracold atoms in optical lattices," *Physical Review Letters*, vol. 111, no. 18, p. 185 301, 2013.

[56] C.-L. Hung, V. Gurarie, and C. Chin, "From cosmology to cold atoms: Observation of Sakharov oscillations in a quenched atomic superfluid," *Science*, vol. 341, no. 6151, pp. 1213–1215, 2013.

[57] J. Steinhauer, "Observation of quantum Hawking radiation and its entanglement in an analogue black hole," *Nature Physics*, vol. 12, no. 10, pp. 959–965, 2016.

[58] A. D. Ludlow, M. M. Boyd, J. Ye, E. Peik, and P. O. Schmidt, "Optical atomic clocks," *Reviews of Modern Physics*, vol. 87, no. 2, pp. 637–701, 2015.

[59] J. Grotti, S. Koller, S. Vogt, *et al.*, "Geodesy and metrology with a transportable optical clock," *Nature Physics*, vol. 14, no. 5, pp. 437–441, 2018.

[60] C. L. Degen, F. Reinhard, and P. Cappellaro, "Quantum sensing," *Reviews of Modern Physics*, vol. 89, no. 3, p. 035 002, 2017.

[61] V. Ménoret, P. Vermeulen, N. Le Moigne, *et al.*, "Gravity measurements below 10^{-9} g with a transportable absolute quantum gravimeter," *Scientific reports*, vol. 8, no. 1, p. 12 300, 2018.

[62] C. Freier, M. Hauth, V. Schkolnik, *et al.*, "Mobile quantum gravity sensor with unprecedented stability," in *Journal of physics: conference series*, IOP Publishing, vol. 723, 2016, p. 012 050.

[63] B. Stray, A. Lamb, A. Kaushik, *et al.*, "Quantum sensing for gravity cartography," *Nature*, vol. 602, no. 7898, pp. 590–594, 2022.

[64] I. Kominis, T. Kornack, J. Allred, and M. V. Romalis, "A subfemtotesla multichannel atomic magnetometer," *Nature*, vol. 422, no. 6932, pp. 596–599, 2003.

[65] N. Aslam, H. Zhou, E. K. Urbach, *et al.*, "Quantum sensors for biomedical applications," *Nature Reviews Physics*, vol. 5, no. 3, pp. 157–169, 2023.

[66] Y. A. El-Neaj, C. Alpigiani, S. Amairi-Pyka, *et al.*, "AEDGE: Atomic experiment for dark matter and gravity exploration in space," *EPJ Quantum Technology*, vol. 7, no. 1, pp. 1–27, 2020.

[67] B. Canuel, A. Bertoldi, L. Amand, *et al.*, "Exploring gravity with the MIGA large scale atom interferometer," *Scientific Reports*, vol. 8, no. 1, p. 14 064, 2018.

[68] C. D. Bruzewicz, J. Chiaverini, R. McConnell, and J. M. Sage, "Trapped-ion quantum computing: Progress and challenges," *Applied Physics Reviews*, vol. 6, no. 2, 2019.

[69] H.-L. Huang, D. Wu, D. Fan, and X. Zhu, "Superconducting quantum computing: A review," *Science China Information Sciences*, vol. 63, pp. 1–32, 2020.

[70] L. Henriet, L. Beguin, A. Signoles, *et al.*, "Quantum computing with neutral atoms," *Quantum*, vol. 4, p. 327, 2020.

[71] N. Schlosser, G. Reymond, I. Protsenko, and P. Grangier, "Sub-poissonian loading of single atoms in a microscopic dipole trap," *Nature*, vol. 411, no. 6841, pp. 1024–1027, 2001.

[72] H. Levine, A. Keesling, G. Semeghini, *et al.*, "Parallel implementation of high-fidelity multiqubit gates with neutral atoms," *Physical Review Letters*, vol. 123, no. 17, p. 170 503, 2019.

[73] O. Mandel, M. Greiner, A. Widera, T. Rom, T. W. Hänsch, and I. Bloch, "Controlled collisions for multi-particle entanglement of optically trapped atoms," *Nature*, vol. 425, no. 6961, pp. 937–940, 2003.

[74] E. Hagley, X. Maitre, G. Nogues, *et al.*, "Generation of Einstein-Podolsky-Rosen pairs of atoms," *Physical Review Letters*, vol. 79, no. 1, pp. 1–5, 1997.

[75] M. Saffman, "Quantum computing with atomic qubits and Rydberg interactions: Progress and challenges," *Journal of Physics B: Atomic, Molecular and Optical Physics*, vol. 49, no. 20, p. 202 001, 2016.

[76] A. Browaeys, D. Barredo, and T. Lahaye, "Experimental investigations of dipole–dipole interactions between a few Rydberg atoms," *Journal of Physics B: Atomic, Molecular and Optical Physics*, vol. 49, no. 15, p. 152 001, 2016.

[77] L. Pitaevskii and S. Stringari, *Bose-Einstein condensation and superfluidity*. Oxford University Press, 2016, vol. 164.

[78] T. Weber, J. Herbig, M. Mark, H.-C. Nägerl, and R. Grimm, "Three-body recombination at large scattering lengths in an ultracold atomic gas," *Physical Review Letters*, vol. 91, no. 12, p. 123 201, 2003.

[79] J. J. Sakurai and J. Napolitano, *Modern quantum mechanics*. Cambridge University Press, 2020.

[80] C. J. Foot, *Atomic physics*. OUP Oxford, 2004, vol. 7.

[81] P. Courteille, R. Freeland, D. J. Heinzen, F. Van Abeelen, and B. Verhaar, "Observation of a Feshbach resonance in cold atom scattering," *Physical Review Letters*, vol. 81, no. 1, p. 69, 1998.

[82] S. Inouye, M. Andrews, J. Stenger, H.-J. Miesner, D. M. Stamper-Kurn, and W. Ketterle, "Observation of Feshbach resonances in a Bose–Einstein condensate," *Nature*, vol. 392, no. 6672, pp. 151–154, 1998.

[83] P. Makotyn, C. E. Klauss, D. L. Goldberger, E. Cornell, and D. S. Jin, "Universal dynamics of a degenerate unitary Bose gas," *Nature Physics*, vol. 10, no. 2, pp. 116–119, 2014.

[84] R. J. Fletcher, A. L. Gaunt, N. Navon, R. P. Smith, and Z. Hadzibabic, "Stability of a unitary Bose gas," *Physical Review Letters*, vol. 111, no. 12, p. 125 303, 2013.

[85] E. A. Donley, N. R. Claussen, S. L. Cornish, J. L. Roberts, E. A. Cornell, and C. E. Wieman, "Dynamics of collapsing and exploding Bose–Einstein condensates," *Nature*, vol. 412, no. 6844, pp. 295–299, 2001.

[86] M. Randeria and E. Taylor, "Crossover from Bardeen-Cooper-Schrieffer to Bose-Einstein condensation and the unitary Fermi gas," *Annu. Rev. Condens. Matter Phys.*, vol. 5, no. 1, pp. 209–232, 2014.

[87] W. Zwerger, *The BCS–BEC crossover and the unitary Fermi gas*. Springer Science & Business Media, 2011, vol. 836.

[88] Y. Chen, M. Horikoshi, M. Kuwata-Gonokami, and K. Yoshioka, "Creating a non-interacting Bose gas in equilibrium at finite temperature," *Physical Review A*, vol. 105, no. 4, p. 043 312, 2022.

[89] A. G. Sykes, J. P. Corson, J. P. D'Incao, *et al.*, "Quenching to unitarity: Quantum dynamics in a three-dimensional Bose gas," *Physical Review A*, vol. 89, p. 021 601, 2 2014.

[90] B. J. DeSalvo, K. Patel, G. Cai, and C. Chin, "Observation of fermion-mediated interactions between bosonic atoms," *Nature*, vol. 568, no. 7750, pp. 61–64, 2019.

[91] L. Chomaz, I. Ferrier-Barbut, F. Ferlaino, B. Laburthe-Tolra, B. L. Lev, and T. Pfau, "Dipolar physics: A review of experiments with magnetic quantum gases," *Reports on Progress in Physics*, vol. 86, no. 2, p. 026 401, 2022.

[92] N. W. Ashcroft and N. D. Mermin, *Solid state physics*. Cengage Learning, 1976.

[93] M. Stöhr, M. Sadhukhan, Y. S. Al-Hamdani, J. Hermann, and A. Tkatchenko, "Coulomb interactions between dipolar quantum fluctuations in Van der Waals bound molecules and materials," *Nature Communications*, vol. 12, no. 1, p. 137, 2021.

[94] T. Köhler, K. Góral, and P. S. Julienne, "Production of cold molecules via magnetically tunable Feshbach resonances," *Reviews of Modern Physics*, vol. 78, no. 4, pp. 1311–1361, 2006.

[95] S. Ospelkaus, K.-K. Ni, D. Wang, *et al.*, "Quantum-state controlled chemical reactions of ultracold potassium-rubidium molecules," *Science*, vol. 327, no. 5967, pp. 853–857, 2010.

[96] A. Chotia, B. Neyenhuis, S. A. Moses, *et al.*, "Long-lived dipolar molecules and Feshbach molecules in a 3D optical lattice," *Physical Review Letters*, vol. 108, no. 8, p. 080 405, 2012.

[97] M. Schmidt, L. Lassablière, G. Quéméner, and T. Langen, "Self-bound dipolar droplets and supersolids in molecular Bose–Einstein condensates," *Phys. Rev. Res.*, vol. 4, p. 013 235, 1 2022.

[98] N. Bigagli, W. Yuan, S. Zhang, *et al.*, "Observation of Bose–Einstein condensation of dipolar molecules," *Nature*, pp. 1–5, 2024.

[99] T. F. Gallagher, "Rydberg atoms," in *Springer Handbook of Atomic, Molecular, and Optical Physics*, Springer, 1994, pp. 231–240.

[100] C. E. Theodosiou, "Lifetimes of alkali-metal—atom Rydberg states," *Physical Review A*, vol. 30, no. 6, pp. 2881–2909, 1984.

[101] C. S. Adams, J. D. Pritchard, and J. P. Shaffer, "Rydberg atom quantum technologies," *Journal of Physics B: Atomic, Molecular and Optical Physics*, vol. 53, no. 1, p. 012 002, 2019.

[102] A. Griesmaier, J. Werner, S. Hensler, J. Stuhler, and T. Pfau, "Bose-Einstein condensation of chromium," *Physical Review Letters*, vol. 94, no. 16, p. 160 401, 2005.

[103] M. Lu, N. Q. Burdick, S. H. Youn, and B. L. Lev, "Strongly dipolar Bose-Einstein condensate of dysprosium," *Physical Review Letters*, vol. 107, no. 19, p. 190 401, 2011.

[104] K. Aikawa, A. Frisch, M. Mark, *et al.*, "Bose-Einstein condensation of erbium," *Physical Review Letters*, vol. 108, no. 21, p. 210 401, 2012.

[105] Y. Miyazawa, R. Inoue, H. Matsui, G. Nomura, and M. Kozuma, "Bose-Einstein condensation of europium," *Physical Review Letters*, vol. 129, no. 22, p. 223 401, 2022.

[106] R. P. Feynman and M. Cohen, "Energy spectrum of the excitations in liquid helium," *Phys. Rev.*, vol. 102, pp. 1189–1204, 5 1956.

[107] D. G. Henshaw and A. D. B. Woods, "Modes of atomic motions in liquid helium by inelastic scattering of neutrons," *Phys. Rev.*, vol. 121, pp. 1266–1274, 5 1961.

[108] L. Chomaz, R. M. van Bijnen, D. Petter, *et al.*, "Observation of roton mode population in a dipolar quantum gas," *Nature physics*, vol. 14, no. 5, pp. 442–446, 2018.

[109] D. Petter, G. Natale, R. van Bijnen, *et al.*, "Probing the roton excitation spectrum of a stable dipolar Bose gas," *Physical Review Letters*, vol. 122, no. 18, p. 183 401, 2019.

[110] Z.-H. Luo, W. Pang, B. Liu, Y.-Y. Li, and B. A. Malomed, "A new form of liquid matter: Quantum droplets," *Frontiers of Physics*, vol. 16, pp. 1–21, 2021.

[111] M. Boninsegni and N. V. Prokof'ev, "Colloquium: Supersolids: What and where are they?" *Rev. Mod. Phys.*, vol. 84, pp. 759–776, 2 2012.

[112] H. Kadau, M. Schmitt, M. Wenzel, *et al.*, "Observing the Rosensweig instability of a quantum ferrofluid," *Nature*, vol. 530, no. 7589, pp. 194–197, 2016.

[113] I. Ferrier-Barbut, H. Kadau, M. Schmitt, M. Wenzel, and T. Pfau, "Observation of quantum droplets in a strongly dipolar Bose gas," *Physical Review Letters*, vol. 116, no. 21, p. 215 301, 2016.

[114] L. Chomaz, S. Baier, D. Petter, *et al.*, "Quantum-fluctuation-driven crossover from a dilute Bose-Einstein condensate to a macrodroplet in a dipolar quantum fluid," *Physical Review X*, vol. 6, no. 4, p. 041 039, 2016.

[115] F. Böttcher, J.-N. Schmidt, M. Wenzel, *et al.*, "Transient supersolid properties in an array of dipolar quantum droplets," *Physical Review X*, vol. 9, no. 1, p. 011 051, 2019.

[116] G. Natale, R. van Bijnen, A. Patscheider, *et al.*, "Excitation spectrum of a trapped dipolar supersolid and its experimental evidence," *Physical Review Letters*, vol. 123, no. 5, p. 050 402, 2019.

[117] M. A. Norcia, C. Politi, L. Klaus, *et al.*, "Two-dimensional supersolidity in a dipolar quantum gas," *Nature*, vol. 596, no. 7872, pp. 357–361, 2021.

[118] L. Tanzi, E. Lucioni, F. Famà, *et al.*, "Observation of a dipolar quantum gas with metastable supersolid properties," *Physical Review Letters*, vol. 122, no. 13, p. 130 405, 2019.

[119] J. Hertkorn, J.-N. Schmidt, M. Guo, *et al.*, "Pattern formation in quantum ferrofluids: From supersolids to superglasses," *Physical Review Research*, vol. 3, no. 3, p. 033 125, 2021.

[120] S. B. Prasad, T. Bland, B. C. Mulkerin, N. G. Parker, and A. M. Martin, "Vortex lattice formation in dipolar Bose-Einstein condensates via rotation of the polarization," *Physical Review A*, vol. 100, no. 2, p. 023 625, 2019.

[121] L. Klaus, T. Bland, E. Poli, *et al.*, "Observation of vortices and vortex stripes in a dipolar condensate," *Nature Physics*, pp. 1–6, 2022.

[122] Z. Hadzibabic, C. Stan, K. Dieckmann, *et al.*, "Two-species mixture of quantum degenerate Bose and Fermi gases," *Physical Review Letters*, vol. 88, no. 16, p. 160 401, 2002.

[123] C. Ravensbergen, V. Corre, E. Soave, *et al.*, "Accurate determination of the dynamical polarizability of dysprosium," *Physical Review Letters*, vol. 120, no. 22, p. 223 001, 2018.

[124] I. Affleck, *Quantum impurity problems in condensed matter physics*, 2009. arXiv: `0809.3474 [cond-mat.str-el]`.

[125] J. Zirbel, K.-K. Ni, S. Ospelkaus, *et al.*, "Heteronuclear molecules in an optical dipole trap," *Physical Review A*, vol. 78, no. 1, p. 013 416, 2008.

[126] A. Schirotzek, C.-H. Wu, A. Sommer, and M. W. Zwierlein, "Observation of Fermi polarons in a tunable Fermi liquid of ultracold atoms," *Physical Review Letters*, vol. 102, no. 23, p. 230 402, 2009.

[127] F. Chevy and C. Mora, "Ultra-cold polarized Fermi gases," *Reports on Progress in Physics*, vol. 73, no. 11, p. 112 401, 2010.

[128] J. Bauer, C. Salomon, and E. Demler, "Realizing a Kondo-correlated state with ultracold atoms," *Physical Review Letters*, vol. 111, no. 21, p. 215 304, 2013.

[129] M.-G. Hu, M. J. Van de Graaff, D. Kedar, J. P. Corson, E. A. Cornell, and D. S. Jin, "Bose polarons in the strongly interacting regime," *Physical Review Letters*, vol. 117, no. 5, p. 055 301, 2016.

[130] N. B. Jørgensen, L. Wacker, K. T. Skalmstang, *et al.*, "Observation of attractive and repulsive polarons in a Bose-Einstein condensate," *Physical Review Letters*, vol. 117, no. 5, p. 055 302, 2016.

[131] N. Mannella, W. L. Yang, X. J. Zhou, *et al.*, "Nodal quasiparticle in pseudogapped colossal magnetoresistive manganites," *Nature*, vol. 438, no. 7067, pp. 474–478, 2005.

[132] A. Lanzara, P. Bogdanov, X. Zhou, *et al.*, "Evidence for ubiquitous strong electron–phonon coupling in high-temperature superconductors," *Nature*, vol. 412, no. 6846, pp. 510–514, 2001.

[133] J. T. Devreese and A. S. Alexandrov, "Fröhlich polaron and bipolaron: Recent developments," *Reports on Progress in Physics*, vol. 72, no. 6, p. 066 501, 2009.

[134] G. E. Marti and D. Stamper-Kurn, "Spinor Bose-Einstein gases," 2015.

[135] T. Sowiński and M. Á. Garcıa-March, "One-dimensional mixtures of several ultracold atoms: A review," *Reports on Progress in Physics*, vol. 82, no. 10, p. 104 401, 2019.

[136] F. Schreck, L. Khaykovich, K. Corwin, *et al.*, "Quasipure Bose-Einstein condensate immersed in a Fermi sea," *Physical Review Letters*, vol. 87, no. 8, p. 080 403, 2001.

[137] A. Trautmann, P. Ilzhöfer, G. Durastante, *et al.*, "Dipolar quantum mixtures of erbium and dysprosium atoms," *Physical Review Letters*, vol. 121, no. 21, p. 213 601, 2018.

[138] C. Ravensbergen, V. Corre, E. Soave, M. Kreyer, E. Kirilov, and R. Grimm, "Production of a degenerate Fermi-Fermi mixture of dysprosium and potassium atoms," *Physical Review A*, vol. 98, no. 6, p. 063 624, 2018.

[139] F. Böttcher, J.-N. Schmidt, J. Hertkorn, *et al.*, "New states of matter with fine-tuned interactions: Quantum droplets and dipolar supersolids," *Reports on Progress in Physics*, vol. 84, no. 1, p. 012 403, 2020.

[140] J. Ulitzsch, D. Babik, R. Roell, and M. Weitz, "Bose-Einstein condensation of erbium atoms in a quasielectrostatic optical dipole trap," *Physical Review A*, vol. 95, no. 4, p. 043 614, 2017.

[141] M. Lecomte, A. Journeaux, L. Renaud, J. Dalibard, and R. Lopes, "Loss features in ultracold ^{162}Dy gases: Two- versus three-body processes," *Physical Review A*, vol. 109, no. 2, p. 023 319, 2024.

[142] B. Seo, Z. Chen, M. Huang, *et al.*, "Apparatus for producing a ^{168}Er Bose–Einstein condensate," *Journal of the Korean Physical Society*, vol. 82, no. 9, pp. 901–906, 2023.

[143] Y. Tang, A. G. Sykes, N. Q. Burdick, J. M. DiSciacca, D. S. Petrov, and B. L. Lev, "Anisotropic expansion of a thermal dipolar Bose gas," *Physical Review Letters*, vol. 117, no. 15, p. 155 301, 2016.

[144] J. Hertkorn, J.-N. Schmidt, M. Guo, *et al.*, "Supersolidity in two-dimensional trapped dipolar droplet arrays," *Physical Review Letters*, vol. 127, no. 15, p. 155 301, 2021.

[145] G. A. Phelps, A. Hébert, A. Krahn, *et al.*, *Sub-second production of a quantum degenerate gas*, 2020. arXiv: `2007.10807 [cond-mat.quant-gas]`.

[146] A. Frisch, K. Aikawa, M. Mark, *et al.*, "Narrow-line magneto-optical trap for erbium," *Physical Review A*, vol. 85, no. 5, p. 051 401, 2012.

[147] L. P. Ardila and T. Pohl, "Ground-state properties of dipolar Bose polarons," *Journal of Physics B: Atomic, Molecular and Optical Physics*, vol. 52, no. 1, p. 015 004, 2018.

[148] B. Kain and H. Y. Ling, "Polarons in a dipolar condensate," *Physical Review A*, vol. 89, no. 2, p. 023 612, 2014.

[149] R. Roy, A. Green, R. Bowler, and S. Gupta, "Rapid cooling to quantum degeneracy in dynamically shaped atom traps," *Physical Review A*, vol. 93, no. 4, p. 043 403, 2016.

[150] Z. Z. Yan, Y. Ni, C. Robens, and M. W. Zwierlein, "Bose polarons near quantum criticality," *Science*, vol. 368, no. 6487, pp. 190–194, 2020.

[151] B. Mukherjee, Z. Yan, P. B. Patel, *et al.*, "Homogeneous atomic Fermi gases," *Physical Review Letters*, vol. 118, no. 12, p. 123 401, 2017.

[152] Y.-C. Zhang, T. Pohl, and F. Maucher, "Phases of supersolids in confined dipolar Bose-Einstein condensates," *Physical Review A*, vol. 104, no. 1, p. 013 310, 2021.

[153] A. Patscheider, L. Chomaz, G. Natale, *et al.*, "Determination of the scattering length of erbium atoms," *Physical Review A*, vol. 105, no. 6, p. 063 307, 2022.

[154] C. d'Errico, M. Zaccanti, M. Fattori, *et al.*, "Feshbach resonances in ultracold ^{39}K," *New Journal of physics*, vol. 9, no. 7, p. 223, 2007.

[155] A. Frisch, M. Mark, K. Aikawa, *et al.*, "Quantum chaos in ultracold collisions of gas-phase erbium atoms," *Nature*, vol. 507, no. 7493, pp. 475–479, 2014.

[156] Z.-X. Ye, A. Canali, E. Soave, *et al.*, "Observation of low-field Feshbach resonances between ^{161}Dy and ^{40}K," *Physical Review A*, vol. 106, no. 4, p. 043 314, 2022.

[157] Y. Tang, W. Kao, K.-Y. Li, and B. L. Lev, "Tuning the dipole-dipole interaction in a quantum gas with a rotating magnetic field," *Physical Review Letters*, vol. 120, no. 23, p. 230 401, 2018.

[158] S. Giovanazzi, A. Görlitz, and T. Pfau, "Tuning the dipolar interaction in quantum gases," *Physical Review Letters*, vol. 89, no. 13, p. 130 401, 2002.

[159] J. Catani, P. Maioli, L. De Sarlo, F. Minardi, and M. Inguscio, "Intense slow beams of bosonic potassium isotopes," *Physical Review A*, vol. 73, no. 3, p. 033 415, 2006.

[160] T. Tiecke, "Properties of potassium," *University of Amsterdam*, 2019.

[161] C. G. Mosander, "On the new metals, lanthanium and didymium, which are associated with cerium; and on erbium and terbium, new metals associated with yttria," *The London, Edinburgh, and Dublin Philosophical Magazine and Journal of Science*, vol. 23, no. 152, pp. 241–254, 1843.

[162] S. J. Blundell and K. M. Blundell, *Concepts in thermal physics*. Oxford University Press, 2009.

[163] J. Böhlke, J. De Laeter, P. De Bievre, *et al.*, "Isotopic compositions of the elements, 2001," *Journal of Physical and Chemical Reference Data*, vol. 34, no. 1, pp. 57–67, 2005.

[164] M. Jackson, "Magnetism of rare earth," *IRM Quarterly*, vol. 3, pp. 1–8, 2000.

[165] C. Hammond, "The elements," *Handbook of chemistry and physics*, vol. 81, 2000.

[166] I. Levine, *Quantum Chemistry* (Pearson advanced chemistry series). Pearson, 2014.

[167] D. P. Wong, "Theoretical justification of Madelung's rule," *Journal of Chemical Education*, vol. 56, no. 11, p. 714, 1979.

[168] B. G. Wybourne and L. Smentek, *Optical spectroscopy of lanthanides: magnetic and hyperfine interactions*. CRC press, 2007.

[169] M. A. Norcia and F. Ferlaino, "Developments in atomic control using ultracold magnetic lanthanides," *Nature Physics*, vol. 17, no. 12, pp. 1349–1357, 2021.

[170] Y. Ralchenko, A. Kramida, J. Reader, *et al.*, *NIST atomic spectra database*, 1997.

[171] W. C. Martin, R. Zalubas, and L. Hagan, *Atomic energy levels - the rare-earth elements*, 1978. DOI: https://doi.org/10.6028/NBS.NSRDS.60.

[172] W. D. Phillips and H. Metcalf, "Laser deceleration of an atomic beam," *Physical Review Letters*, vol. 48, pp. 596–599, 9 1982.

[173] E. L. Raab, M. Prentiss, A. Cable, S. Chu, and D. E. Pritchard, "Trapping of neutral sodium atoms with radiation pressure," *Physical Review Letters*, vol. 59, pp. 2631–2634, 23 1987.

[174] A. Frisch, "Dipolar quantum gases of erbium," Ph.D. dissertation, University of Innsbruck, 2014.

[175] H. Ban, M. Jacka, J. L. Hanssen, J. Reader, and J. J. McClelland, "Laser cooling transitions in atomic erbium," *Optics Express*, vol. 13, no. 8, pp. 3185–3195, 2005.

[176] J. J. McClelland and J. L. Hanssen, "Laser cooling without repumping: A magneto-optical trap for erbium atoms," *Physical Review Letters*, vol. 96, no. 14, p. 143 005, 2006.

[177] E. Den Hartog, J. Chisholm, and J. Lawler, "Radiative lifetimes of neutral erbium," *Journal of Physics B: Atomic, Molecular and Optical Physics*, vol. 43, no. 15, p. 155 004, 2010.

[178] W. H. King, *Isotope shifts in atomic spectra*. Springer Science & Business Media, 2013.

[179] W. Guo Jin, T. Horiguchi, M. Wakasugi, and Y. Yoshizawa, "Hyperfine structure and isotope shift in Er I by the atomic-beam laser spectroscopy," *Journal of the Physical Society of Japan*, vol. 59, no. 9, pp. 3148–3154, 1990.

[180] C. B. Connolly, Y. S. Au, S. C. Doret, W. Ketterle, and J. M. Doyle, "Large spin relaxation rates in trapped submerged-shell atoms," *Physical Review A*, vol. 81, no. 1, p. 010 702, 2010.

[181] S. Methfessel, "Potential applications of magnetic rare earth compunds," *IEEE Transactions on Magnetics*, vol. 1, no. 3, pp. 144–155, 1965.

[182] *Standard specifications for permanent magnet materials*. Magnetic Materials Producers Association, 2019, p. 18.

[183] A. R. Mackintosh, *Rare earth magnetism: structures and excitations*. Clarendon Press, 1991.

[184] B. R. Judd and I. Lindgren, "Theory of Zeeman effect in the ground multiplets of rare-earth atoms," *Phys. Rev.*, vol. 122, pp. 1802–1812, 6 1961.

[185] J. G. Conway and B. G. Wybourne, "Low-lying energy levels of lanthanide atoms and intermediate coupling," *Phys. Rev.*, vol. 130, pp. 2325–2332, 6 1963.

[186] B. Odom, D. Hanneke, B. d'Urso, and G. Gabrielse, "New measurement of the electron magnetic moment using a one-electron quantum cyclotron," *Physical Review Letters*, vol. 97, no. 3, p. 030 801, 2006.

[187] J. J. Tollett, C. C. Bradley, C. A. Sackett, and R. G. Hulet, "Permanent magnet trap for cold atoms," *Phys. Rev. A*, vol. 51, R22–R25, 1 1995.

[188] S. Earnshaw, "On the nature of the molecular forces which regulate the constitution of the luminiferous ether," *Transactions of the Cambridge Philosophical Society*, vol. 7, p. 97, 1848.

[189] J. O. Hirschfelder, C. F. Curtiss, and R. B. Bird, *The molecular theory of gases and liquids*. John Wiley & Sons, 1964.

[190] J. E. Lennard-Jones, "Cohesion," *Proceedings of the Physical Society*, vol. 43, no. 5, p. 461, 1931.

[191] B. J. Alder and T. E. Wainwright, "Studies in molecular dynamics. I. general method," *The Journal of Chemical Physics*, vol. 31, no. 2, pp. 459–466, 1959.

[192] S. Kotochigova, "Controlling interactions between highly magnetic atoms with Feshbach resonances," *Reports on Progress in Physics*, vol. 77, no. 9, p. 093 901, 2014.

[193] S. Kotochigova, H. Levine, and I. Tupitsyn, "Correlated relativistic calculation of the giant resonance in the Gd^{3+} absorption spectrum," *International journal of quantum chemistry*, vol. 65, no. 5, pp. 575–584, 1997.

[194] T. Maier, "Interactions in a quantum gas of dysprosium atoms," Ph.D. dissertation, University of Stuttgart, 2015.

[195] T. Lahaye, C. Menotti, L. Santos, M. Lewenstein, and T. Pfau, "The physics of dipolar bosonic quantum gases," *Reports on Progress in Physics*, vol. 72, no. 12, p. 126 401, 2009.

[196] T. Koch, T. Lahaye, J. Metz, B. Fröhlich, A. Griesmaier, and T. Pfau, "Stabilization of a purely dipolar quantum gas against collapse," *Nature physics*, vol. 4, no. 3, pp. 218–222, 2008.

[197] M. Schmitt, M. Wenzel, F. Böttcher, I. Ferrier-Barbut, and T. Pfau, "Self-bound droplets of a dilute magnetic quantum liquid," *Nature*, vol. 539, no. 7628, pp. 259–262, 2016.

[198] G. Astrakharchik and Y. E. Lozovik, "Super-Tonks-Girardeau regime in trapped one-dimensional dipolar gases," *Physical Review A*, vol. 77, no. 1, p. 013 404, 2008.

[199] G. Lamb, "Toward an ultracold mixture of Er and K," Ph.D. dissertation, University of Oxford, 2022.

[200] F. Scazza, M. Zaccanti, P. Massignan, M. M. Parish, and J. Levinsen, "Repulsive Fermi and Bose polarons in quantum gases," *Atoms*, vol. 10, no. 2, p. 55, 2022.

[201] R. Balakrishnan and I. I. Satija, "Solitons in Bose–Einstein condensates," *Pramana - Journal of Physics*, vol. 77, pp. 929–947, 2011.

[202] N. Parker, B. Jackson, A. Martin, and C. Adams, "Vortices in Bose-Einstein condensates: Theory," in *Emergent Nonlinear Phenomena in Bose-Einstein Condensates*, Springer, 2008.

[203] L. D. Landau and E. M. Lifshitz, *Quantum mechanics: non-relativistic theory*. Elsevier, 2013, vol. 3.

[204] C. J. Pethick and H. Smith, *Bose–Einstein condensation in dilute gases*. Cambridge University Press, 2008.

[205] M. Marinescu and L. You, "Controlling atom-atom interaction at ultralow temperatures by dc electric fields," *Phys. Rev. Lett.*, vol. 81, pp. 4596–4599, 21 1998.

[206] B. Deb and L. You, "Low-energy atomic collision with dipole interactions," *Physical Review A*, vol. 64, no. 2, p. 022 717, 2001.

[207] K. Aikawa, A. Frisch, M. Mark, S. Baier, R. Grimm, and F. Ferlaino, "Reaching Fermi degeneracy via universal dipolar scattering," *Physical Review Letters*, vol. 112, no. 1, p. 010 404, 2014.

[208] B. Gao, "Repulsive $1/r^3$ interaction," *Physical Review A*, vol. 59, no. 4, pp. 2778–2786, 1999.

[209] J. Bohn, M. Cavagnero, and C. Ticknor, "Quasi-universal dipolar scattering in cold and ultracold gases," *New Journal of Physics*, vol. 11, no. 5, p. 055 039, 2009.

[210] J. L. Bohn and D. S. Jin, "Differential scattering and rethermalization in ultracold dipolar gases," *Physical Review A*, vol. 89, no. 2, p. 022 702, 2014.

[211] C. Ticknor, "Collisional control of ground state polar molecules and universal dipolar scattering," *Physical Review Letters*, vol. 100, no. 13, p. 133 202, 2008.

[212] M. A. Baranov, "Theoretical progress in many-body physics with ultracold dipolar gases," *Physics Reports*, vol. 464, no. 3, pp. 71–111, 2008.

[213] S. Yi and L. You, "Trapped atomic condensates with anisotropic interactions," *Physical Review A*, vol. 61, no. 4, p. 041 604, 2000.

[214] S. Yi and L. You, "Trapped condensates of atoms with dipole interactions," *Physical Review A*, vol. 63, no. 5, p. 053 607, 2001.

[215] S. Ronen, D. C. Bortolotti, D. Blume, and J. L. Bohn, "Dipolar Bose-Einstein condensates with dipole-dependent scattering length," *Physical Review A*, vol. 74, no. 3, p. 033 611, 2006.

[216] D. Bortolotti, S. Ronen, J. Bohn, and D. Blume, "Scattering length instability in dipolar Bose-Einstein condensates," *Physical Review Letters*, vol. 97, no. 16, p. 160 402, 2006.

[217] J. G. Danzl, E. Haller, M. Gustavsson, *et al.*, "Quantum gas of deeply bound ground state molecules," *Science*, vol. 321, no. 5892, pp. 1062–1066, 2008.

[218] T. Takekoshi, L. Reichsöllner, A. Schindewolf, *et al.*, "Ultracold dense samples of dipolar RbCs molecules in the rovibrational and hyperfine ground state," *Physical Review Letters*, vol. 113, no. 20, p. 205 301, 2014.

[219] C. Chin, R. Grimm, P. Julienne, and E. Tiesinga, "Feshbach resonances in ultracold gases," *Rev. Mod. Phys.*, vol. 82, pp. 1225–1286, 2 2010.

[220] U. Fano, "Effects of configuration interaction on intensities and phase shifts," *Phys. Rev.*, vol. 124, pp. 1866–1878, 6 1961.

[221] H. Feshbach, "Unified theory of nuclear reactions," *Annals of Physics*, vol. 5, no. 4, pp. 357–390, 1958.

[222] D. Spence and T. Noguchi, "Feshbach resonances associated with Rydberg states of the hydrogen halides," *The Journal of Chemical Physics*, vol. 63, no. 1, pp. 505–514, 1975.

[223] H. Bryant, B. Dieterle, J. Donahue, *et al.*, "Observation of resonances near 11 eV in the photodetachment cross section of the H^- ion," *Physical Review Letters*, vol. 38, no. 5, pp. 228–230, 1977.

[224] A. Moerdijk, B. Verhaar, and A. Axelsson, "Resonances in ultracold collisions of ^{6}Li, ^{7}Li, and ^{23}Na," *Physical Review A*, vol. 51, no. 6, pp. 4852–4861, 1995.

[225] P. Fedichev, Y. Kagan, G. Shlyapnikov, and J. Walraven, "Influence of nearly resonant light on the scattering length in low-temperature atomic gases," *Physical Review Letters*, vol. 77, no. 14, pp. 2913–2916, 1996.

[226] R. Ciuryło, E. Tiesinga, and P. Julienne, "Optical tuning of the scattering length of cold alkaline-earth-metal atoms," *Physical Review A*, vol. 71, no. 3, p. 030 701, 2005.

[227] A. Bambini and S. Geltman, "Feshbach resonances in cold collisions of potassium atoms," *Physical Review A*, vol. 65, no. 6, p. 062 704, 2002.

[228] V. Flambaum, G. Gribakin, and C. Harabati, "Analytical calculation of cold-atom scattering," *Physical Review A*, vol. 59, no. 3, p. 1998, 1999.

[229] R. Santra and C. H. Greene, "Tensorial analysis of the long-range interaction between metastable alkaline-earth-metal atoms," *Physical Review A*, vol. 67, no. 6, p. 062 713, 2003.

[230] A. Petrov, E. Tiesinga, and S. Kotochigova, "Anisotropy-induced Feshbach resonances in a quantum dipolar gas of highly magnetic atoms," *Physical Review Letters*, vol. 109, no. 10, p. 103 002, 2012.

[231] C. Kollath, A. Iucci, T. Giamarchi, W. Hofstetter, and U. Schollwöck, "Spectroscopy of ultracold atoms by periodic lattice modulations," *Physical Review Letters*, vol. 97, no. 5, p. 050 402, 2006.

[232] T. Maier, I. Ferrier-Barbut, H. Kadau, *et al.*, "Broad universal Feshbach resonances in the chaotic spectrum of dysprosium atoms," *Physical Review A*, vol. 92, no. 6, p. 060 702, 2015.

[233] F. Dalfovo, S. Giorgini, L. P. Pitaevskii, and S. Stringari, "Theory of Bose-Einstein condensation in trapped gases," *Reviews of Modern Physics*, vol. 71, no. 3, pp. 463–512, 1999.

[234] S. Giorgini, L. P. Pitaevskii, and S. Stringari, "Theory of ultracold atomic Fermi gases," *Reviews of Modern Physics*, vol. 80, no. 4, pp. 1215–1274, 2008.

[235] Y. Castin, *Basic theory tools for degenerate fermi gases*, 2007. arXiv: `cond-mat/0612613 [cond-mat.other]`.

[236] Y. Castin, "Bose-Einstein condensates in atomic gases: Simple theoretical results," in *Coherent atomic matter waves*, Springer, 2001, pp. 1–136.

[237] E. H. Lieb, R. Seiringer, and J. Yngvason, "Bosons in a trap: A rigorous derivation of the Gross-Pitaevskii energy functional," *Phys. Rev. A*, vol. 61, p. 043 602, 4 2000.

[238] L. Erdős, B. Schlein, and H.-T. Yau, "Derivation of the Gross-Pitaevskii hierarchy for the dynamics of bose-einstein condensate," *Communications on Pure and Applied Mathematics*, vol. 59, no. 12, pp. 1659–1741, 2006.

[239] K. Góral, K. Rzażewski, and T. Pfau, "Bose-Einstein condensation with magnetic dipole-dipole forces," *Physical Review A*, vol. 61, no. 5, p. 051 601, 2000.

[240] S. Vilchynskyy, A. Yakimenko, K. Isaieva, and A. Chumachenko, "The nature of superfluidity and Bose-Einstein condensation: From liquid ^{4}He to dilute ultracold atomic gases," *Low Temperature Physics*, vol. 39, no. 9, pp. 724–740, 2013.

[241] E. P. Gross, "Structure of a quantized vortex in boson systems," *Il Nuovo Cimento (1955-1965)*, vol. 20, no. 3, pp. 454–477, 1961.

[242] L. P. Pitaevskii, "Vortex lines in an imperfect Bose gas," *Soviet Physics - Journal of Experimental and Theoretical Physics*, vol. 13, no. 2, pp. 451–454, 1961.

[243] T. Busch and J. Anglin, "Motion of dark solitons in trapped Bose-Einstein condensates," *Physical Review Letters*, vol. 84, no. 11, pp. 2298–2301, 2000.

[244] Y. Xu, Y. Zhang, B. Wu, *et al.*, "Bright solitons in spin-orbit-coupled Bose-Einstein condensates," *Physical Review A*, vol. 87, no. 1, p. 013 614, 2013.

[245] C. Becker, S. Stellmer, P. Soltan-Panahi, *et al.*, "Oscillations and interactions of dark and dark–bright solitons in Bose–Einstein condensates," *Nature Physics*, vol. 4, no. 6, pp. 496–501, 2008.

[246] G. W. Rayfield and F. Reif, "Quantized vortex rings in superfluid helium," *Physical Review*, vol. 136, no. 5A, A1194–A1208, 1964.

[247] B. Anderson, P. Haljan, C. Regal, *et al.*, "Watching dark solitons decay into vortex rings in a Bose-Einstein condensate," *Physical Review Letters*, vol. 86, no. 14, pp. 2926–2929, 2001.

[248] A. L. Fetter, "Nonuniform states of an imperfect Bose gas," *Annals of physics*, vol. 70, no. 1, pp. 67–101, 1972.

[249] R. Lopes, C. Eigen, N. Navon, D. Clément, R. P. Smith, and Z. Hadzibabic, "Quantum depletion of a homogeneous Bose-Einstein condensate," *Physical Review Letters*, vol. 119, no. 19, p. 190 404, 2017.

[250] N. Bogoliubov, "On the theory of superfluidity," *Journal of Physics*, vol. 11, no. 1, pp. 23–32, 1947.

[251] L. Santos, G. Shlyapnikov, and M. Lewenstein, "Roton-maxon spectrum and stability of trapped dipolar Bose-Einstein condensates," *Physical Review Letters*, vol. 90, no. 25, p. 250 403, 2003.

[252] S. Ronen, D. C. Bortolotti, and J. L. Bohn, "Radial and angular rotons in trapped dipolar gases," *Physical Review Letters*, vol. 98, no. 3, p. 030 406, 2007.

[253] U. R. Fischer, "Stability of quasi-two-dimensional Bose-Einstein condensates with dominant dipole-dipole interactions," *Physical Review A*, vol. 73, no. 3, p. 031 602, 2006.

[254] J.-N. Schmidt, J. Hertkorn, M. Guo, *et al.*, "Roton excitations in an oblate dipolar quantum gas," *Physical Review Letters*, vol. 126, no. 19, p. 193 002, 2021.

[255] P. Blakie, D. Baillie, and R. Bisset, "Roton spectroscopy in a harmonically trapped dipolar Bose-Einstein condensate," *Physical Review A*, vol. 86, no. 2, p. 021 604, 2012.

[256] L. Landau, "The theory of superfluidity of helium II," in *An Introduction to the Theory of Superfluidity*, CRC Press, 2018, pp. 185–204.

[257] Z.-Q. Yu, "Landau criterion for an anisotropic Bose-Einstein condensate," *Physical Review A*, vol. 95, no. 3, p. 033 618, 2017.

[258] A. J. Leggett, *Quantum liquids: Bose condensation and Cooper pairing in condensed-matter systems*. Oxford University Press, 2006.

[259] J. L. Roberts, N. R. Claussen, S. L. Cornish, E. A. Donley, E. A. Cornell, and C. E. Wieman, "Controlled collapse of a Bose-Einstein condensate," *Physical Review Letters*, vol. 86, no. 19, pp. 4211–4214, 2001.

[260] T. D. Lee, K. Huang, and C. N. Yang, "Eigenvalues and eigenfunctions of a Bose system of hard spheres and its low-temperature properties," *Physical Review*, vol. 106, no. 6, pp. 1135–1145, 1957.

[261] A. R. Lima and A. Pelster, "Quantum fluctuations in dipolar Bose gases," *Physical Review A*, vol. 84, no. 4, p. 041 604, 2011.

[262] A. R. Lima and A. Pelster, "Beyond mean-field low-lying excitations of dipolar Bose gases," *Physical Review A*, vol. 86, no. 6, p. 063 609, 2012.

[263] L. Tanzi, J. Maloberti, G. Biagioni, A. Fioretti, C. Gabbanini, and G. Modugno, "Evidence of superfluidity in a dipolar supersolid from nonclassical rotational inertia," *Science*, vol. 371, no. 6534, pp. 1162–1165, 2021.

[264] Y. Pomeau and S. Rica, "Dynamics of a model of supersolid," *Physical Review Letters*, vol. 72, no. 15, pp. 2426–2429, 1994.

[265] A. J. Leggett, "Can a solid be "superfluid"?" *Physical Review Letters*, vol. 25, no. 22, pp. 1543–1546, 1970.

[266] J. Choi, A. A. Zadorozhko, J. Choi, and E. Kim, "Spatially modulated superfluid state in two-dimensional ^{4}He films," *Physical Review Letters*, vol. 127, no. 13, p. 135 301, 2021.

[267] J. S. Hofmann, E. Berg, and D. Chowdhury, "Superconductivity, charge density wave, and supersolidity in flat bands with a tunable quantum metric," *Physical Review Letters*, vol. 130, no. 22, p. 226 001, 2023.

[268] J.-R. Li, J. Lee, W. Huang, *et al.*, "A stripe phase with supersolid properties in spin–orbit-coupled Bose–Einstein condensates," *Nature*, vol. 543, no. 7643, pp. 91–94, 2017.

[269] J. Léonard, A. Morales, P. Zupancic, T. Esslinger, and T. Donner, "Supersolid formation in a quantum gas breaking a continuous translational symmetry," *Nature*, vol. 543, no. 7643, pp. 87–90, 2017.

[270] F. Böttcher, M. Wenzel, J.-N. Schmidt, *et al.*, "Dilute dipolar quantum droplets beyond the extended Gross-Pitaevskii equation," *Physical Review Research*, vol. 1, no. 3, p. 033 088, 2019.

[271] L. Chomaz, D. Petter, P. Ilzhöfer, *et al.*, "Long-lived and transient supersolid behaviors in dipolar quantum gases," *Physical Review X*, vol. 9, no. 2, p. 021 012, 2019.

[272] M. Sohmen, C. Politi, L. Klaus, *et al.*, "Birth, life, and death of a dipolar supersolid," *Physical Review Letters*, vol. 126, no. 23, p. 233 401, 2021.

[273] M. Krstajić, "Experimental platform for a box-trapped dipolar quantum gas," Ph.D. dissertation, University of Cambridge, 2022.

[274] R. Grimm, M. Weidemüller, and Y. B. Ovchinnikov, "Optical dipole traps for neutral atoms," in *Advances in atomic, molecular, and optical physics*, vol. 42, Elsevier, 2000, pp. 95–170.

[275] C. S. Adams, H. J. Lee, N. Davidson, M. Kasevich, and S. Chu, "Evaporative cooling in a crossed dipole trap," *Physical Review Letters*, vol. 74, no. 18, pp. 3577–3580, 1995.

[276] H. J. Metcalf and W. Phillips, "Electromagnetic trapping of neutral atoms," *Metrologia*, vol. 22, no. 4, p. 271, 1986.

[277] N. B. Vilas, "Laser cooling towards a dipolar quantum gas of erbium atoms," Master's Thesis, University of Cambridge, 2018.

[278] D. Castelvecchi, "The Stern–Gerlach experiment at 100," *Nature Reviews Physics*, vol. 4, no. 3, pp. 140–142, 2022.

[279] T. Kishimoto, J. Kobayashi, K. Noda, K. Aikawa, M. Ueda, and S. Inouye, "Direct evaporative cooling of ^{41}K into a Bose-Einstein condensate," *Physical Review A*, vol. 79, no. 3, p. 031 602, 2009.

[280] L. Hofer, "Harnessing machine learning for the analysis of erbium dipolar quantum gas experiments," Ph.D. dissertation, University of Oxford, 2023.

[281] A. Keshet and W. Ketterle, "A distributed, graphical user interface based, computer control system for atomic physics experiments," *Review of Scientific Instruments*, vol. 84, no. 1, 2013.

[282] N. Tammuz, "Thermodynamics of ultracold ^{39}K atomic Bose gases with tuneable interactions," Ph.D. dissertation, University of Cambridge, 2011.

[283] W. D. Phillips, "Nobel lecture: Laser cooling and trapping of neutral atoms," *Reviews of Modern Physics*, vol. 70, no. 3, pp. 721–741, 1998.

[284] Y. Dudin, L. Li, F. Bariani, and A. Kuzmich, "Observation of coherent many-body Rabi oscillations," *Nature Physics*, vol. 8, no. 11, pp. 790–794, 2012.

[285] P. D. Lett, W. D. Phillips, S. Rolston, C. E. Tanner, R. Watts, and C. Westbrook, "Optical molasses," *JOSA B*, vol. 6, no. 11, pp. 2084–2107, 1989.

[286] G. Camy, C. J. Bordé, and M. Ducloy, "Heterodyne saturation spectroscopy through frequency modulation of the saturating beam," *Optics Communications*, vol. 41, no. 5, pp. 325–330, 1982.

[287] J. H. Shirley, "Modulation transfer processes in optical heterodyne saturation spectroscopy," *Optics Letters*, vol. 7, no. 11, pp. 537–539, 1982.

[288] Y.-R. Shen, *Principles of nonlinear optics*. Wiley, 2002.

[289] D. Dreon, L. A. Sidorenkov, C. Bouazza, W. Maineult, J. Dalibard, and S. Nascimbene, "Optical cooling and trapping of highly magnetic atoms: The benefits of a spontaneous spin polarization," *Journal of Physics B: Atomic, Molecular and Optical Physics*, vol. 50, no. 6, p. 065 005, 2017.

[290] T. Chaneliere, L. He, R. Kaiser, and D. Wilkowski, "Three dimensional cooling and trapping with a narrow line," *The European Physical Journal D*, vol. 46, pp. 507–515, 2008.

[291] P. Ilzhöfer, G. Durastante, A. Patscheider, A. Trautmann, M. Mark, and F. Ferlaino, "Two-species five-beam magneto-optical trap for erbium and dysprosium," *Physical Review A*, vol. 97, no. 2, p. 023 633, 2018.

[292] P. Sompet, A. Carpentier, Y. Fung, M. McGovern, and M. Andersen, "Dynamics of two atoms undergoing light-assisted collisions in an optical microtrap," *Physical Review A*, vol. 88, no. 5, p. 051 401, 2013.

[293] A. R. Gorges, N. S. Bingham, M. K. DeAngelo, M. S. Hamilton, and J. L. Roberts, "Light-assisted collisional loss in a $^{85/87}$Rb ultracold optical trap," *Physical Review A*, vol. 78, no. 3, p. 033 420, 2008.

[294] R. W. Drever, J. L. Hall, F. V. Kowalski, *et al.*, "Laser phase and frequency stabilization using an optical resonator," *Applied Physics B*, vol. 31, pp. 97–105, 1983.

[295] E. D. Black, "An introduction to Pound–Drever–Hall laser frequency stabilization," *American Journal of Physics*, vol. 69, no. 1, pp. 79–87, 2001.

[296] P. Langhoff, S. Epstein, and M. Karplus, "Aspects of time-dependent perturbation theory," *Reviews of Modern Physics*, vol. 44, no. 3, p. 602, 1972.

[297] M. Lepers, J.-F. Wyart, and O. Dulieu, "Anisotropic optical trapping of ultracold erbium atoms," *Physical Review A*, vol. 89, no. 2, p. 022 505, 2014.

[298] N. L. Manakov, V. D. Ovsiannikov, and L. P. Rapoport, "Atoms in a laser field," *Physics Reports*, vol. 141, no. 6, pp. 320–433, 1986.

[299] J. H. Becher, S. Baier, K. Aikawa, *et al.*, "Anisotropic polarizability of erbium atoms," *Physical Review A*, vol. 97, no. 1, p. 012 509, 2018.

[300] E. Hecht, *Optics*. Pearson Education, 2017.

[301] Z.-Y. Ma, C. J. Foot, and S. L. Cornish, "Optimized evaporative cooling using a dimple potential: An efficient route to Bose–Einstein condensation," *Journal of Physics B: Atomic, Molecular and Optical Physics*, vol. 37, no. 15, p. 3187, 2004.

[302] A. Korpel, "Acousto-optics," in ser. Applied Solid State Science, vol. 3, Elsevier, 1972, pp. 71–180.

[303] C. Kohstall, *A new toolbox for experiments with ultracold* ^{6}*Li*, 2007.

[304] T. Savard, K. O'hara, and J. Thomas, "Laser-noise-induced heating in far-off resonance optical traps," *Physical Review A*, vol. 56, no. 2, R1095–R1098, 1997.

[305] M. Gehm, K. O'hara, T. Savard, and J. Thomas, "Dynamics of noise-induced heating in atom traps," *Physical Review A*, vol. 58, no. 5, pp. 3914–3921, 1998.

[306] S. Giovanazzi, L. Santos, and T. Pfau, "Collective oscillations of dipolar Bose-Einstein condensates and accurate comparison between contact and dipolar interactions," *Physical Review A*, vol. 75, no. 1, p. 015 604, 2007.

[307] P. Juhász, "Production and characterisation of dipolar Bose–Einstein condensates," Ph.D. dissertation, University of Oxford, 2023.

[308] W. Ketterle and N. Van Druten, "Evaporative cooling of trapped atoms," in *Advances in atomic, molecular, and optical physics*, vol. 37, Elsevier, 1996, pp. 181–236.

[309] H. F. Hess, "Evaporative cooling of magnetically trapped and compressed spin-polarized hydrogen," *Physical Review B*, vol. 34, no. 5, pp. 3476–3479, 1986.

[310] K. B. Davis, M.-O. Mewes, M. A. Joffe, M. R. Andrews, and W. Ketterle, "Evaporative cooling of sodium atoms," *Physical Review Letters*, vol. 74, no. 26, pp. 5202–5205, 1995.

[311] M. Barrett, J. Sauer, and M. Chapman, "All-optical formation of an atomic Bose-Einstein condensate," *Physical Review Letters*, vol. 87, no. 1, p. 010 404, 2001.

[312] T. Kinoshita, T. Wenger, and D. S. Weiss, "All-optical Bose-Einstein condensation using a compressible crossed dipole trap," *Physical Review A*, vol. 71, no. 1, p. 011 602, 2005.

[313] O. Luiten, M. Reynolds, and J. Walraven, "Kinetic theory of the evaporative cooling of a trapped gas," *Physical Review A*, vol. 53, no. 1, pp. 381–389, 1996.

[314] M. C. Garrett, A. Ratnapala, E. D. Van Ooijen, *et al.*, "Growth dynamics of a Bose-Einstein condensate in a dimple trap without cooling," *Physical Review A*, vol. 83, no. 1, p. 013 630, 2011.

[315] D. Stamper-Kurn, H.-J. Miesner, A. Chikkatur, S. Inouye, J. Stenger, and W. Ketterle, "Reversible formation of a Bose-Einstein condensate," *Physical Review Letters*, vol. 81, no. 11, pp. 2194–2197, 1998.

[316] S. Giovanazzi, A. Görlitz, and T. Pfau, "Ballistic expansion of a dipolar condensate," *Journal of Optics B: Quantum and Semiclassical Optics*, vol. 5, no. 2, S208, 2003.

[317] F. Dalfovo, C. Minniti, S. Stringari, and L. Pitaevskii, "Nonlinear dynamics of a Bose condensed gas," *Physics Letters A*, vol. 227, no. 3-4, pp. 259–264, 1997.

[318] M. Greiner, I. Bloch, T. W. Hänsch, and T. Esslinger, "Magnetic transport of trapped cold atoms over a large distance," *Physical Review A*, vol. 63, no. 3, p. 031 401, 2001.

[319] H. J. Lewandowski, D. Harber, D. L. Whitaker, and E. A. Cornell, "Simplified system for creating a Bose–Einstein condensate," *Journal of low temperature physics*, vol. 132, pp. 309–367, 2003.

[320] T. Middelmann, S. Falke, C. Lisdat, and U. Sterr, "Long-range transport of ultracold atoms in a far-detuned one-dimensional optical lattice," *New Journal of Physics*, vol. 14, no. 7, p. 073 020, 2012.

[321] T. Kraemer, J. Herbig, M. Mark, *et al.*, "Optimized production of a cesium Bose–Einstein condensate," *Applied Physics B*, vol. 79, pp. 1013–1019, 2004.

[322] T. Gustavson, A. Chikkatur, A. Leanhardt, *et al.*, "Transport of Bose-Einstein condensates with optical tweezers," *Physical Review Letters*, vol. 88, no. 2, p. 020 401, 2001.

[323] G. Unnikrishnan, C. Beulenkamp, D. Zhang, K. P. Zamarski, M. Landini, and H.-C. Nägerl, "Long distance optical transport of ultracold atoms: A compact setup using a Moiré lens," *Review of Scientific Instruments*, vol. 92, no. 6, p. 063 205, 2021.

[324] J. Léonard, M. Lee, A. Morales, T. M. Karg, T. Esslinger, and T. Donner, "Optical transport and manipulation of an ultracold atomic cloud using focus-tunable lenses," *New Journal of Physics*, vol. 16, no. 9, p. 093 028, 2014.

[325] A. Siegman, *Lasers*. University Science Books, 1986.

[326] U. Govind, "Cooling, transport and mixing of ultracold K and Cs," Ph.D. dissertation, University of Innsbruck, 2022.

[327] D. Bloch, *Optical transport of ultracold atoms*, 2020.

[328] K. F. Riley, M. P. Hobson, and S. J. Bence, *Mathematical Methods for Physics and Engineering: A Comprehensive Guide*, 3rd ed. Cambridge University Press, 2006.

[329] E. Torrontegui, S. Ibáñez, X. Chen, A. Ruschhaupt, D. Guéry-Odelin, and J. Muga, "Fast atomic transport without vibrational heating," *Physical Review A*, vol. 83, no. 1, p. 013 415, 2011.

[330] M. Murphy, L. Jiang, N. Khaneja, and T. Calarco, "High-fidelity fast quantum transport with imperfect controls," *Physical Review A*, vol. 79, no. 2, p. 020 301, 2009.

[331] G. A. Bird, *Molecular gas dynamics and the direct simulation of gas flows*. Oxford University Press, 1994.

[332] A. C. J. Wade, D. Baillie, and P. Blakie, "Direct simulation Monte Carlo method for cold-atom dynamics: Classical Boltzmann equation in the quantum collision regime," *Physical Review A*, vol. 84, no. 2, p. 023 612, 2011.

[333] M. Berninger, A. Zenesini, B. Huang, *et al.*, "Feshbach resonances, weakly bound molecular states, and coupled-channel potentials for cesium at high magnetic fields," *Physical Review A*, vol. 87, no. 3, p. 032 517, 2013.

[334] C. Eigen, J. A. Glidden, R. Lopes, E. A. Cornell, R. P. Smith, and Z. Hadzibabic, "Universal prethermal dynamics of Bose gases quenched to unitarity," *Nature*, vol. 563, no. 7730, pp. 221–224, 2018.

[335] T. Lahaye, J. Metz, B. Froehlich, *et al.*, "D-wave collapse and explosion of a dipolar Bose-Einstein condensate," *Physical Review Letters*, vol. 101, no. 8, p. 080 401, 2008.

[336] S. A. Moses, J. P. Covey, M. T. Miecnikowski, D. S. Jin, and J. Ye, "New frontiers for quantum gases of polar molecules," *Nature Physics*, vol. 13, no. 1, pp. 13–20, 2017.

[337] E. Poli, T. Bland, C. Politi, *et al.*, "Maintaining supersolidity in one and two dimensions," *Physical Review A*, vol. 104, no. 6, p. 063 307, 2021.

[338] K. Baumann, N. Q. Burdick, M. Lu, and B. L. Lev, "Observation of low-field Fano-Feshbach resonances in ultracold gases of dysprosium," *Physical Review A*, vol. 89, no. 2, p. 020 701, 2014.

[339] S. Knoop, T. Schuster, R. Scelle, *et al.*, "Feshbach spectroscopy and analysis of the interaction potentials of ultracold sodium," *Physical Review A*, vol. 83, no. 4, p. 042 704, 2011.

[340] C. Schunck, M. Zwierlein, C. Stan, *et al.*, "Feshbach resonances in fermionic ^{6}Li," *Physical Review A*, vol. 71, no. 4, p. 045 601, 2005.

[341] V. Yurovsky and A. Ben-Reuven, "Three-body loss of trapped ultracold ^{87}Rb atoms due to a Feshbach resonance," *Physical Review A*, vol. 67, no. 5, p. 050 701, 2003.

[342] T. Maier, H. Kadau, M. Schmitt, *et al.*, "Emergence of chaotic scattering in ultracold Er and Dy," *Physical Review X*, vol. 5, no. 4, p. 041 029, 2015.

[343] H. Suno, B. Esry, C. H. Greene, and J. P. Burke Jr, "Three-body recombination of cold helium atoms," *Physical Review A*, vol. 65, no. 4, p. 042 725, 2002.

[344] J. Wang, J. D'Incao, and C. H. Greene, "Numerical study of three-body recombination for systems with many bound states," *Physical Review A*, vol. 84, no. 5, p. 052 721, 2011.

[345] B. D. Esry, C. H. Greene, and H. Suno, "Threshold laws for three-body recombination," *Phys. Rev. A*, vol. 65, p. 010 705, 1 2001.

[346] A. Sykes and J. Bohn, "Nonequilibrium dynamics of an ultracold dipolar gas," *Physical Review A*, vol. 91, no. 1, p. 013 625, 2015.

[347] S. Tojo, A. Tomiyama, M. Iwata, T. Kuwamoto, and T. Hirano, "Collision dynamics between stretched states of spin-2 ^{87}Rb Bose–Einstein condensates," *Applied Physics B*, vol. 93, pp. 403–407, 2008.

[348] A. J. Olson, R. J. Niffenegger, and Y. P. Chen, "Optimizing the efficiency of evaporative cooling in optical dipole traps," *Physical Review A*, vol. 87, no. 5, p. 053 613, 2013.

[349] T. Shobu, H. Yamaoka, H. Imai, A. Morinaga, and M. Yamashita, "Optimized evaporative cooling for sodium Bose-Einstein condensation against three-body loss," *Physical Review A*, vol. 84, no. 3, p. 033 626, 2011.

[350] K. Glaum and A. Pelster, "Bose-Einstein condensation temperature of dipolar gas in anisotropic harmonic trap," *Physical Review A*, vol. 76, no. 2, p. 023 604, 2007.

[351] K. Glaum, A. Pelster, H. Kleinert, and T. Pfau, "Critical temperature of weakly interacting dipolar condensates," *Physical Review Letters*, vol. 98, no. 8, p. 080 407, 2007.

[352] P. Pinkse, A. Mosk, M. Weidemüller, M. Reynolds, T. Hijmans, and J. Walraven, "One-dimensional evaporative cooling of magnetically trapped atomic hydrogen," *Physical Review A*, vol. 57, no. 6, pp. 4747–4760, 1998.

[353] R. L. D. Campbell, "Thermodynamic properties of a Bose gas with tuneable interactions," Ph.D. dissertation, University of Cambridge, 2011.

[354] S. Giorgini, L. Pitaevskii, and S. Stringari, "Condensate fraction and critical temperature of a trapped interacting Bose gas," *Physical Review A*, vol. 54, no. 6, R4633–R4636, 1996.

[355] R. P. Smith, R. L. Campbell, N. Tammuz, and Z. Hadzibabic, "Effects of interactions on the critical temperature of a trapped Bose gas," *Physical Review Letters*, vol. 106, no. 25, p. 250 403, 2011.

[356] J. O. Andersen, "Theory of the weakly interacting Bose gas," *Reviews of Modern Physics*, vol. 76, no. 2, pp. 599–639, 2004.

[357] G. Baym, J.-P. Blaizot, M. Holzmann, F. Laloë, and D. Vautherin, "Bose-Einstein transition in a dilute interacting gas," *The European Physical Journal B-Condensed Matter and Complex Systems*, vol. 24, pp. 107–124, 2001.

[358] M. Holzmann, J.-N. Fuchs, G. A. Baym, J.-P. Blaizot, and F. Laloë, "Bose–Einstein transition temperature in a dilute repulsive gas," *Comptes Rendus Physique*, vol. 5, no. 1, pp. 21–37, 2004.

[359] M. Erhard, H. Schmaljohann, J. Kronjäger, K. Bongs, and K. Sengstock, "Bose-Einstein condensation at constant temperature," *Physical Review A*, vol. 70, no. 3, p. 031 602, 2004.

[360] C. Eberlein, S. Giovanazzi, and D. H. O'Dell, "Exact solution of the Thomas-Fermi equation for a trapped Bose-Einstein condensate with dipole-dipole interactions," *Physical Review A*, vol. 71, no. 3, p. 033 618, 2005.

[361] D. H. O'Dell, S. Giovanazzi, and C. Eberlein, "Exact hydrodynamics of a trapped dipolar Bose-Einstein condensate," *Physical Review Letters*, vol. 92, no. 25, p. 250 401, 2004.

[362] E. J. Routh, *A Treatise in Analytical Statics*. Cambridge University Press, 1892, vol. 2.

[363] S. Giovanazzi, P. Pedri, L. Santos, *et al.*, "Expansion dynamics of a dipolar Bose-Einstein condensate," *Physical Review A*, vol. 74, no. 1, p. 013 621, 2006.

[364] B. Song, C. He, Z. Ren, E. Zhao, J. Lee, and G.-B. Jo, "Effective statistical fringe removal algorithm for high-sensitivity imaging of ultracold atoms," *Physical Review Applied*, vol. 14, no. 3, p. 034 006, 2020.

[365] L. Verlet, "Computer "experiments" on classical fluids. I. Thermodynamical properties of Lennard-Jones molecules," *Physical review*, vol. 159, no. 1, pp. 98–103, 1967.

[366] Y. Kawaguchi and M. Ueda, "Spinor Bose–Einstein condensates," *Physics Reports*, vol. 520, no. 5, pp. 253–381, 2012.

[367] K. Dieckmann, R. Spreeuw, M. Weidemüller, and J. Walraven, "Two-dimensional magneto-optical trap as a source of slow atoms," *Physical Review A*, vol. 58, no. 5, pp. 3891–3895, 1998.

[368] L. Tanzi, C. Cabrera, J. Sanz, P. Cheiney, M. Tomza, and L. Tarruell, "Feshbach resonances in potassium Bose-Bose mixtures," *Physical Review A*, vol. 98, no. 6, p. 062 712, 2018.

[369] G. Modugno, G. Ferrari, G. Roati, R. J. Brecha, A. Simoni, and M. Inguscio, "Bose-Einstein condensation of potassium atoms by sympathetic cooling," *Science*, vol. 294, no. 5545, pp. 1320–1322, 2001.

[370] G. Roati, F. Riboli, G. Modugno, and M. Inguscio, "Fermi-Bose quantum degenerate ^{40}K- ^{87}Rb mixture with attractive interaction," *Physical Review Letters*, vol. 89, no. 15, p. 150 403, 2002.

[371] G. Roati, M. Zaccanti, C. d'Errico, *et al.*, "^{39}K Bose-Einstein condensate with tunable interactions," *Physical Review Letters*, vol. 99, no. 1, p. 010 403, 2007.

[372] G. Salomon, L. Fouché, S. Lepoutre, A. Aspect, and T. Bourdel, "All-optical cooling of ^{39}K to Bose-Einstein condensation," *Physical Review A*, vol. 90, no. 3, p. 033 405, 2014.

[373] G. Salomon, L. Fouché, P. Wang, A. Aspect, P. Bouyer, and T. Bourdel, "Gray-molasses cooling of ^{39}K to a high phase-space density," *Europhysics Letters*, vol. 104, no. 6, p. 63 002, 2014.

[374] H.-Z. Chen, X.-C. Yao, Y.-P. Wu, *et al.*, "Production of large ^{41}K Bose-Einstein condensates using D1 gray molasses," *Physical Review A*, vol. 94, no. 3, p. 033 408, 2016.

[375] D. Nath, R. K. Easwaran, G. Rajalakshmi, and C. Unnikrishnan, "Quantum-interference-enhanced deep sub-Doppler cooling of ^{39}K atoms in gray molasses," *Physical Review A*, vol. 88, no. 5, p. 053 407, 2013.

[376] M. Weidemüller, T. Esslinger, M. A. Ol'shanii, A. Hemmerich, and T. W. Hänsch, "A novel scheme for efficient cooling below the photon recoil limit," *Europhysics Letters*, vol. 27, no. 2, p. 109, 1994.

[377] D. Boiron, C. Triché, D. Meacher, P. Verkerk, and G. Grynberg, "Three-dimensional cooling of cesium atoms in four-beam gray optical molasses," *Physical Review A*, vol. 52, no. 5, R3425–R3428, 1995.

[378] J. Dalibard and C. Cohen-Tannoudji, "Laser cooling below the Doppler limit by polarization gradients: Simple theoretical models," *Journal of the Optical Society of America B*, vol. 6, no. 11, pp. 2023–2045, 1989.

[379] A. Aspect, E. Arimondo, R. e. a. Kaiser, N. Vansteenkiste, and C. Cohen-Tannoudji, "Laser cooling below the one-photon recoil energy by velocity-selective coherent population trapping," *Physical Review Letters*, vol. 61, no. 7, pp. 826–829, 1988.

[380] J. Appel, K.-P. Marzlin, and A. Lvovsky, "Raman adiabatic transfer of optical states in multilevel atoms," *Physical Review A*, vol. 73, no. 1, p. 013 804, 2006.

[381] M. Ol'Shanii and V. Minogin, "Three-dimensional velocity-selective coherent population trapping of a $(3+3)$-level atom," *Optics communications*, vol. 89, no. 5-6, pp. 393–398, 1992.

[382] D. R. Fernandes, F. Sievers, N. Kretzschmar, S. Wu, C. Salomon, and F. Chevy, "Sub-Doppler laser cooling of fermionic ^{40}K atoms in three-dimensional gray optical molasses," *Europhysics Letters*, vol. 100, no. 6, p. 63 001, 2012.

[383] M. Safronova, U. Safronova, and C. W. Clark, "Magic wavelengths for optical cooling and trapping of potassium," *Physical Review A*, vol. 87, no. 5, p. 052 504, 2013.

[384] A. H. Hansen, A. Khramov, W. H. Dowd, A. O. Jamison, V. V. Ivanov, and S. Gupta, "Quantum degenerate mixture of ytterbium and lithium atoms," *Physical Review A*, vol. 84, no. 1, p. 011 606, 2011.

[385] C. Cordova, "Quantum liquid droplets in a mixture of Bose-Einstein condensates," Ph.D. dissertation, Universitat Politecnica de Catalunya, 2018.

[386] M. Sbroscia, "Between order and disorder: Ultracold atoms in a quasicrystalline optical lattice," Ph.D. dissertation, University of Cambridge, 2019.

[387] D. W. Preston, "Doppler-free saturated absorption: Laser spectroscopy," *American Journal of Physics*, vol. 64, no. 11, pp. 1432–1436, 1996.

[388] K. G. H. Viebahn, "Quasicrystalline optical lattices for ultracold atoms," Ph.D. dissertation, University of Cambridge, 2019.

[389] P. Lutkiewicz, "The tightness conditions of UHV all-metal seals subjected to the radiation and inelastic deformation," Ph.D. dissertation, Krakow University of Technology, 2009.

[390] M. Bernardini, S. Braccini, R. De Salvo, *et al.*, "Air bake-out to reduce hydrogen outgassing from stainless steel," *Journal of Vacuum Science & Technology A: Vacuum, Surfaces, and Films*, vol. 16, no. 1, pp. 188–193, 1998.

[391] A. L. Gaunt, "Degenerate Bose gases: Tuning interactions and geometry," Ph.D. dissertation, University of Cambridge, 2014.

[392] P. Zupancic, P. M. Preiss, R. Ma, *et al.*, "Ultra-precise holographic beam shaping for microscopic quantum control," *Optics express*, vol. 24, no. 13, pp. 13 881–13 893, 2016.

[393] J. Stenger, S. Inouye, A. P. Chikkatur, D. Stamper-Kurn, D. Pritchard, and W. Ketterle, "Bragg spectroscopy of a Bose-Einstein condensate," *Physical Review Letters*, vol. 82, no. 23, p. 4569, 1999.

[394] L.-C. Ha, L. W. Clark, C. V. Parker, B. M. Anderson, and C. Chin, "Roton-maxon excitation spectrum of Bose condensates in a shaken optical lattice," *Physical Review Letters*, vol. 114, no. 5, p. 055 301, 2015.

[395] M. R. Andrews, D. M. Kurn, H.-J. Miesner, *et al.*, "Propagation of sound in a Bose-Einstein condensate," *Physical Review Letters*, vol. 79, no. 4, pp. 553–556, 1997.

[396] C. Raman, M. Köhl, R. Onofrio, *et al.*, "Evidence for a critical velocity in a Bose-Einstein condensed gas," *Physical Review Letters*, vol. 83, no. 13, p. 2502, 1999.

[397] W. H. Zurek, "Cosmological experiments in superfluid helium?" *Nature*, vol. 317, no. 6037, pp. 505–508, 1985.

[398] P. C. Hohenberg and B. I. Halperin, "Theory of dynamic critical phenomena," *Reviews of Modern Physics*, vol. 49, no. 3, pp. 435–479, 1977.

[399] J. Beugnon and N. Navon, "Exploring the Kibble–Zurek mechanism with homogeneous Bose gases," *Journal of Physics B: Atomic, Molecular and Optical Physics*, vol. 50, no. 2, p. 022 002, 2017.

[400] T. Bland, E. Poli, C. Politi, *et al.*, "Two-dimensional supersolid formation in dipolar condensates," *Physical Review Letters*, vol. 128, no. 19, p. 195 302, 2022.

[401] C. Ravensbergen, E. Soave, V. Corre, *et al.*, "Resonantly interacting Fermi-Fermi mixture of ^{161}Dy and ^{40}K," *Physical Review Letters*, vol. 124, no. 20, p. 203 402, 2020.

[402] H. Fröhlich, H. Pelzer, and S. Zienau, "XX. Properties of slow electrons in polar materials," *The London, Edinburgh, and Dublin Philosophical Magazine and Journal of Science*, vol. 41, no. 314, pp. 221–242, 1950.

[403] A. G. Volosniev, G. Bighin, L. Santos, and L. A. Peña Ardila, "Non-equilibrium dynamics of dipolar polarons," *SciPost Physics*, vol. 15, no. 6, p. 232, 2023.

[404] H.-P. Breuer and F. Petruccione, *The theory of open quantum systems*. Oxford University Press, 2002.

[405] B. Bylicka, D. Chruściński, and S. Maniscalco, "Non-Markovianity and reservoir memory of quantum channels: A quantum information theory perspective," *Scientific reports*, vol. 4, no. 1, p. 5720, 2014.

[406] H. Shen, S. Xu, S. Yi, and X. Yi, "Controllable dissipation of a qubit coupled to an engineering reservoir," *Physical Review A*, vol. 98, no. 6, p. 062 106, 2018.

[407] J.-B. Yuan, H.-J. Xing, L.-M. Kuang, and S. Yi, "Quantum non-Markovian reservoirs of atomic condensates engineered via dipolar interactions," *Physical Review A*, vol. 95, no. 3, p. 033 610, 2017.

[408] W. C. Swope, H. C. Andersen, P. H. Berens, and K. R. Wilson, "A computer simulation method for the calculation of equilibrium constants for the formation of physical clusters of molecules: Application to small water clusters," *The Journal of chemical physics*, vol. 76, no. 1, pp. 637–649, 1982.

[409] M. Yamashita, M. Koashi, and N. Imoto, "Quantum kinetic theory for evaporative cooling of trapped atoms: Growth of Bose-Einstein condensate," *Physical Review A*, vol. 59, no. 3, pp. 2243–2249, 1999.

[410] K. Berg-Sørensen, "Kinetics for evaporative cooling of a trapped gas," *Physical Review A*, vol. 55, no. 2, pp. 1281–1287, 1997.